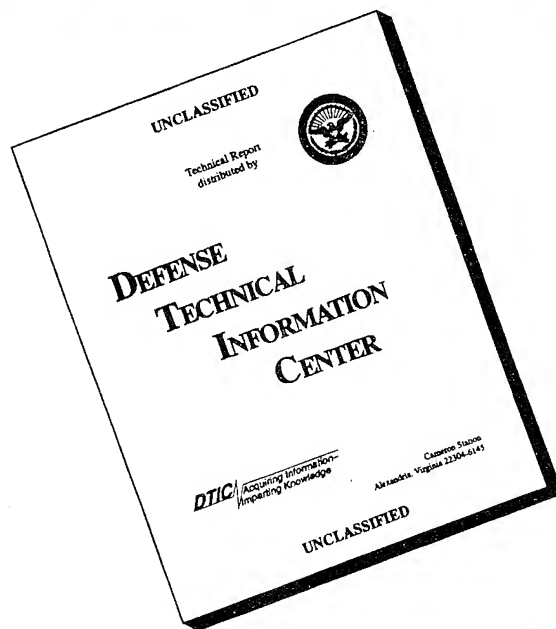


REPORT DOCUMENTATION PAGE			Form Approved OMB NO. 0704-0188	
<small>Public reporting burden for this collection of information is estimated to average 1 hour per response, including the time for reviewing instructions, searching existing data sources, gathering and maintaining the data needed, and completing and reviewing the collection of information. Send comment regarding this burden estimate or any other aspect of this collection of information, including suggestions for reducing this burden, to Washington Headquarters Services, Directorate for Information Operations and Reports, 1215 Jefferson Davis Highway, Suite 1204, Arlington, VA 22202-4302, and to the Office of Management and Budget, Paperwork Reduction Project (0704-0188), Washington, DC 20503.</small>				
1. AGENCY USE ONLY (Leave blank)		2. REPORT DATE		3. REPORT TYPE AND DATES COVERED
				Final 20 Sep 94-29 Sep 95
4. TITLE AND SUBTITLE			5. FUNDING NUMBERS	
Second International Workshop on Ram Accelerators				
6. AUTHOR(S)			DAAH04-94-G-0428	
Adam Bruckner (principal investigator)				
7. PERFORMING ORGANIZATION NAME(S) AND ADDRESS(ES)			8. PERFORMING ORGANIZATION REPORT NUMBER	
University of Washington Seattle, WA 98105				
9. SPONSORING / MONITORING AGENCY NAME(S) AND ADDRESS(ES)			10. SPONSORING / MONITORING AGENCY REPORT NUMBER	
U.S. Army Research Office P.O. Box 12211 Research Triangle Park, NC 27709-2211			ARO 33973.1-EG-CF	
11. SUPPLEMENTARY NOTES				
The views, opinions and/or findings contained in this report are those of the author(s) and should not be construed as an official Department of the Army position, policy or decision, unless so designated by other documentation.				
12a. DISTRIBUTION / AVAILABILITY STATEMENT			12 b. DISTRIBUTION CODE	
Approved for public release; distribution unlimited.				
13. ABSTRACT (Maximum 200 words)				
<p>RAMAC II is the second in a series of workshops on the topic of the ram accelerator, a hypervelocity projectile launcher concept based on ramjet-in-tube principles. The first RAMAC workshop was held in September 1993 at ISL, the French-German Research Institute in Saint-Louis, France, and its success prompted the organization of regular biennial meetings among researchers in this field.</p>				
19960522 098				
14. SUBJECT TERMS			15. NUMBER OF PAGES	
			16. PRICE CODE	
17. SECURITY CLASSIFICATION OF REPORT	18. SECURITY CLASSIFICATION OF THIS PAGE	19. SECURITY CLASSIFICATION OF ABSTRACT	20. LIMITATION OF ABSTRACT	
UNCLASSIFIED	UNCLASSIFIED	UNCLASSIFIED	UL	

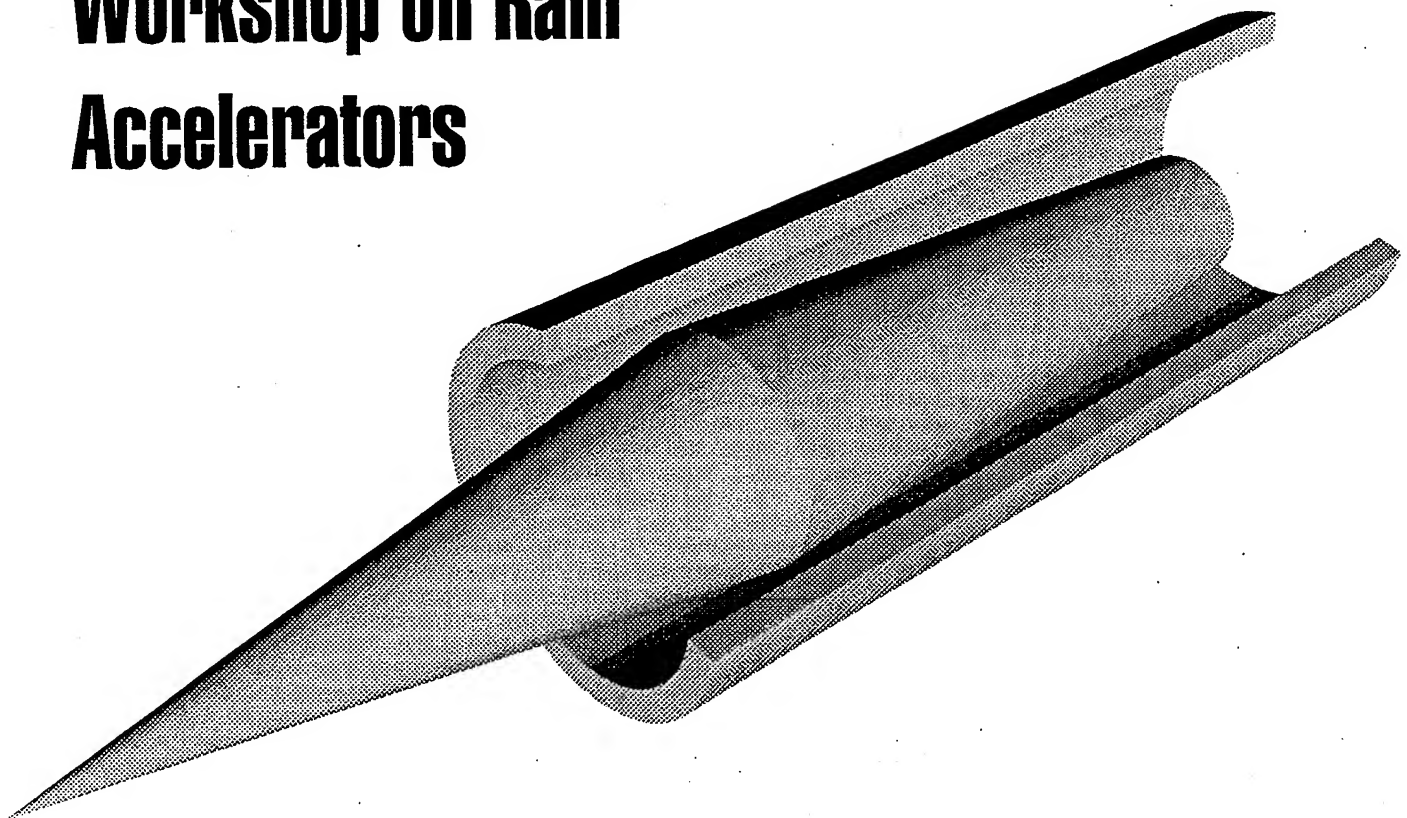
DISCLAIMER NOTICE



THIS DOCUMENT IS BEST QUALITY AVAILABLE. THE COPY FURNISHED TO DTIC CONTAINED A SIGNIFICANT NUMBER OF PAGES WHICH DO NOT REPRODUCE LEGIBLY.

RAMAC II

Second International Workshop on Ram Accelerators



**University of Washington
Seattle, WA USA
July 17-20, 1995**



PREFACE

RAMAC II is the second in a series of workshops on the topic of the ram accelerator, a hypervelocity projectile launcher concept based on ramjet-in-tube principles. The first RAMAC workshop was held in September 1993 at ISL, the French-German Research Institute in Saint-Louis, France, and its success prompted the organization of regular biennial meetings among researchers in this field. The selection of the University of Washington as the venue for the present workshop is significant in that it is the site of the first operational ram accelerator in the world. Research on this technology has come a long way since the first, pioneering experimental efforts began here in 1985. The widely varied applications and the unique phenomena generated by the ram accelerator soon stimulated the interest of researchers around the world. ISL and the U.S. Army Ballistic Research Laboratory (now the Army Research Laboratory) at Aberdeen, MD, established ram accelerator facilities in 1991. Other organizations followed suit, particularly in Japan. At least half a dozen facilities are expected to be operational this summer. Theoretical and computational studies have accompanied these experimental efforts. The broad range of expertise that investigators have brought to ram accelerator research during the past decade has contributed many new insights on the operating characteristics of this device.

The distinctive reacting flow phenomena that have been observed in the ram accelerator are relevant to the aerothermodynamic processes of proposed airbreathing hypersonic propulsion systems, while the inherent scalability of the device offers unique opportunities for its use in a variety of applications, such as high kinetic energy impact studies, tactical and long range defense, hypersonic propulsion research, ballistic range development, and direct launch to orbit.

RAMAC II provides a forum for the exchange of the latest ideas and developments in this rapidly advancing field. The Workshop sessions and the corresponding papers in this volume of Proceedings are organized around the following topics:

- | | |
|------------------------------|-------------------------------|
| 1) Facilities | 5) Theoretical considerations |
| 2) Experiments | 6) Computational modeling |
| 3) Detonation phenomena | 7) Heat transfer |
| 4) Shock and expansion tubes | 8) Unique concepts |

Participants at the Workshop include researchers from all the existing and planned ram accelerator facilities and related experimental installations around the world. Theoretical and computational research programs are also represented, as are potential uses of this emerging technology. A total of 32 papers are included in this volume of Proceedings. Due to the up-to-date, ongoing nature of much of the research presented here, many of the papers consist of extended abstracts and copies of the presentation materials, rather than of full treatises. These works are expected to be published in the near future in various archival journals or as papers at professional society conferences.

Adam P. Bruckner, Chair
Carl Knowlen, Co-Chair

ACKNOWLEDGEMENTS

Support for RAMAC II, the Second International Workshop on Ram Accelerators is provided in part by the U.S. Army Research Office, under grant No. DAAH04-94-G-0428. David Mann is the grant monitor. We are indebted to him for his support, encouragement, and helpful suggestions.

Many thanks are due to William Rogers and Stephanie Strom, of the University of Washington's Engineering Professional Programs, for the tireless administrative support that has been so instrumental in making this Workshop possible. We are also deeply indebted to graduate students Andrew Higgins, Gilbert Chew, Tom Imrich, and Josh Elvander, and to the staff of the Aerospace and Energetics Research Program, Nancy Mattick, Barbara Foster, and Steve Desjardins, for their invaluable contributions to the organization of the Workshop. The assistance of Visiting Scholars Akihiro Sasoh of the Institute of Fluid Science at Tohoku University in Sendai, Japan, and Pascal Bauer of ENSMA in Poitiers and the University of Paris, France, is greatly appreciated. We are also grateful to David Kruczynski and Michael Nusca of the U.S. Army Research Laboratory for their helpful suggestions and moral support. In addition, the interest and cooperation of Walter Christiansen, Chair of the Department of Aeronautics and Astronautics, and J. Ray Bowen, Dean of the College of Engineering, are appreciated. Finally, we would like to extend our sincerest thanks to Abraham Hertzberg for his continued support, encouragement, and wisdom, and for the innovative ideas and perseverance that initiated the field of study that has brought all of us together here. RAMAC II is dedicated to him.

TABLE OF CONTENTS

Session 1: FACILITIES

1. **The Rail Tube in Ram Acceleration: Feasibility Study with ISL's RAMAC 30**
F. Seiler, G. Patz, G. Smeets, J. Srulijes (ISL, France)
2. **Status of ISL's RAMAC 30 with Fin Guided Projectiles Accelerated in a Smooth Bore**
G. Patz, F. Seiler, G. Smeets, J. Srulijes (ISL, France)
3. **RAMAC 25 at the Shock Wave Research Center**
K. Takayama, A. Sasoh (IFS, Tohoku Univ., Japan)
4. **Preliminary Tests of a Rectangular Bore Ram Accelerator**
X. Chang, Y. Shimomura, S. Taki (Hiroshima Univ., Japan)
5. **A Feedback Controlled Gas Mixing System for the Ram Accelerator**
M.R. Jardin, A.P. Bruckner (Univ. of Washington, USA)

Session 2: EXPERIMENTS

6. **RAMAC in 90 mm Caliber or RAMAC 90: Starting Process, Control of the Ignition Location and Performance in the Thermally Choked Propulsion Mode**
M. Giraud, J.F. Legendre, G. Simon, M. Henner, D. Voisin (ISL, France)
7. **Experiments in a 120 mm Multi-Stage Ram Accelerator**
D.L. Kruczynski (ARL, USA)
8. **The Impact of Projectile Geometry on Ram Accelerator Performance**
T. Imrich, J. Elvander, A.P. Bruckner (Univ. of Washington, USA)

Session 3: DETONATION PHENOMENA

9. **90L35 Detonation Tube Experiments: Influence of Diluent Nature on the Detonation Characteristics of Dense Methane-Based Gaseous Explosive Mixtures**
J.F. Legendre, M. Giraud, D. Voisin (ISL, France), P. Bauer (ENSMA, France)
10. **Regular and Mach Reflection of Shock Waves as Detonation Waves**
J. Sterling, K. Ghorbanian (APRI, USA)
11. **Initiation of Detonation by Hypervelocity Projectiles**
A.J. Higgins (Univ. of Washington, USA)

Session 4: SHOCK AND EXPANSION TUBES

12. **Shock Tube Experiments for Modeling Ram-Accelerator-Related Phenomena**
J. Srulijes, A. Eichhorn, G. Smeets, F. Seiler, (ISL, France), M.J. Nusca (ARL, USA)
13. **Expansion Tube Investigation of Combustion Structures in Supersonic Projectile Flowfields**
C. Morris, M. Kamel, M. Thurber, S. Wehe, R.K. Hanson (Stanford Univ., USA)
14. **Computational Study of Flow Establishment in Hypersonic Pulse Facilities**
S. Yungster, K. Radakrishnan (ICOMP, NASA Lewis Rsch. Ctr., USA)
15. **Numerical Study of Some Ignition Regimes of Combustible Supersonic Flows over a Wedge**
L.F. da Silva, B. Deshaies (CNRS-ENSMA, France)

Session 5: THEORETICAL CONSIDERATIONS

16. **Aerothermodynamic Limits of Ram Accelerator Operation**
C. Knowlen (Univ. of Washington, USA)
17. **Real Gas Effects on the Operating Envelope of the Ram Accelerator**
P. Bauer (ENSMA, France), C. Knowlen (Univ. of Washington, USA)
18. **The Effects of Real Material Behavior on Ram Accelerator Performance**
F. Liberatore (ARL, USA)
19. **Theoretical Model for Calculating the Projectile Acceleration in a Ram Accelerator**
F. Gatau, G. Smeets, J. Srulijes (ISL, France)

Session 6: COMPUTATIONAL MODELING

20. **Reacting Flow Simulation of Transient, Multi-Stage Ram Accelerator Operation and Design Studies**
M.J. Nusca (ARL, USA)
21. **An Experimental and Numerical Investigation of the Three-Dimensional Flow Field About a Ram Accelerator Projectile**
J.B. Hinkey (Adroit Systems, Inc., USA)
22. **Pressure Distributions on Ram Accelerator Projectiles**
C. Li, K. Kailasanath, E.S. Oran, J.P. Boris (NRL, USA)

23. Fundamental Studies of Hypersonic Combustion Waves for Ram Accelerators

T. Endo, J.E. Leblanc, J. Kasahara, T. Fujiwara (Nagoya Univ., Japan)

24. Modeling of Unstarts in Ram Accelerator

M.J. Lefebvre (Royal Military Academy, Belgium)

Session 7: HEAT TRANSFER

25. Boundary Layer Model for Calculating the Heat Transfer into a Ram Projectile Fired in a Ram Accelerator

F. Seiler, G. Mathieu (ISL, France)

26. Thermal Stress Due to Aerodynamic Heating of Projectiles During Acceleration in a Ram Accelerator Tube

K.W. Naumann (ISL, France)

27. Computational Study of Projectile Nose Heating in a Ram Accelerator

G. Chew, A.P. Bruckner (Univ. of Washington, USA)

Session 8: UNIQUE CONCEPTS

28. Ram Accelerator Operation with Hollow Projectiles

A. Sasoh (Tohoku Univ., Japan), C. Knowlen, A.J. Higgins, A.P. Bruckner (Univ. of Washington, USA)

29. Recent Developments in the Research on the External Propulsion Accelerator

J. Rom (IIT-Technion, Israel), M. Nusca, D. Kruczynski (ARL, USA), M. Lewis, A.K. Gupta, J. Sabeen (Univ. of Maryland, USA)

30. Feasibility Study of Jet Interaction for Ignition in Chemical Accelerators

J. Brandeis, O. Oettinger (Rafael, Israel)

31. Theoretical Modeling of Detonation Pulse Engine with Application to Ram Accelerator

V.P. Korobeinikov (ICAD, RAS, Russia), S. Wojcicki (Washington State Univ., USA)

32. Ballistic System for Antiasteroid Defense

P.V. Kryukov (Ballistic Technologies [TsNIIMASH], Russia)

Session 1

FACILITIES

THE RAIL TUBE IN RAM ACCELERATION: FEASIBILITY STUDY WITH ISL'S RAMAC 30

F. Seiler, G. Patz, G. Smeets, J. Srulijes

French-German Research Institute of Saint-Louis (ISL)
F 68301 Saint-Louis, France

ABSTRACT

The new concept of accelerating a projectile flying in a tube at supersonic speed by self-synchronized ignition of an explosive gas mixture, the ram accelerator, has generated considerable interest over the last years in different countries: mainly United States, Israel, Japan, France and others. In France ISL has performed experiments in a 30-mm-caliber ram accelerator, called RAMAC 30, at superdetonative flight speeds. The results obtained with this so-called **Scram Accelerator** are described herein using a ram-tube with rails for guiding smooth cylindrical ram-projectiles and present three novel features:

- (1) Scram acceleration was achieved in a single stage tube with a projectile flying in the superdetonative regime from the beginning on. The projectiles have been injected into the ram tube with a conventional gun as pre-accelerator.
- (2) In a rail tube cylindrical projectiles with conical front and back parts were accelerated. In this case, pre-acceleration in a gun without sabot is possible.
- (3) Acceleration could be achieved with hydrogen, methane and ethylen based combustible gas mixtures with a stoichiometric fuel/oxidizer ratio.

INTRODUCTION

The ram accelerator concept was developed and tested successfully in a 38-mm-device by HERZTBERG, BRUCKNER & BOGDANOFF [1] at the University of Washington, Seattle, USA, in 1986. In 1988, based on the need of ISL for hypersonic launching facilities, the decision was taken to build two ram accelerators: a 30-mm-tube, called RAMAC 30, and a 90-mm-one, RAMAC 90 [10]. The RAMAC 90 is designed with the aim to accelerate masses of several kilograms to velocities of up to 3 km/s. The RAMAC 30 facility is used for basic research, mainly in the superdetonative flight regime, with the objective of investigating the ignition and combustion phenomena with regard to the gas mixtures to be used as well as the projectile design.

SMEETS [2] published in 1988 a new concept for a ram accelerator with guiding tube rails for firing rail stabilized projectiles to replace the fin stabilized projectiles originally used at the University of Washington which are accelerated in a cylindrical bore [3-6]. The rail tube idea has some advantages, e. g., no sabot necessary as required for fin guided projectiles, simple projectile geometry, and possibility of varying the inner tube geometry. Therefore it was decided to test the rail tube principle in the RAMAC 30 with rail guided projectiles. These experiments started in November 1992 and continued until August 1994.

In the ram accelerator at the University of Washington the process always starts with subsonic combustion behind the projectile flying initially at subdetonative speeds. For higher velocities, it passes the transdetonative mode and finally switches into the superdetonative combustion mode where combustion occurs in the supersonic flow in the slit between the projectile and the tube wall. To bypass the gasdynamic problems of subdetonative ignition, the direct firing into the superdetonative combustion mode is investigated in the RAMAC 30 used as a scram accelerator.

PRINCIPLE OF SCRAM ACCELERATION

Fig. 1 explains the principle of the scram accelerator process. A vehicle consisting of a cylindrical centerbody with conical portions at its front and rear ends propagates through a combustible gas mixture filled in a cylindrical tube having a diameter greater than that of the centerbody. By mean of fins [1] or rails [2] which are not shown in the figure, the projectile is guided in a centered position inside of the tube. The ram-tube containing the combustible gas mixture is closed at both ends by diaphragms which are destroyed by the moving projectile.

The flow field around the projectile flying at supersonic and superdetonative speed largely corresponds to that of a scramjet motor. On its conical front part, an attached bow shock is formed in the high Mach number upstream flow. That shock undergoes one or more reflections between the wall of the tube and the cylindrical part of the projectile thus creating a series of oblique shocks. By this, the flow is compressed nearly isentropically in the same way as within an inlet of a scramjet engine. The combustible mixture is expected to ignite and combust in the circular section between the cylindrical body and the tube: the combustor. There are still debates whether ignition occurs in an oblique detonation wave or is initiated by hot spots in the stagnation regions formed in the edge between the rails and the projectile surface. The combustion generated high gas pressure produces thrust on the conical back part of the projectile corresponding to the thrust acting on the nozzle of a scramjet engine.

RAIL TUBE CONCEPT

RAMAC 30 set-up

The RAMAC 30 design follows in principle the prototype ram accelerator of HERTZBERG et al. [1] in which fin stabilized bodies are accelerated by combustion in a circular ram tube. The first RAMAC 30 design, however, was chosen for testing the alternative concept of a ram tube with inner rails in combination with cylindrical and finless projectiles. The circular projectile of Fig. 2 has no fins and is guided in a tube with four inner rails, see SEILER et al. [7]. The front cone angle is for the actual projectile 14-16 degrees and the back angle is similar. The combustor zone of constant diameter has a length of 45-60 mm and the projectile mass is 125-135g. The tube cross-section is given in Fig. 3. The total area A_{total} of the cross section of the rail tube is 1241 mm² and the 30 mm caliber projectile cross-section $A_{\text{projectile}}$ is 707 mm².

The whole facility concept is shown in Fig. 4, a) schematic set-up, and b) photography of the whole facility, with a powder gun as pre-accelerator at the right hand side, two dump tanks, and the rail ram tube in between, see Fig. 4c. At the end of the ram accelerator, the projectiles are hitting a set of replaceable steel plates inside of a piston which moves backwards inside of the catcher tube after the impact (Fig. 4d).

In the first experiments we only used one ram-section of 3.6 meters length. In the conventional powder gun having 1.8 meters tube length, aluminium models partially with an inner magnesium core of masses of about 130 g are accelerated to a muzzle velocity of about 1800 m/s being the initial velocity at the entrance of the ram-section. This allows to start in the superdetonative ram accelerator mode, with combustion at the cylindrical part of the projectile as is shown in Fig. 1.

Rail tube experiments

A major challenge for achieving successful scram accelerator experiments to superdetonative speeds is that the test models have to withstand the stresses within both, the launcher and the scram accelerator tube. The light weight models of magnesium, used at the beginning of the experiments, could be accelerated in the existing powder gun to superdetonative speeds without deformation and destruction, but violent reactions occurred in the scram tube between the magnesium and the oxygen as well as the carbondioxide. Fig. 10a shows the x-ray picture of shot no. 34 and Fig. 10b that of no. 36 gathered with magnesium projectiles of about 135 grams in the highly diluted $C_2H_4 + 3O_2 + 26 CO_2$ gas mixture with a velocity gain of 50 m/s along 3.6 m. In both cases the body diameter of originally 30 mm is reduced by ablation and for no. 36 the nose cone is maybe damaged by canting. Firing with less diluent cause more ablation effects followed by an unstart. In that case no x-ray pictures are available due to pre-trigger by the detonation wave in front of the projectile. Fig. 10c contains the original magnesium projectile at rest. Projectiles made of heavier metals like steel were too heavy for reaching the intended muzzle velocities, or projectiles with a thin outer steel envelope were too fragile for surviving the whole firing cycle on the one hand in the gun and on the other hand in the ram-tube without damage. Most of the early experiments failed because of these difficulties. The first experiments leading to positive results were made with aluminum projectiles with an inner magnesium core and a reactive gas mixture based on a stoichiometric hydrogen, oxygen mixture and carbondioxide as the diluent having rather low Chapman-Jouguet detonation velocities.

Fig. 5 shows a set of typical signals received with the electromagnetic sensors and the wall pressure gauges for three measuring locations M16, M18 and M19 of experiment no. 115 along the tube. The electromagnetic signals are received by the interaction of the magnet inside of the moving projectile with a coil sensor placed in the tube wall. The pressure signals are directly correlated in time to the position of the projectile. They show a very strong pressure increase by combustion. More than 1000 bars are acting on the outer surface of the projectile causing a strong mechanical stress at the projectile material. Additionally, the high combustion gas temperature of up to 2500 K leads to a high heat flux into the projectile surface followed by an extraordinary thermal wall stress. Melting processes may occur and also chemical reactions with the oxygen are present, especially when magnesium is used. In case of aluminum the chemical reaction is much smaller as with magnesium and the projectile can survive longer.

We investigated in the RAMAC 30 three different gas mixtures based on hydrogen H_2 , methane CH_4 and ethylene C_2H_4 , mainly with a stoichiometric ratio of fuel and oxidizer and carbondioxide CO_2 as diluent:

- | |
|---|
| (1) ethylen-oxygen-carbondioxide,
(2) methan-oxygen-carbondioxide,
(3) hydrogen-oxygen-carbondioxide. |
|---|

Best ignition and avoidance of unstart effects were obtained with the gas mixture of the following molar components: $2\text{H}_2 + \text{O}_2 + 3.8\text{CO}_2$ having a Chapman-Jouguet detonation velocity of approximately 1450 m/s. The velocity increase found experimentally in a 27 bars gas mixture was about 200 m/s (see Fig. 6, shot no. 97). More CO_2 -contents (shot no. 91 and 93) gives less heat release and consequently less projectile acceleration. A diminishing CO_2 -part increases the heat production by combustion followed by an unstart as shown for shot no. 99. The mean acceleration of 135000 m/s^2 is for firing no. 97 in good accordance with the straightforward gasdynamic estimates done by SMEETS et al. [8] and even exceeds slightly the calculated acceleration.

The results shown in Fig. 6 for hydrogen based mixtures and in Fig. 7 for hydrogen, methane and ethylene fuels were obtained by experiments performed during a period from April to June 1994. The velocities and the accelerations of the projectiles were determined using the signals from the electromagnetic sensors identifying the passage of the magnet to better than one microsecond.

The data describing the experiments and their results are assembled in Table 1: fill pressure p_1 , calculated detonation velocity of the mixture u_{det} , initial (ram-tube entrance) and final projectile velocities u_1 and u_2 , calculated Mach number [8] after supersonic combustion M_2 , accelerating flight distance dx , and projectile mass m . The experimental thrust coefficients TC , as deduced from measured accelerations are compared to predictions resulting from the simple calculations of SMEETS et al. [8]. The non-dimensional thrust coefficient TC is defined here as the ratio of the calculated thrust force F to the product of the propellant fill pressure p and the cross sectional area A of the cylindrical part of the projectile: $TC = F/pA$. For comparison, available experimental data in the superdetonative regime obtained by HERTZBERG et al. in 1989-1991 were also included in the table.

For better perspicuity, the theoretical and experimental thrust coefficients, TC , are plotted against each other in Fig. 8. The overall agreement except for the results of the two experiments Nr. 91 and Nr. 105 with very diluted mixtures is satisfactory and quite remarkable in view of the fact that the calculations [8] are based on an idealized concept of one-dimensional flow which can only very roughly describe the complicated three-dimensional flowfield around the projectile in the tube. It is also interesting to note that the results obtained at ISL with stoichiometric mixtures based on hydrogen, methane and ethylene are in good accordance with data received by HERTZBERG, BRUCKNER and KNOWLEN [3-6] with rather rich methane based mixtures.

Stability limitations

The experiments show that for a quasi stationary flight with acceleration in the superdetonative mode there exist stability limitations. One limit is set by thermal choking followed by an unstart which means that a detonation wave moves in front of the projectile. In this case the calculated Mach number downstream of the reaction is not well above unity.

To avoid thermal choking followed by an unstart, i. e., the flow Mach number after combustion is $M = 1$, the heat release must be adapted to the upstream flow conditions, that means to the flow Mach number M in front of the combustion. ZIEREP [9] shows for a one-dimensional flow, as present in the channel between projectile and wall, that the heat release q must be limited to avoid thermal choking. The formula given by ZIEREP [9] describing the maximal heat input is the following one:

$$\left(\frac{q}{c_p T} \right)_{\max} = \frac{(M^2 - 1)^2}{2(\chi + 1)M^2}$$

In this relation $\chi = c_p/c_v$, with c_p the specific heat at constant pressure and c_v that at constant volume. T is the gas temperature in front of combustion. Fig. 9 shows the distribution of the normalized heat release of the above mentioned equation as a function of the flow Mach number M before combustion. We see two regions: (1) a zone in which no stable combustion occurs and the flow is choked thermally and (2) a zone with stable combustion by limiting the heat input according to the given flow Mach number. This limit defines the maximum heat release and therefore the **lower contents** of the diluent in the combustible gas mixture. Four points are inserted representing the firings no. 91, 93, 97 and 99. Looking to Fig. 6 we see that for shot no. 99 we have a projectile deceleration caused by an unstart and that unstart is also predicted by ZIEREPS's theory [9] shown in Fig. 9. The other three shots are at the border (no. 97) and inside (no. 91 and 93) of the allowed region with no unstart, giving a projectile acceleration as shown in Fig. 6.

Another reason for a failure was found to be the decoupling of the combustion from the projectile in case of mixtures containing too much inert gas. In superdetonative flight, the flow field around the projectile stays in all parts supersonic. The combustion has to be continuously initiated at the side of the cylindrical part of the projectile as shown in Fig. 5. Any reaction, i.e., production of high gas pressure in the supersonic flow downstream of the projectile can produce no more effect on it as described by SEILER et al. [11]. The **upper dilution** limit with decoupling of combustion (or no combustion) will depend on both, the type of combustible gas as well as the inert component of the gas mixture.

CONCLUSION

The experiments performed in the RAMAC 30 at ISL constitute a significant breakthrough in superdetonative ram combustion. The following points can be highlighted:

- (1) Using a conventional gun as preaccelerator, a projectile can be injected into the ram tube flying in the superdetonative regime from the beginning on, showing that the ram accelerator does work in superdetonative mode as scram accelerator.
- (2) Cylindrical bodies with conical front and back parts can be accelerated in a rail tube. In this case, preacceleration in a gun without sabot was possible, and
- (3) there is no problem of an unstart with hydrogen, methane and ethylene based combustible gas mixtures in limiting the heat release.
- (4) Less melting and burning problems using aluminum projectiles.

REFERENCES

1. HERTZBERG, A., BRUCKNER, A. P., BOGDANOFF, D.W., The Ram Accelerator: A new Chemical Method of Achieving Ultra-High Velocities, 37th ARA-Meeting, Québec, Canada, 1986
2. SMEETS, G., Ram-Nachbeschleuniger für aus konventionellen Kanonen verschossene Vollkaliber-Projectile, ISL-Report N 603/88, 1988

3. HERTZBERG, A., Thermodynamics of the Ram Accelerator, 17th International Symposium on Shock Waves and Shock Tubes, Bethlehem, USA, 1989
4. KNOWLEN, C., BURNHAM, E.A., KULL, A. E., BRUCKNER, A. P., HERTZBERG, A., Ram Accelerator Performance in the Transdetonative Velocity Regime, 41st ARA-Meeting, San Diego, USA, 1990
5. HERTZBERG, A., BRUCKNER, A. P., KNOWLEN, C., Experimental Investigation of Ram Accelerator Propulsion Modes, 17th International Symposium on Shock Waves and Shock Tubes, Bethlehem, USA, 1989
6. BRUCKNER, A.P., BURNHAM, E.A., KNOWLEN, C., HERTZBERG, A., BOGDANOFF, D.W., Initiation of Combustion in the Thermally Choked Ram Accelerator, 18th International Symposium on Shock Waves, Sendai, Japan, 1991
7. SEILER, F., PATZ, G., SMEETS, G., SRULIJES, J., Status of ISL's RAMAC 30 with Rail Stabilized Projectiles, First International Workshop on Ram Accelerator, RAMAC I, ISL, France, 1993
8. SMEETS, G., GATAU, F., SRULIJES, J., Rechenprogramm für Abschätzungen zur Ram-Rohrbeschleunigung, ISL-Report RT 507/92, 1992
9. ZIEREP, J., Strömungen mit Energiezufuhr, G. Braun Verlag, Karlsruhe, Germany, 1990
10. GIRAUD, M., LEGENDRE, J.-F., SIMON, G., Ramac 90: Experimental Studies and Results in 60 mm Caliber, Length 108 Calibers, First International Workshop on Ram Accelerator, RAMAC I, ISL, France, 1993
11. SEILER, F., PATZ, G., SMEETS, G., SRULIJES, Gasdynamic limits of ignition and combustion of a gas mixture in ISL's RAMAC 30 Scram accelerator, 20th International Symposium on Shock Waves, California Institute of Technology, Pasadena, California, USA, July 1989

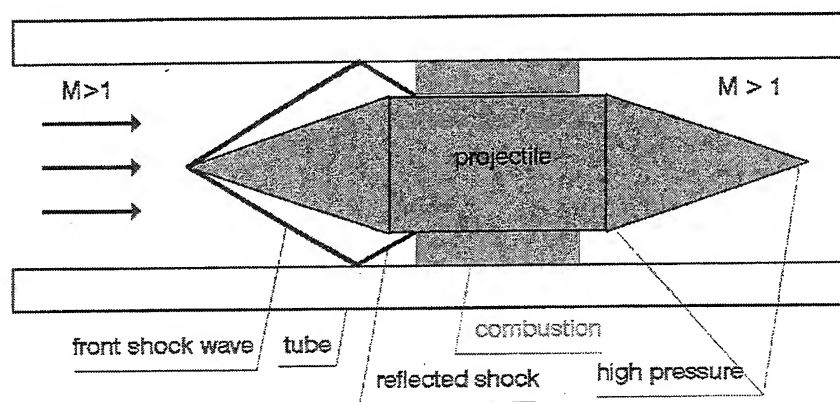


Fig. 1. Principle of the scram accelerator process

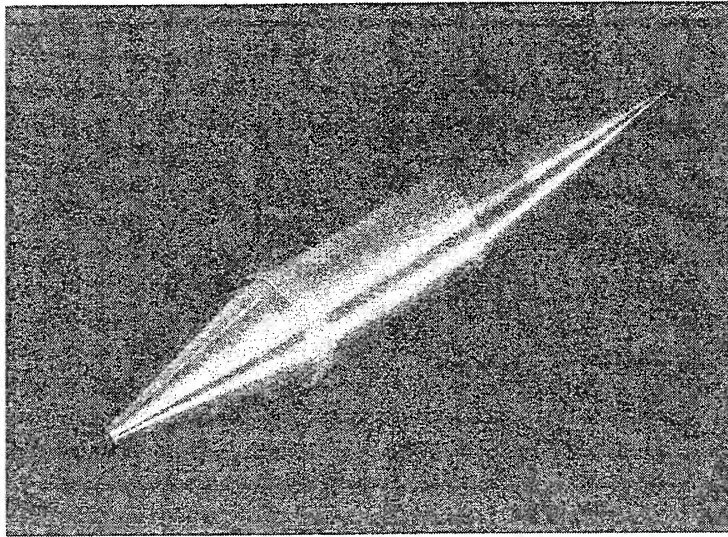


Fig. 2. Smooth cylindrical ram-projectile

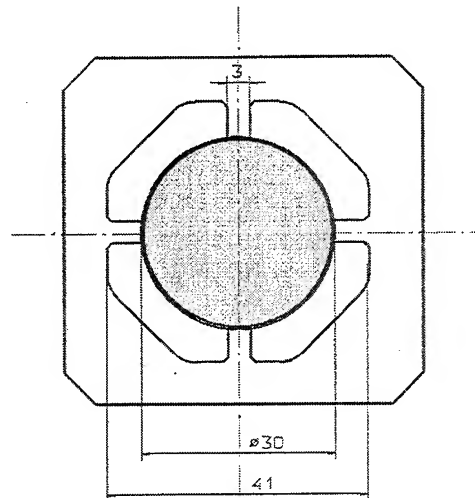


Fig. 3. Ram tube cross-section

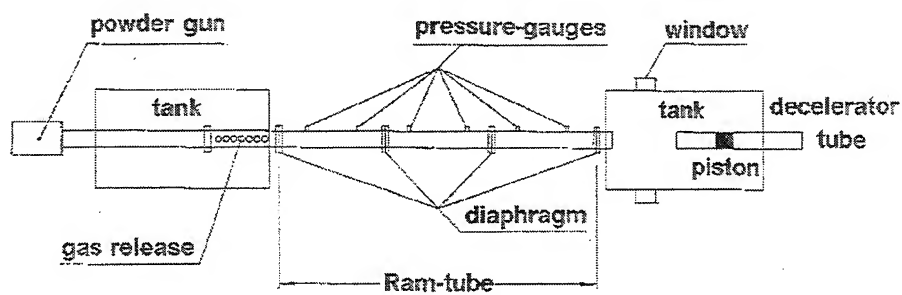


Fig. 4a. Set-up of ISL's ram accelerator

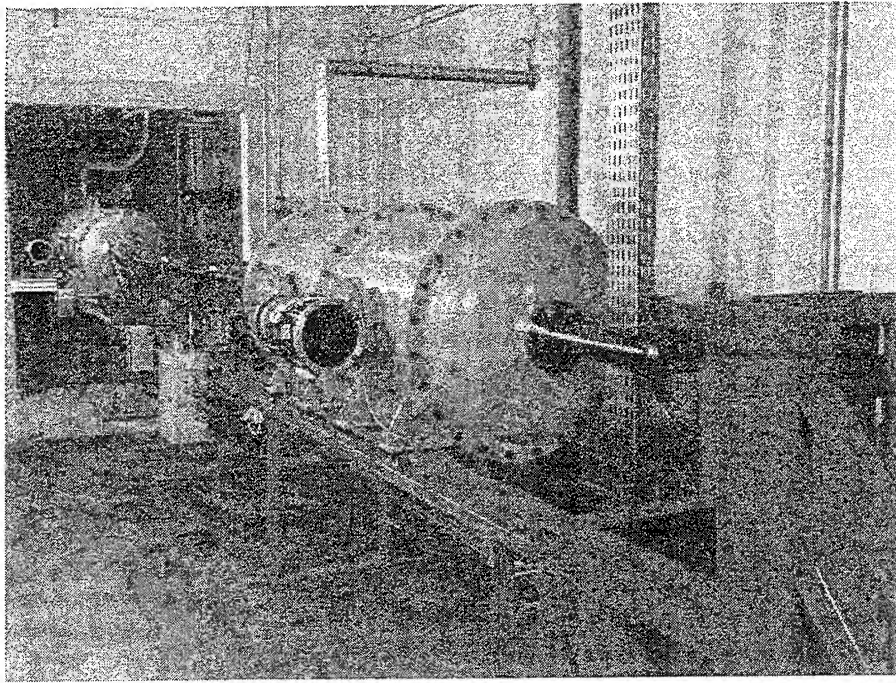


Fig. 4b. View of RAMAC 30 facility with gun, dump tanks and rail tube in between

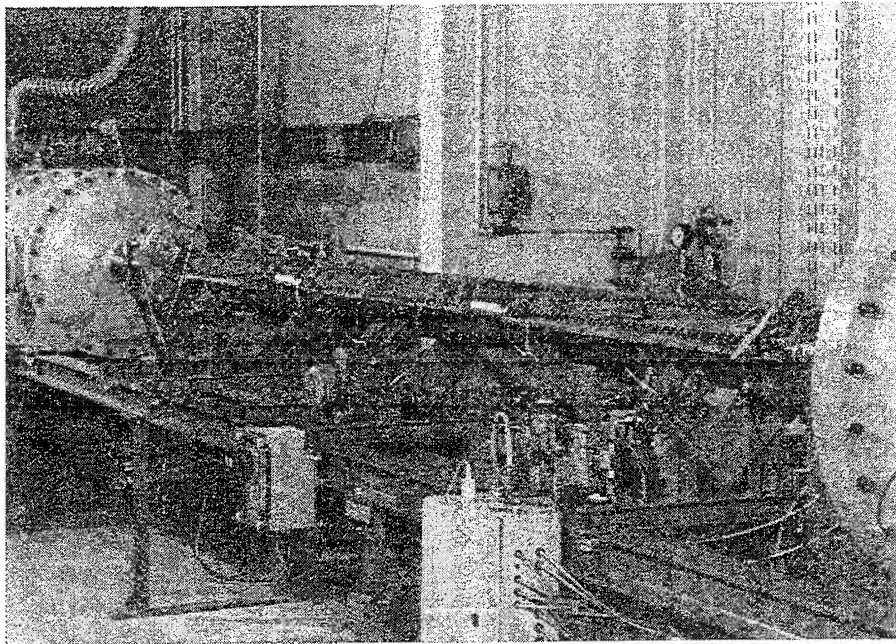


Fig. 4c. Rail tube between the dump tanks

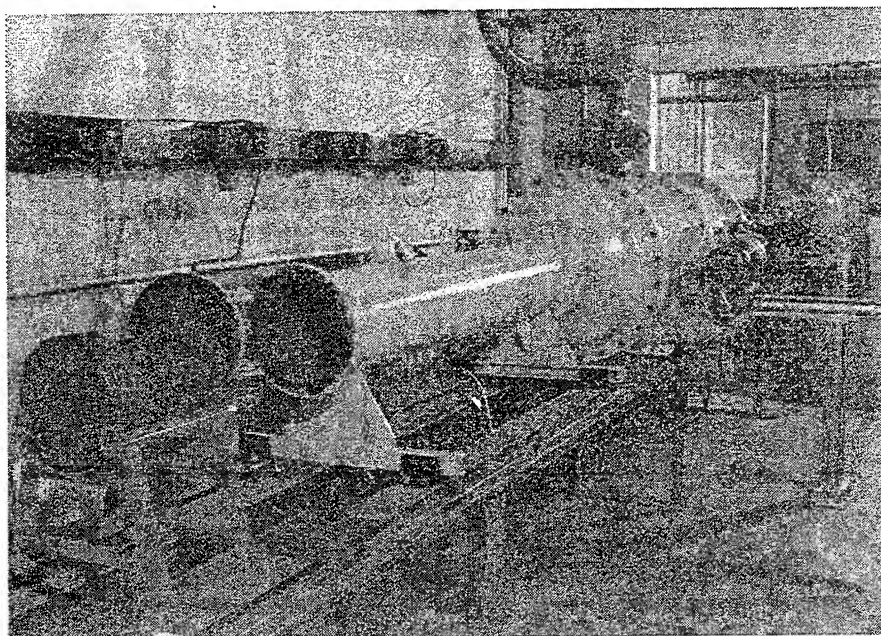


Fig. 4d. Decelerator tube with piston

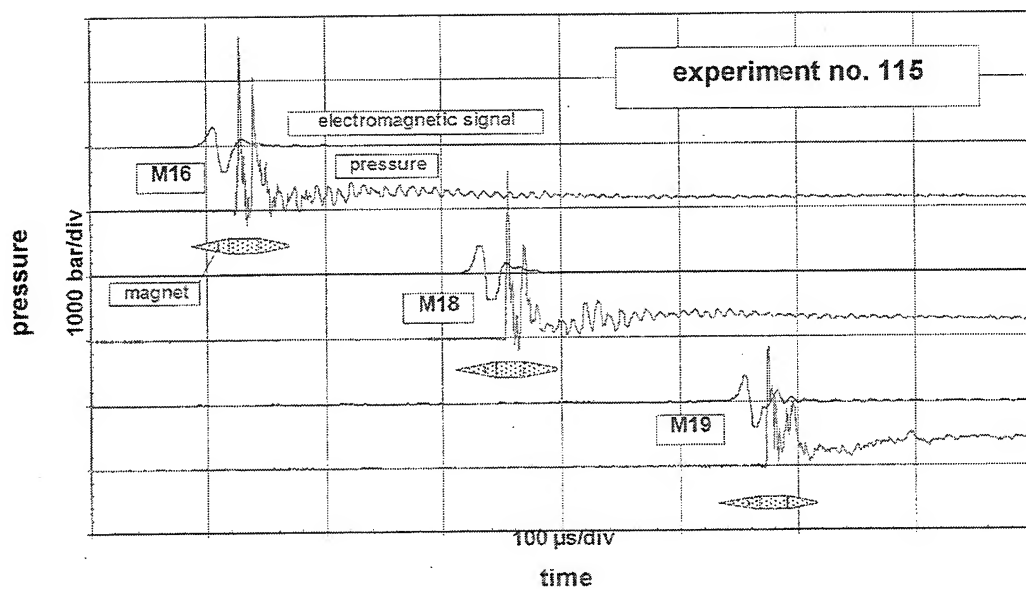


Fig. 5. Signals received with electromagnetic sensors and wall pressure gauges

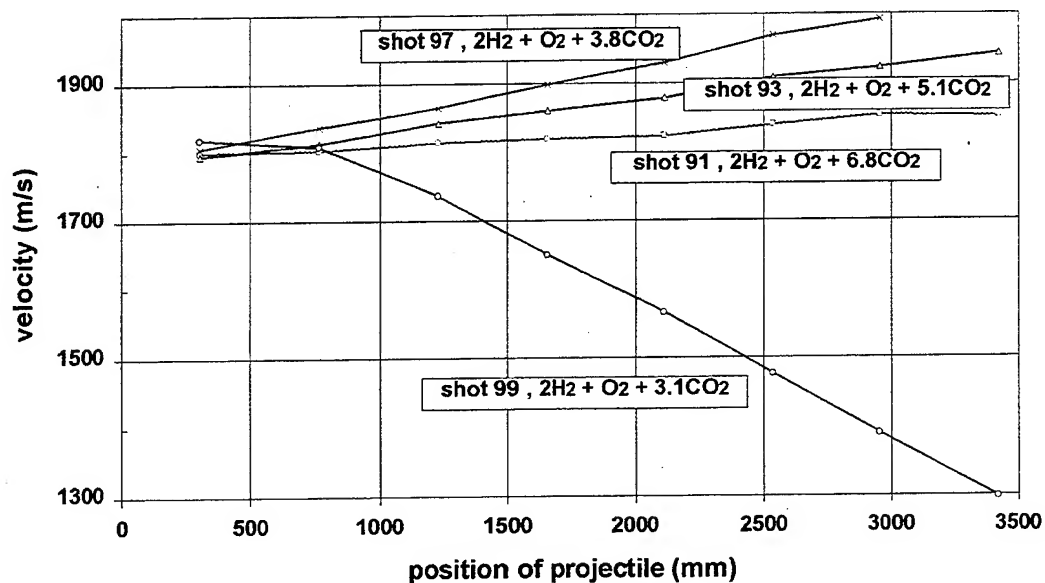


Fig. 6. Flight velocities obtained with hydrogen based mixtures in the rail tube ram accelerator

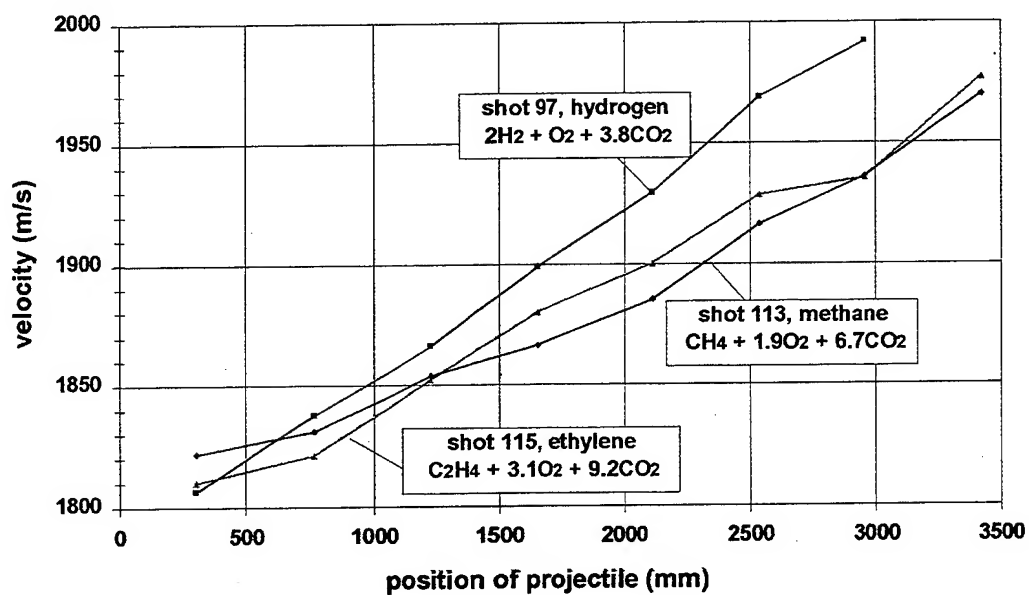


Fig. 7. Flight velocities with mixtures based on hydrogen, methane and ethylene in the rail tube

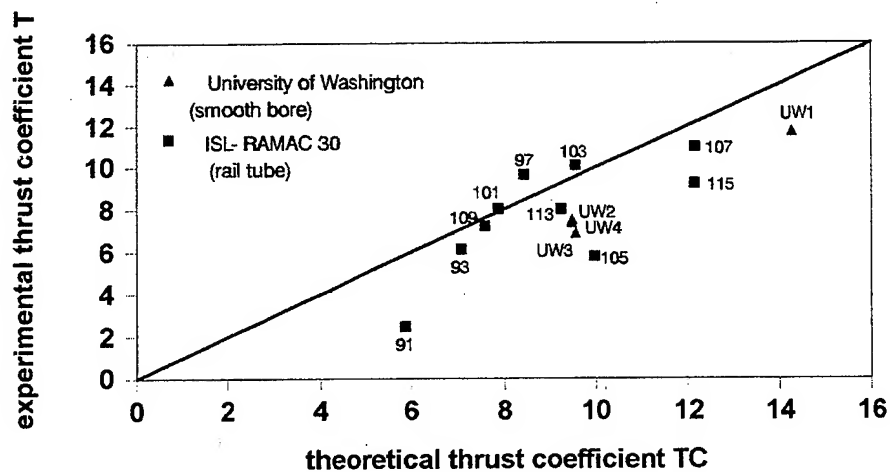


Fig. 8. Comparison of theoretical and experimental thrust coefficients

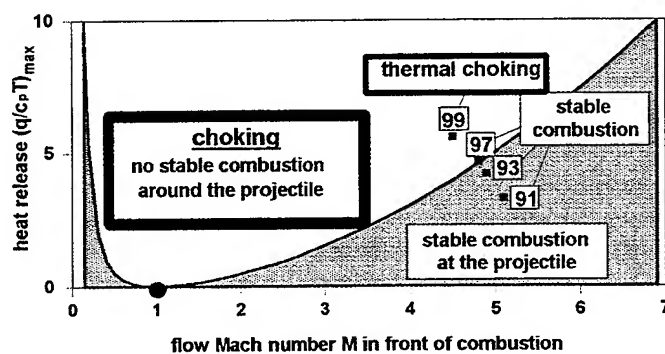


Fig. 9. Maximum heat release for stable combustion

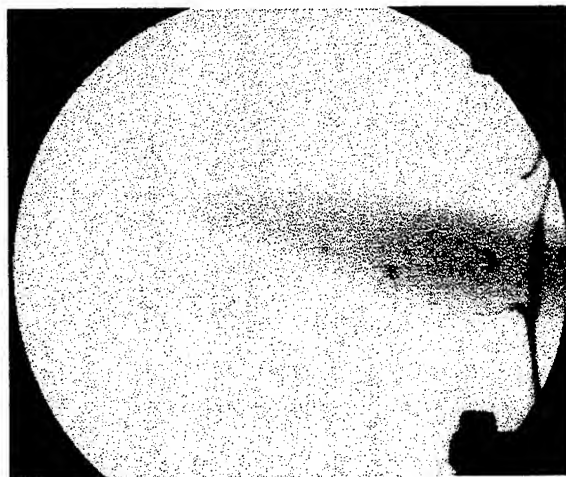


Fig. 10a. x-ray photograph of the magnesium projectile of shot no. 34

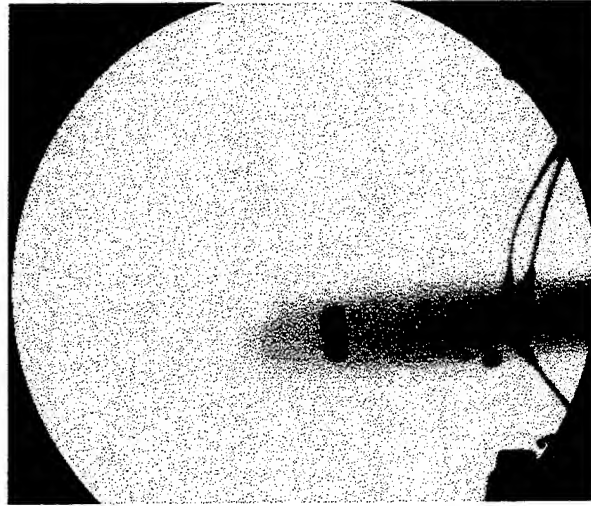


Fig. 10b. x-ray photography of the magnesium projectile of shot no. 36



Fig. 10c. x-ray photography of the magnesium projectile of Fig. 10a at rest

No.	Mixture	p_1/bar	$v_{\text{det}}/\text{m/s}$	$u_1/\text{m/s}$	$u_2/\text{m/s}$	Ma_2	dx/m	m/g	TC_{thoor}	TC_{exp}	Reference
UW1	$0.6\text{C}_2\text{H}_4+2\text{O}_2+3.3\text{CO}_2$	16.00	1627	2210	2465	2.11	3.38	70.00	14.26	11.76	Hertzberg 1989
UW2	$3.1\text{CH}_4+2\text{O}_2+6\text{Ar}$	18.00	1546	1735	1870	1.33	1.70	62.00	9.47	7.52	Knowlen 1990
UW3	$2.7\text{CH}_4+2\text{O}_2+5.8\text{N}_2$	22.00	1700	1835	1990	1.20	2.00	67.00	9.55	6.88	Knowlen 1990
UW4	$2.7\text{CH}_4+2\text{O}_2+5.8\text{N}_2$	22.00	1700	1800	2125	1.00	4.00	67.00	9.46	7.40	Hertzberg 1991
91	$2\text{H}_2+\text{O}_2+6.8\text{CO}_2$	27.00	1182	1800	1853	2.37	2.65	129.50	5.87	2.48	ISL-RAMAC 30
93	$2\text{H}_2+\text{O}_2+5.1\text{CO}_2$	26.80	1312	1796	1943	2.05	3.12	131.80	7.07	6.13	ISL-RAMAC 30
97	$2\text{H}_2+\text{O}_2+3.8\text{CO}_2$	26.80	1452	1806	1969	1.77	2.23	132.70	8.43	9.65	ISL-RAMAC 30
99	$2\text{H}_2+\text{O}_2+3.1\text{CO}_2$	26.30	1550	1820	1297	1.59	3.12	131.20	unstart!	unstart!	ISL-RAMAC 30
101	$2\text{H}_2+1.1\text{O}_2+4.3\text{CO}_2$	25.70	1393	1782	1892	1.85	1.81	131.30	7.87	8.05	ISL-RAMAC 30
103	$\text{CH}_4+2.2\text{O}_2+6.8\text{CO}_2$	23.20	1367	1818	1943	2.00	1.81	127.90	9.54	10.11	ISL-RAMAC 30
105	$\text{C}_2\text{H}_4+3.3\text{O}_2+11.1\text{CO}_2$	24.70	1360	1804	1917	2.00	2.65	127.50	9.97	5.79	ISL-RAMAC 30
107	$\text{C}_2\text{H}_4+2.8\text{O}_2+7.9\text{CO}_2$	24.70	1482	1824	1971	1.78	1.81	125.00	12.15	11.01	ISL-RAMAC 30
109	$2\text{H}_2+1.1\text{O}_2+4.5\text{CO}_2$	20.00	1371	1838	1954	1.99	2.65	123.20	7.59	7.22	ISL-RAMAC 30
113	$\text{CH}_4+1.9\text{O}_2+6.7\text{CO}_2$	20.00	1355	1822	1970	2.04	3.12	125.70	9.32	8.00	ISL-RAMAC 30
115	$\text{C}_2\text{H}_4+2.8\text{O}_2+7.9\text{CO}_2$	20.00	1480	1810	1977	1.76	3.12	128.70	12.14	9.23	ISL-RAMAC 30

Table 1. Summary of available ram shots data

STATUS OF ISL'S RAMAC 30 WITH FIN GUIDED PROJECTILES ACCELERATED IN A SMOOTH BORE

G. Patz, F. Seiler, G. Smeets, J. Srulijes

French-German Research Institute of Saint-Louis (ISL)
F-68301 Saint-Louis, France

ABSTRACT

The new concept of accelerating a projectile flying in a tube at supersonic speed by self-synchronized ignition of an explosive gas mixture filled inside of that tube which is closed at its ends by membranes, the ram accelerator, has generated considerable interest over the last years in different countries: especially in the United States, Israel, Japan, France and others. In France ISL has performed experiments in a 30-mm-caliber ram accelerator, called RAMAC 30, at superdetonative flight speeds. The results and difficulties found in the version with a smooth bore and fin guided projectiles are described herein and can be summarized as follows:

- (1) Scram acceleration was started and achieved in a single stage tube flying in the superdetonative regime from the beginning on, using a conventional gun as preaccelerator for injecting a projectile into the ram tube. Unfortunately, the thrust was very small and significant acceleration could not be obtained.
- (2) From the gasdynamic point of view the combustion was stabilized at the projectile body with hydrogen and methane based gas mixtures.
- (3) Damage of projectile material, especially of fins, by melting and burning when aluminum and titanium is used.

INTRODUCTION

The ram accelerator concept was developed and tested successfully in a 38-mm-device by HERZTBERG, BRUCKNER & BOGDANOFF [1] at the University of Washington, Seattle, USA, in 1986. In 1988, based on the need of ISL for hypersonic launching facilities, the decision was taken to build two ram accelerators: a 30-mm-tube, called RAMAC 30, and a 90-mm-one, RAMAC 90 [8]. The RAMAC 90 is designed to accelerate masses of several kilograms to velocities of up to 3 km/s. The RAMAC 30 facility is used for basic research, mainly in the superdetonative flight regime, with the objective of investigating the ignition and combustion behaviour of different gas mixtures, the influence of projectile geometry and new tube concepts, as published by SEILER et al. [2, 3].

In the ram accelerator at the University of Washington [4-7] the process always starts with subsonic combustion behind the projectile flying initially at speeds lower than the Chapman-

Jouguet detonation velocity of the combustible gas mixture. For higher velocities, it passes the transdetonative mode and finally switches into the superdetonative combustion mode where combustion occurs in the supersonic flow in the slit between the projectile and the tube wall. To bypass the gasdynamic problems of subdetonative ignition, the direct firing into the superdetonative combustion mode (scram accelerator) is investigated in the RAMAC 30. Two ram-tube versions have been tested meanwhile: (a) the rail tube ram accelerator and the „classical“ smooth bore ram-tube. The results gathered with a tube equipped with inner rails for projectile stabilization are described by SEILER et al. [3]. In this paper here the status of the smooth bore concept is discussed and the results obtained till now are presented.

PRINCIPLE

Fig. 1 explains the principle of the scram accelerator process. A vehicle consisting of a cylindrical centerbody with conical portions at its front and rear ends propagates through a combustible gas mixture filled in a cylindrical tube closed at both ends by diaphragms. The tube diameter is greater than that of the projectile centerbody. By means of fins [1] or rails [3] which are not shown in the figure, the projectile is centered inside of the tube.

The flow field around the projectile flying at supersonic and superdetonative speed largely corresponds to that of a scramjet engine. On its conical front part, an attached shock is formed in the high Mach number upstream flow. That shock undergoes several reflections between the wall of the tube and the cylindrical part of the projectile thus creating a series of oblique shocks. By this, the flow is compressed nearly isentropically in the same way as within an inlet of a scramjet engine. The combustible mixture is expected to ignite and combust in the circular section between the cylindrical body and the tube. There are still debates about whether ignition occurs in an oblique detonation wave or is initiated by hot spots in the stagnation regions in front of the positioning fins in the smooth bore version [1] or under the rails in the rail bore version [3]. The combustion generated heat release produces a high gas pressure which gives thrust on the conical back part of the projectile corresponding to the thrust acting on the nozzle of a scramjet.

SMOOTH BORE VERSION

RAMAC 30 facility set-up

After having shown the good application of the rail equipped accelerator tube concept for ram acceleration we are now investigating the conventional smooth bore technique of HERTZBERG et al. [1] with a projectile which is guided by fins fixed at the body of the projectile.

The projectile is injected into the ram tube as in the rail tube case [3] with about 1800 m/s to be superdetonative relative to the combustible gas mixture used. The projectile geometry is depicted in the photography of Fig. 2, showing the fins fixed at the body of the projectile with constant diameter and the conical front and back parts. In this case of fin guided projectile a sabot is necessary for pre-acceleration. Meanwhile we used the projectiles made of aluminum and titanium with four or five fins having a thickness of 2 - 2.5 mm. The front cone angle is 14 - 16 degrees and the back angle is similar. The combustor zone with constant diameter has a length of about 50 mm with a diameter of 20 mm. The projectile mass is 80 - 85 grams with aluminum and about 110 g with titanium and that of the sabot is about 32 grams.

The schematic set-up of the RAMAC 30 facility is depicted in Fig. 3 corresponding in principle to the facility used by SEILER et al. [3] for the rail tube concept. Concerning the 30-mm-caliber smooth ram-tube, we have at the moment in use two 3 m tubes attached to each other with a total length of 6 m, see Fig. 4a with the powder gun at the right hand side. In Fig. 4b the ram-tube is seen at left. In front of the ram-tube a sabot stripper tube (at right) is needed. It has a bigger outer tube diameter than the ram-tube. This stripper tube with 1.5 m length is filled with a heavy gas, e.g., CO₂. Fig. 4c shows the end section of the ram device with the decelerator tube in which a piston is placed with removable steel plates for projectile impact.

Experimental results

The results of shot no. 136 (aluminium) and 138 (titanium) are presented in Fig. 5. There the projectile velocity is shown in dependence of the position of the projectile inside the tube. For both firings, the velocity initially decrease in the sabot stripper tube and then increases, i.e., the combustion starts inside the combustor producing thrust on the back side of the projectile. But, due to the high combustion temperature the heat flux into the ram projectile is enormous maybe initiating melting processes and chemical reactions between the projectile material and the oxygen as well as the diluent CO₂ present in the combustible gas mixture. This chemical reaction produces an additional heat release for that the maximum heat input, see SEILER [3], is surpassed followed by an unstart which begins after a projectile travel of about 4 - 5 m. From x-ray photographs it can be seen that the projectile loose its fins and the combustor body diminishes from 20 mm diameter to about 16 - 18 mm as shown in Fig. 6a for shot no. 134 (projectile travel = 3 m) and Fig. 6b for no. 139 (projectile travel = 6 m). Fig. 6c shows the x-ray image of the projectile of shot no. 142 with maybe weak combustion in the mixture: $2\text{H}_2 + 0.4 \text{O}_2 + 8.2 \text{N}_2$. The fins are well visible in Fig. 6c which is not the case in Figs. 6a and 6b. If the projectile looses its fins canting occurs. In some cases the projectile body is nearly completely burned up during the firing cycle. This behaviour was present with projectiles of aluminum (shot no. 136). Projectiles made of titanium (shot no. 138) behave similar to shot no. 136.

In Fig. 7 a comparison is shown between a shot fired with an aluminum projectile (no. 136), an eloxadized aluminum projectile (no 139), an aluminum projectile with zirconium oxide plasma coating (no. 150) and aluminum with an aluminum oxide plasma coated layer (no. 151). Both coating thicknesses are in the range of about 200 μm . The protected aluminum projectiles survive longer in time than that with pure aluminum. Due to the protection at its outer surface these projectiles are not burned up totally on 6 m acceleration as seen from the impact into the steel plates. The aluminum projectile can survive only a flight of 3 - 4 m (see x-ray image in Fig. 6a). After 6 m flight the aluminum projectile nearly vanishes.

With aluminum projectiles plasma coated with zirconium oxide (ZrO₂) and aluminum oxide (Al₂O₃), the aluminum seems to be protected against the heat influence for about 4 - 5 m flight, but no velocity increase is detected. It seems that the thrust formed by combustion just balances the high-pressure flow drag and the mechanical friction forces of the fins at the tube wall. This outcome shows that the gathered acceleration is small due to the CO₂-dilution used and due to the inefficient geometry of the projectile's boat tail. The velocity increase Δu_p , calculated with the theoretical model of SMEETS et al. [9], is for shot no. 150 about 100 m/s along 6 m ram-tube, which seems to be just balanced by the forces discussed. In shot no. 144 no combustion occurred and the projectile velocity was slowed down, e.g., by $-\Delta u_p \approx 89 \text{ m/s}$ on 6 m tube flight, see Fig. 10.

This velocity rise by ram effect just compensate the flow drag and the tube friction acting on the projectile. If that hypothesis is true, the acceleration present with pure aluminum is caused by burning of the projectile body and its fins forming a second heat source besides the heat release by combustion. The consequence is a undesired velocity gain by burning of projectile material.

The velocity distribution gathered with aluminum projectiles fired with fuel rich (no. 145), stoichiometric (no. 136) and fuel lean (no. 146) hydrogen based gas mixture are drawn in the diagram of Fig. 8. There exists no significant difference in the velocity behaviour of the projectiles. In all three cases the supersonic combustion starts with a projectile acceleration. But after about 3 - 4 m the acceleration stops and is turned in a strong projectile deceleration. The reason for this failure is that the fins and the body are damaged by melting and burning. In each of this three firings practically the whole projectile is burned because nearly no impact is seen in the steel plates of the catcher tube.

The aluminum projectiles fired with fuel rich (no. 149), stoichiometric (no. 148) and fuel lean (no. 152) methane based gas mixtures show in Fig. 9 the same behaviour as discussed for the previous Fig. 8 with variation of the hydrogen fuel contents. As seen in Fig. 8 and Fig. 9 in fuel lean mixtures the projectiles can survive insignificantly longer than in fuel rich mixtures. In stoichiometric mixtures the aluminum projectiles behave better.

CONCLUSIONS

In conclusion, the first firings in ISL's RAMAC 30 with a smooth ram tube and fin guided projectiles carried out from November 1994 up to June 1995 could demonstrate:

- (1) direct firing into the superdetonative combustion mode with fin guided projectiles,
- (2) controlled sabot separation in a sabot stripper tube,
- (3) ignition and stable combustion at the projectile body in order to avoid the unstarting process.
- (4) Weak acceleration with hydrogen and methane based combustible gas mixtures diluted with carbondioxide was obtained. The velocity gain was small due to dilution and ineffective projectile back shape geometry.
- (5) The strong heat flux cause projectile damage, especially at the projectile fins by melting and burning due to chemical reactions of projectile material with the oxygen and the diluent.
- (6) The additional heat input by material burning is an unwellcome heat source and leads to an unstart with a detonation wave moving in front of the projectile. Projectile canting may support the unstart.
- (7) Varying the fuel content from fuel rich to fuel lean with hydrogen and methane based mixtures gave no better results in view of the previous points (5) an (6).
- (8) Results with coatings on aluminum with zirconium oxide (ZrO_2) and aluminum oxide (AL_2O_3) have shown that coating can improve the life-time but not along the whole ram cycle fired.

REFERENCES

1. HERTZBERG, A., BRUCKNER, A. P., BOGDANOFF, D.W., The Ram Accelerator: A new Chemical Method of Achieving Ultra-High Velocities, 37th ARA-Meeting, Québec, Canada, 1986
2. SEILER, F., PATZ, G., SMEETS, G., SRULIJES, J., Status of ISL's RAMAC 30 with Rail Stabilized Projectiles, First Int. Workshop on Ram Accelerator, RAMAC I, ISL, France, 1993
3. SEILER, F., PATZ, G., SMEETS, G., SRULIJES, J., The Rail Tube in Ram Acceleration: Feasibility Study with ISL's RAMAC 30, Second International Workshop on Ram Accelerator, RAMAC II, University of Washington, Seattle, USA, 1995
4. HERTZBERG, A., Thermodynamics of the Ram Accelerator, 17th International Symposium on Shock Waves and Shock Tubes, Lehigh University, USA, 1989
5. KNOWLEN, C., BURNHAM, E.A., KULL, A. E., BRUCKNER, A. P. HERTZBERG, A., Ram Accelerator Performance in the Transdetonative Velocity Regime, 41st ARA-Meeting, San Diego, USA, 1990
6. HERTZBERG, A., BRUCKNER, A. P., KNOWLEN, C., Experimental Investigation of Ram Accelerator Propulsion Modes, 18th International Symposium on Shock Waves, Sendai, Japan, 1991
7. BRUCKNER, A.P., BURNHAM, E.A., KNOWLEN, C., HERTZBERG, A., BOGDANOFF, D.W., "Initiation of Combustion in the Thermally Choked Ram Accelerator", 18th International Symposium on Shock Waves, Sendai, Japan, 1991
8. GIRAUD, M., LEGENDRE, J.-F., SIMON, G., RAM Accelerator in 90 mm Caliber or RAMAC 90:, Experimental Results Concerning the Transdetonative Combustion Mode, 14th International Symposium on Ballistics, Québec, Canada, 26-29 September 1993
9. SMEETS, G., GATAU, F., SRULIJES, J., Rechenprogramm für Abschätzungen zur Ram-Rohrbeschleunigung, ISL-Report RT 507/92, 1992

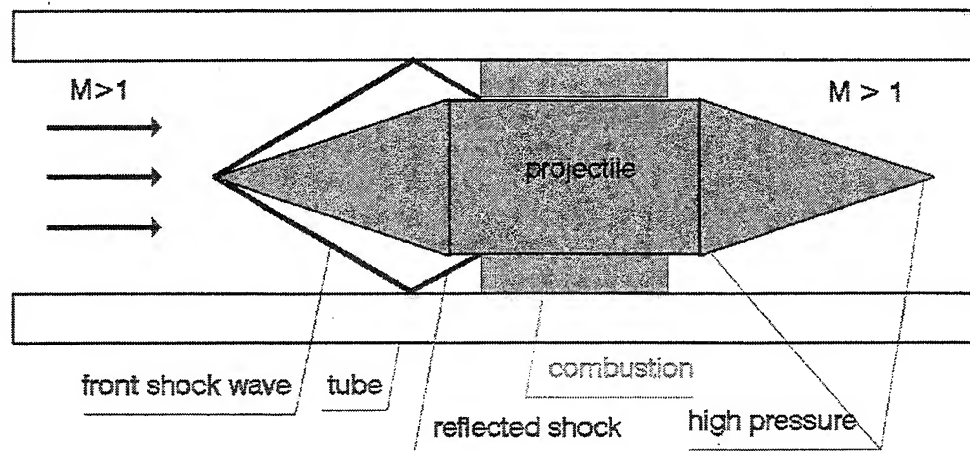


Fig. 1. Principle of the scram accelerator process

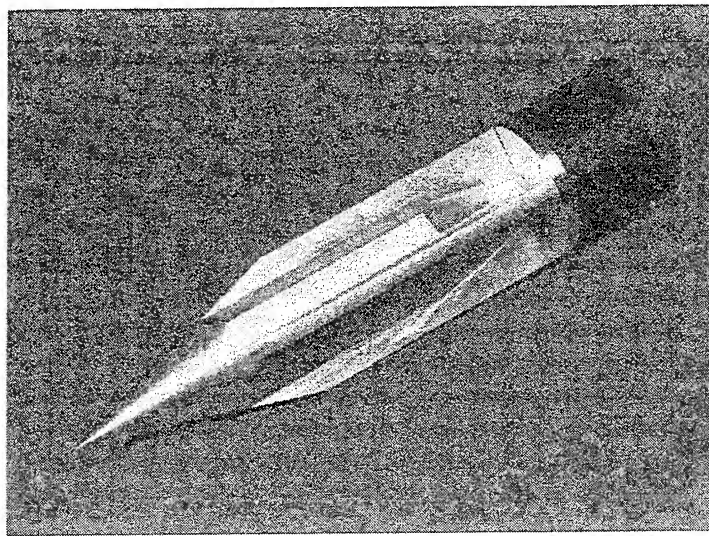


Fig. 2: Ram projectile with guiding fins

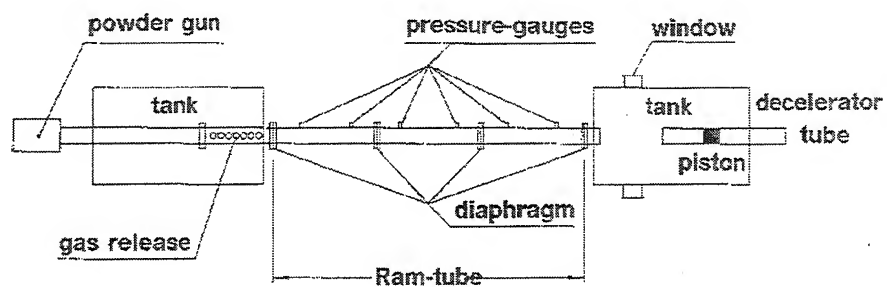


Fig. 3. Set-up of ISL's ram accelerator

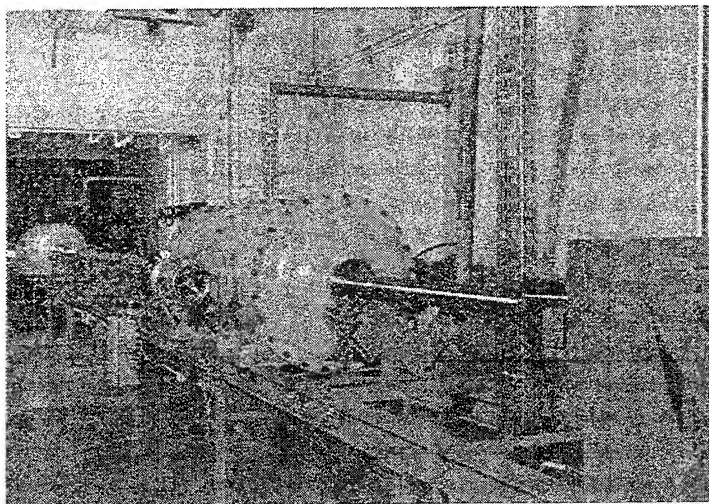


Fig. 4a. Photography of the whole RAMAC 30 facility in June 1995

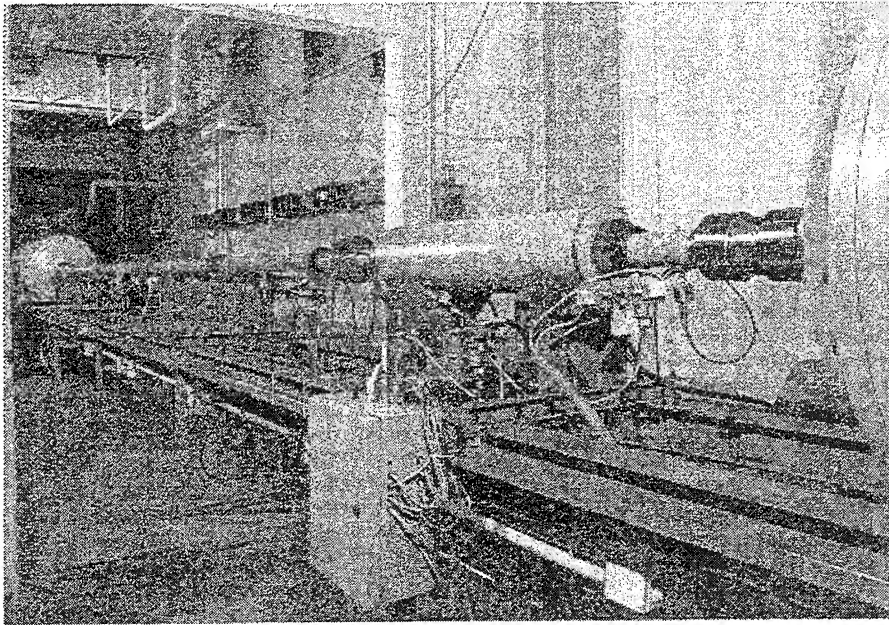


Fig. 4b. Smooth bore 6 m ram tube (left) and 1.5 m sabot stripper tube (right)

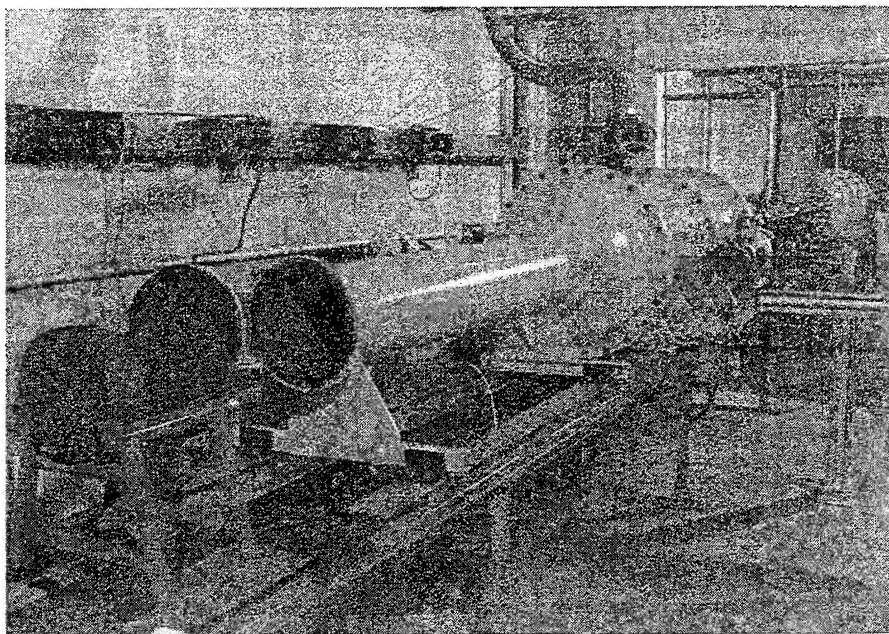


Fig. 4c. Decelerator tube with piston

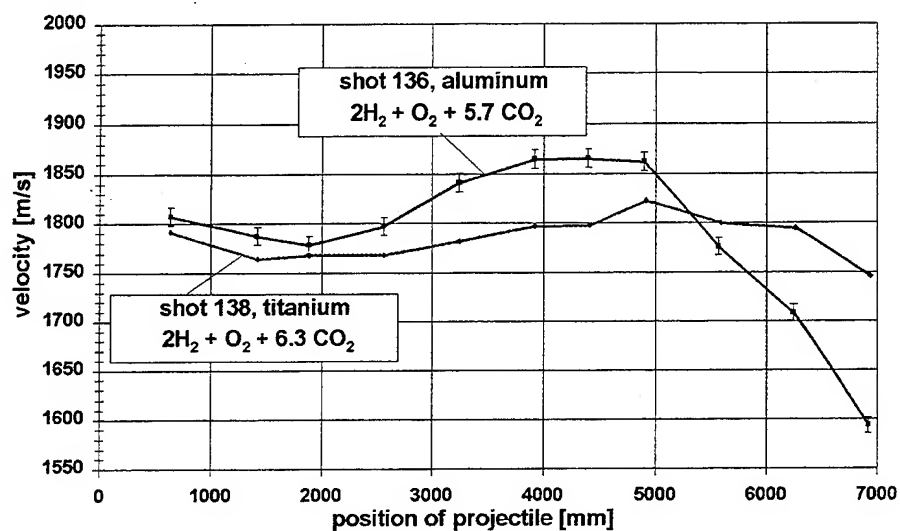


Fig. 5. Velocity increase with projectiles made of aluminum and titanium



Fig. 6a. x-ray image for shot no. 134 after 3 m projectile path with a mixture as for no. 136

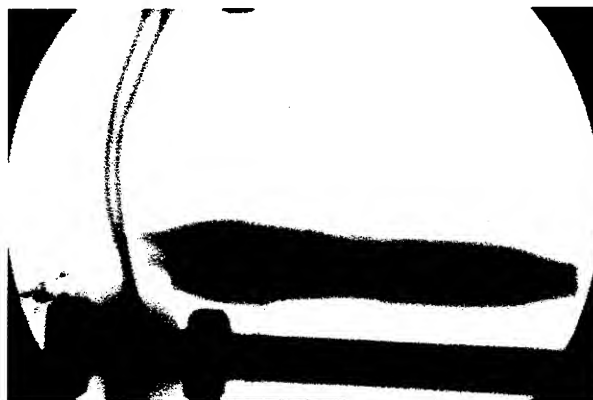


Fig. 6b. x-ray photograph for shot no. 139 after 6 m projectile path



Fig. 6c. x-ray photograph for shot no. 142

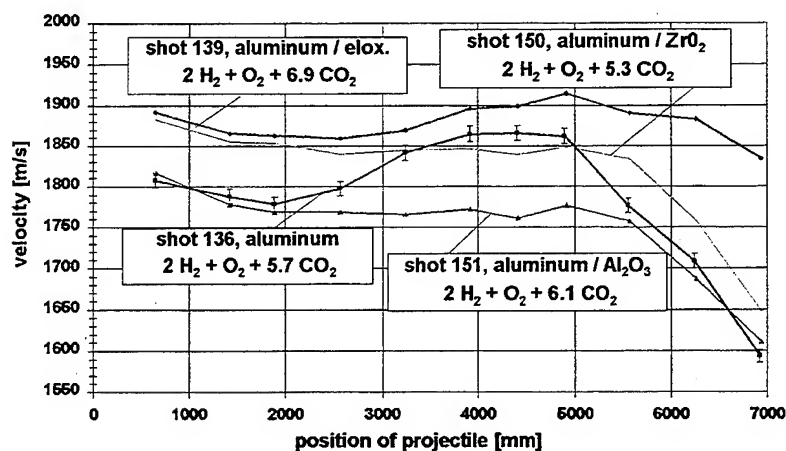


Fig. 7. Velocity increase with projectiles made of aluminum (no. 136), eloxadized aluminum (no. 139), aluminum with zirconium oxide coating (no. 150) and aluminum oxide on aluminum (no. 151)

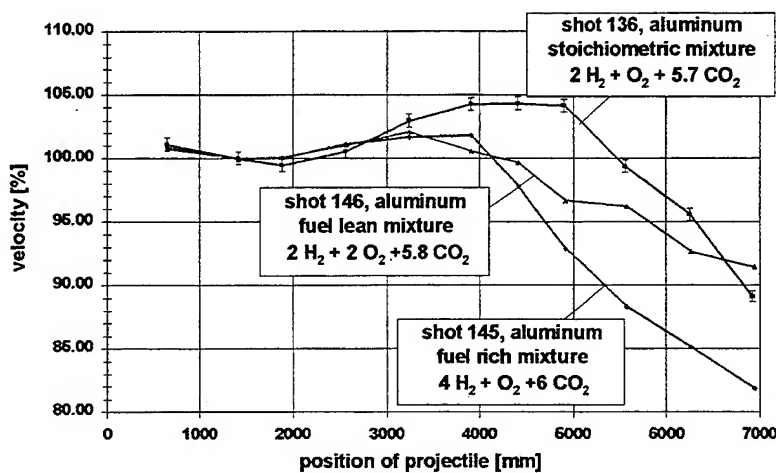


Fig 8. Velocity increase with aluminum projectiles fired with fuel rich (no. 145), stoichiometric no. 136) and fuel lean (no. 146) hydrogen based gas mixture

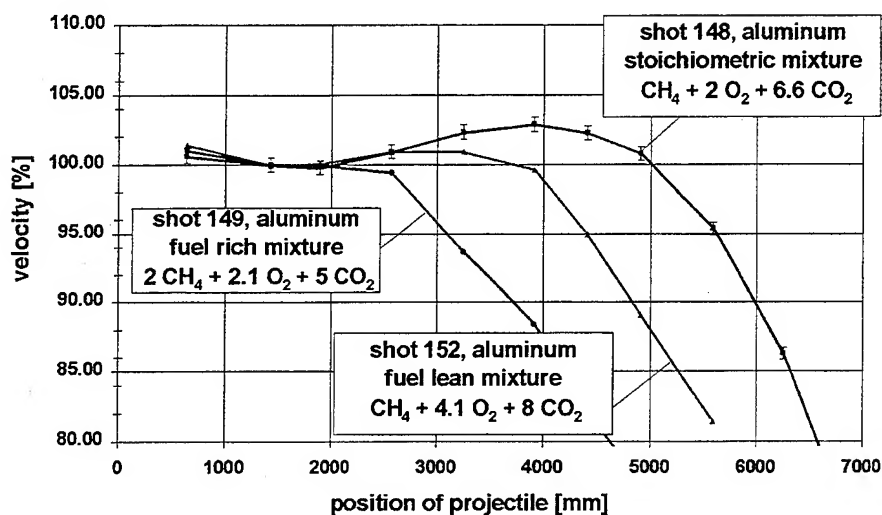


Fig 9. Velocity increase with aluminum projectiles fired with fuel rich (no. 149), stoichiometric (no. 138) and fuel lean (no. 152) methane based gas mixture

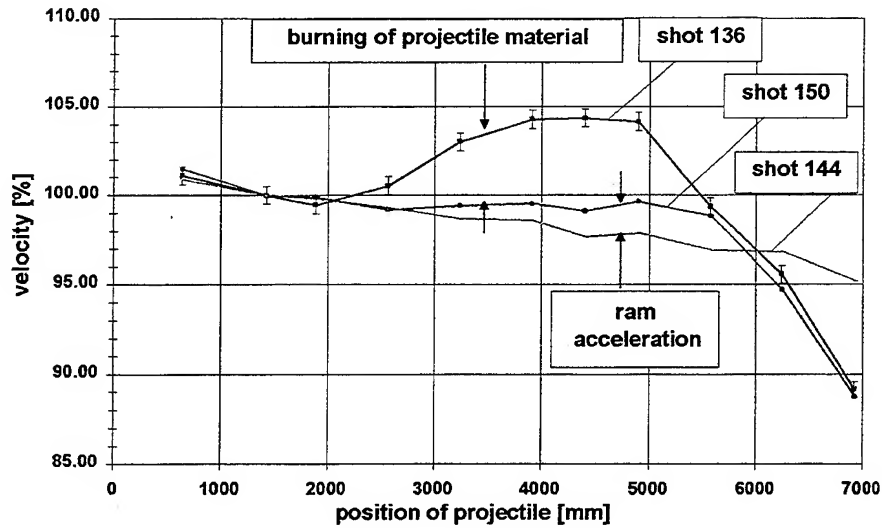


Fig. 10. Flow drag and friction forces balanced by ram acceleration in no. 150 (ram combustion) compared with shot no. 144 (no combustion) and no. 136 (ram combustion and aluminum burning)

RAMAC 25 at Shock Wave Research Center

A. Sasoh and K. Takayama

Shock Wave Research Center
Institute of Fluid Science, Tohoku University
2-1-1 Katahira, Aoba, Sendai 980-77, Japan

ABSTRACT

At Shock Wave Research Center, Institute of Fluid Science, Tohoku University, a 25-mm-bore ram accelerator(RAMAC 25) has been installed. Projects associated with this apparatus aim not only at fundamental research of shock wave dynamics in reactive gas systems but at its various applications to aerospace technologies and to hypervelocity impact. In order to make the flow field model simple, hollow projectiles will be tested first. Also center-body projectiles will be studied on mainly to validate scaling effects on ram accelerator operation and to examine the effect of projectile configuration. The effect of finite rate chemical reaction is being studied theoretically and numerically. CFD studies have been applied to simulate the ram accelerator flow field using a supercomputer Cray C916.

INTRODUCTION

The characteristic of launching a heavy payload to high speeds with high energy conversion efficiencies in using a ram accelerator is most attractive topics in shock wave researches from view points of fundamental research and its application. As was reported at the first RAMAC Workshop held in Saint Louis, a 25-mm-bore ram accelerator has been installed at Shock Wave Research Center (SWRC), Institute of Fluid Science, Tohoku University. Recently, this projects have been in progress through a close collaboration with University of Washington funded by Japan Society of Promotion of Science (JSPS) and International Aircraft Development Fund (IADF).

APPARATUS

Figure 1 shows the schematic illustration of the ram accelerator at SWRC. The ram acceleration section has three two-meter-long tubes. The inner and outer diameters of the tubes are 25 mm and 60 mm, respectively. At axial locations of a 0.4 m separation with each other,

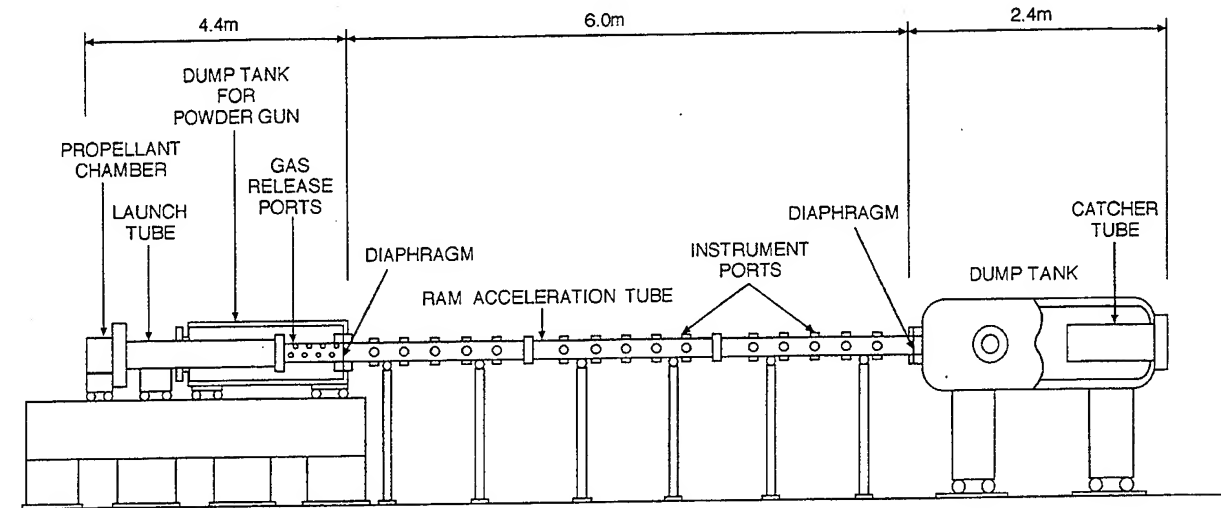


Figure 1: RAMAC 25 at SWRC

the tubes have four instrumentation ports (in total sixty ports). In these ports, the magnetic sensors and pressure transducers are fabricated. The gas feed system is composed of mass flow controllers and backpressure regulators. The flow rate of each species is controlled electrically.

The launch section is a powder gun of the same bore as the ram acceleration tubes. Smokeless powder of 30 gram at maximum can be loaded in the propellant chamber. The launch tube is 4 m in length and is surrounded by a dump tank for the product of the propellant. Between the launch tube and the ram acceleration section, a propellant release port is inserted.

HOLLOW AND CENTER-BODY PROJECTILES

Figures 2 and 3 shows hollow and center-body projectiles which are used in the experiment, respectively. The cross-sectional area of hollow projectile (Fig. 3) is scaled to one to which was tested at University of Washington, [1]. They are made of aluminum alloy A7075T651. It has a converging conical (10 degrees) flow passage on the upstream side and a diverging conical flow passage on the downstream side. The cross-sectional area ratio of the throat to the inlet equals that of a standard center-body projectile at University of Washington.[2] The ratio of the base to the inlet equals that in the center-body projectile.. In order to strengthen the tip of the projectile when it impinges to against rupture diaphragms, it has a lip of a deeper angle of 30 degrees. In this inverse cone type projectile, the area variation, dA/dx (A ; cross-sectional area of the flow passage, x ; axial position), decreases with decreasing the inner radius. In order to increase dA/dx near the throat, the diverging section has a biconic configuration. For

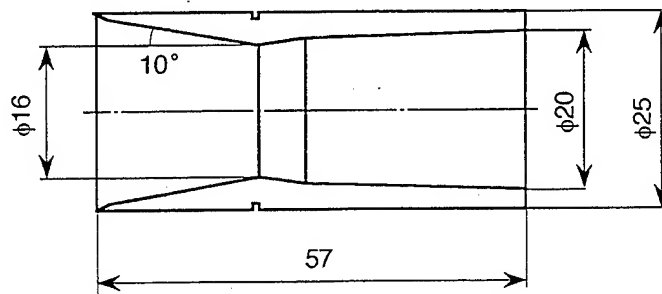


Figure 2: Hollow projectile, dimensions in mm.

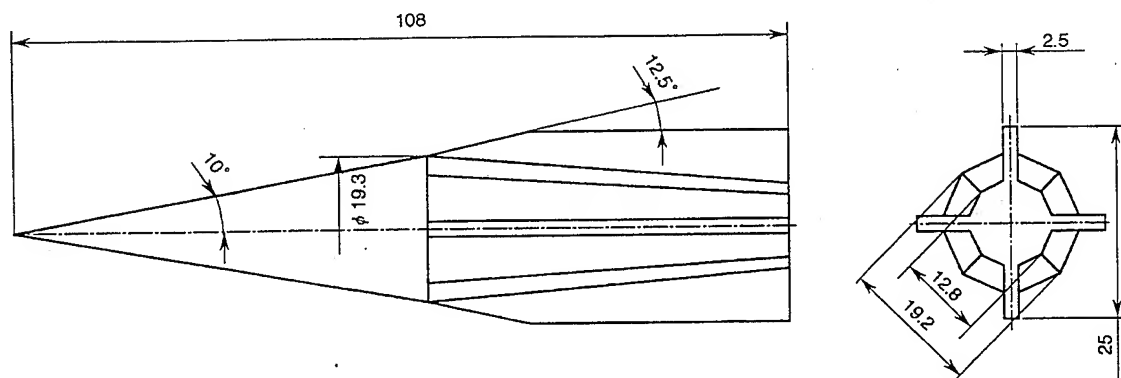


Figure 3: Center-body projectile, dimensions in mm.

measuring an $x-t$ diagram of the projectile, a magnetized plastic ring is so fabricated in the groove on the outer surface as to yield large output signals.

The center-body projectile (Fig. 3) has a similar configuration to that of University of Washington.

Figures 4 and 5 show examples of CFD computation in the case of inert gas flows passing through the hollow projectile. With the same tip angle, a stronger shock is generated by an inverse cone than by a cone. In order to avoid Mach reflection on the axis, the entry speed of the projectile to the ram acceleration section needs to be increased. Furthermore, the effect of the lip of the deeper angle is significant in determining a shock reflection pattern in hollow projectiles, see Figs. 4 and 5 for comparison.

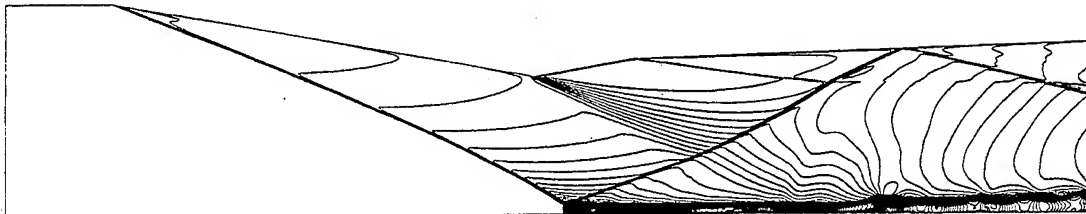


Figure 4: Isopycnics in the hollow projectile without a lip, $\gamma = 1.29$, $M = 4.0$

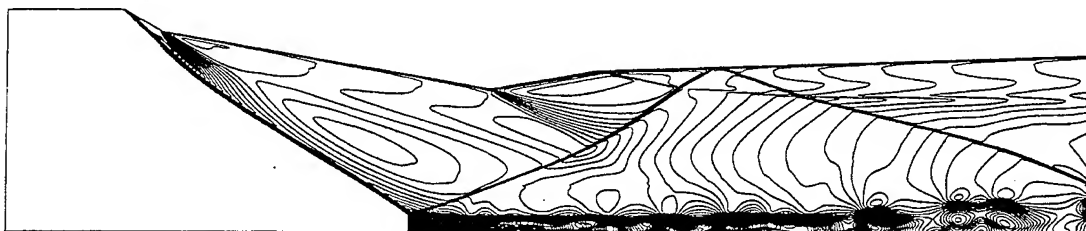


Figure 5: Isopycnics in the hollow projectile with a lip, $\gamma = 1.29$, $M = 4.0$

THEORETICAL AND NUMERICAL WORKS

The study of the effect of finite rate chemical reactions on ram accelerator thrust characteristics was initiated at University of Washington (see Fig. 6)[1]. With a relatively simple quasi-one-dimensional, quasi-steady numerical calculation showed that if the effective induction length of the chemical reactions becomes shorter than a projectile characteristic length a 'transdetonative mode' appears; the flow becomes sonic on the projectile body, being accompanied with supersonic expansion downstream of the sonic point. The thrust in this mode is larger than that in the 'subdetonative' mode in which the flow becomes sonic downstream of the projectile. Further calculations are being conducted at SWRC.

By utilizing existing CFD resources at SWRC, two or three-dimensional CFD codes for the ram accelerator flow simulation are being developed. The calculation was conducted using a supercomputer, Cray C916.

SUMMARY AND FUTURE PLAN

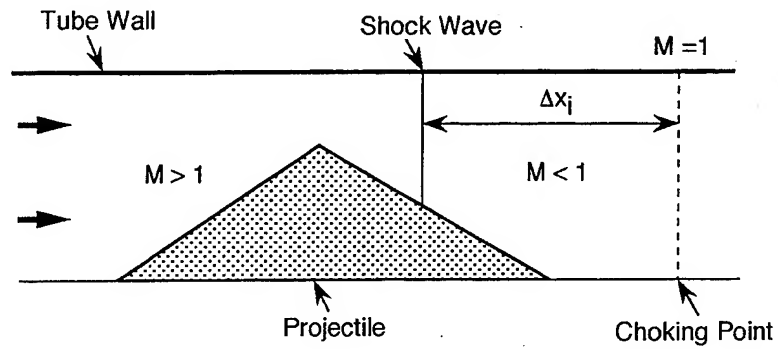
SWRC plans first of all to test hollow projectiles. Then, scaling effects will be investigated with center-body projectiles by comparing the observed performances with others. As an extension of this project, a 100 mm bore ram accelerator as a main facility in SWRC is planned.

ACKNOWLEDGMENT

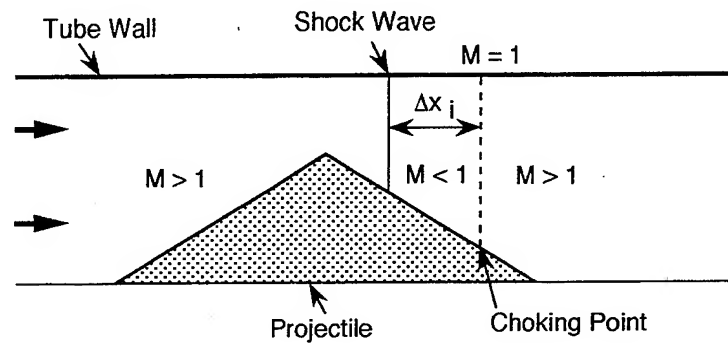
The authors thank valuable helps which have been made by University of Washington. This project is supported by Grant-in Aid for Scientific Research No. 05402033.

References

- 1 Sasoh, A., Knowlen, C. and Bruckner, A. P., "Effects of Finite Rate Chemical Reaction on Ram Accelerator Thrust Characteristics," AIAA 95-2492, 1995.
- 2 Knowlen, C., Higgins A. J. and Bruckner A. P., "Investigation of Operational Limits to the Ram Accelerator," AIAA Paper 94-2967, 1994.



a. Thermally Choked



b. Transdetonative

Figure 6: Schematic illustration of subdetonative and transdetonative modes, from Ref. 1

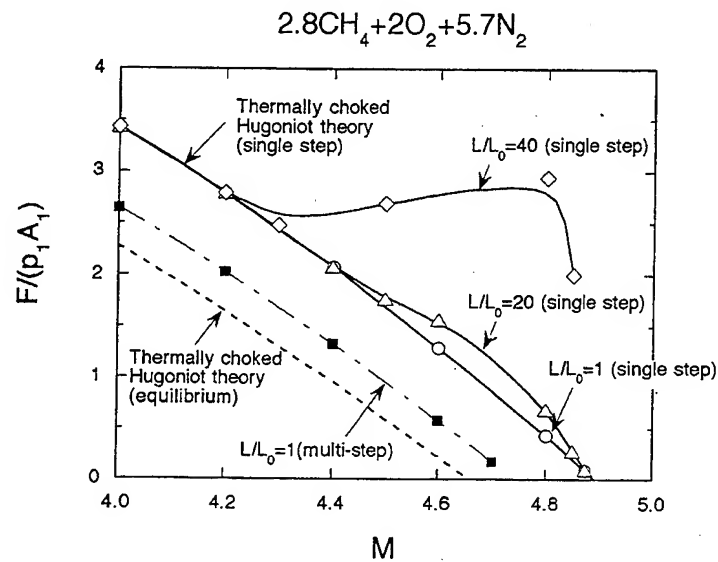
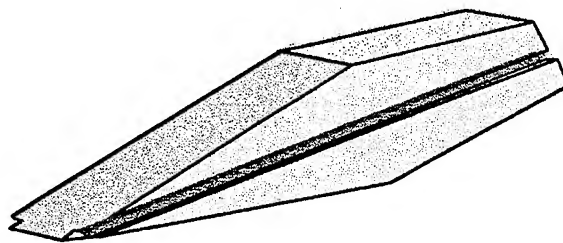


Figure 7: Calculated thrust characteristics, from Ref. 1

Preliminary Tests of a Rectangular Bore Ram Accelerator

Xinyu CHANG, Koji Shimomura and Shiro TAKI
Department of Mechanical Engineering
Hiroshima University, JAPAN



Second International Workshop on
Ram Accelerator
RAMACII
July 17-20, 1995

University of Washington
Seattle, Washington, USA

Preliminary Tests of A Rectangular Bore Ram Accelerator


X. Chang¹, Y. Shimomura² and S. Taki³

ABSTRACT

A new geometry ram accelerator is being made and working at the Hiroshima University of Japan. It consists a two-stage light gas gun as the projectile launcher, a ram acceleration section and a dump section. The light gas gun includes a 55mm bore detonation tube, which drives a free piston, a 55mm bore compression tube, in which the helium gas is compressed by the free piston, and a launch tube, in which the projectile is accelerated by the compressed helium gas and launched into the ram acceleration section. A evacuated tank is located at the end of the launch tube of the light gas gun to serve as a dump for the helium driver gas. In order for the convenience of the visualization of the flowfield around the flying projectile, a rectangular bore ram tube is used. The launch tube of the light gas gun also has the same cross-section. The inner and outer sizes of these tubes are 15x20mm and 55x70mm, respectively. Several observation windows are also located on the side-walls of the ram tube. The projectile in the tubes is centered by two guide rails placed on the side walls of the tube inside. Consequently, the projectile which has the two dimensional structure is shaped to fit the guide rails.

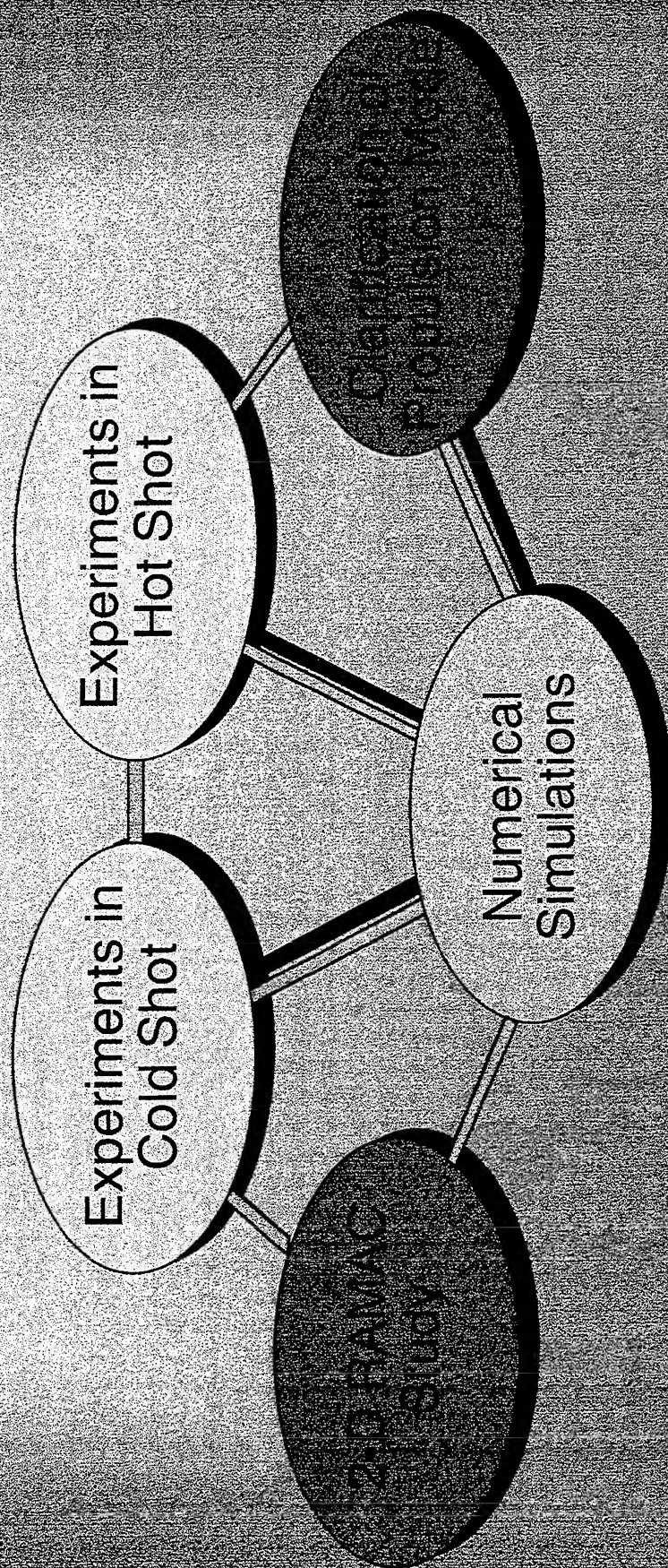
The ram tube is 2m long. Three pressure transducers are mounted along the tube to measure the pressure change when the projectile passes them. Several magnetic detectors are also set along the outside of the walls of the launch tube, dump tube and ram tube to check the passage of the projectile in which a small cobalt magnet is mounted in. The velocity of the projectile can be calculated from these outputs. Schlieren pictures can be taken through the observation windows by the trigger from a pressure transducer or a magnetic detector. Recently the start is obtained at the CO₂ gas compressed to 0.35MPa when the entrance velocity is higher than 1000m/sec.

¹Research Associate, ²Graduate Student, ³Professor
Department of Mechanical Engineering, Hiroshima University,
Higashi-Hiroshima, 724, JAPAN.
Tel: (0824)24-7559, Fax: (0824)22-7193
E-mail: chang@fuji.mec.hiroshima-u.ac.jp

- 
- ©Investigations of the principles of ram jet engine
 - ©Development of a new propulsion technique
 - ©Make a 2-D facility for the visualization of the flowfield around a projectile

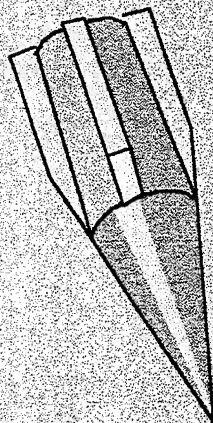
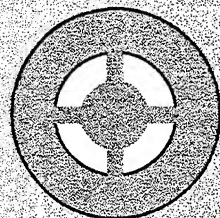
Hurmac

RAMAC Study Procedure

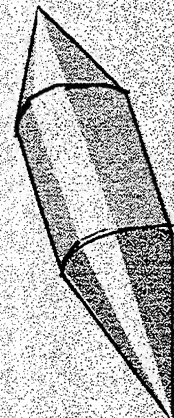
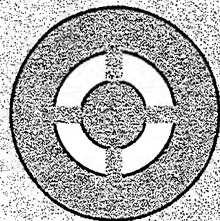


Hur mac

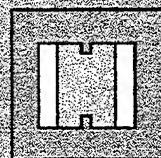
Various Projectiles around the World



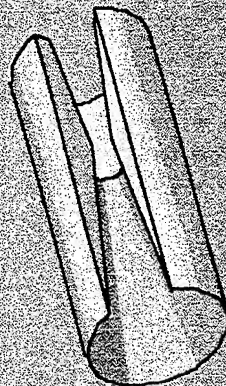
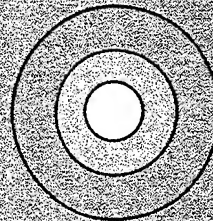
FIN TYPE
(UW, US Army, ISL)



GUIDE-RAIL TYPE
(ISL)



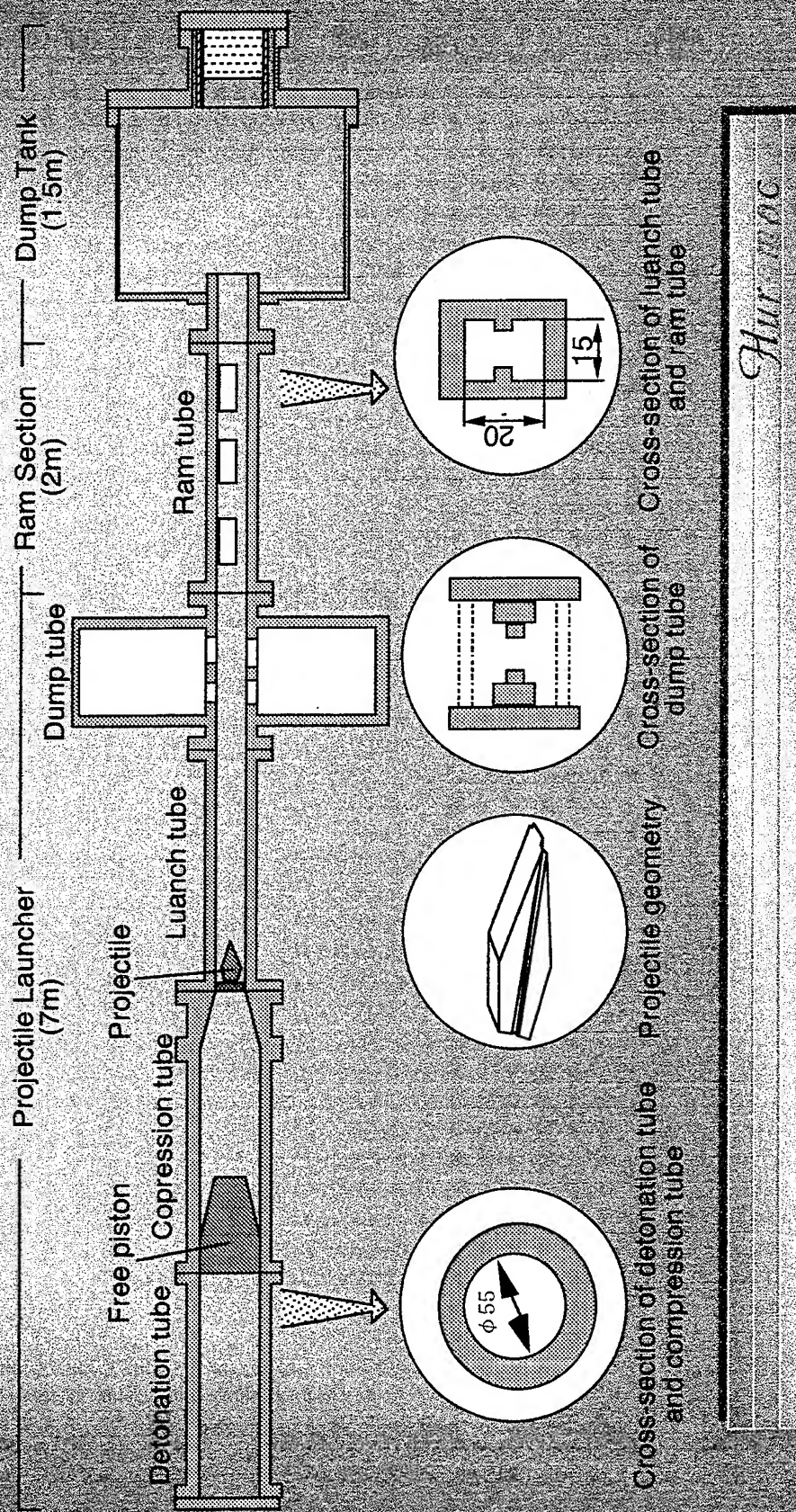
2-D TYPE
(HU)



HOLLOW TYPE
(TU)

Hur noc

Outline of HURAMAC

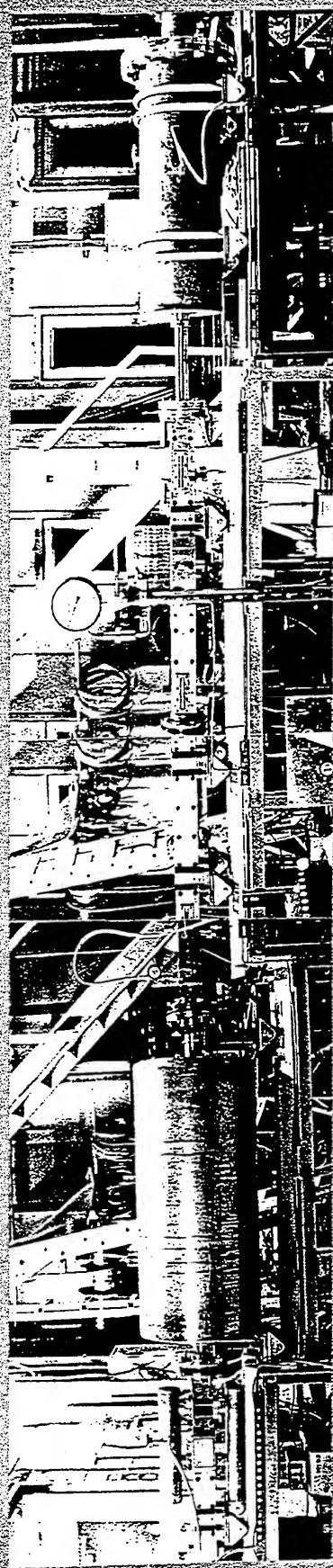
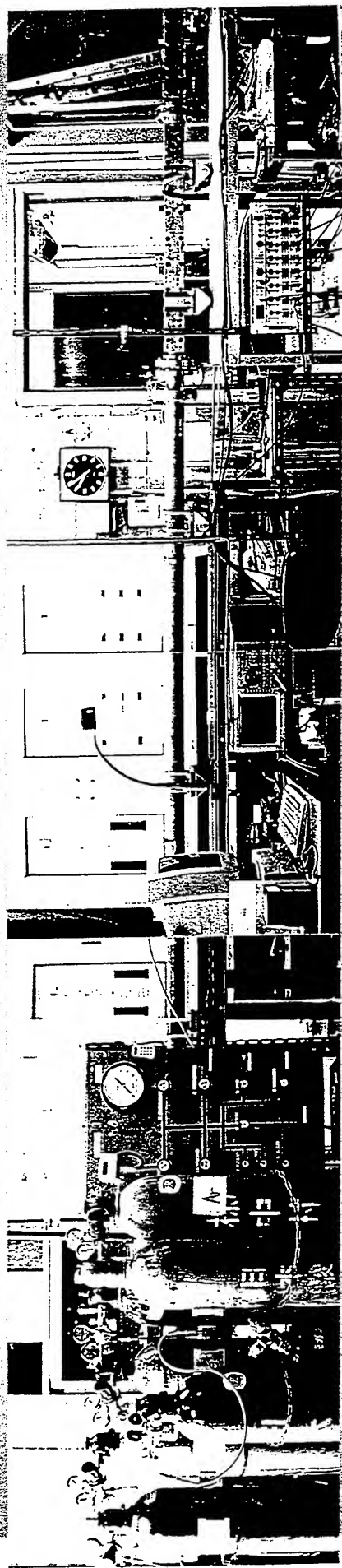


Specifications of HURAMAC

PART	SECTION	GEOMETRY	SIZE
Projectile launcher	Detonation tube	Cylinder	$\phi 55 \times L2000$
	Compression tube	Cylinder	$\phi 55 \times L2000$
	Launch tube	Rectangular	$W15 \times H20 \times L2000$
	He dump tube	Two pieces	$W15 \times L1000$
Accelerator	Ram tube	Rectangular	$W15 \times H20 \times L2000$
Decelerator	Deceleration tube	Cylinder	$\phi 35 \times L500$
	Final dump tank	Cylinder	$\phi 260 \times L1000$
Others	Free piston	Truncated cone	300gr
	Projectile	2-D wedge	5gr
	Obturator	Prism	5gr

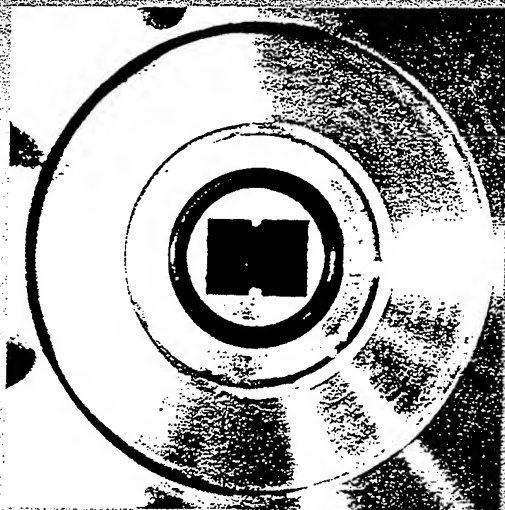
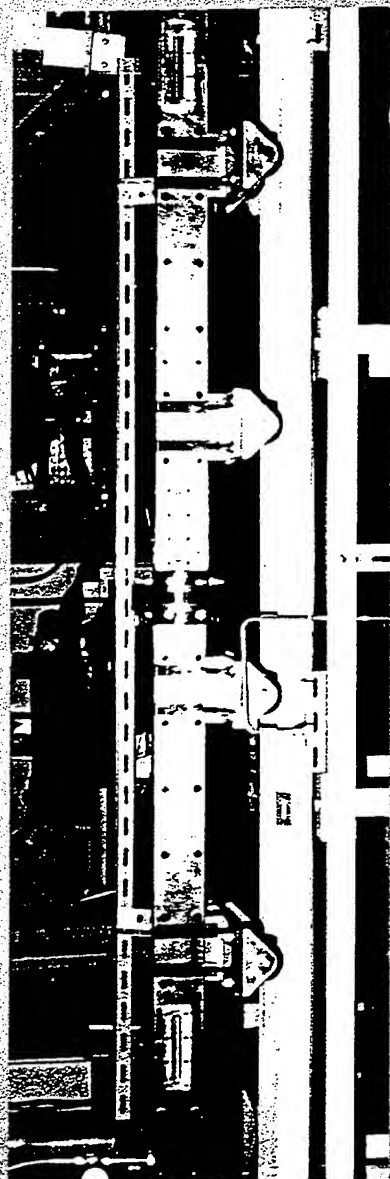
Hurmac

Photographs of UHRAMAC



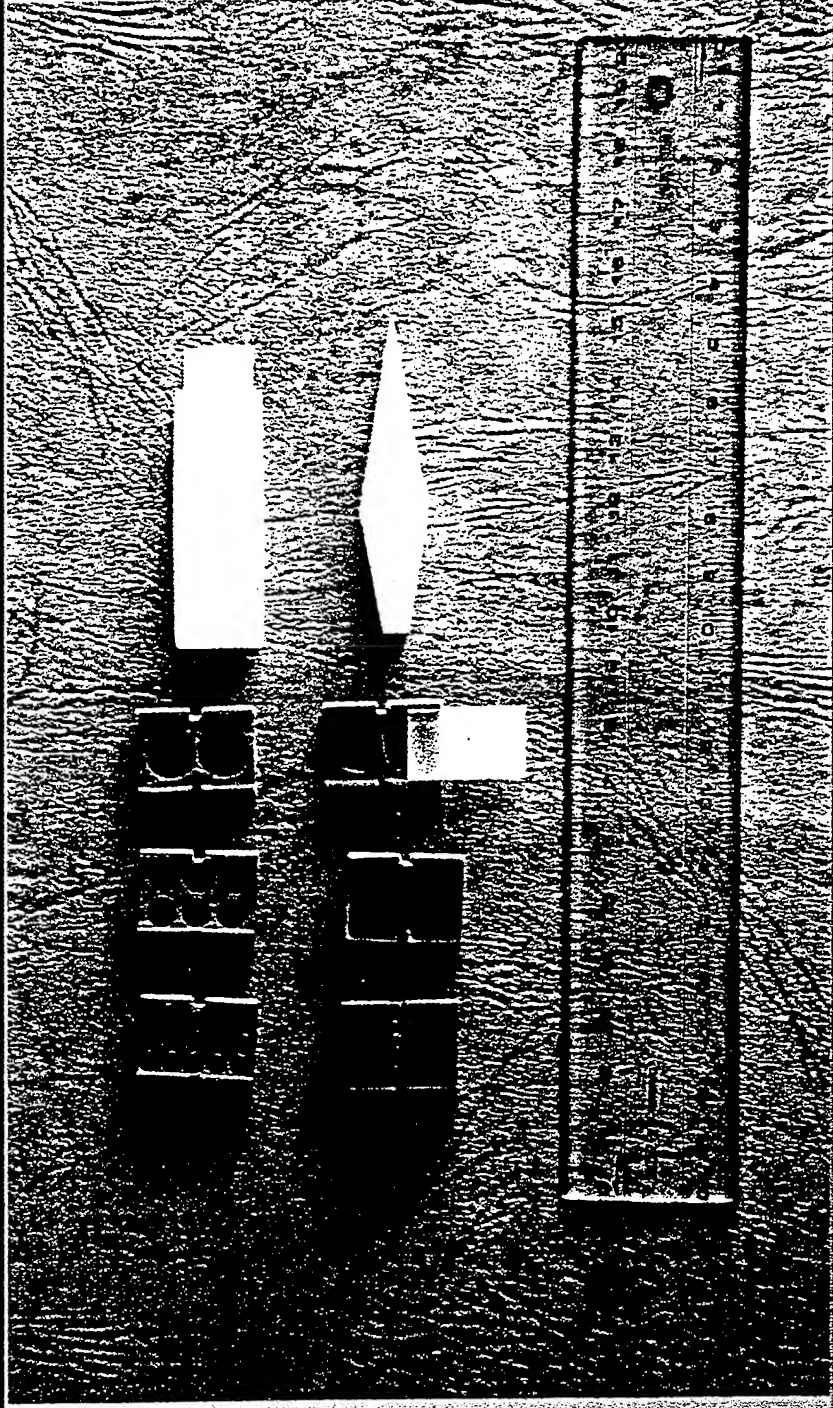
Hurroc

Photographs of Ram Tube



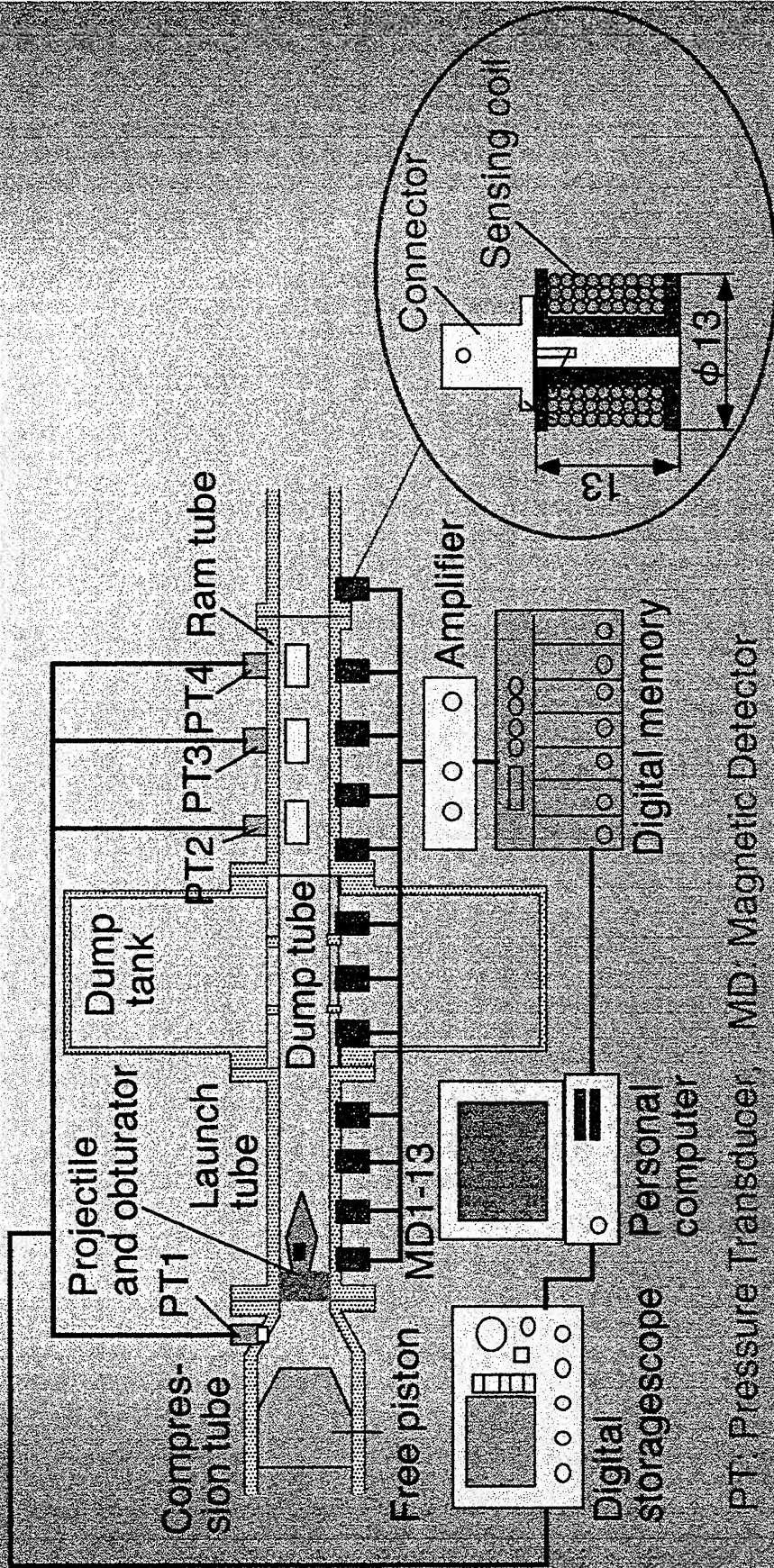
Hurmac

Photograph of Projectiles and Obturators



Hur rcc

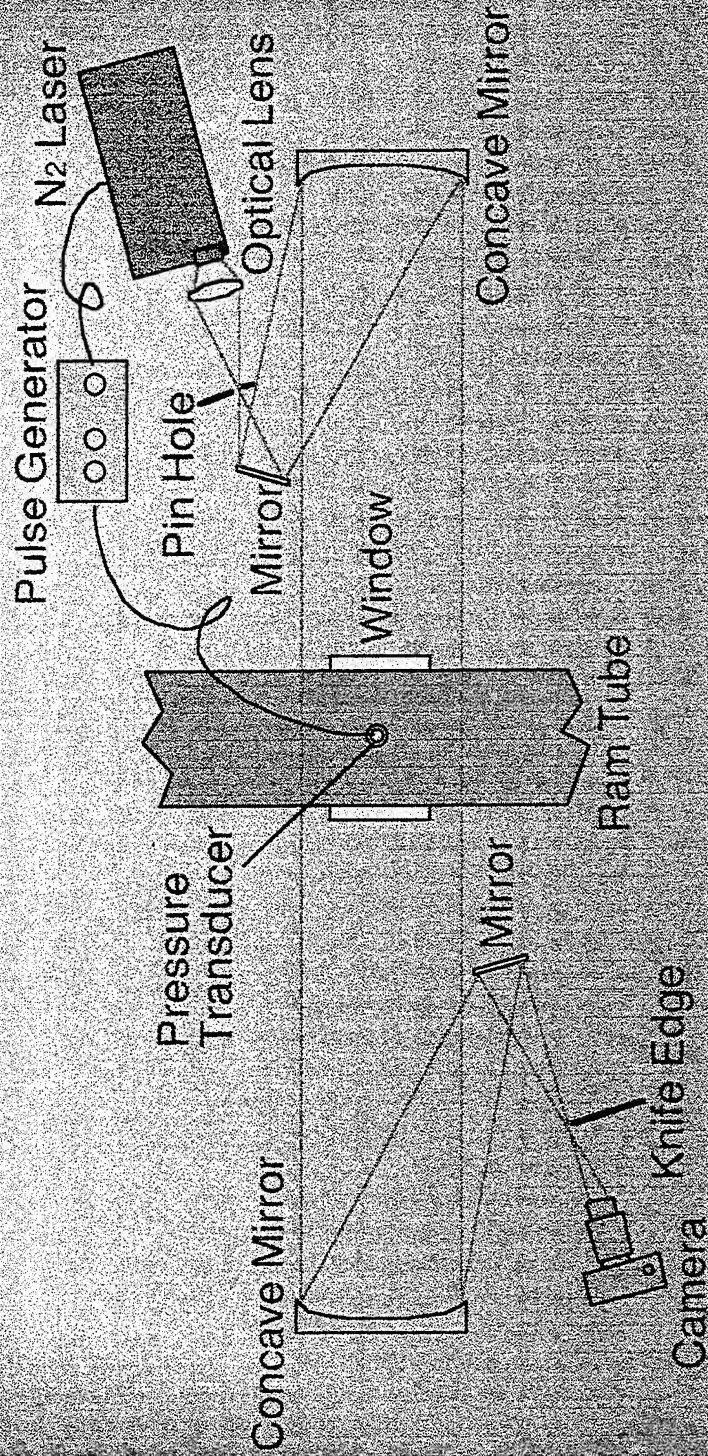
Measurement System



PT: Pressure Transducer, MD: Magnetic Detector

Hur

Visualization System

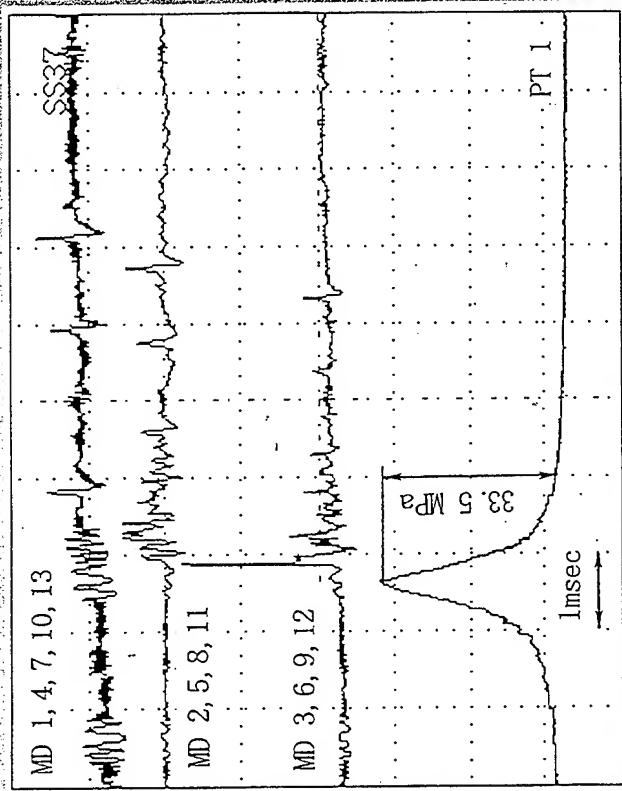


Hurac

Typical Outputs

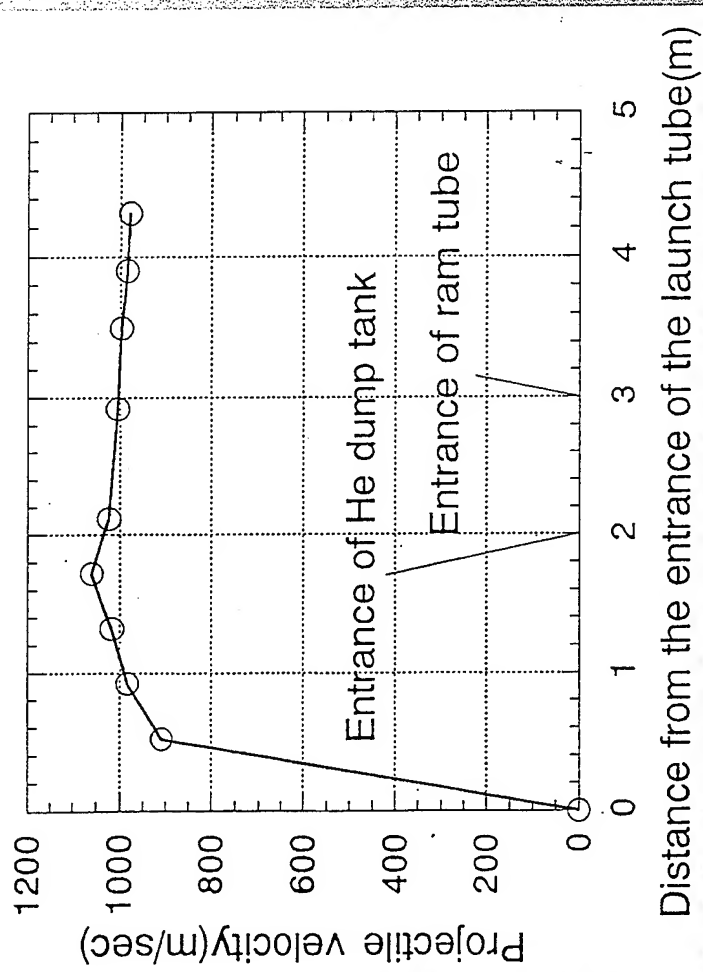
Experimental conditions

Detonation tube	0.4MPa (2H ₂ +O ₂ +Ar)
Compression tube	0.1MPa (He)
Launch tube & He dump tank	120Pa (Air)
Ram tube	0.36MPa (CO ₂)
Final dump tank	0.1MPa (Air)
Free piston	300gr (Al)
Projectile	4.5gr (Polypropylene)
Obturator	4.5gr (with sabot stopper)



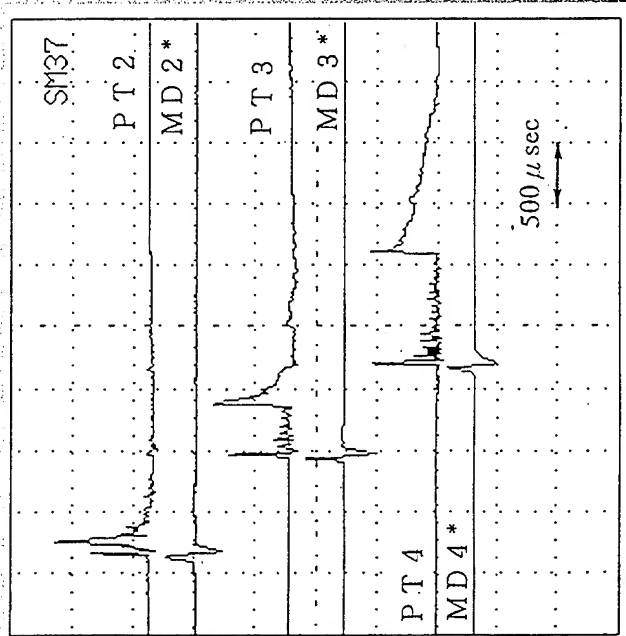
Hurricane

Distributions of Projectile Velocity



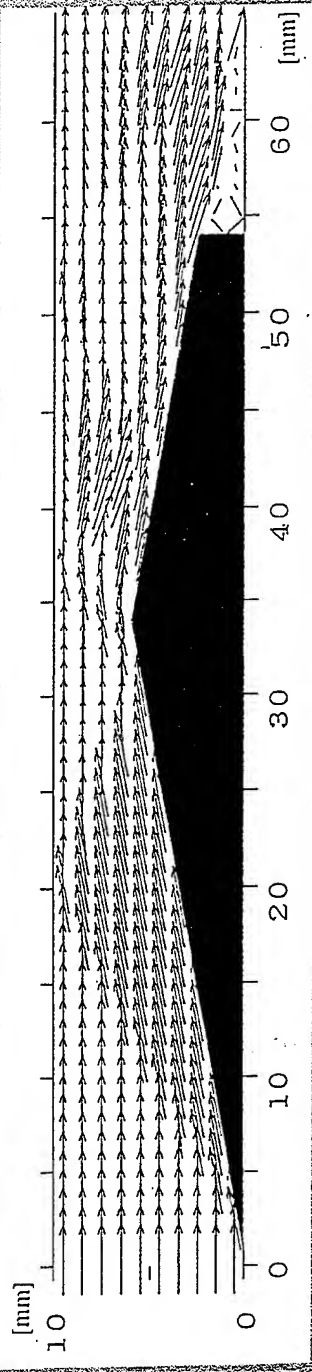
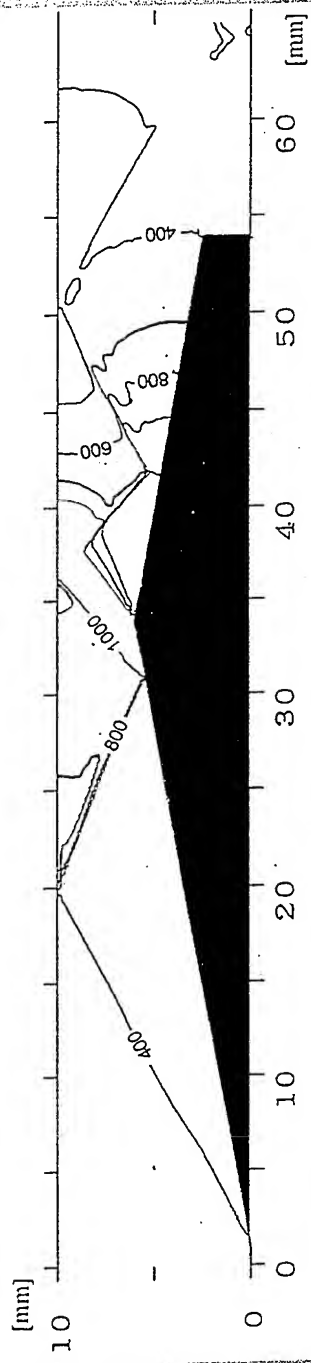
Hurricane

Typical Outputs



500 μ sec

Flowfield around Projectile



($2\text{H}_2 + \text{O}_2 + 3.8\text{N}_2$)

$P_0 = 203 \text{ kPa}$

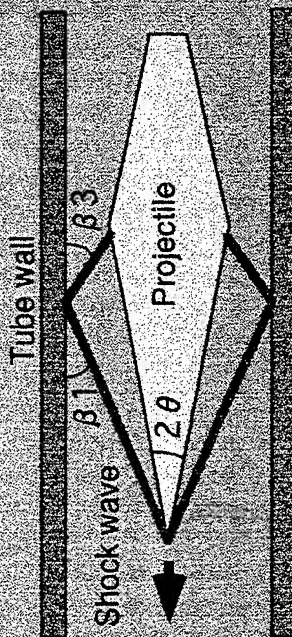
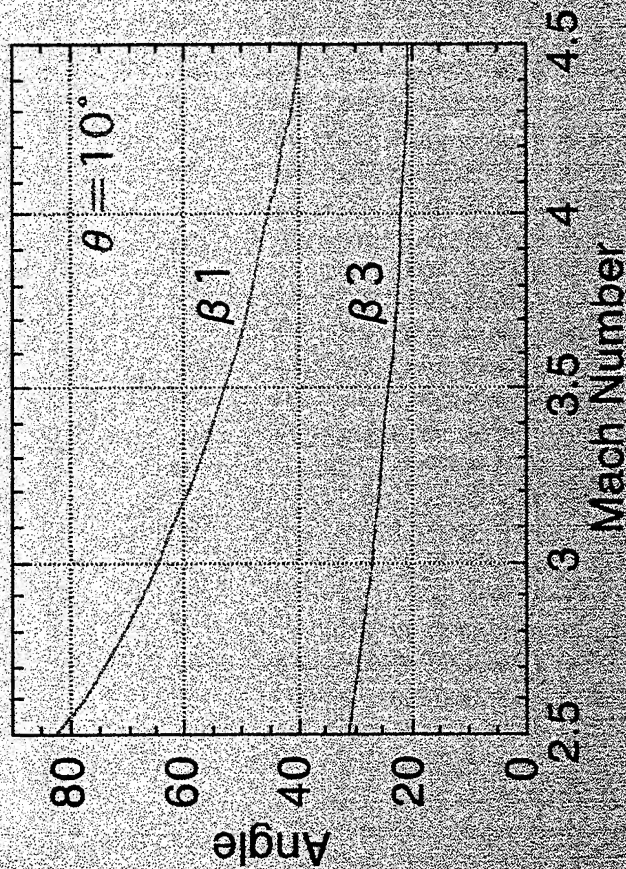
$T_0 = 288 \text{ K}$

$M_s = 3.0$

$dx(\text{min}) = 0.111 \text{ mm}$

Autovac

Shock Angles of Calculation

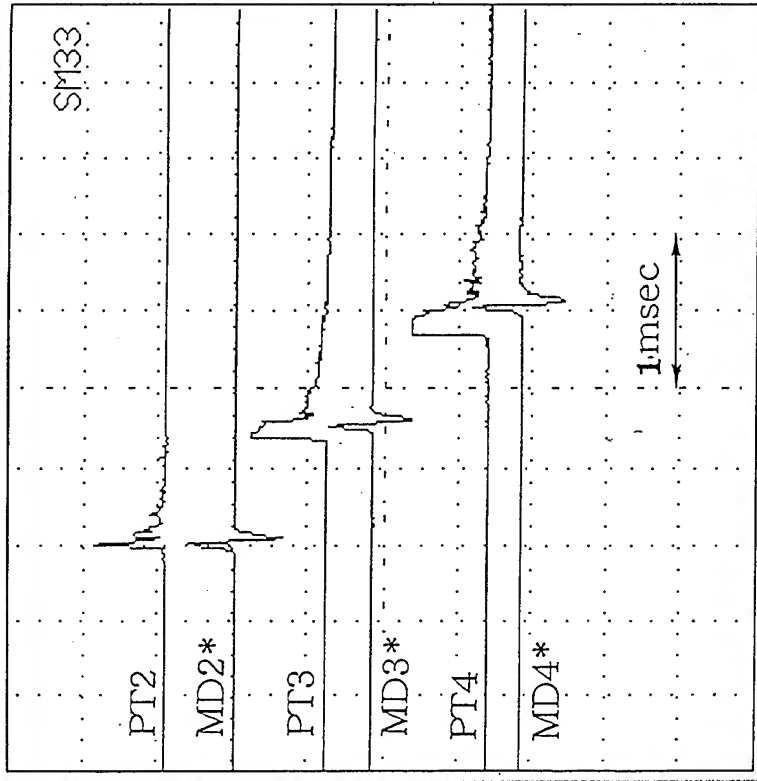


Hur noc

Unstart of Cold Shot in Ar Gas

Experimental conditions

Detonation tube	0.4MPa (2H ₂ +O ₂ +Ar)
Compression tube	0.1MPa (He)
Launch tube & He dump tank	120Pa (Air)
Ram tube	0.2MPa (Ar)
Final dump tank	0.1MPa (Air)
Free piston	300gr (Al)
Projectile	4.5gr (Polypropylene)
Obturator	4.5gr
Entrance velocity	1007.3m/sec



HW 800

Conclusions

- © HURAMAC is working with the cold shots
- © Start at the CO₂ gas when the entrance velocity is higher than 1000m/sec
- © Start at Ar gas is more difficult than it at CO₂ gas
- © Numerical simulation is also being performed

Hurmac

A FEEDBACK CONTROLLED GAS MIXING SYSTEM FOR THE RAM ACCELERATOR

M. R. Jardin and A. P. Bruckner+
Aerospace and Energetics Research Program
University of Washington, FL-10
Seattle, Washington 98195*

Abstract

A feedback-controlled gas mixing system is presented along with operational results for a prototype implementation, which has been developed for the University of Washington ram accelerator hypervelocity launcher facility. The control system is designed to fill high-pressure chambers with a selected number of component gases (four for the ram accelerator) at a chosen set of molar ratios. A mass-flow-rate controller keeps the mass-flow rate of a primary gas constant while secondary gas controllers drive the molar-ratio errors to zero, thereby ensuring that the final gas composition is correct. The sensing elements are resistive thermal detection (RTD) mass-flow meters, and the control elements are switched servo-actuated metering valves. Experimental results for the operation of the prototype system are reported.

Nomenclature

A	= area
c_p	= specific heat at constant pressure
C_v	= valve C_v factor, a measure of pressure loss in gallons per minute of water which will pass through an orifice with a pressure differential of 1 psi.
D	= diameter; denominator polynomial of a transfer function
d_{min}	= minimum fill line diameter
E_D	= discretization error
E_m	= measurement error in mass-flow meter
E_{MR}	= percent error in mass ratio
E	= absolute value of the average of E_m
K_{cf}	= conversion constant in mass-flow-rate equation
K_{cl}	= control law gain
K_{cv}	= proportional constant between orifice area and C_v factor
K_{eff}	= effective closed loop system gain
K_F	= filter gain
K_{fd}	= relational constant between C_v factor and molar flow rate
K_{ss}	= steady-state gain of the control law
K_v	= rate of change of the C_v with respect to time
L	= length of fill pipe
M	= Mach number
M_a	= true accumulated mass

*Aerospace Engineer.; Currently employed with the
Air Traffic Management Branch, NASA Ames Research
Center, MS 210-9, Moffett Field, CA 94035.

+Professor of Aeronautics & Astronautics.

M_e = accumulated mass with error due to discrete integration and measurement error in the mass-flow meter
 \dot{M}_{cl} = voltage signal from control law in feedback loop
 \dot{M}_e = error signal in feedback loop and input to control law
 \dot{M}_{filt} = filtered mass-flow-rate signal
 \dot{M}_m = mass-flow-rate reading from flow meter
 \dot{M}_{max} = maximum mass-flow rate
 \dot{M}_p = mass-flow rate of the primary gas
 \dot{M}_{ref} = input reference mass-flow rate
 \dot{M}_s = mass-flow rate of the secondary gas
 \dot{M}_{SLM} = mass-flow rate in standard liters per minute
 \dot{m} = mass-flow rate in Kg/sec
 N = numerator polynomial of a transfer function
 P = pressure; pole of a transfer function
 P_s = standard pressure (1.01×10^5 MPa)
 P_t = total pressure
 R = ideal gas constant for a given gas
 Re = Reynolds number
 \mathfrak{R} = molar ratio of two gases
 R_u = universal ideal gas constant
 \dot{R}_n = angular speed of valve actuator motor shaft (revolutions/second)
 s = complex variable, Laplace transform analysis
 T = temperature (absolute)
 T_s = standard temperature (273.15 K)
 T_t = total temperature
 u = axial flow velocity
 V = volume
 V_{DZ} = Dead-Zone voltage
 V_e = error voltage
 W = molecular weight
 Z = zero of a transfer function

Greek

γ = ratio of specific heats
 ε = pipe roughness coefficient (inches)
 Φ = friction coefficient
 ρ = density

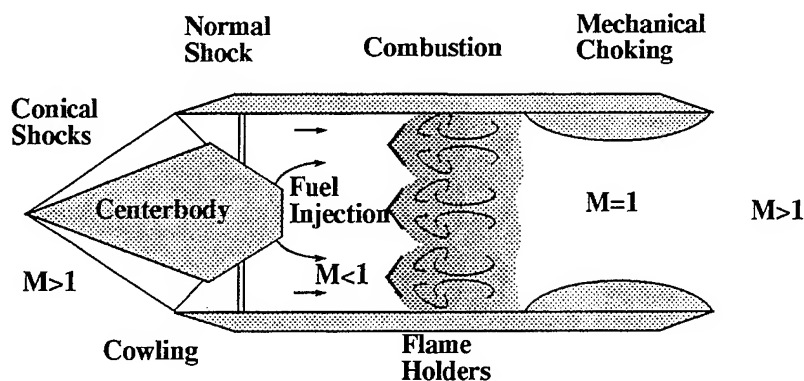
Subscripts

1 = conditions upstream of the valve orifice
 2 = conditions downstream of the valve orifice
 f = conditions in the fill tank
 G = forward path transfer function
 H = feedback path transfer function
 v = conditions at the valve orifice

Introduction

The ram accelerator is a device which accelerates objects to hypersonic velocities by use of a chemical propulsion cycle very similar to that of a conventional ramjet [1]. In the ram accelerator, the projectile is shaped like the center-body of a ramjet and travels freely through a tube filled with a mixture of combustible gases. The shock structure that is developed as the projectile moves through the gases stabilizes combustion behind the projectile, causing acceleration (Fig. 1).

Conventional Ramjet



Ram Accelerator

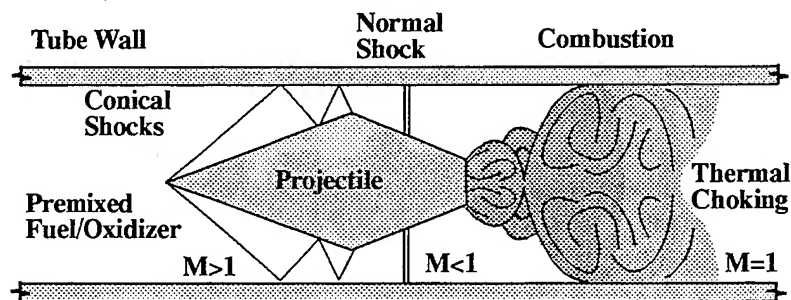


Figure 1. The ram accelerator operates on a chemical propulsion cycle similar to that of a conventional ramjet.

Recent studies [2] suggest that slight changes in gas composition can have significant effects upon ram accelerator performance so that obtaining accurate gas mixtures is very important. In addition to high accuracy, the system used to fill the ram tubes prior to a projectile launch must be quick and efficient if the ram accelerator is to emerge from the research laboratory and become a practical hypersonics test-bed or orbital launch facility in the future.

Both the sonic orifice method for setting ratios of mass-flow rates and partial pressure filling have been used for creating the required combustible gas mixtures, but both methods have inherent problems which have necessitated the search for an alternative gas mixing system. Three

requirements must be met in order to improve upon the current systems: direct measurement of mass-flow rate or of total mass must be made in real time, all gas components should be allowed to flow simultaneously for more efficient operation, and mass *ratios* should be measured and should be able to be set to a specified high degree of accuracy. A feedback-control mechanism which makes use of true mass-flow meters along with integrating capabilities can meet all of the requirements. The concept is to set the mass-flow rate of a primary gas component constant with a mass-flow-rate controller and then to flow the secondary gases through mass-ratio controllers using the mass-flow rate of the primary gas as a reference input (Fig. 2).

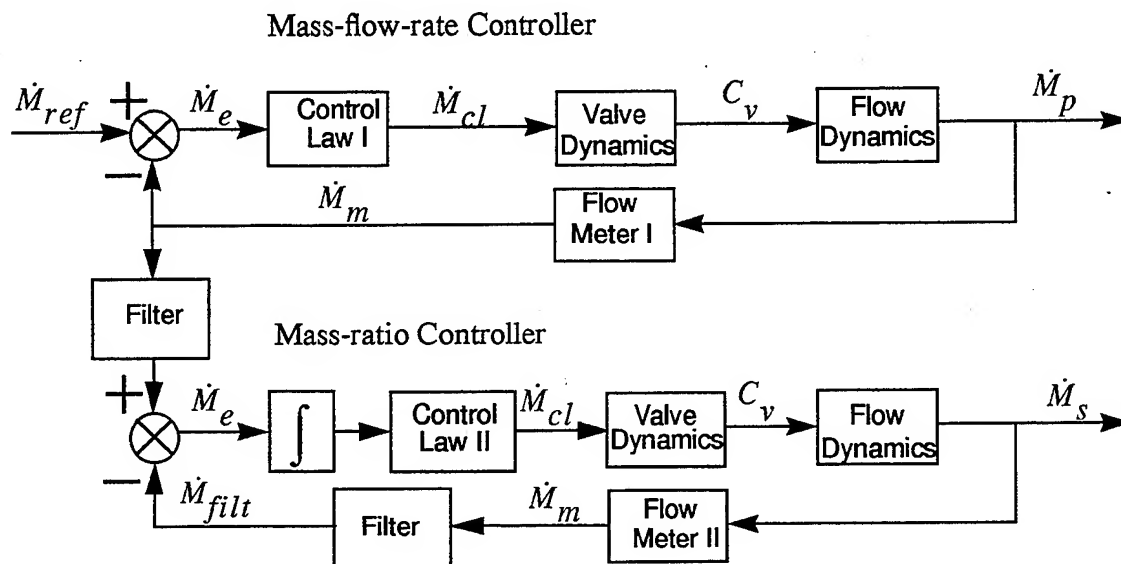


Figure 2. The mass-flow rate of a primary gas is held constant with one control loop, and the output is used as a reference command for a separate control loop which maintains a constant mass ratio between two (or more) gases.

The organization of this paper follows a fairly standard methodology for control system design. The analysis and subsequent selection of control components (mass-flow meter, control valve and actuator) are given first, followed by the dynamic modelling of all elements of the prototype gas mixing system. Once the dynamic modelling has been shown, the mass-flow-rate control law design is given, followed by the design of the mass-ratio control law. Finally, experimental results and conclusions are presented.

Control Component Selection

The resistive thermal detection (RTD) mass-flow meter, which accurately measures the true mass-flow rate (as opposed to *volume*-flow rate) of a gas via heat-transfer principles, best meets the mass-flow-meter requirements as stated in the introduction. Measuring mass-flow rate instead of volume flow rate eliminates the need for extensive pressure and temperature corrections [3].

The RTD mass-flow meter measures mass-flow rates by transferring heat to a diverted stream of the flowing gas and measuring the temperature rise a little further downstream by the use of resistive thermal heating coils in a bridge circuit (Fig. 3). Heat transfer to a flowing gas is primarily

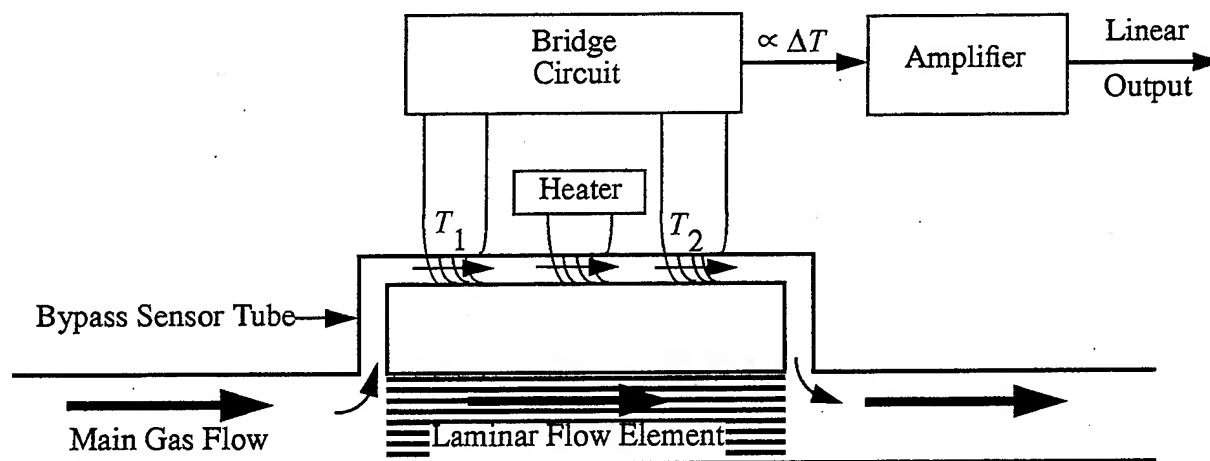


Figure 3. In the RTD measurement concept, heat is transferred to a flowing gas, and the temperature rise of the gas is measured in a bridge circuit and is proportional to the rate of mass flow.

dependent upon mass transport and the specific heat of the gas, so that the mass-flow rate can be detected by this principle. Since c_p is a weak function of temperature, a very small correction factor is needed for variations in gas temperature ($\pm 0.2\%$ of full scale flow per $^{\circ}\text{C}$ between 0 - 50°C).

A micro-metering needle valve is employed as the mass-flow-control element since these valves can withstand high pressures and can provide desirable flow characteristics over the control system operating range. A servo-actuator with a custom designed control board is used for its flexibility in adjusting actuator parameters.

A Macintosh IIci running National Instruments Labview version II software is employed for implementation of the control laws. A National Instruments NB-MIO-16L multifunction analog/digital and timing board provides the hardware/computer interface, and a special termination board, the National Instruments SC-2070, is employed for its thermocouple cold-junction compensation capabilities. Two pressure transducers and two thermocouples are used to make independent measurements of mass vs. time in both the source gas tank and the fill tank into which the gases are to be flowed. These probes and transducers consist of one each of a PX603-1KG5V 1000 psig pressure transducer and a PX603-3KG5V 3000 psig pressure transducer and two JTIN-18E-12 J-type thermocouple probes from Omega Engineering Inc.

Mass-flow Meter Sizing

When choosing the measurement range of mass-flow rates for the mass-flow meter, the total mass to be flowed and the total time required for a fill process must be considered. Knowing the

volume and pressure to which the gases must be filled allows the total mass to be computed, while the required time is a function of the gas dynamic limits of the fill system hardware, the type of gas, the desired gas mixture, and the desired accuracy of the mass-flow meter. After all of the above factors were considered, a Teledyne-Hastings Raydist (model HFM-201) mass-flow meter was selected with a range of 200 Standard Liters per Minute (SLM; the number of liters per minute of a gas flowing at 1 atm and 0° C).

Control Valve and Actuator Sizing

The control valve must be large enough to allow the upper limit mass-flow rates, but must also have desirable control characteristics at the lower mass-flow rates. The actuator must integrate well with the valve to achieve these goals. The objective of the following calculations is to obtain a numerical algorithm which gives the valve C_v factor (an empirical measure of valve size used by most valve manufacturers [4]) as a function of the measurable and independent parameters in the fill system; namely the mass-flow rate (\dot{M}), upstream total pressure (P_1), ram tube fill pressure (P_f), and all of the physical hardware parameters such as tube diameter and the friction coefficient of the tube walls. Once C_v factors have been calculated, the appropriate valve can be chosen. The idealized gas fill system used for these calculations (Fig. 4) has been modelled as a control valve

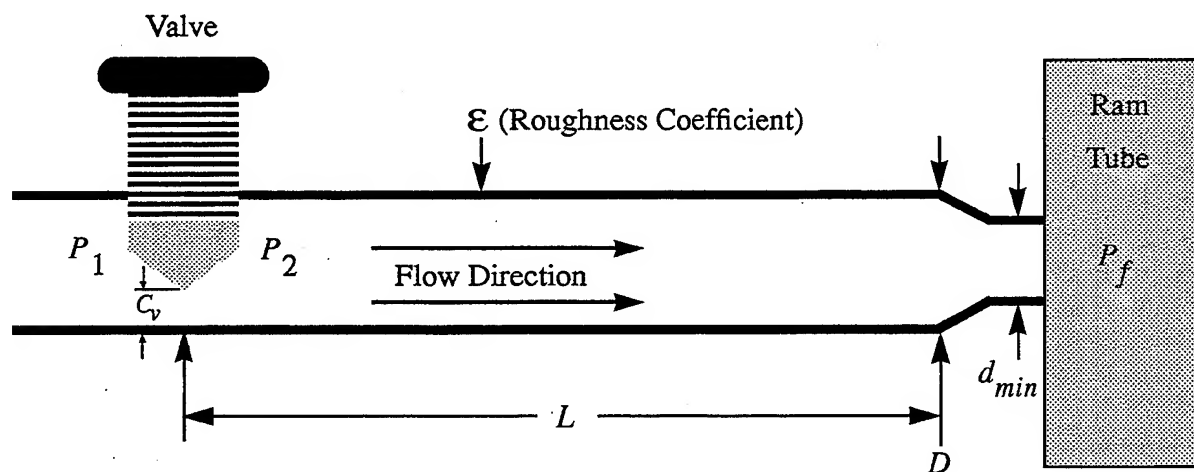


Figure 4. The gas fill system model used for valve sizing calculations.

at the beginning of a high L/D fill tube leading into a large plenum (a section of ram tube). One-dimensional, compressible fluid dynamics with friction accounted for will be used to form the necessary relations among the appropriate variables.

Employing the continuity equation along with isentropic relations gives the well-known equation for the mass flow rate of a calorically perfect gas through a channel of varying cross section, A_v

$$\dot{m} = A_v \left(\frac{2\gamma}{(\gamma-1)RT_1} \right)^{1/2} P_1 \left[\left(\frac{P_v}{P_1} \right)^{2/\gamma} - \left(\frac{P_v}{P_1} \right)^{(\gamma+1)/\gamma} \right]^{1/2} \quad (1)$$

Writing the A_v term as a linear function of the C_v factor, adding a conversion factor to express the mass-flow rate, \dot{M}_{SLM} , in units of Standard Liters per Minute (SLM), and solving for the C_v factor yields

$$C_v = \dot{M}_{SLM} \left\{ K_{cf} \cdot K_{cv} \cdot P_1 \left[\left(\frac{P_v}{P_1} \right)^{2/\gamma} - \left(\frac{P_v}{P_1} \right)^{(\gamma+1)/\gamma} \right]^{1/2} \right\}^{-1} \quad (2)$$

where

$$K_{cf} = 1315.74 \sqrt{\frac{\gamma}{(W)(\gamma-1)}} \left[\frac{L}{N \cdot \text{minute}} \right] \quad (3)$$

and K_{cv} is the proportional constant which relates the C_v factor to the effective orifice area. Note that the $1/\sqrt{T_1}$ term from Eq. (1) is included in K_{cf} , where T_1 is assumed to be room temperature (300 K).

From this point, we need to determine P_v as a function of known values. This will be achieved by working backwards from known conditions at the large plenum, taking into account the pressure losses due to friction along the high L/D fill tube.

Following the work by Shames [5], which addresses pressure loss along the fill pipe due to shear stress at the pipe wall, a relation between the upstream Mach number and other system parameters is given as

$$\left(\frac{1}{M_2} - \frac{1}{M_f} \right) + \left(\frac{\gamma+1}{2} \right) \cdot \ln \left(\frac{M_2^2 (2 + (\gamma-1)M_f^2)}{M_f^2 (2 + (\gamma-1)M_2^2)} \right) = \frac{\Phi \gamma L}{D} \quad (4)$$

where M_2 and M_f are the Mach numbers at upstream station 2 and at the entrance to the ram tube just prior to the fitting restriction, respectively. The constant diameter of the fill pipe is given by D , and L is the length of the fill pipe. The friction coefficient, Φ , is a function of the Reynolds number, the diameter of the fill pipe, and the pipe roughness parameter, ε , and for the Reynolds numbers of interest can be written as

$$\Phi = \frac{0.25}{\left[\log \left(\frac{\varepsilon}{3.7 \cdot D} \right) + \left(\frac{5.74}{(Re)^{0.9}} \right) \right]^2} \quad (5)$$

where the parameters ε and D have been empirically determined for the ram accelerator fill pipe to be 0.03175 mm and 3.861 mm respectively.

Employing the continuity equation, the ideal gas law, the definition of the Mach number, and adding a unit conversion factor, an expression for the Mach number at the entrance to the ram tube can be derived as

$$M_f^2 = \left[\frac{\dot{M}_{SLM} P_s}{P_f A_f (6 \times 10^4)} \right]^2 \frac{W}{\gamma T_f R_u} \quad (6)$$

where all variables must be expressed in SI units, excepting \dot{M}_{SLM} which is in Standard Liters per Minute.

Isentropic relations along with the continuity equation, the definition of the Mach number and the ideal equation of state give

$$P_2 = \frac{\dot{m}}{A_2 M_2} \left(\frac{R \cdot T_{t_2}}{\gamma \{1 + [(\gamma - 1)/2] M_2^2\}} \right)^{1/2} \quad (7)$$

Finally, by assuming isentropic, incompressible conditions from the exit plane of the valve to station 2 and employing the continuity equation and Euler's equation, the pressure at the valve orifice is shown to be

$$P_v = P_2 \left\{ \frac{\gamma M_2^2}{2} \left[1 - \left(\frac{A_2}{C_v \cdot K_{cv}} \right)^2 \right] + 1 \right\} \quad (8)$$

Equations (2) through (8) constitute a complete set of relations which may iteratively solved for the required valve C_v factor as a function of known system parameters and flow conditions. These equations have been numerically solved for the range of flow conditions that the control system must cope with, and, along with considerations of linearity and fine-control capability, have helped to determine that the Whitey SS-21RS4 micro-metering valve ($0 \leq C_v \leq 0.007$) will integrate well with the control system.

The actuation of the valve has been achieved with a switched servo motor provided by ETI Systems. The standard motor speed of 8 rpm yields a 3 SLM/sec rate of change in the mass-flow rate under typical controller operating conditions which provides fine control capability without sacrificing speed of operation.

Prototype Dynamic Modelling

Referring to Fig. 5, the mass-flow meter has been placed immediately upstream of the control valve. In this way the meter and valve can be kept close together, but any turbulence added to the flow by the valve will not affect the meter. Additionally, having the meter upstream of the valve

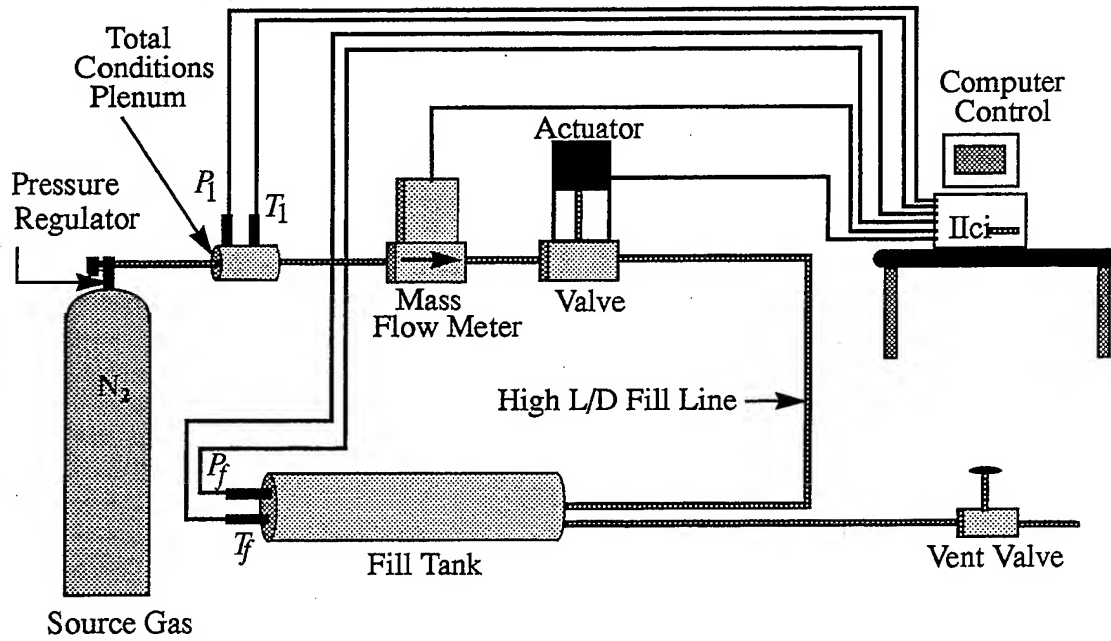


Figure 5. Prototype control system schematic.

keeps the pressure of the gas flowing through the meter roughly constant which increases the precision of the mass-flow measurements.

Mass-flow-meter Dynamic Response Measurements

The time response of the mass-flow meter can be accurately modelled as a simple first-order lag. Step changes in mass-flow rate were applied to the mass-flow meter by quickly opening or closing a valve and recording the meter output voltage. The response data were normalized to a final value of unity and the resulting transfer function for the flow meter has been determined to be

$$\frac{\dot{M}_m(s)}{\dot{M}(s)} = \frac{5.85 \times 10^{-3} \text{ Volts}}{(s + 0.2339) \text{ SLM}} \quad (9)$$

with a conversion factor of 0.025 (V/SLM) included since the output of the meter is in Volts, and the mass-flow rate is treated in SLM (Fig. 6).

Control Valve and Actuator Modelling

The control valve C_v factor is accurately modelled as a linear function of the number of revolutions of the valve stem, and the motor speed of the switched actuator is modelled by a

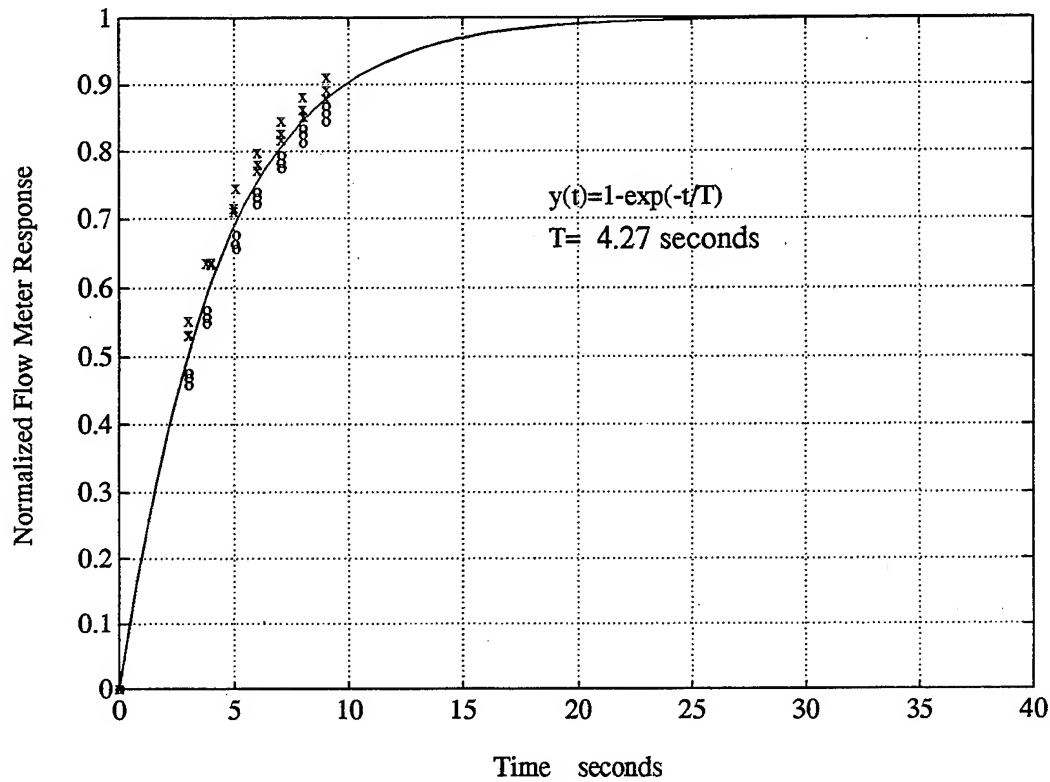


Figure 6. Measurements of the mass-flow-meter response to a step input were made for several mass-flow rates and the results normalized to unity. The data was then fit with a first order exponential function as shown.

constant value, either positive or negative depending upon the sign of the input voltage. The mathematical model for the valve is the following

$$\frac{dC_v}{dt} = \pm K_{v_a} \quad (10)$$

An equation can easily be written for K_{v_a} in terms of measurable quantities in the following way,

$$K_{v_a} = \dot{R}_n \frac{\Delta(C_v)}{\Delta(R_n)} \quad (11)$$

where R_n is the number of revolutions of the valve stem. These quantities have been empirically determined and are given in Table 1 along with the value for K_v , where gpm_1 refers to the units of the C_v factor (gallons per minute of water which will flow through the orifice with a pressure drop of 1 psi).

Due to the actuator motor switch, regardless of the magnitude of the input voltage, the rate at which the motor turns is constant. This simple nonlinearity is easily analyzed in terms of the

Table 1: Valve/Actuator Parameters

$\dot{R}_n \left[\frac{\text{revolution}}{\text{sec}} \right]$	$\frac{\Delta(C_v)}{\Delta(R_n)} \left[\frac{\text{gpm}_1}{\text{revolution}} \right]$	$K_{v_a} \left[\frac{\text{gpm}_1}{\text{sec}} \right]$
1.261×10^{-1}	9.33×10^{-4}	1.177×10^{-4}

equivalent describing function linear model which is a gain term that is a function of the actuator input voltage, \dot{M}_{cl} , as shown here

$$K_v = \frac{4}{\pi} \cdot \frac{K_{v_a}}{|\dot{M}_{cl}|} \quad (12)$$

This gives the following linearized transfer function for the C_v factor

$$\frac{C_v(s)}{\dot{M}_{cl}(s)} = \frac{K_v}{s} \quad (13)$$

The maximum value of K_v will occur near steady-state conditions when $|\dot{M}_{cl}(s)|$ is a minimum. The valve actuator has a dead-zone, V_{DZ} , between ± 0.02 Volts so that the value of K_v will never become infinite in this control system, and the gain of the compensator will be able to change the error value magnitude at which the system reaches steady-state. The maximum value of K_v to be encountered during operation is given approximately by the following relationship

$$K_{v_{max}} = \frac{4}{\pi} \cdot \frac{K_{v_a} \cdot K_{cl} \cdot \prod Z_{cl}}{|V_{DZ}| \cdot \prod P_{cl}} \quad (14)$$

where the subscript, cl , refers to the elements of a forward loop control law (Fig. 2). This relationship will be employed during the control law design phase to help determine stability limits.

Mass-flow-rate Dynamics

A simplified model of the mass-flow-rate dynamics is obtained by rearranging Eq. (2) to obtain

$$\dot{M}_{SLM} = K_{cf} C_v K_{cv} P_1 \left[\left(\frac{P_v}{P_1} \right)^{2/\gamma} - \left(\frac{P_v}{P_1} \right)^{(\gamma+1)/\gamma} \right]^{1/2} \quad (15)$$

K_{cv} is empirically determined by setting the valve to a known C_v factor, and by setting P_1 and P_v to known values and then measuring \dot{M}_{SLM} . These measurements lead to the following value

$$K_{cv} = 7.1475 \times 10^{-5} \quad (16)$$

Making use of Eq. (15), a linearized transfer function for the mass-flow-rate dynamics is obtained by noticing that the pressure terms will generally remain constant during normal operations of the control system (choked flow and regulated upstream pressure, P_1). However, if

P_1 should drop below the regulator level, the volume of the source gas plenum is relatively large so that the rate of change of P_1 will be very small compared to the other dynamic terms in the system. If the flow through the control valve should unchoke, since the ram tubes also have large volumes, the P_v/P_1 terms will also have relatively small rates of change. Therefore, the mass-flow-rate dynamics may be adequately described with the following linear transfer function

$$\dot{M}_{SLM}(s) = K_{fd} \cdot C_v(s) \quad (17)$$

where K_{fd} will have a range of values for which the control laws must be designed to operate.

The upper gain limit, easily determined by the use of Eq. (15), occurs when the flow through the valve is choked and the upstream pressure is at the maximum value of 1000 psig. The minimum gain is slightly more difficult to find, but can be computed with the help of the computer program that was used for sizing the control valve. By running the program for the case where P_f is a minimum (about 400 psig for the ram accelerator) and where the mass-flow rate is a minimum (about 50 SLM for nitrogen), the computed values of P_1 and P_v corresponding to the maximum C_v factor for the valve (0.007) can be used to determine the maximum gain (Eq. (18)).

$$7 \times 10^3 \leq K_{fd} \leq 60 \times 10^3 \quad (18)$$

These limits define the gain range for which the gas mixing system must provide robust control.

Mass-flow-rate Control Law Design

As mentioned in the introduction, the control of the mass ratio of two (or more) gases is achieved by setting the mass-flow rate of a primary gas to a constant value and then controlling the integrated mass ratio of the secondary gas(es) relative to the primary gas with a separate control law.

The block diagram representation of the mass-flow-rate controller appears in Figure 7. As

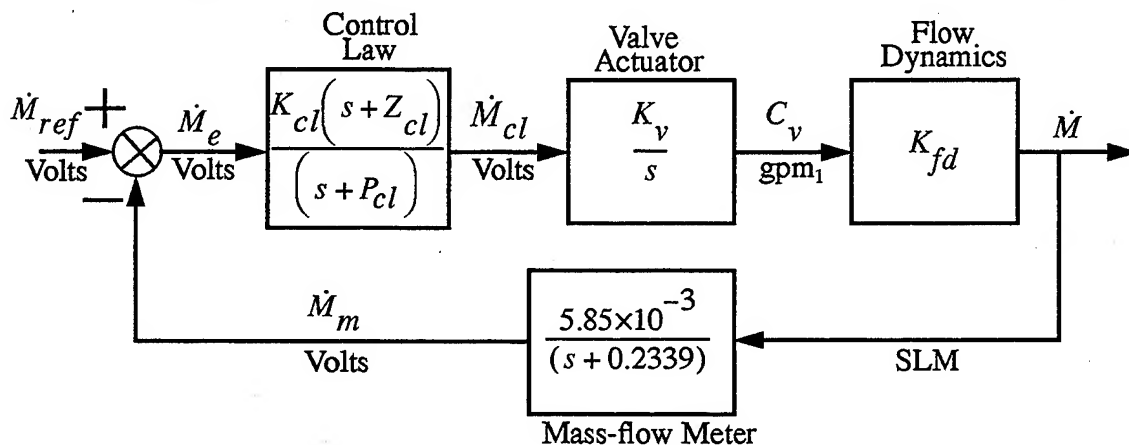


Figure 7. This block diagram represents the system model used for analyzing the mass-flow-rate controller.

noted earlier, the switching action of the valve means that the gain of the control law, K_{cl} , is unable to adjust system dynamics in the usual way. The control law gain can scale the actuator input voltage such that steady-state is reached at a desired level of mass-flow rate accuracy, but the actuator will open (or close) the valve at the same rate regardless of the magnitude of the input voltage; the actuator only differentiates between positive and negative voltage. For this reason, the control law dynamic parameters (poles and zeros) must be chosen such that the system response will be robust over the entire variable gain range.

As previously mentioned, the valve actuator has a dead-zone between ± 0.02 Volts so that if the input to the actuator drops within this range, the control system will be in steady-state. This is not desirable until the mass-flow rate has been set to an acceptable level of accuracy. The control law gain, K_{cl} , can be used to scale the actuator input voltage in order to set the accuracy of the mass-flow-rate controller, carefully noting that too high of a value for K_{cl} may cause continuous small amplitude oscillations due to system noise.

An expression for the steady-state error in terms of percent error is given by

$$\dot{M}_e = \dot{M}_{ref} \left[1 - \frac{\dot{M}_m}{\dot{M}_{ref}} \right] = \dot{M}_{ref} E_p \quad (19)$$

where E_p is the percent error between the measured mass-flow rate and the reference command mass-flow rate.

The steady-state gain of the control law will be given by the following equation

$$K_{ss} = \frac{K_{cl} \cdot \prod Z}{\prod P} \quad (20)$$

When the steady-state gain is multiplied by the desired minimum steady-state error term, the result should equal 0.02 Volts or greater so the valve actuator will still actively control the flow to this point. Multiplying Eqs. (19) and (20) and solving for K_{cl} gives

$$K_{cl} = \frac{(0.02) \prod P}{\prod Z \cdot \dot{M}_{ref} \cdot E_p} \quad (21)$$

This equation is easily programmed to allow the user of the control system to set the control law gain for any desired value of E_p .

For a simple first-order control law, the range of effective system gain for which the compensator must provide robust control can be found by applying Eqs. (14) & (18). Utilizing root locus plots and nonlinear simulations quickly helps to determine that the following control law will

provide robust control without excessive oscillations to set the mass-flow rate to within 1% of the maximum command value (200 SLM, or 5 Volts)

$$\frac{\dot{M}_{cl}(s)}{\dot{M}_e(s)} = \frac{17.1(s + 0.2339)}{(s + 10)} \quad (22)$$

Note that the gain margin for the system with this particular control law can easily be shown to be infinite so that stability of the control system is guaranteed for all positive gain values.

Mass-ratio Control Law Design

For mass-ratio control, as seen in the block diagram (Fig. 8), an integrator must be added to the

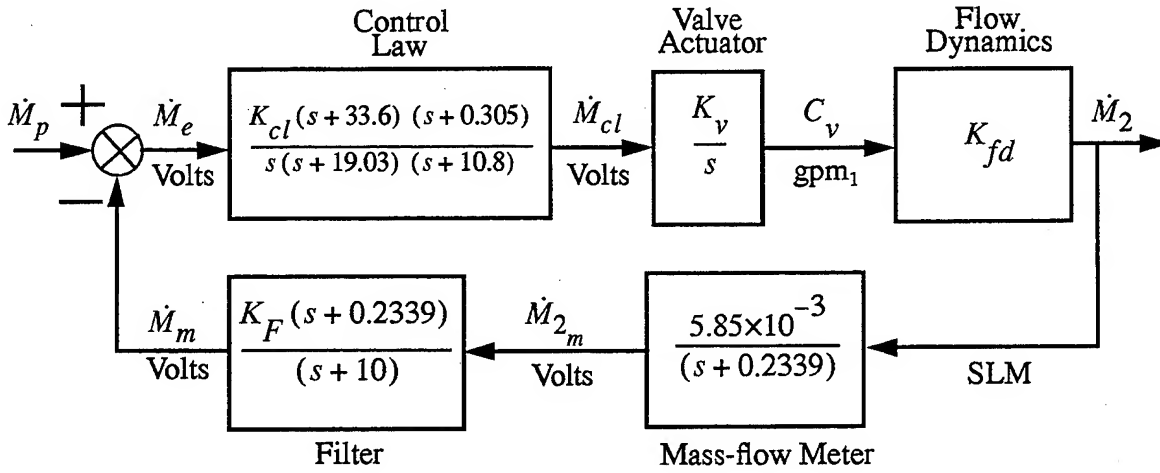


Figure 8. With the addition of the integrator in the forward loop, and the filter in the feedback path, the control of mass ratios can be achieved.

control law in order to drive the mass-ratio error (not just the error in the ratio of mass-flow rates) to zero, and this places a second pole at the origin, bringing the system transfer function to third order.

Since the reference input value, \dot{M}_p , is the mass-flow rate of the primary gas, the feedback value, \dot{M}_{filt} , must be made to represent what the mass-flow rate of the primary gas should be in order to obtain the correct mass ratio between the secondary and primary gases. Defining the desired mass ratio in the following way

$$\mathfrak{R}_s = \left[\frac{\dot{M}_s}{\dot{M}_p} \right]_{desired} \quad (23)$$

the feedback term must be, simply,

$$\dot{M}_{filt} = \frac{\dot{M}_s}{\mathfrak{R}_s} \quad (24)$$

The desired mass ratio, \mathfrak{R}_s , is known, but \dot{M}_s is not directly available in this system. The measurement of the mass-flow rate comes from the mass-flow meter which equals the true mass-flow rate only in steady state. A filter may be employed, however, which effectively compensates for the lag in the reading from the mass-flow meter. This minimizes the integral error so that the mass ratios may be much more quickly set. Without the filter, an overshoot of a few percent with a very long decay time constant must be tolerated as was discovered during nonlinear simulations and during subsequent testing of the mass-ratio control system.

The system transfer function with the mass-flow-meter pole effectively cancelled by the filter is given by

$$\frac{\dot{M}_s}{\dot{M}_p} = \frac{K_{fd}K_vN_{cl}(s+10)}{\left[s^2(s+10)D_{cl} + K_{fd}K_vN_{cl}K_F(5.85 \times 10^{-3}) \right]} \quad (25)$$

where N_{cl} and D_{cl} are the numerator and denominator dynamic terms of the control law, and K_F is defined such that the steady-state gain of the filter is equal to $1/\mathfrak{R}_s$. The definition is, simply,

$$K_F = \frac{10}{(0.2339)\mathfrak{R}_s} \quad (26)$$

The use of a third-order controller (in addition to the integrator) makes the characteristic equation of the closed-loop transfer function sixth-order. The third order controller has six parameters (three poles and three zeros) which may be used to set the poles of the system transfer function as desired. One must only be careful to adhere to any physical limits imposed by the system hardware.

The denominator polynomial of the system transfer function is written as

$$D_W(s) = D_G(s) \cdot D_H(s) \cdot [(s+P_1)(s+P_2)(s+P_3)] \\ + N_G(s) \cdot N_H(s) \cdot [(s+Z_1)(s+Z_2)(s+Z_3)] \quad (27)$$

When the pole and zero terms are expanded, and the constant terms are placed on the right side, Eq. (27) can be written in the following summation form

$$\sum_{j=1}^3 \left[\left(D_G(s_n) \cdot D_H(s_n) \cdot s_n^{(3-j)} \right) \cdot a_{(j-1)} + \left(N_G(s_n) \cdot N_H(s_n) \cdot s_n^{(3-j)} \right) \cdot a_{(j+2)} \right] \\ = -s_n^3 (D_G(s_n) \cdot D_H(s_n) + N_G(s_n) \cdot N_H(s_n)) \quad (28)$$

with

$$a_0 = P_1 + P_2 + P_3 \quad (29)$$

$$a_1 = P_1 \cdot P_2 + P_1 \cdot P_3 + P_2 \cdot P_3 \quad (30)$$

$$a_2 = P_1 \cdot P_2 \cdot P_3 \quad (31)$$

$$a_3 = Z_1 + Z_2 + Z_3 \quad (32)$$

$$a_4 = Z_1 \cdot Z_2 + Z_1 \cdot Z_3 + Z_2 \cdot Z_3 \quad (33)$$

$$a_5 = Z_1 \cdot Z_2 \cdot Z_3 \quad (34)$$

Equation 28 must then be written n times ($n = 6$ in this case), once for each value of s_n that coincides with a desired pole location of the system transfer function. The resulting values for a_n must be used in conjunction with Eqs. (29) through (34) to solve for the control law pole and zero values. The third order control laws found in this way for this system generally have a pole and a zero at nearly equal values which can be cancelled to reduce the control law order to 2. This simplifies the implementation of the control system and through analysis was shown not to significantly alter the system response.

Through iterative frequency response analysis of the linearized system, and through simulations of the nonlinear system, the following control law design has been shown to produce desirable characteristics

$$\frac{\dot{M}_{cl}(s)}{\dot{M}_e(s)} = \frac{K_{cl}(s + 33.6)(s + 0.305)}{s(s + 19.03)(s + 10.8)} \quad (35)$$

and the filter transfer function is given by

$$\frac{\dot{M}_{filt}}{\dot{M}_{s_m}} = \frac{(42.7533)(s + 0.2339)}{\mathfrak{R}_s \cdot (s + 10)} \quad (36)$$

Once again utilizing Eq. (21), a control law gain of $K_{cl} = 8.02$ is determined to set the steady-state mass-flow rate of the secondary gas to within 1% of the maximum mass-flow rate (200 SLM, or 5 Volts). Analysis of this control law demonstrates that the system is stable for the entire effective gain range of the system (computed with Eqs. (14) & (18)). As the effective gain approaches zero (as would happen if the error term approached infinity), the gain margin approaches infinity and the phase margin approaches zero. The gain margin monotonically decreases to a value of 2.13 db at the maximum effective system gain ($K_{eff} = 354$). The phase margin increases to a maximum of 61.0091 deg. at $K_{eff} = 35$ and then decreases to a value of 8.11 deg. at $K_{eff_{max}}$. Note that even if this system is driven to instability (by increasing K_{cl} too much), this will only result in a small amplitude steady-state oscillation. This is due to the manner in which the nonlinear actuator motor switch operates. As the error term increases, the effective system gain decreases, and this brings the effective system gain back into the stable region. Nonlinear

simulations have again been used to verify the results of the linear analysis and have also been used to help tune the controller parameters for a desirable output response.

Experimental Results

A Macintosh IIfx running Labview II software from National Instruments has been employed for data acquisition and the implementation of the discretized continuous time control laws developed previously. Several data runs have been made with both the mass-flow-rate controller and the mass-ratio controller flowing nitrogen gas in order to demonstrate the following:

- That the mass-flow-rate controller is capable of setting and maintaining constant mass-flow rates to within a high degree of accuracy.
- That the mass-ratio controller is capable of setting and maintaining the mass ratio between two gases to within a high degree of accuracy.

Mass-flow-rate Controller

With a unity feedback scheme (no control dynamics), the mass-flow-rate controller is stable, but the step response is oscillatory with a relatively long decay constant (Fig. 9) which shows that a control law is required for mass-flow-rate control. Notice that although the nonlinear simulation data does not match exactly with the empirical measurements, the shape of the response is similar, and the frequency of oscillation is reasonably well matched.

In Fig. 10 appears the response of the mass-flow-rate control system to the same 50 SLM step command input as in Fig. 9, but with the control law implemented as designed. The oscillations have been eliminated, and the speed of response is as quick as the hardware allows. The control voltage input to the valve actuator is plotted vs. time along with the measured mass-flow rate vs. time to demonstrate that although the mass-flow meter shows a lag in response, the control voltage reaches zero very quickly. At this point, the valve has reached steady state meaning that the mass-flow rate has been set constant within about six seconds, while the lagged response of the meter cannot verify this for as long as 25 seconds. The theoretical simulation data appear with the empirical data and show excellent agreement.

The next set of data demonstrates the operation of the mass-flow-rate controller under different upstream pressure conditions. In Figs. 9 and 10, the upstream pressure was set to 1000 psig, while in this case (Fig. 11), the upstream pressure has been reduced to 625 psig. Additionally, the nitrogen was allowed to flow until the pressure had equalized between the source and fill tanks to help determine the limit of the controller's ability to maintain a mass-flow rate under these conditions. The plots show that the control system is operating very well under these lower pressure conditions, and that the mass-flow rate is kept to within 1% of the command value until the fill tank pressure reaches about 85% of the upstream pressure. In this case, the valve orifice unchokes at about 71 seconds yet the mass-flow rate is maintained roughly constant for another 45

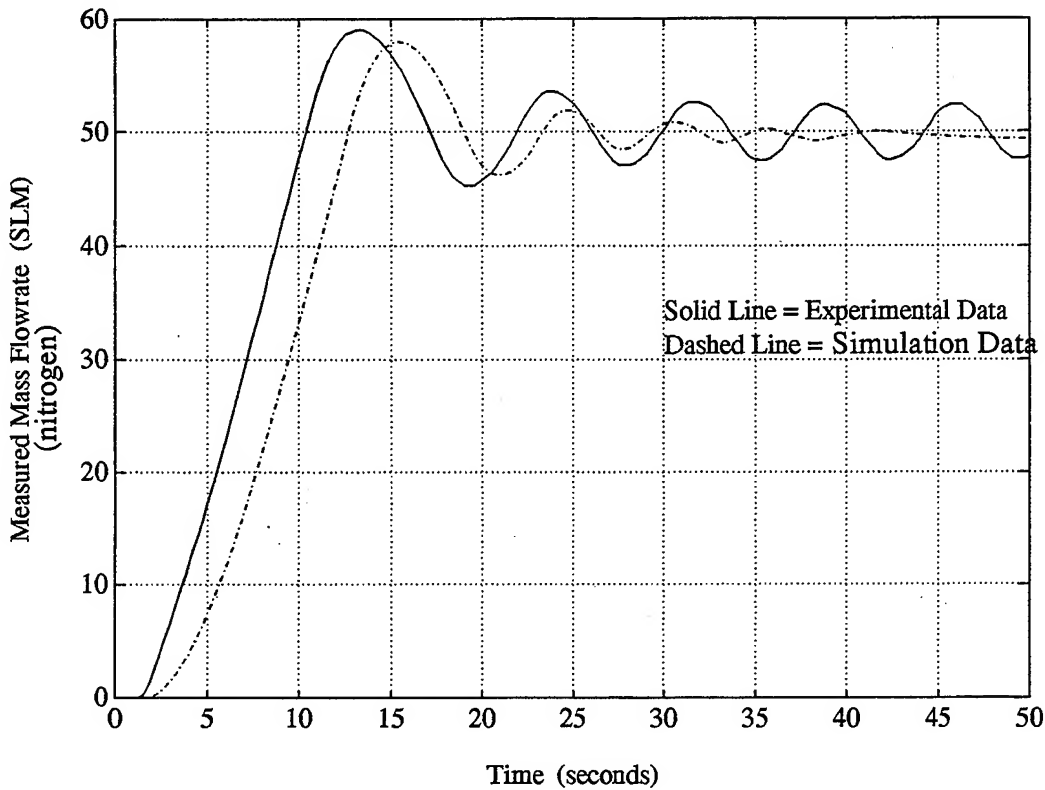


Figure 9. The response of the mass-flow-rate control system to a 50 SLM step command with a simple unity feedback scheme showing that control dynamics are necessary. Both experimental and simulation data appear in the plot. Upstream pressure: 1000 psig

seconds, which is a significant improvement over the sonic orifice method of setting mass-flow rates.

Mass-ratio Controller

Measurements of the mass-ratio control system have been made in order to demonstrate that the control law is operating as designed. Independent measurements of the accumulating mass have also been made during these runs in order to determine the accuracy limitations in the mass-ratio control system.

The error in the final mass ratio to be set by this control system depends upon two factors: the integral error of the mass-flow-meter reading, and the error introduced in the control loop due to

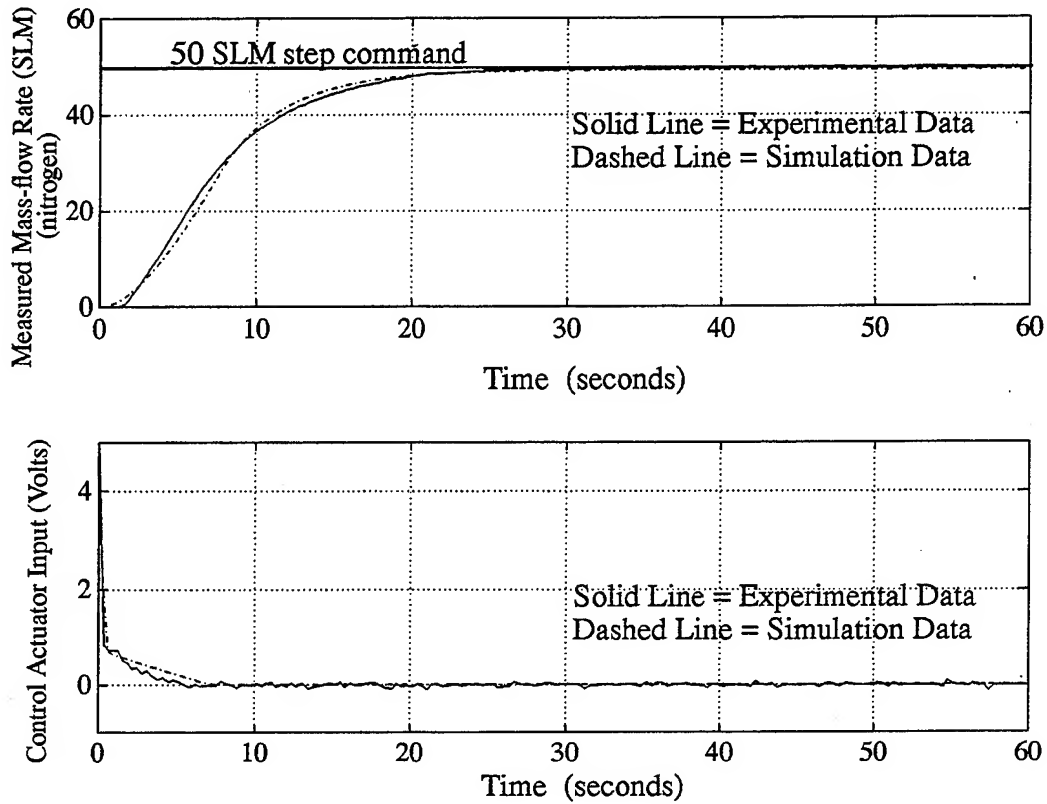


Figure 10. With the first order control law in operation, the step response of the mass-flow-rate controller is greatly improved. Note that the control voltage input to the actuator indicates steady-state conditions have been reached within 6 seconds, approximately 20 seconds before the mass-flow meter can verify this. Upstream pressure: 1000 psig.

discrete integration. With these factors accounted for, the percent error in the final mass ratio is given by

$$E_{MR} = \frac{2E_p}{(1 - E_p)} \quad (37)$$

where the percent error in the mass-flow-meter measurement, E_p , has been assumed to be equal in magnitude for the computation of the command mass error and the feedback mass error. This relationship shows that the error in the mass ratio is about twice that of the error in the mass-flow-rate measurement so that the mass-flow meters must be calibrated to twice the accuracy that the final mass ratio is desired to have.

Since the prototype system consists of only one valve and meter, the command signal to the mass-ratio control system must be simulated. This is accomplished by applying a step command input with the computer software which simulates the case where the primary gas is already flowing at a constant rate when the mass-ratio control system is turned on. All runs use nitrogen

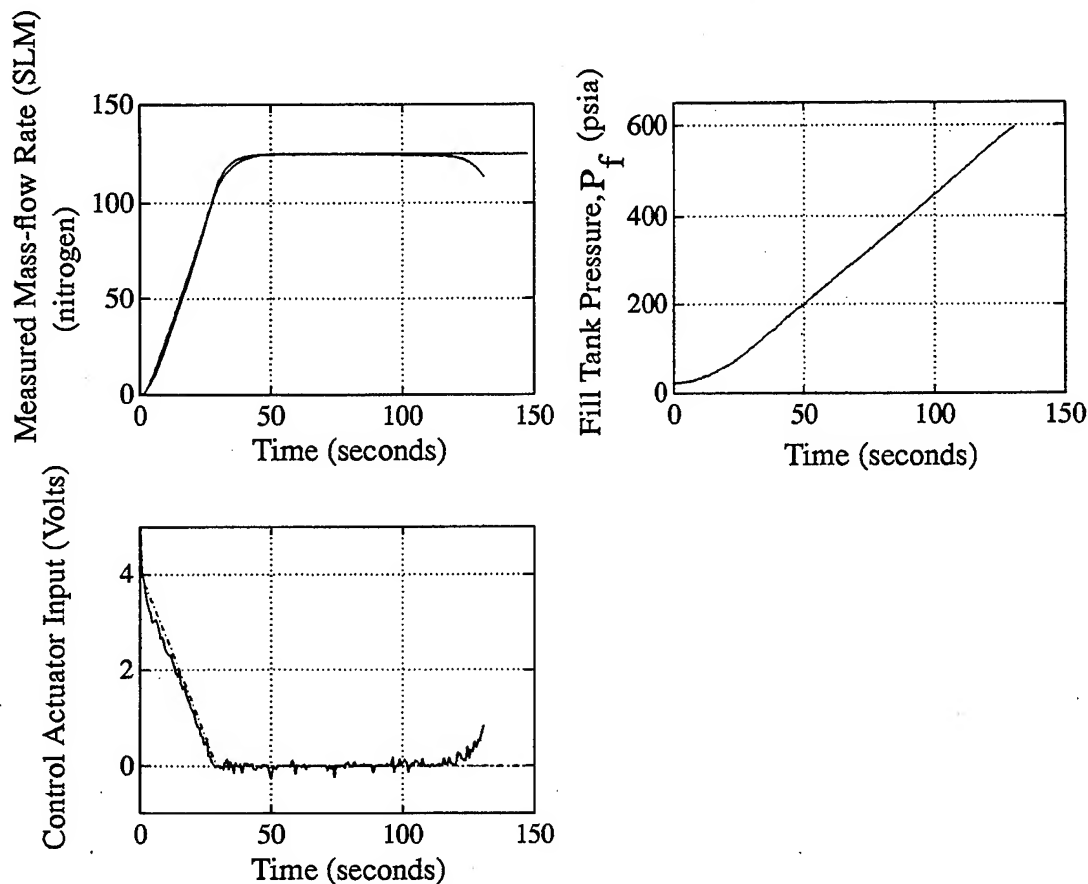


Figure 11. With a lower upstream pressure of 625 psig, the control system still demonstrates excellent performance. The command mass-flow rate is maintained until the fill tank pressure reaches about 85% of the upstream pressure. The theoretical unchoking point occurs at $P_f = 305$ psia which corresponds to $t = 71$ seconds.

gas, and the system is set up to achieve mass ratios equal to unity for simplicity in the data reduction.

The first set of data (Fig. 12) has been recorded with an upstream gas pressure of 1000 psig and a simulated command input of 50 SLM. The plot of mass ratio vs. time shows both the data from within the control loop and that from the pressure and temperature calculations of the accumulated mass. The control loop data demonstrates that the control law is operating properly by setting the mass ratio to the command value of unity. A discrepancy of about 5% between the two independent measurements arises from the error in the pressure and temperature measurements and whatever error exists in the mass-flow-meter calibration. The narrowing of the accuracy limits for the mass-ratio controller may require a more accurate calibration, but the independent measurements are within the experimental error of the measurement probes so that the concept of mass-ratio control has been validated.

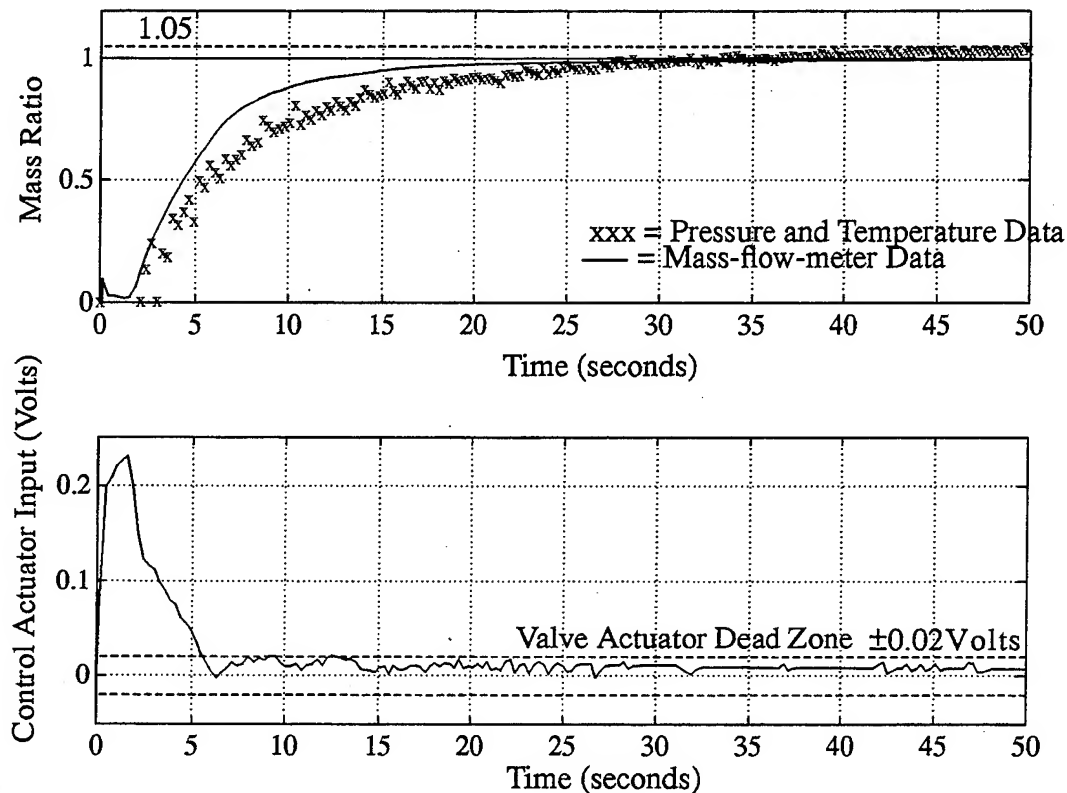


Figure 12. The mass-ratio controller operating with nitrogen gas at an upstream pressure of 1000 psig demonstrates that the control law operates properly. The plot of control actuator input shows that the valve has been set to its steady-state value in under 6 seconds.

The second set of data (Fig. 13) shows the operation of the mass-ratio controller under lower pressure conditions for the same simulated command input of 50 SLM. The control system appears to be very effective in this case and the pressure and temperature data are in better agreement than before. Whether or not this is an effect due to the varying pressure cannot be verified without employing measurement probes with higher accuracy.

Conclusion

The concept of setting mass ratios with a feedback controller employing RTD mass-flow meters and switched servo actuated valves has been validated. The operation of both the mass-flow rate and the mass-ratio control subsystems have been verified through independent measurements of accumulated mass to work within experimental accuracy. Furthermore, the analysis in this paper has shown that the accuracy of this type of feedback controlled gas mixing system is dependent only upon the calibration accuracy of the mass-flow meters that are employed. Subsequent analysis

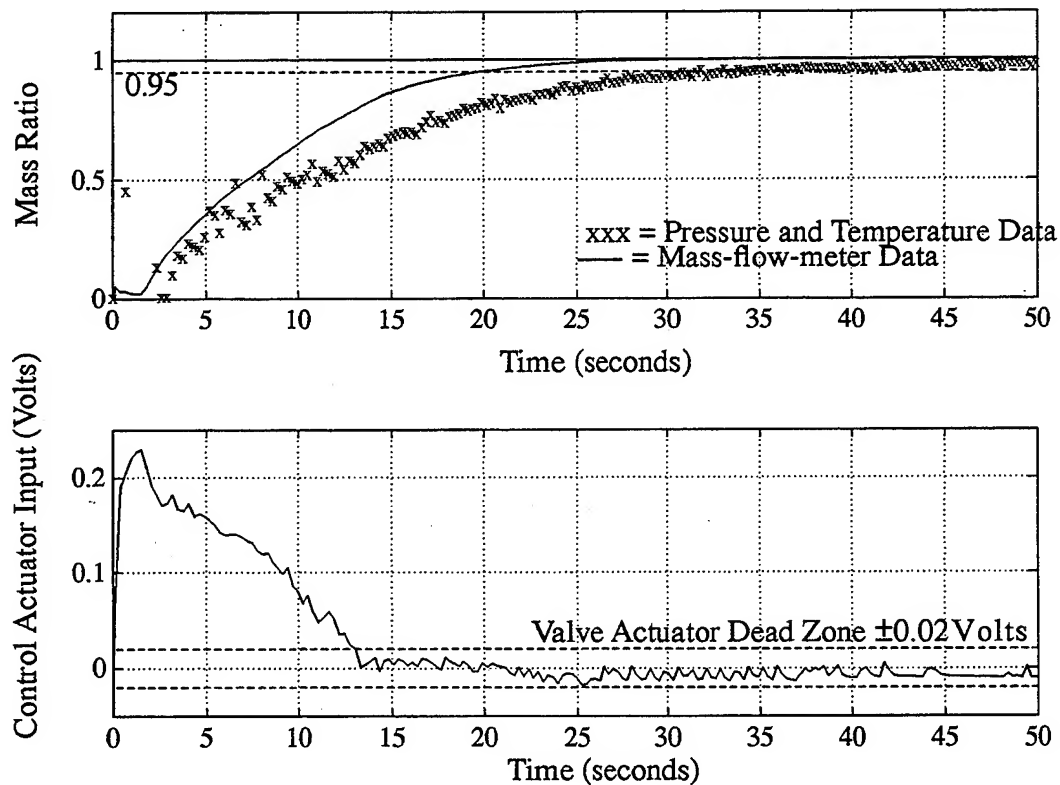


Figure 13. The mass-ratio controller operating with nitrogen gas at an upstream pressure of 600 psig demonstrates that the control law can still maintain an accurate mass-ratio setting under different pressure conditions. The plot of control actuator input vs. time shows that the valve has reached steady state within about 12.5 seconds.

at the University of Washington [6] has demonstrated that this type of control will also work with CO_2 , which exhibits non-ideal behavior.

Acknowledgments

This work was supported in part by USAF Contract No. F08635-89-C-0196. The authors wish to express their gratitude to the following for their research efforts in support of this work: J. Auzias de Turenne, E. Burnham, G. Chew, B. Dunmire, A. Higgins, J. Hinkey and C. Knowlen. The authors also wish to thank Professors A. Hertzberg and T. Mattick for their contributions and discussions, and Dr. D. Bogdanoff for the information and consultations he provided regarding current research in shock tunnel gas mixing systems at NASA Ames Research Center. Finally, the equipment and expertise in control systems supplied by Prof. J. Vagners has greatly enhanced the quality of research presented here.

References

- 1) Hertzberg, A., Bruckner, A. P., and Bogdanoff, D. W., "Ram Accelerator: A New Chemical Method for Accelerating Projectiles to Ultrahigh Velocities," *AIAA Journal*, Vol. 26, No. 2, Feb. 1988, pp. 195-203.
- 2) Higgins, A. J., C. Knowlen, and Bruckner, A. P., "An Investigation of Ram Accelerator Gas Dynamic Limits," AIAA Paper 93-2181, 29th Joint Propulsion Conference and Exhibit, Monterey, CA, June 28-30, 1993.
- 3) Olin et al., United States Patent No. 4,487,062., Dec. 11, 1984.
- 4) Lyons, Jerry L., *Lyons' Valve Designers Handbook*, Van Nostrand Reinhold Co., New York, 1982, pp. 180-185.
- 5) Shames, Irving H., *Mechanics of Fluids*, McGraw-Hill, New York, 1962, Section 11.19.
- 6) Koch, A., "Analysis of a Gas Mixing System Flowing a Non-Ideal Test Gas" 43rd AIAA Region VI Student Conference, Tucson, AZ, April 1-3, 1993.

Session 2

EXPERIMENTS

2nd International Workshop on RAM Accelerators
Seattle / WA, USA, July 17-20, 1995

**RAMAC in 90 mm Caliber or RAMAC 90.
Starting Process, Control of the Ignition Location
and Performance in the Thermally Choked Propulsion Mode**

M. Giraud - J.F. Legendre - G. Simon - M. Henner - D. Voisin*
ISL - French-German Research Institute of Saint-Louis, France

* Laboratoire de Combustion et Systèmes Réactifs (CNRS) Orléans, France

Abstract:

After a description of both the facility organization and the projectile-sabot design, this paper deals in particular with the RAMAC 90 working in the thermally choked propulsion mode or subdetonative combustion mode. The first part of the paper concerns the whole starting process and particularly the fine control of the ignition source location at the rear of the projectile. The second part gives the performances of the RAMAC 90, organized either in single stage (i. e. by using only one ternary explosive gas mixture composed of methane, oxygen and nitrogen) or in two stages (two successive gas mixtures separated by a 3 mm thick PVC diaphragm) working only in the thermally choked propulsion mode. The way through the two different mixtures was achieved without any difficulty. For a projectile mass of 1.340 kg, a RAMAC length at present of 16.2 m (or 180 calibers), an entrance velocity of 1335 m/s and an initial filling pressure P_0 in the range 3 - 4.5 MPa, the maximum exit velocity was about 2 km/s and the average acceleration Γ in the range 3.5 - 7 kg's. The average ballistic efficiency was 0.22. Owing to the results concerning the combustion zone at the rear of the projectile (pulsating phenomenon), the understanding of the thermally choked propulsion mode is now better. According to the projectile velocity achieved, avoiding problems such as a strong balloting motion of the projectile provoked by the crossing of the transdetonative propulsion mode, the RAMAC 90 is now well suitable for the first experiments in the superdetonative propulsion mode (ratio projectile velocity/C.J. detonation speed ≥ 1.20). Nevertheless, to avoid too fast an ablation and an erosion of the fins, the projectile will be realized in a material with better mechanical and thermal properties than the magnesium alloy, such as titanium alloy.

1 Introduction

The feasibility of the ram accelerator as a means of achieving high velocities has been extensively demonstrated in 38 mm caliber at the U.W. (University of Washington, Seattle) since 1986 [1]. The main advantage of a RAMAC for numerous ballistic applications is now well-known: the ability to impart a smooth-tailored acceleration to a projectile or to an instrumented test model, i.e. to realize a "soft launch", particularly at very high velocities. This is due to the fact that the energy is distributed along the ram stages instead of being concentrated in the combustion chamber as is usual in conventional accelerators. In order to study the scale effect for the ram basic principles, in terms of both geometrical, physical and chemical conditions, ISL has developed a 90 mm caliber facility and a 30 mm caliber facility named respectively RAMAC 90 ([2] to [5]) and RAMAC 30 [6].

The goals of the present paper devoted to the RAMAC 90 are:

- to state the experimental conditions in which the reproducibility of the starting process in the thermally choked propulsion mode is better than 99%, i.e. compatible with ballistic applications;
- to demonstrate that a better in-bore guidance of the projectile allows to minimize the balloting phenomenon ([5, 6]) and to obtain an excellent reproducibility of the RAMAC performances in terms of velocity and acceleration also compatible with ballistic applications;

-to highlight experimentally the problems (erosion, ablation) provoked on the projectile materials by too long a flight time into the RAMAC associated with the projectile velocity level [7, 8].

In this paper, results of experimental investigations in the thermally choked propulsion mode are given for an appropriate reactive gas mixture, the projectile body and its sabot remaining unchanged. No on-board or external ignition devices have been used. The parameters are only the filling pressure (in the range 3 - 4.5 MPa) and the number of fins of the projectile, the entrance velocity of the latter being about 1335 m/s (Mach number ≈ 4).

2. Experimental facility [2, 4, 9]

The RAMAC 90 facility is located in the launch room of the aeroballistic range facility at ISL. It is mainly composed by the ram accelerator itself, the gas handling system, the data acquisition system, the gas chromatography system and the X-rays radiography system (Fig. 1).

2.1 The ram accelerator or RAMAC 90 (Fig. 2)
the RAMAC 90 is a modular launcher, every module being a 3 meter long smooth bore. The final configuration of the RAMAC 90 could be easily adapted to the desired velocity level.

The pre-accelerator is a conventional 90L60 (i.e. 90 mm caliber, 60 caliber long) smooth bore powder gun which can accelerate a total mass of 2.5 kg (projectile and sabot) at velocities up to 1800 m/s. The peak acceleration is below 45 kg's. The next element connected to the gun muzzle is a 4 meter long interface largely described in [9, 10].

Finally, the ram accelerator itself is composed of a flexible number of ram modules connected to the interface; each of them can be filled with an appropriate mixture. The realization of the reactive gas mixture, such as methane-oxygen-nitrogen in various amounts of each component, is achieved by means of remote computer-controlled thermal massflow regulators. Samples are collected during the filling phase and analyzed afterwards by gas chromatography [10]. For the present work, the RAMAC 90 has been organized either in single stage or in two stages (two successive gas mixtures separated by a 3-mm thick PVC diaphragm). To date, the

total number of modules is 5. The total length of the ram tube is then 16.2 meters or 180 calibers.

The RAMAC 90 is obturated at both ends with instrumented diaphragms made of PVC [10]. Their thickness depends on the initial gas pressure. For safety reasons, the long interface and the ram accelerator are totally installed inside a large metallic vessel (2 m diameter) which is also modular. At the end of this vessel, through a telescopic device, the projectile penetrates into the decelerator moving along rails in which it is stopped and finally, partially or totally destroyed [5, 9]. To date, the overall length of the facility is 33 meters.

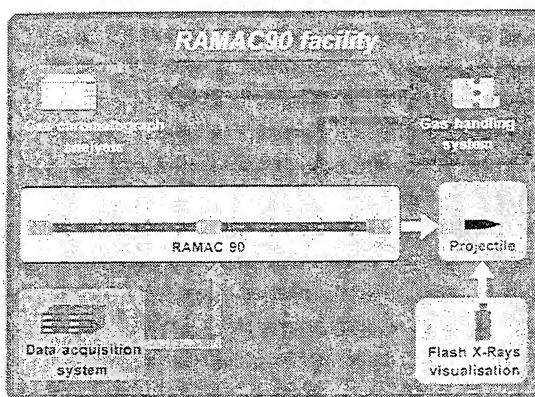


Fig. 1

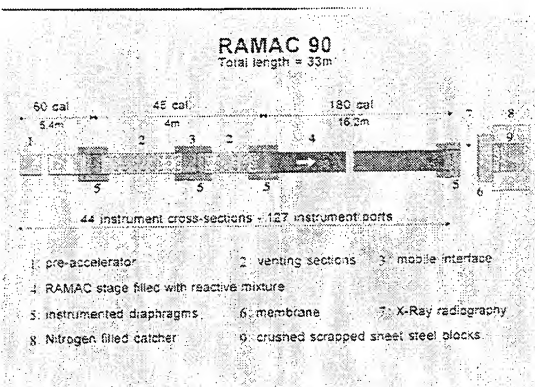


Fig. 2

2.2 The projectile

A projectile for ram accelerators is composed of two main parts: the projectile itself or the ram projectile and its sabot. They are both equipped with a magnetic ring. Accordingly, their trajectories, i.e. time - distance histories, are unambiguously reconstructed through electromagnetic transducers [3, 9, 10].

2.2.1 the ram projectile is a finned projectile.

The conception and the design of such a projectile has been proposed and largely described by Herzberg, Bruckner, Bogdanoff et al. [1, 11].

ISL's projectile shape is very similar to the U.W.'s one [5].

Previously ([2] to [5]), a great number of experiments have been achieved at ISL with the 4-fin model given Fig. 3a.

In the present work, the in-bore guidance of the projectile is upgraded (Fig. 3b): the length of the fins is greater than before, about 1 caliber, and consequently, the center of gravity CG is well placed. The total length of the projectile is 393 mm instead of 322 mm. The number of fins can be 4, 5 or 6. Their thickness is calculated as follows:

a- In a given cross-section of the afterbody, the total area is maintained, whatever the number of fins. Consequently, the mass of the afterbody remains unchanged.

b- The total base area of the projectile is the same as the one given by the first model of projectile (Fig. 3a).

Number of fins	4	5	6
Thickness [mm]	9	7.2	6

Finally, the guiding surface has been increased by the factor 2.55.

A 2 mm deep step is machined at the top of the leading edge of every fin (Fig. 4). These steps are used as cutting tools for the numerous thick diaphragms to avoid a plastic deposit on the wall of the ram tube. The effect of these steps on the flow is given by modelisation (§ 4.1.4.2).

The forebody of the projectile is made of aluminium alloy (dural), the tip being of steel. The afterbody of the projectile is made of light material, the magnesium alloy (Elektron).

The mass of the ram projectile for the present work is 1.340 kg.

2.2.2 The ISL sabot is largely described in the U.S. patent mentioned in [12].

It is relatively light, rather inexpensive, of extremely simple structure, easy to use and suitable for the optimum operation of a RAMAC in large caliber such as the RAMAC 90.

It is composed of 2 main elements (Fig. 5a and Fig. 5b), a ring and the sabot itself, the latter being made up of three parts:

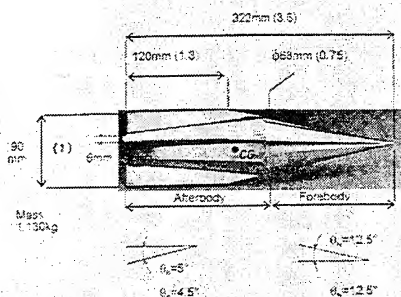


Fig. 3a

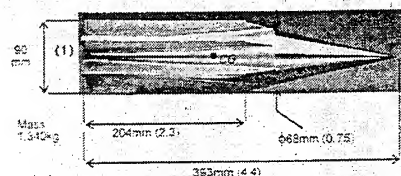


Fig. 3b

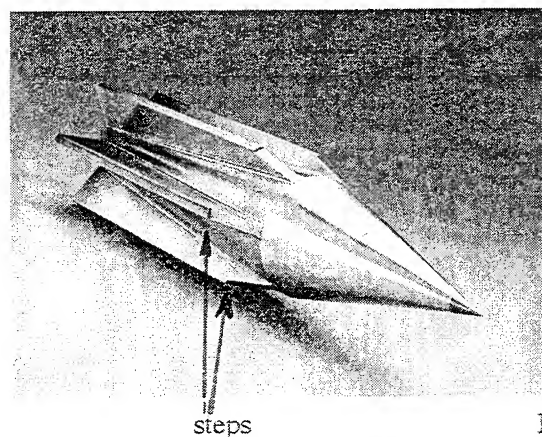


Fig. 4

• the ignition of the reactive gas mixture at the rear of the projectile. It can easily be achieved by a natural process. Preliminary experiments have shown that, for a very great distance between projectile and sabot and by using a well-adapted gas mixture for a subsonic combustion mode, the aerodynamical conditions (pressure, temperature) within the medium at the rear of the projectile are not adequate to initiate the gas mixture [14]. The entrance velocity of the projectile in the RAMAC was limited to 1400 m/s and the initial filling pressure to 5 MPa. Under these initial conditions, the natural process can be obtained either by one of the three following possibilities or by their combination:

- ignition by shock waves (incident and reflected), as largely demonstrated at the U.W. ([1, 11]), generated between sabot and projectile;
- ignition by a jet of hot gases coming from the pre-accelerator; the pusher sabot being subcalibrated, a leakage of gas is possible at a certain moment of the separation between projectile and sabot. Preliminary experiments have shown the reality of such a natural ignition of the reactive gas mixture [14];
- ignition by the flow passing through the ring situated between the pusher sabot and the projectile (Fig. 7). By such means, the temperature level can reach at least 1200 K and the pressure can increase up to 20 times the initial pressure; these are adequate conditions to ignite the reactive mixture. The computation was performed by using the TASCflow code, a full 3D Navier-Stokes code developed by ASC (Advanced Scientific Computed Limited, Canada) [15].

nota: when the diffuser is not initiated, the reactive gas mixture will be systematically ignited by the "gas piston" situated in front of the projectile and accelerated by the latter.

In the present experiments the reactive gas mixture will first meet the flow conditions created by the ring at the rear of the projectile. The ring acts as the main operator of the ignition. Consequently, the control of the ignition source location will be effected by a perfect control of the ring position during the separation phase. Finally, to control perfectly the reproducibility of the ignition source location at the rear of the projectile, the metallic ring previously screwed at the rear of the radial fins (Fig. 5b) is mechanically separated from the projectile by impact on a 5-mm thick annular plastic diaphragm placed at the entrance of the second venting section (Fig. 8), i.e. 1.25 m before the RAMAC entrance. The shock breaks the threading machined on the ring (inside) and on the fins (outside).

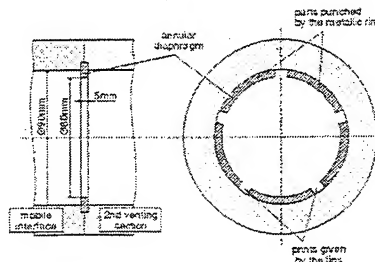


Fig. 8

4 Experimental investigation and performances in the thermally choked propulsion mode

The conditions in which the RAMAC process is successful in such a combustion mode have been clearly identified (Fig. 9), particularly:

- a very well adapted reactive gas mixture;
- a fine ignition source location;
- a great quality of the guidance of the projectile into the RAMAC (number of fins, guiding length).

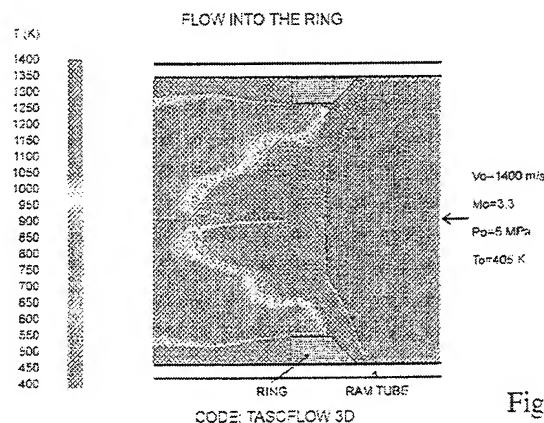


Fig. 7

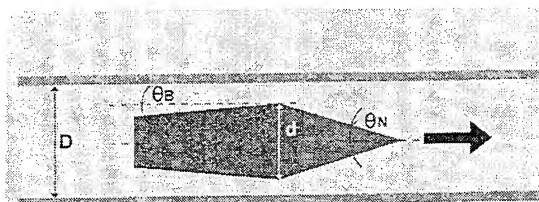
Under these conditions the combustion is well stabilized in the recirculation region behind the projectile (Fig. 10). The additional thrust is communicated to the cross-shaped base. Its area being constant (§ 2.2.1.a) whatever the number of fins, the experiments have shown the noticeable effect of both the base area distribution and the guiding surface of the projectile.

4.1 RAMAC organized in a single stage

The basic composition of the ternary reactive gas mixture chosen for the present experiments is $3\text{CH}_4 + 2\text{O}_2 + 10\text{N}_2$. It is not detonatable [13, 16, 17].

4.1.1 Experimental results in terms of velocity and acceleration versus distance

Velocities are deduced from the experimental values - time t , distance x - obtained prior to and after the entrance of the projectile into the ram stage, by means of a classical mathematical smoothing method and afterwards by derivation. There is a very good agreement between the experimental and the calculated values (Fig. 11).



- Geometry of the projectile
- Entrance Mach number
- Reactive gas mixture :
 - composition
 - initial pressure
- No balloting motion

Fig. 9

THERMALLY CHOKED PROPULSION MODE (T.C.P.M.)

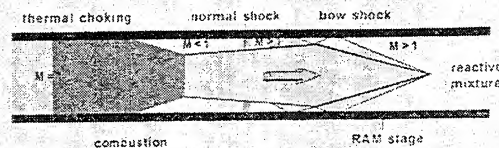


Fig. 10

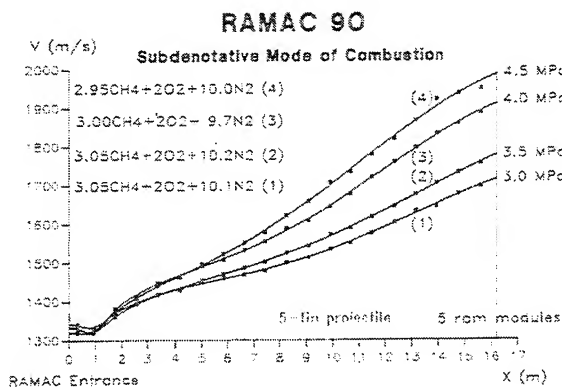


Fig. 11

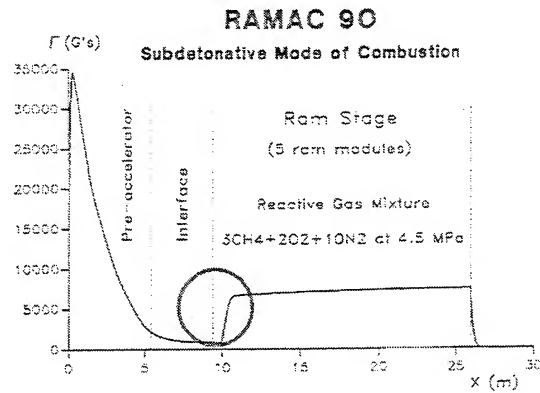


Fig. 12

Figure 11 shows the performances obtained for very similar reactive gas mixtures under an initial pressure of 3 MPa (curve 1), 3.5 MPa (curve 2), 4 MPa (curve 3) and 4.5 MPa (curve 4) and for a projectile equipped with 5 fins. The abscissa x indicates the position of the nose of the projectile. The performances are increasing with P_0 . The results show 3 very interesting aspects:

- the starting process is first characterized by a deceleration of the projectile during the time required for its introduction (from the nose to the base) into the RAMAC and for the ignition of the reactive gas mixture; secondly -and systematically- by the greatest acceleration gradient, in the range 7 to 10 kG's / ms depending on the initial pressure (Fig. 12, encircled part).

The fierce thrust is not rigorously centred on the base of the projectile ([4, 5]) and therefore provokes a small yaw (or pitch) angle of the projectile made in a material with a weak mechanical resistance (§ 2.2.1 .);

→ after the starting process, the acceleration along the ram tube is not constant, whatever the initial pressure. The small and slow oscillation of the projectile introduces a mechanical friction drag variation (between the fins and the tube wall) sufficient to also cause a small and slow oscillation of the acceleration cycle (Fig. 11). To highlight this phenomenon the ram tube has to be long enough. The average acceleration in the ram tube is considered. It is calculated as follows (Fig. 12 and Table 1):

$$\Gamma_{\text{aver}} = \Delta V / \Delta t \quad \left| \begin{array}{l} \Delta V = V_{\text{exit}} - V_{\text{entrance}} \\ \Delta t = \text{flight time into the ram tube;} \end{array} \right.$$

nota: this Γ_{aver} value is an approximation of the derivative of V as a function of time, when the projectile is situated about in the middle of the ram tube;

→ in spite of the prior phenomenon, the reproducibility of the experiments made under the same conditions is very satisfactory and compatible with ballistic applications. For instance, with $P_0 = 3 \text{ MPa}$ and $P_0 = 4.5 \text{ MPa}$, the velocity gains are respectively 373 ± 4 and $655 \pm 6 \text{ m/s}$, i.e. 28% and 49% of the respective entrance velocities. The corresponding average accelerations are respectively 3.53 and 6.64 kG's.

The best performances have been obtained with the projectile equipped with 5 fins (Fig. 13). The maximum exit velocity was 1986 m/s for a 5-fin projectile and 1960 m/s for a 4-fin projectile experimented under the same conditions, the guiding of the projectile being better in the first case.

4.1.2 Experimental results in terms of acceleration versus the initial pressure and in terms of specific impulse and ballistic efficiency

Exp. number	Number of fins	Thick. of the fins (mm)	$V_{\text{ent.}}$ (m/s)	V_{exit} (m/s)	Mach number (mean value)	Acceleration (mean value) $\Gamma_{\text{aver.}}$ (kG's)	P_0 (MPa)	Heat release Q (kJ/l)	$(V_{\text{ej}})_{\text{th}}$ (m/s)	Impulse (mean value) $I_{\text{aver.}}$	$\frac{(V_{\text{aver}})}{(V_{\text{ej}})_{\text{th}}}$ %	Ballistic efficiency P_{bal}
1415/92	5	7.2	1342	1715	4.23	3.53	3.0	36.25	1529	2.48	100.0	0.20
1415/93	5	7.2	1320	1778	4.28	4.39	3.5	42.69	1544	2.64	100.3	0.22
1415/94	5	7.2	1332	1911	4.48	5.77	4.0	50.66	1584	3.04	102.4	0.24
1415/95	5	7.2	1331	1986	4.56	6.64	4.5	57.10	1595	3.11	104.0	0.25
1415/96	4	9	1335	1863	4.43	5.18	4.0	50.47	1581	2.73	101.1	0.22
1415/97	4	9	1337	1960	4.59	6.32	4.5	57.10	1595	2.87	103.4	0.23
1415/98	4	9	1341	1703	4.21	3.423	3.0	36.86	1543	2.41	98.6	0.195
1415/99	4	9	1335	1935	4.53	6.12	4.5	57.50	1601	2.87	102.1	0.22
1415/100	4	9	1328	1725	4.23	3.77	3.5	42.70	1543	2.27	98.9	0.185

Table 1

The theoretical detonation velocity at the Chapman -Jouguet point $(V_{\text{ej}})_{\text{th}}$ given in table 1 has been calculated by means of the Quartet thermochemical code based on the initial conditions (ambient temperature and P_0) and on the Boltzmann Equation of state for the combustion products [13, 16, 17].

The specific impulse I , or non-dimensional thrust coefficient, is given by the relation:

$$I = \frac{\text{thrust}}{S} \cdot \frac{1}{P_0} = \frac{m\Gamma}{S \cdot P_0}$$

m : mass of the projectile [kg]
 Γ : acceleration [m / s^2]
 S : reference area calculated with the ram tube diameter [m^2]
 P_0 : initial pressure [Pa].

A theoretical calculation of the thrust and then of I is undertaken by Henner [18].

The ballistic efficiency ρ_{bal} , a non-dimensional parameter, is given by the classical relation:

$$\rho_{\text{bal}} = \frac{\frac{1}{2} m (V_{\text{exit}}^2 - V_{\text{entrance}}^2)}{Q \cdot \psi}$$

Q = heat release per unit of ram volume [$\text{J} \cdot \text{m}^{-3}$]
 ψ = volume of the ram tube [m^3]

As anticipated, the average acceleration is increasing with the initial pressure P_0 (Fig. 11).

The results given Fig. 13 show that :

- the performances concerning the 5-fin projectile are better than those obtained with the 4-fin projectile;
 - the specific impulse is also increasing with P_0 .
- Indeed, if we assume, in a first approximation, that the law giving the acceleration versus P_0 is linear, we obtain by least square interpolation:

$$\Gamma = 2011 P_0 - 2693 \quad \text{with: } \begin{cases} \Gamma \text{ in G's and} \\ P_0 \text{ in MPa} \end{cases}$$

$$I = m\Gamma / S \cdot P_0 = K1 - K2 / P_0$$

($K1, K2$: constants).

Finally, I is increasing with P_0 (Fig. 14).

In a first approximation, the ballistic efficiency ρ_{bal} equals $\frac{\Gamma_{\text{aver}}}{QS}$ and Q is proportional to P_0 .

Consequently, ρ_{bal} is also slightly increasing with P_0 (Fig. 15). The ballistic efficiency is greater with the 5-fin projectile than with the 4-fin projectile, the guiding of the projectile being better in the first case.

4.1.3 Stabilization of the combustion

4.1.3.1 Combustion totally situated at the rear of the projectile

Observations made from the light emission probes indicate that the combustion is initiated at the rear of the projectile and stabilized in the recirculation region (Fig. 16).

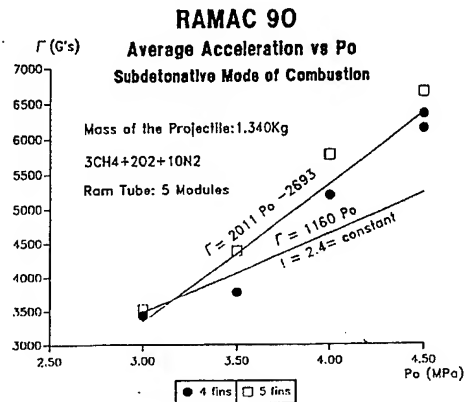


Fig. 13

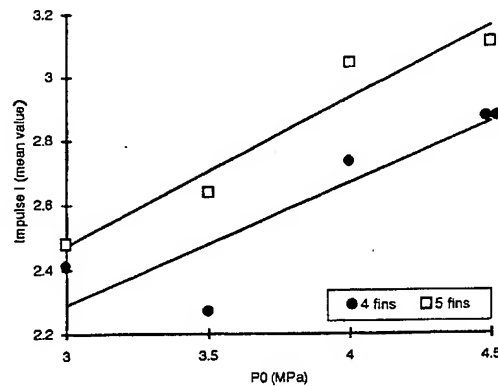


Fig. 14

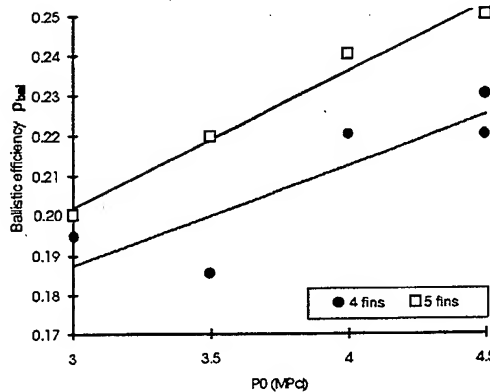


Fig. 15

The heat release from combustion generates high pressures and imparts thrust to the projectile. The mean pressure ratio $\frac{\bar{P}}{P_0}$ in the

combustion volume is in the range 12 to 14 for the reactive gas mixture which is used. The flow and the combustion process are affected by the projectile acceleration itself. The energy is released in large-scale turbulent structures. The pressure oscillations are important.

The combustion front is typically unsteady. Its location versus time can change very rapidly from the base to the position situated about 2 calibers behind the projectile (Fig. 17). The average position of the combustion front is situated at about 1 caliber from the base. The motion is similar to a pulsating phenomenon. Nevertheless, no characteristic frequency at all has been established. The average velocity of the combustion front equals the velocity of the projectile. The differential velocity can reach ± 300 m/s. The projectile pieces recovered in the special catcher used for this purpose show if the material of the projectile afterbody has just been "washed" by the hot gases or eroded. The flash X-ray picture taken at the ram muzzle (Fig. 18) also shows samples of the same material as the one used for the afterbody and with different well-known thicknesses. Taking into account the roll position of the projectile, the quantity of lost material can be evaluated with a good approximation (§ 4.1.4). The perceptible traces on the leading edges of the fins are explained in the same chapter.

4.1.3.2 Combustion not totally situated at the rear of the projectile

In that case, the average position of the combustion front is very close to the base of the projectile (Fig. 26 - First Stage). The pulsating phenomenon is similar to the one described before, but the flame, from time to time, is in contact with the rear part of the afterbody. The part concerned is about one caliber long (i.e. 45% of the guiding length).

Finally, the average position of the front combustion is also directly affected by the unsteadiness of the combustion process. From one experiment to the other, the variation of this position can reach one caliber.

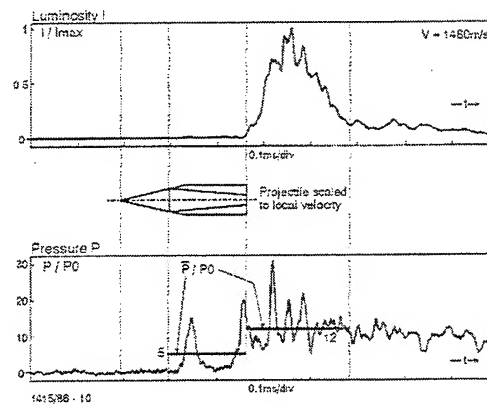


Fig. 16

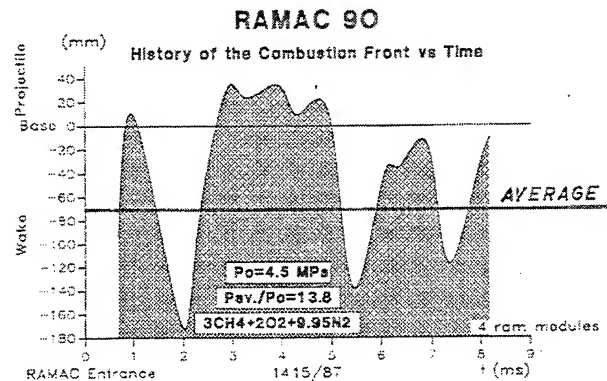


Fig. 17

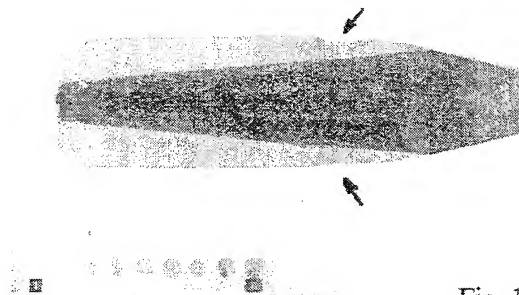


Fig. 18

Example: Experiment 1415/98 $P_0 = 3$ MPa
 4-fin projectile $V_{\text{RAMAC exit}} = 1703$ m/s
 $t_{\text{RAMAC exit}} = 10.76$ ms

4.1.4 Erosion and ablation of the projectile materials

- The different materials (nose, fins, afterbody) of the ram projectile have to resist high mechanical and thermal loads produced by the severe ram flight conditions.

At different places - mainly, the nose (stagnation point), the leading edges of the fins (stagnation points) and the base affected by the combustion itself - the temperature rises extremely fast and reaches a level high enough to melt the material. But the rapid heating also induces thermal stresses on the surface, creating a thermal shock effect that leads to a reduction in material hardness and can cause surface cracks, structural failures and finally mechanical damage.

For the present experiments, the magnesium alloy which is used for the fins and the afterbody and is very interesting for its density (minimum of mass), has not the required properties to resist such mechanical and thermal ram loads for a long time. Therefore, it is interesting to quantify the effect of the severe aerothermodynamic heating of the ram projectile in order to have a better understanding of the overall phenomenon. Indeed, it can change the aerodynamics of the flow, as well as the combustion process (not rigorously monophasic mixture, reactive particles) and unstarts could be provoked by an unsteady phenomenon close to the throat (or diffuser).

- Preliminary experiments have been performed with inert gas (N_2) at different initial pressures P_0 . Under these conditions, the flash X-ray pictures taken 3.4 m after the RAMAC muzzle are used as reference. The pictures in Fig. 19 show the projectile without any deformation, ablation or erosion of the nose (Fig. 19b) and of the base (Fig. 19a), but with a small deformation on the leading edges of the fins (Fig. 19a) provoked by their impact on the thick diaphragms situated at both ends of the ram tube.

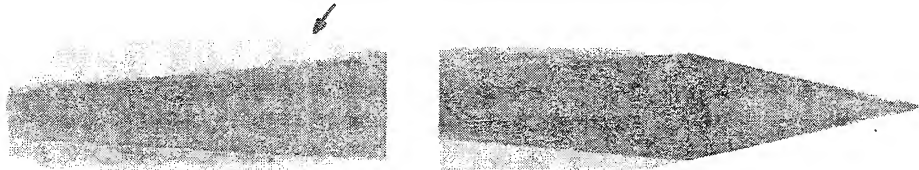


Fig. 19a
(1413/107)

5-fin projectiles
 $N_2 - P_0 = 2.8 \text{ MPa}$
 $V_{\text{entrance}} = 1328 \text{ m/s} \quad V_{\text{exit}} = 1172 \text{ m/s}$

Fig. 19b
(1413/106)

4.1.4.1 Erosion and ablation of the projectile rear part

This phenomenon concerns both the fins and the conical afterbody.

It is difficult to quantify exactly the lost material and its recession velocity. For a given mixture and entrance velocity, they depend on P_0 , on the number of fins (or the total area exposed to the flow) and on the flight time.

The heat conduction within the material used is such that the phenomenon appears after about 6 ms (or flight time in 3 ram modules) and is quantified after about 10 ms (or flight time in 5 ram modules).

Two examples (Fig. 20, 21) are given to highlight the aspects of high heat transfer rates provided by the flow and by the combustion. They correspond to experiments in which the average position of the combustion front is situated behind the projectile (§ 4.1.3.1).

The 2 examples mainly differ in the 2 following points :

- P_0 , respectively 3.5 MPa and 4.5 MPa,
- a combustion front which is from time to time situated on the afterbody, up to 2 cm from the base (Fig. 20), up to 5 cm (Fig. 21).

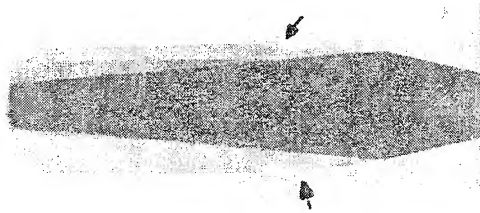


Fig. 20
(1415/93)

$P_0 = 3.5 \text{ MPa}$
 $V_{\text{entrance}} = 1320 \text{ m/s}$
 $V_{\text{exit}} = 1778 \text{ m/s}$
 $t_{\text{RAMAC exit}} = 10.64 \text{ ms}$

- 5-fin projectiles -

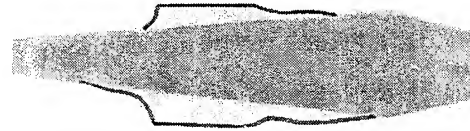


Fig. 21
(1415/95)

$P_0 = 4.5 \text{ MPa}$
 $V_{\text{entrance}} = 1330 \text{ m/s}$
 $V_{\text{exit}} = 1986 \text{ m/s}$
 $t_{\text{RAMAC exit}} = 10.06 \text{ ms}$

An estimation gives the material lost by erosion and ablation at the rear part of the projectile:

- about 50 g (Fig. 20): the thickness of the fins has been strongly reduced (about 3 mm instead of 7.2 mm at the back). The fin length, progressively affected by the phenomenon, is about 1 caliber;

- about 145 g (Fig. 21, Fig. 22): the residual guiding length after 10.06 ms is about 2/3 caliber long, i.e. the strict minimum to ensure the guidance of the projectile into the RAMAC. For a long RAMAC, the flight time will be longer and the quantity of ablated and eroded material will be constantly increasing. The quantity of particles ejected into the combustion zone will be more and more noticeable and will interfere with the combustion process.

By modelisation, the temperature histories of the projectiles could be reconstructed from their velocity histories given by experiments.

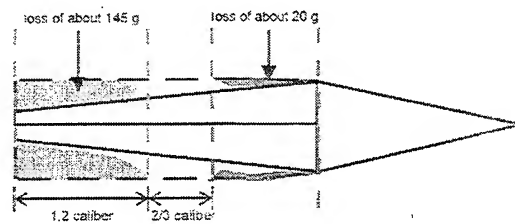


Fig. 22
(1415/95)

4.1.4.2 Ablation and erosion of the leading edges of the fins

The severe aerodynamic heating of every fin leading edge is only due to the flight conditions (P_0 , velocity, flight time). The temperatures produced in the stagnation region are rapidly higher than the melting temperature. Nevertheless, at this place, there is no ignition of the reactive gas mixture during the 10 ms flight time. The light emission probes (Fig. 23) indicate that the ablation of the leading edges begins in the following average conditions:

- velocity 1550 m/s
- time 5.3 ms.

There is no interaction with the combustion zone situated behind the projectile.

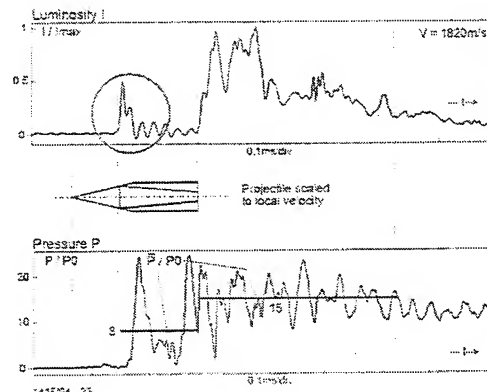
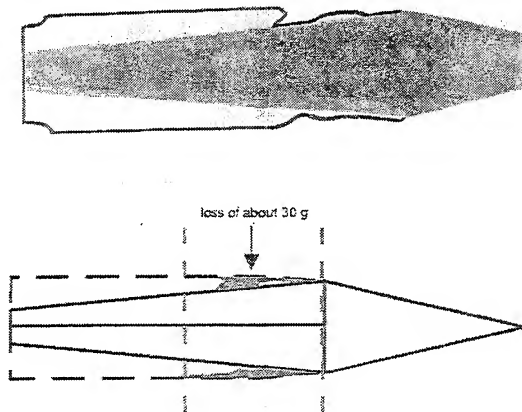


Fig. 23

The perceptible traces on the fin leading edges (Fig. 18,20,21,24) result from ablation and erosion. They are situated just after the stagnation point. The quantity of lost material depends, as explained in § 4.1.4.1, on different parameters: P_0 , the number of fins (taking into account the thickness of each fin) and the flight time. The fin leading edges were not chamfered. An estimation of the quantity of lost material gives 20 g for a 5-fin projectile (fin thickness = 7.2 mm) after about a 10 ms flight time, the exit velocity being 1986 m/s (Fig. 22). For a 4-fin projectile (fin thickness = 9 mm) under similar conditions (Fig. 24), the estimation of lost material averages about 30 g. The precision of the evaluation method is not great enough to establish a difference between the 4- and the 5-fin projectiles.



1415/97

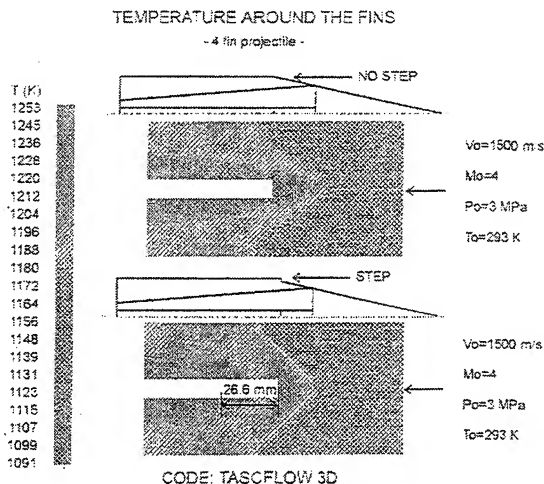
4-fin projectile

Fig. 24

$P_0 = 4.5 \text{ MPa}$

$V_{\text{entrance}} = 1337 \text{ m/s} - V_{\text{exit}} = 1960 \text{ m/s}$

$t_{\text{RAMAC exit}} = 10.04 \text{ ms}$



A computation was performed by using the TASCflow code (§ 3, [15]). It shows the modifications of the flow provoked by the steps machined at the top of the fin leading edges (Fig. 4). The hottest calculated point is situated 26.6 mm behind the step (Fig. 25). The experiments give an average position of the traces, provoked by ablation and erosion, of about 23 mm after the step. The agreement between calculation and experiment is excellent. The temperature level can reach 1250 K, i.e. much higher than the melting temperature of the material (800 - 900 K for magnesium alloy).

Fig. 25

4.1.4.3 Remarks

- After a 10 ms flight time, the nose tip of the projectile made of steel (§ 2.2.1) was not ablated. No light emission has been indicated by the probes.
- A consequence of the ablation and erosion phenomenon of the projectile afterbody is that the performances in terms of velocity and acceleration versus time are affected by the mass reduction. The total quantity of lost material can reach 165 g (§ 4.1.4.1) or 12 % of the ram projectile mass.

4.2 RAMAC organized in two stages

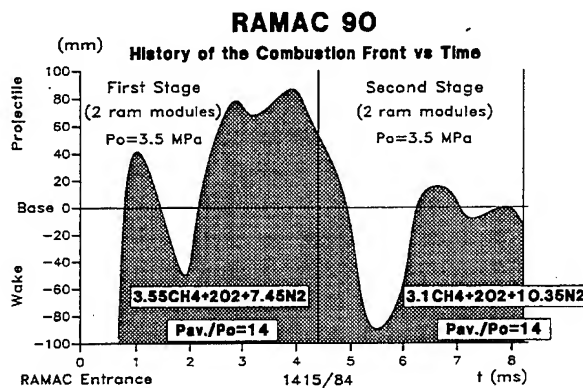


Fig. 26

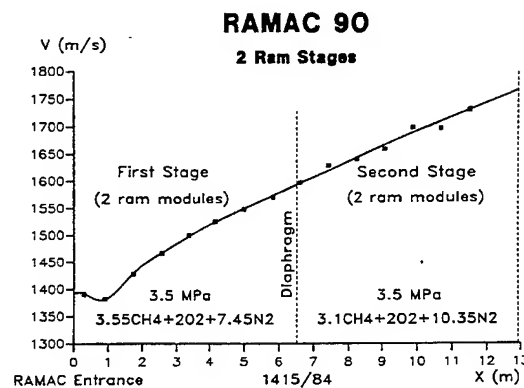


Fig. 27

The experiments have shown that the way through two different mixtures, separated by a 3-mm thick PVC diaphragm, was achieved without any difficulty. In both stages, each of them composed of two ram modules, the combustion mode was thermally choked. An example of experiment performed with a 5-fin projectile is given Fig. 26 and Fig. 27. The ignition of the second mixture was made automatically by the combustion front of the first one. The average position is not in the same place in each stage: very close to the base of the projectile in the first stage and about 4 cm behind the base in the second stage. The mixtures are different. The performances in terms of velocity versus distance (Fig. 27) do not show any discontinuity on the border between the two stages.

5. Conclusion

The present study, concerning the thermally choked propulsion mode and made in 90 mm caliber (RAMAC 90), has clearly highlighted:

- that the reproducibility of the starting process, and therefore the control of the ignition source location at the rear of the projectile, is now very satisfactory and compatible with ballistic applications;
- that the reproducibility of the RAMAC performances in terms of velocity, acceleration and ballistic efficiency is excellent and also compatible with ballistic applications. For instance, the RAMAC length being 16.2 m, for a projectile mass of 1.340 kg, an entrance velocity of 1330 m/s into a mixture composed of $2.95 \text{ CH}_4 + 2\text{O}_2 + 10\text{N}_2$ under a filling pressure of 4.5 MPa, the exit velocity was 1986 m/s (or 149% of the entrance velocity). The reproducibility of the velocity gain was about 1%. The quality of this result has been obtained by:
 - a better control of the ignition source location;
 - using a new projectile with a better in-bore guidance than previously (guiding length increased by a factor 1.7, guiding surface increased by a factor 2.55);
 - using a well-adapted mixture;

-the problems encountered with the high thermal and mechanical ram loads applied on the projectile materials. An estimation of the total material lost by ablation and erosion, at the rear part of the projectile and on the fin leading edges, points to 165 g or 12% of the projectile mass after a 10 ms flight time.

References

- [1] Hertzberg A., Bruckner A., Bogdanoff D.W.
The RAM Accelerator: a New Chemical Method of Achieving Ultrahigh Velocities
37th Meeting of the Aeroballistic Range Association, Quebec, Canada, September 9-12, 1986
- [2] Giraud M., Legendre J.F., Simon G., Catoire L.
RAM Accelerator in 90 mm Caliber. First Results Concerning the Scale Effect in the Thermally Choked Propulsion Mode -
13th International Symposium on Ballistics, Stockholm, Sweden, June 1-3, 1992. ISL CO 210/92
- [3] Giraud M.
First Results concerning the Scale Effect on the Thermally Choked Propulsion Mode -
European Symposium STAR - Properties of Reactive Fluids and their Applications to Propulsion, Poitiers, France, November 24-27, 1992. ISL PU 307/93
- [4] Giraud M., Legendre J.F., Simon G.
RAMAC 90. Experimental Studies and Results in 90 mm Caliber, Length 108 Calibers -
First International Workshop on Ram Accelerator - ISL Saint-Louis, France - September 7-10, 1993. ISL PU 360/93
- [5] Giraud M., Legendre J.F., Simon G.
RAM Accelerator in 90 mm Caliber or RAMAC 90. Experimental Results Concerning the Transdetonative Combustion Mode -
14th International Symposium on Ballistics, Québec, Canada, 26-29 September 1993. ISL PU 363/93
- [6] Seiler F., Patz G., Smeets G., Srujijes J.
Status of ISL's RAMAC 30 with Rail Stabilized Projectiles
First International Workshop on Ram Accelerator, ISL, Saint-Louis, France, September 7-10, 1993. ISL PU 353/93
- [7] Naumann K.W.
Heating and Ablation of Projectiles During Acceleration in the RAMAC 30 Ram Accelerator Tube of ISL
First International Workshop on Ram Accelerator, ISL, Saint-Louis, France, September 7-10, 1993. ISL PU 328/94
- [8] Bruckner A.
A Computational Study of Projectile Nose Heating in the Ram Accelerator
30th AIAA/ASME/SAE/ASEE Joint Propulsion Conference, AIAA 94-2964,
Indianapolis, IN, USA, June 27-29, 1994
- [9] Giraud M., Legendre J.F., Simon G.
RAM Accelerator Studies in 90 mm Caliber -
43rd Meeting of the Aeroballistic Range Association, Columbus, OH, USA,
September 28 - October 2, 1992. ISL CO 233/92
- [10] Giraud M., Legendre J.F., Simon G., Mangold J.P., Simon H., Kauffman H.
RAMAC 90: Facility and Diagnostic Methods
44th Meeting of the Aeroballistic Range Association, Munich, FRG, September 13-17, 1993. ISL PU 362/93
- [11] Bruckner A.
The Ram Accelerator: An Overview
European Symposium STAR - Properties of Reactive Fluids and their Applications to Propulsion, Poitiers, France, November 24-27, 1992.
- [12] Giraud M., Simon H.
Sabot for projectiles of ram accelerators and projectiles equipped with such a sabot
United States Patent Number 5, 394, 805
- [13] Legendre J. F., Giraud M., Bauer P.
Effect of Inert Additives on Detonation Properties of Dense Gaseous Explosives
First International Workshop on RAM Accelerator, ISL, Saint-Louis, France, September 7-10, 1993. ISL PU 359/93
- [14] Giraud M. et al.
ISL Report to be published
- [15] Berner C., Henner M., Giraud M.
Communication given by Berner ISL
ISL Report to be published
- [16] Bauer P., Legendre J.F.
Detonability limits of propellant mixtures used in the RAMAC
14th International Symposium on Ballistics, Québec, Canada, September 26 - 29, 1993. ISL PU 361/93
- [17] Legendre J. F., Giraud M., Bauer P.
90L35 Detonation Tube Experiments: Influence of Diluent Nature on the Detonation Characteristics of Dense Methane - Based Gaseous Explosive Mixtures
Second International Workshop on Ram Accelerator - Seattle, WA, USA, July 17 - 20, 1995. ISL Report to be published
- [18] Henner M.
Ph. D. in preparation - ISL Report to be published

EXPERIMENTS IN A 120 MM MULTI-STAGE RAM ACCELERATOR

D. L. Kruczynski

U.S. Army Research Laboratory, Aberdeen Proving Ground, Md, 21005

ABSTRACT

First experiments using multiple gas fuel stages in the ARL ram accelerator are reported. New criteria for comparative analysis of experiments based on both total heat release and heat release rate are introduced and evaluated relative to these experiments. Finally, experimental data indicating that projectile material can influence the desired experiments through burning and heat release is presented.

INTRODUCTION

Ram acceleration is initiated by injection of a projectile, similar in shape to the center body of a Ramjet engine, into a tube filled with a combustible gaseous fuel/oxidizer/diluent, or simply fuel. As the sub-caliber projectile enters these gases, at supersonic speeds, shock and viscous heating occurs. Properly "timed" this ignites and sustains combustion on the aft section and behind the projectile. This energy release occurs continuously as the projectile accelerates. It is often useful to adjust the fuel composition down the length of the accelerator tube to ensure high efficiency of combustion in accelerating the projectile. In practice this is accomplished by segmenting the accelerator tube with thin plastic diaphragms to separate the fuels. Properties such as sound speed and chemical energy of the fuel are adjusted to maximize acceleration of the projectile¹.

If "low" pressure operation is desired and the length and complexity of the accelerator is not an issue this is a very useful technique for achieving high efficiency conversion of fuel chemical energy into projectile kinetic energy. The use of multiple fuels by segmenting the accelerator is often referred to as "staging" the accelerator.

The U.S Army Research Laboratory (ARL) has been exploring inbore ram acceleration as a technique to obtain hyper-velocities with useful projectile masses. The research has consisted of an integrated program of experiment and gas dynamic modeling. Past research has investigated scaling and pressure effects, and flow visualization²⁻⁴. Current research is ongoing in the areas of projectile geometry and staging effects.

FACILITY

Accelerator and Injection Gun

The ARL facility was created by removing the breeches of 120-mm M256 tank guns and mating the tubes. Each accelerator section (tube) is 4.7 m long. Currently three accelerator tubes are available for a total combined accelerator length of 14.1 m. The accelerator tubes may be segmented with PVC diaphragms and filled with different fuel gases or used without diaphragms for longer runs with single fuel mixtures. The projectile is brought up to injection speed (typically 1200 m/s) using a conventional 120-mm tank gun and a solid propellant. Projectile transition to the first accelerator tube is made through a vented tube section. This section serves to both decouple the conventional gun recoil (through a sliding interface) and vent solid propellant gases to minimize interference with the ram acceleration process. Figure 1 shows the layout of the facility.

Gas Handling and Mixing

A bank of gas storage bottles supplies the required gases. It should be noted that ram acceleration fuels are readily available at bottled gas dealers in standard highway transportable storage bottles. The ARL facility also includes a compressor capable of charging the accelerator to 340 atmospheres. Recent additions to the facility include a pre-mix station and online gas chromatography for analyzing the fuel mixtures used. The pre-mix station was installed to avoid any ambiguity about the content and homogeneity of fuels used in the accelerator and is particularly useful for multi-stage firings since up to three gas mixtures may be mixed, tested, and adjusted, if necessary in advance of firings.

Prior to installation of the pre-mix station the accelerators in the ARL facility were directly filled with the desired fuel by partial pressure methods. Samples taken from the accelerator before firing (but analyzed days later) indicated that in general the actual fuel mixtures were in reasonable agreement with intended mixtures. However it was suspected that the fuel mixture was not homogeneously mixed prior to firing (it was thought that mixing was being completed in the small sample bottles). When the portable gas chromatography (GC) system was installed these suspicions were confirmed. Table 1 shows data from a two accelerator tube shot in which the same mixture was simultaneously pumped into both tubes. Samples from both accelerator tubes were then taken and analyzed immediately after filling (about 10 minutes apart).

Table 1 - Analysis of fuel mixtures taken at different locations in the accelerator tubes

Shot/Stage and Final Fill Pressure	Mixture Component and Order of Fill	Desired Volume Percent (both stages)	GC Analysis of Stage 1	GC Analysis of Stage 2
26/1 & 2 at 57 Atm.	O2	13	15	14
	N2	67	70	64
	CH4	20	15	22
* GC is Gas Chromatography				

Note from Table 1 that there is considerable discrepancy between the two samples.

The premix station consists of a bank of standard 44 liter gas bottles which are remotely filled from the individual source gases many hours (or days) before firing. Using the online GC the banks of bottles may be sampled at any time and their contents adjusted if necessary. Analysis of the premix gases over extended periods of time revealed that, in general, 48 hours or longer is required to ensure the gases have "completely" mixed by diffusion and residue turbulence from the filling process. This can be seen in the samples taken from the first stage mixture of shot 34 and 34 shown in Table 2.

Table 2 - Measurement of fuel mixtures over time

Shot/Stage Number and mixture final pressure	Mixture Component and order of Fill*	Desired Volume Percent in mixture	**GC measurement after 20 hrs	GC measurement after 48 hrs	GC measurement after 68 hrs	GC measurement after 140 hrs	GC measurement after 204 hrs
34/1 at 81 Atm.	N2	67	46	--	69	69	--
	O2	13	9	--	14	14	--
	CH4	20	45	--	17	17	--
35/1 at 81 Atm.	CH4	20	--	17	--	--	17
	N2	67	--	69	--	--	69
	O2	13	--	14	--	--	14

* Mixture were filled in nine steps in the order shown, i.e. N2-O2-CH4 to 1/3 of the desired pressure then repeat sequence two more times to final pressure, ** - GC is Gas Chromatography

When the fuel mixture appears to be within reasonable agreement with the desired mixture it is ready to be pumped to the accelerators for firing. In addition, if desired, multiple shots may be made from the same pre-mixed batch of gas if desired, ensuring repeatability.

To date, no safety problems have been encountered handling these pre-mixed, typically fuel rich, mixtures.

STAGING EXPERIMENTS - RATIONALE, RANKING CRITERIA, AND TEST MATRIX

It has been well documented¹ that peak performance for a ram accelerator, operating below the Chapman-Jouget Detonation Speed, is obtained when the total heat release of the fuel (typically defined as Q/c_pT) is kept as high as possible and the projectile Mach Number is kept as low as possible. However care must be exercised so that the flow neither gas-dynamically chokes at the throat (becomes sonic) nor discharges a normal shock through the throat from behind, during excessive heat addition (an unstart). Finding the optimum conditions is also dependent on the scale and design of the projectile. In addition, the conditions during initial projectile injection into the accelerator and gas dynamic separation (obturator discard, etc.) from the injector gun seem to require lower heat release than for "steady" operation⁴.

ARL has only recently expanded its facility to the point where the "optimum" conditions for efficient operation (after the initial startup) are being explored. Due to the relatively high cost of experimental operation at 120-mm bore size great care is taken in designing new experimental firing matrices to maximize the insights gained from each firing. In the case of the firings reported in this paper a qualitative ranking system was used to screen experiments. The ranking system is based on three simple comparative factors for analyzing experimental potential of a shot. The first two factors, available heat release Q/c_pT , and projectile Mach number (relative to the fuel) were discussed previously.

The third factor is the potential fuel heat release rate currently calculated using a methane/air combustion mechanism developed by the Gas Research Institute which consists of 32 species and 176 reactions and the SENKIN kinetics code. Using such detailed kinetics mechanisms in ARL CFD calculations would result in prohibitively long computer run times. Until better reduced mechanisms are available for CFD use, kinetics codes such as SENKIN appear to provide valuable information for screening new fuel mixtures and making comparative analyses. Further details on the use of this method are available in Reference 5.

The first shot in the staging experiments (Shot 34) was designed to evaluate the potential for operating the 120-mm ram accelerator at elevated (relative to the starting stage) heat release values. The second and third accelerator tubes were filled with the new more energetic mixture. No attempt was made in this experiment to adjust sound speed of the mixture. Since this shot was successful, yet appeared to be close to unstarting at exit, it became the baseline for comparison with subsequent shots. Note that in all the shots in this series the initial stage of the ram accelerator contained nominally the same fuel which has shown excellent repeatability in previous ARL experiments²⁻⁴. The second and third firings of the series were designed to maximize acceleration by raising the heat

release and sound speed of the fuel mixture. This would allow both "high" Q/c_pT and low Mach Number operation. The final shot of the series was made with the same mixture as used in shot 34 however both the projectile design and materials were different. This projectile contained a short straight section (92 mm long) between the nose and aft sections. This isolator design was being evaluated for its potential in preventing unstarts and is fully reported in Reference 6. A Drawing of the "standard" projectile is seen in Figure 2. Table 3 summarizes properties for these experiments. Note that the total heat release, were equal to or less than shot 34 in subsequent shots while the average heat release rates for the shots subsequent to shot 34 (standard or first stage mixture) were longer.

Table 3 - Comparson of Fuel Properties

Table 6 - Comparison of Fuel Properties							
Shot Number	Stage 1 - Fuel Properties and Molar Content			Stage 2 - Fuel Properties			Notes
	Q/c _p T	Release ² Time (ms)	Mach number at entrance	Q/c _p T	Release Time (ms)	Mach number at entrance	
34	3.7	0.6026	3.4	5.23	0.3459	3.7	Standard Projectile
Molar Content ¹	2.6 CH ₄ + 2.1 O ₂ + 10.4 N ₂			2.5 CH ₄ + 2.1 O ₂ + 6.1N ₂			
35	3.7	0.6026	3.3	3.95	0.4141	3.1	Very ³ slight mod
Molar Content	2.6 CH ₄ + 2.1 O ₂ + 10.4 N ₂			3.0 CH ₄ + 2.1 O ₂ + 3.7 N ₂ + 4.3 He			
36	3.49	0.6026	3.4	3.99	0.3866	2.9	Standard Projectile
Molar Content	2.9 CH ₄ + 2.1 O ₂ + 10.1 N ₂			5.0 CH ₄ + 2.0 O ₂ + 4.0 He			
37	3.71	0.6026	3.5	4.33	0.3459	3.93	Proj. with isolator ⁴
Molar Content	2.9 CH ₄ + 2.2 O ₂ + 9.9 N ₂			2.7 CH ₄ + 2.0 O ₂ + 6.3 N ₂			
1 - molar content gas chromatography analysis, 2 - Approximate time to energy release at given temperature, For the first stage the rate is a nominal value based on a 3CH ₄ + 2O ₂ + 10N ₂ mixture, 3 - Small backward steps behind throat between fins (see reference 6), 4 - See projectile description above							

EXPERIMENTAL RESULTS

The first shot of the series (34) exhibited successful ram acceleration in all three accelerator tubes and exited with stable ram combustion established. Photos of the projectile in flight after exit showed no damage. High speed movies of the projectile exiting the last accelerator indicated large light emission around the projectiles forebody at exit. Such evidence generally indicates that significant combustion (but not a normal shock)

exists on the forebody of the projectile and an unstart may be imminent. These results along with similar CFD predictions⁵ indicated that the total heat release of the fuel could not be increased further without causing an unstart. This shot then became the "standard" against which the succeeding tests were compared.

Shot 35 successfully accelerated through the first tube but unstarted 2.355 m (halfway) into the tube two fuel mixture. The projectile's image was captured in-flight at exit from the last accelerator tube. The projectile appeared to be completely intact. This ruled out any question of projectile mechanical failure causing the unstart. The very slight modifications to the projectile noted in Table 3 above did not appear to be involved in the unstart based on its performance in the successful run of the first accelerator stage. Note that the unstart occurred even though the fuel mixtures in accelerator two and three had equal $Q/c_p T$ and longer release rate values than the previous shot.

Shot 36 successfully accelerated through the first stage mixture but again unstarted about halfway into the tube two fuel mixture. Again, an image of the projectile after exit from the accelerators revealed no structural damage. Note that this projectile design was identical to that of shot 34 and the fuels in accelerator tubes two and three again had lower $Q/c_p T$ and longer "release rates".

Shot 37 used a significantly different projectile geometry and was fired primarily to evaluate the performance of projectiles with straight mid bodies (isolators) in ram accelerators. To make direct comparisons with previous "standard" projectiles the mid and aft sections were made from a "high" strength magnesium alloy (ZK-60) to reduce total projectile mass to that of the "standard" projectile design. The nose section was aluminum with a stainless steel tip as in the other shots (see Figure 2). Again the projectile had successful ram acceleration in the first stage. Like the previous two shots, it unstarted (violently) in the middle of the second accelerator. This occurred even though the fuel mixture was the same as that of shot 34 which operated successfully throughout. There was very strong photographic and material evidence that the projectile was burning through at least the later stages of the accelerator. A photo of the projectile after exit was not obtained because extreme light emission over exposed the film. Residue from burning magnesium was also scattered throughout the accelerator. The reason this test is included in this paper, which is looking primarily at kinetics and staging effects, is because it obviously contributed to the heat addition of the ram cycle and sparked a separate study⁷ looking into the effects on fuel kinetics of the projectile's material. This is discussed further in the next section.

A plot of velocity versus travel for the four cases above may be seen in Figure 3.

ANALYSIS

Gas dynamic unstarts occurred in both attempts to raise the fuels sound speed even though other calculated properties such as heat release and release rates were lower (or equal) and longer respectively for these experiments. Since the heat content value $Q/c_p T$ has been used and validated as a experimental parameter it was decided to reexamine the assumption used in calculating the "heat release rate". The first and perhaps most important consideration for these calculations is the temperature selected to begin the combustion calculation. For the cases done to date an "average" temperature in the boundary layer behind the initial bow and reflected shocks over an average range of expected projectile Mach numbers was used. The calculations used in setting these conditions were from previous shots in the ARL first stage "standard" fuel. The initial temperature was set at 1350 K.

Following the unstarts of shot 35 and 36 it was decided to examine the CFD calculations of the flow of shot 36 to assess an "average temperature" using a similar method to that described above. It was found that despite the lower projectile relative Mach number in the helium mixtures, the average temperatures in the flow was about 50 K higher. It is thought that the lower heat capacity of atomic species, in this case helium, (with two energy degrees of freedom) as compared to that of diatomic nitrogen (five energy degree of freedom) may account for this difference. When the "heat release rate" calculations were redone starting at 1400K the release time was found to be shorter that for the nitrogen doped mixtures). The new release times for shots 35 and 36 were calculated to be 0.2388 and 0.2547 ms respectively (compare these to the values in Table 3). Obviously, since such relatively minor temperature changes can make a considerable difference in the kinetic rate calculations, the initial conditions must be considered carefully.

As noted earlier the magnesium projectile (shot 37) did burn and may have contributed significantly to the projectile unstart through this unplanned and excessive heat release. Indeed there is some evidence from the photographs of the aluminum projectiles which survived unstarts (shot 35 and 36) that they may also be some burning around the projectile's base, although this is not conclusive at this time. It is know that aluminum projectiles are failing and perhaps burning at higher Mach numbers. If the projectiles do burn they may have a significant effect on the amount of energy being released around the projectile. This could be responsible for some unexplained unstarts. A study of this potential was done at ARL and is reported seperately⁷.

CONCLUSIONS

It has been shown that the total heat of a ram fuel may be increased once the initial starting process is achieved. This confirms and scales with results in smaller ram accelerators.

A comparative method of screening new ram accelerator fuel mixtures incorporating both total heat release and heat release rates has been suggested. Experiments and subsequent analysis revealed that care must be taken in determining initial conditions for these comparisons to ensure comparable results.

A projectile design which incorporates a straight mid section has been successfully fired through the rigorous starting phase of a ram accelerator. Straight mid sections are desirable to increase projectile cargo space and may also assist in slowing the onset of unstarts and stabilization of combustion beyond the detonation speed of the fuel.

Finally it has been suggested by these experiments that projectile materials may play a role in producing unstarts by unplanned release of energy through the combustion of the projectile material.

ACKNOWLEDGMENTS

Dr. Federico Liberatore for engineering, analytical, and experimental support. Mr. Michael Nusca for critical insights provided by his companion CFD research. Messrs. Robert Hall, John Hewitt, James Tuerk, for continued experimental support. Mr. Albert Horst and Dr. Thomas Minor for continued technical and programmatic support.

REFERENCES

1. Knowlen, C., Bruckner, A. P., and Hertzberg A. "Internal Ballistics of the Ram Accelerator," Proceedings of the 13th International Symposium on Ballistics, Stockholm, Sweden, 1-3 June 1992.

2. Kruczynski, D., "Experimental Demonstration of a 120-mm Ram Accelerator", 29th JANNAF Combustion Meeting", Oct. 1992.

3. Kruczynski D., "New Experiments in a 120-mm Ram Accelerator at High Pressures", AIAA/SAE/ASME/ASEE 29th Joint Propulsion Conference, Monterey, CA, June 28-30, 1993, AIAA Paper 91-2589.

4. Kruczynski D., F. Liberatore, Kiwan M., "Flow Visualization of Steady and Transient Combustion in a 120-mm Ram Accelerator", AIAA/SAE/ASME/ASEE 30th Joint Propulsion Conference, Indianapolis, IN, June 27-29, 1993, AIAA Paper AIAA-94-3344.

5. Nusca M., "Reacting Flow Simulation of Transient Multi-Stage Ram Accelerator Operation and Design Studies", Second International Workshop on Ram Accelerators, July 17-20, 1995.

6. Kruczynski, D., Liberatore F., "Ram Acceleration Experiments with Unique Projectile Geometries", AIAA/SAE/ASME/ASEE 31st Joint Propulsion Conference, San Diego, CA, July 10-12, 1995, AIAA Paper 95-2490.

7. Liberatore F., "The Effects of Real Material Behavior on Ram Accelerator Performance", Second International Workshop on Ram Accelerators, July 17-20, 1995.

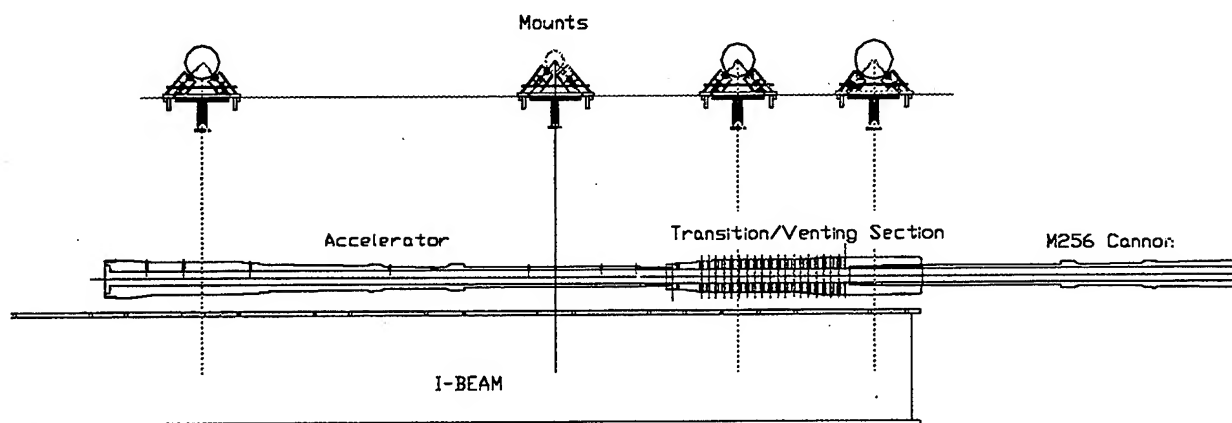


Figure 1 -HIRAM Facility with one accelerator

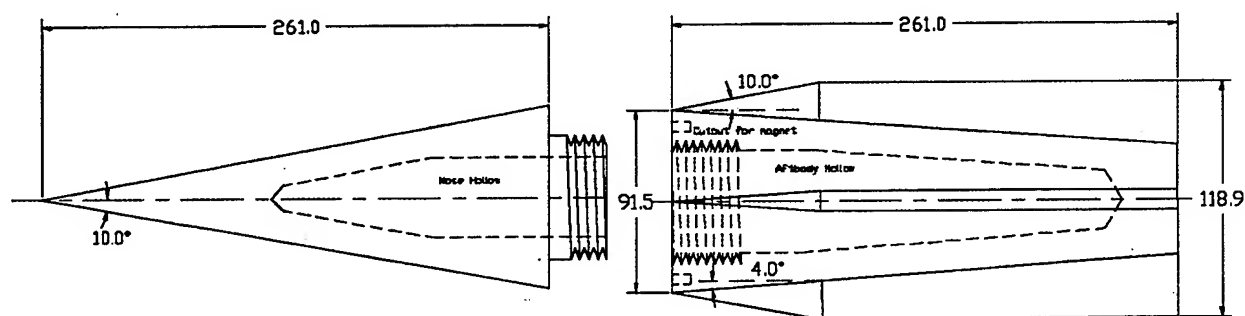
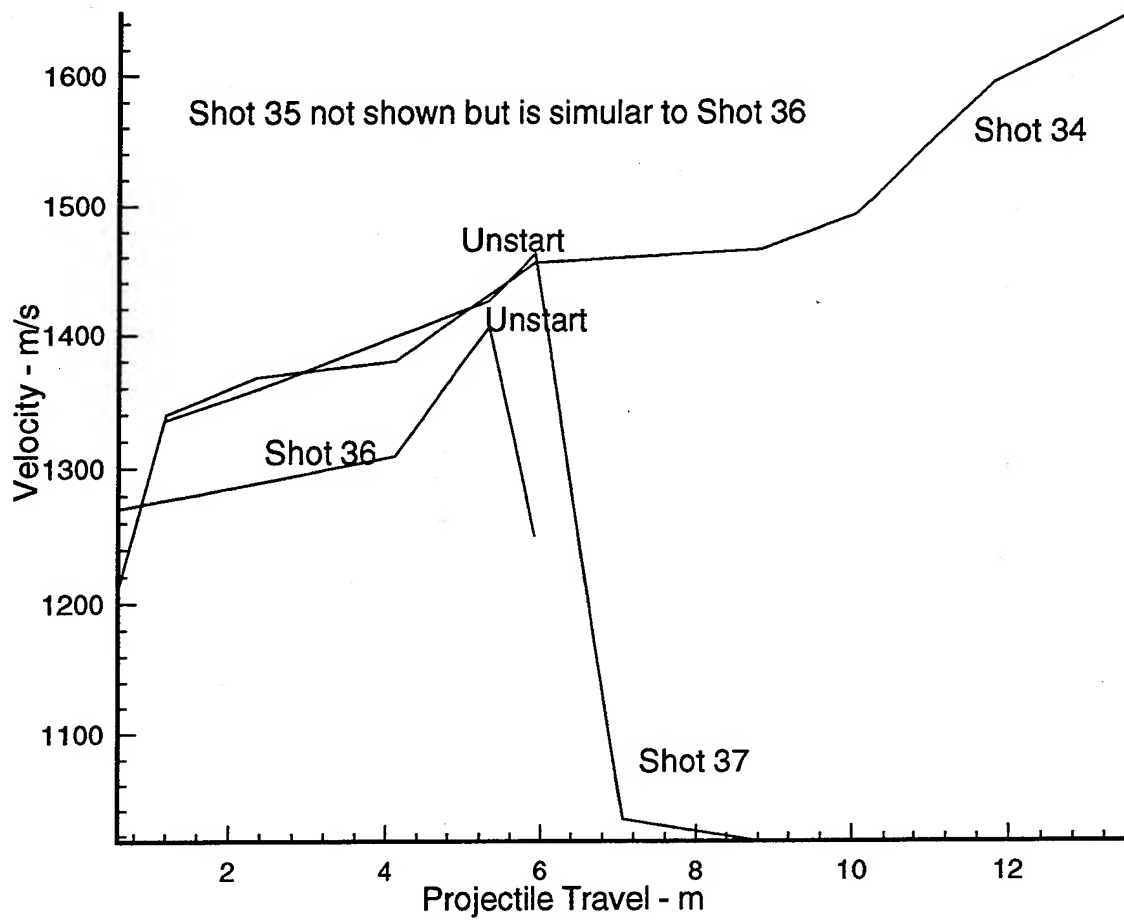


Figure 2 - 120-mm "Standard" HIRAM Projectile

Figure 3. Plot of Velocity Versus Travel



The Impact of Projectile Geometry on Ram Accelerator Performance

T.S. Imrich, J. Elvander, and A.P. Bruckner
Aerospace and Energetics Research Program
University of Washington, Box 353350
Seattle, WA 98195-2250, USA

Abstract

Demonstrating a projectile velocity of 3 km/sec at the UW facility is an important milestone for validating the ram accelerator as a high velocity launch system. Previous research has been directed at modeling various propulsion modes¹⁻⁵ and mapping the ram accelerator's operational envelope in different propellant mixtures.^{6,7} However, to date there has been no systematic attempt to determine the effect of various geometric parameters on ram accelerator operation.

From first principles, acceleration may be increased by either increasing the thrust or decreasing the mass of the projectile. Quasi-one dimensional models developed by Hertzberg et al suggest two ways of increasing thrust. One method is to increase the heat release of the propellant, and the other is to operate at a low Mach number, where the thrust is a maximum for a given amount of heat release. Theoretical models predicted that operation in energetic mixtures could be obtained by increasing the projectile diameter, thus decreasing the flow-throat area. An experimental series was conducted to investigate this promising prediction, but the experiments failed to exhibit a clear sign of improved performance. However, experiments investigating low Mach number operation displayed improved performance, demonstrating higher than nominal accelerations in substantially less energetic mixtures.

To reduce the mass of the projectile, experiments were conducted to study the effects of nose cone angle, body length, and fin configuration. The experiments demonstrated that the projectile's ultimate velocity is very sensitive to nose angle and body length, but the effect of fin configuration is unclear. The unstart velocity is believed to depend of the nose cone angle due to structural limitations of the material, while the influence of the body length is thought to be gasdynamic in nature. The fin configuration does influence the projectile's acceleration performance, but the configuration providing the highest acceleration remains unknown.

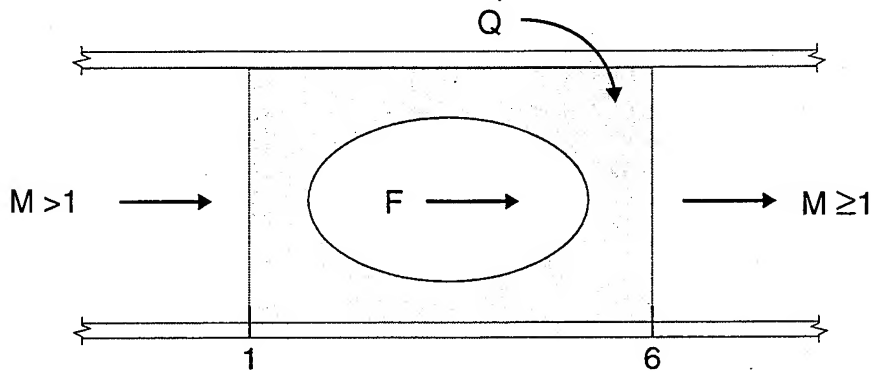
The failure of previous theoretical models to explain the relationship between the unstart velocity and the projectile's body length motivated an investigation of a shock-train model for ram accelerator propulsion. This model is based on previous research of the role of isolators in dual-mode scramjet engines and overexpanded flow in ducts. The limits predicted by the shock-train model correlate well with the results of experiments, and it can provide important insight into the future operation of the ram accelerator.⁸⁻¹²

References

1. Hertzberg, A., Bruckner, A.P., and Bogdanoff, D.W., "Ram Accelerator: A New Chemical Method for Accelerating Projectiles to Ultrahigh Velocities," *AIAA Journal*, Vol. 26, No. 2, February 1988, pp. 195-203.
2. Hertzberg, A., Bruckner, A.P., and Knowlen, C., "Experimental Investigation of Ram Accelerator Propulsion Modes," *Shock Waves*, Vol. 1, 1991, pp.17-25.
3. Burnham, E.A., Kull, A.E., Knowlen, C., Bruckner, A.P., and Hertzberg, A., "Operation of the Ram Accelerator in the Transdetonative Velocity Regime," 26th Joint Propulsion Conference, Orlando, FLA., AIAA 90-1985, July 16-18, 1990.
4. Kull, A.E., Burnham, E.A., Knowlen, C., and Hertzberg, A., "Experimental Studies of Superdetonative Ram Accelerator Modes," 25th Joint Propulsion Conference, Monterey, CA., AIAA 89-2632, July 10-12, 1989.
5. Bruckner, A.P., Knowlen, C., Hertzberg, A., and Bogdanoff, D.W., "Operational Characteristics of the Thermally Choked Ram Accelerator," *Journal of Propulsion and Power*, Vol. 7, No. 5, 1991, pp.828-836.
6. Higgins, A.J., Knowlen, C., and Bruckner, A.P., "An Investigation of Ram Accelerator Gas Dynamic Limits," AIAA Paper 93-2181, June, 1993.
7. Higgins, A.J., "Gas Dynamic Limits of the Ram Accelerator," MS Thesis, University of Washington, 1993.
8. Billig, F.S. "Research on Supersonic Combustion", *Journal of Propulsion and Power*, Vol. 9, No. 4, 1993, pp. 499-514.
9. Pratt, D.T., and Heiser, W.H., "Isolator-Combustor Interaction in a Dual-Mode Scramjet Engine," 31st Aerospace Sciences Meeting and Exhibit, Reno, NV, AIAA 93-0358, January 11-14, 1993.
10. Waltrup, P.J., and Billig, F.S., "Structure of Shock Waves in Cylindrical Ducts," *AIAA Journal*, Vol. 11, No. 10, October 1973, pp. 1404-1408.
11. Heiser, W.H. and Pratt, D.T., *Hypersonic Airbreathing Propulsion*, AIAA Education Series, Washington, DC, 1994, pp. 251-256, 333-370.
12. Van Wie, D.M., "Application of Scramjet Engine Technology to the Design of Ram Accelerator Projectiles," 30th JANNAF Combustion Subcommittee Meeting, Monterey, CA, November 15-18, 1993.

Maximizing Acceleration

The Blackbox Model

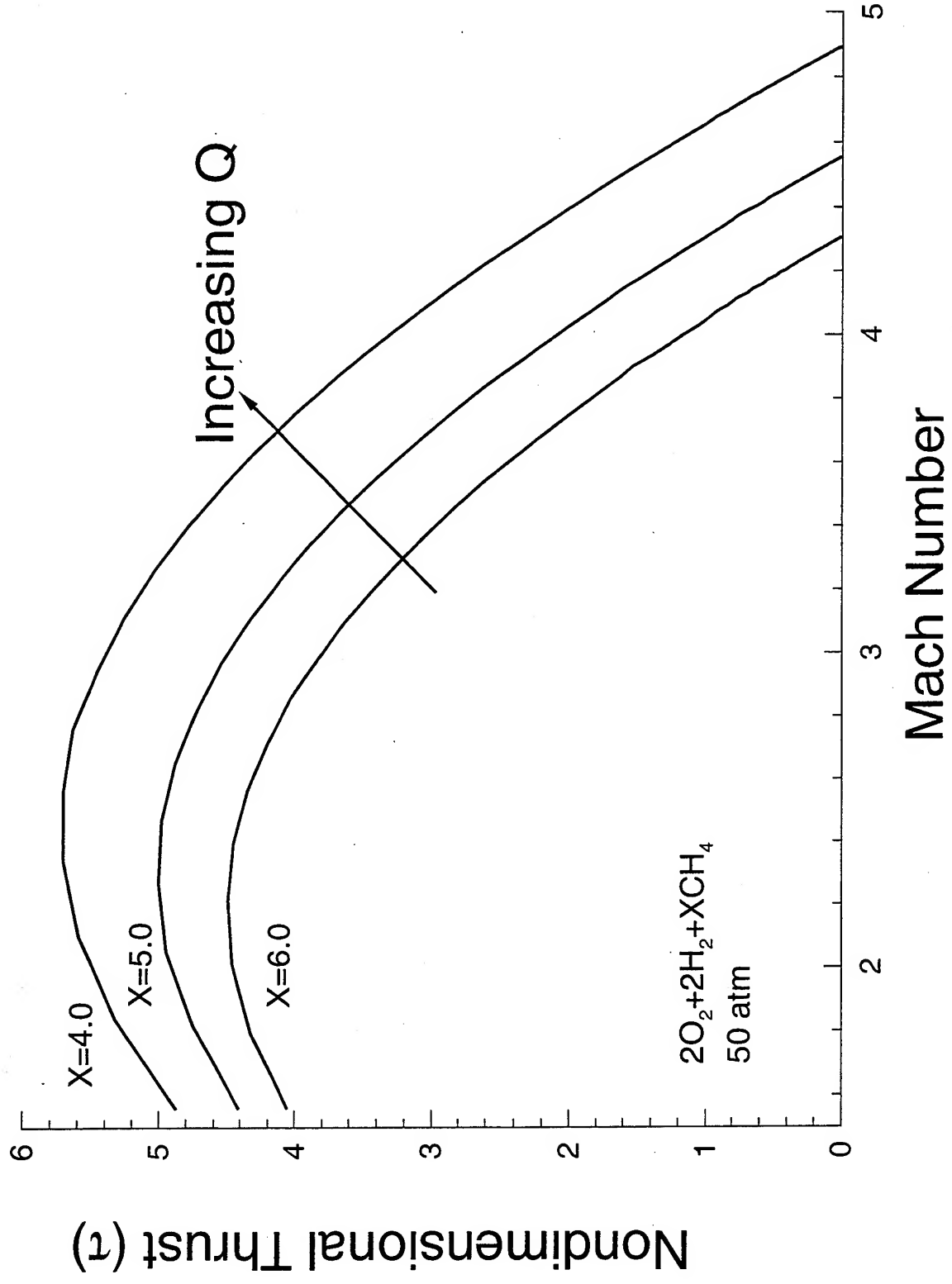


$$a = \frac{F}{m} = \frac{p_1 A \tau}{m} = \frac{p_1 A}{m} \cdot M_1 \left[2(\gamma + 1) \left(1 + \frac{(\gamma - 1)}{2} M_1^2 + Q \right) \right]^{\frac{1}{2}} - (1 + \gamma M_1^2)$$

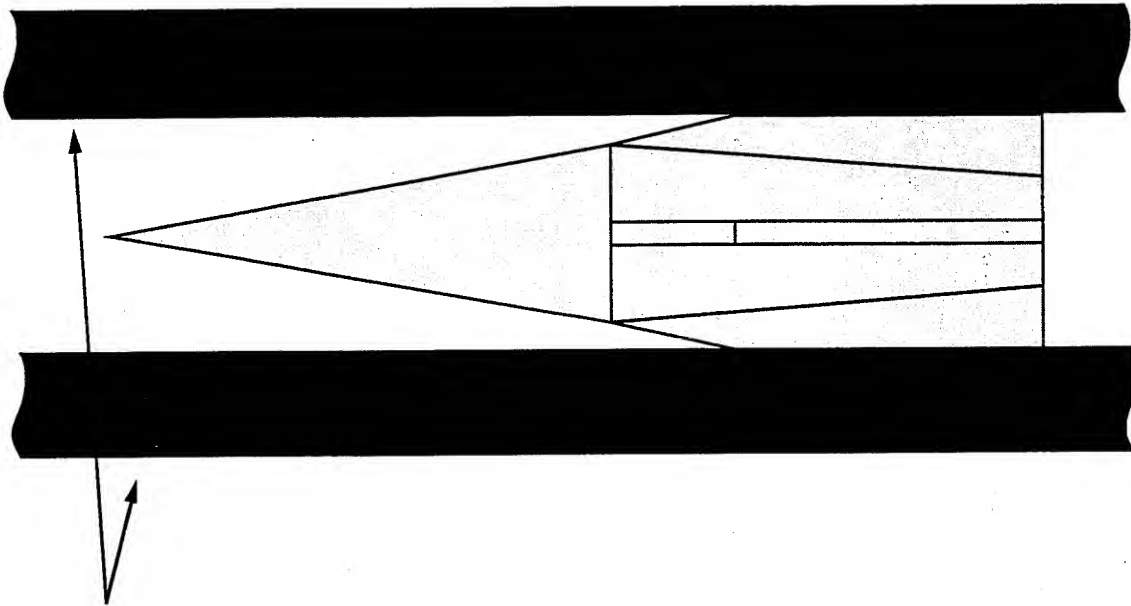
Strategies for Increasing Acceleration:

- **Increase Thrust**
 - **Increase Tube Fill Pressure (p_1)**
 - **Increase Tube Cross Sectional Area (A)**
 - **Increase Heat Release (Q)**
 - **Operate at Lower Mach Number (M_1)**
- **Decrease Projectile Mass**

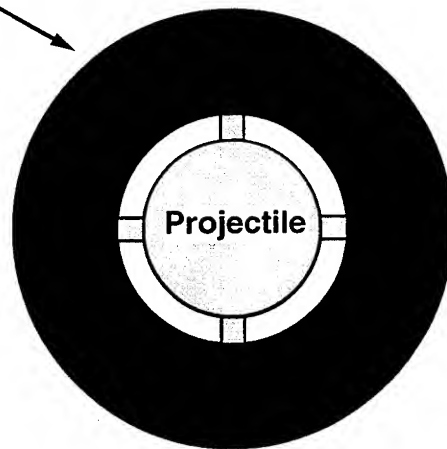
The Effect of Increasing Mixture Energetics



Projectile Flow Throat

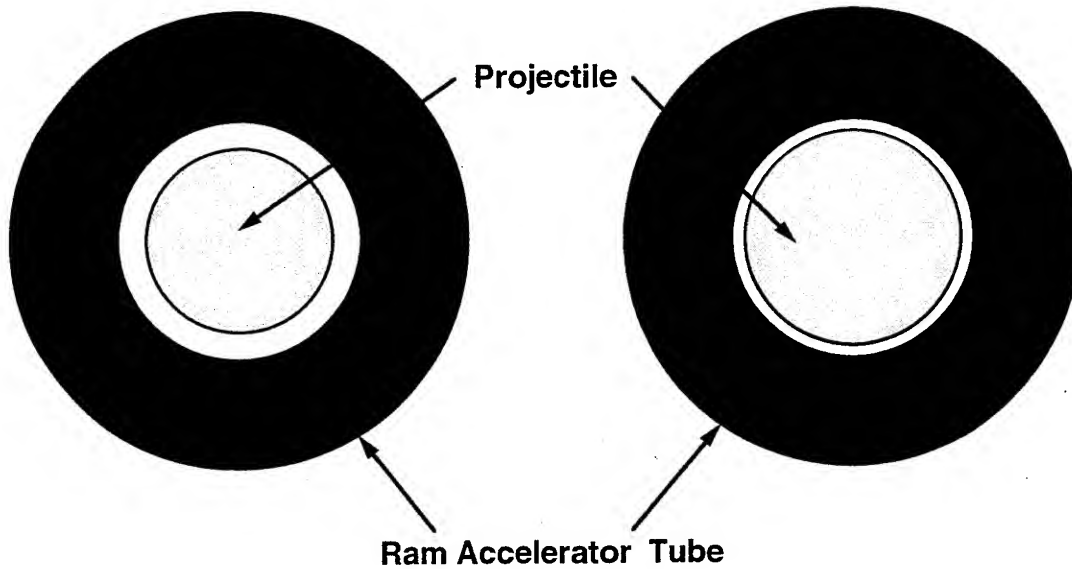
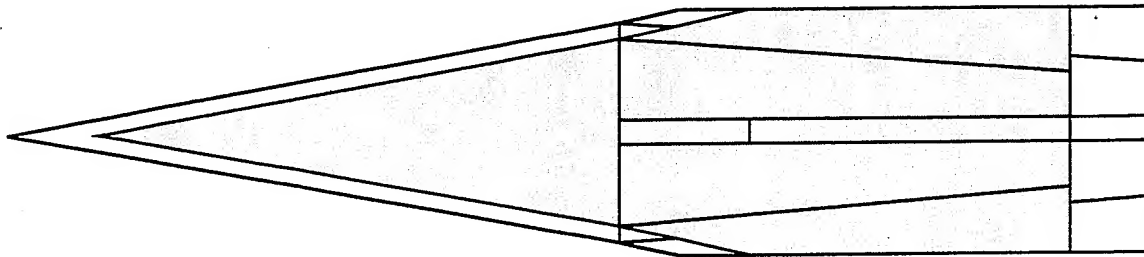


Ram Accelerator Tube



Nominal Flow Throat
($A_{throat}/A_{tube} = 0.42$)

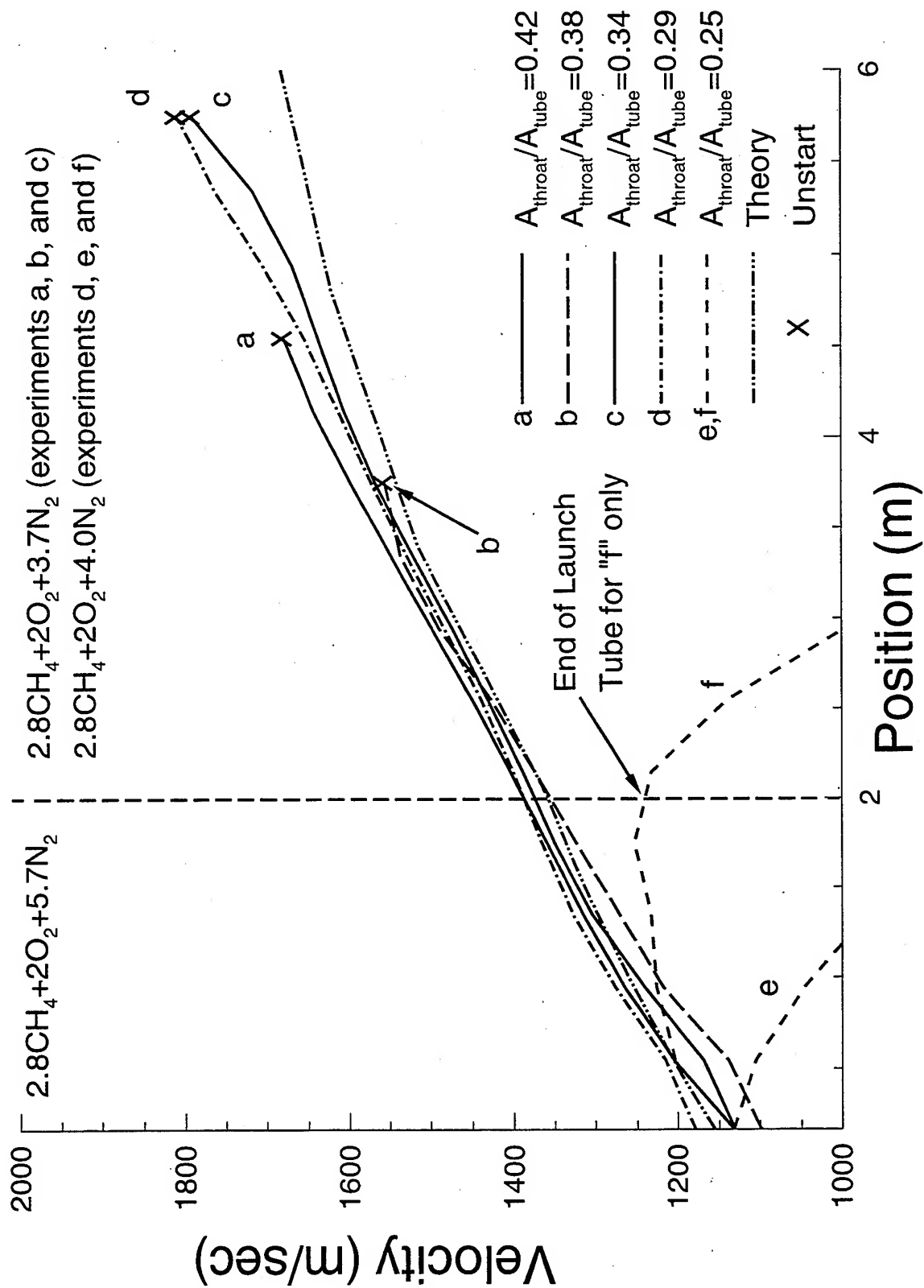
Throat Variation Series



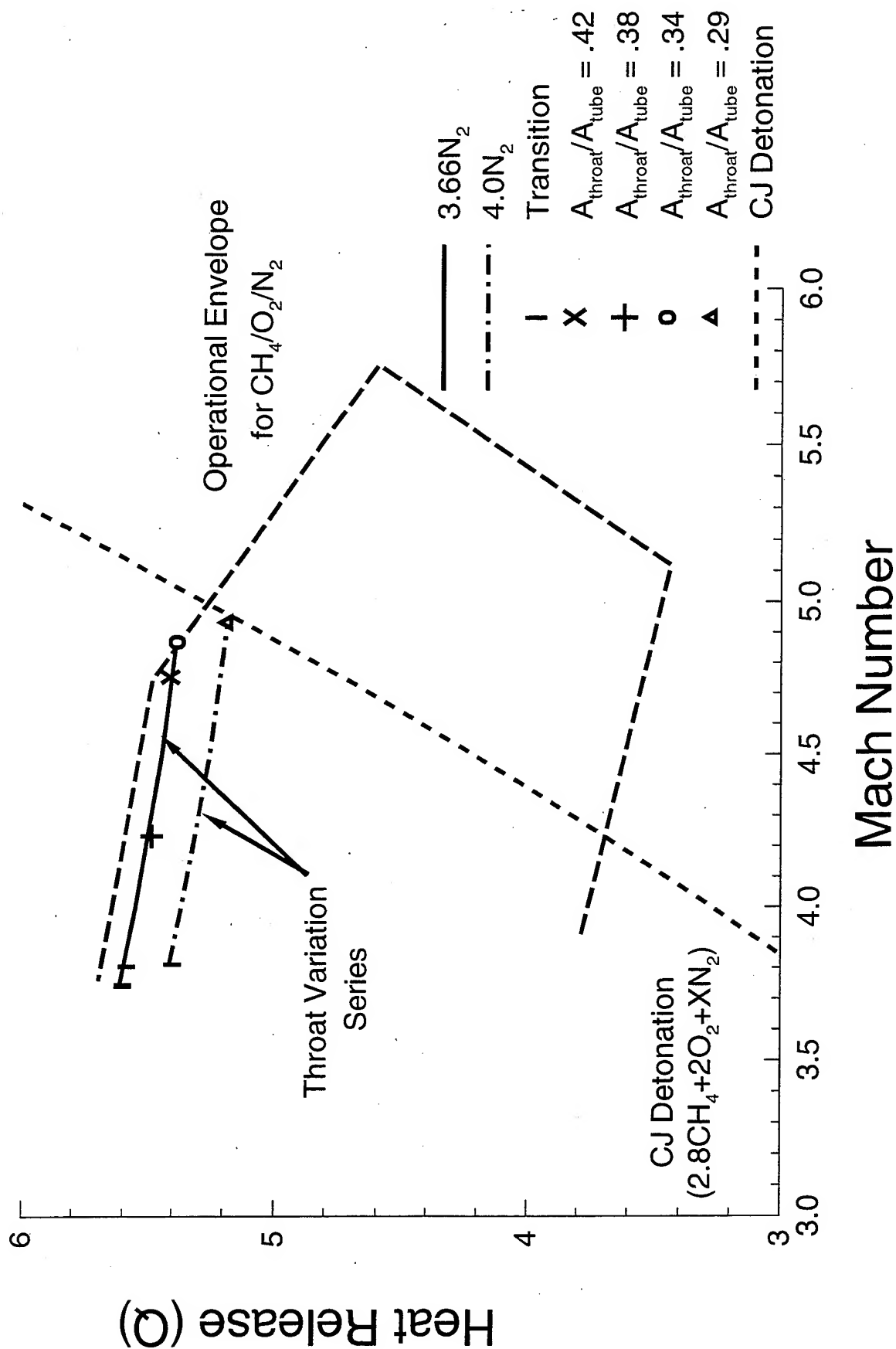
Nominal Flow Throat
($A_{throat}/A_{tube} = 0.42$)

Smallest Flow Throat
($A_{throat}/A_{tube} = 0.29$)

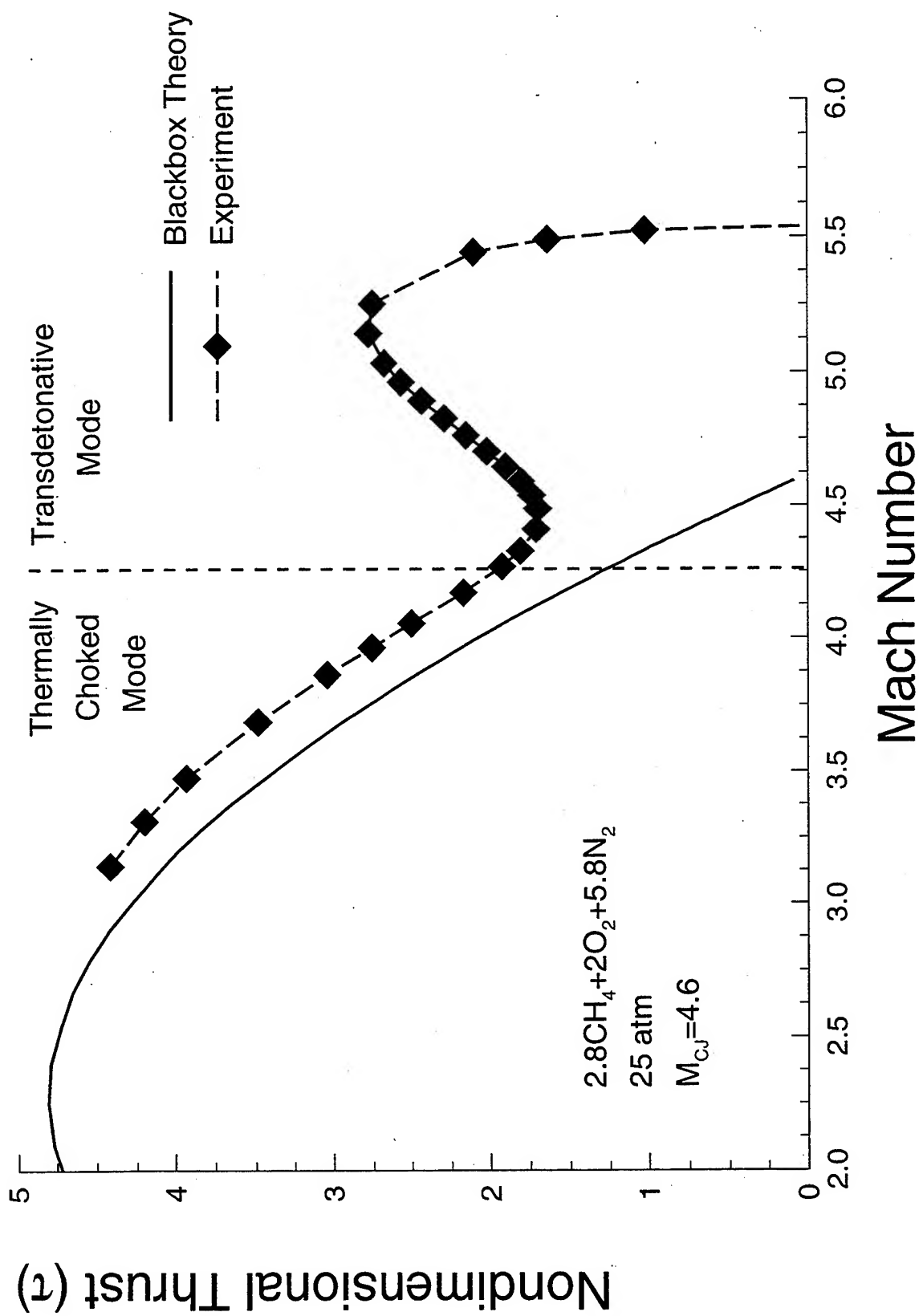
Velocity-Position Data for the Throat Variation Series



Results from the Throat Variation Series

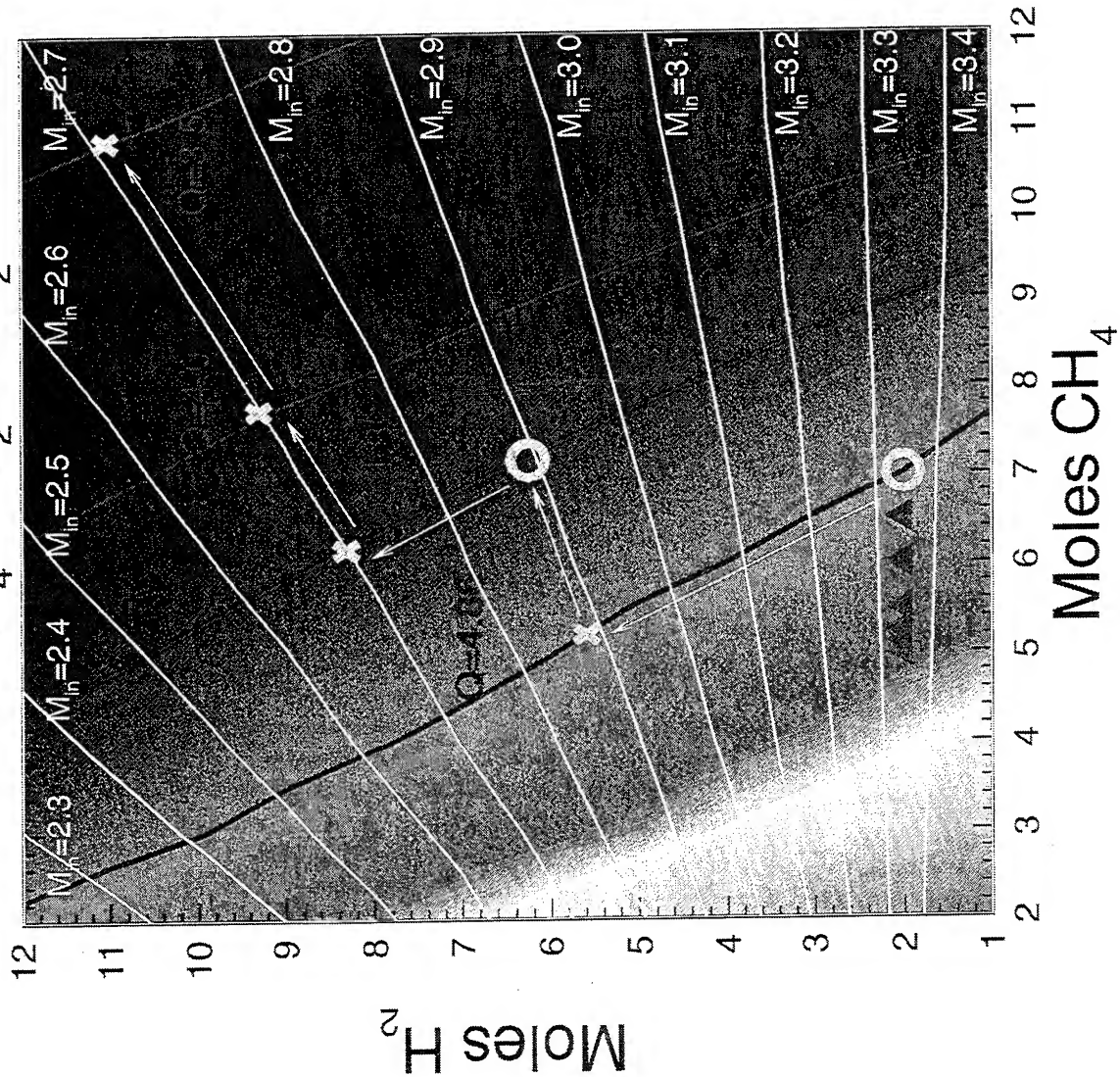


Experimental Experience vs. Theoretical Predictions



Mixture Selection For Low Mach Number Experiments

$X \text{CH}_4 + 2\text{O}_2 + Y \text{H}_2$



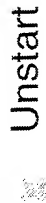
Q



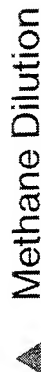
2m Starter Stage
 $2.8\text{CH}_4 + 2\text{O}_2 + 5.7\text{N}_2$
 50 atm
 $V_{in} = 1500 \text{ m/sec}$



Drive Out

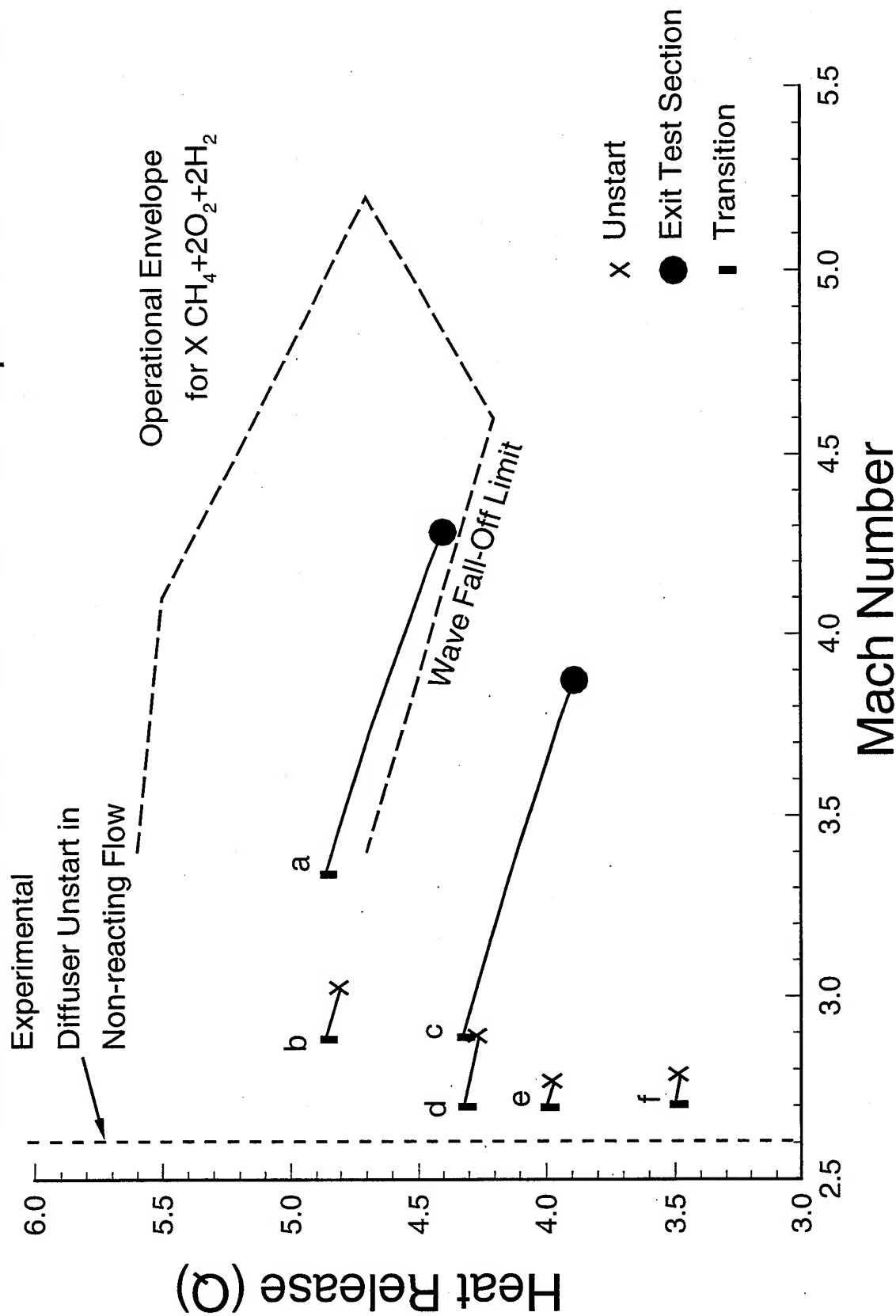


Unstart

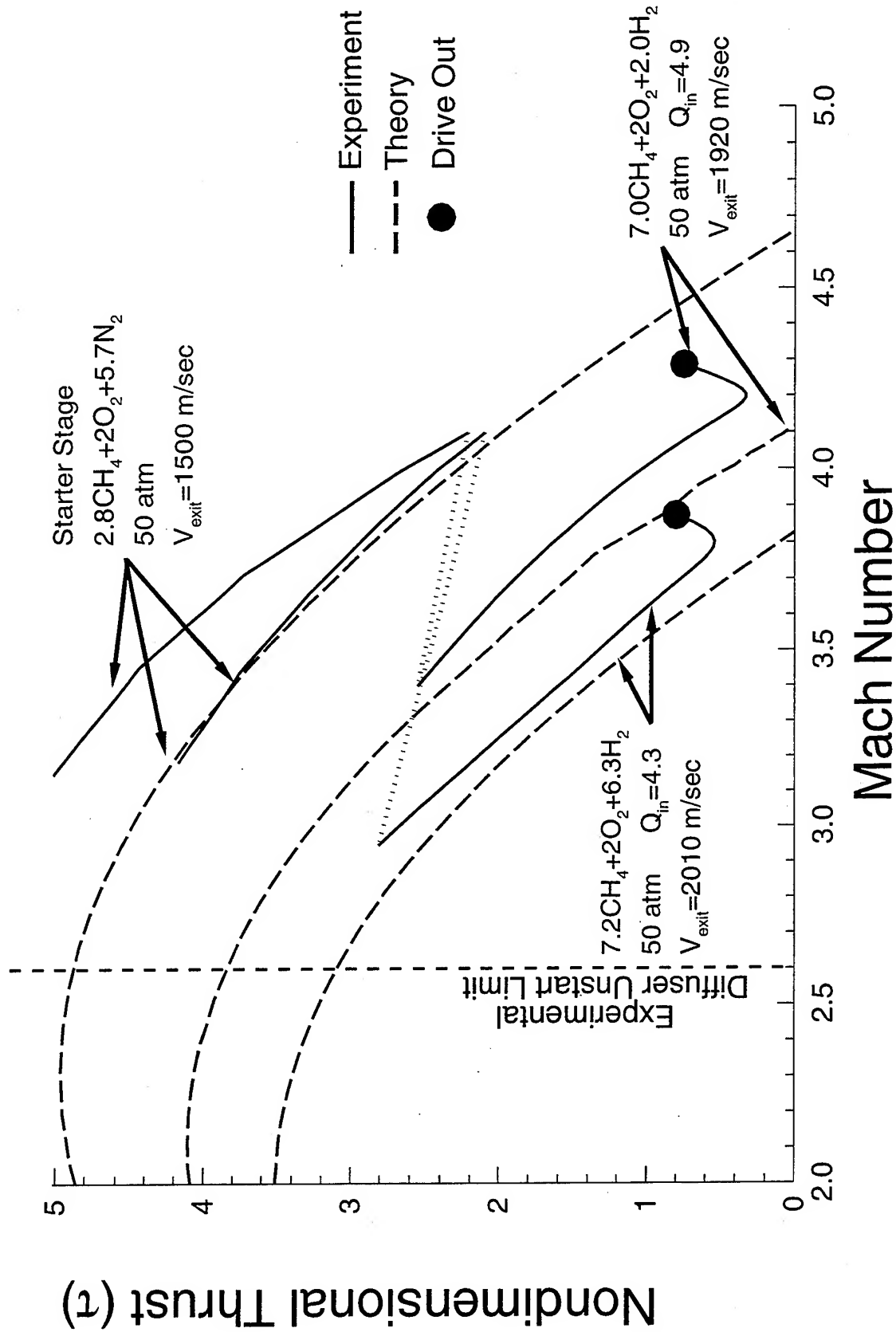


Methane Dilution Series Start

Results of the Low Mach Number Operation Series

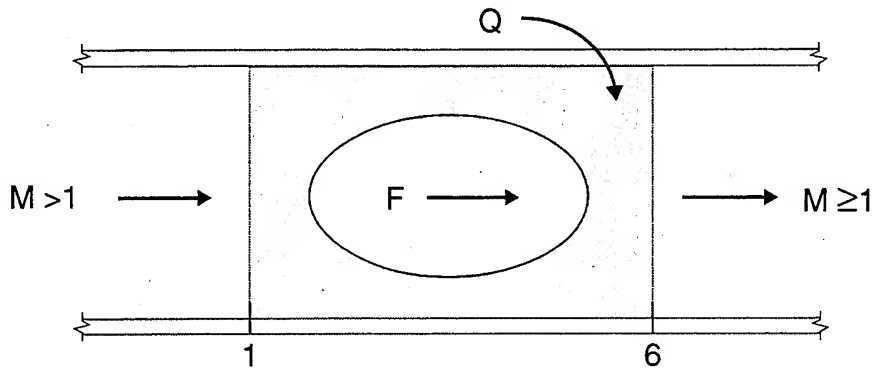


Thrust Profile for a Low Mach Number Experiment



Maximizing Acceleration

The Blackbox Model



$$a = \frac{F}{m} = \frac{p_1 A \tau}{m} = \frac{p_1 A}{m} \cdot M_1 \left[2(\gamma + 1) \left(1 + \frac{(\gamma - 1)}{2} M_1^2 + Q \right) \right]^{\frac{1}{2}} - (1 + \gamma M_1^2)$$

Strategies for Increasing Acceleration:

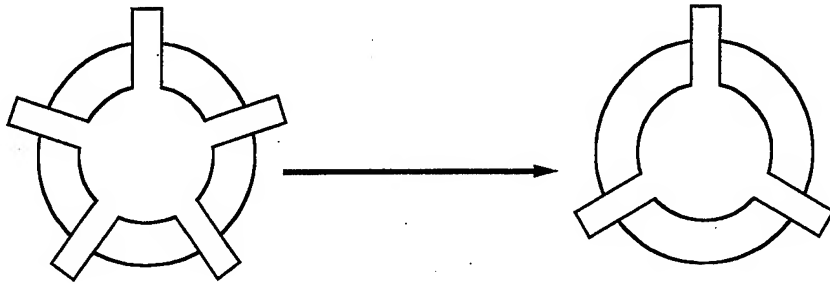
- **Increase Thrust**

- **Increase Tube Fill Pressure (p_1)**
- **Increase Tube Cross Sectional Area (A)**
- **Increase Heat Release (Q)**
- **Operate at Lower Mach Number (M_1)**

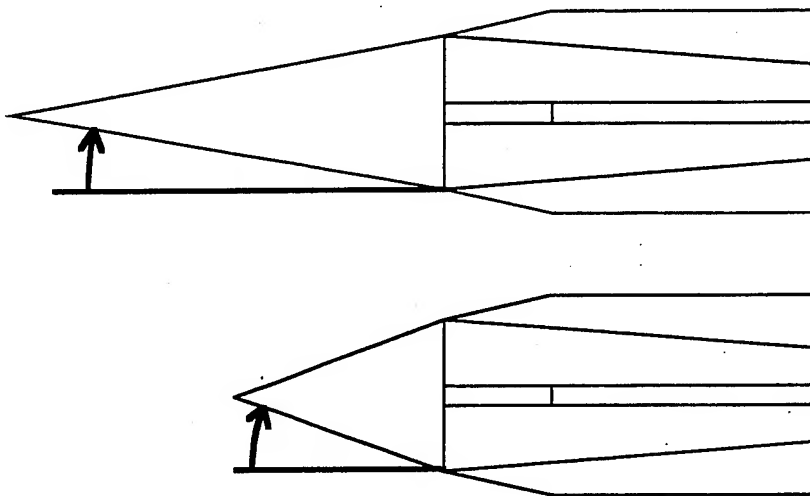
- **Decrease Projectile Mass**

Reducing Projectile Mass

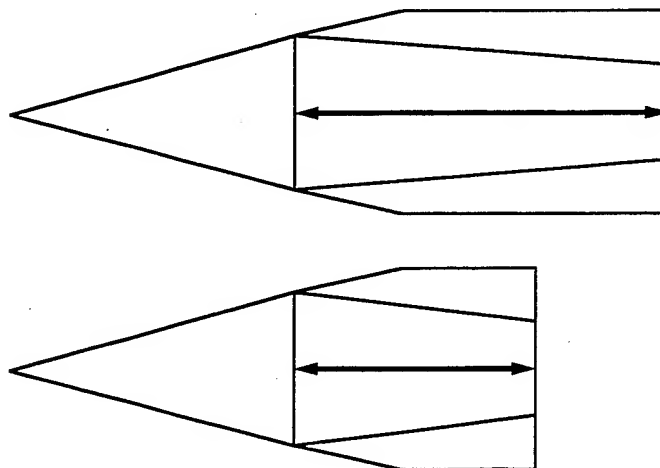
Reduce Fin Number



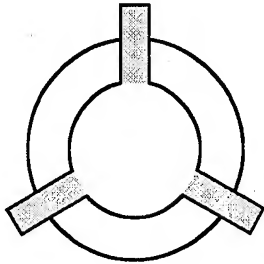
Increase Nose Cone Angle



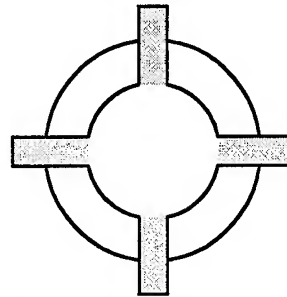
Decrease Body Length



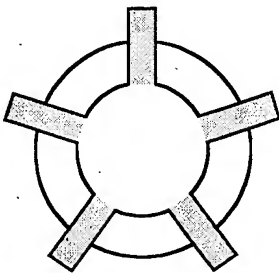
Fin Variation Series



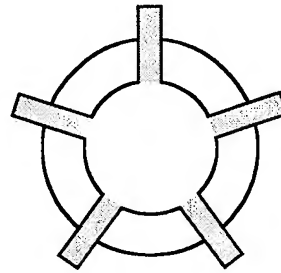
Fin Area: 113 mm²



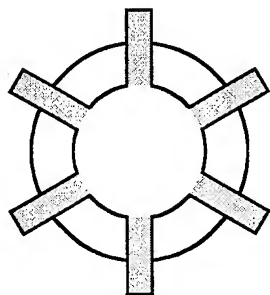
Fin Area: 155 mm²



Fin Area: 186 mm²

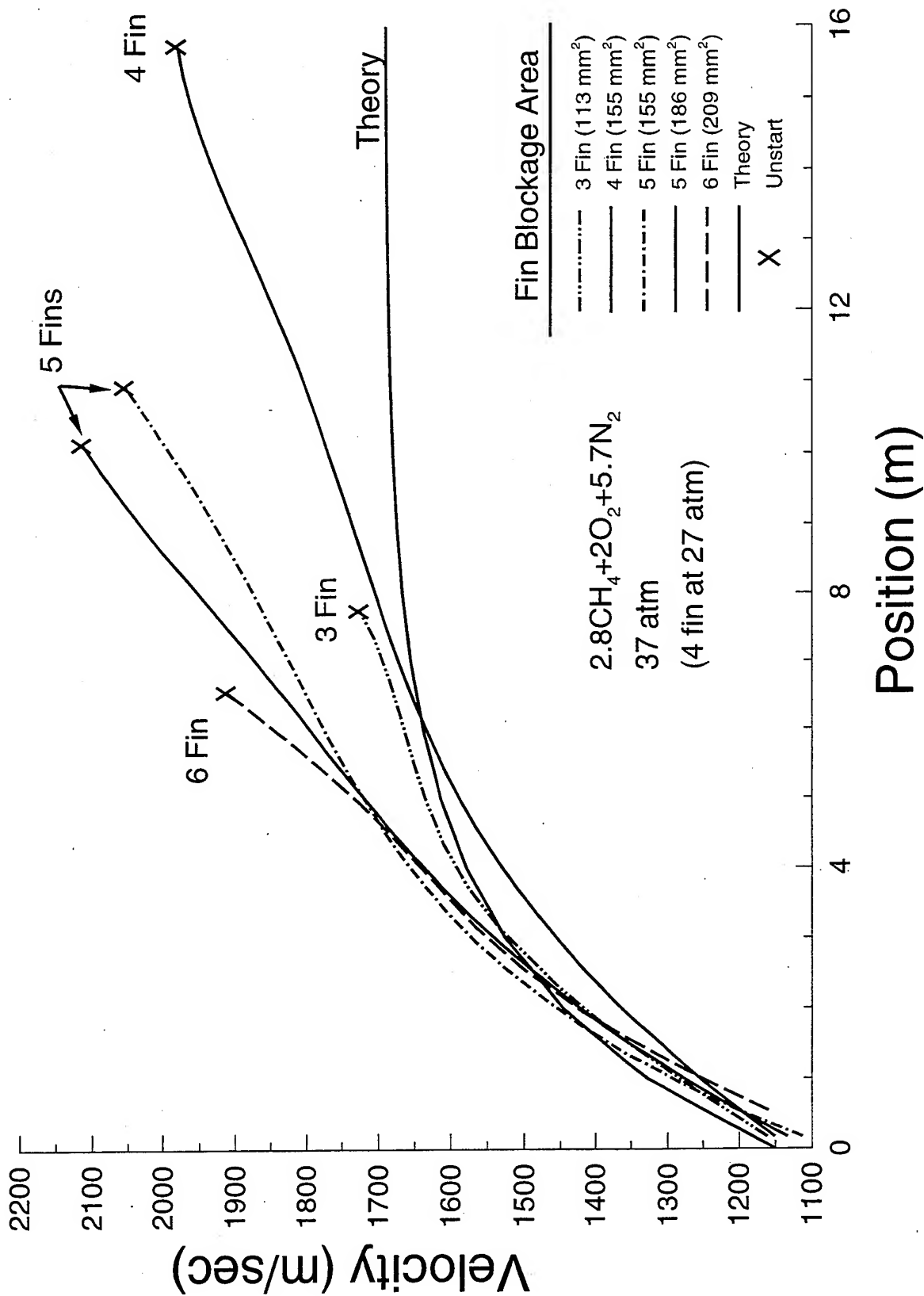


Fin Area: 155 mm²

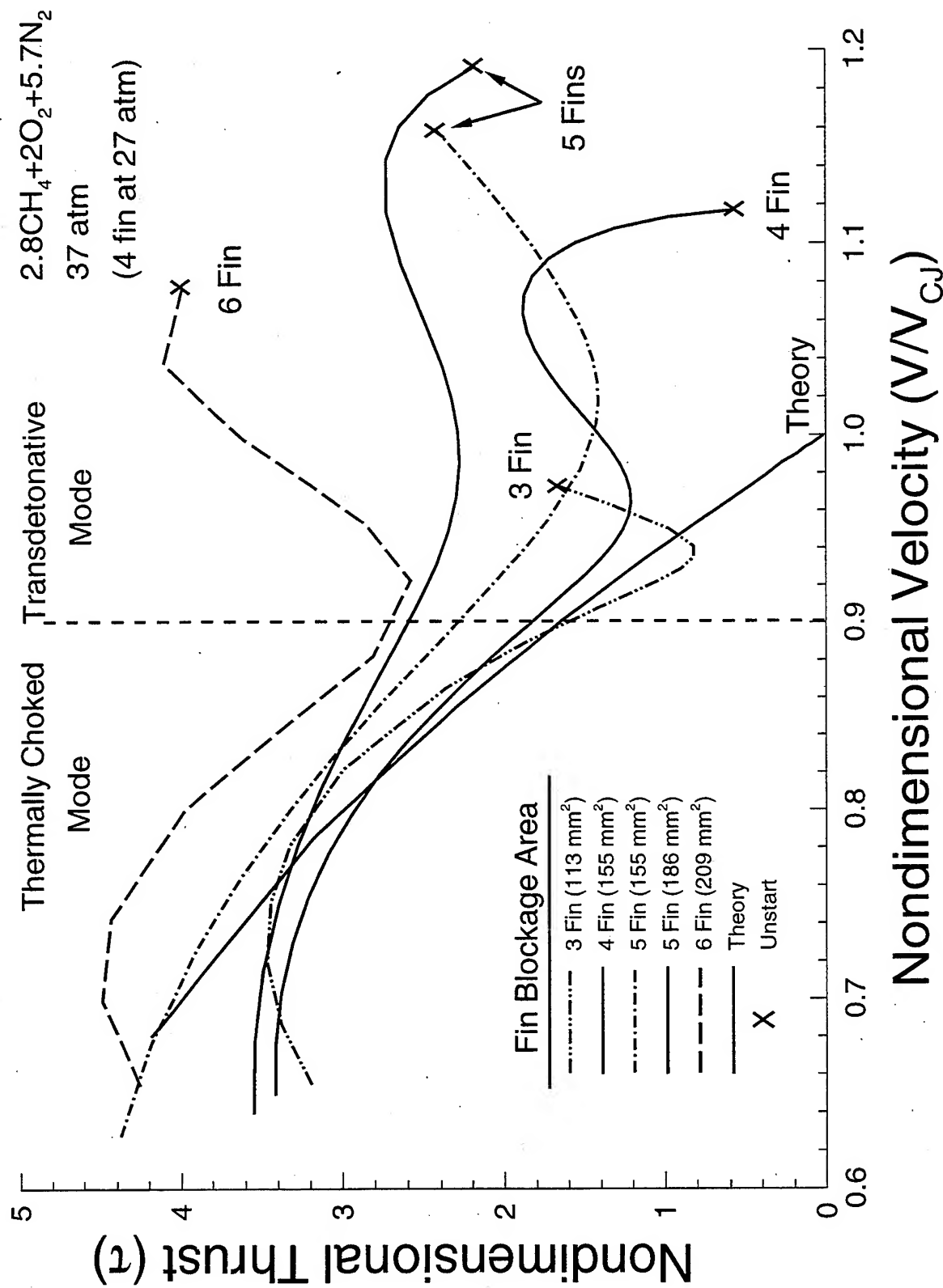


Fin Area: 209 mm²

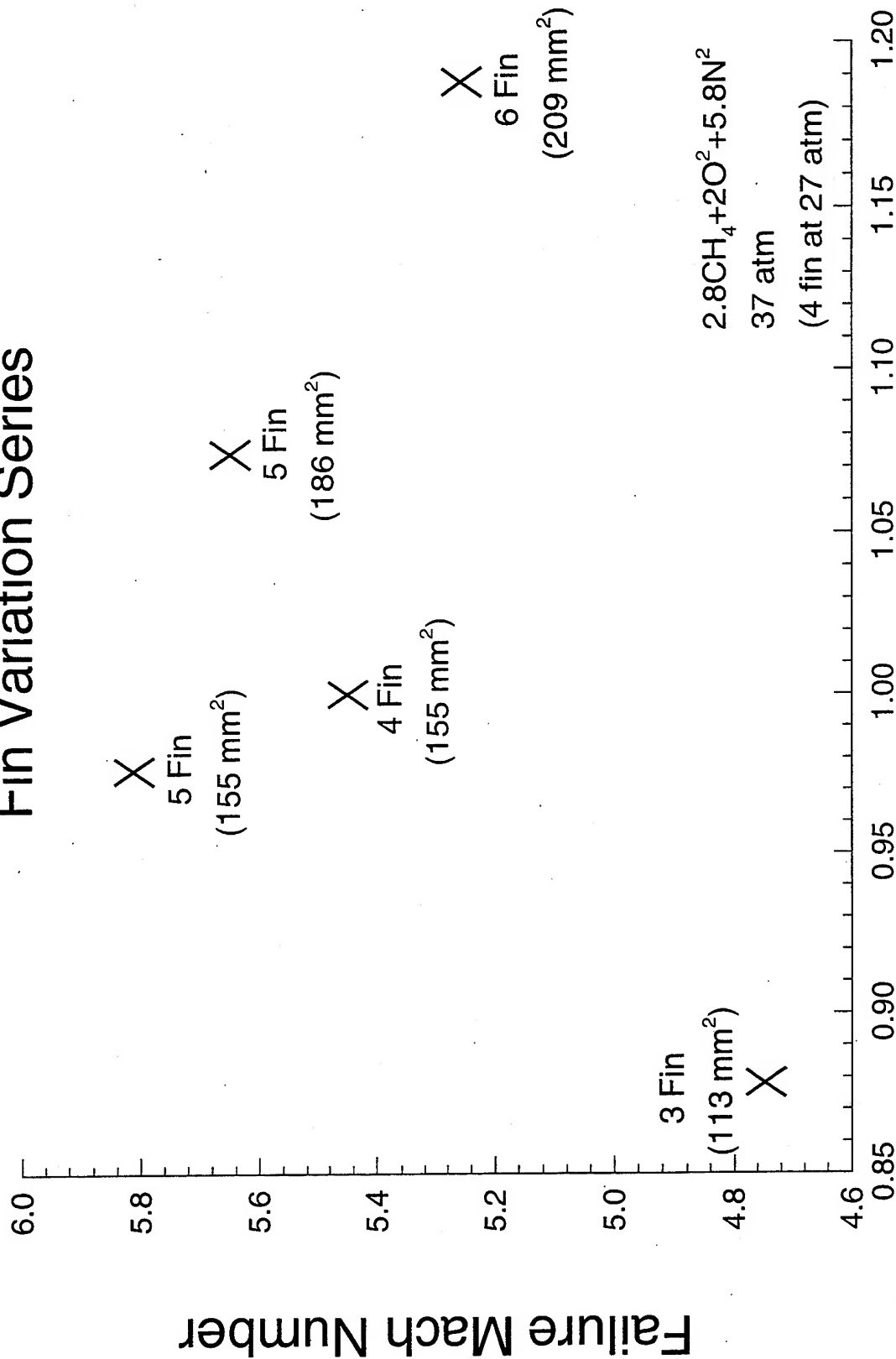
Velocity-Position Data for the Fin Variation Series



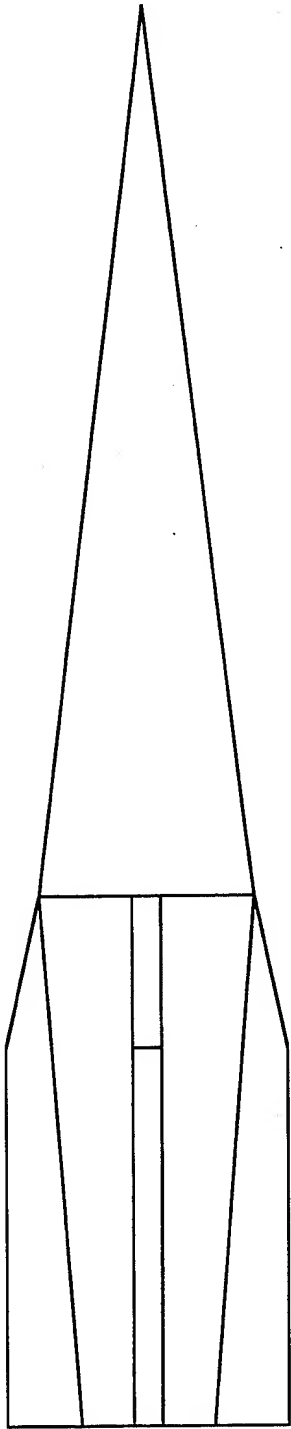
Nondimensional Thrust Profiles for the Fin Variation Series



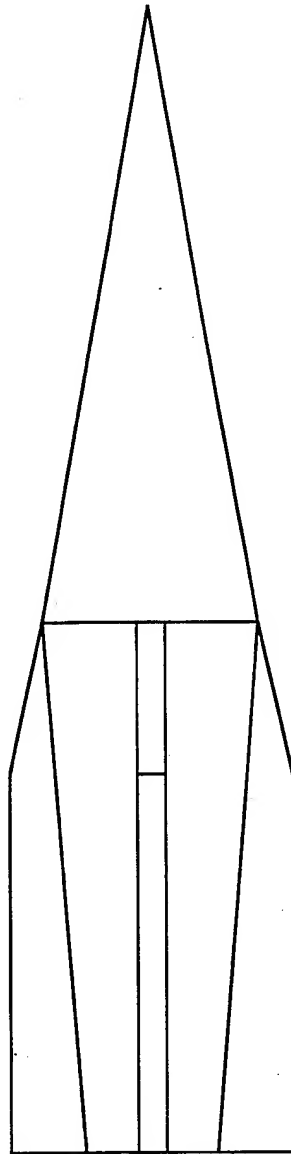
Fin Variation Series



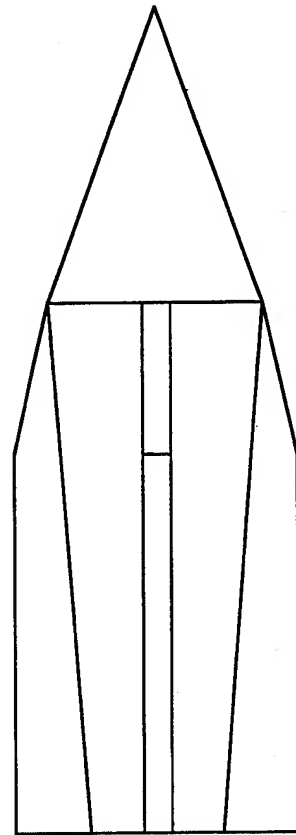
Nose Angle Series



7° Nose

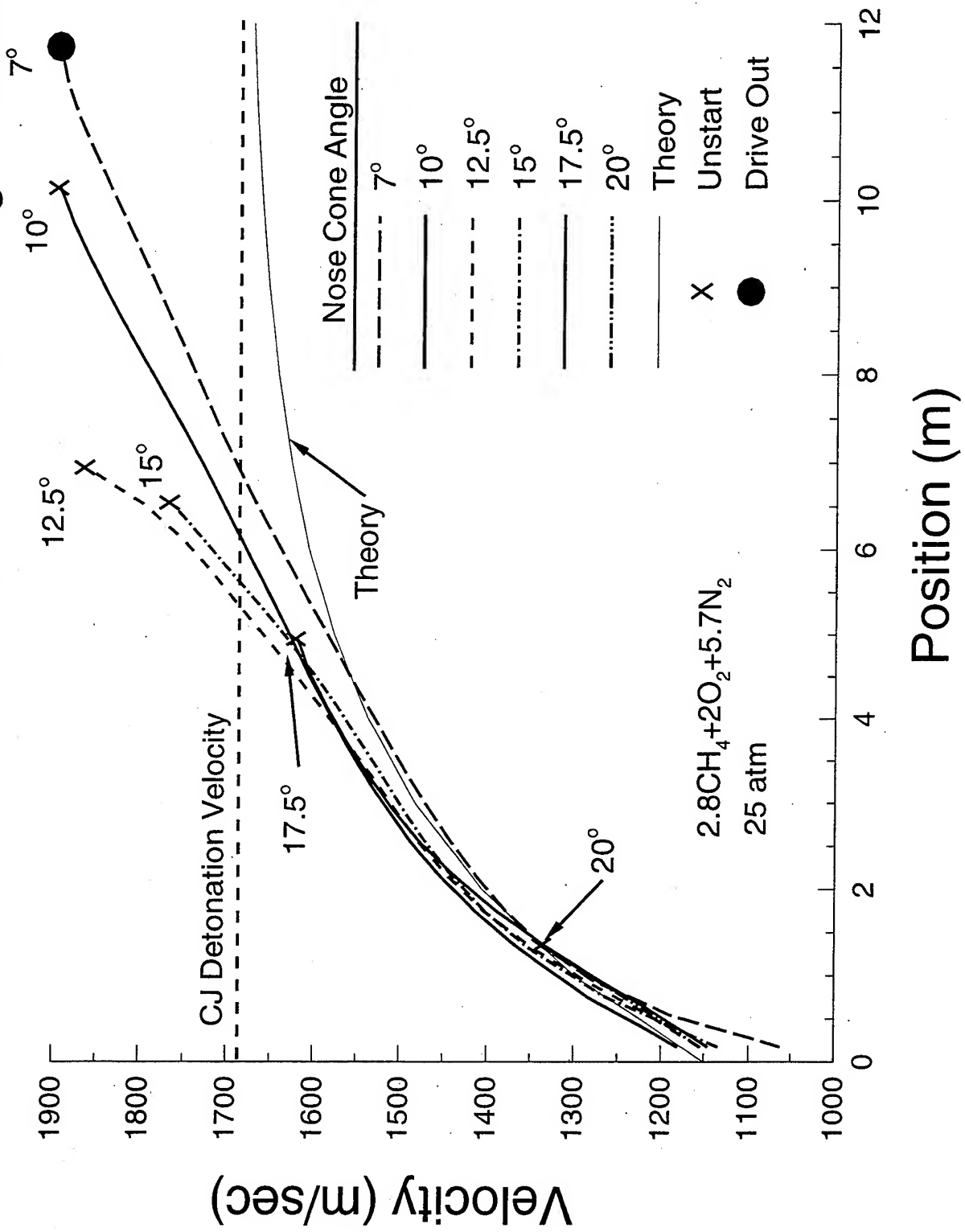


**10° Nose
Standard Projectile**

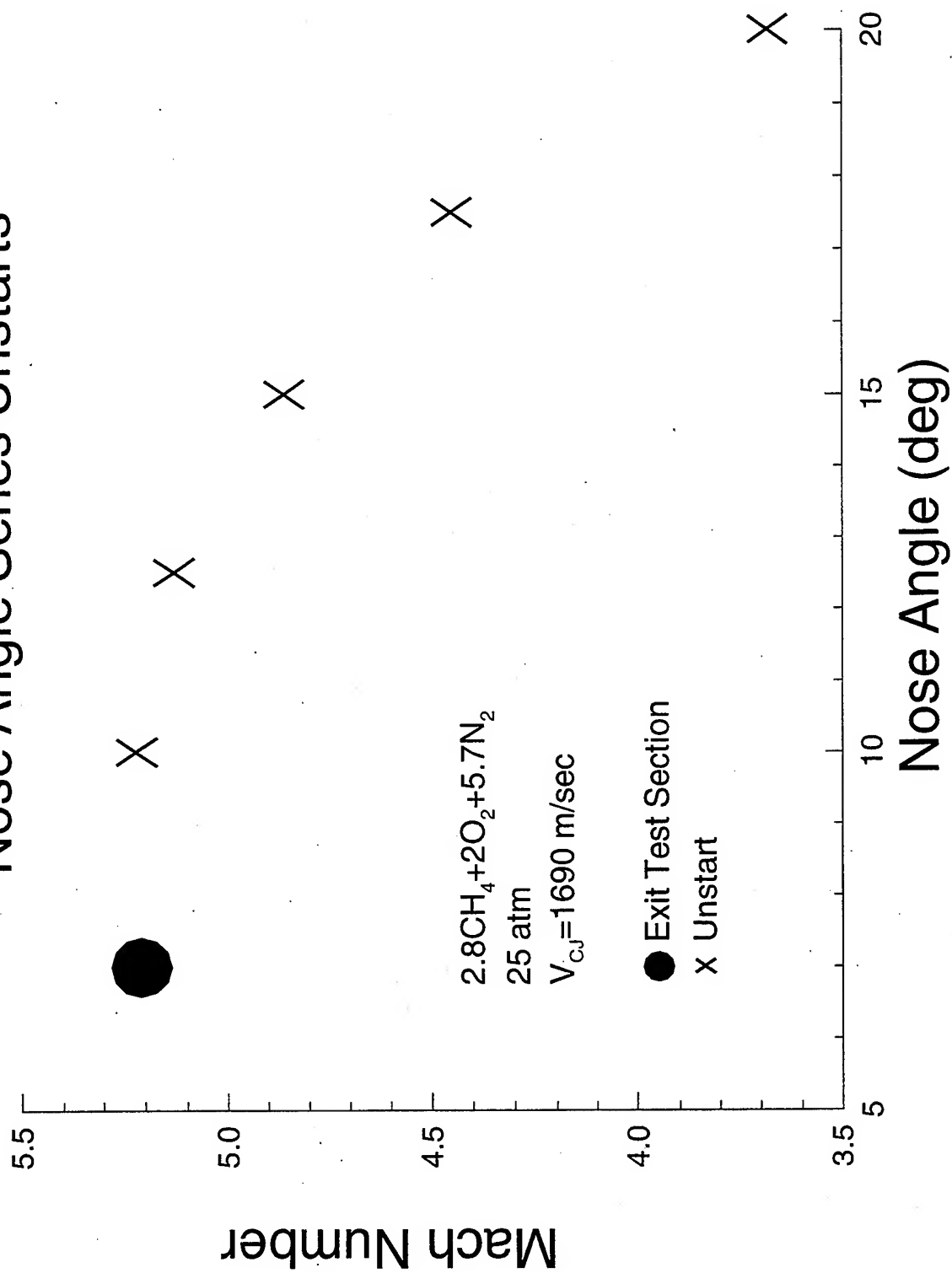


20° Nose

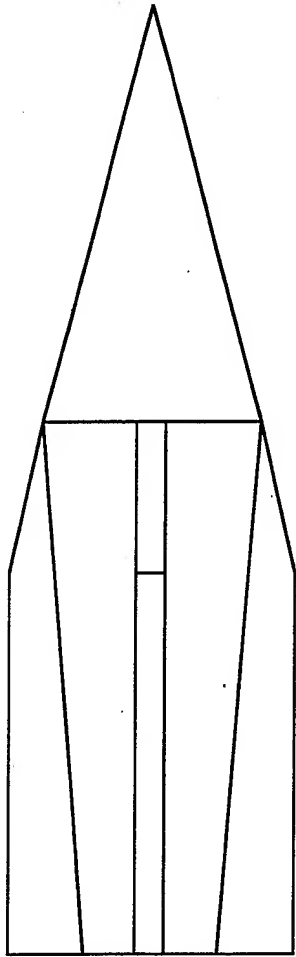
Velocity-Position Data for the Nose Cone Angle Series



Nose Angle Series Unstarts

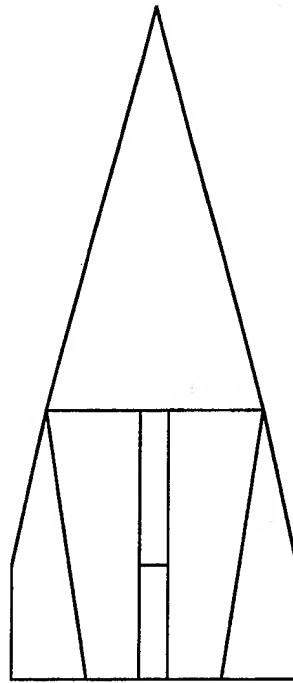


Body Length Series



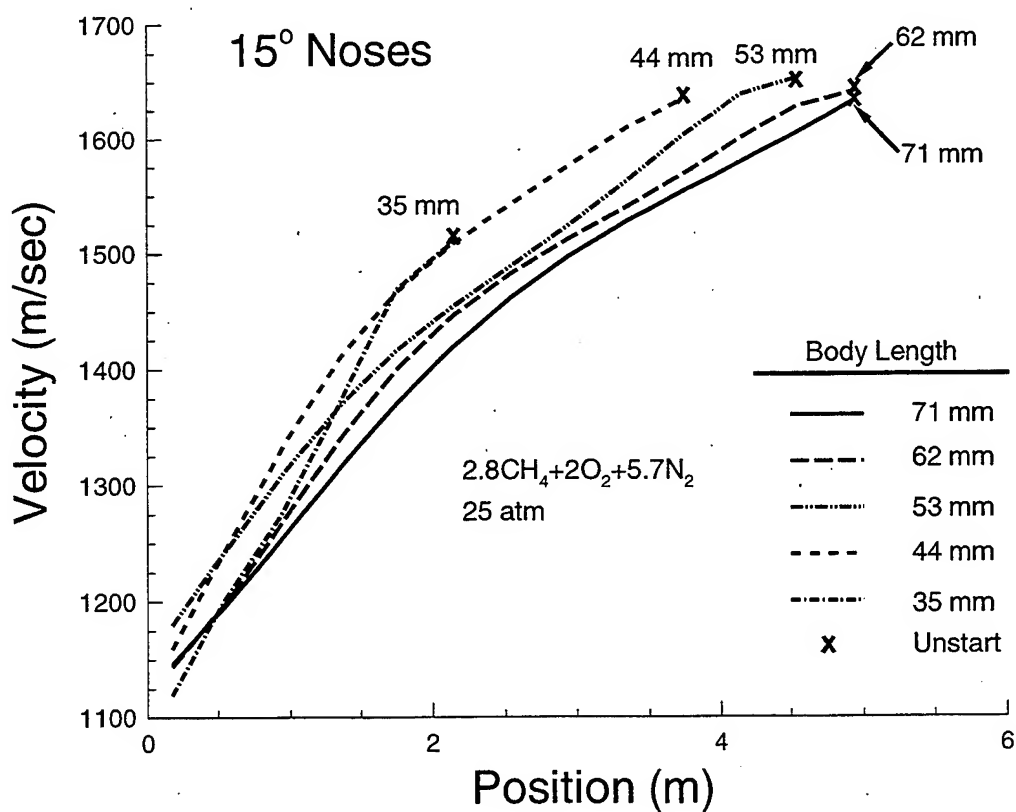
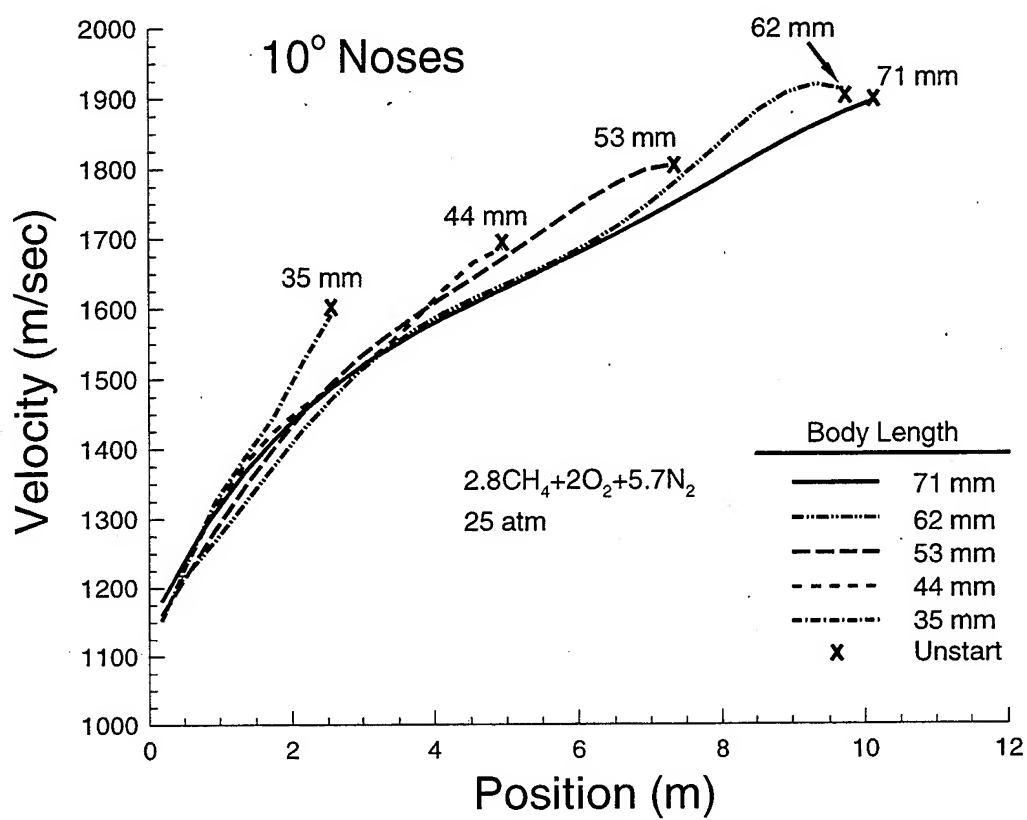
Standard Body

71 mm

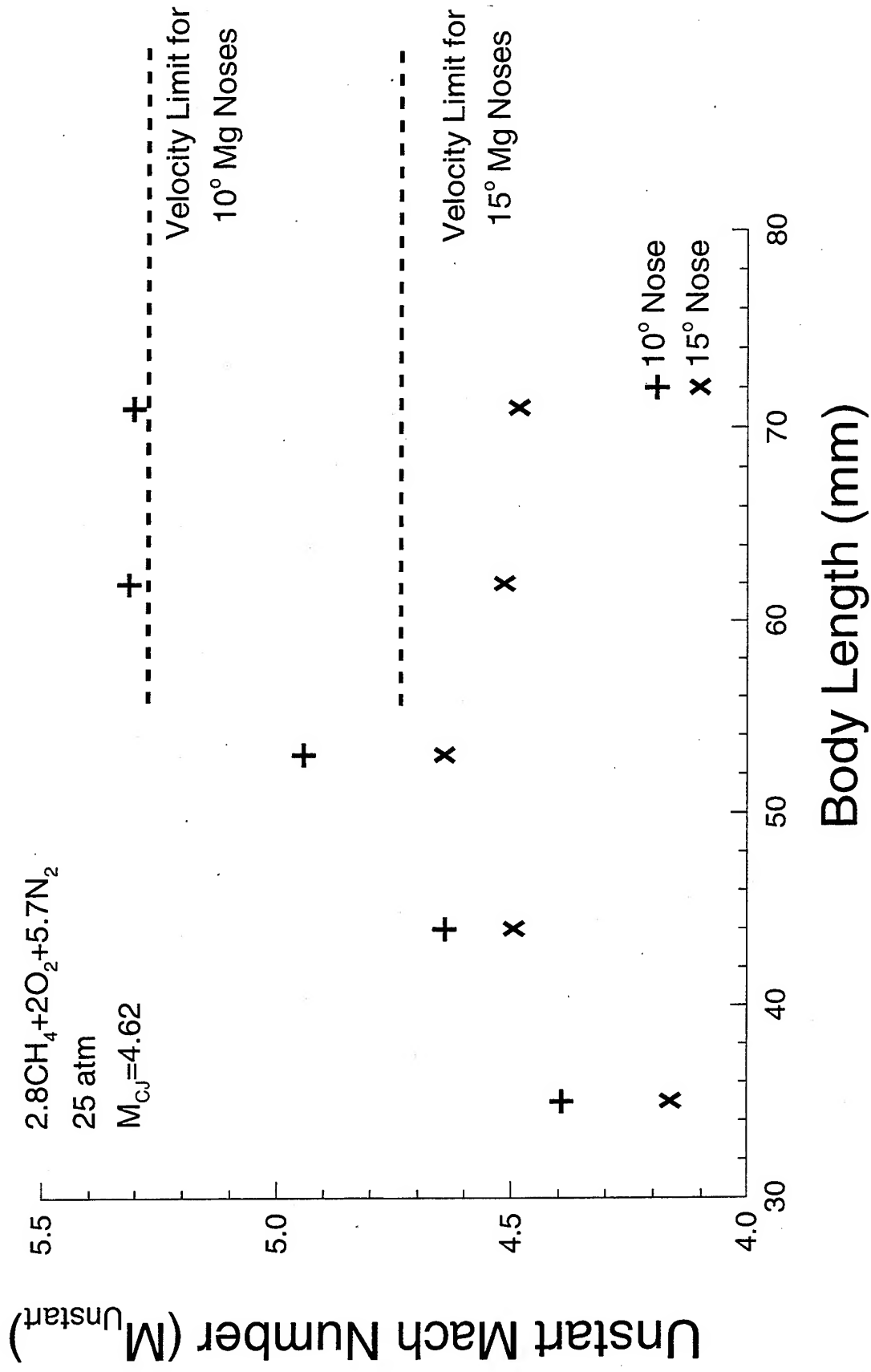


35 mm

Velocity-Position Data for the Body Length Series

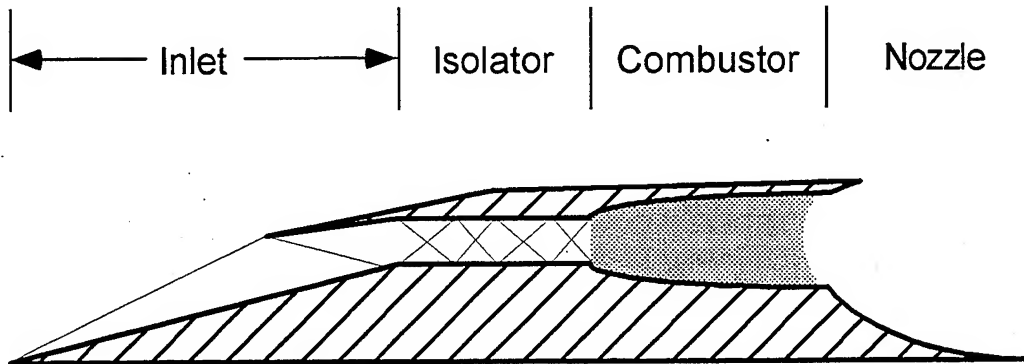


The Effect of Reducing Body Length

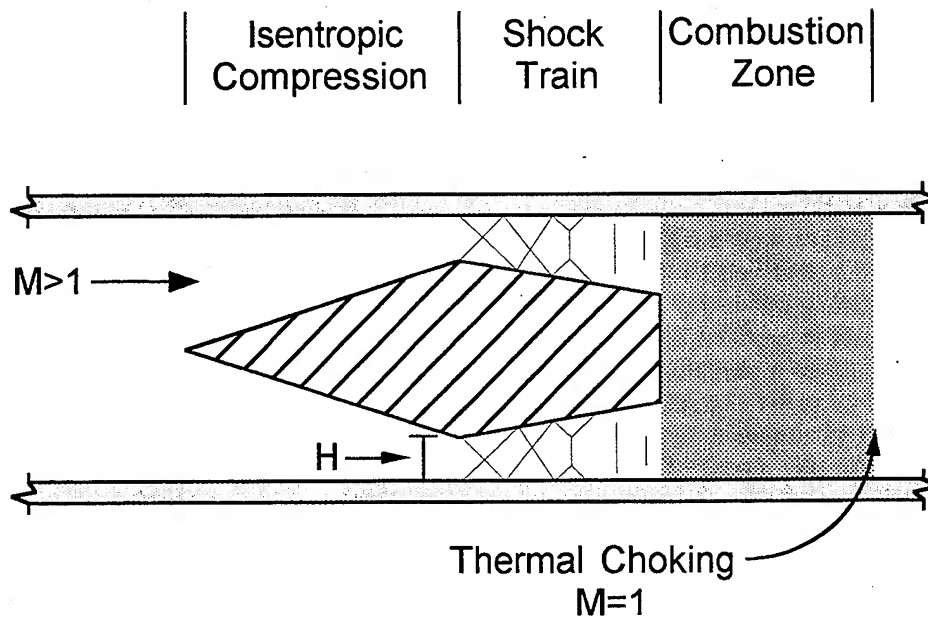


Shock Train Model

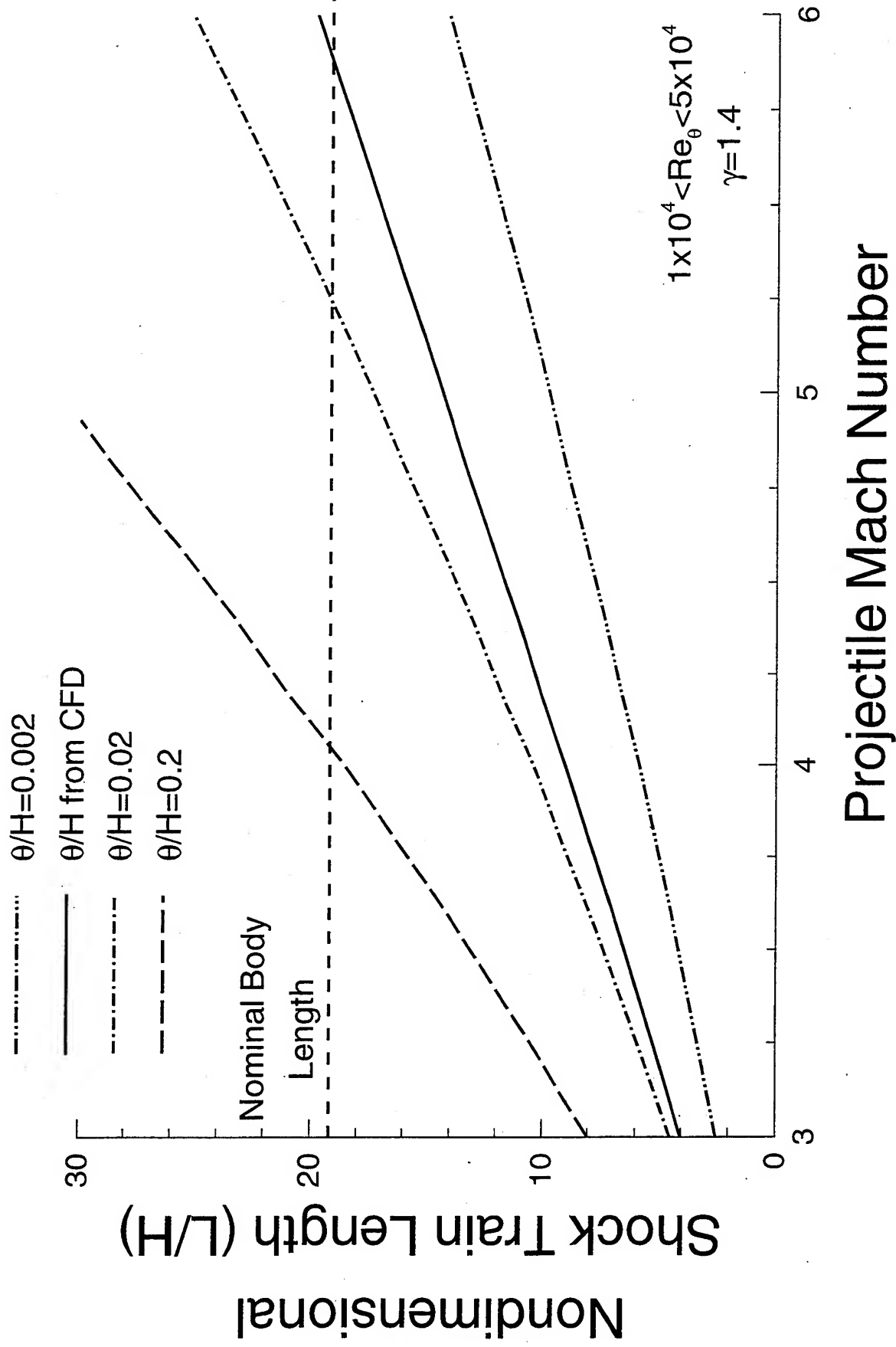
Dual-Mode Scramjet



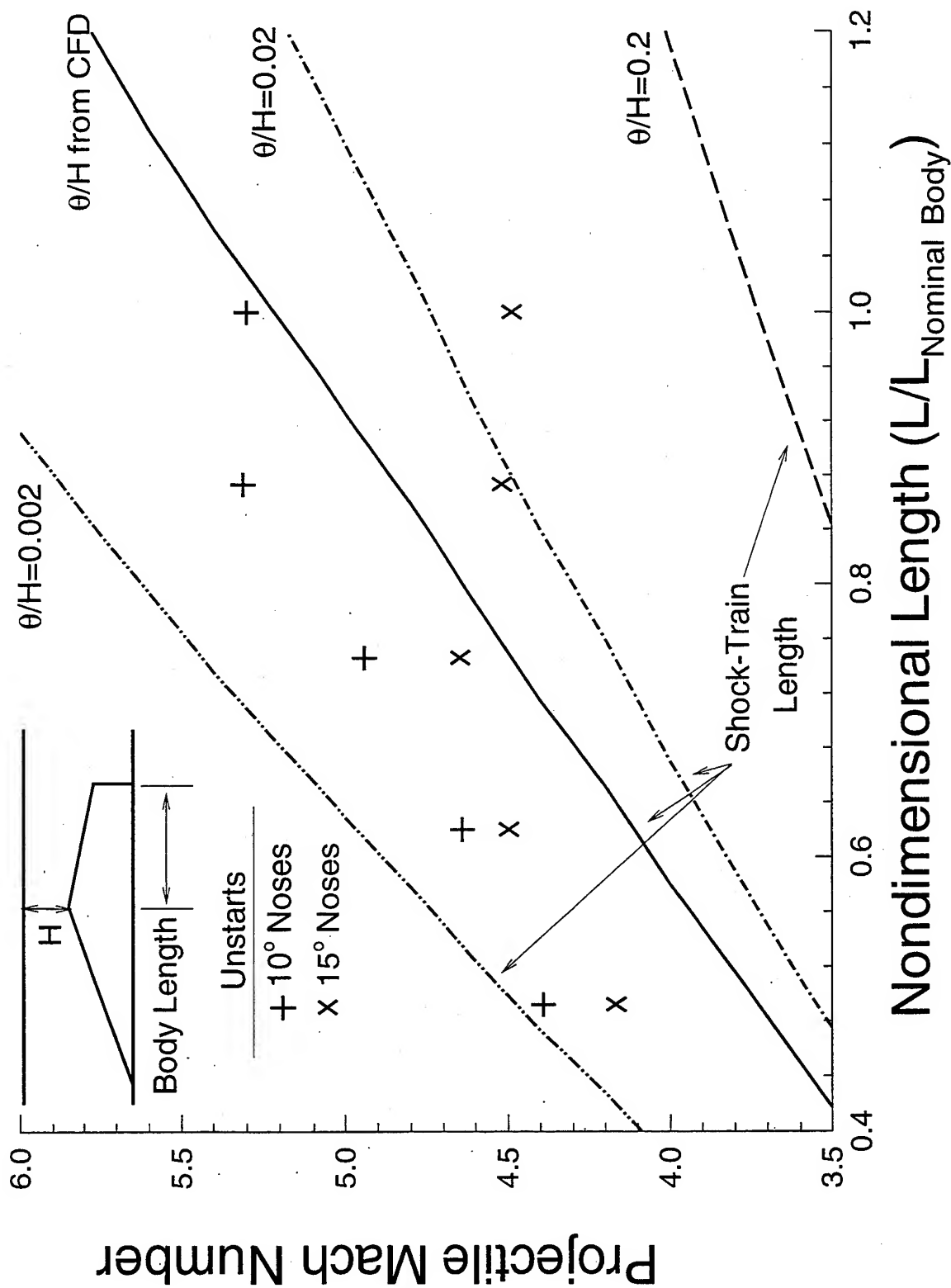
Ram Accelerator



Predicted Shock Train Length



Predicted Unstart Mach Number



Session 3

DETONATION PHENOMENA

90L35 Detonation Tube Experiments : Influence of Diluent Nature on the Detonation Characteristics
of Dense Methane-Based Gaseous Explosive Mixtures

J-F LEGENDRE ⁽¹⁾, M. GIRAUD ⁽¹⁾, P. BAUER ⁽²⁾, D. VOISIN ⁽³⁾

(1) ISL, French-German Research Institute of Saint-Louis
5, rue du Général Cassagnou BP 34, F-68301 Saint-Louis Cedex, France

(2) LCD, Laboratory of Combustion and Detonics
ENSMA BP109, F-86960 Futuroscope Cedex, France

(3) LCSR, Laboratory of Combustion and Reactive Systems
1C, Av. de la Recherche Scientifique, F-45071 Orléans Cedex 2, France

Abstract:

Using a 90L35 detonation tube, experimental detonation characteristics (detonability limits, detonation velocities and peak pressures) of stoichiometric Methane-Oxygen-diluent mixtures at an initial pressure up to 3,5MPa have been investigated.

A parametric study has been carried out as a function of both amount and nature of diluent -namely Carbon Dioxide, Nitrogen and Helium-.

The experimental results allowed the adjustment and validation of computations of the Chapman-Jouguet characteristics by means of the Quartet thermochemical code.

These experimental data associated with validated computations provide a valuable tool, among others, for the interpretation of the effect of mixture compositions in the RAMAC superdetonative combustion mode, and in particular for the RAMAC 90 taking into account the different multi-stage configurations available.

1. Introduction

Studies and researches conducted at ISL on a 90mm caliber RAM Accelerator (RAMAC 90) [1], [2] have demonstrated the importance of the scale effect in terms of both geometrical, physical and chemical conditions [3]. To date, the RAMAC 90 maximum performance enables an exit velocity of about 2km/s in the thermally choked propulsion mode along a 16.2m long RAM stage (180 calibers) for a 1.34kg projectile and an initial entrance velocity of 1335m/s [4]. According to the results obtained in terms of projectile velocity, whereas continuous sufficient in-bore guiding has been achieved, superdetonative combustion mode can now be safely considered.

Among different key-elements ruling the superdetonative combustion mode, the composition of the dense gaseous explosive mixture obviously plays a very important role. Therefore, a better knowledge of the detonation behavior of these dense gaseous reactive mixtures is required in terms of both detonability and Chapman-Jouguet equilibrium characteristics (detonation velocity, peak pressure, temperature, heat release...). The experimental and numerical analysis presented in this paper are aimed at providing a set of data that should help interpret the experimental behavior of the RAMAC in the superdetonative regime, especially the RAMAC 90 for which this combustion mode is expected to be achieved by the beginning 1996.

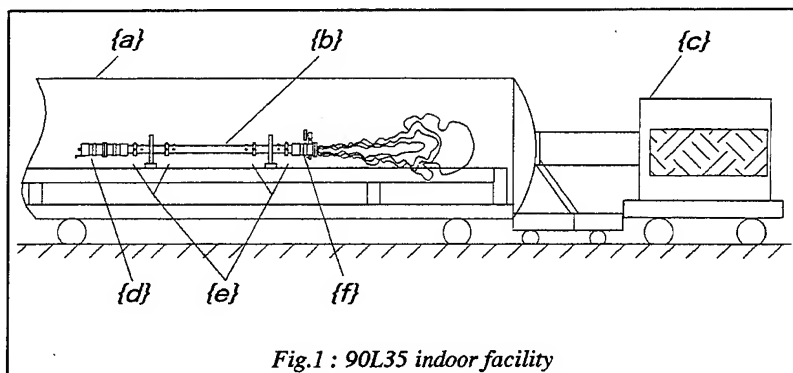
In order to provide experimental data that would match as closely as possible the RAMAC 90 behavior, an experimental setup, namely 90mm caliber detonation tubes, was designed. One must be aware, as it shows in these experiments, that there is a tremendous gap between the ignition process in the RAMAC and that occurring in the so-called "static" experiments involving a conventional ignition source. The shock generation due to a blasting cap is in no way comparable to the shock wave pattern of the flow around the RAMAC projectile. Nevertheless, bearing in mind this important aspect, one may expect some important issues, by just a mere comparison of the detonabilities of the mixtures in "static" conditions.

Concerning the first superdetonative experiments foreseen in the RAMAC 90, it has been chosen for both safety and technological reasons to keep Methane as the combustible gas. Thereby diluent nature and initial filling pressure are two parameters to play upon. Basically three diluents have been investigated in the 90mm caliber detonation tubes, namely Nitrogen, Carbon Dioxide and Helium.

2. Experimental setup.

To date two 90mm caliber detonation tubes are in use at ISL, respectively 1.35m long (15 calibers) noted 90L15 and 3.15m long (35 calibers) noted 90L35. Experiments with the 90L15 have already been described basically dealing with Nitrogen diluted mixtures [5] [6]. In these first experiments, it has been determined that a tube length of 15 calibers, although theoretically long enough to state on a stable self-sustained detonation, did not allow to state unambiguously on the stability of some detonation waves especially at the vicinity of the detonability limit for low diluted mixtures [7].

Accordingly, a second longer detonation tube has been installed with a tube length of 35 calibers. On this purpose a 3m long RAM tube has been used which, besides its length, has also the advantage to allow the statement on the mechanical stress resistance of this type of RAM tube under most severe detonation conditions. A first series of experiments has been conducted outdoor on ISL proving ground, therefore allowing to safely check the proper behaving of the overall facility and especially the newly designed probes to be used in the RAMAC 90 facility. A second series of experiments has been conducted indoor in the launch room of the Aeroballistic tunnel where the RAMAC 90 is installed.



For safety reasons the 90L35 detonation tube (Fig.1{b}) has been installed in the blast protecting tank (Fig.1{a}) which normally hosted the RAMAC 90 stages. Detonation experiments in this tank provided also data on both the ability of this vessel to withstand the muzzle blast from the

expansion of the detonation products and data on the effect on the structure of the surrounding buildings. The exit of this expansion vessel is connected, like for RAMAC 90 experiment, with the projectile catcher moving along rails (Fig.1{c}). The blast protecting tank has proved satisfactory even in case of most severe detonation conditions of stoichiometric pure Methane-Oxygen at 4MPa initial pressure - it can be noted that in this case the blast wave exiting the tank and expanding in the

projectile catcher caused this 5-ton cart to move 1m backwards. As described in former papers [7] [8], one end of this tube is obturated by a breech block (Fig.1{d}) in which is installed the initiation device, the other end (Fig.1{f}) being fitted with the RAMAC muzzle device, allows the installation of a breakable PVC diaphragm and the high-pressure valve for connection with the gaseous feeding line. This 90L35 tube is originally fitted with 24 instrumentation ports divided along 8 cross sections. For the sake of the probes, only reinforced gage-ports along 4 cross-sections (Fig.1{e}) are presently in use. Three measuring bases - respectively 60cm, 106cm and 60cm long- are then considered. Since detonation velocity measurements are at most accurate - i.e. a deviation less than 0.5%- these have always been used as a reliable check of the detonation stability, as well as a criterion regarding Equation of State (henceforth noted EoS) validity. Therefore, ionization together with light probes were used on this facility. Piezoelectric pressure gages are also installed to get values of the detonation peak pressure but it has been determined that such experimental data are not accurate and reliable enough, at least to give valuable comparison with calculated values. The initiation source consisting of a #8 detonator (1g equivalent tetryl) remained unchanged among all detonation tubes experiments. This relatively low energy ignition source by means of a direct blast wave drives to the referred to "fast mode of initiation" where the detonation is formed instantaneously [9]. According to both tube diameter and initial pressure, the locally spherical initiation mode drives to planar propagation at least before the detonation wave reaches the first instrument cross-section [10]. The detonation front, if any, is then rapidly and unambiguously decoupled from the ignition source. However, this type of ignition source is totally inaccurate to simulate the development of a detonation in the RAMAC in case either of an unstart through the aerodynamic obturation of the diffuser (referred to "piston initiation") or in the transdetonative propulsion mode. In the latter case, a "slow mode of initiation" [11] could be considered via an accelerating flame thus driving to a deflagration-to-detonation-transition; however this type of experiments is beyond the scope of this paper.

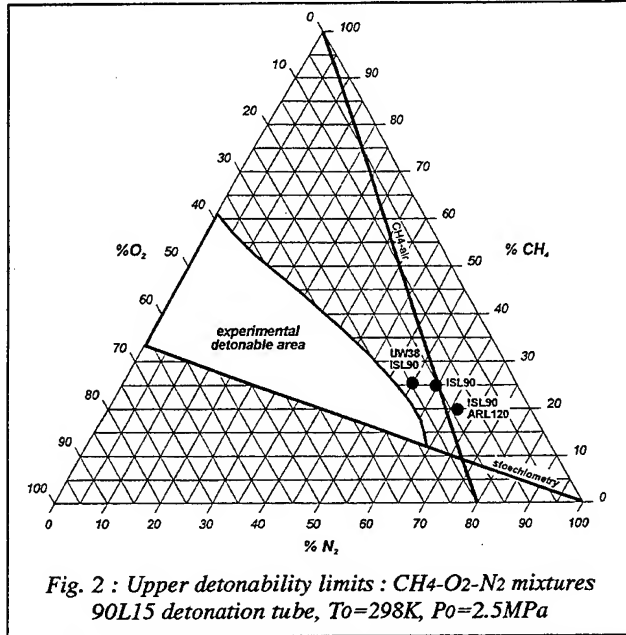
3. Results and discussion.

The detonability region was investigated for mixtures of CH₄/O₂, diluted in various inert gases, namely N₂, CO₂ and He. Some data on detonability limits are available in the litterature but they solely deal with explosive mixtures in standard conditions. Data related to high pressure systems are extremely scarce if any. Therefore, our present measurements may be regarded as a unique set of data that can be further applied to RAMAC, provided one keeps in mind our preceeding comments on their extent of application. Regarding the operational limits of the RAMAC, a thorough study of the energetic content should be done. Stoichiometric mixtures are very energetic ones. Most mixtures that were used so far for RAMAC experiments happen to have quite a low energetic content, since it was shown that operational limits of the RAMAC correspond to this type of mixture. A decrease of the energetic content can be obtained by either increasing the equivalence ratio or the inert amount. In the present scope, we mostly deal with equivalence ratios less than 3 and inert dilution (termed as β) in the range of 0 to 5. The Quartet Thermochemical code [12] was used for each series of calculations that are presented hereafter.

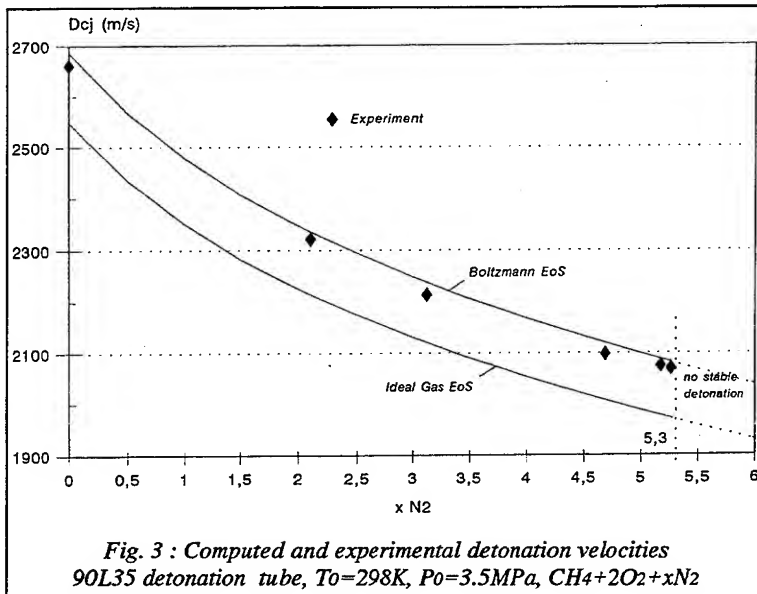
3.1 Nitrogen dilution.

Results concerning the detonable area have already been extensively presented [6]. As a reference, they are recalled on Fig.2. The three Methane-based mixtures used in ISL RAMAC 90 are presented on this plot - i.e. 2.7CH₄+2O₂+5.6N₂, 3.2CH₄+2O₂+7.5N₂ and 3.0CH₄+2O₂+10.0N₂ - which both exhibit a high equivalence ratio and a high inert ratio. 2.7CH₄+2O₂+5.6N₂ mixtures extensively used in the University of Washington in the 38mm caliber RAMAC (UW38) [13] always yielded to

transdetonative combustion in the RAMAC90 [3]. However, heavily inerted mixtures ($3.0\text{CH}_4 + 2\text{O}_2 + 10.0\text{N}_2$) also used in the Army Research Laboratory in the 120mm caliber RAMAC (ARL120) [14] have yielded to pure thermally choked propulsion mode in the RAMAC 90, even for projectile velocities above 120% of the calculated Chapman-Jouguet detonation velocity [4].



For this type of mixture, detonation characteristics may be readily obtained with the Boltzmann Equation of State [15] for the combustion products as it was shown earlier [6]. Even at the vicinity of the detonability limits corresponding to these experiments, it shows on Fig. 3, that the deviation between calculation and experiments remain less than 1%.



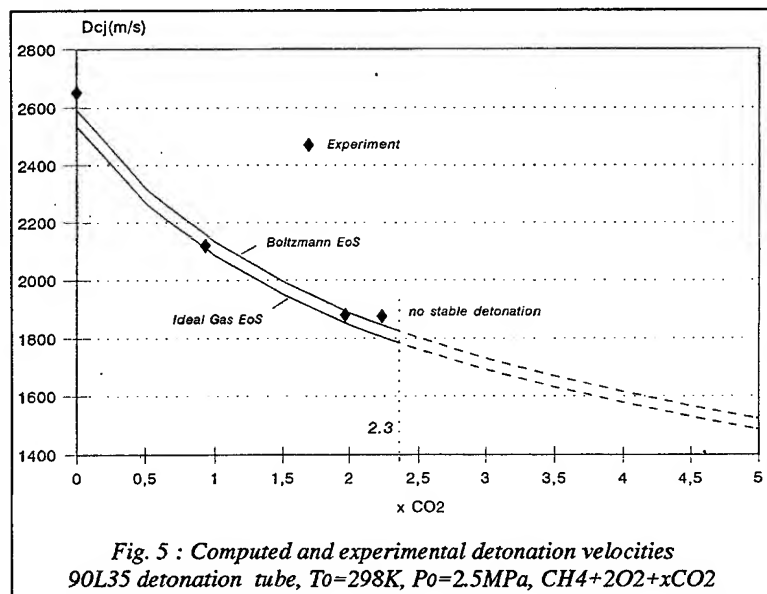
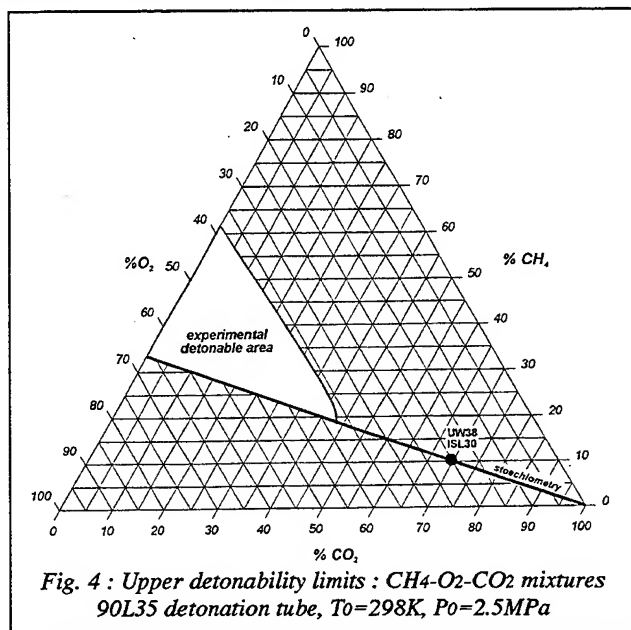
3.2 Carbon Dioxide dilution

In order to look for gaseous mixtures which should exhibit lower detonation velocities, keeping Methane as the combustible and initial pressure around 3MPa, it has been required to look for the upper detonable area of Carbon Dioxide diluted mixtures. This study has been undertaken with the 90L35 detonation tube installed indoor in the RAMAC 90 blast protecting tank. This experimental setup allowed to use very conveniently without any modification all security controls, gas monitoring

and analysis systems as well digital data acquisition system involved in RAMAC 90 experiments [16]. According to the overall gas handling system available to date, the upper detonability limits of $\text{CH}_4\text{-O}_2\text{-CO}_2$ mixtures have been determined at $T_0=298\text{K}$ and $P_0=2.5\text{MPa}$ (Fig.4).

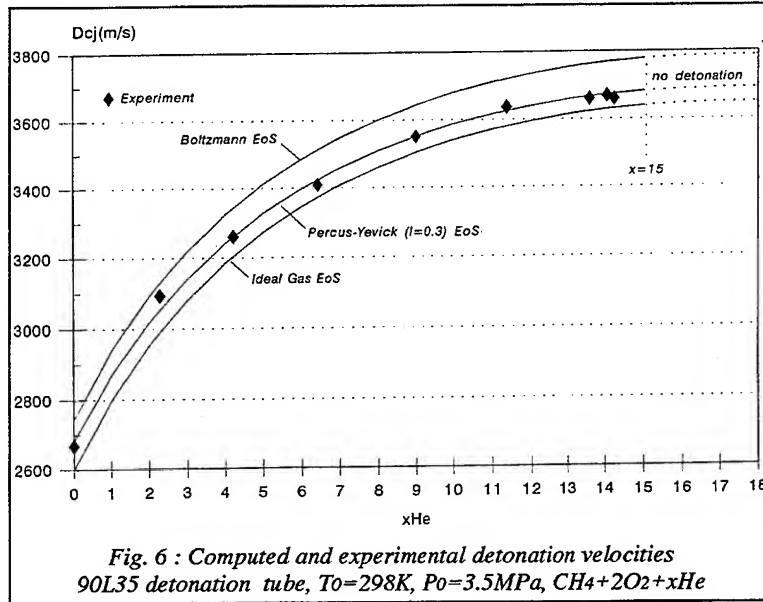
As awaited, from the respective flammability areas of Methane-Oxygen mixtures diluted with Nitrogen or Carbon Dioxide at atmospheric pressure [17], the detonable area with CO_2 is noticeably smaller than that of N_2 dilution. $\text{CH}_4+2\text{O}_2+7\text{CO}_2$ mixture, represented on this graph, was used for the thermally choked propulsion mode at the University of Washington (UW38) [18] and for the superdetonative propulsion mode at ISL RAMAC 30 using rail tube with 30mm cone-cylinder projectile [19]. As to

predicting the detonation characteristics of such mixtures, the Boltzmann EoS, again turns out to be reliable, even for a diluent ratio $\beta=1.15$ ($\text{CH}_4+2\text{O}_2+2.3\text{CO}_2$) where the detonation happens to remain very stable. Calculated and experimental values are presented on Fig. 5.



3.3 Helium dilution.

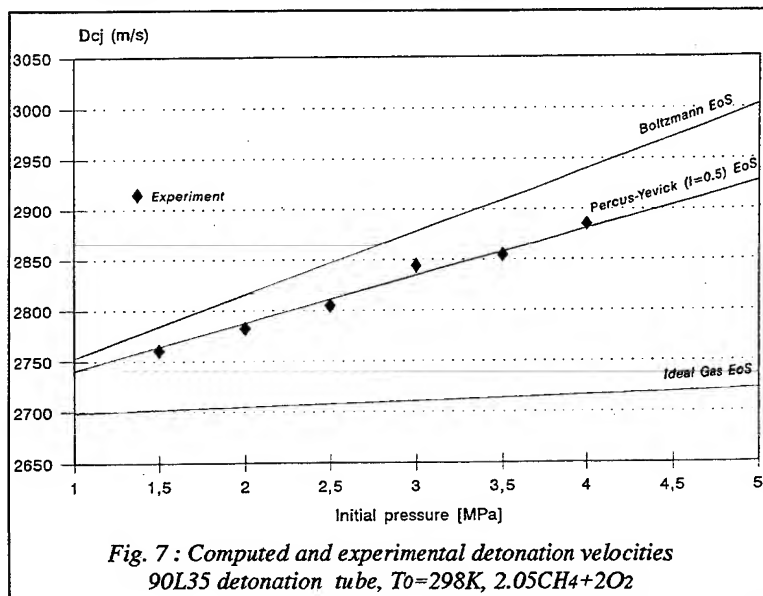
These close to stoichiometric mixtures ($1.1\text{CH}_4 + 2\text{O}_2 + x\text{He}$) were found to be detonable up to the high dilution ratio $\beta=7.5$ ($1.1\text{CH}_4 + 2\text{O}_2 + 15\text{He}$, i.e. a molar fraction of Helium in the mixture up to $\sim 83\%$). Even at the vicinity of this limit, a very stable self-sustained detonation wave has been



observed. In the present case, the Boltzmann EoS was no more adapted for the prediction of the detonation characteristics. The Percus-Yevick EoS [20], already used in some instance with condensed explosives appeared to drive to good results. This theory is based on hard spheres [21], and enables to take into account interactions between molecules of different nature. Calculated and experimental values are presented on Fig. 6.

3.4 Pure Methane-Oxygen mixtures.

To proof-test the resistance of the RAM tube itself as well as different gages to be used in RAMAC 90, very reactive non diluted mixtures were detonated. Non-diluted Methane-Oxygen mixtures for an equivalence ratio of ~ 2 were detonated for an increasing initial pressure in the range 1.5 to 4MPa [22]. It must be emphasized that for $P_0=4.0\text{MPa}$ the propagating detonation peak



pressure caused irreversible damage to gages installed on the tube, even though the tube-wall itself did not exhibit permanent deformation. If any super-detonative propulsion mode should be foreseen in the RAMAC 90 with Chapman-Jouguet characteristics similar to those encountered for these conditions, all gages and instrument ports should be redesigned to cope with these high pressure oscillations. Experimental detonation velocities for these mixtures investigated in the 90L35 detonation tube are compared

on Table 1 and Fig. 7. It can be noticed as well that the Boltzmann Equation of State yields to greater discrepancy with the experiment.

P0(MPa)	1.5	2.0	2.5	3.0	3.5	4.0
Equivalence ratio	2.05	2.01	2.06	2.05	1.98	1.97
DCJ(experimental) (m/s)	2765	2790	2811	2844	2857	2885
DCJ(Ideal Gas EoS)	2702	2713	2709	2713	2727	2730
Deviation(%)	2.28%	2.76%	3.63%	4.61%	4.55%	5.37%
DCJ(Boltzmann EoS)	2784	2822	2847	2879	2920	2951
Deviation(%)	0.69%	1.15%	1.28%	1.23%	2.21%	2.29%
DCJ(Percus Yevick EoS)	2764	2795	2811	2836	2871	2895
Deviation(%)	0.04%	0.18%	0.00%	0.28%	0.49%	0.35%

In this case of very energetic detonable mixtures, the Percus Yevick EoS could be adjusted so that to allow the prediction of detonation velocities in very good agreement with the experiment.

Table 1 : CH₄-O₂ calculated and measured detonation velocities [22]

It has been previously shown [10][22] that most EoS used in the code fail to accurately predict the detonation properties of pure fuel-oxygen mixtures. The parameters of the EoS are to be necessarily re-adjusted in each particular case. The absence of inerts that account for as energetic sinks therefore greatly affects the thermochemical response of the system.

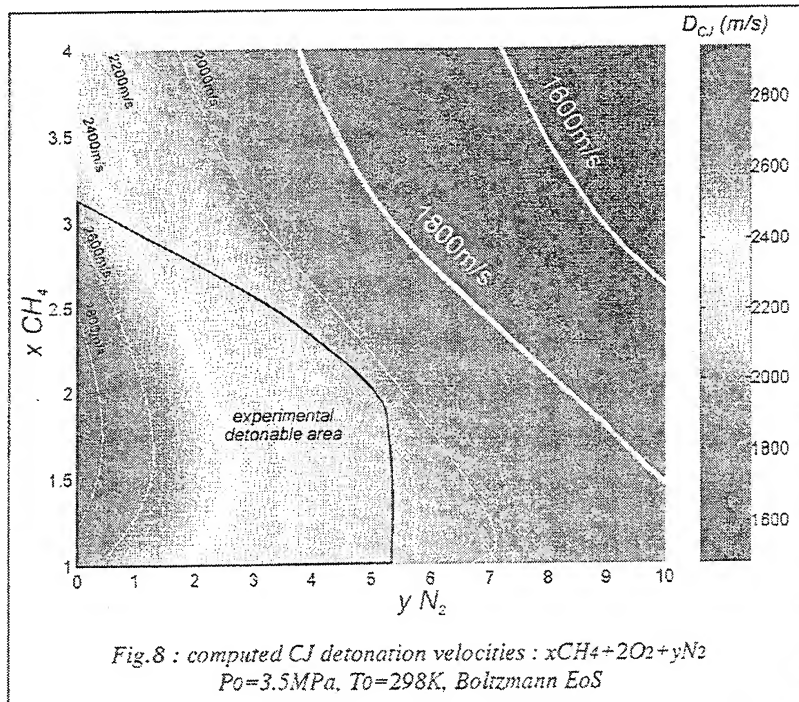
4. First considerations for the choice of the RAMAC 90 superdetonative mixture.

Among the numerous and complex parameters ruling and limiting the superdetonative propulsion mode, we shall examine in the following only the point of view of the detonation properties of the mixtures. According to the results presented above, we can dispose of experimental and validated computations of detonation properties for dense gaseous mixtures usable in the RAMAC 90. Disposing of a reliable method of calculating the Chapman-Jouguet detonation properties (in particular the detonation velocity noted D_{CJ}) it is possible to represent a validated colormap of the variation of D_{CJ} as a function of amount of both combustible and diluent. The main interest of these maps is to offer a wide variety of possible systems that would yield a given set of detonation parameters. As a reference, the detonability limits of these systems in our present conditions, i.e. so-called "static" detonations, are exhibited on these plots as well.

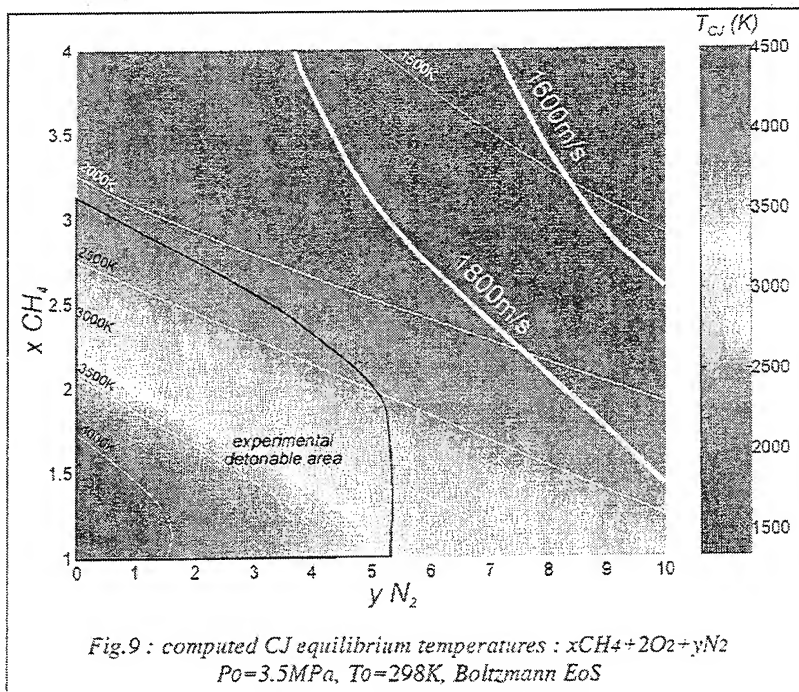
To date, the RAMAC 90 for its 16.2m long Ram-stage (180cal.) configuration allows a maximum exit velocity of about 2000m/s in the thermally choked propulsion mode [4]. Accordingly, for the first RAM stage in which the superdetonative regime is awaited, the mixture should be at least detonable in the RAMAC propagation, and with a detonation velocity noticeably smaller than 2000m/s. Two detonation velocities, 1600m/s and 1800m/s, are then considered, in which cases the entering velocity of the projectile, depending on the performance in the thermally choked propulsion mode, could be of the order of 1.20 the CJ detonation velocity. This makes sense regarding the current experience in superdetonative modes.

For safety reasons, in the RAMAC 90, it has been decided to keep Methane as the combustible for both thermally choked and first superdetonative experiments. Oxygen remaining the oxidizer, diluent nature is then the last parameter to play upon.

The first diluent considered is Nitrogen for which the color map of the computed CJ detonation velocity and CJ equilibrium temperatures are presented respectively on Fig.8 and Fig.9. These calculations were made for $P_0=3.5\text{MPa}$, $T_0=298\text{K}$, and were based on the Boltzmann EoS for the detonation products. The detonable area is presented on this graph as well. The $D_{CJ}=1600\text{m/s}$ and 1800m/s are highlighted on this plot since these velocities could be regarded as matching those required for the onset of a superdetonative regime for a projectile entering at the Mach number corresponding to our experiments [4].



Although this doesn't seem likely to meet the detonability requirement, according to the detonability range as depicted here, one should bear in mind that these limits may not be directly applied to the actual RAMAC operational range. Besides, some combustion temperature measurements were conducted in the tube during flame propagations (deflagration) [23] [24]. The results were in good agreement with values calculated on the basis of a constant volume assumption. The detonation temperatures presented on Fig. 9 have not been experimentally confirmed so far. A thorough investigation of the detonation temperature as function of composition is definitely one of our objectives. It remains a highly difficult task but it would provide crucial results as, for example, a set of data for most heat transfer studies, in an attempt to improve the knowledge of the ablation phenomenon.



In order to look for a Methane-based mixture allowing lower stable detonation velocities, it has been investigated to use Carbon Dioxide as diluent (although it can not be considered as completely inert). This high molar weight component, compared to N_2 , allows to get lower detonation velocities for a given dilution ratio.

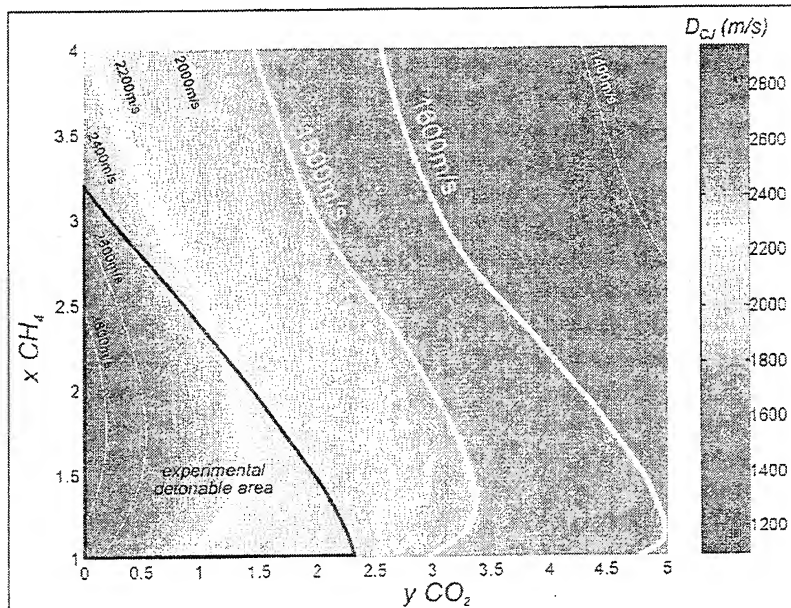


Fig.10 : computed CJ detonation velocities : $x\text{CH}_4 + 2\text{O}_2 + y\text{CO}_2$
 $P_0 = 3.5\text{MPa}$, $T_0 = 298\text{K}$, Boltzmann EoS

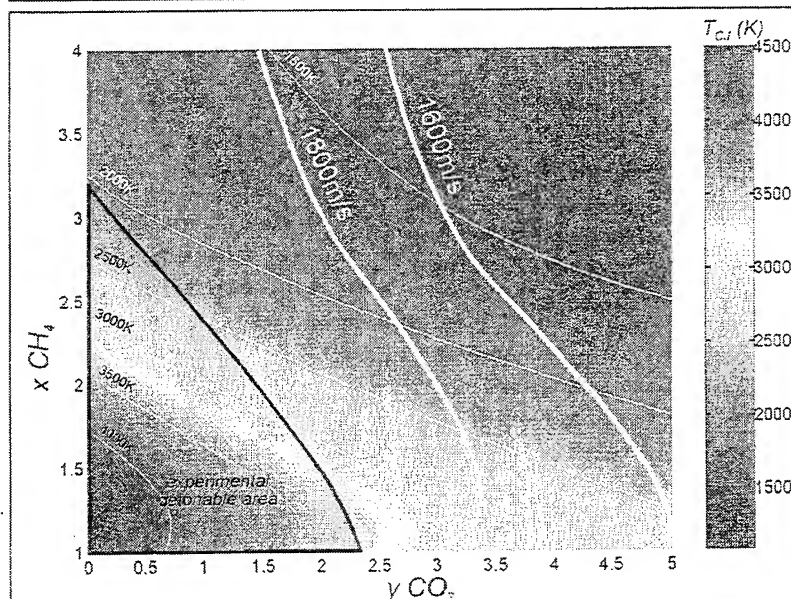


Fig.11 : computed CJ detonation velocities : $x\text{CH}_4 + 2\text{O}_2 + y\text{CO}_2$
 $P_0 = 3.5\text{MPa}$, $T_0 = 298\text{K}$, Boltzmann EoS

Fig. 10 shows the color map of computed CJ detonation velocities of Carbon Dioxide diluted mixtures ($P_0 = 3.5\text{MPa}$, $T_0 = 298\text{K}$, Boltzmann EoS of the combustion products). Here again is represented the experimental detonable area where stable self-sustained detonation has propagated. The contour curves at 1600m/s and 1800m/s are also highlighted. It can be noticed that in this case the curve at 1600m/s is again far away from the experimental detonable area. Concerning the contour at 1800m/s, stoichiometric mixtures with an inert dilution ratio $1 < \beta = [\text{CO}_2]/[\text{O}_2] < 1.5$ could be considered to fulfill the requirements for a self-sustained detonable mixture at $D_{CJ} \sim 1800\text{m/s}$ in the RAMAC conditions. Fig. 11 shows computations of the CJ equilibrium temperature colormap. According to the latest experiments carried out in the RAMAC 90 [4], the thermal ablation of projectiles has been determined to be a very limiting parameter especially for very long RAMAC (i.e. long duration spent in combustion zone). This means that the characteristic of heat release playing upon the level of thrust must also be considered from both its

ablating and eroding effect on projectile material point of view. If we take the exemple of the stoichiometric mixtures with inert dilution ratio $1 < \beta = [\text{CO}_2]/[\text{O}_2] < 1.5$ ($D_{CJ} \sim 1800\text{m/s}$) that have been considered for their detonation velocity properties, equilibrium temperatures are computed between 3000K and 3500K. Obviously, this level of temperature would even more dramatically increase the ablation of the projectile.

5. Conclusions and perspectives.

This paper was aimed at presenting the upper detonable areas for which a stable self-sustained detonation has been observed for two types of mixtures : namely Methane-Oxygen-Nitrogen and Methane-Oxygen-Carbon Dioxide for the following experimental conditions : initial pressure $P_0=2.5\text{MPa}$, initial temperature $T_0=298\text{K}$, 90mm caliber detonation tube and #8 detonator direct blast initiation source. It must be emphasized that the geometry of the domain depends very closely on the mode of initiation used. According to the different strong initiation modes that could be encountered in the RAMAC depending on the flow field around the projectile, the "static" detonability areas show the range of compositions for which a detonation will propagate in any RAMAC condition. To a certain extent for specific RAMAC conditions, mixtures situated outside these domains could propagate a detonation as well depending on the initiation conditions. However, in this latter case, one could wonder whether these detonation waves are either stable or even self-sustained.

It has been determined for these two types of mixtures that the Boltzmann EoS yields to calculated detonation velocities that are in very good agreement with experimental values - i.e. a deviation less than 1 %-. For both Methane-Oxygen-Helium and pure Methane-Oxygen mixtures, the Percus-Yevick EoS was preferably used. These investigations allow to regard our code and present panel of EoS as most reliable tools for further computations related to RAMAC investigations. On this basis, detonation temperatures could also be calculated. Depending on the mixture composition, high values of temperature should be accounted for in the studies of ablation and/or eroding of the projectile.

The future works under consideration will emphasize the need for better computer modeling and simulation. First will be studied a computation method which could a-priori predict the detonability limits of gaseous mixtures as a function of constituting components and initial pressure/temperature. Studies on this subject, although limited to atmospheric pressure, are already carried out at the University of London [25]. Furthermore, it will be needed to quantify precisely the relative influence of the variations of initial pressure and temperature on the geometry of detonable areas which could then be included in CFD models used for the Ramac. Second, the modeling of the phenomena occurring during the transition from deflagration to detonation encountered for the RAMAC transdetonative combustion mode would be most useful. Evaluation of the range of mixtures at the border of the detonable area which could exhibit transition will help choosing mixture compositions for pure thermally choked propulsion mode.

Future experimental work on the detonation properties of dense gaseous mixtures will cope with the investigation on the detonation initiation and propagation phenomena in conditions closer to those found in the RAMAC. Different new types of initiations will then be experimented, in particular "piston initiation" (for simulating RAMAC unstart) and accelerating flames (for simulating transdetonative regime). This will allow a better correlation between the detonation phenomena observed in detonation tube and in real RAMAC experiments. Thereby this should help to state on the variation of the detonable area geometry as function of initiation conditions.

Finally detonation tube experiments will allow to design new gages to be used in the future on the RAMAC. Supersonic combustion front temperature measurement techniques and specific wavelength light probes will be experimented. Investigation on new pressure gages based on PVDF foils will also be continued.

References :

- [1] M. Giraud - J.F. Legendre - G. Simon - L. Catoire
RAM Accelerator in 90mm Caliber. First Results Concerning the Scale Effect in the Thermally Choked Propulsion Mode - ISL CO 210/92
13th International Symposium on Ballistics - Stockholm, Sweden, June 1-3, 1992.
- [2] M. Giraud - J.F. Legendre - G. Simon
RAM Accelerator in 90mm Caliber or RAMAC 90, Experimental Results Concerning the Transdetonative Combustion Mode - ISL PU 363/93
14th International Symposium on Ballistics - Québec, Canada, 26-29 September 1993.
- [3] M. Giraud - J.F. Legendre - G. Simon
RAMAC 90. Experimental Studies and Results in 90mm Caliber, Length 108 Calibers - ISL PU 360/93 - First International Workshop on RAM Accelerator - ISL Saint-Louis, France - September 7-10, 1993
- [4] M. Giraud - J.F. Legendre - G. Simon - M. Henner - D. Voisin
RAMAC in 90mm caliber or RAMAC 90 : Starting process, control of the ignition location and performances in the thermally choked propulsion mode - ISL report to be published - Second International Workshop on RAM Accelerator - UW in Seattle, WA USA - July 17-20, 1995
- [5] J-F Legendre - M. Giraud - P. Bauer
Effect on inert additives on the detonation properties of dense gaseous explosives - ISL PU 359/93 - First International Workshop on RAM Accelerator - ISL Saint-Louis, France - September 7-10, 1993
- [6] P. Bauer, J-F Legendre
Detonability limits of propellant mixtures used in the RAMAC - ISL PU 361/93
14th International Symposium on Ballistics - Québec, Canada, September 26-29, 1993
- [7] P. Bauer, M. Giraud, J-F Legendre, L. Catoire
Detonability limits of Methane-Oxygen mixtures at elevated initial pressure ISL CO 222/92 - Propellants, Explosives, Pyrotechnics 19, 311-314 (1994)
- [8] J-F Legendre
Detonability limits of propellant mixtures used in the RAMAC - ISL PU 306/93
European Symposium STAR - Properties of Reactive Fluids and their Application to Propulsion -, Poitiers, France, November 24-27, 1992
- [9] H.S. Lee
Dynamic parameters of gaseous detonations
Ann. Rev. Phys. Chem. 1984.16: 311-336 p. 327 (1984)
- [10] P. Bauer
Contribution à l'étude de la détonation de mélanges explosifs gazeux à pression initiale élevée - Thèse de Doctorat ès Sciences Physiques, Université de Poitiers, France, pp.108-111, (1985)
- [11] H.S. Lee
Initiation of gaseous detonation
Ann. Rev. Phys. Chem. 1977.28:75-104 p.76 (1977)
- [12] O. Heuzé, P. Bauer, H.N. Presles
Quatuor :A thermochemical code for computing thermodynamic properties of detonation and combustion products
GTPS Juan les Pins, France, pp. 91-96, (1987)

- [13] C. Knowlen - E.A. Burnham - A.E. Kull - A.P. Bruckner - A. Hertzberg
RAM Accelerator performance in the transdetonative velocity regime
41st Meeting of the Aeroballistic Range Association, San diego , CA -USA, 1990
- [14] D.L. Kruczynski
Analysis of firings in a 120mm RAM Accelerator at high pressures
First International Workshop on RAM Accelerator - ISL Saint-Louis, France - September 7-10, 1993
- [15] L. Boltzmann
Lectures on Gas Theory, Vol. 2, Chap. 51
University of California Press, USA, (1964)
- [16] M. Giraud - J-F Legendre - G. Simon - J-P Mangold - H. Simon - H. Kauffmann
RAMAC 90 : Facility and diagnostic methods - ISL PU 362/93
44th Meeting of the Aeroballistic Range Association, Munich - Germany, September 13-17, 1993
- [17] A. Van Tiggelen
Oxydations et combustions, éditions Technip Paris, tome I, p.306 (1968)
- [18] A. Bruckner
The RAM Accelerator: An Overview
European Symposium STAR - Properties of Reactives Fluids and their Application to Propulsion. Poitiers, France, November 24-27, 1992
- [19] G. Smeets - F. Seiler - G. Patz - J. Srulijes
First results obtained in a 30mm caliber scram accelerator using a rail tube for cylindrical projectiles - ISL PU 327/94
25th International Symposium on Combustion, Irvine, CA - USA, July 31-August 5, 1994
- [20] J.K. Percus - G.J. Yevick
Analysis of classical statistical mechanics by means of collective coordinates
Physical Review vol.110 n°1, pp. 1-13 (1958)
- [21] J.L. Lebowitz
Exact solution of generalized Percus-Yevick equation for mixture of hard spheres
Physical Review vol.133 n°4A, pp. A895-A899 (1964)
- [22] P. Bauer - H.N. Presles - O. Heuzé - J-F Legendre
Prediction of detonation characteristics of dense gaseous explosives on the basis of the virial equations of state - ISL PU 308/95
20th International Pyrotechnics Seminar, Colorado Springs, CO -USA, July 25-29, 1994
- [23] H. Mach - U. Werner - H. Masur
Erste Temperatur Messungen beim Abbrand eineses CH₄-O₂-N₂ Gemisches unter hohem Anfangsdruck - ISL N610/92
- [24] H. Mach - A. Eichorn - U. Werner - H. Masur
Untersuchung der Deflagrazion eines CH₄-O₂-N₂ Gemisch unter 3.0MPa Anfangsdruck - ISL 1995 report to be published
- [25] A.I. Asewando
A physico-chemical theory of marginal detonation
Ph.D. thesis, University of London, 1994

Regular and Mach Reflection of Shock Waves as Detonation Waves

James D. Sterling and Kaveh Ghorbanian
Advanced Projects Research Incorporated
4674 Paulette Place
Santa Rosa, CA 95403

Abstract

In this paper we analyze the reflection of non-reacting shock waves as oblique detonation waves. The 2-d, steady, inviscid analysis makes use of detonation polar diagrams to identify incident shock angles that lead to reflected overdriven and Chapman-Jouguet detonations, with and without detonation Mach stem formation. The implications of the results for ram accelerator design and operation are discussed.

1. Introduction

Oblique detonation wave ram accelerators are designed in a manner that a non-reacting shock wave is generated at the tip of the projectile. This shock wave reflects from the tube wall as an oblique detonation wave (ODW). As with detonations observed in shock tube experiments, ODWs exhibit unsteady, three-dimensional cellular structure that becomes suppressed as the Mach number increases above the Chapman-Jouguet (C-J) Mach number of the reactants. If the size of the cellular structure is small compared to other relevant length scales, the detonation wave may be idealized as having the classical Zel'dovich, von Neumann, Döring (ZND) structure of a non-reacting shock wave followed by a deflagration wave. The best experimental data regarding ODWs have been obtained in two-layer shock tube experiments discussed in references [1] [2] and [3]. These papers demonstrate close agreement between experimental results and the steady, 2-D, Rankine-Hugoniot analysis of ODWs. The Rankine-Hugoniot analysis of ODWs is contained in references [4] and [5]. Further historical reviews of ODW research may be found in references [4] and [6].

Returning to ODW ram accelerator design, the reactants and initial conditions must be appropriately selected so that the chemical induction length downstream of the nonreacting shock wave is much larger than the characteristic projectile length and that the chemical induction length downstream of the reflected wave is much smaller than the characteristic length. With this propellant selection, there are still several obvious criteria that must be met for the leading non-reacting shock wave to be reflected as an ODW. First, the Mach number downstream of the non-reacting shock must be above the local C-J Mach

number. Second, the projectile cone half-angle must be large enough that a supported or *weak, overdriven* ODW can form. References [4] and [5] contain discussion of the conditions required for generation of weak, overdriven ODWs. In this mode of operation, the flow relative to a ram accelerator projectile is compressed by both the leading non-reacting shock wave, and the non-reacting part of the ODW structure. Heat is added in the deflagrative part of the ODW and the flow expands along the afterbody of the projectile to complete the thermodynamic engine cycle. The flow remains supersonic with respect to the projectile throughout. The lowest Mach number occurs downstream of the non-reacting part of the ODW which “overtakes” the flow away from the wall before the deflagration accelerates the flow and returns it to be parallel to the wall.

The above discussion was based on the assumption that the ODW was formed by the *regular* reflection of the leading non-reacting shock wave from the wall. In this paper we investigate additional criteria for ODW stabilization based on the need to avoid formation of a detonation Mach stem upon shock reflection. This occurrence would result in subsonic flow downstream of the strong, overdriven detonation stem and may lead to ram accelerator unstart. Detailed study of Mach reflection of non-reacting shock waves has been performed [7] [8] and although several investigators have studied the Mach reflection of detonation waves [9] [10], there have been no analogous studies of a non-reacting shock reflecting as a detonation wave.

In the following section, we begin with a discussion of traditional Rankine-Hugoniot analysis and a review of the resulting *reaction polars* (p - θ diagrams) for 2-d, steady combustion waves. As will be shown, the polar diagrams are particularly useful for the investigation of wave interaction processes, including Mach reflection phenomena. Some definitions of special values of the projectile cone half-angle are then presented using the reaction polar diagrams. The variation of these special angles with Mach number and heat release is presented. Since this study makes use of two-dimensional Rankine-Hugoniot analysis, it is directly applicable to ODW scramjet engines and rectangular ram accelerators that have primarily 2-d cross sectional flows. The implications of the results for supersonic flameholding as well as inlet unstart phenomena are discussed. Axisymmetric ram accelerators can be expected to demonstrate the same qualitative behavior so the present results may be used as a guide for axisymmetric projectile design.

2. Rankine-Hugoniot Analysis

2.1. General Features of Reaction Polars

Before delving into the analysis of regular and Mach reflection of shock waves in detonable mixtures, it is useful to review the traditional Rankine-Hugoniot analysis, in order to establish limit cases and nomenclature. The Rankine-Hugoniot relations are particularly useful for investigating, understanding, and classifying systems in which the major changes in the values of the flow variables, as well as the effects of viscosity, diffusion, and thermal conductivity are collapsed into a discontinuity, i.e. compression- and combustion waves. A clear presentation of standing ODWs based on the Rankine-Hugoniot analysis is provided in reference [4]. In this section, we offer more insight on the subject matter by presenting the general features of *reaction polars*.

Figure 2.1 depicts the supersonic flow of an ideal gas through an oblique discontinuity

that is inclined at an angle β from the incoming flow direction. The flow is turned through a deflection angle θ . For both adiabatic and diabatic flows, the conservation laws of mass, normal momentum, tangential momentum, and energy yield:

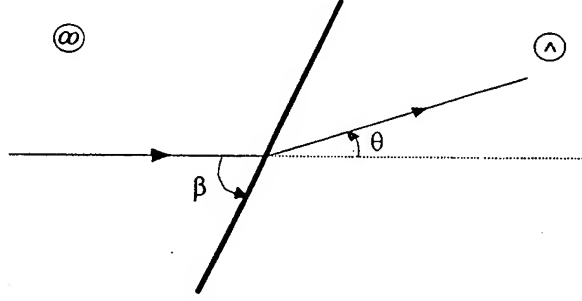


Figure 2.1: Plane oblique discontinuity geometry

$$\rho_{\infty} u_{\infty n} = \hat{\rho} \hat{u}_n, \quad (2.1)$$

$$p_{\infty} + \rho_{\infty} u_{\infty n}^2 = \hat{p} + \hat{\rho} \hat{u}_n^2, \quad (2.2)$$

$$(\rho_{\infty} u_{\infty n}) u_{\infty t} = (\hat{\rho} \hat{u}_n) \hat{u}_t, \text{ or } u_{\infty t} = \hat{u}_t, \quad (2.3)$$

and

$$h_{\infty} + \frac{u_{\infty n}^2}{2} = \hat{h} + \frac{\hat{u}_n^2}{2} \quad (\text{since } u_{\infty t}^2 = \hat{u}_t^2) \quad (2.4)$$

where the subscripts “ ∞ ” and “ λ ” denote upstream and downstream conditions respectively. To complete the system of the equations, the ideal gas equation of state is assumed to apply,

$$p = \rho RT. \quad (2.5)$$

With the assumption of heat released implicitly due to chemical reaction, Eq. (4) may be used as is, provided the enthalpies h_{∞} and \hat{h} include both the chemical enthalpy of formation and the sensible enthalpy. Accurate results at high temperature and pressure require the use of variable specific heats and complex chemical equilibrium and kinetics calculations [11]. For purposes of exposition, it is assumed that Q_{∞} units of heat per unit mass are added to the fluid to represent the sensible heat release due to combustion. Further, assuming that the fluid has a constant specific heat capacity and does not change composition by heat addition, Eq. (4) may be rewritten as

$$c_p T_{\infty} + \frac{u_{\infty n}^2}{2} + Q_{\infty} = c_p \hat{T} + \frac{\hat{u}_n^2}{2}. \quad (2.6)$$

Notice that the above set of equations hold for combustion waves in general – that is, deflagration as well as detonation. Combination of the conservation equations, the equation

of state, and the kinematic relations of the geometry from Figure 2.1 result in a density ratio expressed by

$$\frac{\rho_\infty}{\hat{p}} = \frac{\hat{u}_n}{u_{\infty n}} = \frac{\tan(\beta - \theta)}{\tan \beta} \quad (2.7)$$

which after some algebraic manipulations may be rewritten as

$$\frac{\rho_\infty}{\hat{p}} = \frac{1 + \gamma M_{\infty n}^2}{(\gamma + 1) M_{\infty n}^2} \pm \frac{\sqrt{(1 - M_{\infty n}^2)^2 - 2(\gamma + 1) M_{\infty n}^2 \tilde{Q}_\infty}}{(\gamma + 1) M_{\infty n}^2} \quad (2.8)$$

where \tilde{Q}_∞ is the second Damköhler parameter defined as

$$\tilde{Q}_\infty = \frac{Q_\infty}{c_p T_\infty}. \quad (2.9)$$

Furthermore, the Mach number is defined as

$$M_\infty \equiv \frac{u_\infty}{\sqrt{\gamma R T_\infty}} \quad (2.10)$$

where $M_{\infty n} \equiv M_\infty \sin \beta$, and $\gamma = c_p/c_v$ is the ratio of constant specific heats.

Substituting Eq. (8) into the normal momentum equation and rearranging gives

$$\frac{\hat{p}}{p_\infty} = 1 + \gamma M_{\infty n}^2 \left(1 - \frac{\rho_\infty}{\hat{p}} \right). \quad (2.11)$$

In the analysis of steady two-dimensional flow, a useful set of results for computing wave interactions is obtained by plotting the pressure ratio \hat{p}/p_∞ versus the turning angle θ for various \tilde{Q}_∞ . These curves are presented in Figure 2.2 and will be referred to as *reaction polars*. It is apparent from inspection of Figure 2.2 that the reaction polars are divided into two nonoverlapping branches: an upper branch for which the pressure ratio \hat{p}/p_∞ increases, called *detonation polars*, and a lower branch for which the pressure \hat{p}/p_∞ decreases, called *deflagration polars*. It can be readily shown that for the detonation (deflagration) polars the normal component of the freestream Mach number $M_{\infty n}$ is supersonic (subsonic).

We first consider the general characteristics of detonation polars. As illustrated in Figure 2.2, for adiabatic flows, for a given deflection angle θ there are either two solutions to the oblique shock relations, or none at all. In addition, the detonation polar solutions may be divided by the sonic line SL and termed *weak* solutions corresponding to downstream supersonic flow and *strong* solutions corresponding to downstream subsonic flow. Further examination of Figure 2.2 indicates that an additional classification for diabatic flows is necessary. This classification is based on whether the normal component of the downstream Mach number \hat{M}_n is subsonic, sonic, or supersonic. For diabatic flows, states with $\hat{M}_n = 1$, corresponding to C-J detonation waves, are represented by the CJ curve. Points on the constant \tilde{Q}_∞ dashed lines to the left of the C-J point are *underdriven* waves with $\hat{M}_n > 1$. Points on the constant \tilde{Q}_∞ solid lines to the right of the C-J point have $\hat{M}_n < 1$ and are thus *overdriven*. To be consistent with the terms weak and strong as applied to adiabatic oblique shock waves, points within the C-J curve and below the sonic line will be referred to as *weak overdriven*, and above the sonic line, as *strong overdriven*. However, since all

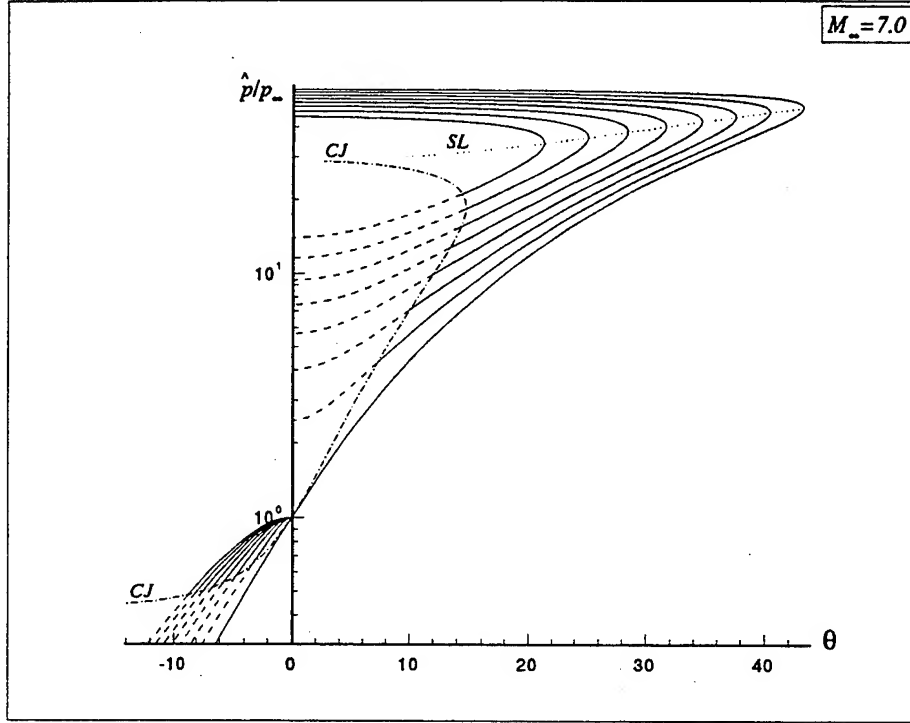


Figure 2.2: Generalized reaction polars

strong oblique shock waves are overdriven, they will be called simply strong ODWs. It is also apparent from inspection that, there is a *maximum* turning angle θ_{max} beyond which an oblique detonation wave will detach or *unstart*, just as in the case of oblique shock waves without heat addition, but with a reduced range of turning angles with increasing amounts of heat release.

2.2. Significance of the C-J Condition

As noted above, there are three distinct classes of ODWs which must be considered in detonation wave stability analyses for applications to propulsive devices. The boundary between underdriven ODWs and weak overdriven ODWs is delimited by the C-J state, which is the point of minimum wave angle β on each locus of states for diabatic flows [4]. Since total pressure loss increases both with the amount of heat release \tilde{Q} and wave angle β , the C-J turning angle θ_{cj} corresponds to the minimum total pressure loss for given approach condition. Consequently, the C-J state provides a limiting condition for ODW engine design.

Having established the significance of the C-J state as a bound, Rankine-Hugoniot relations at the C-J point provide the most convenient forms for the analysis of ODWs. The maximum possible heat addition satisfying the conservation equations for a given value of approach Mach number M_∞ , is defined as the C-J heat addition \tilde{Q}_{cj} , which is given by

$$\tilde{Q}_{cj} \equiv \frac{(1 - M_\infty^2)^2}{2(\gamma + 1)M_\infty^2}. \quad (2.12)$$

By definition, the C-J wave angle β_{cj} is

$$\beta_{cj} \equiv \sin^{-1} \left(\frac{M_{cj}}{M_\infty} \right) \quad (2.13)$$

where M_{cj} is given by

$$M_{cj} \equiv \sqrt{[1 + \tilde{Q}_\infty(\gamma + 1)] \pm \sqrt{[1 + \tilde{Q}_\infty(\gamma + 1)]^2 - 1}}. \quad (2.14)$$

$M_{cj}^{(+)}$ and $M_{cj}^{(-)}$ correspond to the C-J Mach numbers of normal detonation and deflagration waves, respectively, in which heat \tilde{Q}_∞ is released. Further, the C-J density and pressure ratios can be shown to be

$$\left(\frac{\rho_\infty}{\hat{\rho}} \right)_{cj} \equiv \frac{1 + \gamma M_{cj}^2}{(\gamma + 1) M_{cj}^2}, \quad (2.15)$$

$$\left(\frac{\hat{p}}{p_\infty} \right)_{cj} \equiv \frac{1 + \gamma M_{cj}^2}{\gamma + 1}. \quad (2.16)$$

Finally, making use of Eq. (7) with the trigonometric identity

$$\tan(\sin^{-1} x) = \frac{x}{\sqrt{1 - x^2}} \quad (2.17)$$

the C-J turning angle θ_{cj} is given by

$$\theta_{cj} \equiv \beta_{cj} - \tan^{-1} \left(\frac{1 + \gamma M_{cj}^2}{(\gamma + 1) M_{cj}^2 \sqrt{(M_\infty/M_{cj})^2 - 1}} \right). \quad (2.18)$$

The different regions of reaction polars presented in this section are not all physically accessible and their physical occurrence is sensitive to the particular geometrical configuration and freestream conditions. As mentioned above, a detonation may be idealized as a shock wave followed by a pressure coupled deflagration front – that is, the ZND model. The normal component of the velocity downstream of the nonreacting shock wave is subsonic. As is well known, it is not possible to have heat addition to a subsonic flow and proceed past the sonic condition. Therefore, the first restriction on the reaction polars presented above is that the underdriven detonation branch is not accessible. For the same reason, the strong deflagration branch is not physically accessible.

3. Definitions of Special Values of θ

In this section we present definitions of the special turning angles that result in 1) reflection of the non-reacting shock wave as a regularly reflected C-J ODW, $\theta_{CJ,R}$, 2) the pressure rise of a regularly reflected ODW becoming equal to that of a normal detonation (referred to as the von Neumann condition), θ_N , 3) the maximum deflection condition for which the reflected ODW can just return the flow to be parallel to the wall, θ_D , and 4) Mach reflection with the formation of a detonation Mach stem and a reflected C-J ODW, $\theta_{CJ,M}$.

Consider the ram accelerator geometry shown in Fig. 3.1. For a given freestream Mach number, M_∞ , and normalized heat release \tilde{Q}_∞ , we will consider the reflection of the nonreacting shock wave, denoted I , from the upper wall. Reaction polar diagrams will be used to determine the nature of the reflected detonation, R , and the formation of a detonation Mach stem, S .

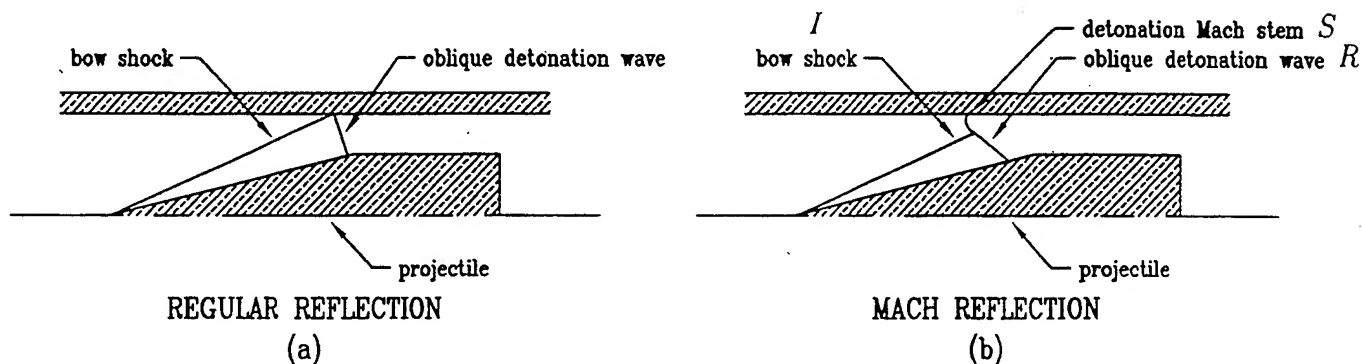


Figure 3.1: ODW ram accelerator geometry

We begin with $M_\infty = 4.0$ and $\tilde{Q}_\infty = 1.0$ which for fixed $\gamma = 1.4$ yields $M_{c_j} = 2.58$. The relevant reaction polar diagram for small values of the turning angle is presented in Fig. 3.2. The curve labelled SP denotes the locus of states that can be reached when the freestream gas passes through a non-reacting shock wave. Similarly, DP denotes the locus of states that can be reached by passing through an ODW with the prescribed heat release. The solid dot represents the state downstream of the nonreacting shock wave formed by a $\theta = 7$ degree turning angle. In addition, the reflected detonation polar, R_{DP} , represents the locus of states that can be reached by the gas that has already passed through the non-reacting shock as it passes through a detonation wave. The portion of this curve with $\theta < 7$ degrees corresponds to a reflected ODW, i.e. the family of ODWs that decrease the flow angle. Since the flow downstream of the wave should be parallel to the wall, we look for the intersections of the R_{DP} curve with the p-axis yielding the reflected wave that returns the flow angle to zero. The solutions are called *regular reflections*.

The dashed-dotted curves on both DP and R_{DP} represent weak, underdriven ODWs that are not physically attainable. We observe that for $\theta = 7$, the reaction polar diagram indicates that the shock wave will reflect as an underdriven weak detonation or as a strong detonation with a pressure rise of a factor of around 27. Since underdriven waves are not possible, the strong detonation solution will occur if the kinetics are sensitive enough to maintain a pressure-coupled reaction front. Alternatively, the shallow shock wave may not increase the pressure, temperature and the corresponding kinetic rates sufficiently to maintain a strong detonation. In this case, the *shock-induced-combustion* is uncoupled from a regularly reflected non-reacting shock wave.

As the turning angle is increased to $\theta = 11$ degrees, we see in Fig. 3.3 that the C-J point on the reflected detonation polar occurs at the intersection of the R_{DP} curve with the pressure axis at a pressure ratio of about 10. Thus, for a specified M_∞ and \tilde{Q}_∞ , we define

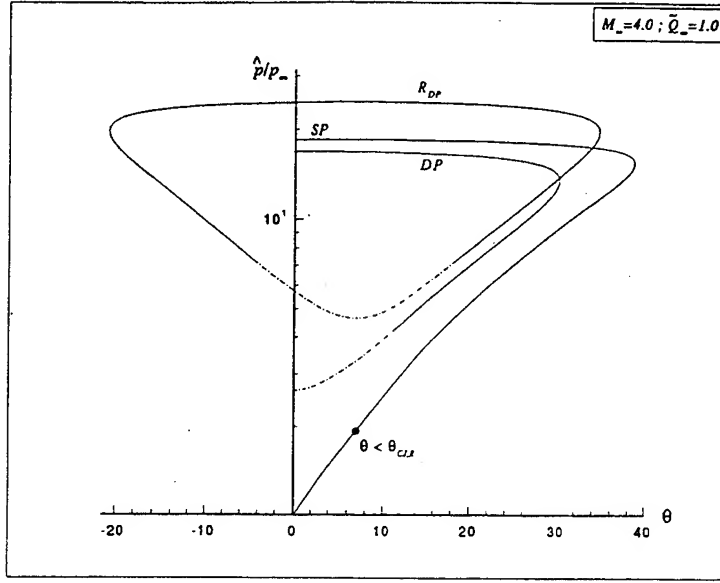


Figure 3.2: Reaction Polar Diagram for Small Turning Angle

the turning angle required to obtain a regularly-reflected C-J ODW as $\theta_{CJ,R}$.

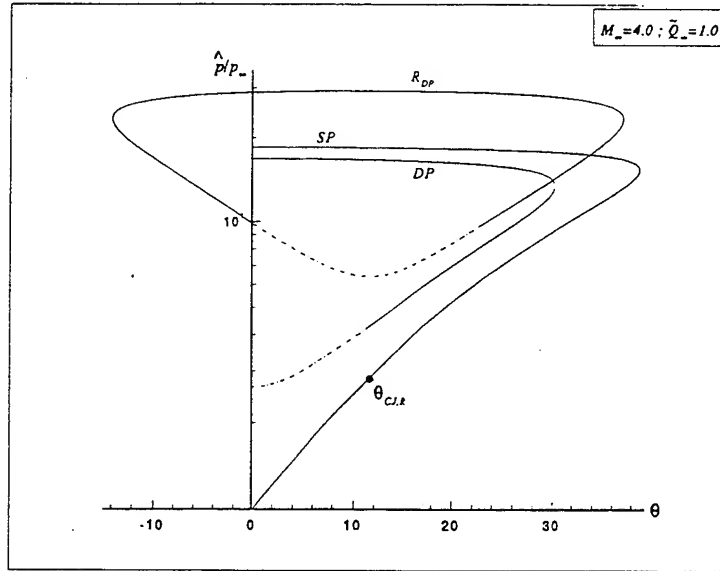


Figure 3.3: Turning Angle Required for Regularly-Reflected C-J ODW

As observed in Fig. 3.4, the turning angle may be increased until the reflected detonation polar intersects the p-axis to provide the same pressure rise that would occur across a normal detonation wave. This condition, that the R_{DP} and DP curves intersect on the p-axis, will be referred to as the *von Neumann condition* with turning angle, θ_N – in analogy to the definition for non-reacting shock waves [7] [8]. This condition corresponds to incipient *Mach reflection*. In other words, any increase of θ above θ_N may lead to the formation of a detonation Mach stem.

The detonation Mach stem is a curved detonation that provides zero flow turning through

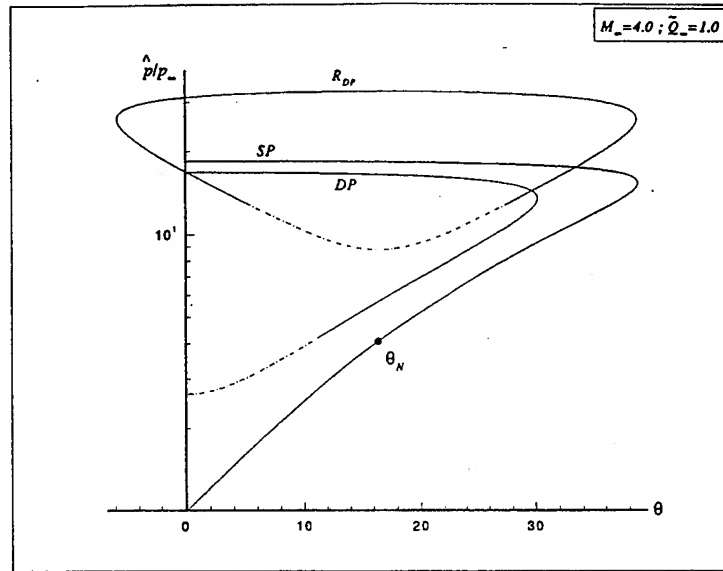


Figure 3.4: Turning Angle for Incipient Detonation Mach Reflection

a normal detonation at the wall and a subsonic downstream flow of products. As presented in Fig. 3.1b, the stem, S , intersects with both the incoming non-reacting shock, I , and the reflected ODW, R , at point P . The vortex sheet, V , separates the flow downstream of the detonation Mach stem from the flow downstream of the reflected ODW. The pressure rise and turning angle of these two flows must match so that both downstream flows can be represented as a point on the reaction polar diagram. A reaction polar diagram for a Mach stem configuration is shown in Fig. 3.5. The detonation Mach stem is represented by the nearly horizontal portion of the DP curve between its intersection with the p -axis and its intersection with the R_{DP} curve.

Figure 3.5 also represents the turning angle that makes the R_{DP} curve just tangent to the p -axis. This *maximum-deflection condition*, with a turning angle defined as θ_D , provides a nearly sonic downstream Mach number. Under some conditions, $\theta_D < \theta_N$, such that the maximum-deflection condition provides incipient Mach reflection. As will be shown, for propulsively useful fuels and freestream Mach numbers, $\theta_D > \theta_N$. Thus, we will consider the von Neumann condition to represent incipient Mach reflection for the remainder of this paper.

As the turning angle is increased further, a point is reached where the reflected ODW intersects the DP curve at the C-J point. We define the turning angle providing this condition as $\theta_{CJ,M}$ as seen in Fig. 3.6. For turning angles larger than this value, the pressure rise across the non-reacting shock wave is so large that, for a reflected wave to provide a pressure that equals that of any strong detonation Mach stem, only a weak underdriven ODW is needed. Underdriven waves are unphysical but there are two other solutions that may occur. First, it is likely that as θ approaches $\theta_{CJ,M}$, and the detonation Mach stem grows in length, the projectile throat will choke and the entire shock structure will propagate upstream and the inlet will unstart. Second, the highly reactive propellant gases may cause the leading shock wave to become an attached or detached detonation wave regardless of the wall interaction processes [5].

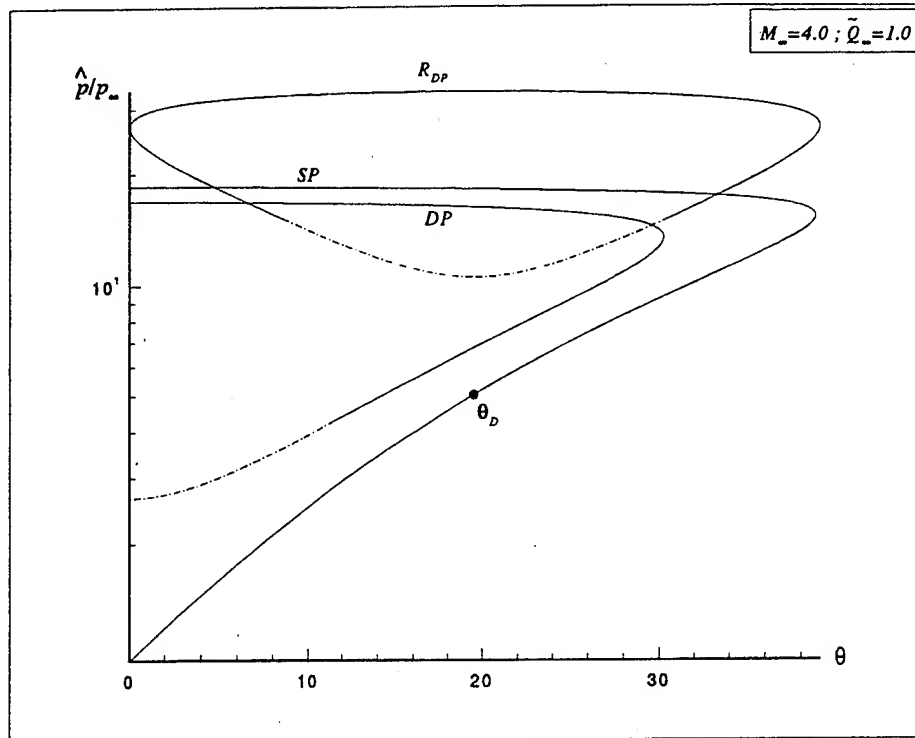


Figure 3.5: Turning Angle for Maximum Deflection Condition

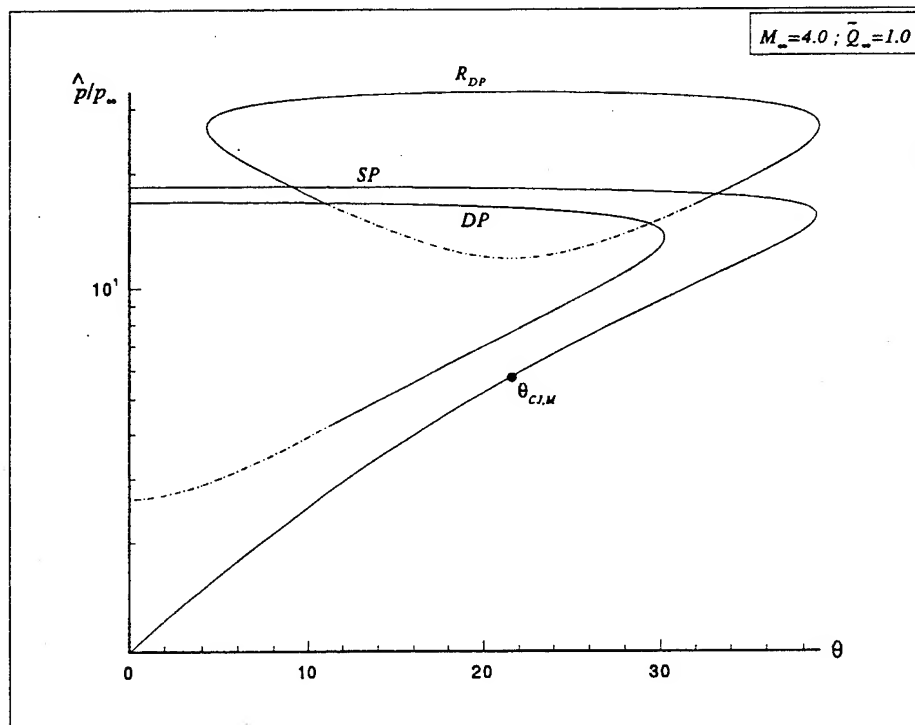


Figure 3.6: Turning Angle for Mach-Reflected C-J ODW

4. Variation of Special θ Values with M_∞ and \tilde{Q}_∞

Recall that the above figures were representative of $M_\infty = 4.0$ and $\tilde{Q}_\infty = 1.0$. In this section we first investigate the nature of the special turning angles for $M_\infty = 5.8$ and $M_\infty = 12.0$ for fixed $\tilde{Q}_\infty = 5.0$ (i.e. $M_{CJ} = 5.1$). Figs. 4.1 and 4.2 contain these results. A series of R_{DP} curves are shown for various turning angles of the incident shock wave. The turning angles vary from 1° to a value that nearly provides a downstream Mach number equal to the local C-J Mach number (i.e. 17° when $M_\infty = 5.8$ and 39.5° when $M_\infty = 12.0$). The locus of the C-J states is shown by the dotted curve in each figure. For the smaller superdetonative projectile speed, Fig. 4.1 presents the locus of C-J states that crosses the p-axis above the pressure of a normal detonation wave. Thus, there is no solution for θ_N or $\theta_{CJ,M}$ if the Mach number is near that of a C-J wave. Additionally, there is no flow turning angle that results in the regular reflection of an overdriven ODW.

Fig. 4.2 contains the results for the higher degree of overdriving. In this figure the locus of C-J states passes the p-axis below the pressure rise of a normal detonation. Thus, the ordering of the special angles is similar to the ordering for $M_\infty = 4.0$ and $\tilde{Q}_\infty = 1.0$. Here we obtain $\theta_{CJ,R} < \theta_N < \theta_D$ and $\theta_N < \theta_{CJ,M}$ which may be greater than or less than θ_D , depending on the particular M_∞ and \tilde{Q}_∞ .

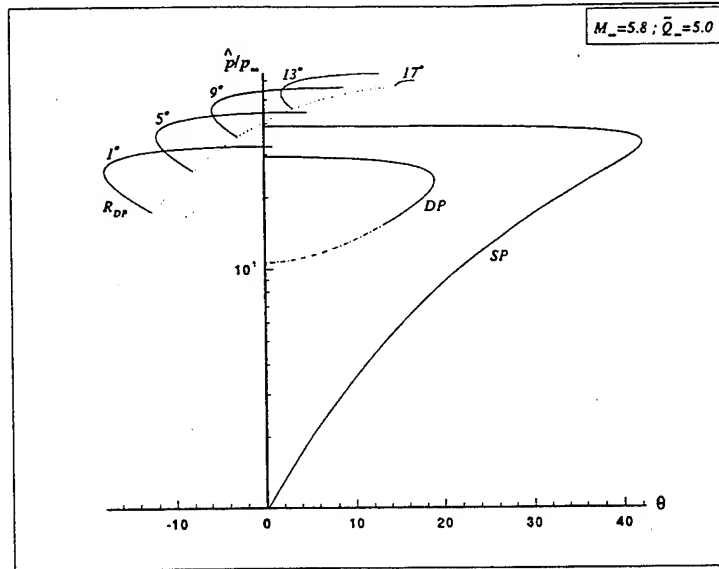


Figure 4.1: Reflected Detonation Polars for Varying Turning Angle for $M_\infty=5.8$, $\tilde{Q}_\infty=5.0$

For a prescribed \tilde{Q}_∞ , there is a unique small superdetonative M_∞ , for which the locus of C-J states will just cross the p-axis at the normal detonation pressure rise value. For these conditions, θ_N and $\theta_{CJ,M}$ come into existence and $\theta_{CJ,R} = \theta_N = \theta_{CJ,M} < \theta_D$. We now investigate the variation of $\theta_{CJ,R}$ and θ_N with M_∞ above the value required for $\theta_{CJ,R} = \theta_N$ for $\tilde{Q}_\infty = 1.0, 3.0$, and 5.0 . The results are shown in Fig. 4.3. The Mach number is normalized by the C-J Mach number so that the abscissa represents the amount of overdriving that a normal detonation wave travelling with the projectile experiences. For $\tilde{Q}_\infty = 1.0$, as the Mach number increases we observe that $\theta_{CJ,R}$ also increases to a maximum angle of nearly 12° until the overdriving exceeds 1.4 and then it decreases monotonically to near 7° at

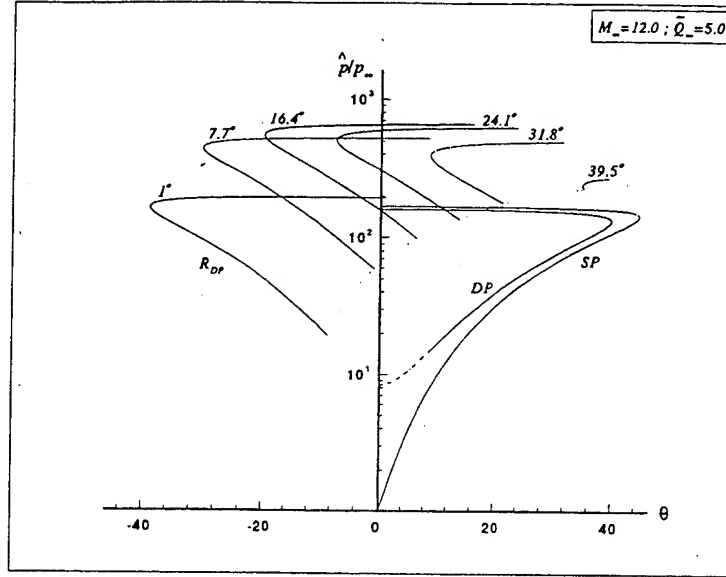


Figure 4.2: Reflected Detonation Polars for Varying Turning Angle for $M_\infty=12.0$, $\tilde{Q}_\infty=5.0$

$M_\infty/M_{CJ} = 3$. The turning angle for incipient Mach reflection, θ_N , increases monotonically from near 7° at $M_\infty/M_{CJ} = 1.1$ to near 19° at $M_\infty/M_{CJ} = 3$.

We also observe in Fig. 4.3 that the range of turning angles providing regularly-reflected ODW operation increases with M_∞ for fixed \tilde{Q}_∞ , but decreases as \tilde{Q}_∞ increases for fixed M_∞ . For example, if $M_\infty/M_{CJ} = 2$ and \tilde{Q}_∞ is increased from 1 to 5, the range of regularly reflected ODW operation decreases from about a 9° range to around a 5° range.

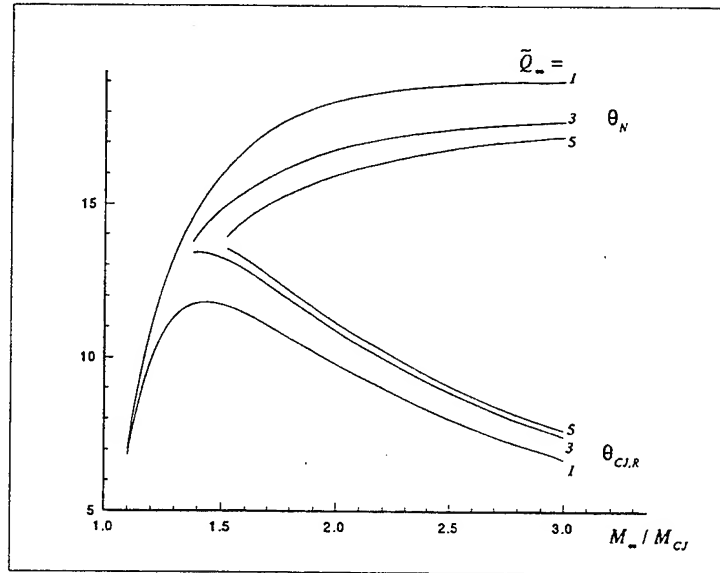


Figure 4.3: Variation of Special Angles with Heat Release and Mach Number

5. Summary

This discussion summarizes the character of the reflection of a non-reacting shock wave in a detonable gaseous mixture and the implications for ram accelerator operation. The primary assumption of the study is that the pressure and temperature rise across the non-reacting shock wave generated at the tip of the projectile is insufficient to initiate chemical reaction in a distance that is comparable to any other length scale in the problem; but, that any further pressure rise will result in immediate reaction so that a detonation wave will form.

For turning angles of the non-reacting shock wave below the regularly-reflected C-J ODW turning angle, θ_{CJR} , a strong ODW will result if the kinetics are truly sensitive enough to any further pressure and temperature increase. Since the flow downstream of the strong ODW is subsonic, downstream information can propagate to the strong wave and may force it to move upstream in an unsteady manner. This is one condition that may lead to unstart of a ram accelerator. However, a more likely scenario for small turning angles is that a small pressure rise will be insufficient to result in rapid chemical reaction so that a regularly-reflected shock wave should occur and be followed by supersonic deflagration or shock-induced-combustion. In this case, the engine cycle efficiency depends on the extent to which the supersonic combustion occurs near the projectile throat: no thrust will be generated if the combustion occurs downstream of the projectile.

For turning angles above θ_{CJR} but below the von Neumann turning angle, θ_N , a regular reflection of a weak overdriven ODW should occur. This operating mode assures supersonic flow over the projectile and avoids possible Mach reflection and associated unstart.

The formation of a detonation Mach stem occurs when the turning angle is above θ_N . While some conditions may provide a steady configuration with a detonation Mach stem, the length of the stem is not easily determined. Furthermore, since the flow downstream of the stem is subsonic, it may move upstream in an unsteady manner that leads to ram accelerator unstart. For this reason, we consider θ_N to represent the turning angle for incipient unstart of a ram accelerator.

Thus, assuming that propellants have been selected with the appropriate kinetics characteristics, one may use the results presented in this paper to determine the turning angle and minimum injection Mach number (i.e. ODW takeover velocity) to achieve ODW operation while avoiding both shock-induced-combustion and detonation Mach stem formation.

References

- [1] E. K. Dabora, D. Desbordes, C. Gueraud, and H. G. Wagner, "Oblique detonations at hypersonic velocities," *Prog. Aero. Astro.*, vol. 133, AIAA, pp. 187-204, 1991.
- [2] J. C. Liu, J. J. Liou, M. Sichel, C. W. Kaufmann, and J. A. Nicholls, "Diffraction and transmission of a detonation into a bounding explosive layer," *21st International Symposium on Combustion*, 1987.
- [3] D. Desbordes, L. Hamada, and C. Gueraud, "Supersonic h₂-air combustion behind oblique detonation waves," *Shock Waves*, vol. 4, pp. 339-345, 1995.
- [4] D. T. Pratt, J. W. Humphrey, and D. E. Glenn, "Morphology of a standing oblique detonation wave," *Journal of Propulsion and Power*, vol. 7, pp. 837-845, sep-oct 1991.

- [5] K. Ghorbanian and J. D. Sterling, "Influence of formation processes on oblique detonation wave stabilization," *submitted to Journal of Propulsion and Power*, 1995.
- [6] J. E. Shephard, "Detonation waves and propulsion," *Graduate Aeronautical Laboratories, California Institute of Technology*, vol. FM93-4, 1993.
- [7] H. Hornung, "Regular and mach reflection of shock waves," in *Ann. Rev. Fluid Mech.*, vol. 18, pp. 33-58, 1986.
- [8] L. F. Henderson, "The reflexion of a shock wave at a rigid wall in the presence of a boundary layer," in *J. Fluid Mech.*, vol. 30, pp. 699-722, 1967.
- [9] J. Meltzer, J. E. Shepherd, R. Akbar, and A. Sabet, "Mach reflection of detonation waves," in *Dynamic Aspects of Detonations*, vol. 153, Progress in Astronautics and Aeronautics, July 1991.
- [10] T. P. Gavrilenko and E. S. Prokhorov, "Overdriven gaseous detonations," in *Shock Waves, Explosions, and Detonations*, vol. 87, pp. 244-250, Progress in Astronautics and Aeronautics, 1983.
- [11] D. T. Pratt, *Calculation of Chemically Reacting Flows with Complex Chemistry*, vol. II. New York: B. E. Launder, Academic Press, 1977.

INITIATION OF DETONATION BY HYPERVELOCITY PROJECTILES

A. J. Higgins

Aerospace and Energetics Research Program
University of Washington, Box 352250
Seattle, WA 98195-2250, USA

EXTENDED ABSTRACT

Introduction

The conditions under which a supersonic blunt projectile will initiate a detonation wave are investigated experimentally. A blunt body of sufficient size and velocity injected into a reactive mixture can initiate a detonation wave which, if the projectile velocity is less than the mixture detonation velocity, will propagate ahead of the projectile. If the projectile does not initiate an unsupported detonation, the mixture may still react in a combustion wave which is not fully coupled to the projectile bow shock. The boundary between these two phenomena is the subject of this investigation.

The first examination of the projectile velocity and size required for detonation initiation was made by Zeldovich and Leipunsky in the early 1940's.¹ Investigations in the 1960's used flow visualization to examine the steady and periodic regimes of shock induced combustion around spheres and blunt cylinders at projectile speeds above and below the detonation speed of the mixture.^{2,3,4,5} These investigations focused on oscillating combustion instabilities behind the bow shock of the projectile, although a few instances of detonation initiation were noted.^{4,5} No systematic investigation of the conditions under which initiation occurs has been conducted.

Recently, the problem of detonation initiation by supersonic blunt bodies has received renewed attention, largely as a result of interest in the ram accelerator. In 1994, Lee⁶ and Vasiljev⁷ independently developed similar theories for the condition under which detonation will occur. Their theories equate the critical energy required to initiate a cylindrical detonation with the work done by the drag force on the projectile, as given by the hypersonic blast wave analogy. A rigorous comparison of this theory with experiment has not yet been performed. Experiments to investigate this problem are underway at the University of Washington.

Experiment Description

The boundary between steady flow and unsteady detonation initiation is currently being examined experimentally as a function of projectile velocity and fill pressure. In these experiments, a sphere-carrying sabot is fired from a single-stage light gas gun up to 2 km/sec using helium as the propelling gas. The sabot is stripped gasdynamically, leaving the sphere free-flying supersonically down the tube (Fig. 1a). The sphere then passes through a thin Mylar diaphragm into a large diameter tube (18 cm) filled with combustible gas (Fig. 1b). Experiments

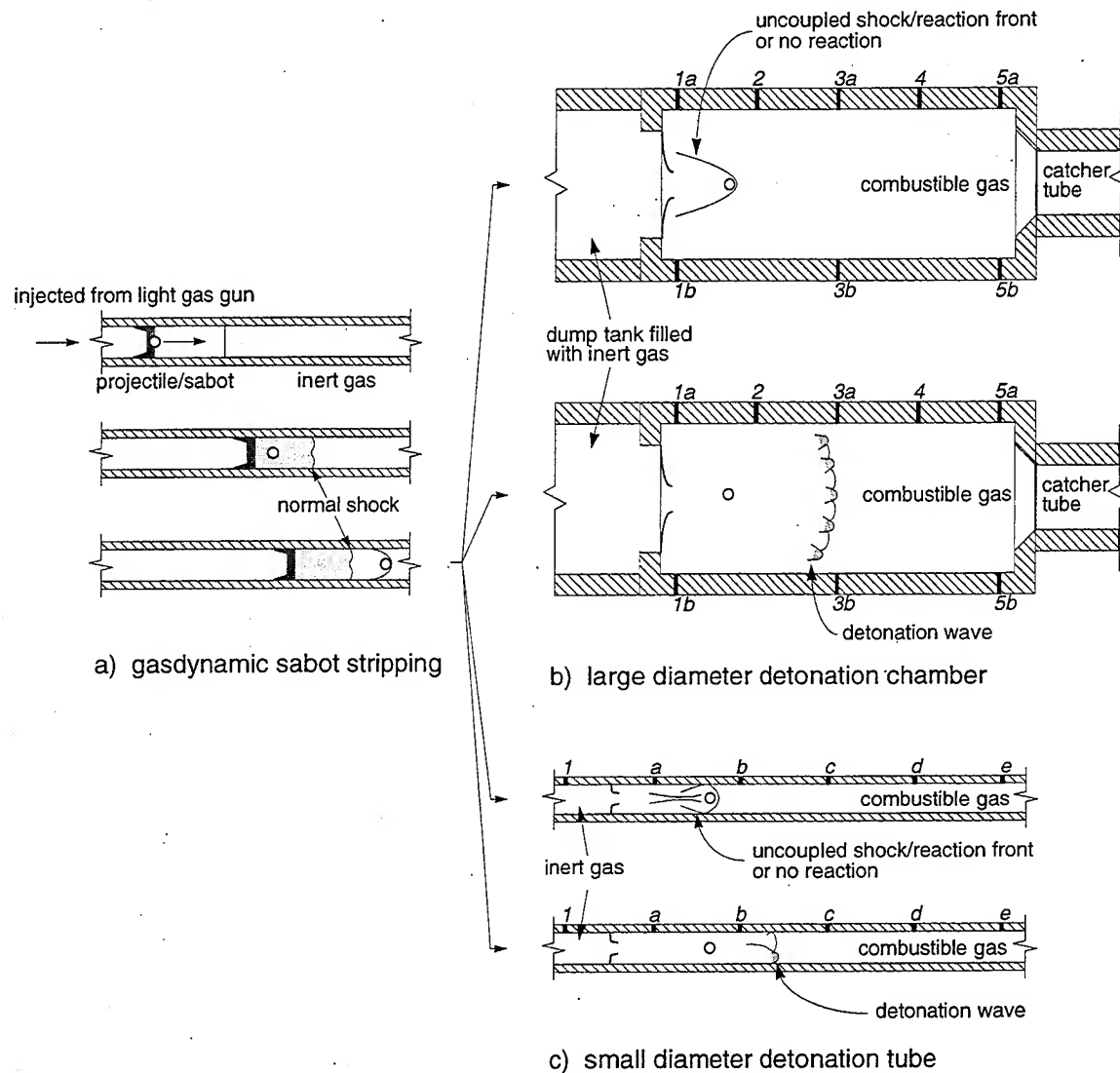


Fig. 1 Schematic of experiments to study detonation initiation via blunt bodies in both detonation chambers and confined tubes.

are also conducted with a smaller diameter (3.8 cm), confined tube to examine the influence of the multiple bow shock reflections off the tube wall downstream of the sphere (Fig. 1c). The results of the experiment are monitored by pressure transducers mounted on the tube wall.

The occurrence of a successful detonation initiation is identified by a pressure pulse traveling in front of the sphere at approximately the Chapman-Jouguet (CJ) detonation speed (Fig. 2a). An experiment which does not induce detonation is not necessarily without combustion; the mixture may react behind the bow shock in a smooth, uncoupled wave or in a weakly coupled oscillating pattern. A sphere-initiated detonation wave can be differentiated from a non-detonating bow shock by the arrival time and amplitude of the first pressure pulse seen by a transducer on the wall of the chamber (Fig. 2b). Yet another possible outcome of the experiment

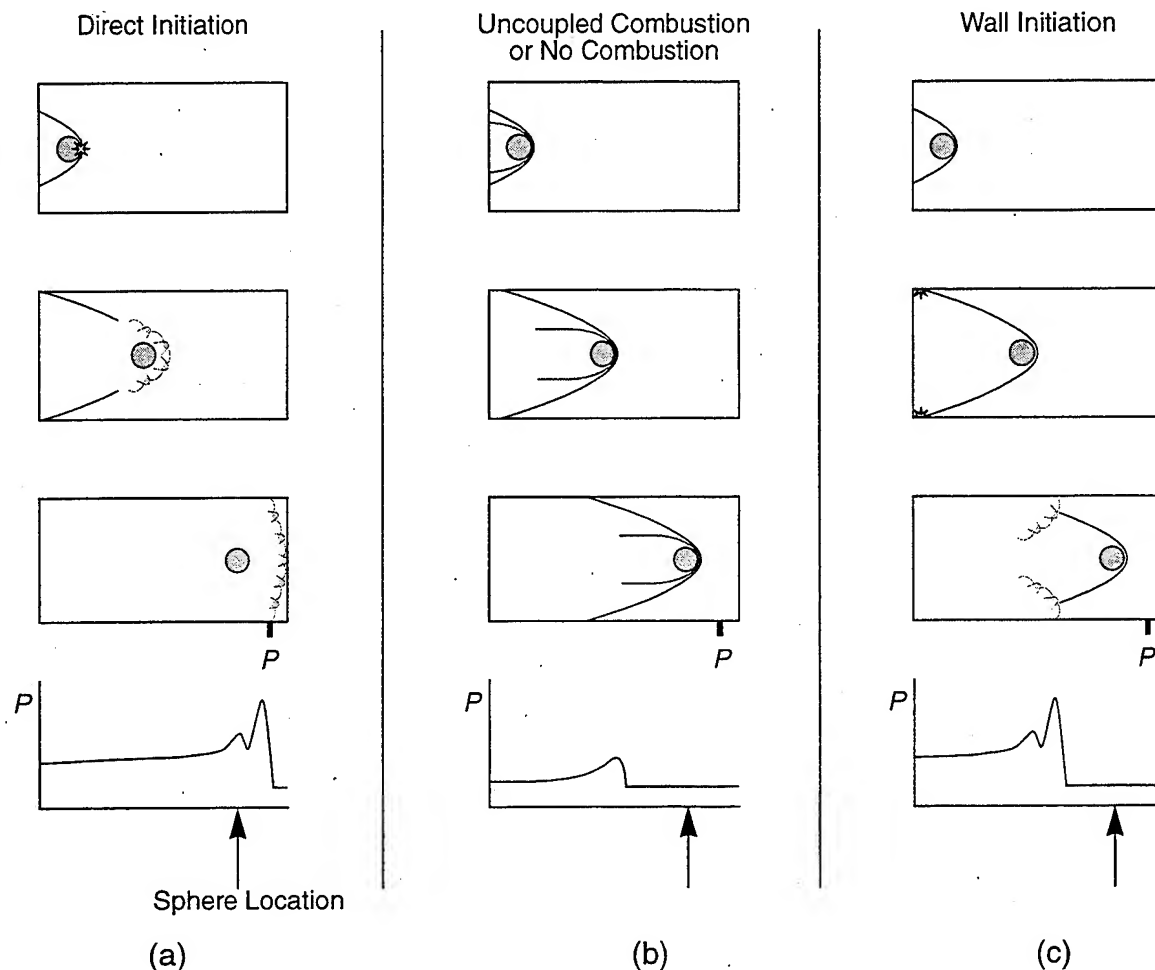


Fig. 2 Schematics of different experimental results. The stylized pressure traces demonstrate how these different regimes of combustion are identified.

is the initiation of detonation by secondary effects, such as the interaction of the bow shock with the confinement of the tube wall. This phenomenon can be isolated from "direct" initiation by the sphere, since the bow shock of a hypersonic projectile does not reach the tube wall until a considerable time after the projectile enters the test section. Since any detonation initiated by the interaction of the bow shock with the tube wall cannot overtake the original sphere within the ~1 m length of test section, there is no possibility of these wall effects confusing the results of an experiment (Fig. 2c).

Preliminary Results

A sample of results is shown in Figs. 3 and 4 from a large diameter tube, as illustrated schematically in Fig. 1b. The tube is 178 mm in diameter and 902 mm long. In these experiments, a 12.7 mm diameter chrome steel sphere is injected into a gas at 7.5 atm fill pressure. Fig. 3 shows the results from a sphere traveling at 1650 m/sec (Mach 4.7) through a tube filled with nitrogen, an inert gas. The pressure transducers are spaced 215 mm apart, with the first

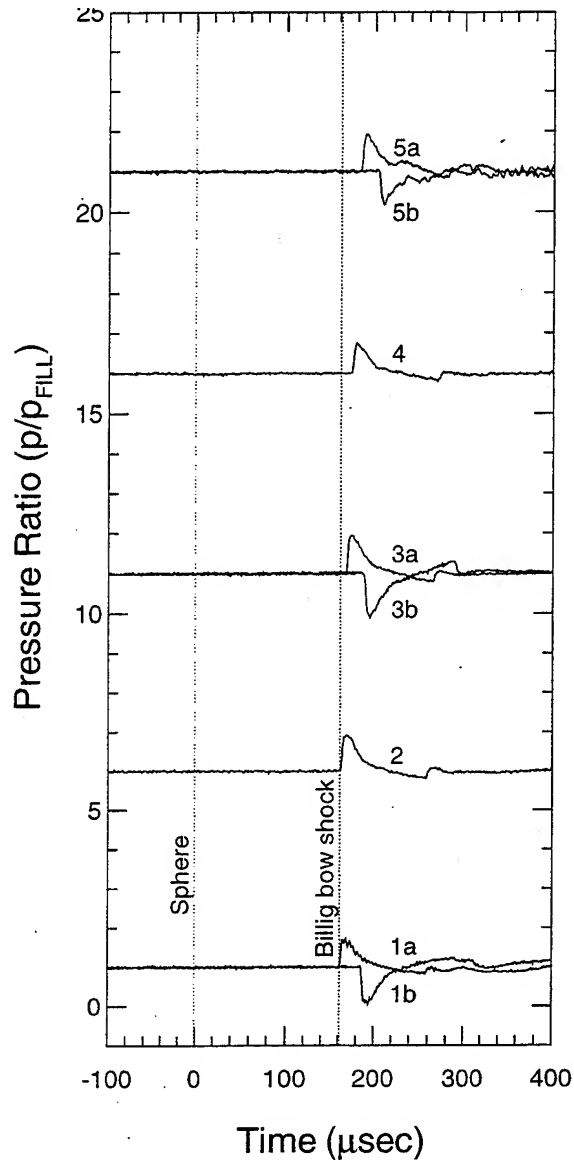


Fig. 3 Pressure data for sphere traveling at 1650 m/sec (Mach 4.7) through 7.5 atm of nitrogen, compared to Billig's prediction of bow shock location. Traces from the opposite side of the tube are inverted.

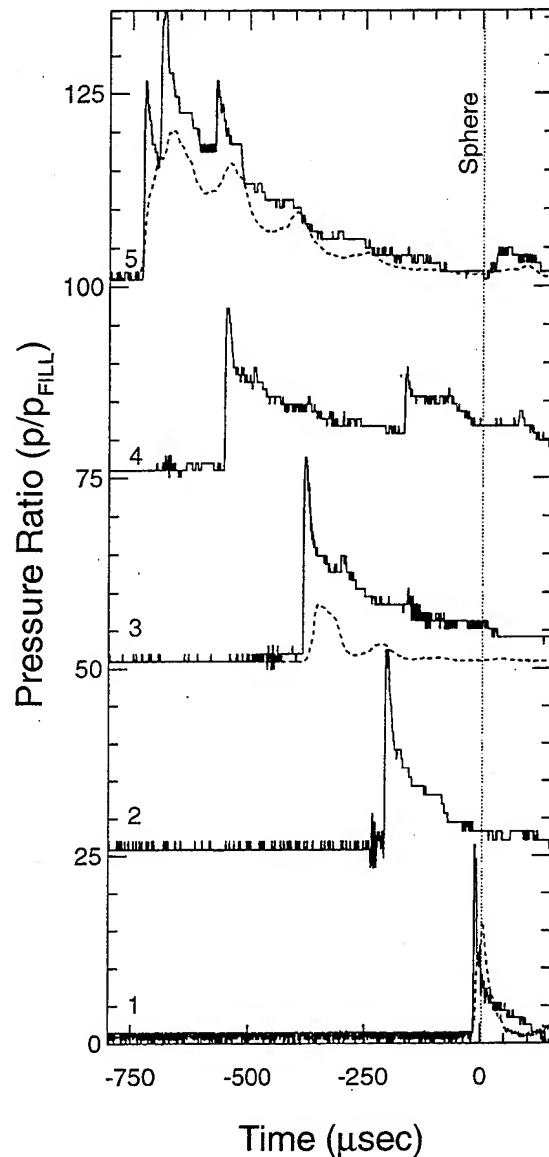


Fig. 4 Pressure (solid line) and luminosity (dashed line) data for a detonation initiated by a sphere traveling at 730 m/sec (Mach 2.1) through $2\text{H}_2 + \text{O}_2 + 7\text{Ar}$ at 7.5 atm. See Fig. 1b for transducer locations.

probe just 21 mm from the entrance diaphragm. The data are scaled to the fill pressure of 7.5 atm. The pressure transducers show the bow shock impinging on the wall approximately 160 μs after the passage of the sphere, which occurs at time $t = 0$ μs . This delay correlates well with the expected bow shock location as predicted by an empirical correlation after Billig, shown as a dotted line.^{8,9} A difference in arrival time of 20 μs can be observed on opposite sides of the tube. Using the Billig correlation and the known speed of the sphere, this difference can be computed to

result from less than a 5 mm displacement of the sphere from the tube axis. The lagging of the bow shock behind its predicted location in traces 3, 4, and 5 is due to drag losses in the sphere's velocity, which are not taken into account here.

Results from a firing into a combustible mixture are shown in Fig. 4. A sphere identical to the one from Fig. 3 is injected at 733 m/sec (Mach 2.1) into a mixture of $2\text{H}_2 + \text{O}_2 + 7\text{Ar}$, again at 7.5 atm. In addition to the pressure transducers, data are also shown from photoelectric sensors, which are connected to the tube wall via fiber optic cable. The data from the photoelectric sensor (shown as a dashed line) are largely qualitative and are left unscaled, though they do give an indication of the presence and location of combustion. Both the pressure and luminosity data show a detonation wave forming immediately in front of the sphere and propagating ahead of it. The wave initially appears overdriven, traveling at greater than 120% of the CJ speed between traces 1 and 2. The wave quickly decays; the velocity of the wave between traces 4 and 5 is 1760 m/sec, within 1% of the theoretical CJ speed. Since the detonation was observed well in front of the sphere even before the bow shock had time to reach the tube wall, the conclusion is that this detonation was initiated directly by the impact of the sphere into the combustible gas (corresponding to the case shown in Fig. 2a).

Sample results from an experiment in a smaller diameter, confined tube are shown in Figs. 5 and 6. In these experiments, a 12.7 mm diameter steel sphere is again fired into a mixture of $2\text{H}_2 + \text{O}_2 + 7\text{Ar}$. The tube diameter, however, is significantly reduced to 38.1 mm. The fill pressure has also been reduced to 1 atm. The first pressure trace in Fig. 5 is taken from the inert gas used to strip the sabot (Fig. 1a) and shows a typical nonreacting pressure profile generated by the impingement of the bow shock on the tube wall. The impingement now occurs almost concurrently with the passage of the sphere. The sphere is traveling at a velocity of 1100 m/sec, or 65% of the theoretical CJ speed in the combustible mixture. A small silhouette of a sphere shows its position and diameter relative to the data. The next five traces (a-e) are from sensors spaced 40 cm apart, beginning 20 cm after the thin diaphragm separating the inert and combustible gases. Both pressure and luminosity data show a distinct combustion wave developing in the wake and overtaking the projectile. By the time of trace c, a free running detonation has been initiated in front of the sphere and by trace e has settled down to a velocity of 1680 m/sec, within 1% of the theoretical CJ speed. Similar results were obtained with projectile velocities over the range from 900 m/sec up to the CJ speed, although detonation initiation was more prompt in the higher velocity cases.

Fig. 6 shows an identical experiment, only with the sphere velocity reduced to 800 m/sec. No combustion activity is seen, and the projectile proceeds supersonically down the tube. This result implies a critical velocity of 800-900 m/sec, or 50% of the detonation speed, is required to initiate a detonation in $2\text{H}_2 + \text{O}_2 + 7\text{Ar}$ at 1 atm with this projectile and tube geometry.

Conclusion

Experiments in progress are studying the critical velocity for detonation initiation by spheres as a function of pressure. The simplicity of geometry and the isolation of wall influence and confinement effects allow these experiments to bridge the gap between contemporary ram accelerator research and classical detonation parameters such as cell size and critical tube

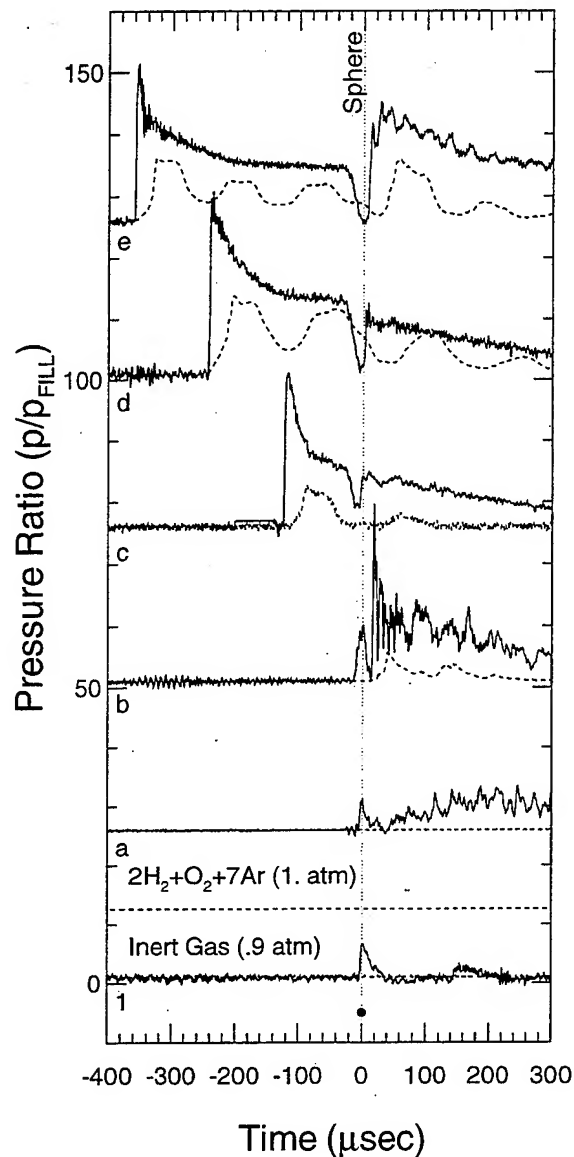


Fig. 5 Pressure (solid line) and luminosity (dashed line) data for a detonation initiated by a sphere traveling at 1100 m/sec (65% CJ speed).

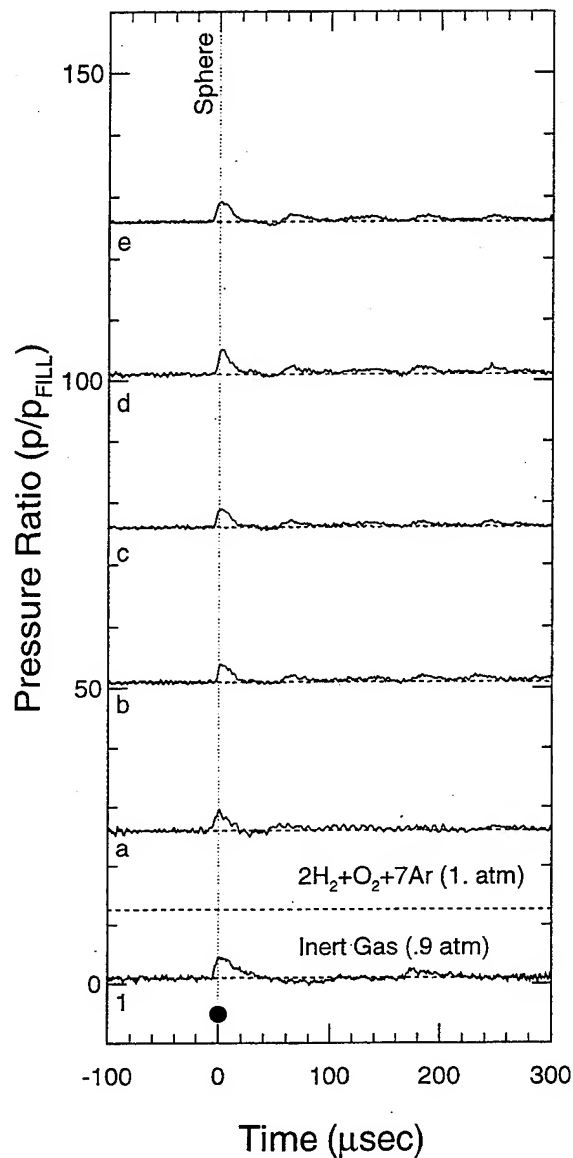


Fig. 6 Pressure (solid line) and luminosity (dashed line) data for sphere traveling at 800 m/sec (50% CJ speed). Note no detonation was initiated.

diameter. The results could illuminate important aspects of the ram accelerator, such as combustion and detonation stabilization, unstart phenomena, and the possible merits of operating without interaction with the tube wall.

Acknowledgments

Carl Knowlen was instrumental in the early stages of planning these experiments. Dennis Peterson furnished invaluable assistance in the design and construction of the facility. Pascal Bauer provided pertinent discussion on detonation waves. Adam Bruckner is thanked for his support and guidance.

References

1. Zeldovich, J., and Leipunsky, O., "A Study of Chemical Reactions in Shock Waves," *Acta Physicochimica U.R.S.S.*, Vol. 18, 1943, pp. 167-171.
2. Ruegg, F.W., and Dorsey, W.W., "A Missile Technique for the Study of Detonation Waves," *Journal of Research of the National Bureau of Standards-C. Engineering and Instrumentation*, Vol. 66C, 1962, pp. 51-58.
3. Behrens, H., Struth, W., and Wecken, F., "Studies of Hypervelocity Firings into Mixtures of Hydrogen with Air or with Oxygen," *Tenth Symposium (International) on Combustion*, 1965, pp. 245-252.
4. McVey, J.B., and Toong, T.Y., "Mechanism of Instabilities of Exothermic Hypersonic Blunt-Body Flows," *Combustion Science and Technology*, Vol. 3, 1971, pp. 63-76.
5. Lehr, H.F., "Experiments on Shock-Induced Combustion," *Astronautica Acta*, Vol. 17, 1972, pp. 589-597.
6. Lee, J.H.S., "On the Initiation of Detonation by a Hypervelocity Projectile," Zeldovich Memorial Conference on Combustion, Voronovo, Russia, Sept. 12-17, 1994.
7. Vasiljev, A.A., "Initiation of Gaseous Detonation by a High Speed Body," *Shock Waves*, Vol. 3, 1994, pp. 321-326.
8. Anderson, J.D., *Hypersonic and High Temperature Gas Dynamics*, McGraw-Hill, Inc., New York, 1989, p. 189.
9. Billig, F.S., "Shock-Wave Shapes Around Spherical- and Cylindrical-Nosed Bodies," *Journal of Spacecraft and Rockets*, Vol. 4, No. 6, 1967, pp. 822-823.

Session 4

SHOCK AND EXPANSION TUBES

SHOCK TUBE EXPERIMENTS FOR MODELING RAM-ACCELERATOR-RELATED PHENOMENA

J. Srulijes, A. Eichhorn, M. J. Nusca*, G. Smeets, F. Seiler

French-German Research Institute of Saint-Louis (ISL), F-68301 Saint-Louis, France

*Army Research Laboratory (ARL), USA-MD, Aberdeen Proving Ground

ABSTRACT

This paper presents the ISL expansion tube as a useful means for investigating the gasdynamic phenomena occurring inside a ram-accelerator. It could be demonstrated that with a specially devised expansion tube, a combustible gas mixture can be accelerated to a superdetonative velocity without autoignition. The experiments in the expansion tube are carried out for basic research purposes on ram-accelerator-related combustion phenomena and also for supporting and optimizing the operation of the 30 mm and 90 mm ram accelerator facilities at ISL.^{1,2} In this paper we discuss some experiments performed using the expansion tube. These experiments were carried out to demonstrate the establishment and stabilization of combustion at a step or a second small cone following the forebody cone. This second cone represents a small step on a projectile flying at hypersonic speed in an external propulsion accelerator, as proposed by Rom.³ Using a modified CCD-camera we succeeded in recording the emission in the wavelength range 300 nm to 320 nm, emitted by the OH band "A $2\Sigma^+ - X 2\Pi_1$ ". By this method we can measure the onset of combustion, its spatial extension and its duration. The experimental results are compared to fluid dynamics calculations using a CFD code that solves the 2D-axisymmetric, Reynolds-Averaged Navier Stokes (RANS) equations including equations for chemical kinetics (finite-rate and equilibrium), as given by Nusca.⁴

INTRODUCTION

The worldwide first ram accelerator was devised and successfully operated by Hertzberg et al.⁵ and Bruckner et al.⁶ The ram accelerator is based on the ramjet principle. A sharp-nosed projectile, which resembles the centrebody of a conventional ramjet runs inside a tube filled with a combustible gas mixture. The tube acts as the outer cowl of the ramjet and the energy release by combustion produces high pressure at the base of the projectile providing thrust. The reason for testing the gasdynamic ram-accelerator-related phenomena in an expansion tube is the difficulty to obtain reliable information about the details of the combustion processes occurring around a moving projectile. On the contrary, with our expansion tube and a fixed projectile in a moving gas, information can be obtained in a much simpler way. We succeeded in accelerating combustible gas mixtures, without autoignition, to superdetonative velocities under well-known conditions, see Srulijes et al.⁷

We employed a special shock tube with a third section at a very low pressure filled with hydrogen, called expansion section, beyond the driven section. Because of the non-stationary expansion, this set-up provides high gas velocities with very high stagnation temperatures in the expansion section. The shock tube was modified by mounting an additional section filled with an inert gas (hydrogen or nitrogen), named buffer section, placed between the driver tube containing hydrogen and the driven tube filled with the combustible gas mixture. This buffer section is indis-

pensable to avoid pre-ignition caused by the rupture of the steel diaphragm. The geometry of the expansion shock tube used for the experiments presented in this paper is as follows: inner diameter = 0.1 m, driver length = 2.7 m, buffer length = 3.5 m, driven tube length = 6.7 m and expansion tube length = 8.5 m.

The mean flow parameters were: velocity = 2280 m/s, static pressure = 0.65 bar and static temperature = 285 K. Both, the calculated and the measured test time for our expansion tube (constant flow parameters) is about 650 μ s before the flow begins to decay. All the experiments shown in the paper were carried out using a stoichiometric gas mixture of methane and air and for the comparative experiments, without combustion, we used nitrogen instead of air. The Chapman-Jouguet velocity of the gas mixture is 1823 m/s, calculated with the real gas code MEGEC of Gatau⁸. The calculated velocity was checked by measuring the pressure history on the surface of a wedge with $\theta_2 = 15^\circ$ and also by Pitot measurements using PCB pressure gauges type 113A24. Both, wedge surface as well as Pitot pressures, were measured in the Mach cone flow.

With our expansion tube a hypersonic and superdetonative flow can be produced and used for testing the flow around models of different shapes. As an interesting test example for experimental study using our expansion tube, we chose a model based on Rom's idea of the external propulsion accelerator. Using his words: "the question of establishment and stabilization of a combustion or detonation front on a projectile flying at hypersonic speeds in a detonable mixture is of interest both as a fundamental combustion problem and for practical application in the external propulsion accelerator. It is also relevant to the oblique detonation wave engine, the ram accelerator, and various scramjet engines."

The overall reaction time for combustion processes, as described by Anderson et al.⁹, is generally inversely proportional to pressure (or density) to an exponent one for binary collisions (two-body reactions), and to an exponent two for ternary reactions, and exponentially dependent on temperature. Taking the binary scaling law as an approximation, the results obtained in the expansion tube experiment can be transformed to the actual conditions, i.e., Rom's external propulsion accelerator or the ram accelerator itself.

FLOW VISUALIZATION

General

The flow visualization was done by means of differential interferometry as described by Smeets and George¹⁰. This optical measuring technique allows the visualization of density gradient fields. We visualized the flow by two means - framing pictures and streak records - using a rotating drum camera in both cases. For the framing pictures the whole window is focused on the rotating film and illuminated by eight successive air sparks ($\Delta t = 200 \mu$ s). For the streak records only a section of the flow field limited by a small slit is focused onto the rotating drum, by using a flash light for illumination (duration time ≈ 4.0 ms).

We studied the behaviour of the flow around various geometries: a two-dimensional wedge followed by a step, a three-dimensional model consisting of a cone followed by a ring cowl where the onset of combustion with different cowl thicknesses was studied and extensively, a double-cone configuration. The angle of the forebody cone θ_2 for the double-cone model was calculated to have, for the given freestream conditions, a θ_2 resulting in a $T_2 \approx 800$ K, i.e., $\theta_2 = 25^\circ$; a second small cone, with an angle θ_1 , follows the forebody cone representing a small step with height h . For this second cone we used different angles (measured from the model axis) and

different step heights, varying from $\vartheta_1 = 50^\circ$ to 85° and $h = 1$ mm to 4 mm. Two different diameters for the cylindrical body were used (34 mm and 50 mm). All models were placed outside, shortly after the end cross-section of the expansion tube (Mach cone), to allow the low Mach number hydrogen flow leaving the tube before the test gas arrives. Some experiments were carried out with off-axis position of the model, having a displacement of 25 mm from the flow axis, to use as much as possible of the core of the Mach cone flow.

The interferogram at the left of Fig. 1 shows the combustion flow configuration obtained with a wedge of 40 mm width, with $\vartheta_2 = 15^\circ$ and with a step of $h = 4$ mm. The model is mounted off-axis. The picture at the right shows the corresponding control experiment with no combustion. The flow configuration with combustion, especially in the recirculation zone in front of the step, can be compared to the one without combustion.

In Fig. 2 we see the flow configuration with and without combustion for a three-dimensional model with a ring, consisting of a cone of $\vartheta_2 = 13^\circ$ (similar to the angle used for the ram projectiles) and a ring cowling with $h = 3$ mm. This ring is designed in a way to have the cone bow shock impinging at the inner corner of the front edge of the ring, as can be seen in the control experiment. This configuration, as opposed to the double-cone configuration, leads to a normal shock in front of the ring cowling. The large combustion zone induced by the shock at the ring can thus be seen.

Double-cone

Fig. 3 presents two interferograms showing a combustion front wave and the corresponding flow configuration for the control experiment for a double-cone $\vartheta_2 = 25^\circ / \vartheta_1 = 50^\circ / h = 4$ mm with 34 mm body diameter. A steeper front wave and a different flow pattern, due to combustion, compared to the control experiment, can be recognized.

The interferograms in Fig. 4 show the combustion front wave and the corresponding flow configuration for the control experiment for a double-cone $\vartheta_2 = 25^\circ / \vartheta_1 = 50^\circ / h = 4$ mm, here with a 50 mm body diameter. The model is mounted off-axis.

On the upper side of Fig. 5 we see a streak record for the double-cone configuration of Fig. 4, taken through a 0.25 mm wide slit placed parallel to the body at 2 mm distance from the wall. This streak picture shows all three regimes, i.e., super-, trans- and subdetonative. The expansion wave produced by the bursting of the diaphragm reaches the test section during the time of the streak record reducing the gas velocity. It allows to pass through all three regimes in only one experiment. In the superdetonative domain the combustion front wave position is practically steady. After the transdetonative region in the subdetonative regime a pulsating combustion takes place, for the methane-air case, due to the periodic ignition and separation of the combustion. The streak shows the instationarity of the combustion front wave. For the comparative experiment with methane-nitrogen, the position of the shock wave is, as expected, nearly constant during the whole measuring cycle.

Two differential interferograms can be seen in Fig. 6 showing a combustion front wave and the corresponding flow configuration for the control experiment for a double-cone $\vartheta_2 = 25^\circ / \vartheta_1 = 85^\circ / h = 2.5$ mm with 50 mm body diameter. The model is mounted off-axis. We used this model geometry exclusively for both, the OH-emission measurements and the CFD calculations discussed below.

DOUBLE-CONE

Recording of OH-emission

By means of a substantially modified CCD-camera (LHESA mod. 5018), as described by Eichhorn et al.¹¹, we recorded in different ways the emission in the wavelength range 300 nm to 320 nm, which contains the OH band " $A^2\Sigma^+ - X^2\Pi_1$ ". The camera is equipped with a CCD image sensor (THOMSON TH7864) consisting of two parts: a light sensitive image zone and a memory zone where the charges generated in the image zone by the incoming light intensity can be rapidly stored. Each zone consists of 288 lines and 550 columns. By appropriately transferring whole frames or partial frames up to single lines from the image zone to the memory zone, a large variety of registration modes from framing to streak modes can be used. In the streak mode the possible time resolution is better than 10 μ s per line.

The experimental set-up for these registrations is shown in Fig. 7. The double-cone shown in flow direction is mounted off-axis with its upper wall being on the axis of the flow (displacement 25 mm). The image of the test model and its flow field is formed by means of a quartz lens ($f = 80$ mm) through an interference filter (transmission peak at 310 nm, half width 12 nm) at the entrance plane of a gateable micro channel plate. The amplified image is recorded by means of the CCD-camera described above. In the framing mode the exposure time is defined by the gate of the image amplifier, while in the streak mode the gate remains activated and the time resolution is defined by the timing of the transfer of the lines or line groups from the image zone to the memory zone.

Figs. 8 and 9 show two registrations of the emission in the framing mode with different exposure times: 200 μ s and 100 μ s respectively. The exposure started about 150 μ s after the beginning of combustion. The side view contour of the model is superposed as a reference for position and size. If we assume that OH chemiluminescent emission is correlated with gas combustion, then the images show, for the given exposure time, the extension of the combustion zone.

Fig. 10 shows a series of seven partial images with an exposure time of 50 μ s and $\Delta t = 100$ μ s between each of them, thus showing the development of the combustion during the first 500 μ s. For this registration the camera was rotated by about 25 degrees to become parallel to the cone surface. The flow direction is indicated by the right part of the contour superposed in Fig. 10. These images clearly show that the flow ignites at the step and from there the combustion propagates towards the cone and the cylinder.

The result of a streak recording is shown in Figs. 11 and 12. The orientation of the camera is the same as in Fig. 10. The time resolution is 50 μ s per line. The intensity distribution is shown as a function of time along a line, parallel to the cone surface, cutting the step of the model. Fig. 11 shows 100 lines in a pseudo-colour-plot, while Fig. 12 shows 28 lines covering the first 1.4 ms of the combustion in a pseudo-3D-plot. These figures show the location of combustion maxima and inform quantitatively about the combustion time. A strong combustion occurs during the first 700 μ s and then a weak combustion continues for some milliseconds as described by Srulijes et al.⁷ Our "clean" test time is of the same order as measured here. Combustion is also observed in front of a detachment flow region of about 7 mm in front of the step. Due to the subsonic regions in the boundary layer, the combustion beginning at the step can obviously influence the upstream supersonic flow near the leading cone.

Pressure Measurements

The static pressure is measured at the end of the tube with a PCB gauge type 113A21. Using PCB pressure gauges type 113A24 and 113A34 we measured the static pressure on the cylindrical body, i.e., measuring stations G1 = 5 mm, G2 = 35 mm and G3 = 45 mm after the second cone. The pressure gauges were quasi-dynamically calibrated already mounted in the test model. We used a special device that generates pressure pulses of about 1 ms, giving calibration values better than one percent. All pressure gauges exposed to high temperature are protected with a 0.2 mm wax layer.

Fig. 13 shows pressure time histories for one of the experiments with non-reacting flow. All three gauges show, first the pressure histories corresponding to the low Mach number hydrogen flow for about 750 μ s and then, the arrival of the high Mach number $\text{CH}_4 + \text{N}_2$ test gas is clearly seen with gauges G1 and G2. The gauge at the end of the expansion tube G0 shows the pressure history of the free stream flow. G1 shows the pressure increase due to shock compression. G2 gives the corresponding pressure history behind the expansion wave.

Fig. 14 presents pressure time histories for an example experiment with reacting flow. As can be seen, both, G1 and G2 show a significant pressure increase due to combustion.

The mean wall pressure ratio (reacting/inert) taken from 13 different experiments are 2.02 for G1, 2.51 for G2 and 2.35 for G3. The pressures measured at G2 and G3 are in good agreement with CFD-calculation shown in Fig. 18. The value of G1 is smaller than the calculated value, maybe due to the position near the step, where the pressure increase is quite steep. The CFD absolute values of pressure are rather high compared with the experiments, the reason can be found in the difference between calculated and measured shape of the shock.

CFD-Calculations

The computational fluid dynamics effort was performed at the US Army Research Laboratory using a computer code that solves the 2D-axisymmetric Reynolds Average Navier-Stokes equations (RANS) with nonequilibrium chemical reactions. Chemical kinetics are fully coupled to the gas dynamics equations. Molecular diffusion, thermal conduction and viscosity (including a mixing-length turbulence model) are included. A co-volume equation of state is used. The governing equations are rendered in conservative finite-volume form and solved using an upwind implicit numerical scheme. For the present application a 3-step global kinetics mechanism was employed for seven methane/air species (CH_4 , O_2 , N_2 , H_2 , CO , CO_2 , H_2O). Further details are given by Nusca.⁴ The computational mesh was generated in a zonal body-fitted fashion such that sharp geometric corners and the details of the geometry are preserved. Approximately 12700 grid points were used to represent the computational domain around the model (the tunnel walls were assumed to be 200 mm from the model centerline) The code was executed for approximately 3.3 hours of computer time on a CRAY2 computer to yield a steady flow solution. The freestream Mach number, pressure, temperature were 6.651, 0.592 atm, 285 K, respectively. Plotted results are presented in form of density colour plot (the density being normalized by the freestream values). Combustion is calculated in a 5 mm detachment flow region in front of the second cone, on the leading cone and on the cylindrical body, which is in good agreement with the OH-measurements described above. The reaction was not extinguished by expansion after the second cone, thus resulting in a pressure increase around the cylinder, see similar results by Rom, Nusca, et. al.¹²

Fig. 15 presents a colour contour plot of the x-component of velocity for non-reacting flow, showing the separated flow region of about 5 mm near the step. This separated flow region plays an important role for flow ignition, as could be deduced from the OH-registrations. The freestream u-velocity is plotted in red, light blue is low speed attached flow, dark blue is reverse flow. The wall boundary layers can be clearly seen as well.

Fig. 16 shows a colour contour plot of density for reacting flow, normalized by the freestream value, showing an extensive combustion on the step and after the step. By plotting the H_2O contours a small amount of combustion can be seen in the boundary layer of the forebody cone. This result is in good agreement with our OH-records. The shape of the calculated shock wave due to the second cone is less steep than the experimental one shown in Fig. 6.

Fig. 17 shows a colour contour plot of density for non-reacting flow, normalized by the freestream value, showing in red a strong (i.e., red is high density) oblique shock generated by the separated flow region about one step height in front of the step. This oblique shock merges with the weaker (i.e., orange is lower density) oblique nose shock and generates a nearly-normal curved transmitted shock above the step, similar to what can be seen in the interferograms. The difference between experiment and CFD is that the calculated separated region is smaller. A grid refinement before the step may give a weaker oblique shock and thus result in a different shape shock system. The grid refinement will be done until the computed results become grid independent.

Fig. 18 shows the calculated wall pressure ratio (reacting/inert), G1 corresponds to 53 mm, G2 to 83 mm and G3 to 93 mm.

SUMMARY AND CONCLUSIONS

The expansion tube combined with differential interferometry, OH-records and pressure measurements is used to study the problem of the establishment and stabilization of combustion at a small step following a forebody cone. Various test models and different geometries were used.

Time resolved recording of OH-emission in an expansion tube generated flow was used here for the first time. This method allows to localize combustion and to measure its duration in time. This technique, as presented here, is a good method for studying combustion related phenomena if planar laser-induced fluorescence (PLIF) as used by Kamel et al.¹³ is not available.

OH-records, differential interferograms and pressure measurements proved that the combustion is not extinguished after the step and, therefore, the resulting pressure increase can be used for external propulsion accelerator purposes. The experiments show that the combustion is induced at the step and also influences the upstream supersonic flow near the leading cone.

The experimental results were compared with CFD-calculations performed at the US Army Research Laboratory. The combustion at the step and at the forebody cone, the detachment region in front of the step as well as the pressure increase due to combustion around the cylindrical body were well predicted by the calculations. The shock shape and the resulting pressure distribution after the shock will be subject of new calculations with a mesh refinement in front of the second cone. The 3-step global kinetics mechanism employed for the seven species given above was successfully validated by the good agreement of computer and experimental results.

REFERENCES

1. Seiler, F., Patz, G., Smeets, G., Srulijes, J., "The Rail Tube in Ram Acceleration: Feasibility Study with ISL's RAMAC 30," Second International Workshop on Ram Accelerators, Seattle, July 1995.
2. Giraud, M., Legendre, J.F., Simon, G., Henner, M., Voisin, D., "RAMAC 90 Starting Process: Control of the Ignition Location and Performance in the Thermally Choked Propulsion Mode," Second International Workshop on Ram Accelerators, Seattle, July 1995.
3. Rom, J., "Method and Apparatus for Launching a Projectile at Hypersonic Velocity," US: Patent 4,932,306, 1990.
4. Nusca, M.J., "Reacting Flow Simulation for a Large Scale Ram Accelerator," AIAA Paper 94-2963, 1994.
5. Hertzberg, A., Bruckner, A.P., Bogdanoff, D.W., "The Ram Accelerator: A new Chemical Method for Achieving Ultrahigh Velocities," 37th Meeting of the Aeroballistic Range Association, Québec, Canada, 1986.
6. Bruckner, A. P., Bogdanoff, D.W., Knowlen, C., Hertzberg, A., "Investigation of Gasdynamic Phenomena Associated with the Ram Accelerator Concept," AIAA Paper 87-1327, 1987.
7. Srulijes, J., Smeets, G., Seiler, F., "Expansion Tube Experiments for the Investigation of Ram-Accelerator-Related Combustion and Gasdynamic Problems," AIAA Paper-92-3246, 1992.
8. Gatau, F., "Propriétés thermodynamiques d'un mélange de gaz en équilibre thermochimique Programme MEGEC," ISL-Report R 109/79, 1979.
9. Anderson, G.Y., Kumar, A., Erdos, J.I., "Progress in Hypersonic Combustion Technology with Computation and Experiment," AIAA Paper 90-5254, AIAA Second International Aerospace Planes Conference, Orlando, Florida, 1990.
10. Smeets, G., George, A., "Anwendungen des Laserdifferentialinterferometers in der Gasdynamik," ISL-Report 28/73, 1973.
11. Eichhorn, A., Werner, U., Mach, H., Masur, H., "Zeitaufgelöste Strahldichtemessungen an Stoßwelleninduzierten Blitzen in Argon, Luft und Xenon," ISL-Report 120/94, 1994.
12. Rom, J., Nusca, M.J., Kruczynski, D., Lewis, L., Gupta, A., Sabean, J., "Investigation of the combustion Induced by a Step on a Projectile Flying at Hypersonic Speed in an External Propulsion Accelerator," AIAA Paper No. 95-0259, 1995.
13. Kamel, M.R., Morris, C.I., Thurber, M.C., Wehe, S.D., Hanson, R.K., "New Expansion Tube Facility for the Investigation of Hypersonic Reactive Flow," AIAA Paper No. 95-0233, 1995.

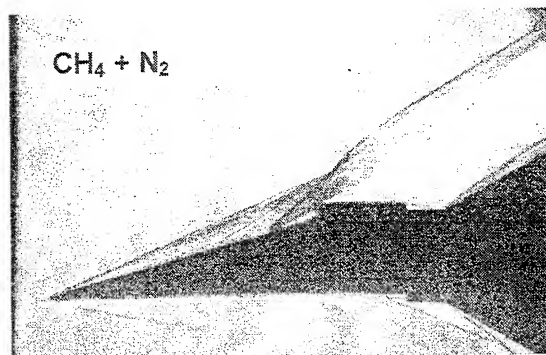
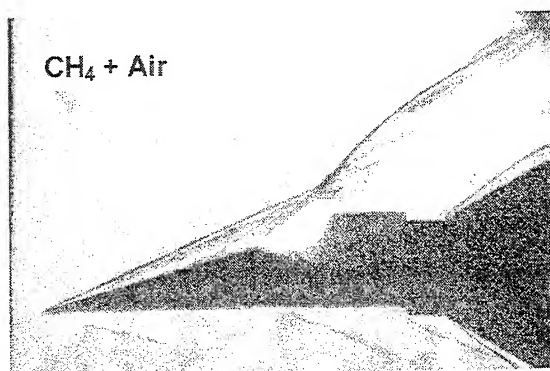


Fig. 1. Differential interferograms showing a wedge with $\theta_2 = 15^\circ$ and a step of $h = 4 \text{ mm}$, with combustion and the corresponding control experiment without combustion.

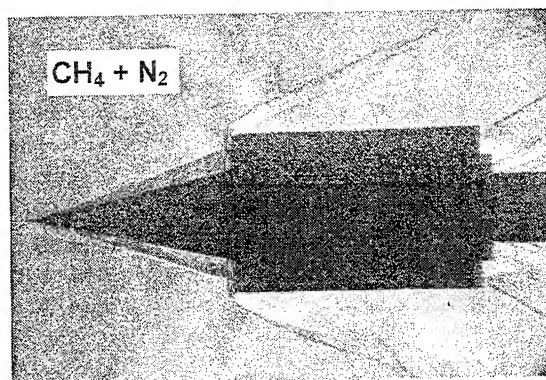
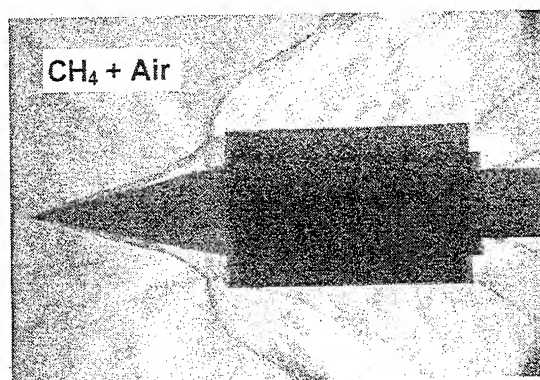


Fig. 2. Differential interferograms showing the flow configuration for a three-dimensional model consisting of a leading cone of $\theta_2 = 13^\circ$ followed by a body surrounded by a hollow cylinder (ring cowl) with $h = 3 \text{ mm}$, with combustion and the corresponding control experiment without combustion.

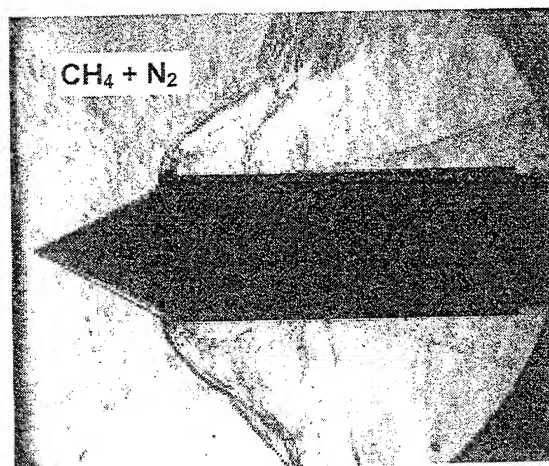
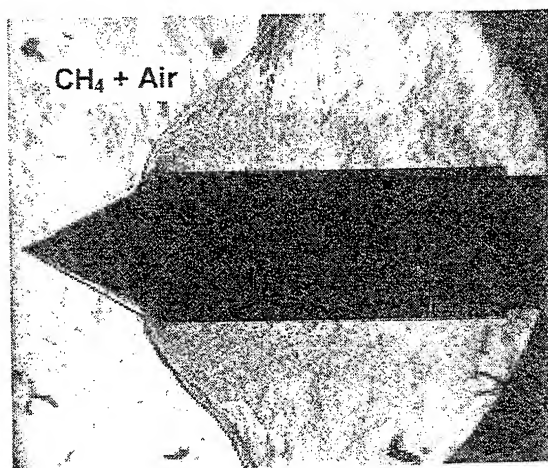


Fig. 3. Differential interferograms showing combustion front wave and the corresponding control experiment with no combustion for a double-cone $\theta_2 = 25^\circ / \theta_1 = 50^\circ / h = 4 \text{ mm}$ with a 34 mm body diameter.

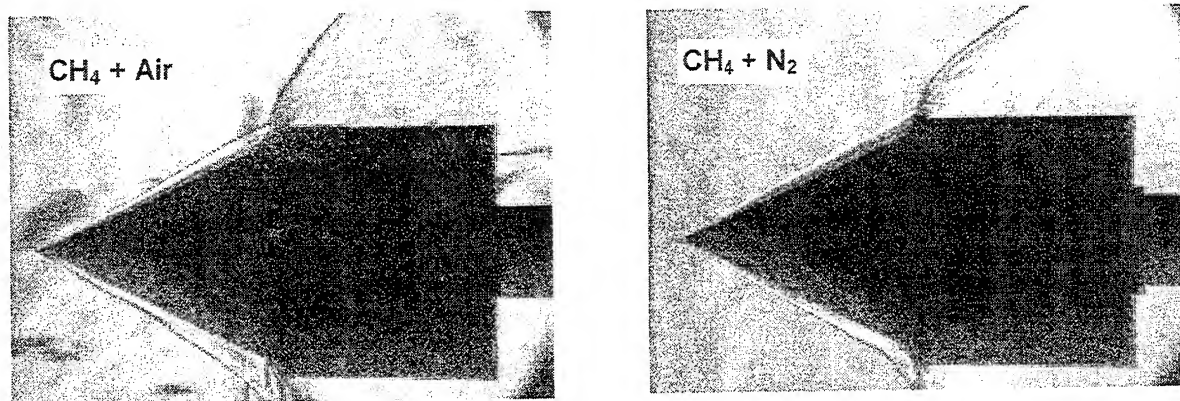


Fig. 4. Differential interferograms showing combustion front wave and corresponding control experiment with no combustion for an off-axis mounted double-cone $\theta_2 = 25^\circ / \theta_1 = 50^\circ / h = 4 \text{ mm}$ with a 50 mm body diameter.



Fig. 5. Streak records, showing each 2.5 ms, for the double-cone configuration of Fig. 4, with 0.25 mm slit at a distance of 2 mm parallel to the body in the step region; showing for the combustion case, the three regimes, i.e., super-, trans-, and subdetonative, and the comparison experiment streak record with no combustion.

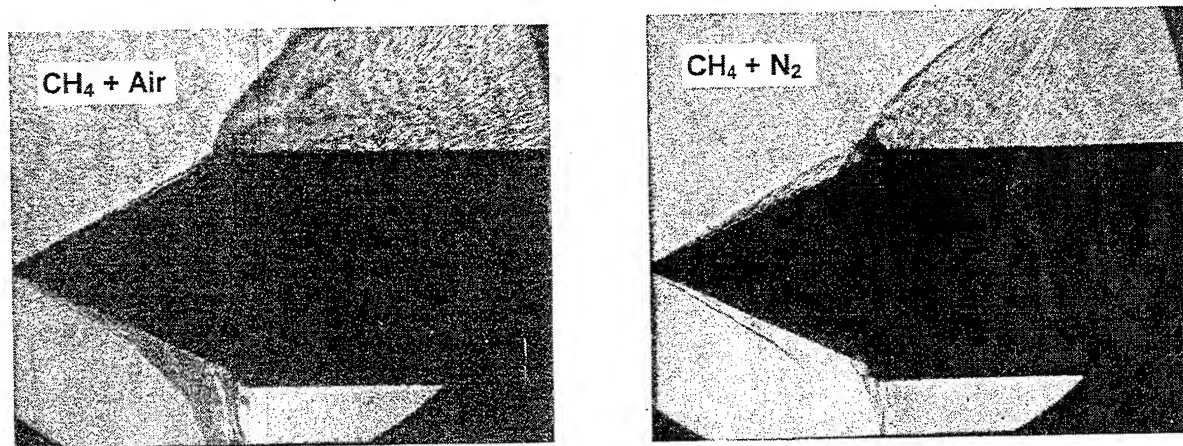


Fig. 6. Differential interferograms showing combustion front wave and corresponding control experiment with no combustion for an off-axis mounted double-cone $\theta_2 = 25^\circ / \theta_1 = 85^\circ / h = 2.5 \text{ mm}$ with a 50 mm body diameter.

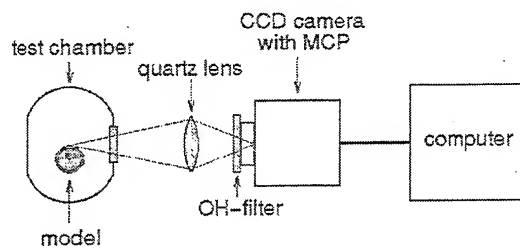


Fig. 7. Set-up used for OH-registrations.

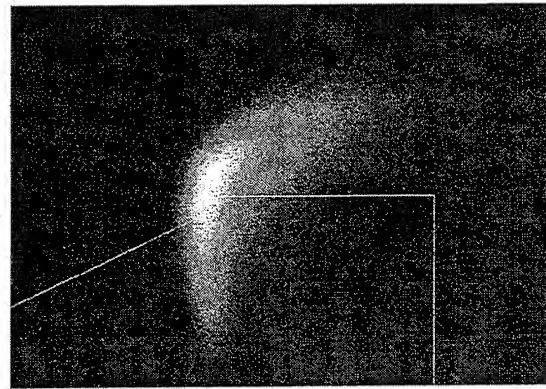


Fig. 8. OH-emission in framing mode, exposure time 200 μ s, showing the combustion zone, visualized from the side, for the off-axis mounted cone of Fig. 6.

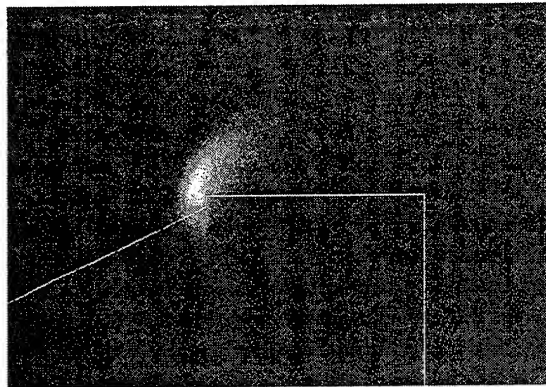


Fig. 9. OH-emission in framing mode, as described in Fig. 8, with a shorter exposure time of 100 μ s.

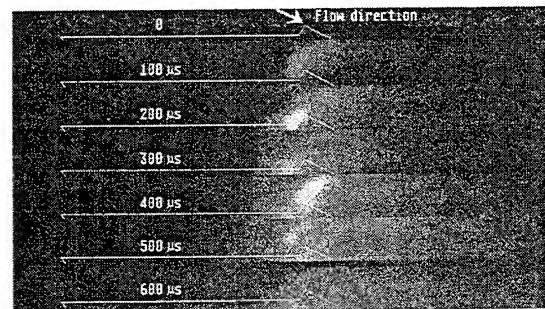


Fig. 10. Series of seven images showing the combustion development during the first 500 μ s for the off-axis mounted cone of Fig. 6.

Fig. 11. Pseudo-color-plot of a streak record with 50 μ s time resolution showing the position and time development of combustion for the off-axis mounted cone of Fig. 6 with the camera rotated by about 25 degrees.

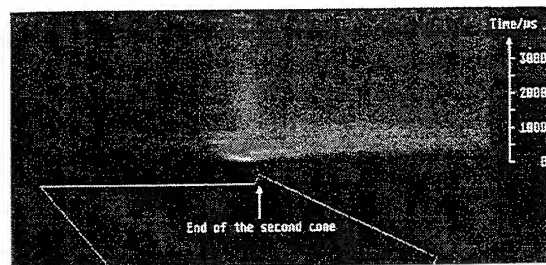
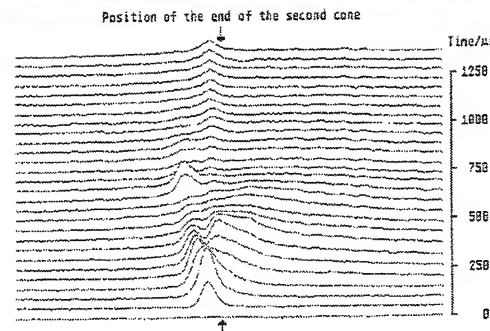


Fig. 12. Pseudo-3D-plot of the streak record in Fig. 11 showing the position and time development of combustion.



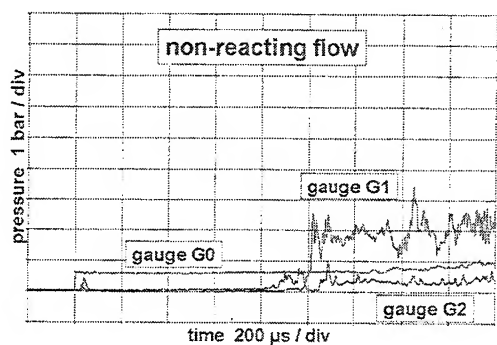


Fig. 13. Pressure time histories for non-reacting flow

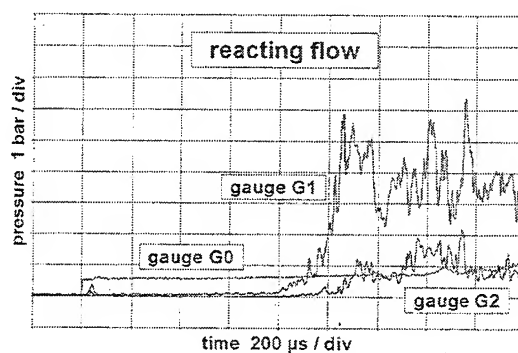


Fig. 14. Pressure time histories for reacting flow

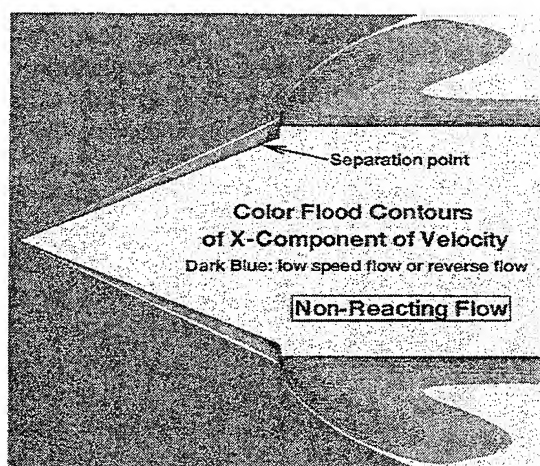


Fig. 15. CFD-calculated x-component velocity

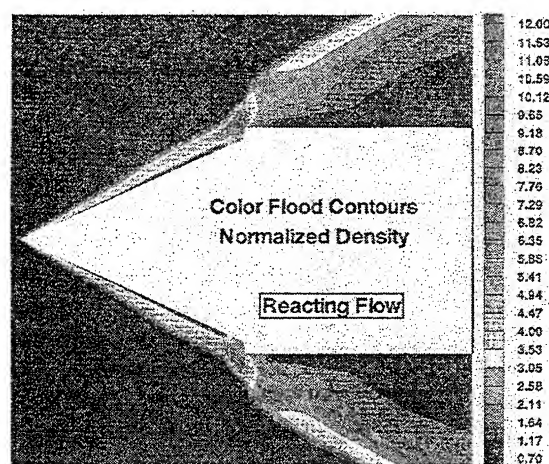


Fig. 16. CFD-calculated density for reacting flow

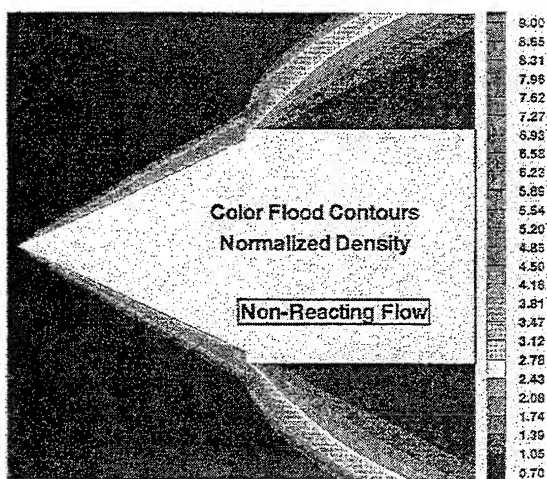


Fig. 17. CFD-calculated density for non-reacting flow

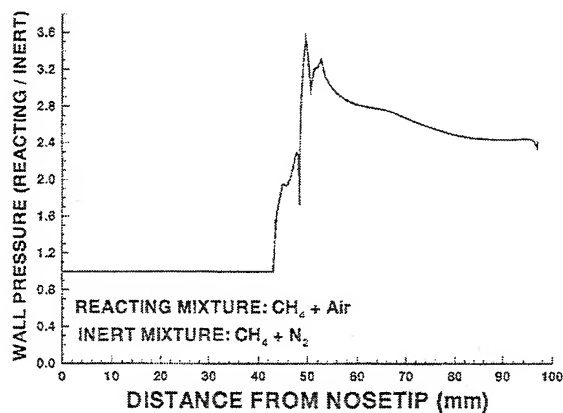


Fig. 18. CFD-calculated wall pressure ratio

Expansion Tube Investigation of Combustion Structures in Supersonic Projectile Flow Fields

Christopher Morris, Michel Kamel, Mark Thurber, Shawn Wehe and Ronald K. Hanson

High Temperature Gasdynamics Laboratory
Stanford University, Stanford, California 94305

ABSTRACT

Submitted to *The Second International Workshop on Ram Accelerators*

An expansion tube facility has been built at Stanford University to enable spatially resolved, instantaneous optical measurements of supersonic reactive flow fields. The device is similar to a conventional shock tunnel, except that the steady, 2-D expansion process of a shock tunnel is replaced by a low-pressure expansion section which accelerates the flow via an unsteady, 1-D rarefaction. Here, we report on continuing efforts to characterize the performance of our facility as well as to perform planar laser induced fluorescence (PLIF) measurements in a supersonic reactive flow field.

The work at Stanford is intended to complement the ongoing international development of the ram-accelerator concept proposed by Herzberg et al. (1986.) The ram-accelerator has been studied experimentally at the University of Washington (Herzberg, 1987), Institut Saint-Louis (Giraud, 1992) and the U.S.Army Research Laboratory (Kruczynski, 1993.) However, flow field diagnostics have been limited mainly to high-speed cameras, pressure transducers, photo diode sensors, and Doppler radar. In our approach, the projectile is fixed in the laboratory reference frame, and the expansion tube generates a flow over the body similar to that experienced by a projectile in a real accelerator. This allows use of modern optical diagnostic techniques, such as PLIF, to obtain information about the reacting flow field surrounding a fixed body. The utility of an expansion tube for ram-accelerator related research has been verified by Srulijes, Smeets, and Seiler at ISL, France (1992.)

A schematic of the facility is shown in Fig. 1. The apparatus is designed to accelerate a fuel-air test gas (typically stoichiometric $\text{CH}_4\text{-Air}$) to Mach 4-7 without premature ignition

of the mixture. The test gas is initially shocked to an intermediate velocity and temperature ($\approx 1000\text{K}$) in the driven section. The conditions are limited to avoid autoignition. When the primary shock reaches the expansion section, it initiates an unsteady rarefaction which simultaneously accelerates and cools the test gas.

Here, we report the experimental results of our ongoing expansion tube characterization efforts. A preliminary description of the facility, as well as initial shock and flow speed results, was published by Kamel et al. (1995.) New experiments address the issues of test time and flow uniformity. The experimental test time is determined by comparison of wall pressure traces and absorption measurements of a tracer in the test gas. Pressure measurements from a pitot rake installed at the exit of the tube are used to determine core flow uniformity. We compare these results with boundary layer theory and the data obtained at other installations.

We also report on our effort to apply PLIF imaging to supersonic reacting flow over a body in an expansion tube. Schlieren and OH PLIF images of reacting flow over a cylinder are shown in Fig. 2. Note that OH PLIF provides positive confirmation of combustion at the front of the cylinder, while the Schlieren image is useful for discerning the position of the bow shock. We present results which demonstrate the extension of PLIF to supersonic reacting flow over wedges and blunt bodies, configurations which are relevant to the ram-accelerator community. The work provides combustion and flow field information critically needed to validate the computational codes that support ram-accelerator development.

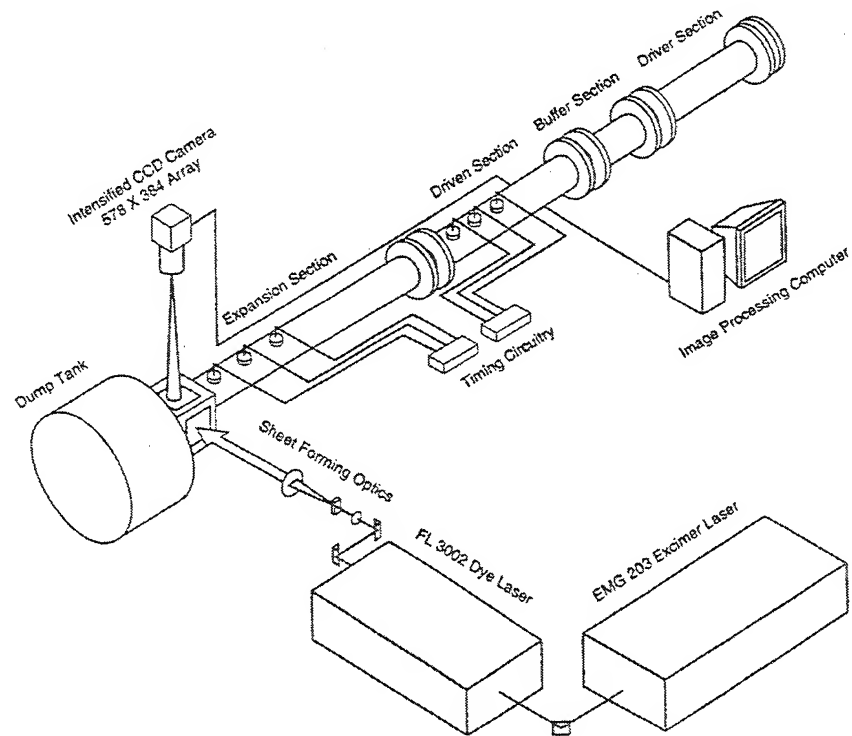


Figure 1: Sketch of expansion tube with PLIF diagnostic.

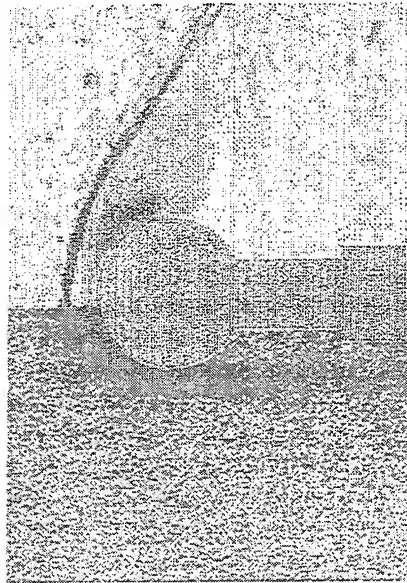


Figure 2: A Schlieren result (top half) is compared with a PLIF image (bottom half) that has been flipped across the flow plane of symmetry. Calculated flow conditions are the same for both cases: $M_{\infty} = 4.5$, $T_{\infty} = 480K$, and $P_{\infty} = 0.81$ psi

COMPUTATIONAL STUDY OF FLOW ESTABLISHMENT IN HYPERSONIC PULSE FACILITIES

S. Yungster

*Institute for Computational Mechanics in Propulsion
NASA Lewis Research Center, Cleveland, OH 44135*

and

K. Radhakrishnan

NYMA, Inc.

NASA Lewis Research Center, Cleveland, OH 44135

ABSTRACT

This paper presents a study of the temporal evolution of the combustion flowfield established by the interaction of ram-accelerator-type projectiles with an explosive gas mixture accelerated to hypersonic speeds in an expansion tube. The Navier-Stokes equations for a chemically reacting gas are solved in a fully coupled manner using an implicit, time accurate algorithm. The solution procedure is based on a spatially second order, total variation diminishing (TVD) scheme and a temporally second order, variable-step, backward differentiation formula method. The hydrogen-oxygen chemistry is modeled with a 9-species, 19-step mechanism. The accuracy of the solution method is first demonstrated by several benchmark calculations. Numerical simulations of expansion tube flowfields are then presented for two different configurations. In particular, the development of the shock-induced combustion process is followed. In one case, designed to ensure ignition only in the boundary layer, the lateral extent of the combustion front during the initial transient phase was surprisingly large. The time histories of the calculated thrust and drag forces on the ram accelerator projectile are also presented.

INTRODUCTION

A major difficulty associated with ground testing of hypersonic propulsion systems in pulse facilities is the short test time available (on the order of a millisecond). In some cases, the test time may be less than the time required to fully establish the reacting flow, especially if recirculation zones and shock wave/boundary layer or detonation wave/boundary layer interactions are present. Numerical simulation of the temporal evolution of the combustion process can supplement experimental work by providing detailed information about reaction initiation and flow establishment time in pulse facilities.

In this paper we investigate numerically the combustion process generated by the interaction between an axisymmetric projectile and an explosive gas mixture that has been accelerated to hypersonic speeds in an expansion tube. The principal advantage of the expansion tube over the shock tube or shock tunnel for this type of flow is that its operating cycle does not involve stagnation of the test gas. Therefore, with proper care, explosive mixtures can be accelerated to superdetonative velocities without autoignition, as demonstrated by Srulijes et al [1] in their experimental investigation of ram

accelerator [2,3] flowfields. In fact, ram accelerator type flowfields can be studied more easily in a fixed projectile, moving gas frame of reference than in the ram accelerator itself, where measurements are difficult to make.

However, important differences exist between the ram accelerator and an expansion tube experiment in the boundary layer growth along walls and flow characteristics during startup. Specifically, in the expansion tube the test time begins after passage of the shock wave and contact discontinuity over the projectile, as described below. On the other hand, startup in the ram accelerator follows the bursting of the first diaphragm by the projectile, a process that generates shock and expansion waves. In addition, the high fill pressures typical of ram accelerator operation cannot be duplicated in an expansion tube. The effects of these differences can be examined by using CFD methods.

An expansion tube consists of a single tube divided into three or four sections by diaphragms, as shown in Figure 1, which is a schematic of the classic expansion tube described by Trimpi [4]. When the test gas consists of an explosive mixture, a buffer zone containing an inert gas is added between the test gas and the driver gas to prevent autoignition following rupture of the primary diaphragm [1].

A brief explanation of the operation of the expansion tube is necessary in order to clarify the assumptions made in the numerical simulations. Following the rupture of the primary diaphragm at time $t = 0$ (see Fig. 1), a primary shock wave propagates into the test gas and an expansion wave into the driver gas. The numbering of the flow states in Fig. 1 corresponds to that defined by Trimpi [4]. On reaching the end of the driven section, the primary shock ruptures the secondary diaphragm and a secondary shock wave propagates into the expansion section, while an expansion wave moves into the test gas. This expansion wave is washed downstream, since the gas in region 2 is moving at supersonic speeds. Test time begins with the passage of the test gas/accelerating gas contact discontinuity over the model and ends with the arrival of the expansion wave. The state of the gas in region 5 determines the test conditions. Test times in expansion tubes are typically tens to hundreds of microseconds long [5]. An advantage of CFD analysis is that the test time can be extended arbitrarily, in order to estimate the flow establishment time.

Previous computational studies by Jacobs [5] and Wilson [6] simulated the flow of nonexplosive mixtures inside the expansion tube for the time interval $0 \leq t \leq t_2$ (see Fig. 1). In contrast, the goal of the present work was to examine the establishment of the flow of an explosive mixture over the test model. Therefore, our simulations were performed for times $t \geq t_2$.

NUMERICAL FORMULATION

Governing Equations

The conservation form of the nonequilibrium Navier-Stokes equations describing two-dimensional or axisymmetric chemically reacting flow involving n species can be written in general curvilinear coordinates (ξ, η) as follows:

$$\frac{\partial Q}{\partial t} + \frac{\partial (F - F_v)}{\partial \xi} + \frac{\partial (G - G_v)}{\partial \eta} + j(S - S_v) = W \quad (1)$$

where the parameter j is zero for two-dimensional flow and one for axisymmetric flow and Q is the vector of dependent variables:

$$Q = J^{-1}[\rho_1, \rho_2, \dots, \rho_n, \rho u, \rho v, e]^T \quad (2)$$

The dependent variables are the mass density of the i th species ρ_i , the velocity components u and v , and the total energy per unit volume e . J is the grid Jacobian and F and G are the inviscid flux vectors in the ξ and η directions, respectively. F_v and G_v are analogous viscous fluxes. S and S_v are axisymmetric source terms and W is the chemical source term. A detailed description of the terms in Eq. (1) and additional state and constitutive equations needed for system closure are given by Yungster [7].

Numerical Method

The numerical method used for solving Eq. 1 is described in detail in Ref. [8] and summarized briefly here. For simplicity, only the two-dimensional Euler equations are considered in this description; however, extension to the viscous case is straightforward [8]. The equation set is discretized using a temporally second-order, variable-step backward differentiation formula (BDF) method, which can be written as:

$$\Delta Q_{j,k}^n = \gamma \Delta Q_{j,k}^{n-1} - \beta \Delta t^n [\tilde{F}_{j+1/2,k} - \tilde{F}_{j-1/2,k} + \tilde{G}_{j,k+1/2} - \tilde{G}_{j,k-1/2} - W_{j,k}]^{n+1} \quad (3)$$

$$\Delta Q_{j,k}^n = Q_{j,k}^{n+1} - Q_{j,k}^n \quad (4)$$

where γ and β are variable-step BDF method coefficients [8], and Δt^n is the time step. The terms \tilde{F} and \tilde{G} are the numerical fluxes in the ξ and η directions. They are computed using Yee's second order total variation diminishing (TVD) scheme [9]. Equation 3 is then linearized in a conservative manner and solved iteratively, using a lower-upper relaxation procedure consisting of successive Gauss-Seidel (LU-SGS) sweeps. At each time step the iterative process of producing successively improved approximate solutions to equation (3) is continued until a suitable convergence criterion is satisfied. The inversion of large matrices is avoided by partitioning the system into reacting and non-reacting parts; however, a fully coupled interaction is still maintained. Consequently, the matrices that have to be inverted are of the same size as those that arise in the commonly used point implicit methods. An important advantage of the present method is that it remains stable for large values of the CFL number, so that large time steps can be used.

RESULTS

Benchmark test cases

Before applying the present method to the study of expansion tube reacting flows, its accuracy was first established by computing various benchmark test cases. Two such cases are presented below for reacting and nonreacting, inviscid flows.

The first case was a simulation of Lehr's ballistic range experiments [10], which consisted of spherical nosed projectiles of diameter 15-mm being fired into a premixed, stoichiometric hydrogen-air mixture. Figure 2a shows a shadowgraph image obtained by Lehr [10] for a Mach number $M = 4.79$. The corresponding computational result, obtained with a 9-species, 19-step reaction mechanism for hydrogen-oxygen [8], is shown in Fig. 2b in the form of density contours. Under the conditions of the test, the reacting flow was unstable, resulting in a highly regular, periodic flow structure. An experimental oscillation frequency of 720 kHz was reported [10]. The computed frequency of oscillation varied from 701 to 716 kHz. Computations of other flow conditions also produced excellent agreement with experimental data [8].

The second test case was the regular reflection of an incident shock wave from a 55° wedge. Experiments were conducted in a 60 mm x 150 mm shock tube at the Institute of Fluid Science of Tohoku University and results reported by Falcovitz et al [11], who also performed numerical simulations for several cases. Figure 3 gives their experimental holographic interferograms and our computed density contours at three different times during the reflection process for an incident shock Mach number of 1.488. The spacing of the contours was selected to match that observed in the experimental interferograms. The computational results were generated with a 400 x 316 uniform grid. Figures 3a and 3b show the reflected shock wave prior to its collision with the shock tube end-wall. Figures 3b to 3g show the wave configuration at two different times after collision with the end-wall. It should be pointed out that due to a small air gap between the end wall of the shock tube and its upper wall an expansion wave was generated at the upper edge of the end-wall [11]. This expansion wave can be observed in Fig. 3c near the upper right corner of the holographic interferogram and in Fig. 3e near one of the reflected shocks. The air gap was not modeled in our computations.

The agreement between the computational and experimental results is excellent at all times. The computations match almost every fringe in the experiments, except immediately after the head-on collision near the right corner (Fig. 3d), where the grid is not fine enough to resolve the details of the reflection. The overall resolution of the flowfield compared well with the numerical results computed by Falcovitz et al [11]. However, near the walls the present method produced superior results. Note especially that the small, closed fringe near the bottom corner was reproduced in our calculation (Figs. 3d and 3g), whereas it was not captured by Falcovitz et al.

Expansion tube reacting flows

Two cases are presented, the first involving only boundary layer ignition, and the second a ram accelerator type configuration. Both cases employed pure hydrogen as the accelerating gas and the mixture $H_2 + 2.75O_2 + 2.5Ar$ as the test gas. The $H_2 - O_2$ reaction mechanism consisted of 19 reac-

tions among 9 species [8].

Case 1

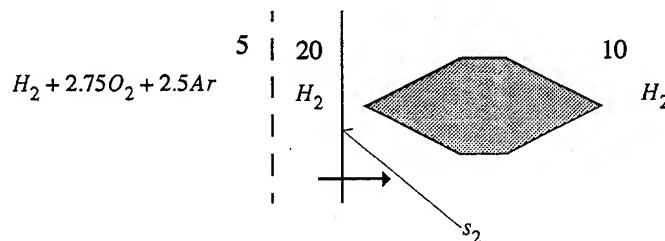
This case considered an axisymmetric projectile composed of two 30° half angle cones and a short straight section. The corners of the projectile were rounded. The projectile overall length and maximum diameter were 1.45 cm and 0.693 cm, respectively. The flow conditions for this test are shown in the schematic below:

$$c_{s_2} = 2.0$$

$$p_{10} = 1 \text{ atm} \quad T_{10} = 300 \text{ K}$$

$$p_{20} = p_5 = 4.5 \text{ atm} \quad T_{20} = 506.25 \text{ K} \quad T_5 = 300 \text{ K}$$

$$M_{20} = 0.9623 \quad M_5 = 4.748$$



Here c denotes the shock speed and p , T and M are the pressure, temperature and Mach number, respectively. The conditions for this case were selected to produce ignition in the boundary layer. The flow was assumed to be laminar and the projectile surface adiabatic. A 320x110 nonuniform grid was utilized. The time evolution of the flowfield is shown in Fig. 4 by means of nondimensional temperature (T/T_{10}) contours. In Fig. 4a the secondary shock has just reached the tip of the projectile. The shock is partly reflected from the projectile surface and continues to travel downstream. The reflection is too weak for the temperature range used and is therefore not apparent in Fig. 4. As the high Mach number test gas reaches the projectile (Fig. 4b), a conical shock begins to form over its nose. A short time later (Fig. 4c), combustion begins in the boundary layer. Subsequently, the reacting boundary layer penetrates region 20 of the accelerating gas. Once the reacting gas reaches the projectile shoulder, its lateral expansion is considerable. The penetration of the reacting boundary layer can be explained by the fact that as the conical shock begins to form over the nose of the projectile, a large pressure is established over this region. The shock has not yet formed downstream, thereby creating a substantial pressure gradient, which forces the boundary layer gases downstream. After the transient phase, combustion is observed only along the boundary layer (Fig. 4i), which separates over the rear of the projectile. The computation was stopped at $t = 13.52 \mu\text{sec}$, although the flow had not yet reached steady state. This simulation required 6200 iterations and 12.4 hrs. of CPU time on a Cray C90 computer, with a maximum CFL number of between 3 and 10.

Case 2

This case considered a ram accelerator configuration that included an axisymmetric projectile and a ram accelerator tube. As shown in Fig. 5a, the front end of the tube was positioned slightly behind

the projectile shoulder, in order to limit the boundary layer growth and thus simulate conditions in the actual ram accelerator. The projectile comprised a 15° half angle nose cone, a 30° axisymmetric ramp, a constant diameter section and a specially configured tail. The total length of the projectile, its maximum diameter and the ram accelerator tube diameter were 10.85 cm, 2.82 cm and 3.8 cm, respectively. These dimensions are based on the experimental device currently operating at the University of Washington [2,3]. The flow conditions for this test case were:

$$c_{s_2} = 2.35$$

$$p_{10} = 1 \text{ atm} \quad T_{10} = T_5 = 300 \text{ K} \quad T_{20} = 597.93 \text{ K}$$

$$p_{20} = p_5 = 6.276 \text{ atm} \quad M_{20} = 1.136 \quad M_5 = 6.058$$

The flow was assumed to be turbulent, and a constant wall temperature of 300 K was specified at the projectile surface and at the tube wall. The Baldwin-Lomax turbulence model [12] was used in this calculation. A 315×125 nonuniform grid was utilized. The time evolution of the flowfield is shown in Fig. 5 in the form of nondimensional temperature (T/T_{10}) contours (bottom half of each figure) and pressure (p/p_{10}) contours (top half). Note that for clarity in presentation the pressure and temperature contour ranges are not the same for all the plots. Each color bar defines the contour range both for the figure in which it appears and for every subsequent plot until a new color bar appears.

The initial flow development for this case is similar to that described for the previous one. That is, the flow begins with the arrival of the secondary shock (Fig. 5a), its reflection off the projectile (Fig. 5b) and the formation of the conical shock over its nose (Fig. 5c). At subsequent times, the secondary shock is reflected off the projectile's ramp (Fig. 5d) and a series of wave reflections from the tube wall and projectile surface can be observed in Figs. 5e and 5f. The conical shock reflected off the tube wall begins to establish in Fig. 5g and shortly after it hits the projectile surface ignition occurs in the boundary layer (Fig. 5h). Combustion spreads both downstream and towards the tube wall and, at the same time, propagates upstream through the boundary layer (Fig. 5i-k). A shock-induced combustion wave is established, creating a large pressure over the back of the projectile, and positive thrust begins to be generated at $t = 68 \mu\text{sec}$ approximately. The combustion continues to propagate upstream along the projectile boundary layer and also along the tube wall boundary layer (Fig. 5l-n), until unstart occurs (Fig. 5o). For this calculation the maximum CFL number varied between 5 and 15. The computational work requirement was 7000 iterations and 11.3 hrs. on a Cray C90 computer.

The total thrust and viscous drag forces on the projectile are plotted in Fig. 6. During flow initiation, the projectile is subjected to an increasing drag force, as the conical wave system is established over the projectile. When combustion begins, a progressive reduction in total drag is observed, but positive thrust is produced only after the shock-induced combustion wave is reflected off the projectile surface, resulting in the steep increase in total thrust shown in Fig. 6. The viscous drag builds up in a similar manner and decreases significantly once the combustion process starts. Note that the viscous drag accounts for less than 1% of the total thrust.

CONCLUSION

The expansion tube is a useful tool for investigating ram-accelerator-type phenomena. However, important issues such as boundary layer growth along walls, startup characteristics and operating pressures will prevent the expansion tube from duplicating exactly the conditions in a ram accelerator. In addition, the short test time available may be insufficient to establish fully the reacting flow-field. Computational studies can support experimental efforts by providing answers to these issues. A methodology for simulating the combustion process in expansion tube flowfields was described, and computations for two cases were presented to illustrate the capability of the numerical approach. The unexpected combustion phenomenon observed during the initial transient phase emphasizes the need for further study of this type of flow. The efficiency of our time-accurate, fully implicit numerical method was demonstrated by computing high-speed, reacting, turbulent flows at CFL numbers as high as 15.

REFERENCES

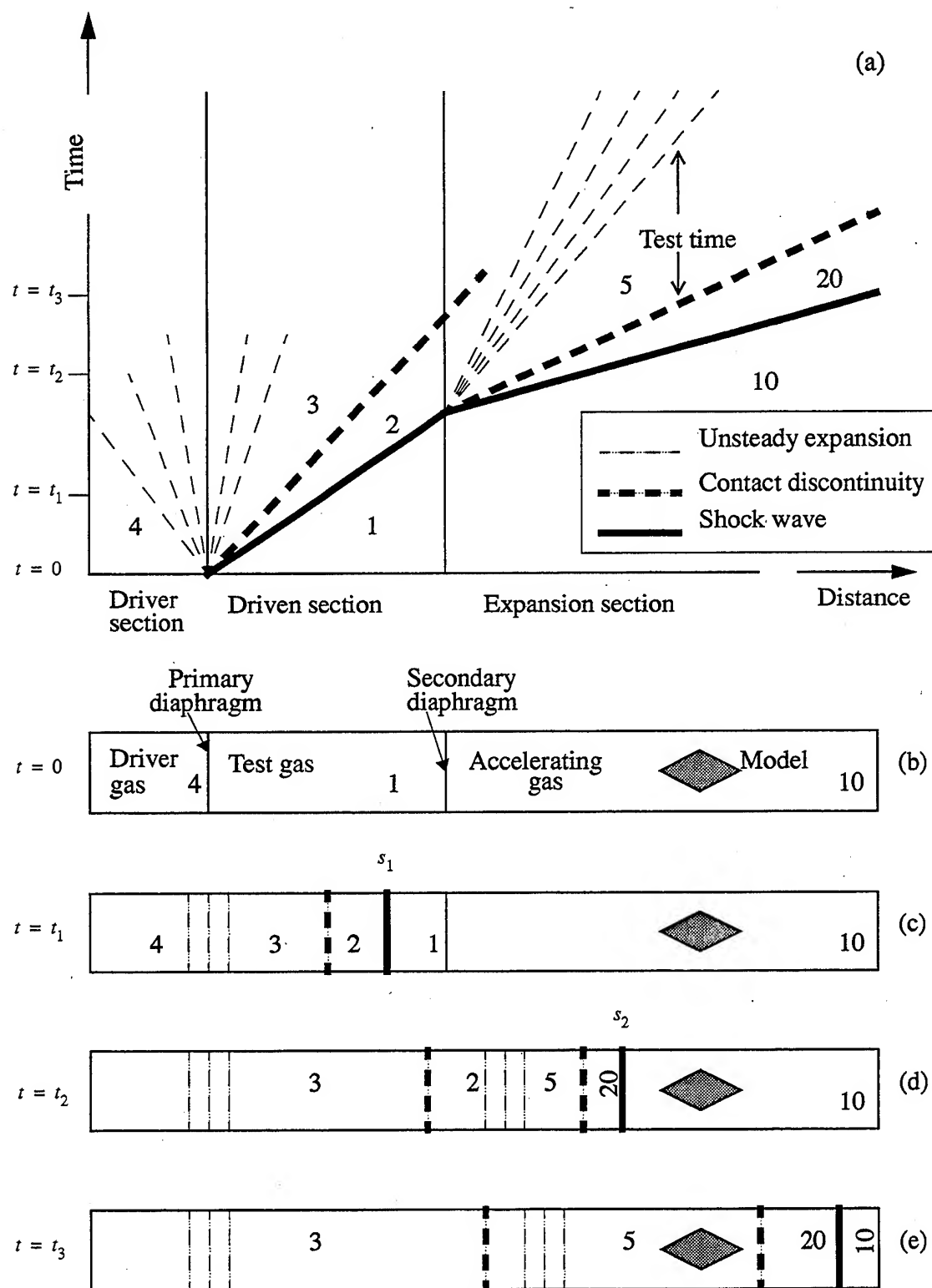
- 1.- Srulijes, J., Smeets, G., and Seiler, F., "Expansion Tube Experiments for the Investigation of Ram Accelerator Related Combustion and Gasdynamic Problems," AIAA paper 92-3246, 1992.
- 2.- Hertzberg, A., Bruckner, A.P., and Bogdanoff, D.W., "Ram Accelerator: A New Chemical Method for Accelerating Projectiles to Ultrahigh Velocities," AIAA Journal, Vol. 26, 1988, pp. 195-203.
- 3.- Bruckner, A.P., Knowlen, C., Hertzber, A., and Bogdanoff, D.W., "Operational Characteristics of the Thermally choked Ram Accelerator," Journal of Propulsion and Power, Vol. 7, 1991, pp. 828-836.
- 4.- Trimpi, R.L., "A Preliminary Theoretical Study of the Expansion Tube, a New Device For Producing High-Enthalpy Short Duration Hypersonic Gas Flows," NASA Technical Report R-133, 1962.
- 5.- Jacobs, P.A., "Numerical Simulation of Transient Hypervelocity Flow in an Expansion Tube," NASA CR 189601 (also ICASE Report 92-20), 1992.
- 6.- Wilson, G., "Time-Dependent Quasi-One-Dimensional Simulations of High Enthalpy Pulse Facilities," AIAA paper 92-5096, 1992.
- 7.- Yungster, S., "Numerical Study of Shock-Wave Boundary Layer Interactions in Premixed Combustible Gases," AIAA Journal, Vol. 30, No. 10, October 1992, pp. 2379-2387.
- 8.- Yungster, S., and Radhakrishnan, K., "A Fully Implicit Time Accurate Method for Hypersonic Combustion: Application to Shock-Induced Combustion Instability," NASA TM-106707, AIAA-94-2965, 1994. (To appear in Shock Waves Journal 1995).
- 9.- Yee, H.C., "Construction of Explicit and Implicit Symmetric TVD Schemes and Their Applica-

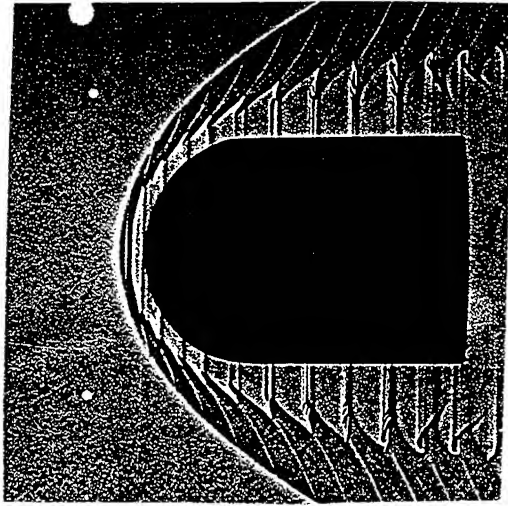
tions. Journal of Computational Physics Vol. 68, 1987, pp. 151-179

10.- Lehr, H.F., "Experiments on Shock-Induced Combustion," Acta Astronautica, Vol. 17, Nos. 4 & 5, 1972, pp. 589-596.

11.- Falcovitz, J., Alfandary, G., and Ben-Dor, G., "Numerical Simulation of the Head-On Reflection of a Regular Reflection," International Journal for Numerical Methods in Fluids, Vol. 17, 1993, pp. 1055-1077.

12.- Baldwin, B. and Lomax, H., "Thin Layer Approximation and Algebraic Model for Separated Turbulent Flows," AIAA paper 78-257, 1978.



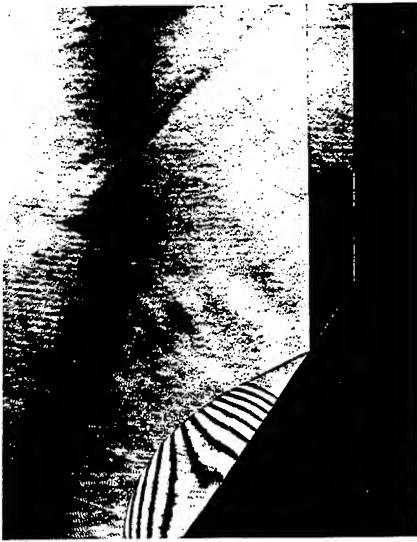


(a)

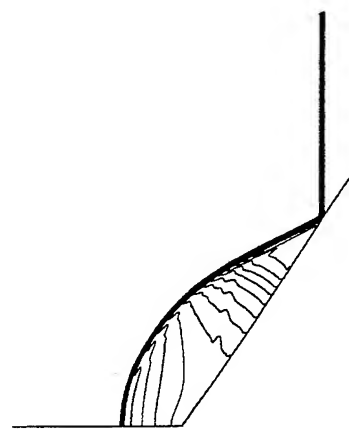


(b)

Figure 2. Experimental and computational results for a projectile moving at $M = 4.79$ in a stoichiometric hydrogen-air mixture: (a) experimental shadowgraph image (Lehr [10]); (b) density contours.



(a)

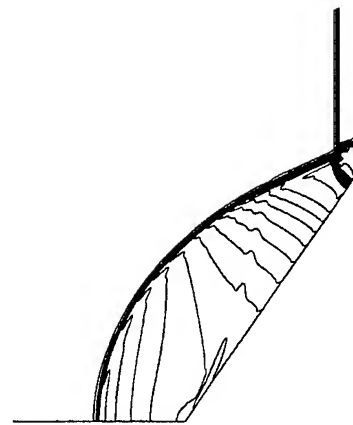


(b)

Figure 3. Temporal evolution of the regular reflection of a $M = 1.488$ shock wave with a $\theta = 55^\circ$ wedge. (a) Holographic interferogram prior to its interaction with the end wall [11]; (b) computed density contours.



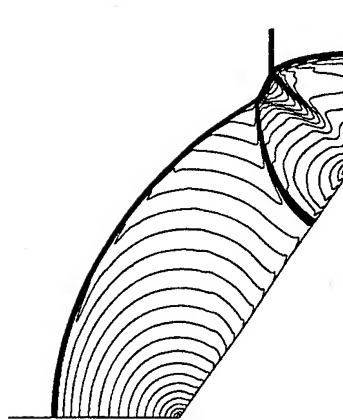
(c)



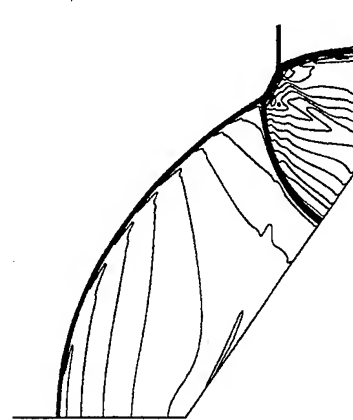
(d)



(e)



(f)



(g)

Figure 3 continued. (c), (e) Holographic interferograms at two time intervals after collision with the shock tube end-wall [11]; (d), (g) computed density contours; (f) computed Mach number contours.

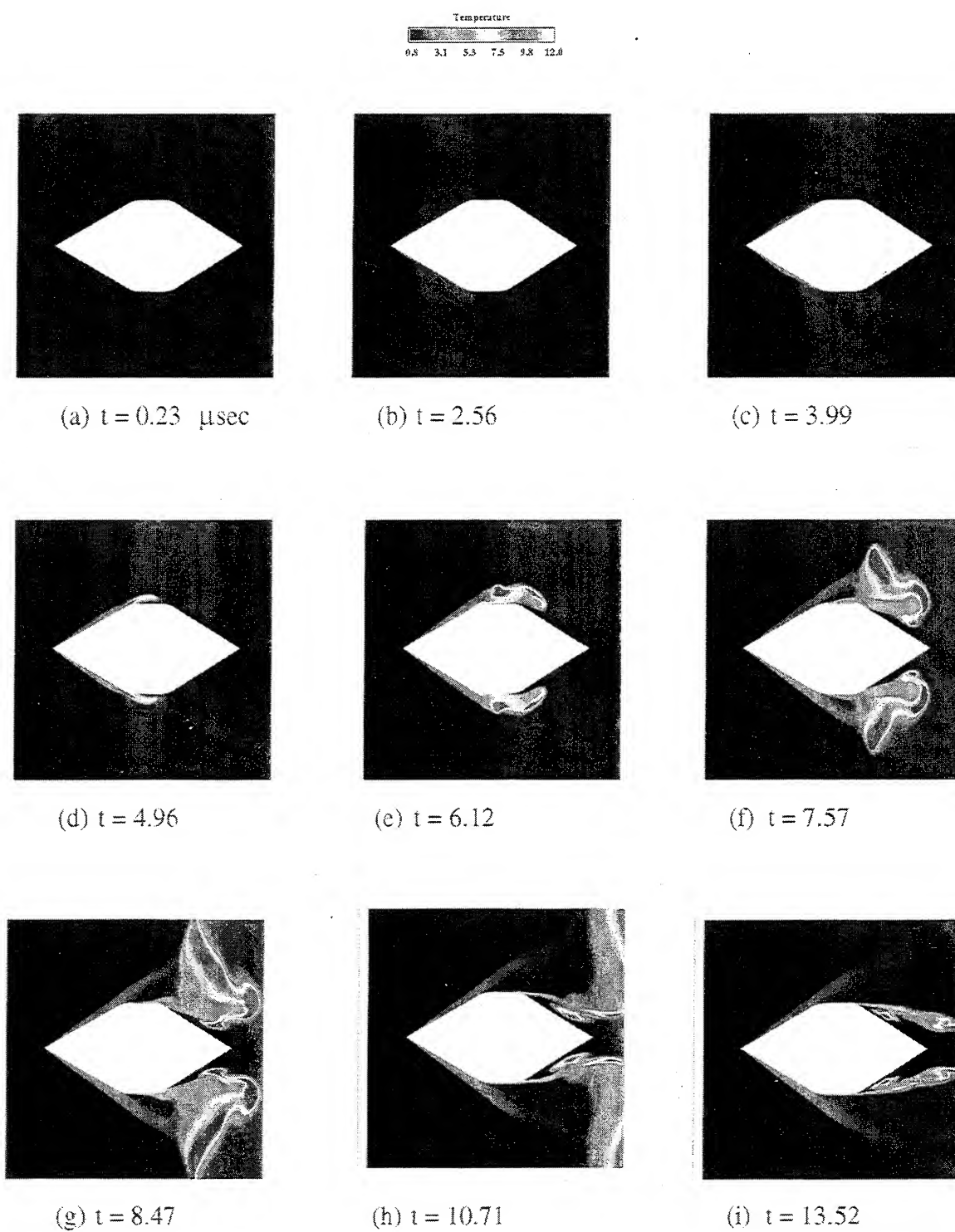


Figure 4. Nondimensional temperature contours T/T_{10} showing temporal evolution of expansion tube flow over an axisymmetric projectile. Test gas: $H_2 + 2.75O_2 + 2.5Ar$.

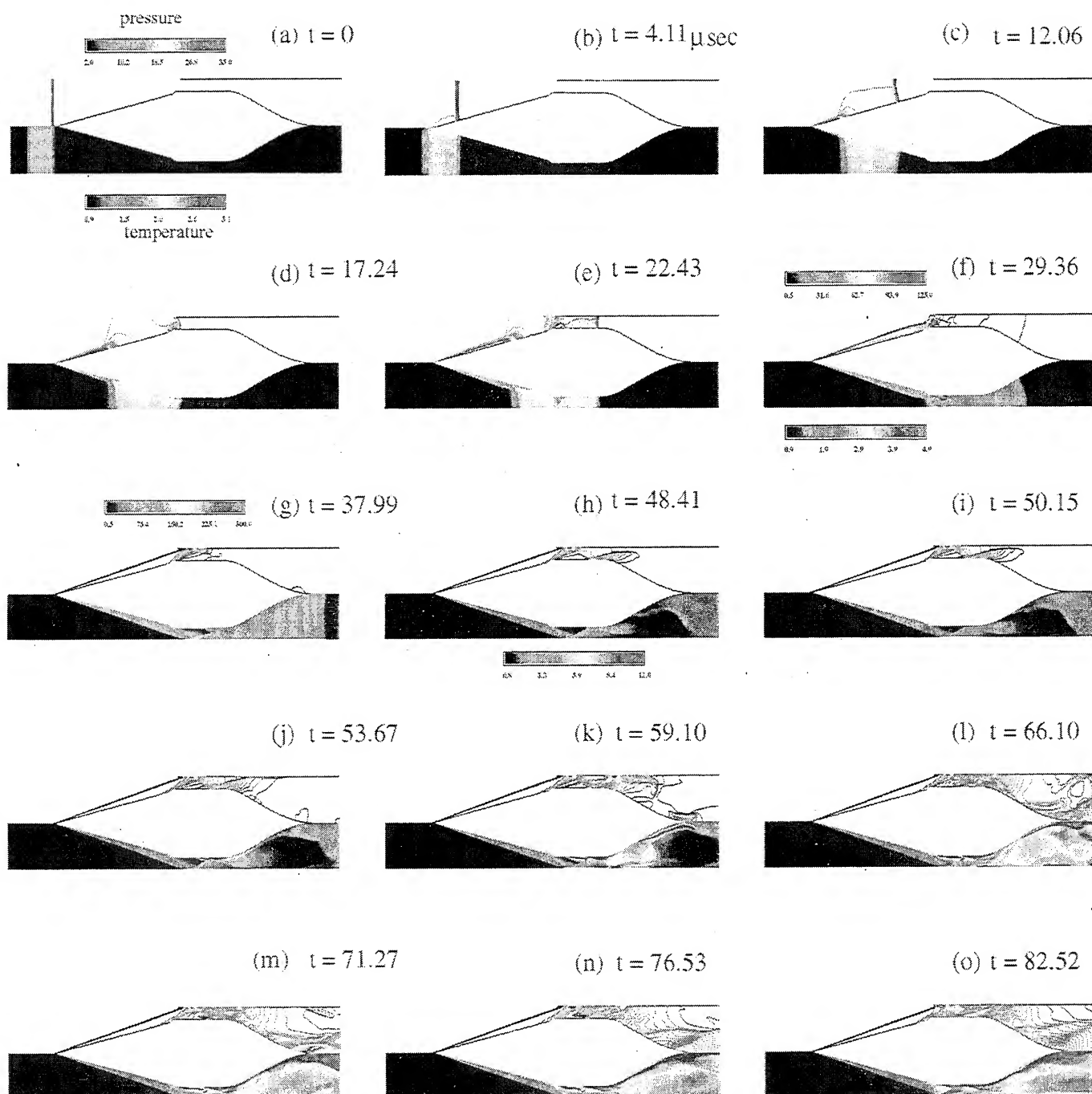


Figure 5. Nondimensional pressure (p/p_{10} , top half) and temperature (T/T_{10} , bottom half) showing temporal evolution of expansion tube flow over a ram accelerator configuration. Test gas: $H_2 + 2.75O_2 + 2.5Ar$. Note: color bar defines contour range both for the plot in which it appears and for every subsequent plot until a new color bar appears.

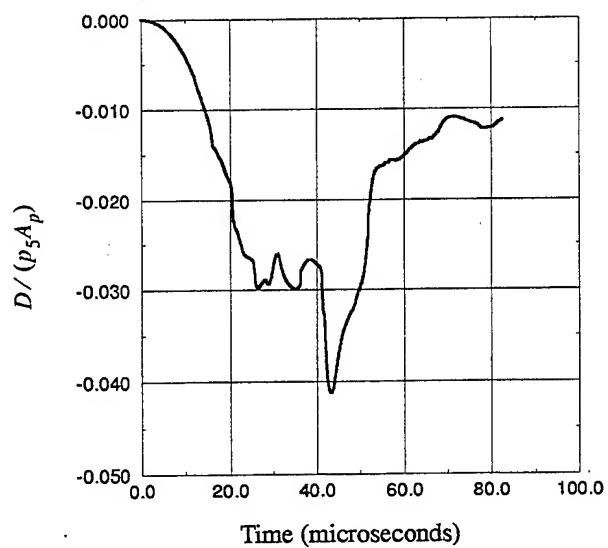
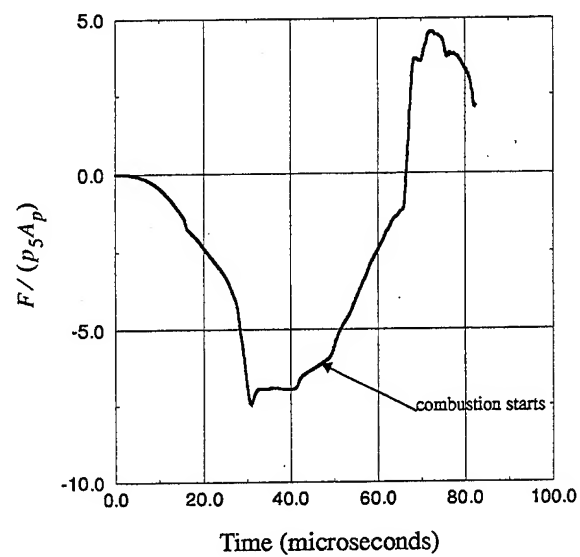


Figure 6. Nondimensional net thrust (a) and viscous drag (b) forces on ram accelerator projectile. (Here, A_p is the maximum cross-sectional area of the projectile).

Numerical Study of some Ignition Regimes of Combustible Supersonic Flows over a Wedge

Luís Fernando Figueira da Silva & Bruno Deshaies
Laboratoire de Combustion et de Détonique (UPR 9028 CNRS)
ENSMA et Université de Poitiers
86960 Futuroscope Cedex FRANCE
tel. (33) 49 49 82 77; fax (33) 49 49 81 76
e-mail: da-silva@univ-poitiers.fr

Abstract

In this work we study two basic ignition mechanisms which are of practical importance to ramaccelerator applications. In such cases two different flow phenomena are source of compressibility and of temperature increase, and thus may trigger ignition: (i) boundary layers and (ii) shock waves. Although a strong coupling may occur between these two phenomena and chemistry, limitations due to computation power preclude the systematic study of this triple interaction. Therefore we present here studies concerning the coupling between (i) and (ii) and chemistry separately.

The first mechanism investigated is ignition within the boundary layer that develops over the projectile. Indeed, viscous dissipation heating may sufficiently increase the temperature of the gas so that a thermal runaway of the mixture is possible. In the *First International Workshop on Ram Accelerators* we have presented a detailed parametric study of this ignition regime for supersonic hydrogen-air flows over a flat plate as a function of the temperature, pressure and equivalence ratio. This study is now extended to the flow conditions of practical interest to Ramac applications, *i.e.* using hydrogen and methane – air/oxygen mixtures.

In addition to this first mechanism, ignition may occur behind oblique shock waves during the transdetonative/superdetonative flight of the projectile, giving birth to oblique detonations. We present a study of the transition from an oblique shock wave to an oblique detonation wave in a supersonic flow over a wedge, with emphasis on the transient regime. More specifically we attempt to precise the critical conditions that lead to the formation of a detonation. These two-dimensional calculations are performed using a detailed chemical kinetic scheme for hydrogen-air combustion.

Acknowledgement: This work has been accomplished under the contract no. 93-053 "Combustion Supersonique PREPHA" of the Direction des Recherches et Etudes Techniques DRET/DGA.

References

- [1] George D. Byrne and Anthony M. Dean. The Numerical Solution of Some Kinetics Models with VODE and CHEMKIN II. *Computers Chem.*, 17(3):297–302, 1993.
- [2] L. F. Figueira da Silva and B. Deshaies. The Influence of Equivalence Ratio and Sorêt Effect on the Ignition of Hydrogen-Air Mixtures in Supersonic Boundary Layers. In *25th Symposium (International) on Combustion*, Irvine, 1994. The Combustion Institute, The Combustion Institute.
- [3] L. F. Figueira da Silva and B. Deshaies. Numerical analysis of the self-ignition of hydrogen-air supersonic flows over a wedge. In *Submitted to the 3rd Asian-Pacific Symposium on Combustion and Energy Utilisation*, Hong-Kong, 1995. APISCEU.
- [4] L. F. Figueira da Silva, B. Deshaies, and M. Champion. A Numerical Study of Ignition within Hydrogen-Air Supersonic Boundary Layers. *AIAA Journal*, 31(5):884–890, May 1993.
- [5] L. F. Figueira da Silva, B. Deshaies, and M. Champion. Boundary Layer Ignition of Hydrogen-Air Mixtures in Supersonic Flows. *Journal of Thermal Science*, 1994.
- [6] C. Hirsch. *Numerical Computations of Internal and External Flows*, volume 2, chapter 21, pages 493–594. Wiley, 1990.
- [7] R. J. Kee, G. Dixon-Lewis, J. Warnatz, M. E. Coltrin, and J. A. Miller. A Fortran Computer Code Package for the Evaluation of Gas Phase Multicomponent Transport Properties. Technical Report SAND89-86246/UC-401, Sandia National Laboratories, December 1986.
- [8] R. J. Kee, F. M. Rupley, and J. A. Miller. CHEMKIN-II: A Fortran Chemical Kinetics Package for the Analysis of Gas Phase Chemical Kinetics. Technical Report SAND89-8009B/UC-706, Sandia National Laboratories, November 1991.
- [9] M. H. Lefebvre and T. Fujiwara. Numerical Modeling of Combustion Processes Induced by a Supersonic Conical Blunt Body. *Combustion and Flame*, 100(1/2):85–93, January 1995.
- [10] B. Lewis and G. von Elbe. *Combustion, Flames and Explosions of Gases*. New York: Academic Press, 1961.
- [11] C. Li, K. Kailasanath, and E. Oran. Detonation Structures Behind Oblique Shocks. *Physics of Fluids*, 6(4):1600–1611, April 1994.
- [12] M.-S. Liou. A Continuing Search for a Near-Perfect Numerical Flux Scheme – Part I: AUSM+. Technical Report TM-106524, NASA, March 1994.
- [13] D. J. Singh, J. K. Ahuja, and M. K. Carpenter. Numerical Simulation of Shock-Induced Combustion/Detonation. In *Symposium on High-Performance Computing for Flight Vehicles*, December 1992.

- [14] G. Smeets, F. Seiler, G. Patz, and J. Strulijes. First Results Obtained in a 30-millimeter-caliber Scram Accelerator using a Rail Tube for Cylindrical Projectiles. In *25th Symposium (International) on Combustion*, Irvine, 1994. The Combustion Institute, The Combustion Institute.
- [15] Y. Tan, P. Dagaut, M. Cathonnet, and J.C. Boettner. Acetylene oxidation in JSR from 1 to 10 atm and comprehensive kinetic modeling. *Combustion Science and Technology*, 102:21-55, 1994.
- [16] Y. Tan, P. Dagaut, M. Cathonnet, and J.C. Boettner. Oxidation and ignition of methane-propane and methane-ethane-propane mixtures: experiments and modeling. *Combustion Science and Technology*, 103:133-151, 1994.
- [17] V. V. Vlasenko and V. A. Sabel'nikov. Numerical Simulation of Inviscid Flows with Hydrogen Combustion after Shock Waves and in Detonation Waves. In *AIAA 94-3177*. 30th AIAA/ASME/SAE/ASEE Joint Propulsion Conference, 1994.
- [18] H. C. Yee. A Class of High-Resolution Explicit and Implicit Shock-Capturing Methods. Technical Report TM-101088, NASA, February 1989.

*Numerical Study of some Ignition Regimes of
Combustible Supersonic Flows over a Wedge*

Luis Fernando Figueira da Silva & Bruno Deshaies
Laboratoire de Combustion et de Detonique

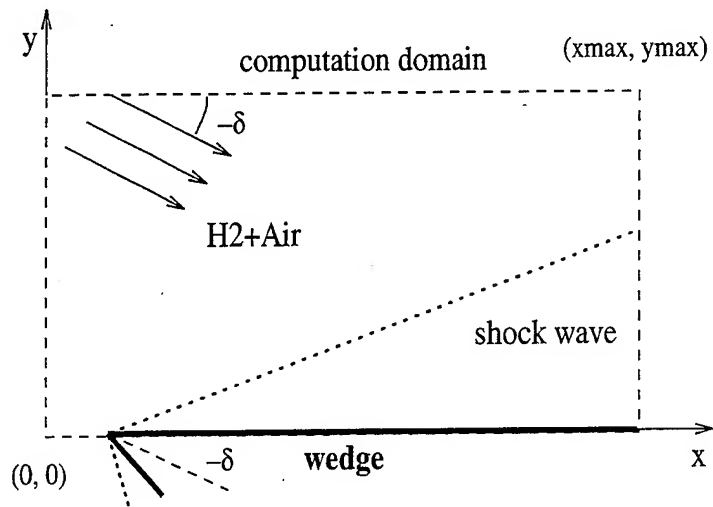
UPR 9028 du CNRS

ENSMa & Universite de Poitiers
Futuroscope FRANCE

Recall of some of the results obtained for H_2 -Air
boundary layer combustion;

RAMAC30 of ISL: boundary layer combustion results for
methane/oxygen/dilutant mixture;

Transition from an oblique shock wave to an oblique
detonation wave: two different types of transition,
unsteady thermal choking.



Two basic ignition mechanisms:

- ignition is triggered within the boundary layer only (viscous dissipation heating effects);
- ignition occurs behind the oblique shock wave, leading to the formation of an oblique detonation wave;

Mathematical Formulation of the Problem under Boundary Layer Assumptions

Equations:

$$\begin{aligned}\frac{\partial \rho u}{\partial x} + \frac{\partial \rho v}{\partial y} &= 0 \\ \rho u \frac{\partial u}{\partial x} + \rho v \frac{\partial u}{\partial y} &= -\frac{\partial p}{\partial x} + \frac{\partial}{\partial y} \left(\mu \frac{\partial u}{\partial y} \right); \quad \frac{\partial p}{\partial y} = 0 \\ \rho u c_p \frac{\partial T}{\partial x} + \rho v c_p \frac{\partial T}{\partial y} &= u \frac{\partial p}{\partial x} + \frac{\partial}{\partial y} \left(\lambda \frac{\partial T}{\partial y} \right) - \sum_{k=1}^K \rho Y_k V_k c_{p_k} \frac{\partial T}{\partial y} + \mu \left(\frac{\partial u}{\partial y} \right)^2 - \sum_{k=1}^K h_k \omega_k \\ \rho u \frac{\partial Y_k}{\partial x} + \rho v \frac{\partial Y_k}{\partial y} &= -\frac{\partial}{\partial y} (\rho Y_k V_k) + \omega_k \quad k = 1, \dots, K \\ p &= \rho R T \sum_{k=1}^K \frac{Y_k}{M_k}; \quad h_k = h_k^0 + \int_{T_0}^T c_{p_k} dT \\ V_k &= -\rho D_k \frac{1}{X_k} \frac{\partial X_k}{\partial y} + \frac{D_k \Theta_k}{X_k} \frac{1}{T} \frac{\partial T}{\partial y} + V_c\end{aligned}$$

Boundary Conditions

- Initial (upstream) condition at $x = x_0$: compressible self similar boundary layer solution for a chemically frozen flow.
- Freestream conditions $y \rightarrow \infty$: $T = T_\infty$, $p = p_\infty$, $u = u_\infty$, $Y_k = Y_{k\infty}$
- Plate conditions $y = 0$: $u = v = 0$, non-catalytic $\partial Y_k / \partial y = 0$

Both adiabatic $\partial T / \partial y = 0$ and non adiabatic $T = T_w$

Numerical Procedure:

Thermodynamic and physico-chemic properties computed as functions of local temperature, pressure and composition (CHEMKIN, Kee et al.)

Second order finite differences for the transverse direction

First order finite differences for the streamwise direction

Modified (damped) Newton method, numerical calculation of the Jacobian (Deuflard, Kee et al.)

Adaptative mesh in the transverse direction, using the gradient and the curvature of the unknowns (Giovangigli and Smooke)

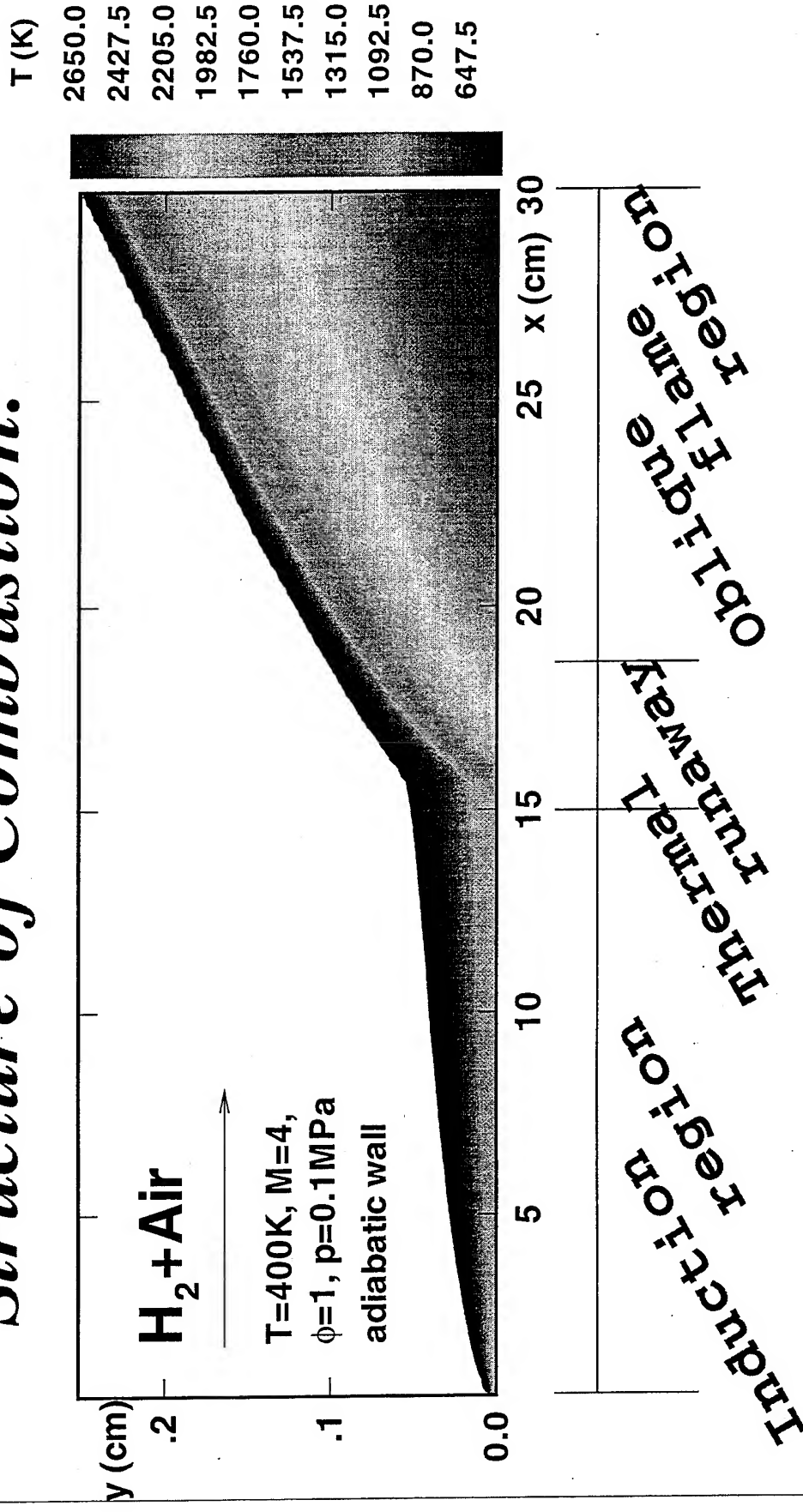
Chemical Kinetics:

For hydrogen-Air mixtures, the chemical scheme we use involves nine species: H_2 , O_2 , H_2O , OH , H , O , HO_2 , H_2O_2 and N_2 .

For the $\text{CH}_4/\text{O}_2/\text{CO}_2$ mixture we have performed a systematic reduction of a detailed chemical kinetics mechanism by Tang et al., resulting in a scheme with 26 species:

CH_4 O_2 H_2O CO CO_2 H H_2 O OH HO_2 H_2O_2 HCO CH_3 C_2H_6 CH_2O C_2H_5 CH_2
 CH_3O CH C_2H_2 C_2H_4 C_2H_3 C_2H CH_2CO HCCO CH_3CO

Structure of Combustion:



Strong coupling between chemical kinetics and compressible aerodynamics

Ignition is triggered by viscous dissipation heating within the boundary layer

Length of the induction region?

$t_1 = (\text{chemical time}) \cdot (\text{charact. velocity})$

Characteristic velocity $\Rightarrow u_\infty$ (??)

Chemical induction time: $\tau_i = \tau_i(T, p, \phi)$

T : wall temperature $T_w = T_w(T_\infty, M_\infty, Pr)$

Pr : Prandtl number, $Pr = Pr(\phi)$

ϕ : local equivalence ratio \Rightarrow Soret effect

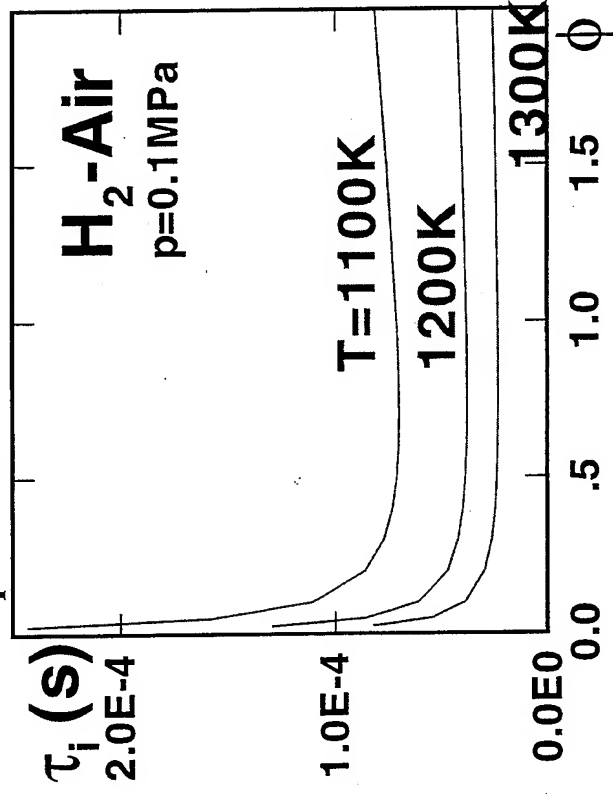
p : pressure \Rightarrow second explosion limit

: b.l. thickness \Rightarrow transverse transports

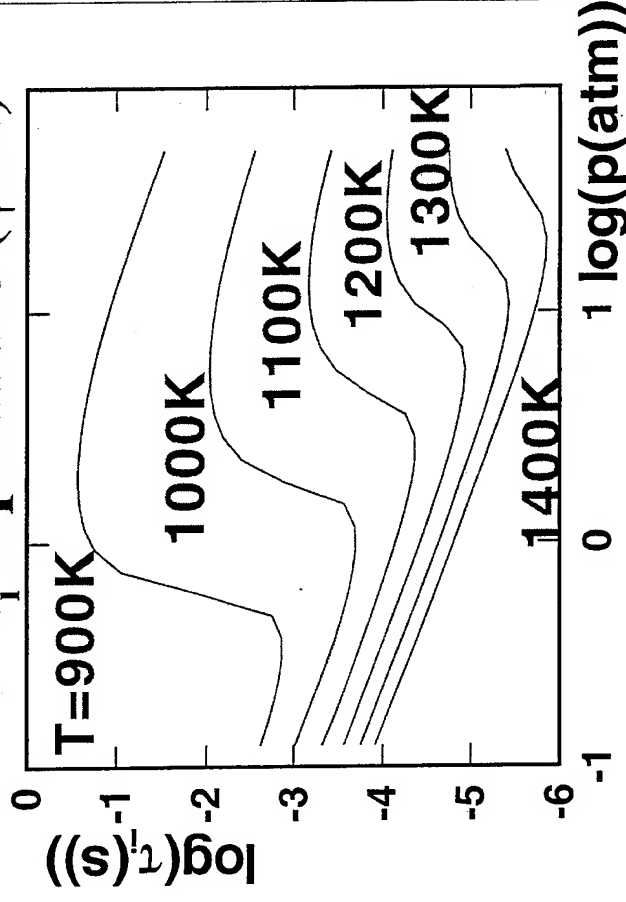
Complex variation of the induction length with the flow parameters

Induction time - Thermal explosion:

τ_i x equivalence ratio



τ_i x pressure ($\phi=1$)



Induction time: 10% of equilibrium H₂O mass fraction

Constant pressure (Semenov) thermal

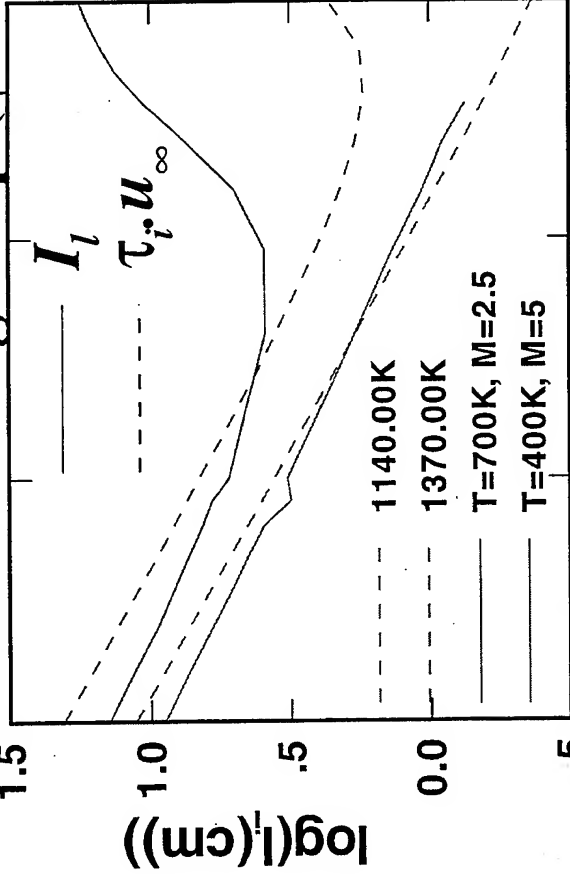
explosion: T increases $\Rightarrow \tau_i$ decreases

Rapid increase in τ_i for $\phi < 0.2$

Second explosion limit: τ_i increases with p

The influence of the pressure on the I_i :

Induction length $\times p$ ($\phi=1$)



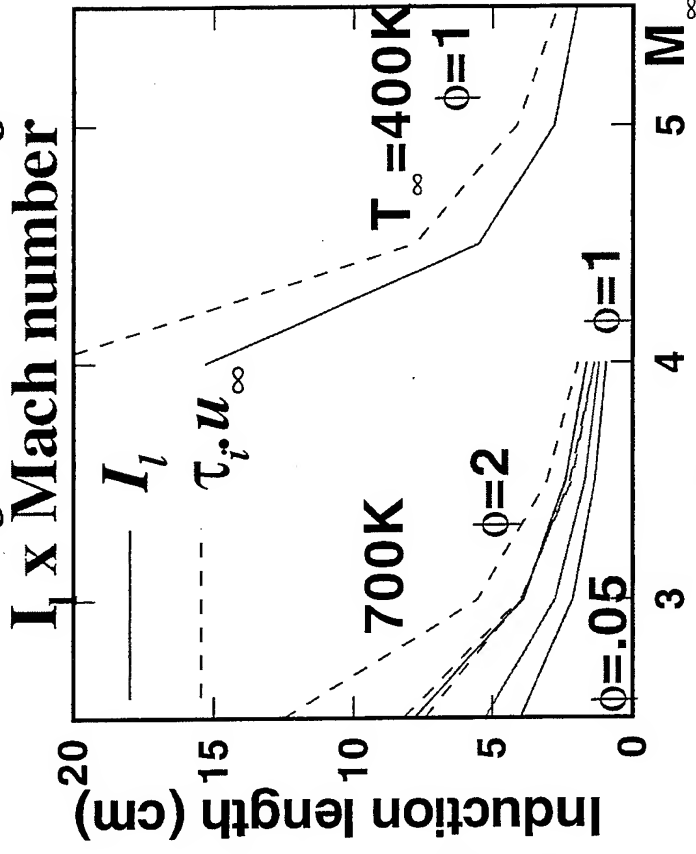
I_i : b.l. induction length
 $\tau_i \cdot u_\infty$: (thermal explosion induction time).(freestream velocity)
 τ_i is a direct function of p

$\log(I_i)$ (cm) $0.5 \log(p(\text{atm}))$

At constant M_∞ and T_∞ , the b.l. thickness:
 $\delta \propto 1/\sqrt{Re} \approx \rho^{-1/2} \approx p^{-1/2} \Rightarrow$ as p increases, δ decreases
 As δ decreases, the transverse transports increase.

The induction length is a function of both p and $\delta(p)$

The influence of M_∞ and ϕ on the I_i :



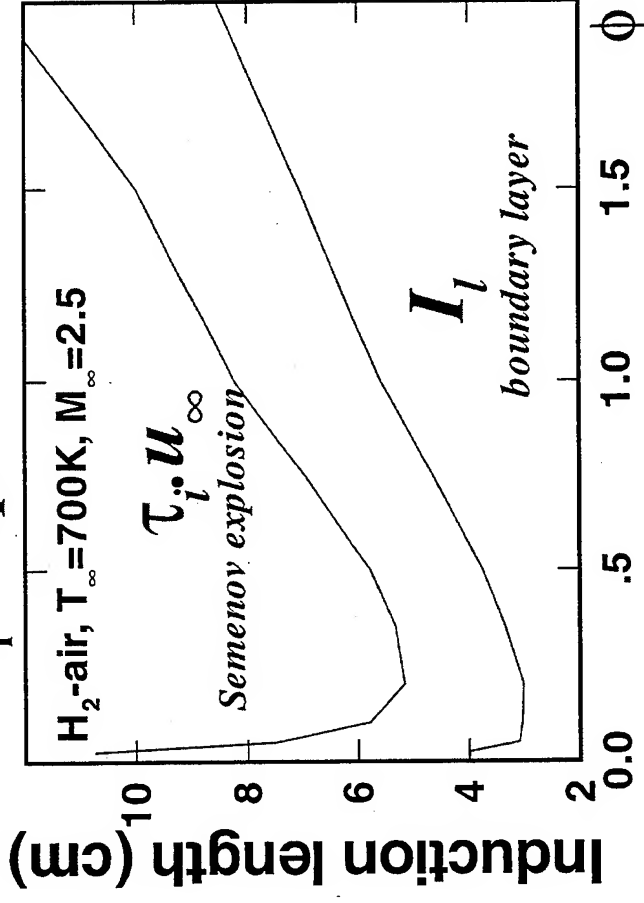
I_i : b.l. induction length
 τ_i : induction time (Semenov thermal explosion)
 u_∞ : freestream velocity

As M_∞ increases, the ratio $I_1 / (\tau_i \cdot u_\infty)$ approaches unity

The thickness of the b.l. $\delta_\infty M_\infty^2 / \sqrt{\text{Re}}$ increases with M_∞ , thus preserving the wall region from the external flow:
 Influence of the Lewis number

Boundary layer x Thermal explosion:

I_1 x equivalence ratio



τ_i calculated at the wall temperature at the beginning of the boundary layer and using the freestream

equivalence ratio

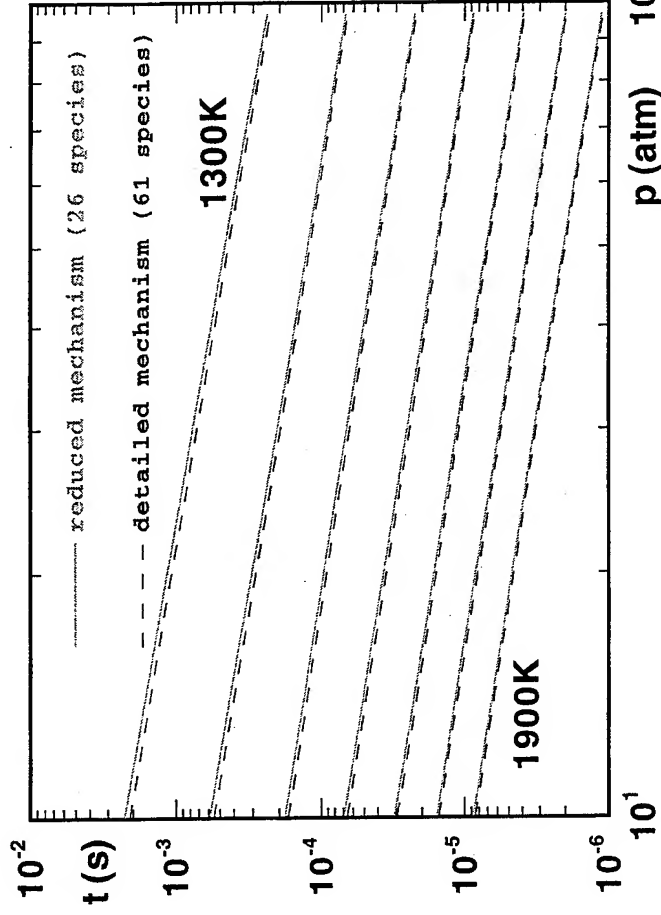
u_∞ - freestream velocity

τ_i is a function of ϕ

Steep increase in the b.l. induction length for $\phi < 0.1$

The product $\tau_i \cdot u_\infty$ overpredicts the b.l. induction length for all equivalence ratios, with the same overall behaviour I_1 is a function of both ϕ and $T_w(\phi)$

Induction time of the 0D thermal explosion:



used in the RAMAC30 of ISL

Detailed hydrocarbon-oxygen chemical kinetics mechanism from Tan et al.

(LCSR Orleans)

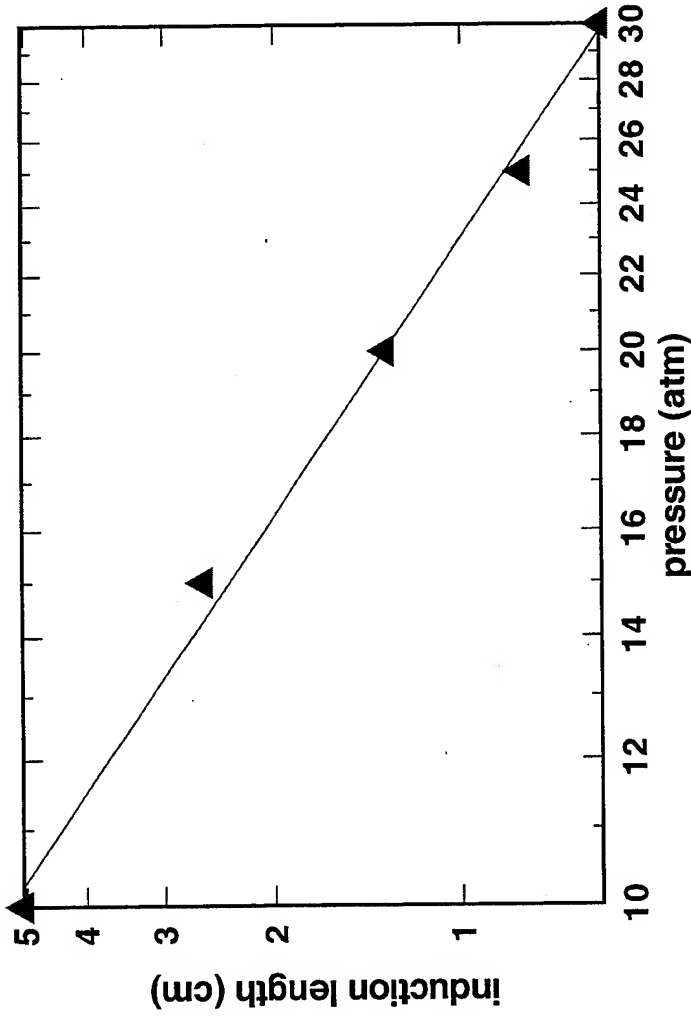
Limitation of the calculations shown:
 perfect gas equation of state.

(future work will include real gas effects)

As opposed to the hydrogen-air mixtures, the induction time has a monotonous decrease with pressure.

The induction times of the $\text{CH}_4 + 1.9\text{O}_2 + 6.7\text{CO}_2$ mixture are 100 to 1000 times longer than those corresponding to H_2 -air.

Induction length as a function of the pressure



for the mixture $\text{CH}_4 + 1.9\text{O}_2 + 6.7\text{CO}_2$
used in the RAMAC30 of ISL

External conditions to the
boundary layer calculation are
representative of the theoretical
test conditions:

$T_\infty = 400\text{K}$

$u_\infty = 2000\text{m/s}$

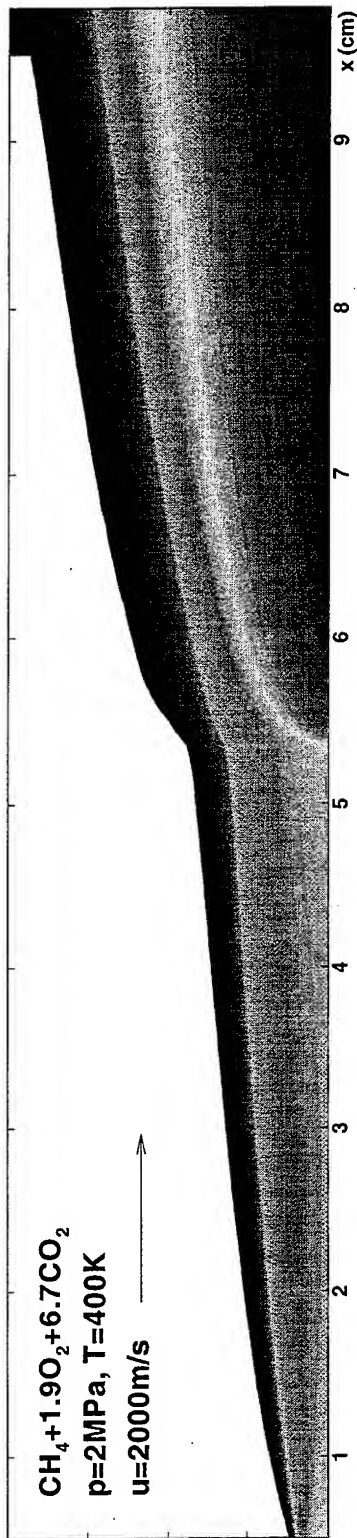
$p > 20\text{atm}$

(adiabatic non catalytic surface)

Boundary layer combustion may occur over the forebody of
the RAMAC30 in these superdetonative conditions

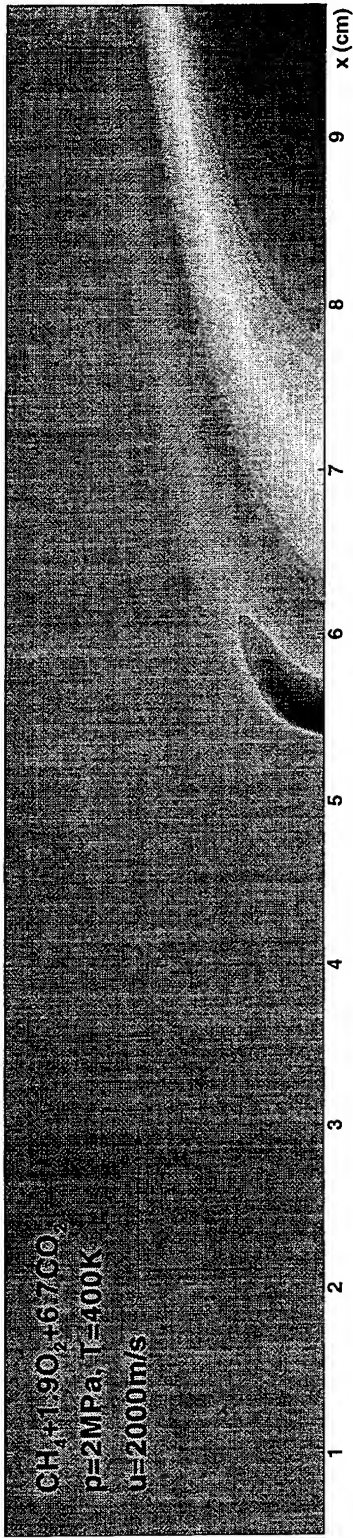
T (K)

2399
2180
1960
1740
1520
1301
1081
861
642



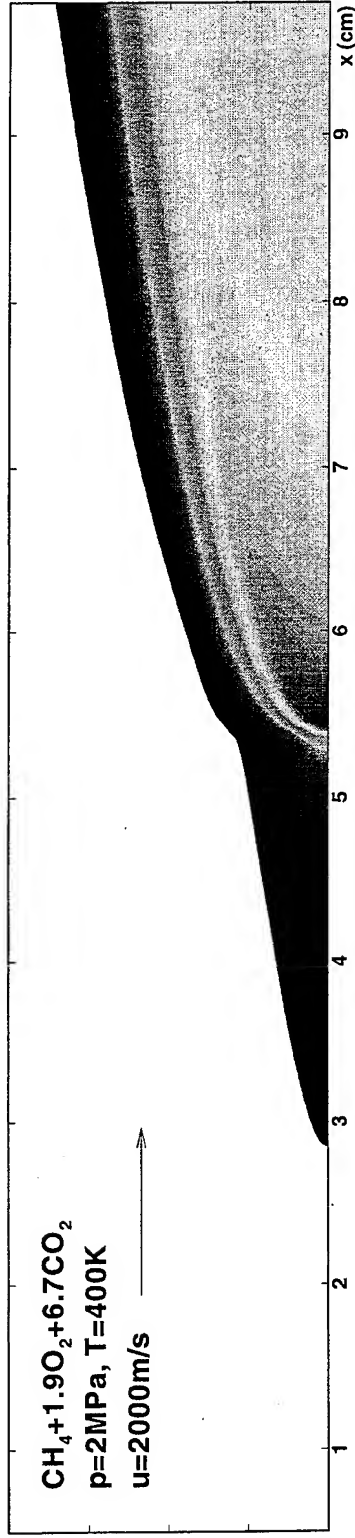
CO₂

0.813
0.809
0.804
0.800
0.795
0.791
0.786
0.782
0.777
0.773



CO

0.089
0.079
0.070
0.060
0.050
0.040
0.030
0.021
0.011



Onset of combustion behind an oblique shock wave

boundary layer combustion only: ignition occurs due to viscous dissipation heating near the surface of the wedge;

Ignition of the flow as a whole behind the oblique shock wave, with two different types of transition to the oblique detonation wave that corresponds to the wedge angle. Smooth vs. abrupt transition.

Thermal choking of the flow behind the oblique detonation wave: unsteady unstart of the shock structure, influence of the downstream boundary conditions.

The Navier Stokes equations for a multicomponent chemically reacting mixture can be written as follows:

$$\frac{\partial U}{\partial t} + \frac{\partial F}{\partial x} + \frac{\partial G}{\partial y} = W$$

$$U = \begin{bmatrix} \rho \\ \rho u \\ \rho v \\ \rho E \\ \rho Y_1 \\ \rho Y_2 \\ \vdots \\ \rho Y_{K-1} \end{bmatrix} \quad F = \begin{bmatrix} \rho u \\ \rho u^2 + p - \tau_{xx} \\ \rho uv - \tau_{xy} \\ u(\rho E + p) - \Omega_x \\ \rho Y_1(u + V_{x1}) \\ \rho Y_2(u + V_{x2}) \\ \vdots \\ \rho Y_{K-1}(u + V_{xK-1}) \end{bmatrix}$$

$$G = \begin{bmatrix} \rho v \\ \rho uv - \tau_{xy} \\ \rho v^2 + p - \tau_{yy} \\ v(\rho E + p) - \Omega_y \\ \rho Y_1(v + V_{y1}) \\ \rho Y_2(v + V_{y2}) \\ \vdots \\ \rho Y_{K-1}(v + V_{yK-1}) \end{bmatrix} \quad W = \begin{bmatrix} 0 \\ 0 \\ 0 \\ 0 \\ W_1\omega_1 \\ W_2\omega_2 \\ \vdots \\ W_{K-1}\omega_{K-1} \end{bmatrix}$$

$$Y_K = 1 - \sum_{k=1}^{K-1} Y_k; \quad p = \rho RT \sum_{k=1}^K \frac{Y_k}{W_k}$$

$$h_k = h_k^0 + \int_{T_0}^T c_{pk} dT = e_k + \frac{p}{\rho}$$

$$E = e + \frac{1}{2} (u^2 + v^2) = \sum_{k=1}^K Y_k e_k + \frac{1}{2} (u^2 + v^2)$$

$$\rho Y_k V_{x_{ik}} = -\rho D_k \partial Y_k / \partial x_i$$

$$\tau_{x_i x_j} = \mu \left(\frac{\partial u_i}{\partial x_j} + \frac{\partial u_j}{\partial x_i} - \frac{2}{3} \delta_{ij} \frac{\partial u_l}{\partial x_l} \right)$$

$$\Omega_{x_i} = u_i \tau_{x_i x_i} + u_j \tau_{x_i x_j} + \lambda \frac{\partial T}{\partial x_i} - \rho \sum_{k=1}^K h_k Y_k V_{x_{ik}}$$

Boundary conditions:

- slip or no-slip ($u=0$) adiabatic ($\partial T / \partial y = 0$), non catalytic boundary conditions at the wedge surface ($y=0$);
- non-reflecting characteristic boundary conditions at the exit ($x=x_{max}$).

Numerical method for the solution of the unsteady

2D Navier-Stokes Equations

"Advection Upstream Splitting Method" applied on the inviscid fluxes (AUSM+, Liou, 1994)

2nd order MUSCL extrapolation using MINMOD limiter on the primitive variables (ρ , u , v , p , Y_k) (van Leer, 1982)

Chemical kinetics and physico-chemical properties (c_p , λ , μ , etc.): CHEMKIN-II (Kee et al., 1989)

Time step splitting for the chemistry calculations; stiff ODE solver VODE (Byrne & Dean, 1993) for the chemistry, 2nd order runge-kutta for the fluid dynamics

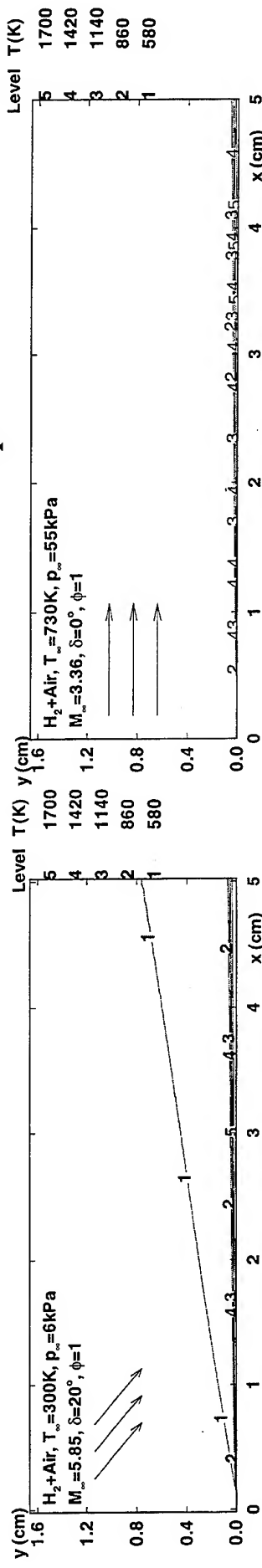
Boundary layer combustion only:

The b.l. induction length calculated using the N.S. program is smaller than the one obtained using the b.l. code, due to the heating at the leading edge of the wedge.

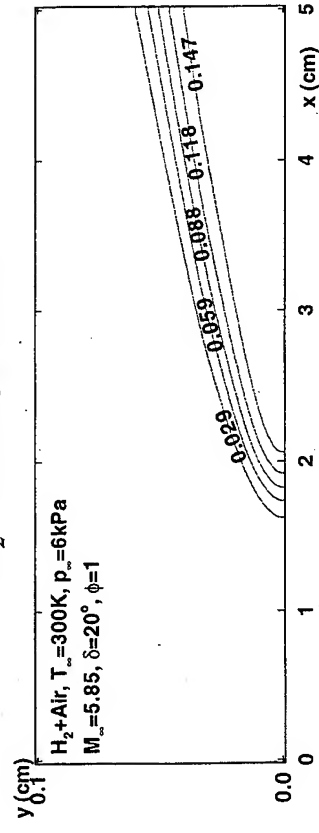
The basic structure of flow remains unchanged

Navier-Stokes vs. boundary layer calculations

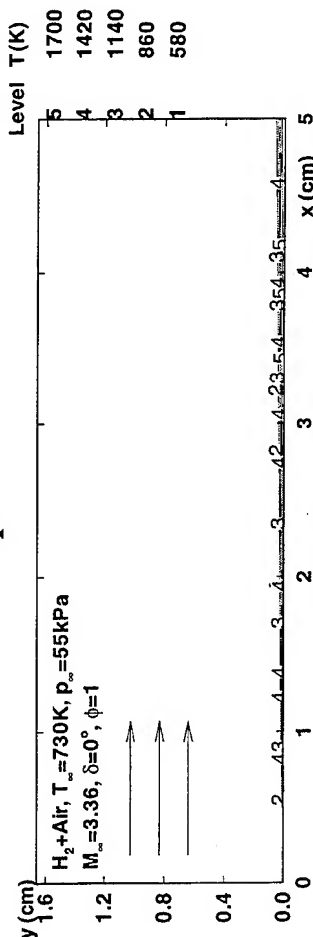
Temperature



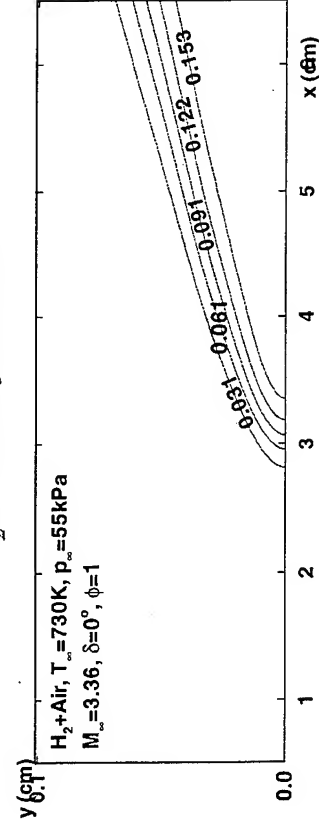
H_2O mass fraction



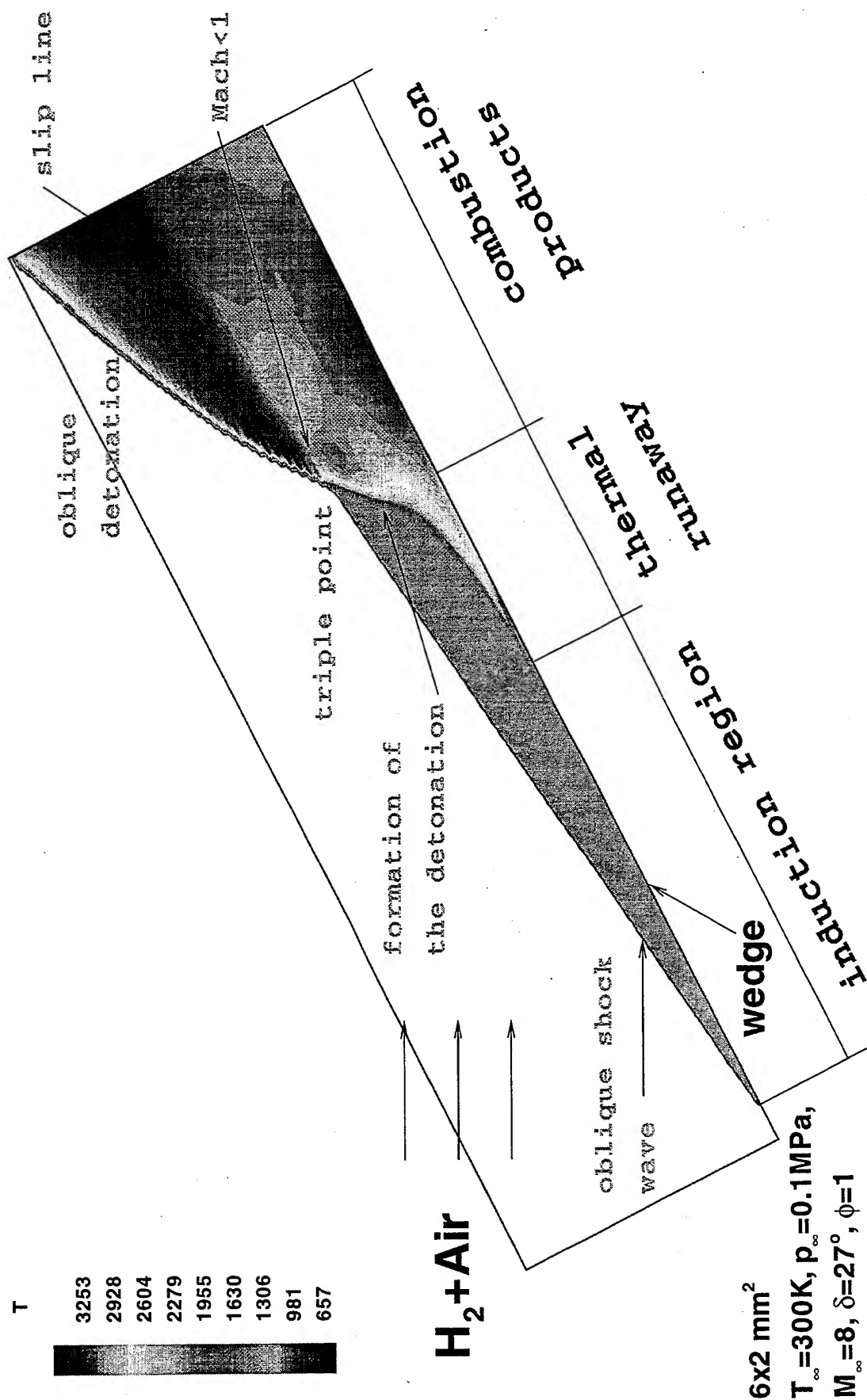
Temperature



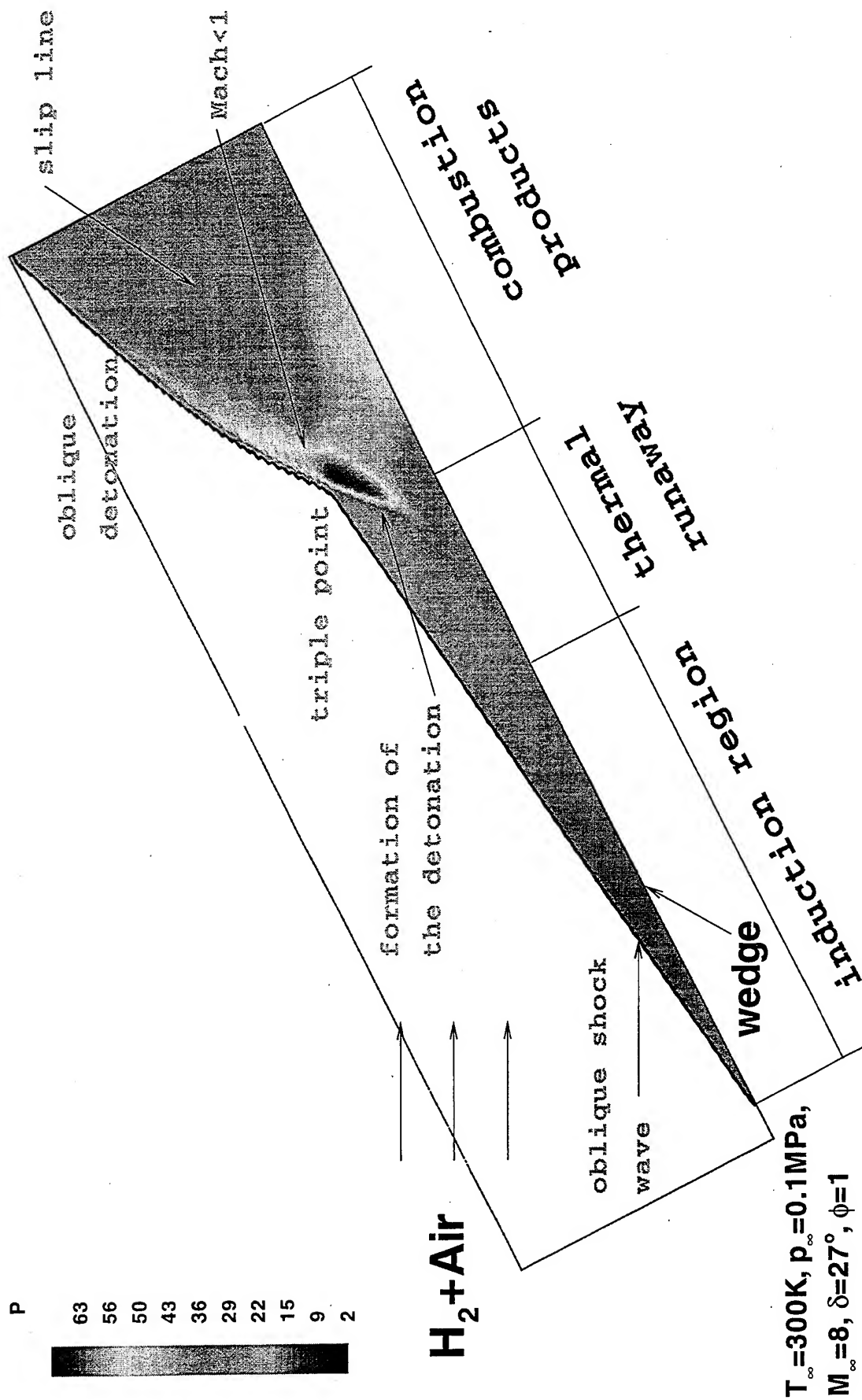
H_2O mass fraction



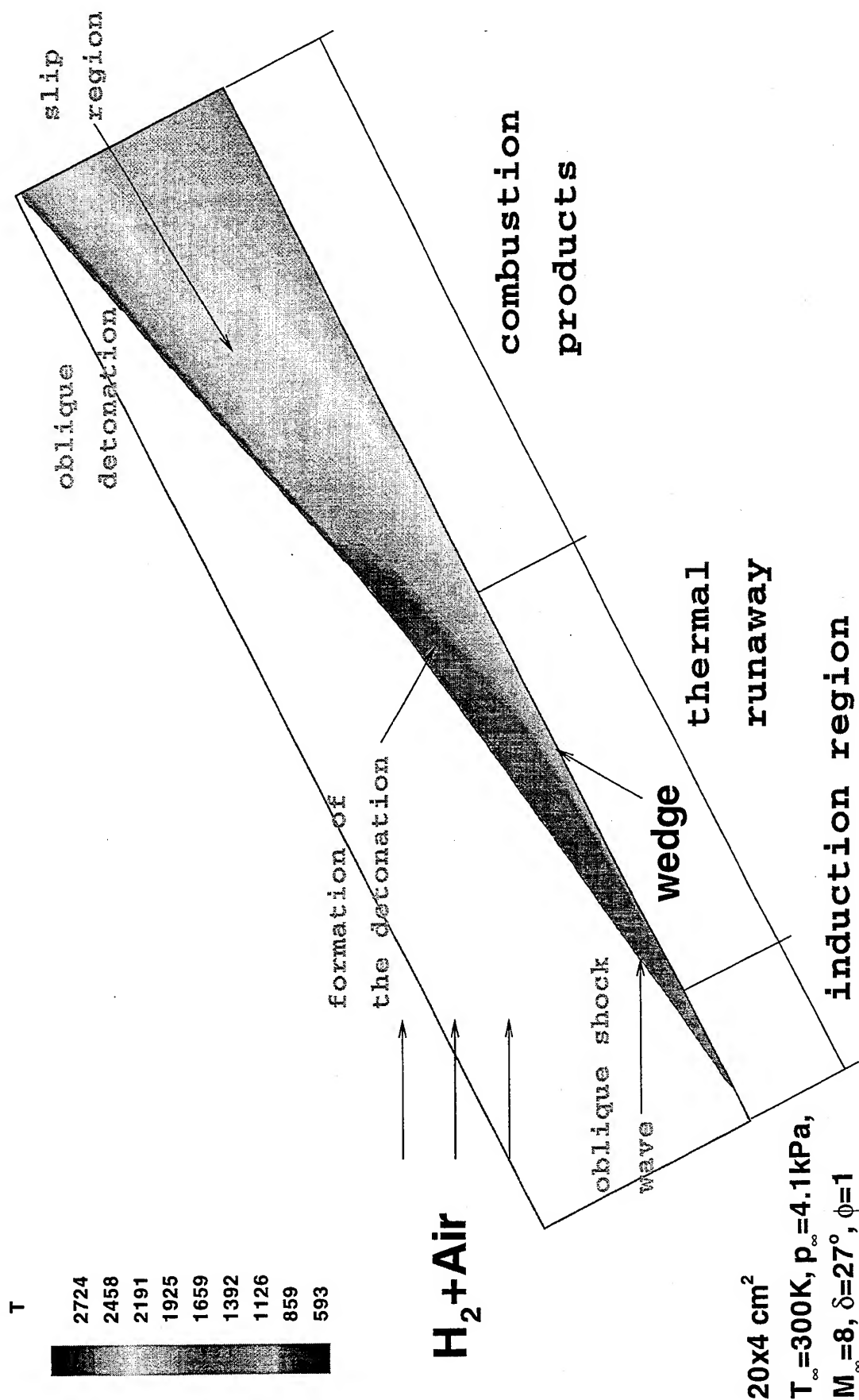
Development of combustion over a supersonic wedge



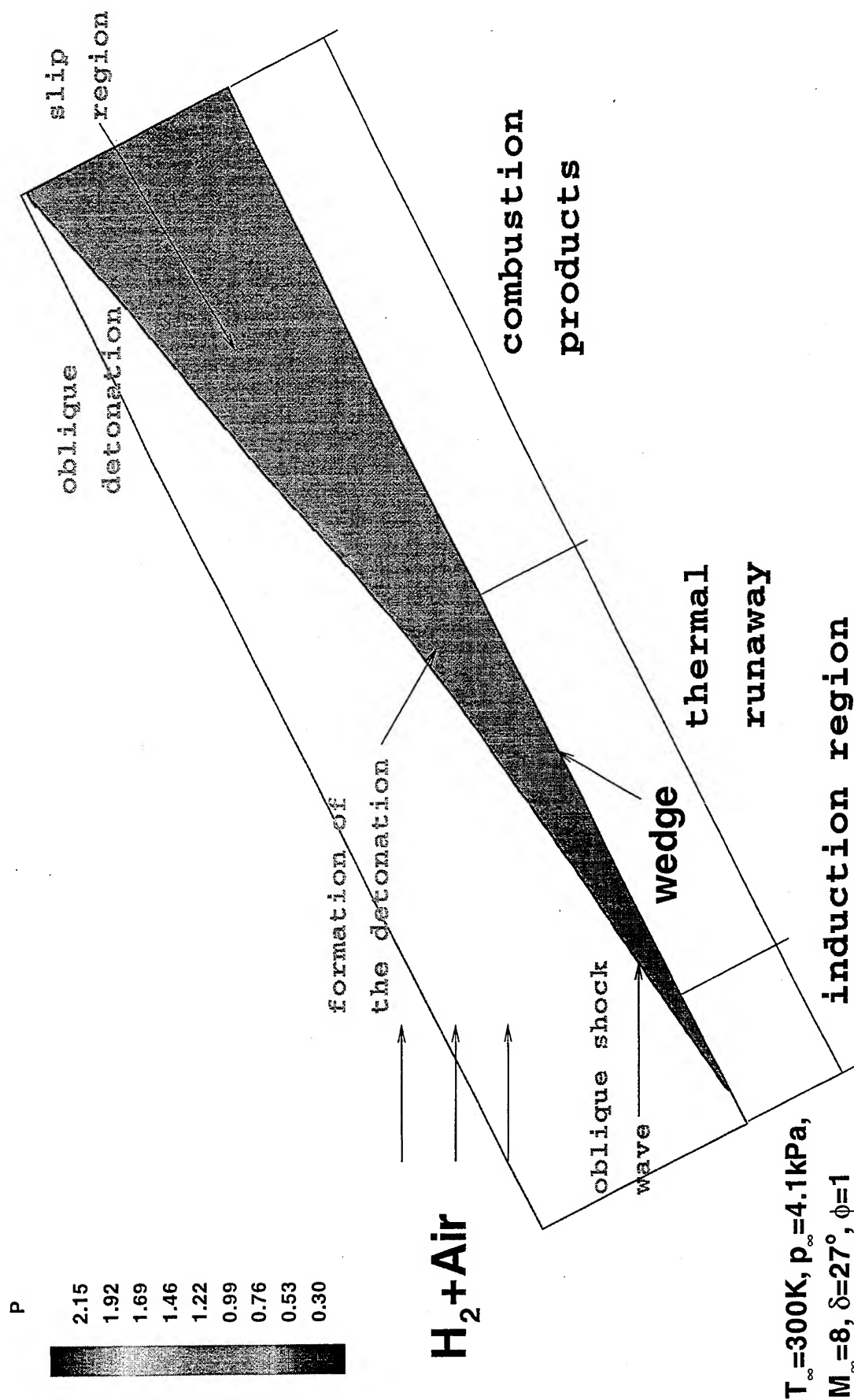
Development of combustion over a supersonic wedge



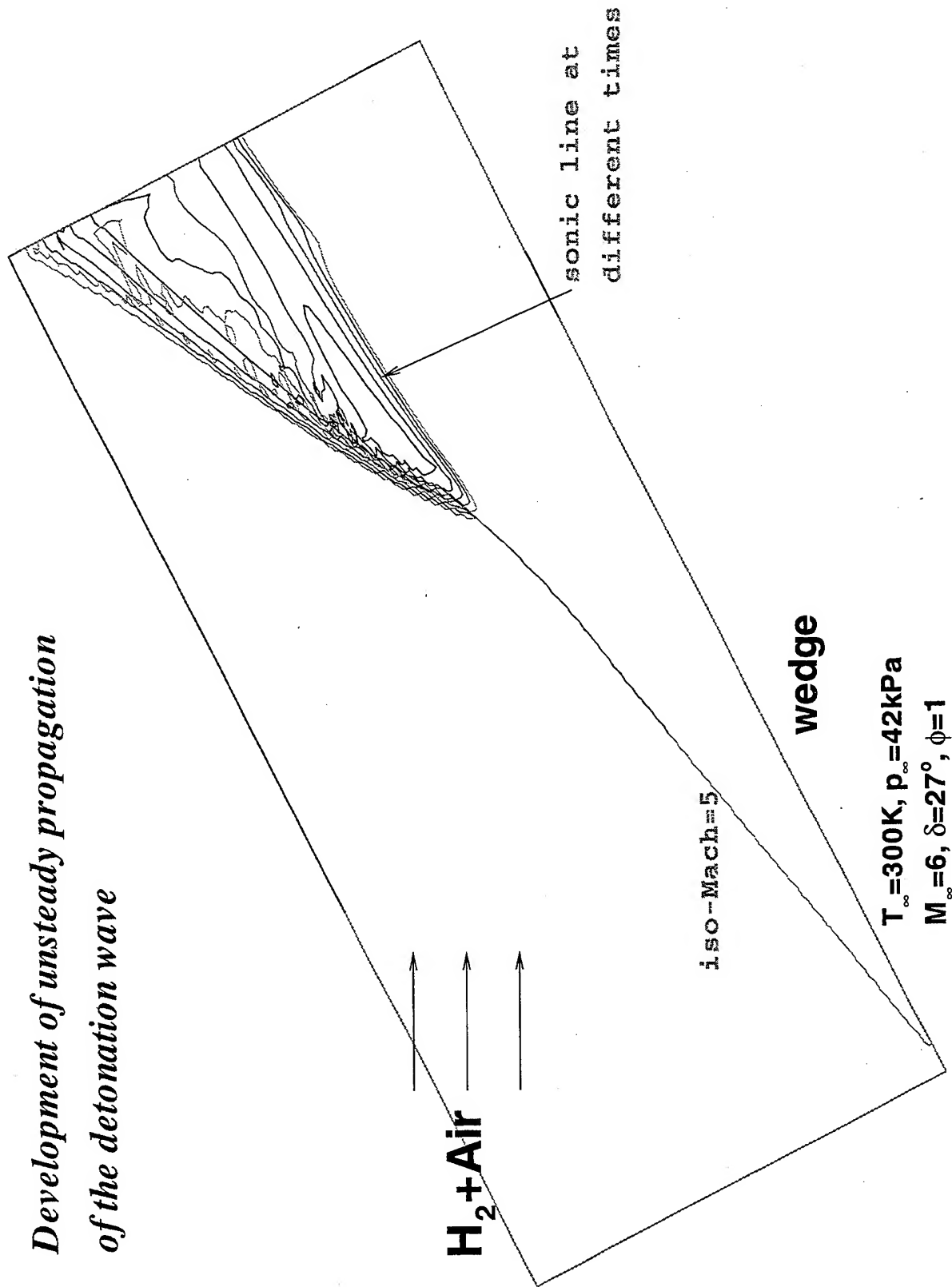
Development of combustion over a supersonic wedge



Development of combustion over a supersonic wedge



*Development of unsteady propagation
of the detonation wave*



REACTION	A	β	E
$\text{H} + \text{O}_2 \rightleftharpoons \text{OH} + \text{O}$	5.13E16	-.816	16507.
$\text{O} + \text{H}_2 \rightleftharpoons \text{OH} + \text{H}$	1.80E10	1.00	8826.
$\text{OH} + \text{H}_2 \rightleftharpoons \text{H}_2\text{O} + \text{H}$	1.17E09	1.30	3626.
$\text{OH} + \text{OH} \rightleftharpoons \text{O} + \text{H}_2\text{O}$	6.00E08	1.30	0.
$\text{H}_2 + \text{M} \rightleftharpoons \text{H} + \text{H} + \text{M}^b$	2.23E12	0.50	92600.
$\text{H} + \text{OH} + \text{M} \rightleftharpoons \text{H}_2\text{O} + \text{M}^c$	7.50E23	-2.60	0.
$\text{O}_2 + \text{M} \rightleftharpoons \text{O} + \text{O} + \text{M}$	1.85E11	0.50	95560.
$\text{H} + \text{O}_2 + \text{M} \rightleftharpoons \text{HO}_2 + \text{M}^c$	2.10E18	-1.00	0.
$\text{H} + \text{HO}_2 \rightleftharpoons \text{OH} + \text{OH}$	2.50E14	0.00	1900.
$\text{H} + \text{HO}_2 \rightleftharpoons \text{H}_2 + \text{O}_2$	2.50E13	0.00	700.
$\text{H}_2 + \text{O}_2 \rightleftharpoons \text{OH} + \text{OH}$	1.70E13	0.00	47780.
$\text{O} + \text{HO}_2 \rightleftharpoons \text{O}_2 + \text{OH}$	4.80E13	0.00	1000.
$\text{OH} + \text{HO}_2 \rightleftharpoons \text{H}_2\text{O} + \text{O}_2$	5.00E13	0.00	1000.
$\text{HO}_2 + \text{HO}_2 \rightleftharpoons \text{H}_2\text{O}_2 + \text{O}_2$	2.00E12	0.00	0.
$\text{H}_2\text{O}_2 + \text{M} \rightleftharpoons \text{OH} + \text{OH} + \text{M}$	1.30E17	0.00	45500.
$\text{H}_2\text{O}_2 + \text{H} \rightleftharpoons \text{HO}_2 + \text{H}_2$	1.60E12	0.00	3800.
$\text{H} + \text{O}_2 + \text{O}_2 \rightleftharpoons \text{HO}_2 + \text{O}_2$	6.70E19	-1.42	0.
$\text{H} + \text{O}_2 + \text{N}_2 \rightleftharpoons \text{HO}_2 + \text{N}_2$	6.70E19	-1.42	0.
$\text{H}_2\text{O}_2 + \text{OH} \rightleftharpoons \text{H}_2\text{O} + \text{HO}_2$	1.00E13	0.00	1800.

Third-body efficiencies:

a- $f_{\text{H}_2\text{O}}=21$, $f_{\text{H}_2}=3.3$, $f_{\text{N}_2}=f_{\text{O}_2}=0$; b- $f_{\text{H}_2\text{O}}=6$, $f_{\text{H}}=2$, $f_{\text{H}_2}=3$; c- $f_{\text{H}_2\text{O}}=20$.

REACTION	A	β	E
H + H + M = H ₂ + M	7.310E+17	-1.0	0.0
O + O + M = O ₂ + M	1.140E+17	-1.0	0.0
O + H + M = OH + M	6.200E+16	-0.6	0.0
H ₂ + O ₂ = OH + OH	1.700E+13	0.0	47780.0
O + H ₂ = OH + H	3.870E+04	2.7	6260.0
H + O ₂ = OH + O	1.900E+14	0.0	16812.0
H + O ₂ + M = HO ₂ + M	8.000E+17	-0.8	0.0
H + OH + M = H ₂ O + M	8.615E+21	-2.0	0.0
H ₂ + OH = H ₂ O + H	2.161E+08	1.51	3430.0
H ₂ O + O = OH + OH	1.500E+10	1.14	17260.0
HO ₂ + OH = H ₂ O + O ₂	2.890E+13	0.0	-497.0
HO ₂ + O = OH + O ₂	1.810E+13	0.0	-400.0
H + HO ₂ = H ₂ + O ₂	6.620E+13	0.0	2130.0
H + HO ₂ = OH + OH	4.951E+13	0.0	143.0
H + HO ₂ = H ₂ O + O	3.010E+13	0.0	1721.0
HO ₂ + HO ₂ = H ₂ O ₂ + O ₂	4.075E+02	3.321	1979.0
H ₂ O ₂ + M = OH + OH + M	3.100E+16	-0.5	36402.0
H ₂ O ₂ + OH = HO ₂ + H ₂ O	5.800E+14	0.0	9557.0
H ₂ O ₂ + H = HO ₂ + H ₂	1.700E+12	0.0	3750.0
H ₂ O ₂ + H = H ₂ O + OH	1.000E+13	0.0	3590.0
H ₂ O ₂ + O = HO ₂ + OH	2.800E+13	0.0	6400.0
CO + HO ₂ = CO ₂ + OH	1.500E+14	0.0	23650.0
CO + OH = CO ₂ + H	5.230E+06	1.4	-980.0
CO + O + M = CO ₂ + M	2.830E+13	0.0	-4540.0
CO + O ₂ = CO ₂ + O	2.530E+12	0.0	47700.0
HCO + M = H + CO + M	1.850E+17	-1.0	17000.0
HCO + OH = CO + H ₂ O	1.000E+14	0.0	0.0
HCO + O = CO + OH	3.000E+13	0.0	0.0
HCO + O = CO ₂ + H	3.000E+13	0.0	0.0
HCO + H = CO + H ₂	7.224E+13	0.0	0.0
HCO + O ₂ = CO + HO ₂	4.723E+12	0.0	250.0
HCO + CH ₃ = CO + CH ₄	1.200E+14	0.0	0.0
HCO + HO ₂ = CO ₂ + OH + H	3.000E+13	0.0	0.0
HCO + C ₂ H ₆ = CH ₂ O + C ₂ H ₅	4.700E+04	2.72	18235.0
HCO + HCO = CH ₂ O + CO	1.800E+13	0.0	0.0
HCO + HCO = H ₂ + 2CO	3.000E+12	0.0	0.0
CH ₄ = CH ₃ + H	2.132E+31	-5.30	104906.0
CH ₄ + HO ₂ = CH ₃ + H ₂ O ₂	1.122E+13	0.0	24641.0
CH ₄ + OH = CH ₃ + H ₂ O	1.548E+07	1.83	2774.0
CH ₄ + O = CH ₃ + OH	3.150E+12	0.50	10290.0
CH ₄ + H = CH ₃ + H ₂	8.583E+03	3.05	7941.6
CH ₄ + CH ₂ = CH ₃ + CH ₃	4.300E+12	0.0	10038.0
CH ₄ + O ₂ = CH ₃ + HO ₂	4.040E+13	0.0	56913.0

REACTION	A	β	E
$\text{CH}_3 + \text{M} = \text{CH}_2 + \text{H} + \text{M}$	1.900E+16	0.0	91600.0
$\text{CH}_3 + \text{M} = \text{CH} + \text{H}_2 + \text{M}$	6.900E+14	0.0	82460.0
$\text{CH}_3 + \text{HO}_2 = \text{CH}_3\text{O} + \text{OH}$	8.000E+12	0.0	0.0
$\text{CH}_3 + \text{OH} = \text{CH}_3\text{O} + \text{H}$	5.740E+12	-0.23	13931.0
$\text{CH}_3 + \text{OH} = \text{CH}_2\text{O} + \text{H}_2$	3.190E+12	-0.53	10810.0
$\text{CH}_3 + \text{O} = \text{CH}_2\text{O} + \text{H}$	8.430E+13	0.0	0.0
$\text{CH}_3 + \text{H} = \text{CH}_2 + \text{H}_2$	7.000E+13	0.0	15100.0
$\text{CH}_3 + \text{O}_2 = \text{CH}_3\text{O} + \text{O}$	1.280E+13	0.0	28000.0
$\text{CH}_3 + \text{O}_2 = \text{CH}_2\text{O} + \text{OH}$	4.361E+14	0.0	30749.0
$\text{CH}_3 + \text{CH}_3 = \text{C}_2\text{H}_5 + \text{H}$	3.011E+13	0.0	13513.0
$\text{CH}_3 + \text{CH}_3 = \text{C}_2\text{H}_6$	2.393E+38	-7.581	11359.0
$\text{CH}_3 + \text{CH}_3\text{O} = \text{CH}_4 + \text{CH}_2\text{O}$	2.409E+13	0.0	0.0
$\text{CH}_2 + \text{OH} = \text{CH} + \text{H}_2\text{O}$	1.130E+07	2.0	3000.0
$\text{CH}_2 + \text{OH} = \text{CH}_2\text{O} + \text{H}$	2.500E+13	0.0	0.0
$\text{CH}_2 + \text{O} = \text{CO} + \text{H} + \text{H}$	5.000E+13	0.0	0.0
$\text{CH}_2 + \text{O} = \text{CO} + \text{H}_2$	6.000E+13	0.0	0.0
$\text{CH}_2 + \text{H} = \text{CH} + \text{H}_2$	1.000E+18	-1.56	0.0
$\text{CH}_2 + \text{O}_2 = \text{HCO} + \text{OH}$	4.300E+10	0.0	-500.0
$\text{CH}_2 + \text{O}_2 = \text{CO}_2 + \text{H}_2$	3.450E+11	0.0	1000.0
$\text{CH}_2 + \text{O}_2 = \text{CO}_2 + \text{H} + \text{H}$	1.600E+12	0.0	1000.0
$\text{CH}_2 + \text{O}_2 = \text{CO} + \text{H}_2\text{O}$	1.870E+10	0.0	-1000.0
$\text{CH}_2 + \text{O}_2 = \text{CO} + \text{OH} + \text{H}$	8.640E+10	0.0	-500.0
$\text{CH}_2 + \text{O}_2 = \text{CH}_2\text{O} + \text{O}$	5.000E+13	0.0	9000.0
$\text{CH}_2 + \text{CO}_2 = \text{CH}_2\text{O} + \text{CO}$	1.100E+11	0.0	1000.0
$\text{CH}_2 + \text{CH}_2 = \text{C}_2\text{H}_2 + \text{H}_2$	3.200E+13	0.0	0.0
$\text{CH}_2 + \text{CH}_2 = \text{C}_2\text{H}_2 + \text{H} + \text{H}$	4.00E+13	0.0	0.0
$\text{CH}_2 + \text{CH}_3 = \text{C}_2\text{H}_4 + \text{H}$	4.000E+13	0.0	0.0
$\text{CH}_2 + \text{CH} = \text{C}_2\text{H}_2 + \text{H}$	4.000E+13	0.0	0.0
$\text{CH}_2 + \text{C}_2\text{H}_6 = \text{CH}_3 + \text{C}_2\text{H}_5$	6.500E+12	0.0	7911.0
$\text{CH} + \text{OH} = \text{HCO} + \text{H}$	3.000E+13	0.0	0.0
$\text{CH} + \text{O} = \text{CO} + \text{H}$	1.000E+14	0.0	0.0
$\text{CH} + \text{O}_2 = \text{HCO} + \text{O}$	3.300E+13	0.0	0.0
$\text{CH} + \text{O}_2 = \text{CO} + \text{OH}$	2.000E+13	0.0	0.0
$\text{CH} + \text{CO}_2 = \text{HCO} + \text{CO}$	3.400E+12	0.0	690.0
$\text{CH} + \text{CH}_4 = \text{C}_2\text{H}_4 + \text{H}$	6.000E+13	0.0	0.0
$\text{CH} + \text{CH}_3 = \text{C}_2\text{H}_3 + \text{H}$	3.000E+13	0.0	0.0
$\text{CH}_3\text{O} + \text{M} = \text{CH}_2\text{O} + \text{H} + \text{M}$	4.880E+15	0.0	22773.0
$\text{CH}_3\text{O} + \text{HO}_2 = \text{CH}_2\text{O} + \text{H}_2\text{O}_2$	3.000E+11	0.0	0.0
$\text{CH}_3\text{O} + \text{OH} = \text{CH}_2\text{O} + \text{H}_2\text{O}$	1.000E+13	0.0	0.0
$\text{CH}_3\text{O} + \text{O} = \text{CH}_2\text{O} + \text{OH}$	1.300E+13	0.0	0.0
$\text{CH}_3\text{O} + \text{H} = \text{CH}_2\text{O} + \text{H}_2$	2.000E+13	0.0	0.0
$\text{CH}_3\text{O} + \text{O}_2 = \text{CH}_2\text{O} + \text{HO}_2$	2.349E+10	0.0	1788.0
$\text{CH}_3\text{O} + \text{C}_2\text{H}_5 = \text{CH}_2\text{O} + \text{C}_2\text{H}_6$	2.410E+13	0.0	0.0
$\text{CH}_3\text{O} + \text{C}_2\text{H}_3 = \text{CH}_2\text{O} + \text{C}_2\text{H}_4$	2.410E+13	0.0	0.0
$\text{CH}_3\text{O} + \text{C}_2\text{H}_4 = \text{CH}_2\text{O} + \text{C}_2\text{H}_5$	1.200E+11	0.0	7000.0

REACTION	A	β	E
$\text{CH}_2\text{O} + \text{M} = \text{HCO} + \text{H} + \text{M}$	5.540E+15	0.0	75000.0
$\text{CH}_2\text{O} + \text{HO}_2 = \text{HCO} + \text{H}_2\text{O}_2$	4.000E+12	0.0	11665.0
$\text{CH}_2\text{O} + \text{OH} = \text{HCO} + \text{H}_2\text{O}$	1.716E+09	1.18	-447.0
$\text{CH}_2\text{O} + \text{O} = \text{HCO} + \text{OH}$	1.807E+13	0.0	3088.0
$\text{CH}_2\text{O} + \text{H} = \text{HCO} + \text{H}_2$	2.190E+08	1.77	3000.0
$\text{CH}_2\text{O} + \text{O}_2 = \text{HCO} + \text{HO}_2$	2.040E+13	0.0	39000.0
$\text{CH}_2\text{O} + \text{CH}_3 = \text{HCO} + \text{CH}_4$	8.376E-02	4.33	4365.0
$\text{C}_2\text{H}_6 = \text{C}_2\text{H}_5 + \text{H}$	2.080E+38	-7.08	106507.0
$\text{C}_2\text{H}_6 + \text{HO}_2 = \text{C}_2\text{H}_5 + \text{H}_2\text{O}_2$	1.210E+12	0.0	17600.0
$\text{C}_2\text{H}_6 + \text{OH} = \text{C}_2\text{H}_5 + \text{H}_2\text{O}$	5.125E+06	2.06	860.0
$\text{C}_2\text{H}_6 + \text{O} = \text{C}_2\text{H}_5 + \text{OH}$	1.930E-02	4.85	2029.0
$\text{C}_2\text{H}_6 + \text{H} = \text{C}_2\text{H}_5 + \text{H}_2$	5.250E+14	0.0	12800.0
$\text{C}_2\text{H}_6 + \text{O}_2 = \text{C}_2\text{H}_5 + \text{HO}_2$	1.000E+13	0.0	51000.0
$\text{C}_2\text{H}_6 + \text{CH}_3 = \text{C}_2\text{H}_5 + \text{CH}_4$	7.536E+00	3.727	9883.0
$\text{C}_2\text{H}_5 + \text{HO}_2 = \text{C}_2\text{H}_4 + \text{H}_2\text{O}_2$	3.000E+11	0.0	0.0
$\text{C}_2\text{H}_5 + \text{OH} = \text{C}_2\text{H}_4 + \text{H}_2\text{O}$	2.409E+13	0.0	0.0
$\text{C}_2\text{H}_5 + \text{OH} - \text{CH}_3 + \text{CH}_2\text{O} + \text{H}$	2.409E+13	0.0	0.0
$\text{C}_2\text{H}_5 + \text{O} = \text{CH}_2\text{O} + \text{CH}_3$	4.238E+13	0.0	0.0
$\text{C}_2\text{H}_5 + \text{O} = \text{C}_2\text{H}_4 + \text{OH}$	3.046E+13	0.0	0.0
$\text{C}_2\text{H}_5 + \text{H} = \text{C}_2\text{H}_4 + \text{H}_2$	1.250E+14	0.0	8000.0
$\text{C}_2\text{H}_5 + \text{O}_2 = \text{C}_2\text{H}_4 + \text{HO}_2$	2.560E+19	-2.77	1977.0
$\text{C}_2\text{H}_5 + \text{CH}_3 = \text{C}_2\text{H}_4 + \text{CH}_4$	1.144E+12	0.0	0.0
$\text{C}_2\text{H}_5 + \text{C}_2\text{H}_5 = \text{C}_2\text{H}_4 + \text{C}_2\text{H}_6$	1.400E+12	0.0	0.0
$\text{C}_2\text{H}_4 + \text{M} = \text{C}_2\text{H}_2 + \text{H}_2 + \text{M}$	3.000E+17	0.0	79350.0
$\text{C}_2\text{H}_4 + \text{M} = \text{C}_2\text{H}_3 + \text{H} + \text{M}$	2.970E+17	0.0	96560.0
$\text{C}_2\text{H}_4 + \text{OH} = \text{C}_2\text{H}_3 + \text{H}_2\text{O}$	1.807E+13	0.0	5941.0
$\text{C}_2\text{H}_4 + \text{O} = \text{CH}_3 + \text{HCO}$	1.117E+08	1.44	530.0
$\text{C}_2\text{H}_4 + \text{O} - \text{CH}_2 + \text{HCO} + \text{H}$	2.073E+08	1.44	530.0
$\text{C}_2\text{H}_4 + \text{H} = \text{C}_2\text{H}_3 + \text{H}_2$	1.000E+14	0.0	15009.0
$\text{C}_2\text{H}_4 + \text{H} = \text{C}_2\text{H}_5$	1.051E+14	-0.5	655.0
$\text{C}_2\text{H}_4 + \text{O}_2 = \text{C}_2\text{H}_3 + \text{HO}_2$	4.000E+13	0.0	61500.0
$\text{C}_2\text{H}_4 + \text{C}_2\text{H}_4 = \text{C}_2\text{H}_5 + \text{C}_2\text{H}_3$	5.000E+14	0.0	64700.0
$\text{C}_2\text{H}_4 + \text{CH}_3 = \text{C}_2\text{H}_3 + \text{CH}_4$	4.280E+11	0.0	11114.0
$\text{C}_2\text{H}_3 = \text{C}_2\text{H}_2 + \text{H}$	1.574E+43	-9.589	48492.0
$\text{C}_2\text{H}_3 + \text{HO}_2 - \text{CH}_3 + \text{CO} + \text{OH}$	3.000E+13	0.0	0.0
$\text{C}_2\text{H}_3 + \text{OH} = \text{C}_2\text{H}_2 + \text{H}_2\text{O}$	3.000E+13	0.0	0.0
$\text{C}_2\text{H}_3 + \text{H} = \text{C}_2\text{H}_2 + \text{H}_2$	3.000E+13	0.0	0.0
$\text{C}_2\text{H}_3 + \text{O} = \text{CH}_3 + \text{CO}$	3.000E+13	0.0	0.0
$\text{C}_2\text{H}_3 + \text{O}_2 = \text{CH}_2\text{O} + \text{HCO}$	4.000E+12	0.0	-250.0
$\text{C}_2\text{H}_3 + \text{CH} = \text{CH}_2 + \text{C}_2\text{H}_2$	5.00E+13	0.0	0.0
$\text{C}_2\text{H}_3 + \text{CH}_3 = \text{C}_2\text{H}_2 + \text{CH}_4$	3.910E+11	0.0	0.0
$\text{C}_2\text{H}_3 + \text{C}_2\text{H}_6 = \text{C}_2\text{H}_4 + \text{C}_2\text{H}_5$	1.500E+13	0.0	10000.0
$\text{C}_2\text{H}_3 + \text{C}_2\text{H} = \text{C}_2\text{H}_2 + \text{C}_2\text{H}_2$	3.000E+13	0.0	0.0
$\text{C}_2\text{H}_3 + \text{HCO} = \text{C}_2\text{H}_4 + \text{CO}$	9.034E+13	0.0	0.0
$\text{C}_2\text{H}_3 + \text{CH}_2\text{O} = \text{C}_2\text{H}_4 + \text{HCO}$	5.420E+03	2.81	5862.0
$\text{C}_2\text{H}_3 + \text{C}_2\text{H}_3 = \text{C}_2\text{H}_2 + \text{C}_2\text{H}_4$	1.084E+13	0.0	0.0

REACTION	A	β	E
$C_2H_2 = C_2H + H$	2.373E+32	-5.28	130688.0
$C_2H_2 + O_2 = HCCO + OH$	2.000E+07	1.5	30100.0
$C_2H_2 + O_2 = C_2H + HO_2$	1.210E+13	0.0	74520.0
$C_2H_2 + HO_2 = CH_2 + CO + OH$	1.508E+11	0.0	7948.0
$C_2H_2 + OH = C_2H + H_2O$	2.710E+13	0.0	10500.0
$C_2H_2 + OH = CH_2CO + H$	2.192E-04	4.5	-1000.0
$C_2H_2 + H = C_2H + H_2$	7.830E+00	3.2	477.0
$C_2H_2 + O = CH_2 + CO$	2.896E+06	2.09	1560.0
$C_2H_2 + O = HCCO + H$	4.344E+06	2.09	1560.0
$C_2H_2 + CH_3 = C_2H + CH_4$	1.800E+11	0.0	17290.0
$C_2H + OH = HCCO + H$	2.000E+13	0.0	0.0
$C_2H + O = CO + CH$	1.000E+13	0.0	0.0
$C_2H + O_2 = CO + HCO$	2.410E+12	0.0	0.0
$CH_2CO + M = CH_2 + CO + M$	3.600E+15	0.0	59270.0
$CH_2CO + O_2 = CH_2O + CO_2$	2.000E+13	0.0	61500.0
$CH_2CO + HO_2 = CH_2O + CO + OH$	6.000E+11	0.0	12738.0
$CH_2CO + OH = HCCO + H_2O$	7.500E+12	0.0	2000.0
$CH_2CO + O = CH_2 + CO_2$	1.760E+12	0.0	1349.0
$CH_2CO + O = HCCO + OH$	1.000E+13	0.0	8000.0
$CH_2CO + H = CH_3 + CO$	3.715E+13	0.0	3660.0
$CH_2CO + H = HCCO + H_2$	5.000E+13	0.0	8000.0
$CH_2CO + CH_3 = C_2H_5 + CO$	1.000E+12	0.0	3000.0
$CH_2CO + CH_2 = C_2H_4 + CO$	2.000E+12	0.0	3000.0
$HCCO + M = CH + CO + M$	6.000E+15	0.0	58821.0
$HCCO + OH = HCO + CO + H$	1.000E+13	0.0	0.0
$HCCO + O = CO + CO + H$	1.930E+14	0.0	590.0
$HCCO + H = CH_2 + CO$	1.500E+14	0.0	0.0
$HCCO + O_2 = CO_2 + CO + H$	1.400E+09	1.0	0.0
$HCCO + CH_2 = C_2H + CH_2O$	1.000E+13	0.0	2000.0
$HCCO + CH_2 = C_2H_3 + CO$	3.000E+13	0.0	0.0
$HCCO + CH = C_2H_2 + CO$	5.00E+13	0.0	0.0
$HCCO + HCCO = C_2H_2 + 2CO$	1.00E+13	0.0	0.0

Third-body efficiencies:

$f_{H_2O}=16$, $f_{C_2O}=3.75$, $f_{CO}=1.875$, $f_{H_2}=2.5$, $f_{CH_4}=f_{C_2H_6}=f_{C_2H_4}=f_{C_2H_2}=16$;

Session 5

THEORETICAL CONSIDERATIONS

AEROTHERMODYNAMIC LIMITS OF RAM ACCELERATOR OPERATION

C. Knowlen
University of Washington
Seattle, WA, U.S.A.

ABSTRACT

Ram accelerator operation has proven to be a reliable means for launching projectiles to velocities well over 2 km/sec in the 38 mm bore facility at the University of Washington.¹⁻³ Propulsion cycle analyses indicate that useful thrust levels can be sustained at velocities above 7 km/sec;⁴⁻⁶ however, experiments at the UW facility are restricted to approximately 3 km/sec due to the limitations of the initial launcher and the length and pressure rating of the test section.⁷ Even though the ultrahigh velocities are not attainable with the current facility, essential investigations of ram accelerator operating characteristics are being conducted in the corresponding Mach number regimes. Understanding the velocity limiting mechanisms in the range of 2 to 3 km/sec will facilitate the engineering of ram accelerator systems capable of launching large payloads at near orbital velocities.

Fundamental studies of the effects of propellant energetics on ram accelerator performance have helped determine several mechanisms that limit the peak velocity of a given projectile configuration.⁸⁻¹¹ High resolution pressure measurements of the transient flow fields of projectiles in the process of unstating have shown that projectile canting is often a precursor.^{12,13} The projectile's geometry and materials have also been varied in experiments designed to distinguish between unstart inducing phenomena that are gas dynamic and structural in nature.^{14,15} Computational and analytical investigations of aerodynamic heat transfer indicate that parts of the thin-walled projectiles will reach the melting temperature of aluminum and magnesium alloys within the typical 10 msec duration of the experiment.¹⁶⁻¹⁹

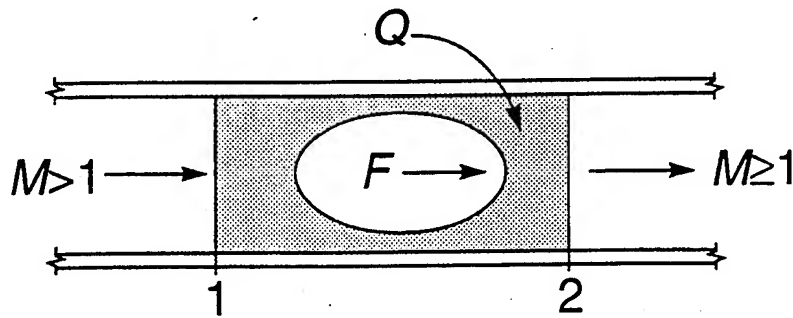
Theoretical considerations indicate that for all propellant mixtures there is a limiting velocity at which the ram accelerator thrust is exactly balanced by the projectile drag. One-dimensional, quasi-steady Hugoniot analysis indicates that the thrust goes to zero when the flow leaving the vicinity of the projectile is at the Mach number corresponding to the flow behind a Chapman-Jouguet or oblique detonation wave traveling at the projectile Mach number.^{20,21} Equating the work done by the projectile drag force to the maximum work output possible for a ram accelerator propulsive cycle provides another approach to estimating the peak operating velocity of a given propellant mixture.^{22,23} Experiments in which the projectile coasted at constant velocity for several meters are presented and the applicability of these velocity limiting theories is discussed.

REFERENCES

1. Hertzberg, A., Bruckner, A.P., and Bogdanoff, D.W., "Ram Accelerator: A New Chemical Method for Accelerating Projectiles to Ultrahigh Velocities," *AIAA Journal*, Vol. 26, 1988, pp. 195-203.
2. Bruckner, A.P., Knowlen, C., Hertzberg, A., and Bogdanoff, D.W., "Operational Characteristics of the Thermally Choked Ram Accelerator," *J. Propulsion and Power*, Vol. 7, 1991, pp. 828-836.
3. Hertzberg, A., Bruckner, A.P., and Knowlen, C., "Experimental Investigation of Ram Accelerator Propulsion Modes," *Shock Waves*, Vol. 1, 1991, pp. 17-25.
4. Knowlen, C., Bogdanoff, D.W., Bruckner, A.P., and Hertzberg, A., "Performance Capabilities of the Ram Accelerator," AIAA Paper 87-2152, AIAA/SAE/ASME/ASEE 23rd Joint Propulsion Conference, June 1987.
5. Brackett D.C. and Bogdanoff D.W., "Computational investigation of oblique detonation ramjet-in-tube concepts," *J Propulsion and Power*, Vol. 5, 1988, pp. 276-281
6. Yungster S. and Bruckner A.P., "Computational Studies of a Superdetonative Ram Accelerator Mode," *J Propulsion and Power*, Vol. 8, 1992, pp. 457-463.
7. Knowlen, C., Li, J.G., Hinkey, J., and Dunmire, B., "University of Washington Ram Accelerator Facility," Proc. of 42nd Meeting of the Aeroballistic Range Association, Adelaide, Australia, October 22-25, 1991.
8. Higgins, A.J., Knowlen, C., and Bruckner, A.P., "An Investigation of Ram Accelerator Gas Dynamic Limits," AIAA Paper 93-2181, AIAA/SAE/ASME/ASEE 29th Joint Propulsion Conference, June 1993.
9. Higgins A.J., Gas Dynamic Limits of the Ram Accelerator, MSAA Thesis, University of Washington, 1993.
10. Knowlen, C., Higgins, A.J., and Bruckner, A.P., "Investigation of Operational Limits to the Ram Accelerator," AIAA Paper 94-2967, AIAA/SAE/ASME/ASEE 30th Joint Propulsion Conference, June 1994.
11. Knowlen, C., Higgins, A.J., and Bruckner, A.P., "Aerothermodynamics of the Ram Accelerator," AIAA Paper 95-0289, 33rd Aerospace Sciences Meeting and Exhibit, January 1995.
12. Hinkey, J.B., Burnham, E.A., and Bruckner, A.P., "Investigation of Ram Accelerator Flow Fields Induced by Canted Projectiles," AIAA Paper 93-2186, June 1993.
13. Hinkey, J.B., An Experimental and Numerical Investigation of the Three-Dimensional Flow Field About a Ram Accelerator Projectile, Ph.D. Dissertation, University of Washington, March 1994.
14. Imrich, T.S., The Impact of Projectile Geometry on Ram Accelerator Performance, MSAA Thesis, University of Washington, June 1995.
15. Imrich, T.S., Elvander, J., and Bruckner, A.P., "Effect of Projectile Geometry on Ram Accelerator Performance," 2nd International Workshop on Ram Accelerators, July 1995.

16. Naumann, K.W., "Heating and Ablation of Projectiles During Acceleration in a Ram Accelerator Tube," AIAA Paper 93-2184, AIAA/SAE/ASME/ASME 29th Joint Propulsion Conference, June 1993.
17. Seiler, F. and Naumann, K.W., "Bow Shock Heating and Ablation of a Sharp-Nosed Projectile Flying at Supersonic Velocity Inside a Ram Accelerator," 19th International Symposium on Shock Waves, Marseille, France, July 1993.
18. Chew, G. and Bruckner, A.P., "A Computational Study of Projectile Nose Heating in the Ram Accelerator," AIAA Paper 94-2964, AIAA/SAE/ASME/ASME 30th Joint Propulsion Conference, June 1994.
19. Chew, G., Projectile Nose Heating in the Ram Accelerator, Ph.D. Dissertation, University of Washington, June 1995.
20. Knowlen, C., Theoretical and Experimental Investigation of the Thermodynamics of the Thermally Choked Ram Accelerator, Ph.D. Dissertation, University of Washington, 1991
21. Knowlen, C. and Bruckner, A.P., "A Hugoniot Analysis of the Ram Accelerator," Shock Waves, edited by K. Takayama, Springer-Verlag, Berlin, 1992, pp. 617-622.
22. Lee, J.H.S., "On the Initiation of Detonation by a Hypersonic Projectile," Zeldovich Memorial Conference on Combustion, Voronovo, Russia, September 1994.
23. Rom, J., "Analysis of the Initiation of Detonation on a Hypervelocity Projectile and It's Maximum Velocity in the External Propulsion Accelerator," TAE No. 729, Technion-Israel Institute of Technology, Israel, December 1994.

Derivation of the Thrust Equation



Mass:

$$p_1 M_1 \sqrt{\frac{\gamma_1}{R_1 T_1}} = p_2 M_2 \sqrt{\frac{\gamma_2}{R_2 T_2}}$$

Momentum:

$$1 + \gamma_1 M_1^2 + \frac{F}{p_1 A} = \frac{p_2}{p_1} (1 + \gamma_2 M_2^2)$$

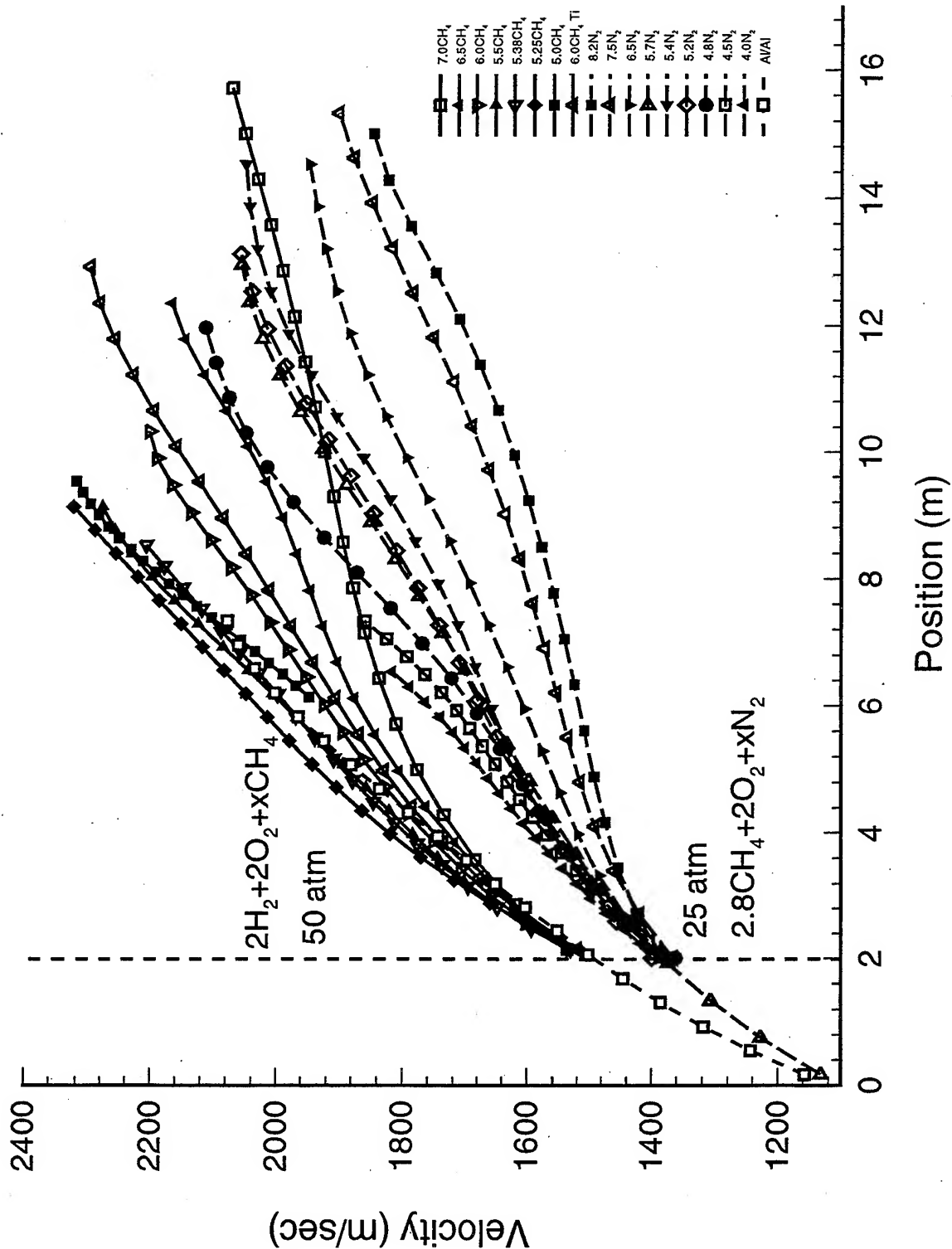
Energy:

$$c_{p_1} T_1 \left(\frac{h_1}{c_{p_1} T_1} + \frac{\gamma_1 - 1}{2} M_1^2 + \frac{\Delta q}{c_{p_1} T_1} \right) = c_{p_2} T_2 \left(\frac{h_2}{c_{p_2} T_2} + \frac{\gamma_2 - 1}{2} M_2^2 \right)$$

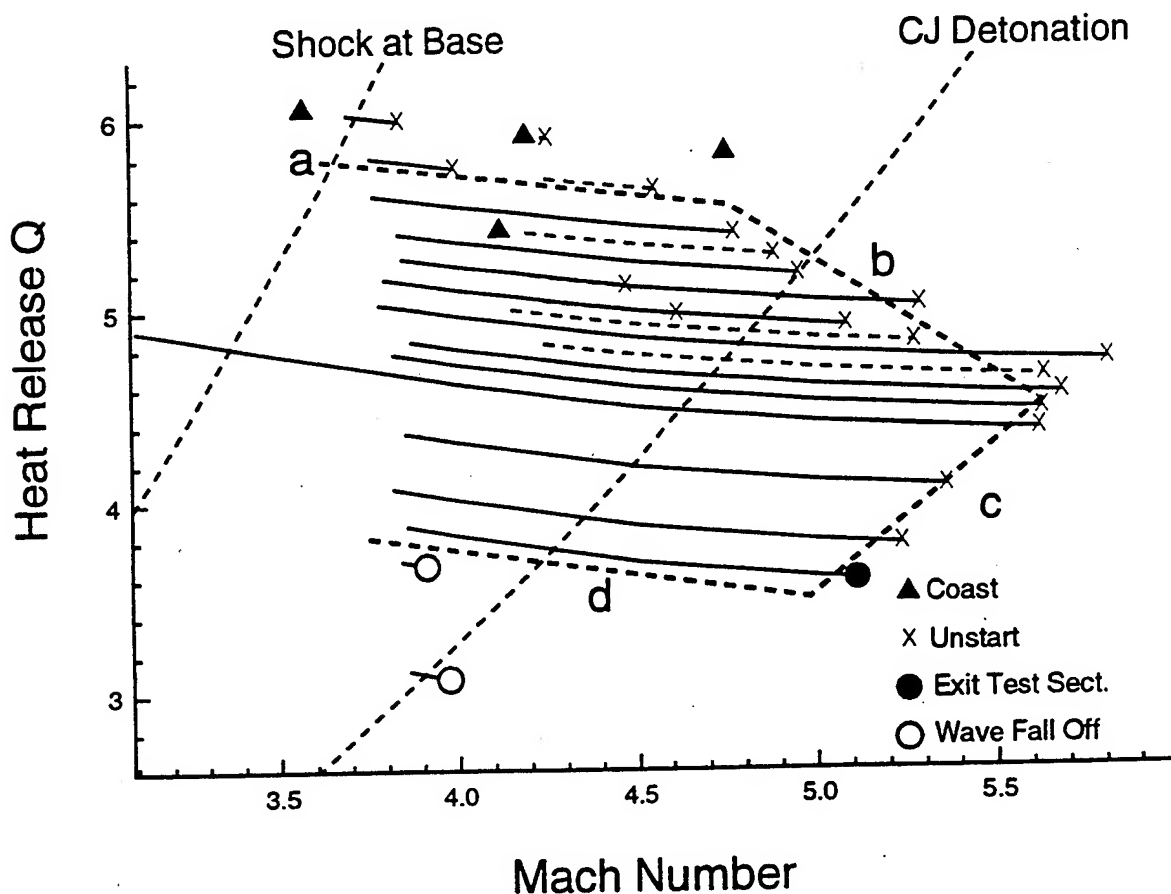
Thrust Equation:

$$\frac{F}{p_1 A} = \frac{M_1 \gamma_1}{M_2 \gamma_2} \sqrt{\left(\frac{\gamma_2 - 1}{\gamma_1 - 1} \right) \frac{\frac{h_1}{c_{p_1} T_1} + \frac{\gamma_1 - 1}{2} M_1^2 + Q}{\frac{h_2}{c_{p_2} T_2} + \frac{\gamma_2 - 1}{2} M_2^2}} (1 + \gamma_2 M_2^2) - (1 + \gamma_1 M_1^2)$$

Velocity-Distance Data for Variable Propellant Dilution



Observed Limits to the Ram Accelerator



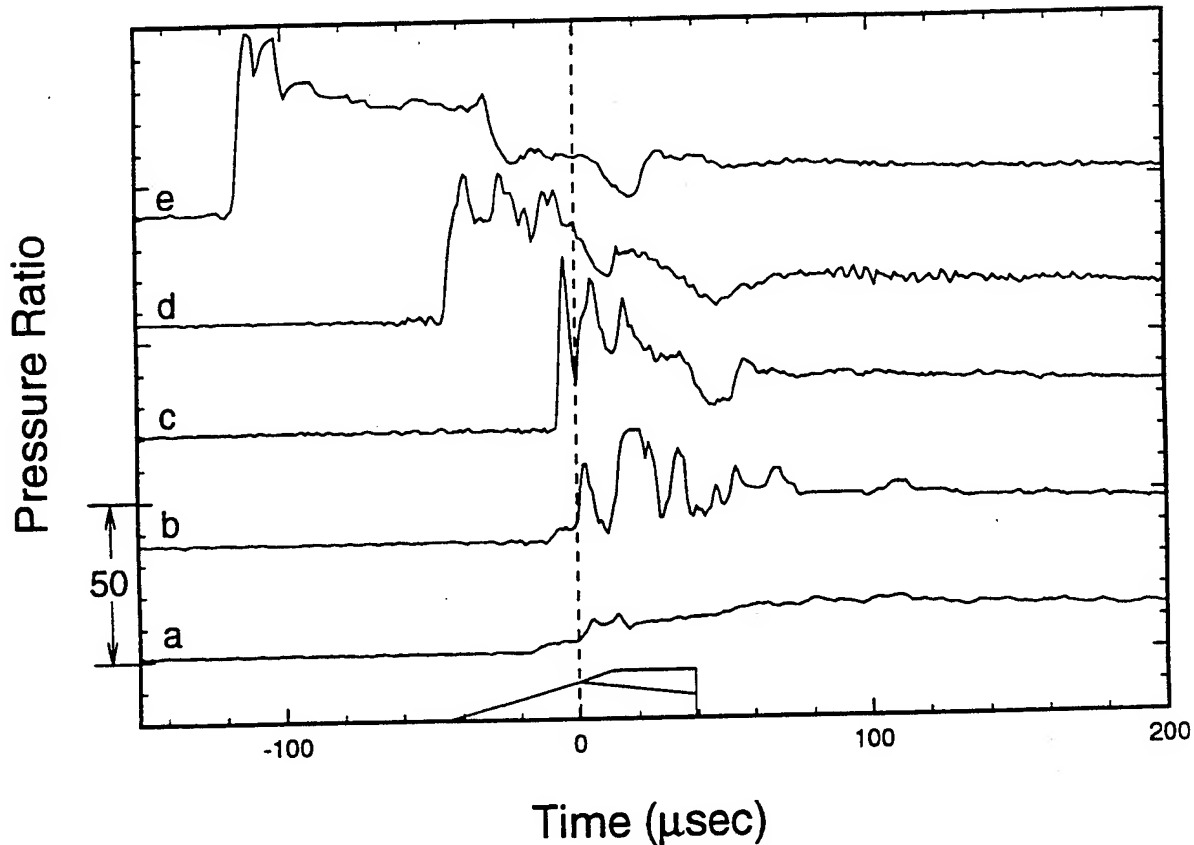
a maximum heat release

b maximum velocity for projectile with combustion wave attached

c not purely gas dynamic phenomena

d minimum heat release required to support combustion

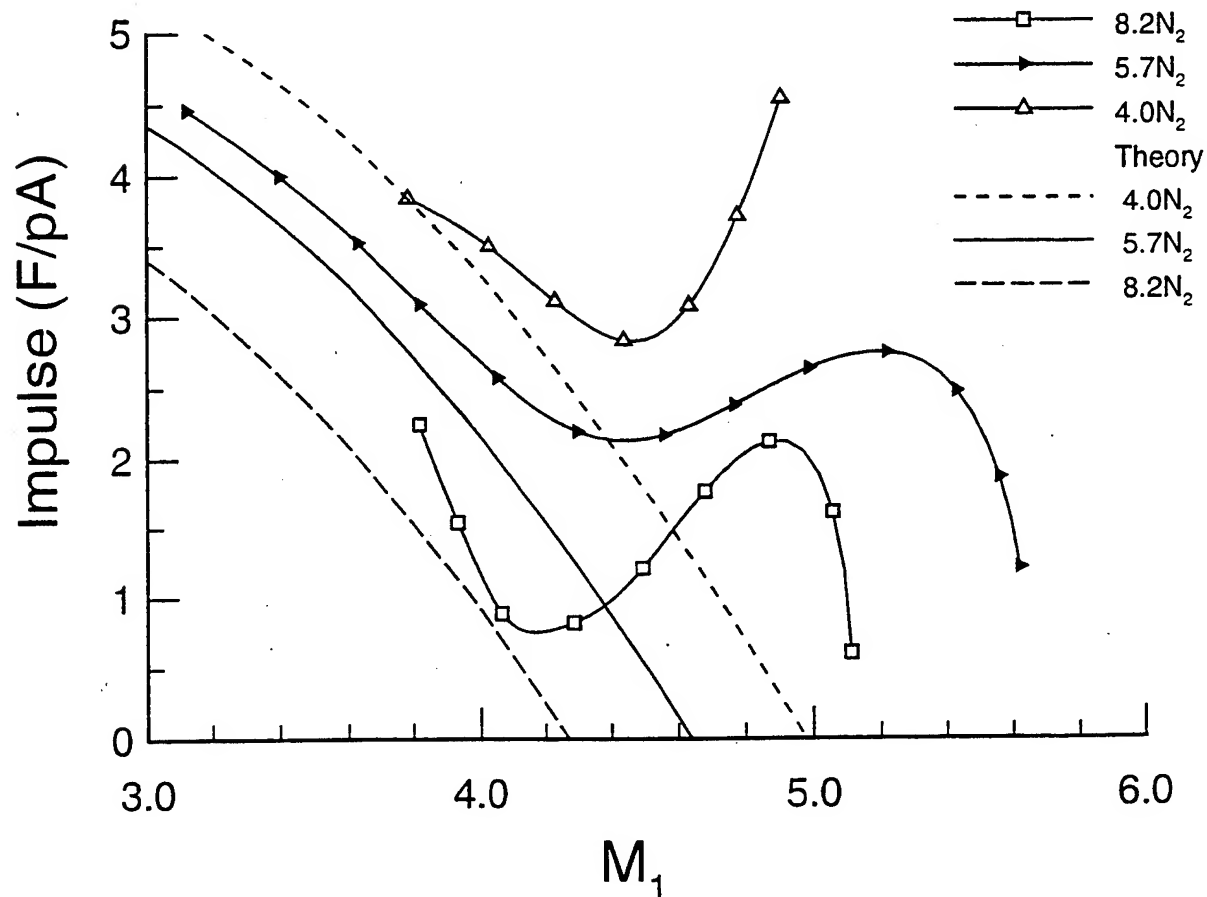
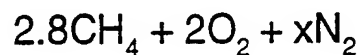
Evolution of an Unstart



Attempts to operate in more energetic mixtures often result in an unstart.

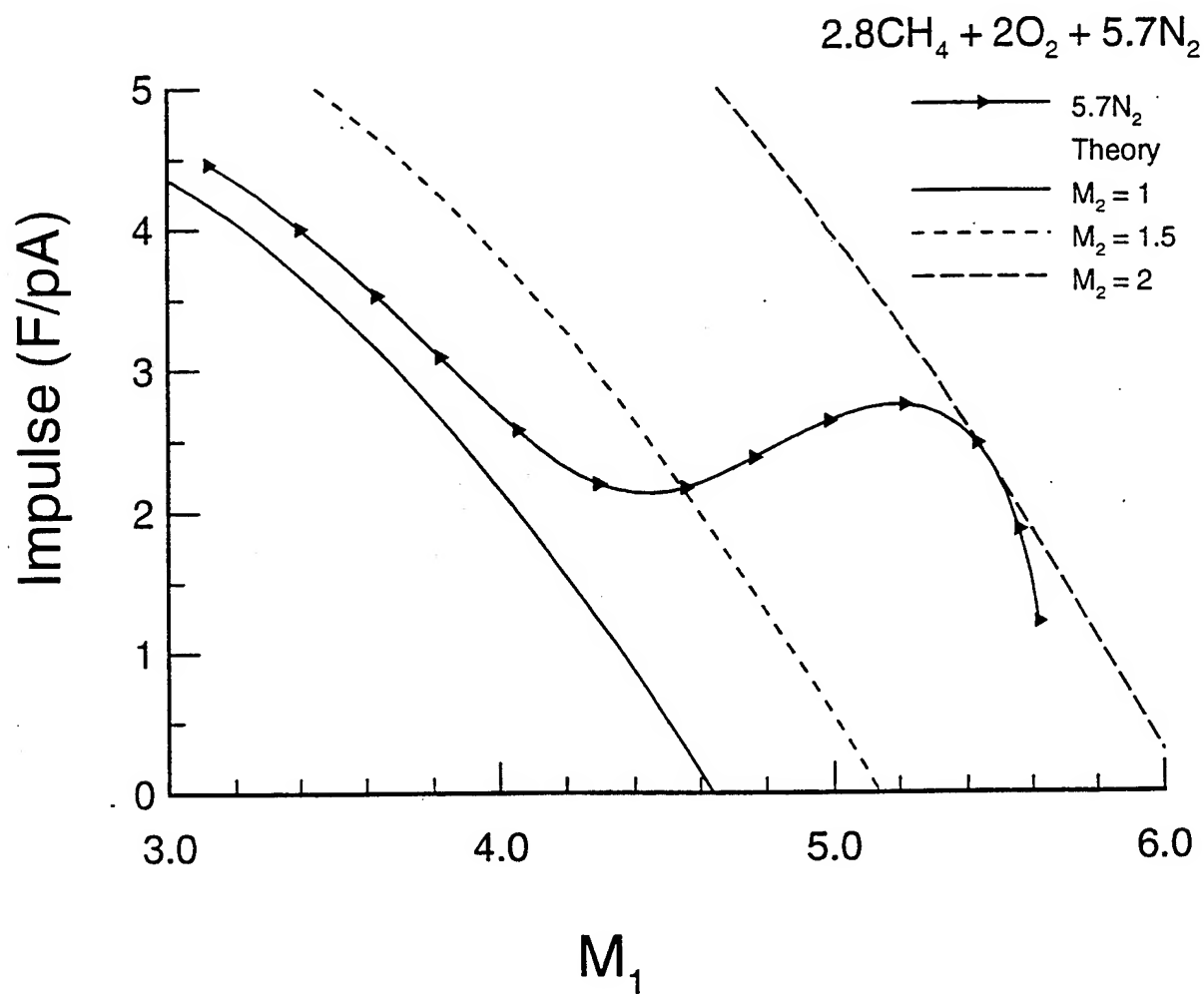
An unstart is seen here in pressure traces from tube wall.

Thrust-Mach Profiles for Variable Dilution



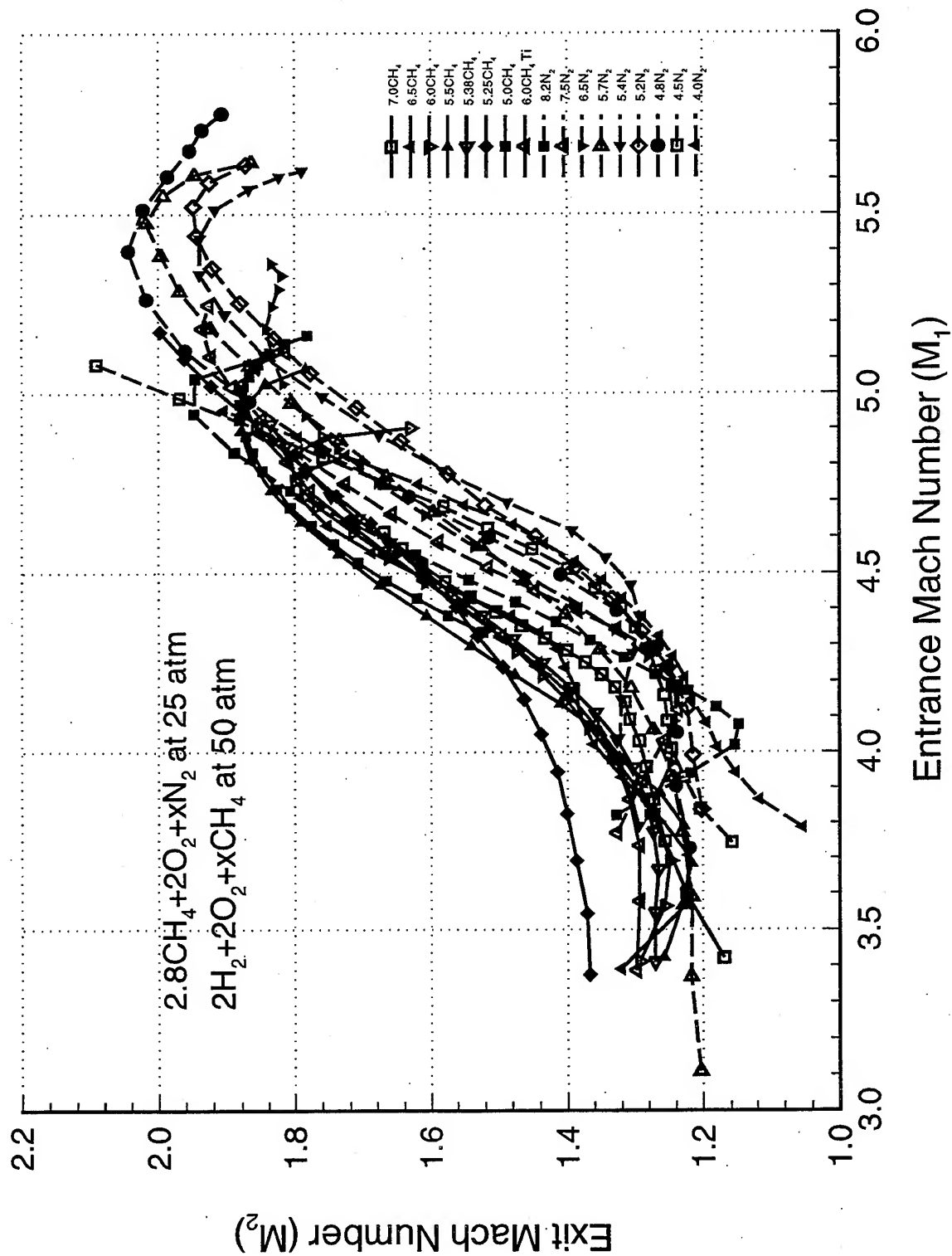
Theory determined for thermally choked exit flow.

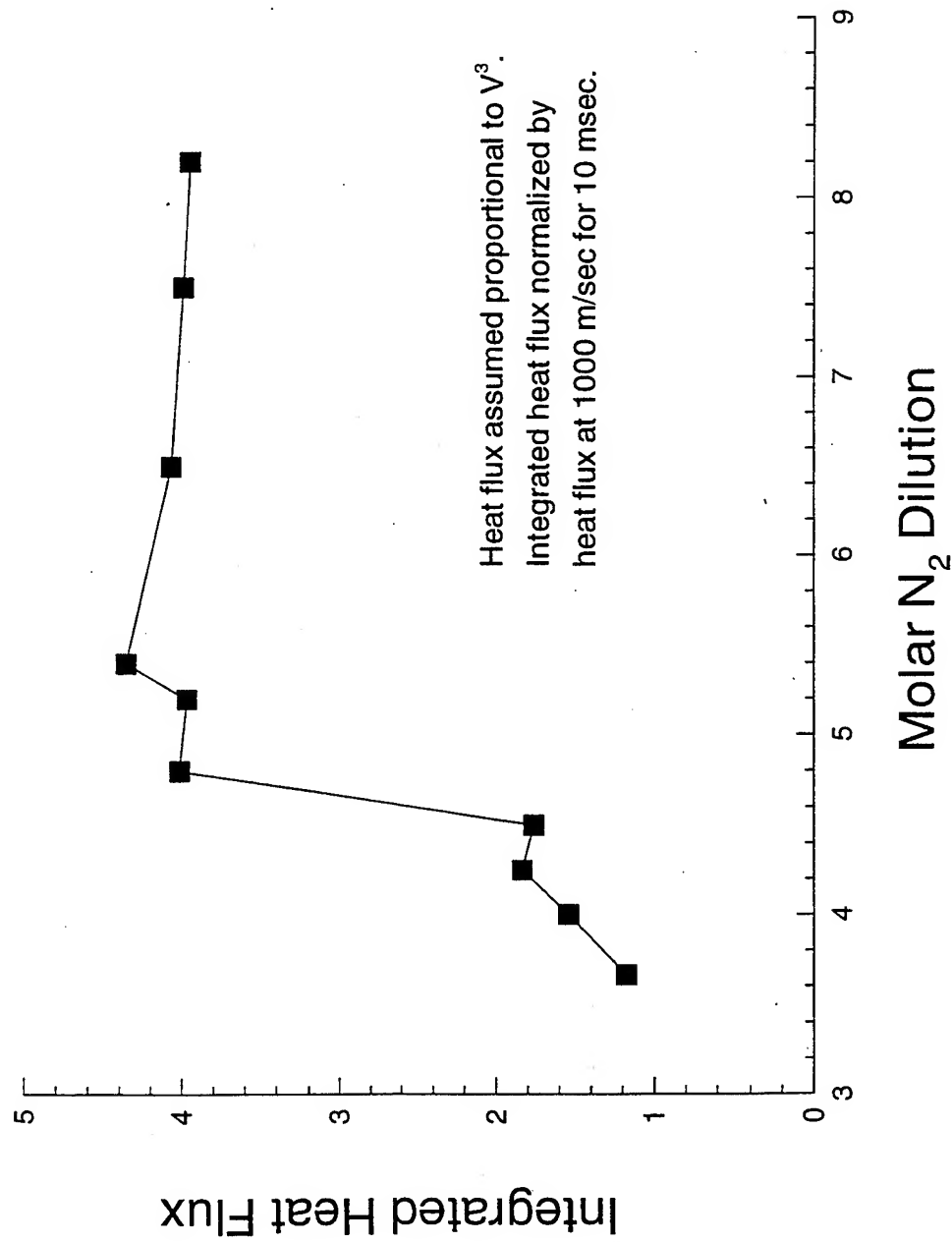
Thrust-Mach Profiles for Various M_2

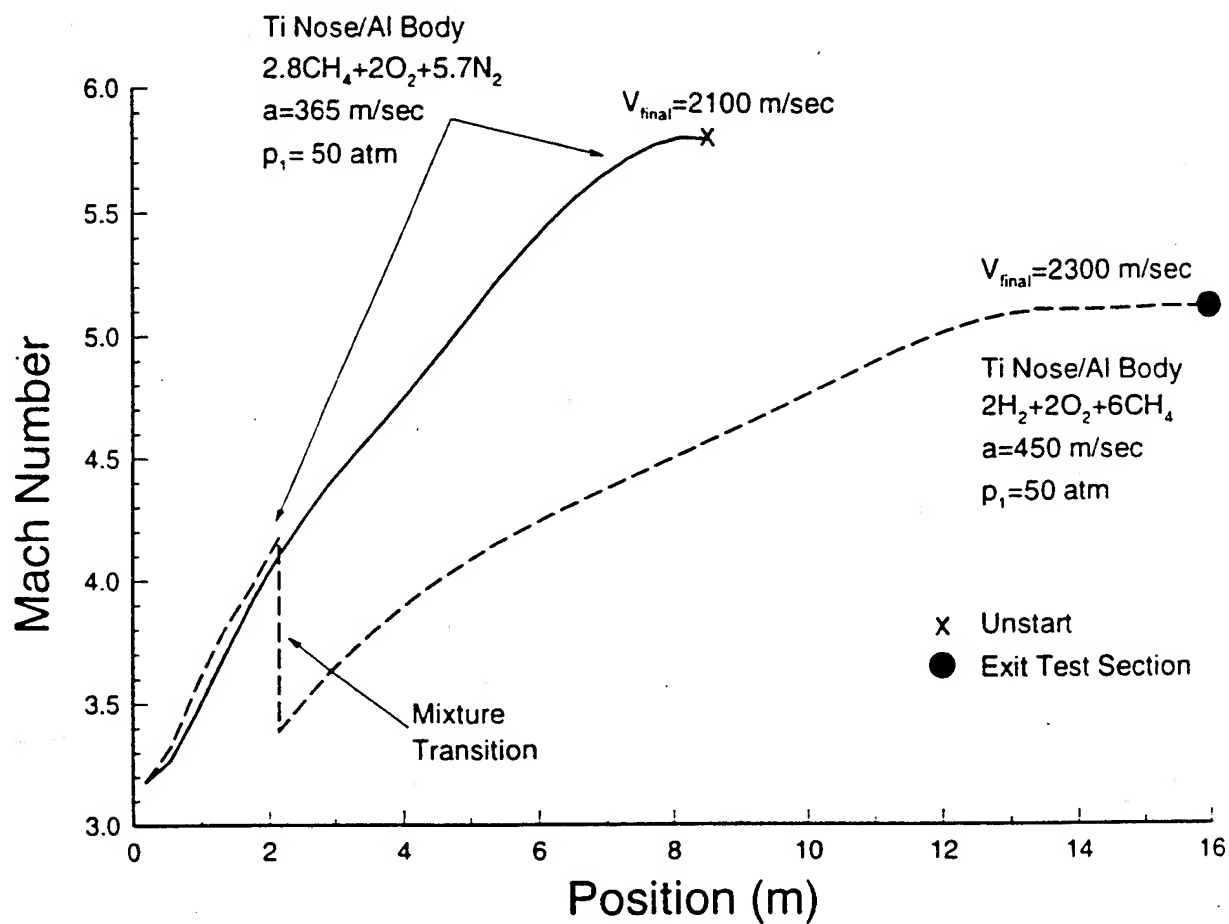


Exit flow in thermodynamic equilibrium for given M_2 .

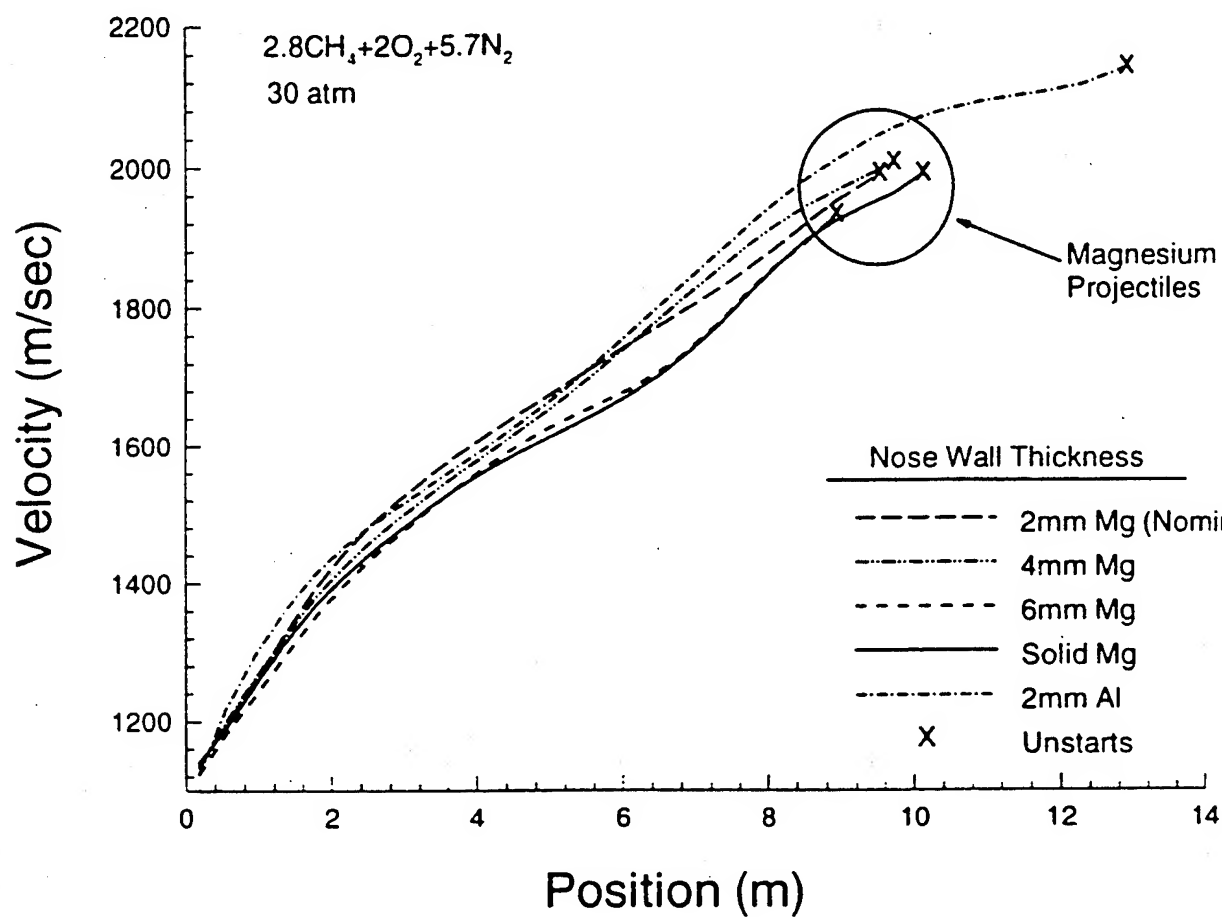
Exit Mach vs Entrance Mach for Variable Dilution







Mach-position histories for two projectiles in mixtures with differing sound speeds.



Velocity-position histories for projectiles with different nose wall thicknesses.

REAL GAS EFFECTS ON THE OPERATING ENVELOPE OF THE RAM ACCELERATOR

Pascal Bauer [§] and Carl Knowlen
Aerospace and Energetics Research Laboratory
University of Washington, Box 352250
Seattle, WA 98195-2250, USA

ABSTRACT

The analysis of ram accelerator performance is based on one-dimensional modelling of the flow process that propels the projectile. The conservation equations are applied to a control volume travelling with the projectile, and quasi steady flow is assumed. When the flow is leaving the control volume at sonic velocity, this modelling yields results that are in good agreement with the experimental observations.^{1,2,3}

To date the solutions obtained, namely the generalized Hugoniot and the thrust equation, have been based on the ideal gas assumption. At the high level of pressure that is encountered during the ram accelerator process, this assumption can not be regarded as adequate. Thus a more appropriate equation of state (EOS) should be used instead. Depending upon the level of pressure, several equations of state are available for dense gaseous energetic materials.⁴ The virial type of EOS can be more or less sophisticated, depending upon the extent of complexity of the intermolecular modelling.^{5,6} It turns out to be totally appropriate for most gaseous explosives mixtures that have been investigated at moderate initial pressures,^{7,8} i.e., less than $p_0=10$ MPa. As soon as the initial pressure exceeds this value, this EOS is no longer valid and a more sophisticated one is needed.⁹ Of course when dealing with most energetic systems, a powerful thermochemical computation program is required. This is the aim of the QUARTET code that was used in this investigation,^{10,11} especially for determining chemical equilibrium composition.¹²

In the present case the Boltzmann EOS was applied.¹³ It is based on very simplified molecular interactions which makes it relatively easy to use in calculations. Moreover, the energetic EOS needs to be taken into account. This concerns all the calorimetric coefficients, as well as the thermodynamic parameters which can not be expressed anymore as only a function of temperature. The higher the pressure level, the more sophisticated these corrections, but the main relationships that account for real gas effects are basically the same. These include the use of a general form of analytical operators applied to correct the thermodynamic functions and coefficients.¹⁴

The equations governing the one-dimensional modelling were taken as a basis for the real gas corrections. They were solved in an analytical way. The parameters which play a most crucial role in this correction may thus be highlighted. A complete set of equations, involving the real gas effects are presented in this paper. This more accurate model can better predict the projectile acceleration of the thermally choked propulsive mode. Although the present analysis is applied to the fuel rich Methane/Oxygen/Nitrogen mixture currently used in the ram accelerator experiments,^{15,16} its general formulation makes it readily applicable to any other mixture. The projectile velocity and acceleration histories determined by the Hugoniot analysis for the thermally choked ram accelerator mode, assuming a Boltzmann EOS, turn out to be in much better agreement with experimental observations up to the CJ detonation velocity.

[§] Current address: Laboratoire de Combustion et Détonique
ENSMA - CNRS - University of Poitiers - Futuroscope, France

REFERENCES

1. C. Knowlen, "Theoretical and Experimental Investigation of the Thermodynamics of the Thermally Choked Ram accelerator" PhD dissertation, University of Washington, USA, 1991
2. C. Knowlen, and A.P. Bruckner, "A Hugoniot Analysis of the Ram accelerator", Proc. of the 18th Int. Symposium on Shock Waves, Sendai, Japan, July 21-26, 1991
3. A.P. Bruckner, J.B. Hinkey, E.A. Burnham, and C. Knowlen, "Investigation of 3-D Reacting Flow Phenomena in a 38 mm Ram Accelerator", Proc. of the First Int. Workshop on Ram Accelerator RAMAC I, French German Research Institute (ISL), Saint Louis, France
4. W. Byers Brown, and A. Amaee, "Review of Equations of State of Fluids Valid to High Densities", Report # 39/1992, Dept of Chemistry, University of Manchester, U.K., 1992
5. P. Bauer, H.N. Presles, O. Heuzé, and C. Brochet, "Equation of State for Dense Gases", Archivum Combustionis, 5, 1, 1985, pp. 315-320
6. O. Heuzé, "Equations of State of Detonation Products", Phys. Rev., 34(1), 1986, pp. 428-432
7. P. Bauer, "Contribution a l'Etude de la Detonation de Melanges Explosifs Gazeux a Pression Elevée", Thèse de Doctorat ès Sciences, Université de Poitiers, France, 1985
8. P. Bauer, H.N. Presles, O. Heuzé, and J.F. Legendre, "Prediction of Detonation Characteristics of Dense Gaseous Explosives on the Basis of Virial Equation of State", Proc. of 20th Int. Pyrotechnics Seminar, Colorado Springs, CO, USA, July 25-29, 1994
9. P. Bauer, M. Dunand and H.N. Presles, "Detonation Characteristics of Methane Oxygen and Nitrogen at Extremely High Initial Pressures", 12th ICDERS, AIAA, Progress in Aeronautics and Astronautics, Vol. 133, 1991, pp. 56-62
10. O. Heuzé, P. Bauer, H.N. Presles, and C. Brochet, "Equations of State For Detonation Products and their Incorporation into the Quatuor Code", Proc. of the 8th Symp. (Int.) on Detonation, 1986, pp. 762-769
11. O. Heuzé, P. Bauer, and H.N. Presles, "Quatuor: A Thermochemical Code for Computing Thermodynamic Properties of Detonation and Combustion Products", 12th Int. Pyrotechnics Seminar, Ed. SERIEP, Paris, France, 1987, pp. 91-96
12. O. Heuzé, H.N. Presles, and P. Bauer, "Computation of Chemical Equilibria", J. Chem. Phys., 38, 9, 1985, pp. 4734-4737
13. P. Bauer, and C. Brochet, "Properties of Detonation Waves in Hydrocarbon-Oxygen-Nitrogen Mixtures at High Initial Pressures", 8th ICOGERS, AIAA, Progress in Aeronautics and Astronautics, Vol. 87, 1983, pp. 231-243

14. O. Heuzé, P. Bauer and H.N. Presles, "Compressibility and Thermal Properties of Gaseous Mixtures at a High Temperature and High Pressure", High Temperatures, High Pressures, 19, 1987, pp. 611-620
15. M. Giraud, J.F. Legendre, and G. Simon, "RAMAC 90: Experimental Studies and Results in 90 mm Caliber Length 108 Calibers", Proc. of the First Int. Workshop on Ram Accelerator RAMAC I, French German Research Institute (ISL), Saint Louis, France
16. D.L. Kruczynski, "Analysis of Firings in a 120 mm Ram Accelerator at High Pressures", Proc. of the First Int. Workshop on Ram Accelerator RAMAC I, French German Research Institute (ISL), Saint Louis, France

EQUATION OF STATE

General form of the equation of state (EOS) of the combustion (or detonation) products:

$$pv = \sigma RT$$

THERMODYNAMIC EQUATION OF STATE

Enthalpy: $H^{rg}(p, T, x_1, x_2, \dots, x_n) = H^{ig}(T, x_1, x_2, \dots, x_n) + \tilde{H}(p, T, x_1, x_2, \dots, x_n)$

Int. energy: $U^{rg}(V, T, x_1, x_2, \dots, x_n) = U^{ig}(T, x_1, x_2, \dots, x_n) + \tilde{U}(V, T, x_1, x_2, \dots, x_n)$

where \tilde{H} and \tilde{U} are the imperfect, residual or excess term. These are the corrections which will be affected by the EOS:

$$\tilde{H} = V - T \left(\frac{\partial V}{\partial T} \right)_p \quad \tilde{U} = T \left(\frac{\partial p}{\partial T} \right)_V - p$$

THERMODYNAMIC PROPERTIES

Heat capacities ratio: $\gamma = \frac{c_p}{c_v}$

Sound speed: $a^2 = \Gamma RT$ with R : universal gas constant related to 1 kg of mixture

and $\Gamma = - \left(\frac{\partial \ln p}{\partial \ln V} \right)_S = f(\gamma, p, T, x_i)$ (Adiabatic gamma)

IMPULSE OF THE PROPULSIVE CYCLE OF THE RAMAC

ASSUMPTION # 1: IDEAL GAS

$$I = \frac{\gamma_1}{\gamma_6} \frac{M_1}{M_6} (1 + \gamma_6 M_6^2) \sqrt{\left(\frac{\gamma_6 - 1}{\gamma_1 - 1} \right) \frac{Q + 1 + \frac{\gamma_1 - 1}{2} M_1^2}{1 + \frac{\gamma_6 - 1}{2} M_6^2}} - (1 + \gamma_1 M_1^2)$$

$$\text{with } \sigma = 1 \quad ; \quad \frac{h}{c_p T} = 1$$

ASSUMPTION # 2: IDEAL GAS (but thermally real)

$$I = \frac{\gamma_1}{\Gamma_6} \frac{M_1}{M_6} (1 + \Gamma_6 M_6^2) \sqrt{\left(\frac{\Gamma_6 - 1}{\gamma_1 - 1} \right) \frac{Q + \frac{H_1}{c_{p1} T_1} + \frac{\gamma_1 - 1}{2} M_1^2}{\frac{H_6}{c_{p6} T_6} + \frac{\Gamma_6 - 1}{2} M_6^2}} - (1 + \gamma_1 M_1^2)$$

$$\text{with } \sigma = 1 \quad ; \quad \frac{h}{c_p T} \neq 1 \quad ; \quad \Gamma_6 = \gamma_6 \left(1 - \frac{V}{n} \frac{\partial n}{\partial V} \right)_T \quad (\text{where } n = \sum x_i)$$

ASSUMPTION # 3: REAL GAS

$$I = \sigma \sqrt{\frac{M_1}{M_6} \frac{\gamma_1}{\Gamma_6} \frac{R_6}{R_1} \frac{c_{p1}}{c_{p6}}} \sqrt{\frac{Q + \frac{H_1}{c_{p1} T_1} + \frac{\gamma_1 - 1}{2} M_1^2}{\frac{H_6}{c_{p6} T_6} + \frac{\Gamma_6 R_6 M_6^2}{2 c_{p6}}} \left(1 + \frac{\Gamma_6 M_6^2}{\sigma} \right) - (1 + \gamma_1 M_1^2)}$$

$$\text{with } \sigma \neq 1 \quad ; \quad \frac{h}{c_p T} \neq 1 \quad ; \quad \Gamma_6 = \gamma_6 \left(1 - \frac{V}{\sigma} \frac{\partial \sigma}{\partial V} \right)_T - \frac{V}{n} \frac{\partial n}{\partial V} \bigg|_T$$

$$\text{and } h_6 = h_6^{id} + \tilde{h}_6$$

APPLICATION

In this range of pressure, i.e. $0.1 \text{ MPa} < p_0 < 6 \text{ MPa}$, the most appropriate EOS is the BOLTZMANN EOS:

$$pv = \sigma RT$$

where:

$$\sigma = 1 + \frac{b}{v} + 0.625\left(\frac{b}{v}\right)^2 + 0.287\left(\frac{b}{v}\right)^3 + 0.193\left(\frac{b}{v}\right)^4 + O\left(\left(\frac{b}{v}\right)^n\right)$$

High order terms expressed in $O\left(\left(\frac{b}{v}\right)^n\right)$ are neglected and molecular interactions are described by the following law:

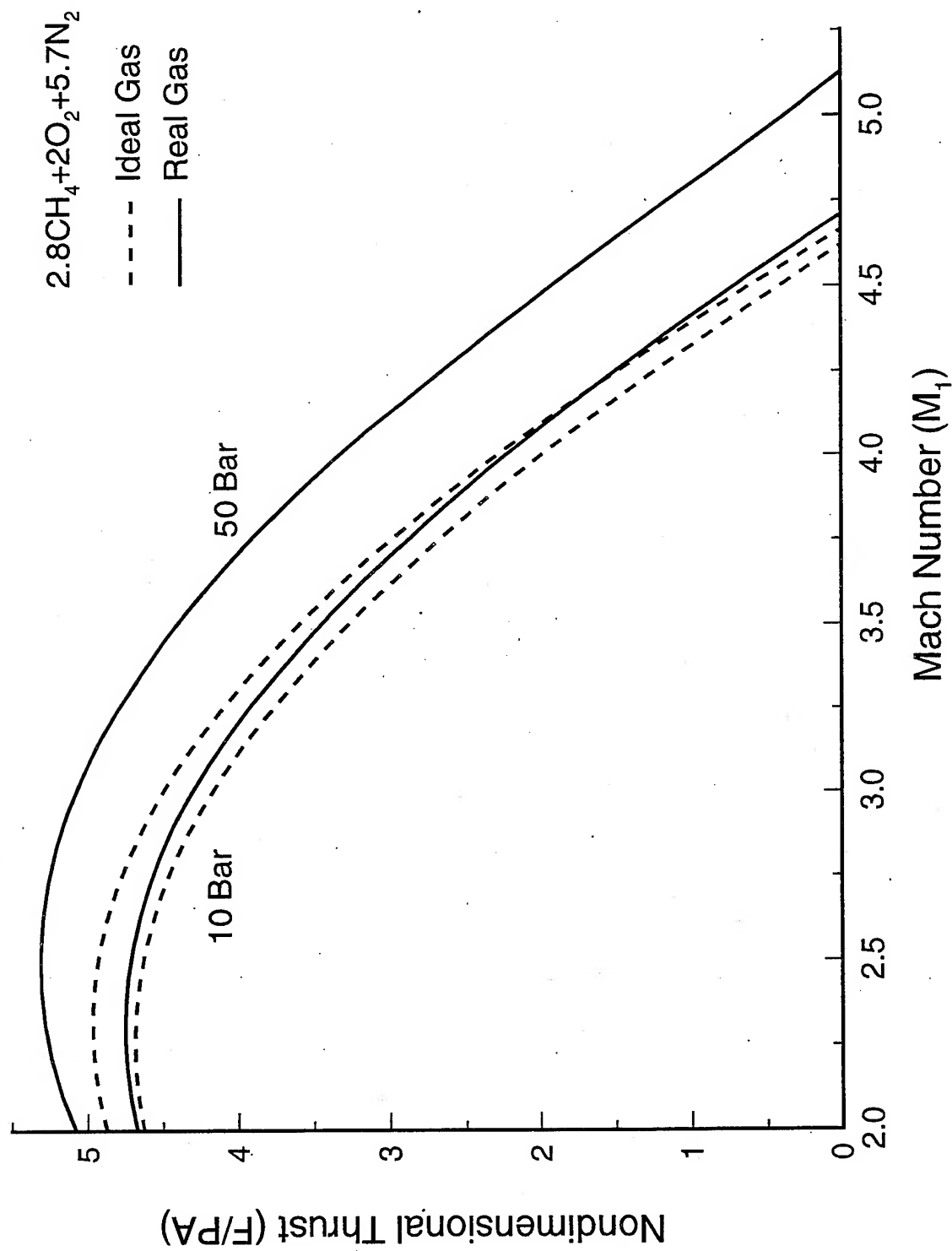
with $b = \sum x_i b_i$

This particular form of the EOS yields:

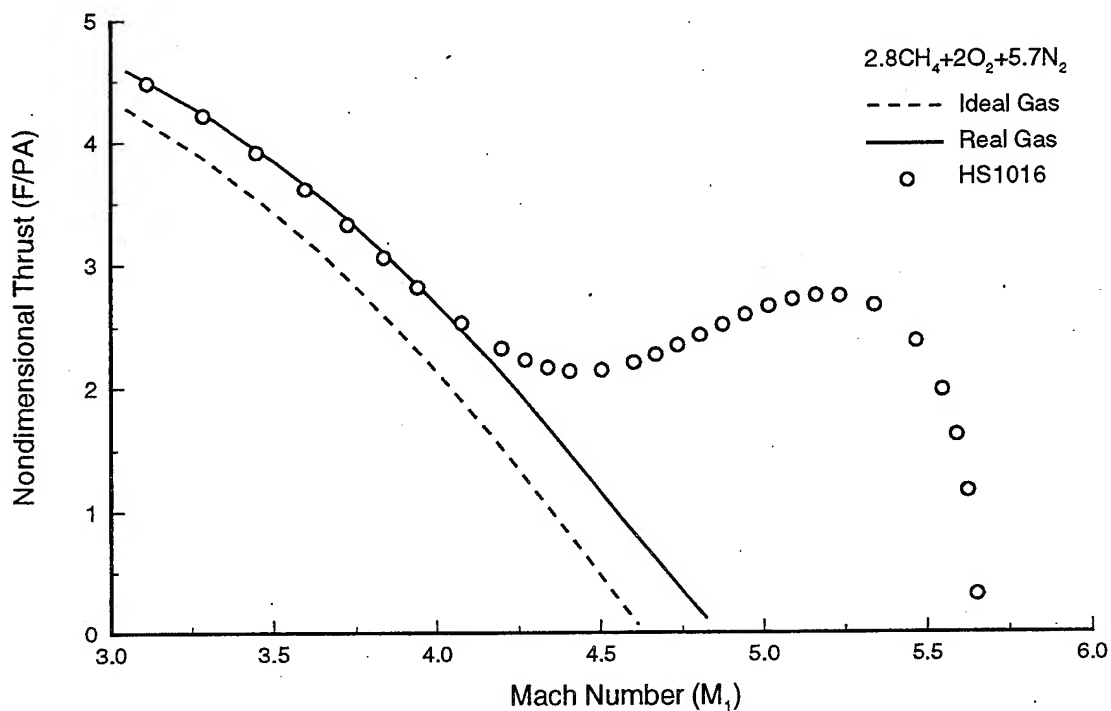
$$\tilde{U} = 0 \quad \text{and} \quad \tilde{H}(p, T, x_1, x_2, \dots, x_n) = (\sigma - 1)RT$$

Impulse can thus be readily calculated.

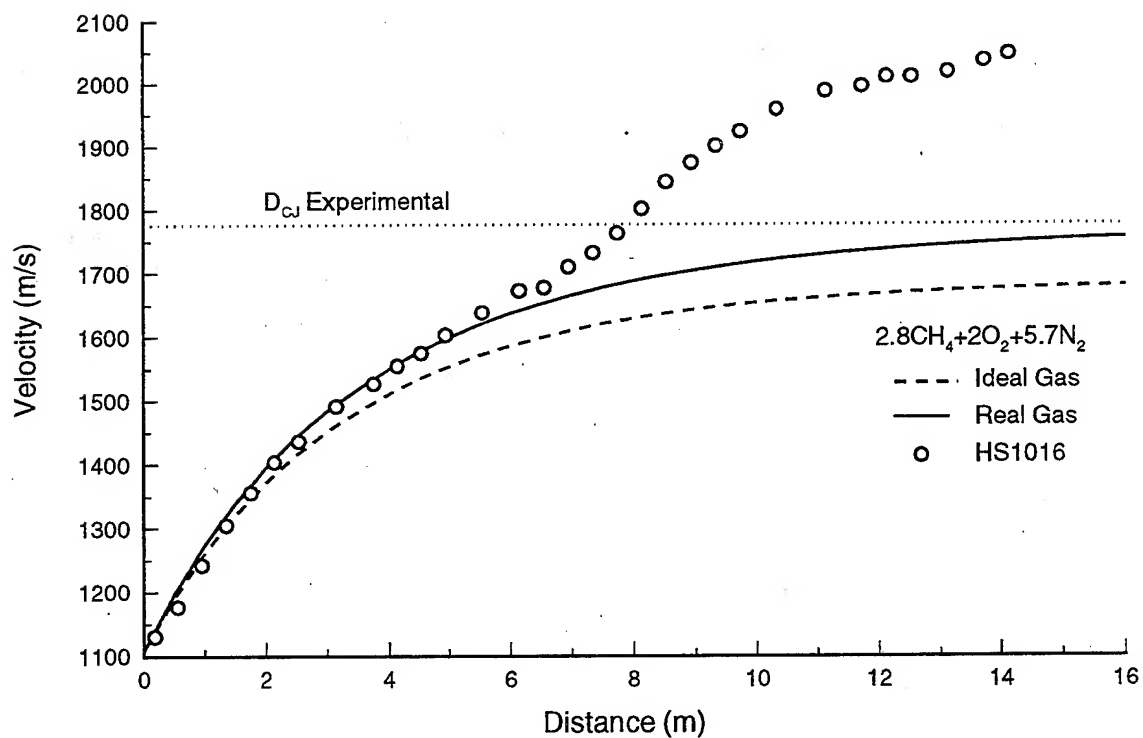
Thrust vs Mach Number for Ideal and Real Gas EOS



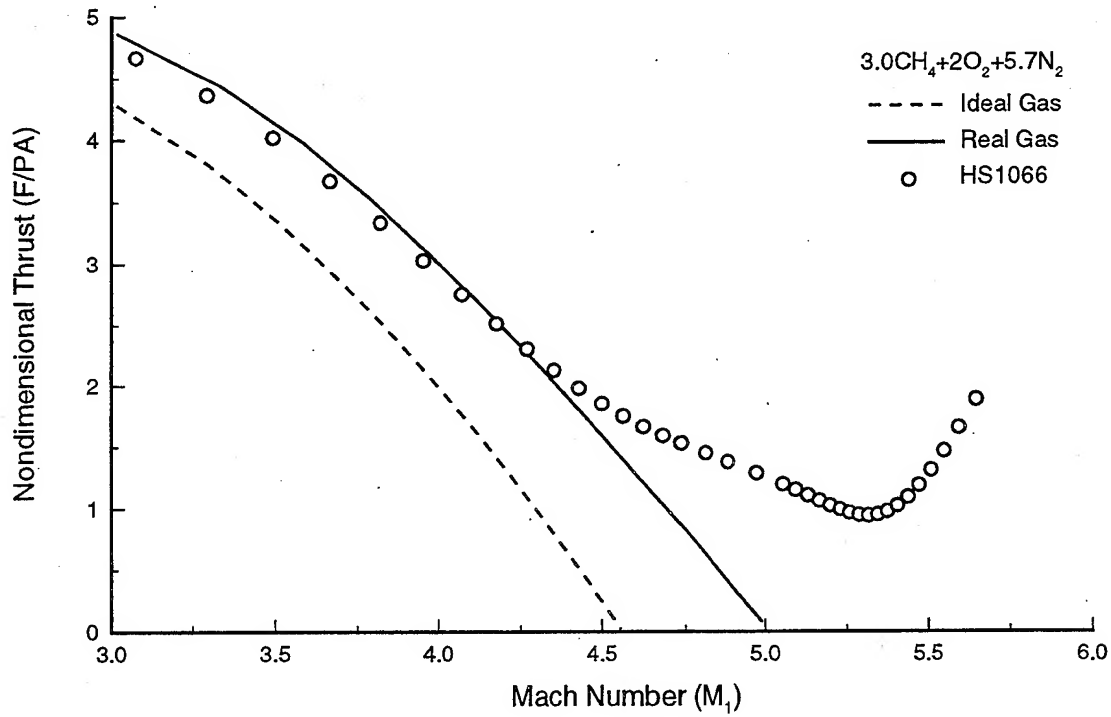
Thrust vs Mach Number for Theory and Experiment at 25 Bar



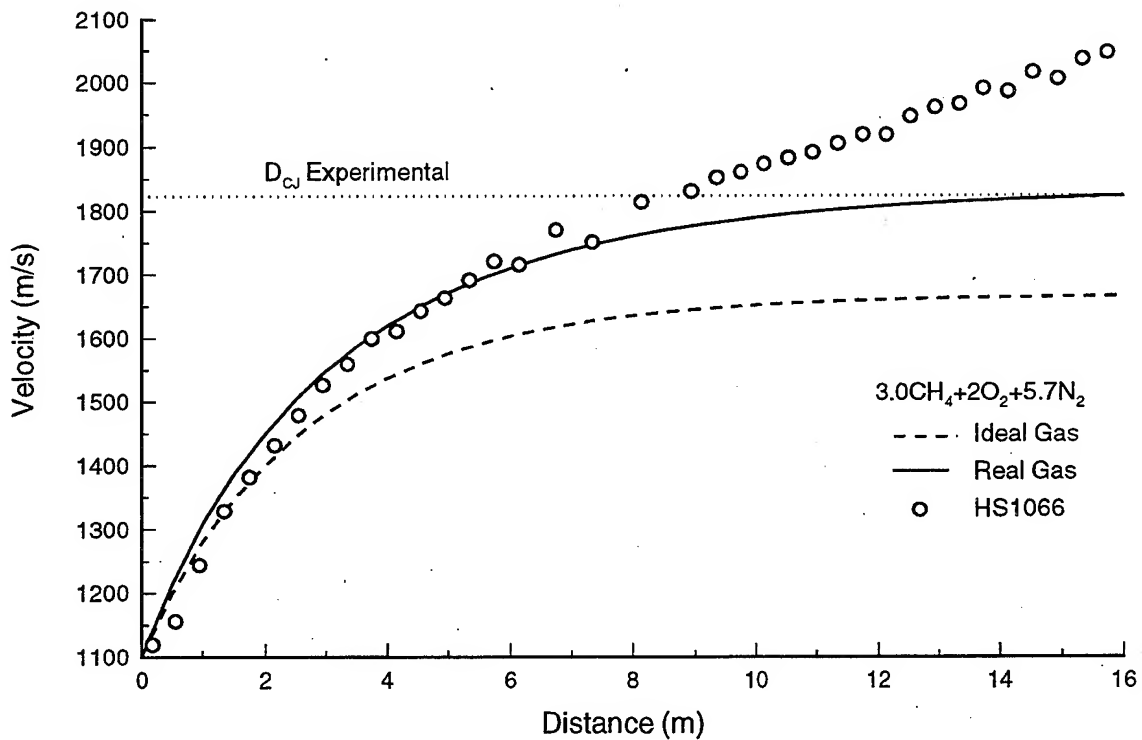
Velocity vs Distance for Theory and Experiment at 25 Bar



Thrust vs Mach Number for Theory and Experiment at 50 Bar



Velocity vs Distance for Theory and Experiment at 50 Bar



The Effects of Real Material Behavior on Ram Accelerator Performance

Federico Liberatore

Propulsion and Flight Division, Weapons Technology Directorate

U.S. Army Research Laboratory, AMSRL-WT-PA

Aberdeen Proving Ground, MD 21005-5066

ABSTRACT

Recent firings of the HIRAM facility at Aberdeen Grounds produced evidence strongly implying ablation of projectiles which were of either all-aluminum or mixed aluminum/magnesium construction. Beyond the immediate concern of loss of projectile structural integrity caused by ablation, there is the issue of impact on projectile performance caused by the introduction of aluminum and/or magnesium into the reacting freestream.

The modifications needed to attempt to accurately analyze the situation using an existing one-dimensional equilibrium chemistry code are discussed. It is found that the changes to the gas dynamic equations are minor and solution of the equations should present little problem once the mass flow rate of metal into the freestream is known. Calculating the mass flow rate of metal into the freestream is found to be a more difficult problem because of complex physics and uncertainties of material properties, particularly liquid metal properties.

The existing one-dimensional equilibrium chemistry performance code is used to ascertain the significance of the performance changes caused by increasing levels of metal introduced into typical HIRAM reactants, fuel rich methane, oxygen, and nitrogen mixtures of moderate energy release values, $3.5 \leq \frac{\Delta q}{C_p T_1} \leq 5.4$. Without knowing the exact rates of projectile material loss, various levels of rate of material loss are assumed (0%, 1%, 5%, 10%, and 25% over a fixed distance of two accelerator tube lengths) so that comparisons can be made. Examination of the results reveals that the change in energy release value caused by introduction of metal as a reactant is not excessive. The increase in equilibrium temperature brought about by increasing amounts of reacting metal can be dramatic, pushing combustion temperatures to $3000^\circ K$ and above for cases of very high metal loss rates (as would be expected in total projectile failure and consummation). Very low loss rates (1%) were found to cause temperature increases great enough to have a serious impact on the kinetics of the fuel mixture.

NOMENCLATURE

A	area
F	thrust
H	enthalpy
Δh_{fg}	enthalpy of evaporation
h	convective heat transfer coefficient
k	thermal conductivity
L	latent heat of fusion
\dot{m}	mass flow rate
P	pressure
q''	heat flux
T_i	initial temperature
T_f	melting temperature
T_{ev}	evaporation temperature
t	time
U	velocity in axial direction
V	velocity in transverse direction
v_i	velocity of liquid-gas interface
v_s	velocity of liquid-solid interface
y	vertical dimension
α	thermal diffusivity
δ	thermal penetration depth
ε	metal vapor to gas mass flow rate ratio
ρ	density

INTRODUCTION

Overview

Recent firings of the HIRAM facility have shown evidence of the aluminum and magnesium material used in projectile construction burning. The use of these materials has long been questioned for purely structural reasons. The consequence of metal erosion is the introduction of another reactant into the fuel mixture. The effect of adding another reactant to the nominal fuel mixture has, to date, not been investigated.

The expense of operating a large-bore facility puts a premium on utilizing results obtained from smaller facilities such as those given in Reference 1. The HIRAM projectile has been found to be operable over a limited range of energy release values and the sensitivity to energy release rates is only now being quantified. The presence of an unaccounted reactant could very possibly cause the resulting fuel mixture to have undesirable characteristics. The purpose of this paper is twofold; 1) describe a methodology for analyzing the problem using an existing one-dimensional equilibrium chemistry performance code and 2) use the existing code to attempt to explain the recent failures.

Fluid Mechanical Governing Equations

Figure 1 shows a diagram of the control volume describing the problem. The major departure from previously reported analyses is the secondary stream crossing the control surface that envelopes the projectile. This is the flux of metal that occurs when projectile material ablates. The existing one-dimensional equations have to be modified to include mass, momentum, and energy that cross the control surface.

It should be apparent that the momentum equation presents a complication to the analysis. It would be reasonable to assume that the metal vapor leaves the projectile in a direction normal to the surface. This assumption would then require the addition of a surface integral term with a variable integrand in the momentum equation. A simplification can be achieved if the projectile is assumed to be a flat plate as shown in Figure 2. The flat plate geometry would give equal flux streams on top and bottom that have no component in the axial direction.

The expression for continuity is given by Equation 1.

$$\rho_1 U_1 A_1 + \rho \cdot V \cdot A \cdot = \rho_2 U_2 A_2 \quad (1)$$

Note that $V \cdot$ is perpendicular to the axial velocity and $A \cdot$ is the reference area of the flat plate. The entrance area, A_1 , is equal to the exit area, A_2 . The expression for momentum is given by Equation 2.

$$P_1 A_1 + \rho_1 U_1^2 + F = P_2 A_2 + \rho_2 U_2^2 \quad (2)$$

Because of the flat plate assumption and vertical only outflow velocity, the momentum equation is identical to the case of no outflow velocity. The expression for energy is given by equation (3).

$$\left(H_1 + \frac{U_1^2}{2} \right) \rho_1 U_1 A_1 + \left(H \cdot + \frac{V \cdot^2}{2} \right) \rho \cdot V \cdot A \cdot = \left(H_2 + \frac{U_2^2}{2} \right) \rho_2 U_2 A_2 \quad (3)$$

The continuity equation can be rearranged to help clarify the deviation from the more familiar no outflow case by dividing through by $\rho_1 U_1 A_1$ and defining a perturbation parameter.

$$1 + \varepsilon = \frac{\rho_2 U_2}{\rho_1 U_1} \quad \text{where} \quad \varepsilon = \frac{\rho \cdot V \cdot A}{\rho_1 U_1 A_1} \quad (4)$$

The perturbation parameter, ε , corresponds to the mass flow ratio of metal to gas. Continuity is now substituted into momentum and energy to give Equations 5 and 6.

$$\frac{P_2}{P_1} = \frac{1 + \frac{F}{AP_1}}{1 - \gamma_2 M_2^2 \left[\frac{\rho_2 / \rho_1}{(1 + \varepsilon)^2} - 1 \right]} \quad (5)$$

$$\left(H_2 + \frac{U_2^2}{2} \right) = \frac{\left(H_1 + \frac{U_1^2}{2} \right) + \left(H_\infty + \frac{V_\infty^2}{2} \right) \varepsilon}{1 + \varepsilon} \quad (6)$$

When $\varepsilon \rightarrow 0$, Equations 5 and 6 reduce to the governing equations used in Reference 2 to calculate ram accelerator thrust curves.

Heat Transfer with Phase Changes

Though it has not yet been done, the calculation of a thrust curve with the presence of the parameter ε does not appear to have any great difficulties. A more difficult problem is the calculation of ε which involves calculating the flow rate of metal into the freestream. The mass flow rate of metal crossing the control surface and entering the freestream will be determined by the amount of heat transfer into the projectile and the thermal properties of the material. The situation is shown schematically in Figure 3.

Heat flux into the projectile will raise the temperature of the projectile above its initial temperature, T_i . During the initial portion of the heating process, heating of the projectile results in the growth of the penetration depth. At some time, the penetration depth reaches the centerline of the plate which is, because of symmetry, an adiabatic surface. After the penetration depth extends to the plate centerline, the temperature of the centerline begins to rise above T_i . The temperature at the surface will continue to climb until the fusion temperature, T_f , is reached and then a melt layer will begin to propagate into the slab. Further heating will raise the temperature at the surface to the evaporation temperature, T_{ev} , and metal will then enter the free stream in

the gas phase. The mass flow rate of metal is then used to calculate the parameter, ϵ , allowing the fluid dynamic equations to be solved.

The situation just described is a complicated one and there are several problems that impact the accuracy of any calculated results. The freestream flow will certainly be turbulent so calculated heat transfer from the freestream into the projectile will be depend on the turbulence model used. The melt layer also presents a challenging problem. The freestream will be exerting a shearing stress on the fluid, so the melt layer will actually be flowing. The nature of the melt layer flow will depend on the applied shear stress, viscosity, and depth of the layer. Previous work reported in Reference 3 used the assumption that shear stress was so great that as soon as the material reached the liquid phase, ablation occurred. For the purpose of calculating material loss disregarding interaction with the flow field, this is a reasonable approach. However, if material interaction with the flow field is desired, it is necessary to continue the thermal analysis until the the metal evaporates because it will react in the gas phase.

An initial search did not obtain all the needed information on the properties of aluminum and magnesium in the liquid state. This might indicate that such information is not readily available or widely circulated. In the absence of data, assumptions need to be made about the conductivity and viscosity of liquid aluminum and magnesium and this introduces large uncertainties into the calculations. It might be necessary to use generalized property relations for liquids such as given in Reference 4 in order to estimate the needed information. As a first approximation, it seems reasonable to assume a small film height and relatively large viscosity suggesting, therefore, that the melt layer is a creeping flow. The portion of the problem that deals with heat transfer in the solid phase is purely conductive in nature and can probably be well characterized even with a simple analysis.

Attention will be focused on outlining a simplified analysis that can be used to calculate the mass flow rate of metal vapor into the ram accelerator freestream. The application of integral methods to various situations is covered extensively in Reference 5. It was previously speculated that the melt layer would be a creeping flow situation. In the interest of making the thermal analysis as simple as possible, it will be assumed that flow in the melt layer will have no impact on heat transfer so the problem will be reduced to one that is purely conductive in nature.

The governing equation for unsteady, conductive heat transfer is given by Equation 7.

$$\frac{\partial^2 T}{\partial y^2} = \frac{1}{\alpha} \frac{\partial T}{\partial t} \quad (7)$$

The simplifying assumption of constant properties is also made. Integrating both sides of Equation 7 from $y = 0$ to $y = \delta(t)$, the penetration depth of the temperature profile, gives the integral version of the heat transfer equation.

$$\left. \frac{\partial T}{\partial y} \right|_{y=\delta} - \left. \frac{\partial T}{\partial y} \right|_{y=0} = \frac{1}{\alpha} \left[\frac{\partial}{\partial t} \int_{y=0}^{y=\delta(t)} T dy - T \right]_{y=\delta(t)} \frac{d\delta(t)}{dt} \quad (8)$$

A cubic polynomial will be used to represent the temperature profile.

$$T(y,t) = a_1 + a_2 y + a_3 y^2 + a_4 y^3 \quad (9)$$

The constants of the polynomial expression will be determined by applying the necessary boundary and initial conditions.

The boundary conditions that apply at the initial stage of the problem are identical to those that apply to heat conduction into a semi-infinite solid. When the penetration depth reaches the midplane of the plate, it can no longer advance forward. At this point in time it will become necessary to solve the same governing equations with different boundary conditions. When a phase change temperature is reached, another change in boundary conditions occurs. In addition, a second temperature profile is needed for the liquid phase. The phase changes also involve fronts that advance into the the material. These relations are expressed by the following two equations

liquid-solid phase change:
$$\left[\begin{array}{c} \text{heat flux in} \\ \text{(liquid phase)} \end{array} \right] - \left[\begin{array}{c} \text{heat flux out} \\ \text{(solid phase)} \end{array} \right] = \left[\begin{array}{c} \text{heat absorbed} \\ \text{(melting)} \end{array} \right]$$

$$-k \left. \frac{\partial T}{\partial y} \right|_{liq} + k \left. \frac{\partial T}{\partial y} \right|_{sol} = \rho L v_s \quad (10)$$

liquid gas phase change:
$$\left[\begin{array}{c} \text{heat flux in} \\ \text{(gas phase)} \end{array} \right] - \left[\begin{array}{c} \text{heat flux out} \\ \text{(liquid phase)} \end{array} \right] = \left[\begin{array}{c} \text{heat absorbed} \\ \text{(evaporation)} \end{array} \right]$$

$$h (T_2 - T_{ev}) + k \left. \frac{\partial T}{\partial y} \right|_{liq} = \rho \Delta h_{fg} v_v \quad (11)$$

where L is the latent heat of fusion, Δh_{fg} is the heat of evaporation, v_s is the velocity of the liquid-solid interface, and v_v is the velocity of the gas-liquid interface. Performing a continuity balance on the gas-liquid interface gives the mass flow rate of metal vapor into the freestream.

$$\rho_1 v_1 A_1 = \rho V A. \quad (12)$$

At this moment, it is not certain that the integral heat transfer approach just outlined will actually be used. The use of a purely numerical approach will also be investigated and a decision on which to use will be based on their relative merits.

DISCUSSION

As previously mentioned, the modifications necessary to correctly include the flow of metal into the control volume have not yet been incorporated into the equilibrium chemistry performance code. Nevertheless, some preliminary calculations were made with the existing code in the interest of attempting to get some insight to the problem of magnesium and aluminum entering the freestream. The actual rate of metal erosion was not calculated so, instead, several different rates of steady erosion were assumed. The assumed erosion rates were 0%, 1%, 5%, 10%, and 25% projectile mass over two tube lengths (9 m). The mass of metal lost was added to the mass of the gas mixture in the same length of tubing and from this total mass of reactant, a modified mixture composition was used as the input to the equilibrium chemistry performance code. The initial temperatures used for the metal reactants were their respective evaporation temperatures which are 2770 °K for aluminum and 1380 °K for magnesium.⁶ Without going any further, it should be apparent that the relatively low evaporation temperature of magnesium might present serious problems when exposed to the combustion environment inside a ram accelerator.

Lumping the metal together with the gas reactants is equivalent to mixing the metal with the gas. Instead of forming a secondary stream into the control volume, the metal vapor enters the control volume at the entrance face (see Figure 1) with the same velocity as the gas reactants. Equations 4-6 are presented with ϵ as a perturbation parameter. As long as ϵ is sufficiently small, the true solution won't deviate much from the approximate solution.

Three different base methane, oxygen, nitrogen mixtures were investigated. These mixtures were chosen because they cover the range of energy release values that are normally used currently in ram accelerators, $3.5 \leq \frac{\Delta q}{C_p T_1} \Big|_{\text{det}} \leq 5.4$. A summary of the cases run is shown in Table 1. The measured weights of aluminum and magnesium standard geometry HIRAM projectiles (no isolators inserts) were used to calculate metal weight fractions.

Table 1: metal to gas reactant fractions for all calculations.

	3CH ₄ +2O ₂ +8.5N ₂ $\left. \frac{\Delta q}{C_p T_1} \right _{\text{det}} = 3.5$ $m_{\text{gas}} = 5.509 \text{ kg}$	3CH ₄ +2O ₂ +6N ₂ $\left. \frac{\Delta q}{C_p T_1} \right _{\text{det}} = 4.1$ $m_{\text{gas}} = 5.409 \text{ kg}$	3CH ₄ +2O ₂ +2.5N ₂ $\left. \frac{\Delta q}{C_p T_1} \right _{\text{det}} = 5.4$ $m_{\text{gas}} = 5.157 \text{ kg}$
Mg projectile 1% loss	$\frac{m_{\text{metal}}}{m_{\text{gas}}} = 0.0055$	$\frac{m_{\text{metal}}}{m_{\text{gas}}} = 0.0056$	$\frac{m_{\text{metal}}}{m_{\text{gas}}} = 0.0059$
Mg projectile 5% loss	$\frac{m_{\text{metal}}}{m_{\text{gas}}} = 0.0274$	$\frac{m_{\text{metal}}}{m_{\text{gas}}} = 0.0279$	$\frac{m_{\text{metal}}}{m_{\text{gas}}} = 0.0292$
Mg projectile 10% loss	$\frac{m_{\text{metal}}}{m_{\text{gas}}} = 0.0548$	$\frac{m_{\text{metal}}}{m_{\text{gas}}} = 0.0558$	$\frac{m_{\text{metal}}}{m_{\text{gas}}} = 0.0585$
Mg projectile 25% loss	$\frac{m_{\text{metal}}}{m_{\text{gas}}} = 0.1369$	$\frac{m_{\text{metal}}}{m_{\text{gas}}} = 0.1394$	$\frac{m_{\text{metal}}}{m_{\text{gas}}} = 0.1462$
Al projectile 1% loss	$\frac{m_{\text{metal}}}{m_{\text{gas}}} = 0.0077$	$\frac{m_{\text{metal}}}{m_{\text{gas}}} = 0.0079$	$\frac{m_{\text{metal}}}{m_{\text{gas}}} = 0.0083$
Al projectile 5% loss	$\frac{m_{\text{metal}}}{m_{\text{gas}}} = 0.0387$	$\frac{m_{\text{metal}}}{m_{\text{gas}}} = 0.0394$	$\frac{m_{\text{metal}}}{m_{\text{gas}}} = 0.0413$
Al projectile 10% loss	$\frac{m_{\text{metal}}}{m_{\text{gas}}} = 0.0774$	$\frac{m_{\text{metal}}}{m_{\text{gas}}} = 0.0788$	$\frac{m_{\text{metal}}}{m_{\text{gas}}} = 0.0827$
Al projectile 25% loss	$\frac{m_{\text{metal}}}{m_{\text{gas}}} = 0.1935$	$\frac{m_{\text{metal}}}{m_{\text{gas}}} = 0.1970$	$\frac{m_{\text{metal}}}{m_{\text{gas}}} = 0.2067$

The results of all the calculations performed are shown in Figures 4-15. The effect of metal addition to a base gas mixture is represented by 4 plots. The first plot shows energy release, $\frac{\Delta q}{C_p T_1}$, and thrust, $\frac{F}{AP_1}$, as functions of velocity with increasing levels of the first metal (magnesium). The second plot shows temperature ratio, $\frac{T_2}{T_1}$, as a function of velocity for the first metal. These two plots are then repeated for the second metal (aluminum). The entire sequence is then repeated for the other two gas mixtures.

Calculation of the aluminum thrust curves produced an unexpected problem. The program would only calculate a few points (out of 43) of the thrust curve and then stop because it was not able to converge on the solution (P,T) and that point. The curves for 5% aluminum loss with a mixture of 3C H₄ + 2O₂ + 6N₂, Figures 10 and 11, are entirely missing because the program was unable to converge on the first point, the Chapman-Jouget detonation point. It is believed that when a certain temperature was reached, a phase change was occurring within the equilibrium

combustion products and this caused the ideal gas based iteration scheme of the flow-solver to fail. While this problem is significant and warrants further investigation, it was decided to use the results obtained because the portions of the curves that were calculated were sufficient to support the trouble-free magnesium calculations.

The initial topic of concern regarding combustion of metal with ram-accelerator methane/oxygen/nitrogen fuel mixtures was that an inordinate amount of additional energy would be released and this would cause an unstart. Examination of the energy release vs velocity plots shows that energy release does rise but not excessively and, for aluminum, energy release reaches a maximum and decreases with larger percentages of aluminum erosion. The erroneous conclusion one could reach from studying only energy release calculations is that large percentages of metal erosion can be tolerated without provoking an unstart.

Energy release, however, is not the only factor that determines the successful operation of a ram accelerator projectile. Energy release rate also plays a significant role and was strongly believed to be responsible for the unstarts experienced in the latest series of firings of the HIRAM facility.^{7,8} Temperature was found to strongly affect the ignition delay time of a given mixture. An increase of 50 °K shortened the delay time of a mixture by 43%.⁸ The increase in average flow field temperature from 1350 °K to 1400 °K was caused by the use of helium as a diluent.⁸ Examination of the temperature plots shows that an approximate increase of 50 °K throughout the calculated velocity range caused by the loss of 1% mass of a magnesium projectile. The temperature gain from a loss of 1% of an aluminum projectile is approximately double. Equilibrium temperatures increase monotonically with increasing levels of metal reactant for the levels investigated in this study. The temperatures associated with a total projectile failure reach or exceed 3000 °K.

It is possible to piece together a plausible explanation for the unstarts observed in the latest series of HIRAM firings, shots 34-37. Shot 34 successfully used an all aluminum projectile flying through an methane/oxygen/nitrogen mixture. Shots 35 and 36 unstarted using all aluminum projectiles flying through helium diluted mixtures. Shot 37 unstarted using a composite aluminum/magnesium projectile flying through the same mixture used successfully in shot 34. Photographic evidence showing the combustion very close to the projectile throat led to the conclusion that shot 34 was operated very close to permissible limits of energy release levels and energy release rate.⁷ Shots 35 and 36 unstarted because higher operating temperatures caused

the energy release rate to become too high.⁸ The same increase in operating temperature can be caused through the loss of a relatively small amount of magnesium. This is a conservative approach to estimating magnesium's effect on kinetics and doesn't begin to answer questions regarding the effect magnesium has on the reaction mechanism.

Given magnesium's low evaporation temperature of 1380 °K which is comparable to the average temperature throughout the ram accelerator flow field, it seems very likely that this is what happened. After the unstart becomes established, the temperature increases and this will cause the mass flow rate of magnesium into the freestream to increase which further increases temperature leading to a very violent and hot destruction of the projectile. Aluminum projectiles, on the other hand, survived the unstarts in shots 35 and 36 but the bases appeared to be on fire. This result is supported by aluminum's much higher evaporation temperature of 2770 °K which would inhibit participation of aluminum in combustion except for localized hot spots. Higher temperatures caused by greater speeds or more energetic reactants should cause aluminum to be as vulnerable as magnesium is at current operating temperatures.

CONCLUSIONS

The computation of projectile ablation remains a challenging problem because of complicated physics and uncertain material data. The effect assumed rates of ablation have on projectile performance is much easier to calculate. Despite these current limitations, it is possible to demonstrate that projectile material loss can have a profound and devastating effect on projectile performance by increasing energy release rates beyond acceptable limits and causing a projectile unstart. In HIRAM shot 37 a material loss rate on the order of 1% mass occurring over 9 meters of travel would have been sufficient to push a kinetically marginal fuel mixture to having too quick an ignition delay time thus causing the projectile to unstart.

REFERENCES

- 1 Higgins, A. J., Knowlen, C., and Bruckner, A. P., "An Investigation of Ram Accelerator Gas Dynamic Limits", AIAA-93-2181, 29th Joint Propulsion Conference , June 1993.
- 2 Liberatore, F. , Ram Accelerator Performance Calculations Using a Modified Version of the NASA Lewis CET89 Equilibrium Chemistry, Army Research Lab-Tech Report-647, December, 1994.
- 3 Naumann, K. W., "Heating and Ablation of Projectiles During Acceleration in a Ram Accelerator Tube", AIAA 93-2184, 29th Joint Propulsion Conference , June 1993
- 4 Bird, R. B., Stewart, W. E., and Lightfoot, E. N., Transport Phenomenon, John Wiley&Sons, 1960.
- 4 Ozisik, M., Heat Conduction, John Wiley & Sons, 1980.
- 5 Stull, D. and Prophet, H., JANAF Thermochemical Tables, Second Edition, NBS 37, U.S. Government Printing Office, 1971.
- 6 Kruczynski, D.L., "Experiments in a 120mm Multi-Stage Ram Accelerator", 2nd International Workshop on Ram Accelerators, July 17-20, 1995.
- 7 Nusca, M. J., "Reacting Flow Simulation of Transient, Multi-Stage Ram Accelerator Operation and Design Studies", 2nd International Workshop on Ram Accelerators, July 17-20, 1995.

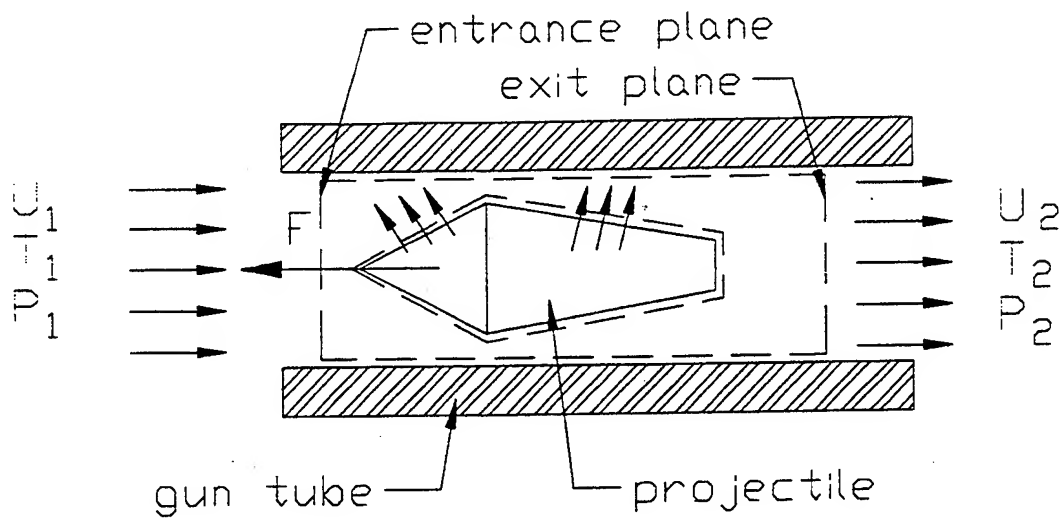


Figure 1: Ram accelerator control volume

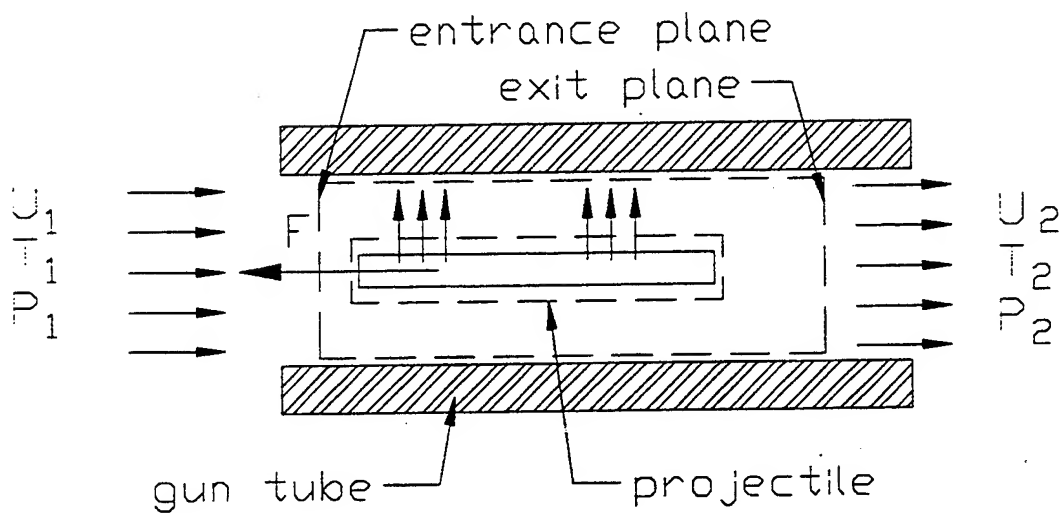


Figure 2: Simplified ram accelerator control volume.

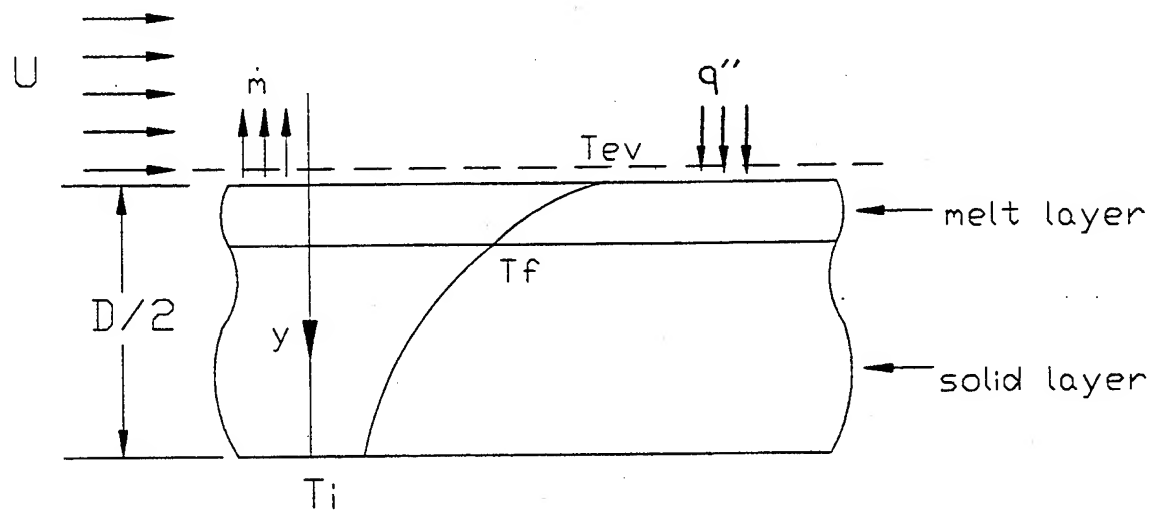


Figure 3: 1D heat transfer with phase changes

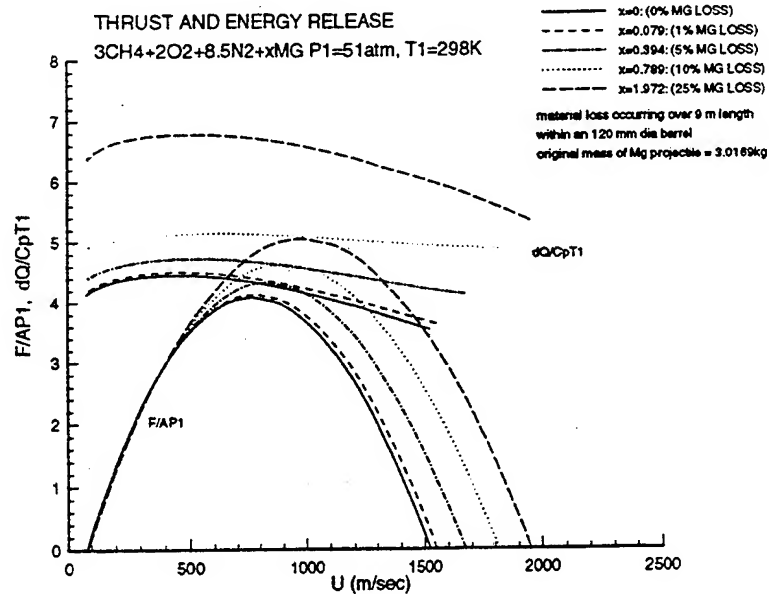


Figure 4: Thrust and Energy Release; "Cool" mix + Mg

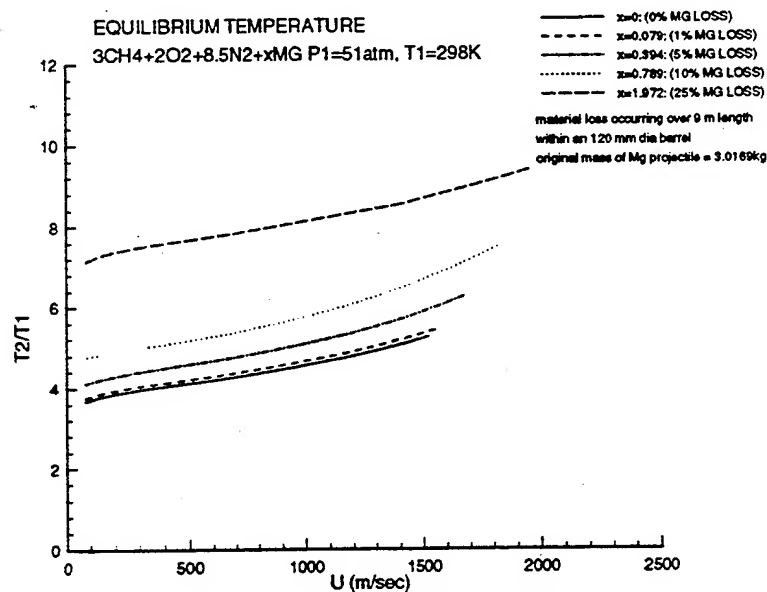


Figure 5: Temperature; "Cool" mix + Mg

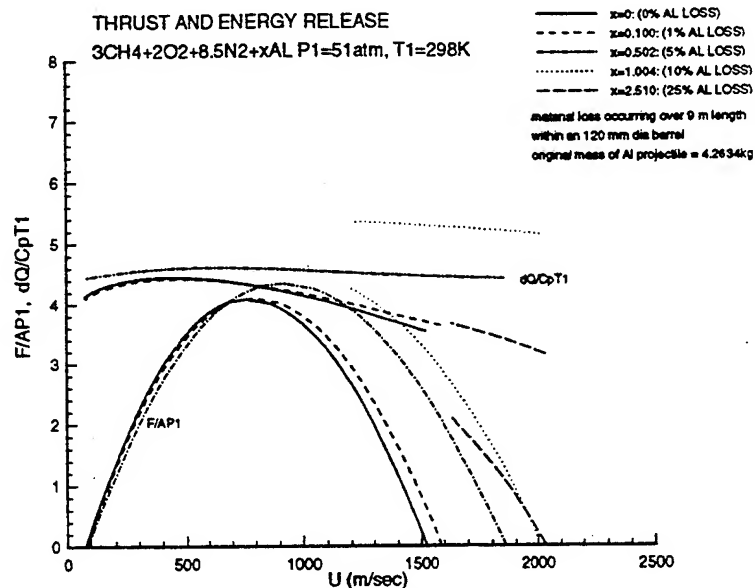


Figure 6: Thrust and Energy Release; "Cool" mix + Al

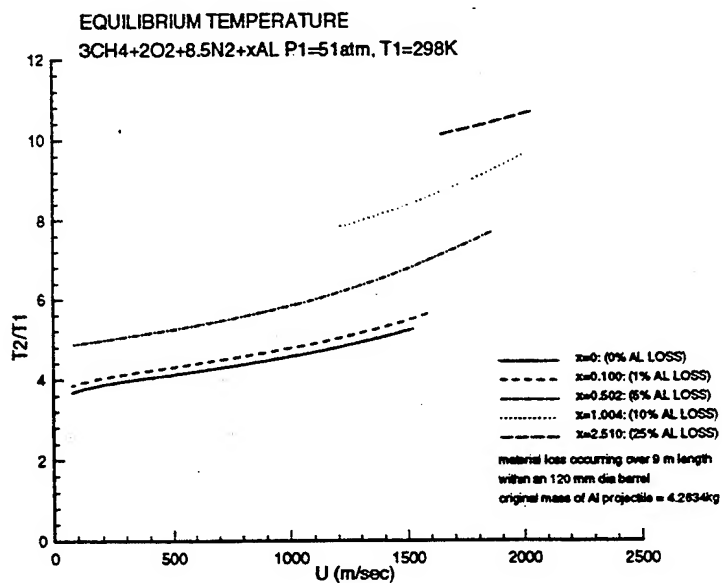


Figure 7: Temperature; "Cool" mix + Al

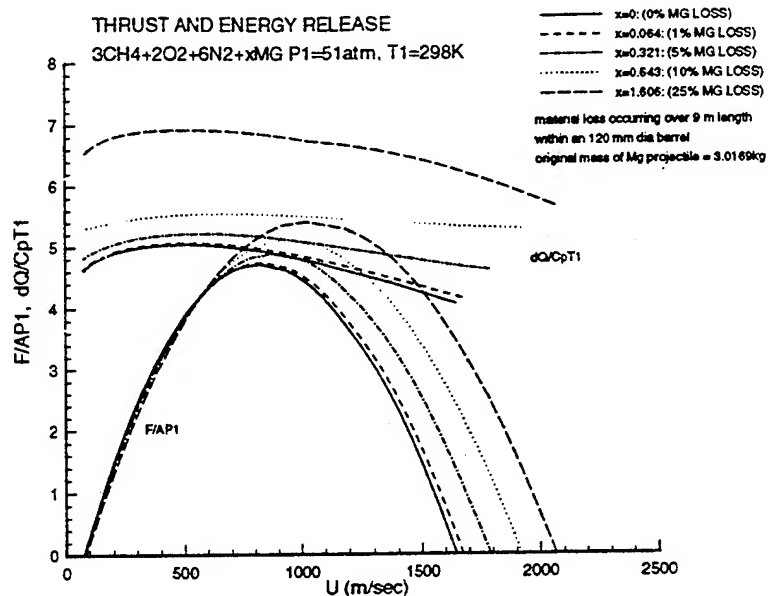


Figure 8: Thrust and Energy Release: "Mild" mix + Mg

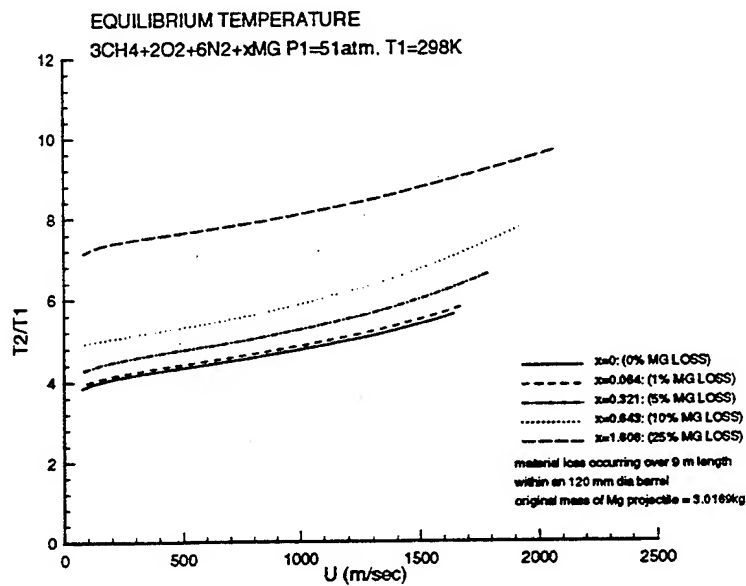


Figure 9: Temperature; "Mild" mix + Mg

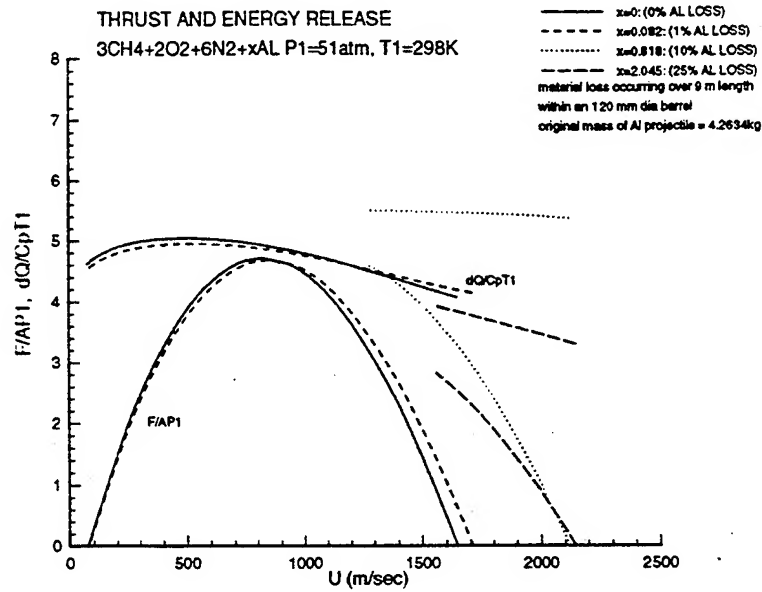


Figure 10: Thrust and Energy Release; "Mild" mix + Al

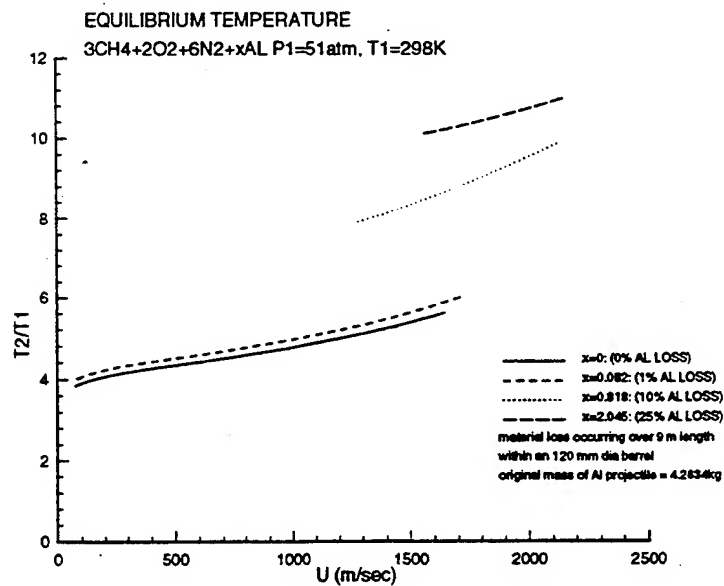


Figure 11: Temperature; "Mild" mix + Al

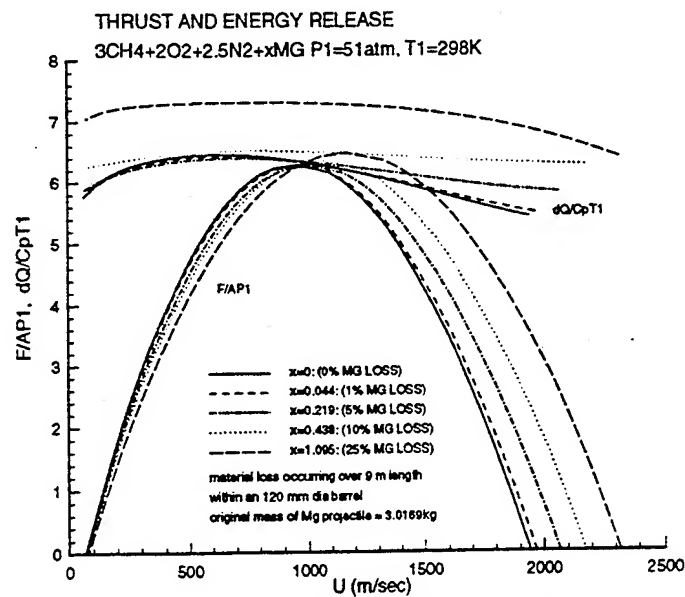


Figure 12: Thrust and Energy Release; "Hot" mix + Mg

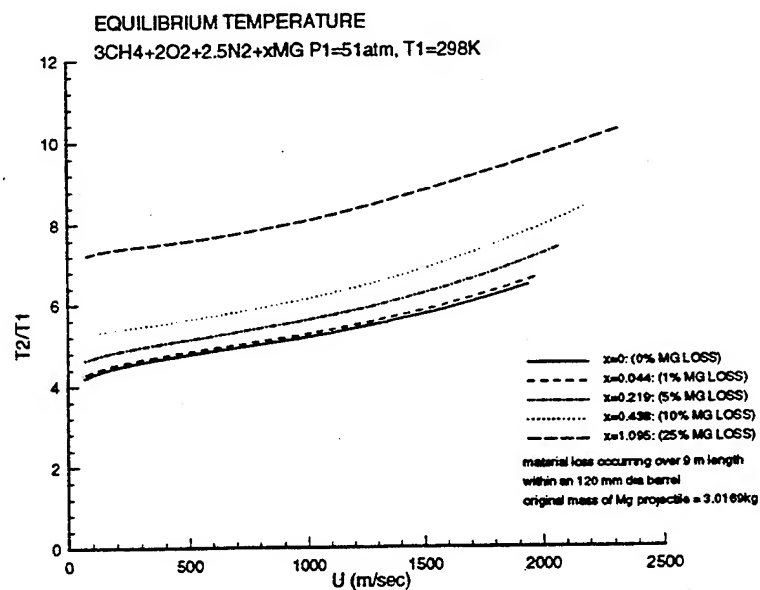


Figure 13: Temperature; "Hot" mix + Mg

THEORETICAL MODEL FOR CALCULATING THE PROJECTILE ACCELERATION IN A RAM ACCELERATOR

F. Gatau, G. Smeets, J. Srulijes

French-German Research Institute of Saint-Louis (ISL)
F-68301 Saint-Louis, France

ABSTRACT

In a ram accelerator a sharp-nosed-body flies at supersonic velocity through a tube initially filled with a highly compressed combustible gas mixture. By shock compression, i.e., bow wave and its reflections at the tube wall, the gas mixture is heated progressively and is ignited in subdetonative combustion mode at the body's back giving a forward thrust to the ram-projectile. In superdetonative mode, as investigated in the RAMAC 30 of ISL, the combustion takes place in the channel between the projectile body and the tube wall.

The experimental work is progressing well at ISL with both ram accelerators, the 30 mm caliber RAMAC 30 [4, 5] and the 90 mm caliber RAMAC 90 [7, 8]. The computer code MEGEC [9], which was initially developed to evaluate the composition and the thermodynamic properties of a gas mixture, has been applied for comparing and predicting both, the detonation velocity of the combustible gas mixtures used in the RAMAC and the projectile acceleration with theoretical calculations. This code takes into account, on the basis of a gas kinetic model, the chemical reactions between fuel and oxidizer which are produced by combustion. The modeling of real gas effects begins by using in the equation of state the virial coefficients given by BOLTZMANN [3].

To calculate the pressure increase caused by the gas reaction that results in a projectile acceleration, the velocity history is calculated using a time-step procedure. For each time step the combustion model is applied in a one-dimensional scheme for calculating, on the basis of the conservation equations the pressure force exerted at the projectile's boat tail. The whole firing cycle is subdivided in n time intervals $\Delta t_1, \Delta t_2, \dots, \Delta t_n$, with constant acceleration in each of the time intervals.

INTRODUCTION

The ram accelerator concept was developed and tested successfully in a 38-mm-device by HERZTBERG, BRUCKNER & BOGDANOFF [1] at the University of Washington, Seattle, USA, in 1986. In 1988, based on the need of ISL for hypersonic launching facilities, the decision was taken to build two ram accelerators: a 30-mm-tube, called RAMAC 30, and a 90-mm-one, RAMAC 90. The RAMAC 90 is designed to accelerate masses of several kilograms to velocities up to about 3 km/s. The RAMAC 30 facility is used for basic research, see SEILER et al. [5], mainly in the superdetonative flight regime, with the objective of obtaining highest possible projectile velocities.

Parallel to the ram accelerator experiments at ISL there was a need for a theoretical description of the combustion phenomena running off around the ram projectile. The aim of this calculation is

to be able to study the influence of interesting parameters on projectile acceleration such as: gas mixture composition, projectile mass, projectile velocity, bypass ratio, initial pressure and others. A numerical solution of the full Navier-Stokes equations was not taken into account due to the amount of work involved and the excessive computer time required. Therefore a one-dimensional model was developed by SMEETS et al. [2] to calculate the time history of projectile acceleration by solving the conservation equations applied to the flow around a ram projectile. There, in the energy equation the heat release due to combustion has to be modeled taking into account the chemical reactions of fuel and oxidizer.

SMEETS et al. [2] used a straightforward model based on a perfect gas for calculating the change of state 1 before reaction to state 2 after reaction. Since the assumption of a perfect gas is not a good one, it was replaced by using real gas equations to improve the results. Therefore, in the computer code MEGEC, see Fig. 1, real gas effects have been introduced taking into account the interaction between the species of the gas mixture on a gaskinetic level. Herewith, the high gas pressures can be modeled much more precisely.

DESCRIPTION OF THE CODE MEGEC

Perfect gas and "real" gas: thermodynamic properties

The energy of an gas molecule can be divided into two parts: the kinetic energy of translation due to the linear motion of its mass center, and the internal energy of the molecule, i.e., the rotation energy, vibration energy and electronic excitation.

According to the mechanical statistics developed by BOLTZMANN [3], these different parts of the total energy of a gas, that contains N molecules in a volume V at temperature T , can be described with the partition function $Q(V, T)$.

For a perfect gas the Boltzmann's partition function can be written as:

$$Q(V, T) = Q_t Q_{int},$$

$$\text{and} \quad Q_{int}(T) = Q_r Q_v Q_e,$$

$$\text{with} \quad Q_t(V, T) = \left(\frac{2\pi m k T}{h^2} \right)^{\frac{3}{2}} V$$

Each of the internal partition functions Q_r , Q_v and Q_e can be expressed as follows:

$$Q = \sum_i g_i \exp\left(-\frac{\varepsilon_i}{kT}\right).$$

The parameter g_i is the number of quantum states of energy ε_i . These parameters are available in spectroscopic tables.

For a "real" gas we must consider the intermolecular forces, especially for high pressures. If we introduce the covolume b of a molecule, the equation of state can be developed as an virial expansion. For that purpose, a corrective term must be added to the translation partition function, as follows:

$$Q_t(V, T) = \left(\frac{2\pi m k T}{h^2} \right)^{\frac{3}{2}} V \left(1 - \frac{Nb}{V} \right)$$

The thermodynamic properties of the gas, especially the chemical potential μ , are all deduced from the partition function $Q(V, T)$. They are listed in Fig. 2.

Thermodynamic properties of a gas mixture

We will consider a reacting gas as a mixture of several components which can react with each other. This mixture of j components formed from m chemical elements (e.g., C, H, N, O,.....), will contain the reacting species and the species produced by the reactions. If N_i is the number of molecules of the species i , the thermodynamics properties of each of the species i , given in Fig. 3, can be determined with the formulae shown in Fig. 2.

By using the Dalton law we can write the gas properties of the mixture as a sum of these for each species. For example, the pressure p and energy E are given by the following expressions:

$$p = \sum_i p_i$$

$$E = \sum_i E_i = \sum_i N_i k T e_i^0$$

At equilibrium we can determine the composition of the mixture, i.e., the N_i for each species, because there the Gibbs free energy has its minimum value. In addition we have to take into account the conservation of the number of atoms (see Fig. 4). This gives a system of equations which is solved with the help of the multipliers of Lagrange π_k . At least, the composition will be given by the mole fractions $x_i = N_i/N$, with $N = \sum_i N_i$.

"Real" gas model

As can be seen in Fig. 5 the equation of state is modeled by using the factor σ . Then the change of state in a reacting gas mixture will be calculated on the basis of a perfect gas with $\sigma = 1$. To take into account the real gas effects we use $\sigma > 1$, which is determined by the evaluation of BOLTZMANN [3].

CALCULATION OF DETONATION VELOCITY WITH THE CODE MEGEC

Fig. 6 shows the results of the code MEGEC for (a) perfect gas and (b) real gas effect using Boltzmann's equation. It can be seen that for gas pressures in the range of 1 bar there exist only small differences. For increasing gas pressure, the deviation becomes considerable and for, e.g., 40 bars the difference in detonation velocity is about 100 m/s. The calculation for the real gas

description using the equation of state of BOLTZMANN [3] is in good agreement with the experiment of BAUER [6]. This comparison shows that for gas pressures much higher than 1 bar the real gas assumption becomes necessary.

APPLICATION OF CODE MEGEC TO RAM ACCELERATION

Fig. 7 explains the principle of the scram accelerator process. A vehicle consisting of a cylindrical centerbody with conical portions at its front and rear end propagates through a combustible gas mixture filled in a cylindrical tube having a diameter greater than that of the centerbody. By means of fins [4] or rails [5] which are not shown in the figure, the projectile is guided into a centred position inside the tube.

The flow field around the projectile flying at a supersonic and superdetonative speed largely corresponds to that of a scramjet engine. On its conical front part, an attached shock is formed in the high Mach number upstream flow. That shock undergoes one or more reflections between the wall of the tube and the cylindrical part of the projectile, thus creating a series of oblique shocks. Herewith, the flow is compressed nearly isentropically in the same way as within an inlet of a scramjet engine. The combustible mixture is expected to ignite and combust in the circular section between the cylindrical body and the tube. The combustion generated high gas pressure produces thrust on the conical back part of the projectile, corresponding to the thrust acting on the nozzle of a scramjet.

The thrust can be estimated by considering an equivalent one-dimensional and stationary flow and by calculating its global changes using the equations for mass, momentum and energy, between reference planes, positioned as shown in Fig. 8. As assumed in Fig. 8, the upstream flow first undergoes an isentropic compression between the upstream flow 1 and plane S. Its mass flux, energy flux as well as the entropy of the gas are all conserved. Combustion is assumed to occur within the portion of constant cross section between the cylindrical part of the projectile and the tube wall.

While the fluxes of mass and momentum are conserved, the energy of the gas increases by the chemical reaction. It is assumed that, after combustion, at plane 2, the gas mixture has reached its new thermal equilibrium. In the last step, the flow undergoes an isentropic expansion between plane 2 and the downstream flow 3 in the tube. During its passage over the projectile, the flow obtains a net increase of momentum flux. The total momentum gain has to be calculated by integration of the momentum around the projectile. Its thrust and acceleration result from this calculation.

In order to consider the projectile acceleration, a time-step-procedure with ongoing time-steps $\Delta t_1, \Delta t_2, \dots, \Delta t_n$, was developed (Fig. 9). From step to step the projectile velocity is increased by calculating the pressure distribution around the projectile. Fig. 10 shows the calculation result for shot no. 97 and for the first time-step t_1 at $u = 1806$ m/s, which is the entrance velocity to the ram accelerator. Using the acceleration γ , obtained with the effective gas pressure p_{eff} acting on the projectile's back, see Fig. 11, the velocity gain is obtained for each time step n : $v_{n+1} = v_n + \gamma_n \Delta t_n$.

RAMAC 30 RAIL TUBE CONCEPT

Best ignition and avoidance of unstart effects were obtained in the RAMAC 30 rail tube [5] with the gas mixture of the following molar components: 2 hydrogen + 1 oxygen + 3.8 carbondioxide having a Chapman-Jouguet detonation velocity of approximately 1500 m/s. The result of calculation obtained with the combustion model for experiment no. 97 of RAMAC 30 is shown in the path-velocity plot of Fig. 12 for both, the experimentally as well as the calculated velocity gain. The velocity increase found experimentally in a 27 bars gas mixture was about 200 m/s. The mean acceleration of 135000 m/s^2 is in good accordance with the gasdynamic estimates and even slightly exceeds the calculated acceleration probably due to a mass loss by melting and burning of the projectile material (aluminum) during the acceleration cycle, especially towards the end cross-section of the ram-tube.

The comparison shows that the one-dimensional combustion model can be successfully applied for calculating in a few seconds CPU-time on a PC-486 the whole ram-acceleration cycle. Therefore it is possible to do parameter studies immediately and parallel to the RAMAC experiments in order to find an optimal operation level. CFD calculations are too expensive for this purpose and their precision is not necessary for a fast prediction of the influence of the governing parameters.

CONCLUSION

A computer code called MEGEC was developed for calculating the change of gas conditions for a gas with chemical reactions. In the equation of state, real gas effects are modeled using the virial expansion of BOLTZMANN [3].

The calculation of the detonation velocity shows the need for using the real gas model, especially at high gas pressures ($p > 1 \text{ bar}$).

The real gas code MEGEC was introduced in the scheme of SMEETS et al. [2] for solving the conservation equations. This scheme was applied to the firing cycle in RAMAC 30 of ISL using a time-step-procedure for modeling the whole ram shot. The deviation between experiment and calculation is very small at the gas conditions present in the RAMAC 30. The applicability of the model at other conditions will be tested when RAMAC 30 is operated at higher projectile velocities and higher fill pressures. The aim is to become a projectile velocity of about 3000 m/s along a tube length of 12 m. The calculated velocity prediction for RAMAC 30 is given in Fig. 13. Furthermore, a comparison with experimental results of ISL's RAMAC 90 is planned.

REFERENCES

1. HERTZBERG, A., BRUCKNER, A. P., BOGDANOFF, D. W., The Ram Accelerator: A new Chemical Method of Achieving Ultra-High Velocities, 37th ARA-Meeting, Québec, Canada, 1986

2. SMEETS, G., GATAU, F., SRULIJES, J., Rechenprogramm für Abschätzungen zur Ram-Rohrbeschleunigung, ISL-Report RT 507/92, 1992
3. BOLTZMANN, L. Lectures on Gas Theory, Vol. 2, Chapter 5, University of California Press, 1964
4. PATZ, G., SEILER, F., SMEETS, G., SRULIJES, J., Status of ISL's RAMAC 30 with Fin Guided Projectiles Accelerated in a Smooth Bore, RAMAC II, Second International Workshop on Ram Acceleration, University of Washington, Seattle, USA, July 1995
5. SEILER, F., PATZ, G., SMEETS, G., SRULIJES, J., The Rail Tube in Ram Acceleration: Feasibility Study with ISL's RAMAC 30, RAMAC II, Second International Workshop on Ram Acceleration, University of Washington, Seattle, USA, July 1995
6. BAUER, P.; PRESLES, H. N., HEUZE, O., BROCHET, C., Recherche des limites de validité des équations d'état des produits de détonation, Sciences et Techniques de l'Armement, 60, 4^e Fasc., 1986
7. GIRAUD, M., LEGENDRE, J. F., SIMON, G., HENNER, M., VOISIN, D., RAMAC 90 Starting Process: Control of the Ignition Location and Performance in the Thermally Choked Propulsion Mode, RAMAC II, Second International Workshop on Ram Acceleration, University of Washington, Seattle, USA, July 1995
8. GIRAUD, M., LEGENDRE, J.-F., SIMON, G., RAM Accelerator in 90 mm Caliber or RAMAC 90: Experimental Results Concerning the Transdetonative Combustion Mode, 14th International Symposium on Ballistics, Québec, Canada, 26-29 September 1993
9. GATAU, F., Propriétés thermodynamiques d'un mélange de gaz en équilibre thermochimique, programme MEGEC, ISL-Report R 109/79, 1979

Calculation of the change of the gas conditions from one state to another

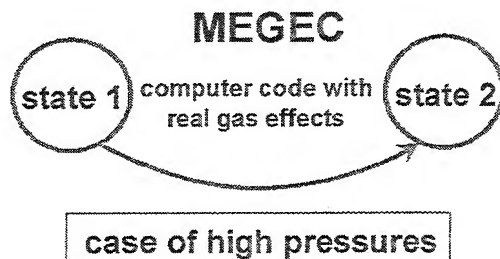


Fig. 1. Performance of code MEGEC

$$p = \frac{NkT}{V} \left(1 + \frac{N}{V}b + \dots \right)$$

$$\mu = -kT \left\{ \ln \left[\left(\frac{2\pi mkT}{h^2} \right)^{\frac{3}{2}} \frac{kT}{p} \right] + \ln Q_{\text{int}} \right\}$$

$$E = \frac{3}{2}NkT + NkT^2 \frac{d}{dT} (\ln Q_{\text{int}})$$

$$H = E + pV$$

$$S = \frac{E + NkT - N\mu}{T}$$

$$c_v = \left(\frac{\partial E}{\partial T} \right)_v$$

$$c_p = \left(\frac{\partial H}{\partial T} \right)_p$$

Fig. 2. Thermodynamic properties

For each species i it is valid:

$$p_i = N_i \frac{kT}{V} \left(1 + \frac{N_i}{V} b_i + \dots \right)$$

$$\mu_i = kT \left(\mu_i^0 + \ln \frac{p_i}{p_0} \right)$$

$$E_i = N_i kT e_i^0$$

$$S_i = N_i k \left(e_i^0 + 1 - \mu_i^0 - \ln \frac{p_i}{p_0} \right)$$

$$C_{vi} = N_i k c_{vi}^0$$

with

$$\mu_i^0 = -\ln \left[\left(\frac{2\pi m_i kT}{h^2} \right)^{\frac{3}{2}} \frac{kT}{p_0} \right] - \ln Q_i$$

$$e_i^0 = \frac{3}{2} + T \frac{d}{dT} (\ln Q_i)$$

$$c_{vi}^0 = \frac{3}{2} + T \frac{d^2}{dT^2} (T \ln Q_i)$$

Fig. 3. Gas mixture

$$\sum_i \mu_i dN_i = 0$$

$$\sum_i n_{ik} dN_i = 0 \quad m \text{ equations, } k = 1, \dots, m$$

multiplier of Lagrange: $kT\pi_k$

$$\sum_i \left[\mu_i - kT \sum_k n_{ik} \pi_k \right] dN_i = 0$$

$$\mu_i = kT \sum_k n_{ik} \pi_k$$

$$x_i = \frac{N_i}{N} = \frac{p_i}{p} = \frac{p_0}{p} e^{(\sum_k n_{ik} \pi_k - \mu_i^0)}$$

$$\sum_i n_{ik} x_i = \text{constant}$$

Fig. 4. Description of thermodynamic equilibrium of a gas mixture

$$E = RT \sum_i x_i e_i^0$$

$$S = R \sum_i x_i (e_i^0 + 1 - \mu_i^0 - \ln \frac{p}{p_0} x_i)$$

$$C_{v0} = R \sum_i x_i c_{vi}^0$$

$$H = E + pV$$

$$p = \sigma \frac{RT}{V}$$

$\sigma = 1$: perfect gas mixture

if not: real gas mixture

Boltzmann: $\sigma = 1 + u + 0,625 u^2 + 0,287 u^3 + 0,193 u^4$

with $u = \frac{\sum_i x_i b_i}{V}$, b_i = covolume

$$\rho = \frac{m}{V} \quad m = \sum_i x_i m_i$$

Fig. 5. Thermodynamic function valid for a gas mixture

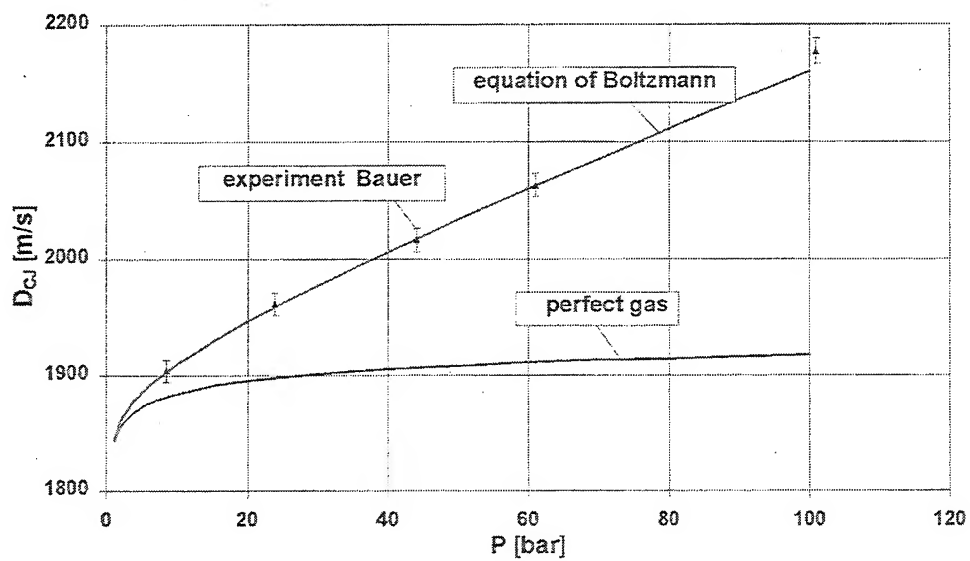


Fig. 6. Comparison of detonation velocity: ethylene - air

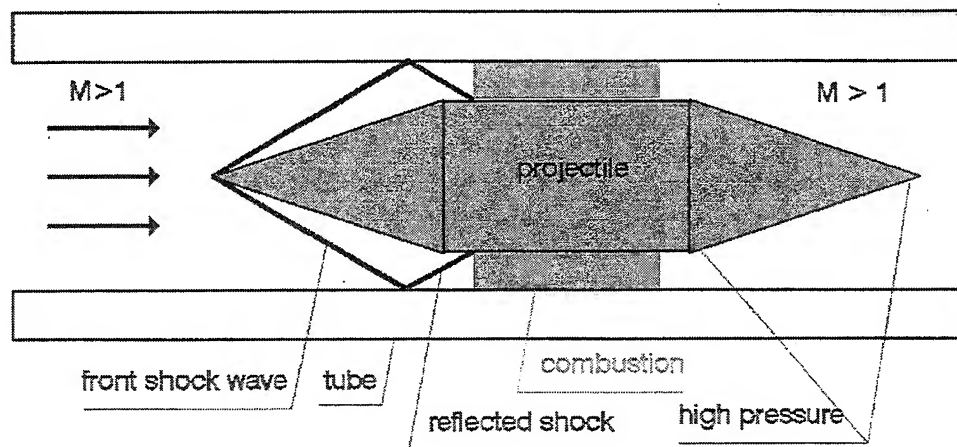
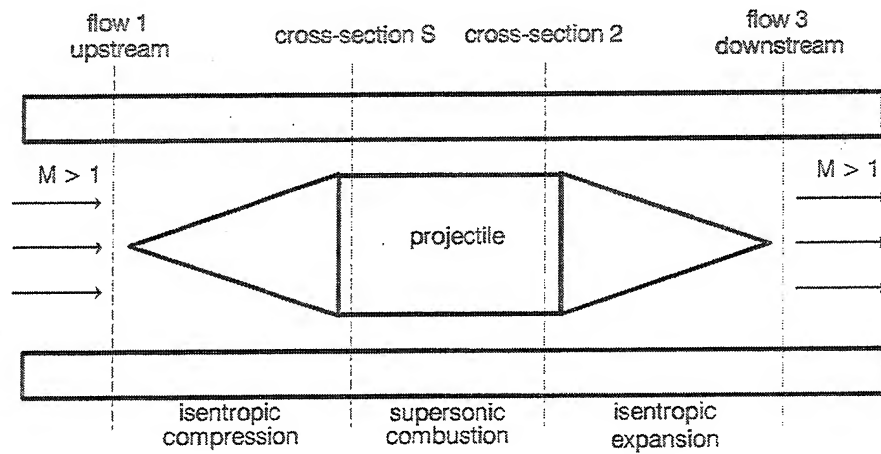


Fig. 7. Principle of the superdetonative ram accelerator mode



isentropic compression: (1) \Rightarrow (S)

$$\rho_S u_S F_S = \rho_1 u_1 F_1$$

$$s_S = s_1$$

$$h_S + \frac{u_S^2}{2} = h_1 + \frac{u_1^2}{2}$$

$$p = \sigma \rho \frac{R}{m} T$$

combustion in constant cross-section: (S) \Rightarrow (2)

$$\rho_2 u_2 = \rho_S u_S$$

$$p_2 + \rho_2 u_2^2 = p_S + \rho_S u_S^2$$

$$h_2 + \frac{u_2^2}{2} = h_S + \frac{u_S^2}{2}$$

$$p = \sigma \rho \frac{R}{m} T$$

Fig. 8. Application of conservation laws to the flow around a ram projectile

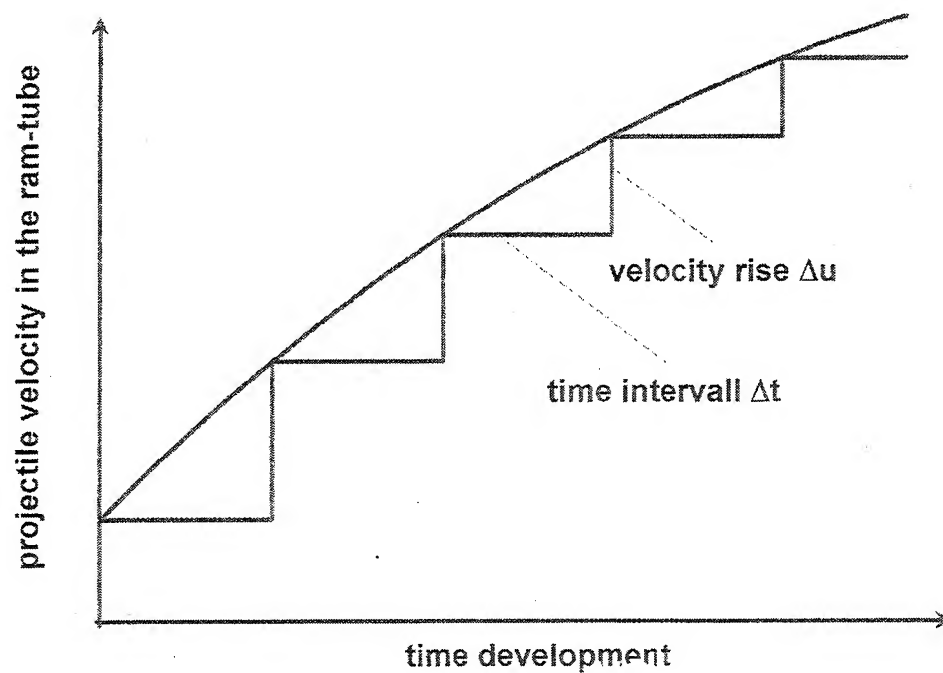


Fig. 9. Schematic time-step procedure

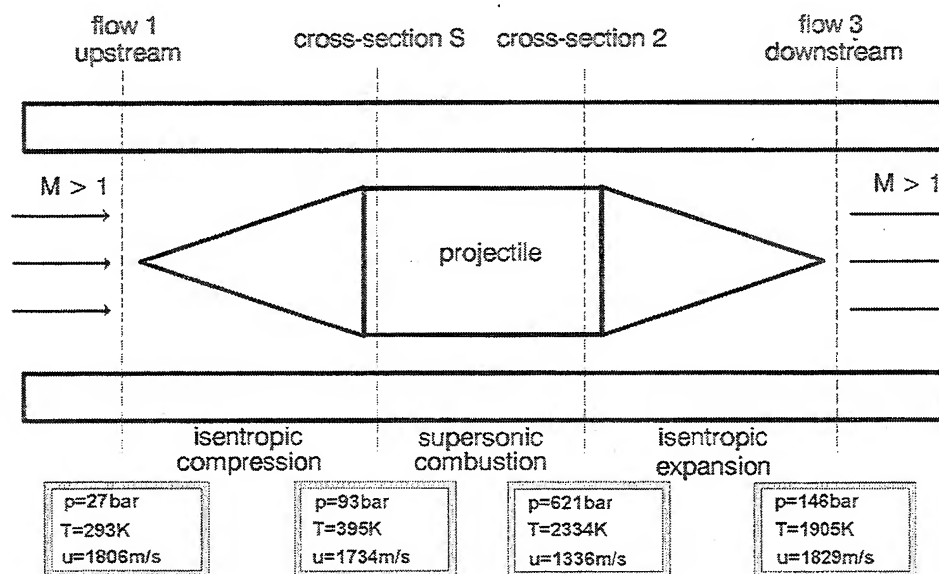


Fig. 10. Calculation of flow around the ram projectile for shot no. 97

$$p_{\text{eff}} = [p_3 + \rho_3 u_3^2 - (p_1 + \rho_1 u_1^2)] / \text{FLPR}$$

$$\gamma = \frac{p_{\text{eff}} F_p}{m_p}$$

$$v = v_0 + \gamma \Delta t$$

Fig. 11. Calculation of the acceleration and velocity

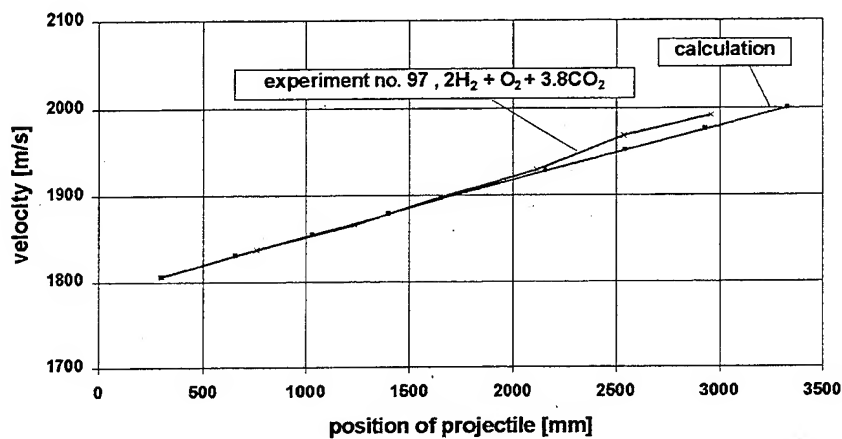


Fig. 12: Comparison of real gas calculation and experimental result

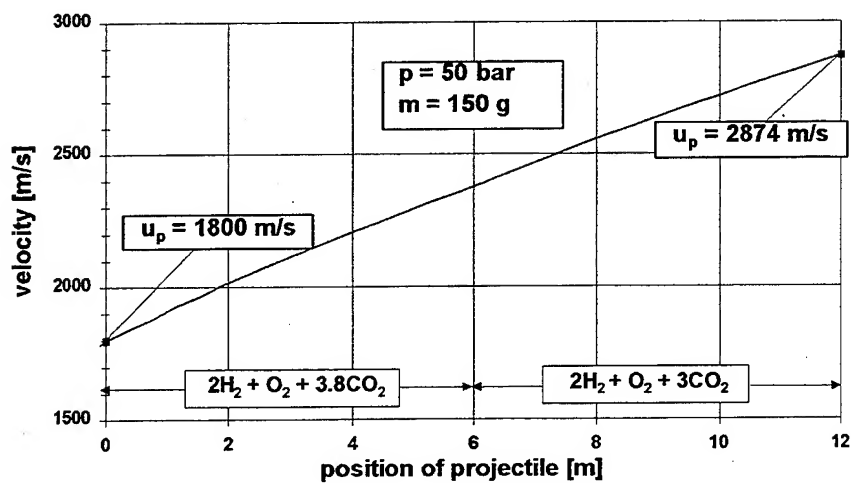


Fig. 13. Expected velocity increase in RAMAC 30 along 12 m ram-tube

Session 6

COMPUTATIONAL MODELING

REACTING FLOW SIMULATION OF TRANSIENT, MULTI-STAGE RAM ACCELERATOR OPERATION AND DESIGN STUDIES

Michael J. Nusca

Propulsion and Flight Division, Weapons Technology Directorate
U.S. Army Research Laboratory, Aberdeen Proving Ground, MD 21005, USA

ABSTRACT

Computational fluid dynamics solutions of the full Navier-Stokes equations have been used to numerically simulate the reacting in-bore flowfield for the ram accelerator projectile propulsion system. In this system a projectile and obturator are injected at supersonic velocity into a stationary tubes filled with pressurized mixtures of hydrocarbon, oxidizer and inert gases. Flow stagnation on the obturator initiates combustion of the mixture. A system of shock waves generated around the projectile, in conjunction with viscous heating, sustains combustion. The resulting energy release, which travels with the projectile, also generates high pressures that impart thrust to the projectile. Numerical simulations utilizing finite-rate chemical kinetics have been used to investigate this flow field for a single-stage as well as multi-stage ram accelerator. The chemical ignition time is investigated and compared to the gas dynamic flow time yielding performance evaluations for various gas mixtures used in these stages.

NOMENCLATURE

A	preexponential constant for rate law
b	co-volume
c_p	specific heat capacity, constant p
c_v	specific heat capacity, constant volume
C	specific reaction rate constant
D	mass diffusion coefficient
Da	Damkohler number (Eq. 21)
e	specific total internal energy
E_a	activation energy (kJ/kgmole)
F, G	flux vectors (Eq. 1)
h	molar specific enthalpy
i	i -th species
L	projectile length
m	mass or mixture quantity (subscript)
M	molecular weight (kg/kgmole)
n	number of moles
N	total number of species
p	static pressure
Q	heat released, $\Delta H_{f,react} - \Delta H_{f,prod}$
\mathfrak{R}	specific gas constant, \mathfrak{R}/M
$\bar{\mathfrak{R}}$	universal gas constant (8.314 kJ/kgmole-K)
Re	Reynolds Number, $\rho UL/\mu$

Sc	Schmidt Number, $\mu_m/\rho D$
t	time
T	static temperature
u	axial velocity
v	radial velocity
U	magnitude of the local velocity vector
V	specific volume ($1/\rho$)
W	dependent variable vector (Eq. 1)
x, y	cartesian coordinates
X	species mole fraction
α	0 for 2D, 1 for axisymmetric flow
γ	ratio of specific heats, c_p/c_v
ΔH_f	enthalpy of formation
κ	thermal conductivity
μ	molecular viscosity
ν	stoichiometric coefficient
ρ	density
σ	species mass fraction
τ	shear stress tensor
ω	chemical production term (Eq. 18)
Ω	source term vector (Eq. 1)

INTRODUCTION

Experimental testing and gasdynamic modeling of the ram acceleration technique for in-bore projectile propulsion are being investigated at the U.S. Army Research Laboratory (ARL) under the Hybrid Inbore RAM (HIRAM) propulsion program.^{1,2} This research program seeks to provide a highly efficient method of achieving hypervelocity (3 km/s) projectile launch for use in high speed impact testing applications. The ARL ram accelerator system uses 120-mm (bore diameter) tubes and is modeled after the 38-mm system at the University of Washington,³ where the technology was first demonstrated. Ram acceleration has also been demonstrated at the Institute of St. Louis (ISL) in France.^{4,5} Numerical solutions of the Navier-Stokes equations have been obtained via computational fluid dynamics (CFD) for chemically reacting, two- and three-dimensional flows at ARL. A variety of CFD techniques have been brought to bear on this problem, including models for finite-rate global- and multiple-step chemical kinetics, and equilibrium chemical processes. Accurate numerical simulation of hydrocarbon-based reacting flow creates a very great demand on computational resources since the number of intermediate species and the number of reaction steps for typical hydrocarbon fuels are prohibitively large. The ARL CFD simulation uses 3 reaction steps and 6 species. Within several hours of time on supercomputers, viscous and chemically reacting gas dynamic simulations are used to assess the influence of projectile velocity, fill pressure, mixture composition, and projectile geometry on species consumption, launch tube wall pressure and projectile thrust. These studies are being used to seek optimum performance for the ARL ram accelerator with minimal gun firings. In addition, a finite-rate kinetics code consisting of 176 reactions and 32 species is used to evaluate the ignition delay time (heat release rate) and heat released by mixtures at a constant pressure and an initial

temperature, without regard to the gas dynamic flow. Important conclusions concerning the relative performance of these mixtures can be obtained from both the CFD analysis and kinetics analysis.

The ARL facility consists of accelerator tubes made from 120-mm M256 tank guns (see Figure 1). The projectile is made of high strength aluminum alloy (4.29 kg) and consists of an axisymmetric cone-boattail body with stabilizing fins for centering in the tube (see Figure 1). Projectile transition from the conventional (solid propellant) launcher to the accelerator is made through a transition/vent section. This section decouples the launch gun movement from the accelerator (via a sliding interface) and vents combustion gases from the conventional charge. The accelerator tubes are filled with gas mixtures of hydrocarbon fuel (CH_4), oxidizer (O_2) and diluents (e.g. N_2 , HE) at a pressure of 50 to 100 atm. Ignition of the gas is achieved by flow stagnation on the projectile backplate (.514 kg circular disk), initially mated to the projectile in the launch gun tube, then gas-dynamically discarded in the first accelerator tube. This process has been numerically simulated by Nusca² and is reviewed in this paper. Ends of the accelerator tubes are sealed with PVC diaphragms. The tubes can be separately filled with different gas mixtures. Numerical simulation of projectile transition between these tubes or stages is the subject of the present paper. When the injection velocity of the projectile is greater than the sound speed of the gas, a system of oblique and normal shock waves develops on the projectile which act to sustain combustion. This energy release travels with the projectile and thrust is generated by the action of high pressure reacting gases on the rear part of the projectile. Diluents are used to tailor the acoustic speed of the mixture to prevent flow choking, and tailor the ignition delay such that combustion takes place on the projectile afterbody.

REACTING FLOW MODEL

CFD flow simulations for the ARL ram accelerator are performed using the Rockwell Science Center USA-RG (Unified Solution Algorithm Real Gas) code.⁶⁻⁸ This CFD code solves the full, 3D, unsteady Reynolds-Averaged Navier-Stokes (RANS) equations including equations for chemical kinetics. These partial differential equations are cast in conservation form and converted to algebraic equations using an upwind finite-volume formulation. Solution takes place on a mesh of nodes distributed in a zonal fashion around the projectile and throughout the flow field such that sharp geometric corners and other details are accurately represented. The conservation law form of the equations assures that the end states of regions of discontinuity (shocks, detonations, deflagrations) are physically correct even when smeared over a few computational cells. The Total Variation Diminishing (TVD) technique is employed to discretize inertia terms of the conservation equations, while the viscous terms are evaluated using an unbiased stencil. Flux computations across cell boundaries are based on Roe's scheme for hyperbolic equations.⁹ Spatial accuracy of third-order can be maintained in regions of the flow field with continuous variation while slope limiting, used near large flow gradients, reduces the accuracy locally to avoid spurious oscillations.

The RANS equations for 2D/axisymmetric reacting flow (N species mixture) are written in the following conservation form.⁷

$$\frac{\partial W}{\partial t} + \frac{\partial(F_1 - G_1)}{\partial x} + \frac{\partial(F_2 - G_2)}{\partial y} + \frac{\alpha(F_2 - G_2)}{y} = \Omega \quad (1)$$

$$\begin{aligned}
W &= \begin{pmatrix} e \\ \rho \\ \rho u \\ \rho v \\ \rho \sigma_1 \\ \vdots \\ \vdots \\ \vdots \\ \rho \sigma_{N-1} \end{pmatrix}, F_1 = \begin{pmatrix} (e+p)u \\ \rho u \\ \rho u^2 + p \\ \rho uv \\ \rho u \sigma_1 \\ \vdots \\ \vdots \\ \vdots \\ \rho u \sigma_{N-1} \end{pmatrix}, F_2 = \begin{pmatrix} (e+p)v \\ \rho v \\ \rho v u \\ \rho v^2 + p \\ \rho v \sigma_1 \\ \vdots \\ \vdots \\ \vdots \\ \rho v \sigma_{N-1} \end{pmatrix}, \Omega = \begin{pmatrix} 0 \\ 0 \\ 0 \\ \alpha \tau_+ \\ \sum_k \omega_{1k} \\ \vdots \\ \vdots \\ \vdots \\ \sum_k \omega_{(N-1)k} \end{pmatrix} \\
G_1 &= \begin{pmatrix} \kappa_m \frac{\partial T}{\partial x} + \sum_i \rho D(h_i - h_N) \frac{\partial \sigma_i}{\partial x} + u \tau_{xx} + v \tau_{xy} \\ 0 \\ \tau_{xx} \\ \tau_{xy} \\ \rho D \frac{\partial \sigma_1}{\partial x} \\ \vdots \\ \vdots \\ \vdots \\ \rho D \frac{\partial \sigma_{N-1}}{\partial x} \end{pmatrix} \\
G_2 &= \begin{pmatrix} \kappa_m \frac{\partial T}{\partial y} + \sum_i \rho D(h_i - h_N) \frac{\partial \sigma_i}{\partial y} + u \tau_{yx} + v \tau_{yy} \\ 0 \\ \tau_{yx} \\ \tau_{yy} \\ \rho D \frac{\partial \sigma_1}{\partial y} \\ \vdots \\ \vdots \\ \vdots \\ \rho D \frac{\partial \sigma_{N-1}}{\partial y} \end{pmatrix}
\end{aligned}$$

The shear stress terms are given by,

$$\tau_{xx} = 2\mu_m \frac{\partial u}{\partial x} - \frac{2}{3}\mu_m \left(\frac{\partial u}{\partial x} + \frac{\partial v}{\partial y} + \frac{v\alpha}{y} \right) \quad (2)$$

$$\tau_{yy} = 2\mu_m \frac{\partial v}{\partial y} - \frac{2}{3}\mu_m \left(\frac{\partial u}{\partial x} + \frac{\partial v}{\partial y} + \frac{v\alpha}{y} \right) \quad (3)$$

$$\tau_{xy} = \tau_{yx} = \mu_m \left(\frac{\partial u}{\partial y} + \frac{\partial v}{\partial x} + \frac{v\alpha}{y} \right) \quad (4)$$

$$\tau_+ = 2\mu_m \frac{v\alpha}{y} - \frac{2}{3}\mu_m \left(\frac{\partial u}{\partial x} + \frac{\partial v}{\partial y} + \frac{v\alpha}{y} \right) \quad (5)$$

The species viscosity and thermal conductivity are referenced to μ_o , κ_o and T_o using Sutherland's law,

$$\frac{\mu_i}{\mu_{oi}} = \left(\frac{T}{T_{oi}} \right)^{3/2} \frac{T_{oi} + S_\mu}{T + S_\mu} \quad (6)$$

$$\frac{\kappa_i}{\kappa_{oi}} = \left(\frac{T}{T_{o\kappa}}\right)^{3/2} \frac{T_{o\kappa} + S_\kappa}{T + S_\kappa} \quad (7)$$

where T_o and S vary with species.¹⁰ The mixture viscosity and thermal conductivity are determined using Wilke's law¹¹ denoting f as μ or κ ,

$$f_m = \sum_{i=1}^N \left[X_i f_i \left(\sum_{j=1}^N X_j \phi_{ij} \right)^{-1} \right] \quad (8)$$

$$\phi = (8)^{-1/2} \left(1 + \frac{M_i}{M_j} \right)^{-1/2} \left[1 + \left(\frac{f_i}{f_j} \right)^{1/2} \left(\frac{M_j}{M_i} \right)^{1/4} \right]^2 \quad (9)$$

Fick's law is used to relate the mixture diffusivity to the mixture viscosity through the Schmidt number, $Sc = \mu_m/(\rho D)$, which can be equated to the Prandtl number, $Pr = \mu_m c_{pm}/\kappa_m$. The specific heat and enthalpy of each species (per mass) are given by the following fourth order polynomial curve fits with coefficients $A - E$,¹²

$$\frac{c_{pi}}{\mathfrak{R}_i} = A_i + B_i T + C_i T^2 + D_i T^3 + E_i T^4 \quad (10)$$

$$h_i = \mathfrak{R}_i \left(A_i + \frac{B_i}{2} T + \frac{C_i}{3} T^2 + \frac{D_i}{4} T^3 + \frac{E_i}{5} T^4 \right) T + \Delta H_{fi} \quad (11)$$

The mixture enthalpy, total energy per unit volume, and ratio of specific heats are given by,

$$h = \sum_{i=1}^N \sigma_i \int^T c_{pi} dT + \sum_{i=1}^N \sigma_i \Delta H_{fi} \quad (12)$$

$$e = \frac{p}{\gamma - 1} + \rho \frac{(u^2 + v^2)}{2} + \sum_{i=1}^N \rho \sigma_i \Delta H_{fi} \quad (13)$$

$$\gamma = 1 + \left[\frac{c_{pm}}{\mathfrak{R} \sum_i (\sigma_i / M_i)} - 1 \right]^{-1} \quad (14)$$

$$c_{pm} = \frac{1}{T} \sum_{i=1}^N \sigma_i \int^T c_{pi} dT \quad (15)$$

A co-volume equation of state is used,

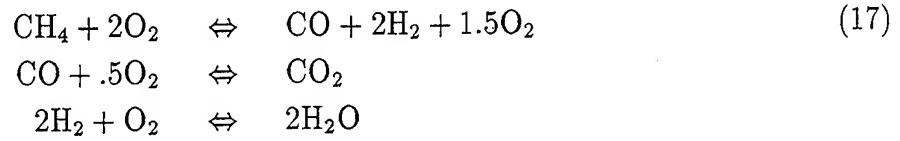
$$p(V - b) = n \mathfrak{R} T; \quad b = \sum_{i=1}^N n_i b_i \quad (16)$$

where covolume can be obtained from literature.¹³

The system of Navier-Stokes equations (Eq. 1) is valid for the laminar flow of a viscous, Newtonian fluid. In reality, the flow will remain laminar up to a certain critical value of the Reynolds number, $\rho U L / \mu$. Above this critical value the flow becomes turbulent and is characterized by the appearance of fluctuations in all variables (U, p, ρ, T , etc.) around mean values. These fluctuations are statistical in nature and cannot be described in a deterministic way. The current model uses the Reynolds-averaging approximation along with algebraic

turbulence models that relate fluid viscosity (μ) to other variables. See Reference 2 for further details.

Hydrocarbon mixtures ($3\text{CH}_4 + 2\text{O}_2 + 10\text{N}_2$), pressurized to 50-100 atm, are commonly used for ram accelerator testing at ARL. Fuel rich mixtures are used with fuel equivalence ratios of about 3. For this value a complete understanding of CH_4/O_2 chemical kinetics, especially for $P \geq 10$ atm, is not available.¹⁴ Accurate numerical simulation of hydrocarbon-based reacting flow is very demanding in terms of computational resources since the number of intermediate species and the number of kinetic steps are prohibitively large (i.e., ≥ 15). For high pressure systems the computational investment may not be justified due to uncertainty in measured reaction kinetics. Thus, a global reaction mechanism (neglecting intermediate steps) has been used,



The reaction rate is defined using the Law of Mass Action and an Arrhenius expression for C , the specific reaction rate constant.

$$\begin{aligned}\omega &= C \prod_{i=1}^N \sigma_i^{\nu_i} \\ &= AT^\beta \exp\left(\frac{-E_a}{RT}\right) \sigma_{\text{CH}_4}^a \sigma_{\text{O}_2}^b \sigma_{\text{CO}}^c \sigma_{\text{H}_2}^d \sigma_{\text{CO}_2}^e \sigma_{\text{H}_2\text{O}}^f\end{aligned}\quad (18)$$

where AT^β is the collision frequency ($\beta = 0$ for the present work) and the exponential term is the Boltzmann factor. Exponents a thru f are originally chosen to fit results from flame experiments using large kinetic mechanisms (see Table 1) but can be adjusted so that computed results more closely match experimental observations.

Table 1. Reduced Reaction Rate Data

Equ.	E_a	A	a	b	c	d	e	f
17 (1)	30.0	8.3×10^5	1.0	3.5	1.0	2.0	0.0	0.0
17 (2)	44.7	3.0×10^6	0.0	0.5	1.0	0.0	1.0	0.0
17 (3)	37.6	1.0×10^5	0.0	1.0	0.0	2.0	0.0	2.0

CHEMICAL KINETICS MODEL

The chemical energy (non-dimensional) released by ram accelerator gas mixtures, $Q/c_p T$, has been used as a relative figure of merit in predicting performance.^{3,20} Here, the specific heat, c_p , and temperature, T , are taken as the fill conditions for the gas mixture. However, in rating ram accelerator performance, it is required to determine if a specific mixture will result in significant chemical heat release (with attendant pressure rise) on the afterbody and base of the projectile, thus generating thrust. If significant release occurs on the forebody, either a reduction in thrust or an unstart (i.e., negative thrust) will result. This determination requires knowledge of the chemical ignition delay time (energy release rate) of the mixture,

the gas dynamic flow time, the projectile geometry and velocity. CFD analysis provides a good overall picture of the gas dynamic flow field but is limited to reduced chemical kinetics mechanisms that do not accurately represent the ignition delay time (especially at high pressures) without empirical adjustment. In order to investigate the ignition delay time (i.e., the time for rapid heat release to occur after the temperature of a gas mixture has been raised), a full kinetics mechanism must be used. Chemical kinetics analysis does not consider the gas dynamic flow over the projectile, as does the CFD analysis, but requires far less computer time. Full mechanisms for methane/air combustion have been the subject of intense research by several institutions including the Gas Research Institute (GRI).¹⁵ The GRI mechanism consists of 32 species and 176 reactions. The species are: H_2 , H , O_2 , O , OH , H_2O , HO_2 , H_2O_2 , C , CH , CH_2 , CH_2^* , CH_3 , CH_4 , CO , CO_2 , HCO , CH_2O , CH_2OH , CH_3O , CH_3OH , C_2H , C_2H_2 , C_2H_3 , C_2H_4 , C_2H_5 , C_2H_6 , $HCCO$, CH_2CO , $HCCOH$, N_2 , AR . The reactions are given in Table 2. The effectiveness of this mechanism at high pressures (i.e., > 10 atm) is not known. To link this full kinetics mechanism to the CFD code would provide a coupled chemical time and flow time analysis, but would require prohibitively long computer run times. Therefore, the ARL has adopted both a CFD solution of the nonequilibrium Navier-Stokes equations with a 3-step reduced methane reaction mechanism (Eq. 17), and a kinetics analysis of a full mechanism as two primary tools for predicting mixture performance.

The SENKIN kinetics code¹⁶ predicts the time dependent chemical kinetics behavior of a homogeneous gas mixture in a closed system. In addition to predicting the species and temperature histories, the code can also compute the first-order sensitivity coefficients with respect to the elementary reaction rate parameters. Once the kinetics mechanism has been specified, the code can be configured for a variety of scenarios including an system (i.e., specified initial mole fractions of the reactants) assumed adiabatic at constant pressure and an initial temperature; the system is free to expand, and the enthalpy of the system is constant. The governing equations follow from conservation of mass and energy.

$$\frac{d\sigma_i}{dt} = \frac{V\omega_i\mathcal{M}_i}{m}, \quad i = 1, N \quad (19)$$

$$c_p \frac{dT}{dt} + \frac{V}{m} \sum_{i=1}^N h_i \omega_i \mathcal{M}_i = 0 \quad (20)$$

The chemical production term, ω for each species i , is specified in Arrhenius form (see Eq. 18). An initial value problem for the system of ordinary differential equations is formulated given the constant pressure, initial temperature and initial composition of the system. The equations are numerically stiff, in general, and require special integration techniques.¹⁶ Typical run time on an SGI Indigo Elan is 5 minutes. The results include total heat release versus time and temperature. The total non-dimensional heat released by the mixture, $Q/c_p T$, is the area under the heat released versus time curve. In the present work, the SENKIN code was run with initial conditions of the fill pressure, fill composition, and an initial temperature typical of the pre-combustion flowfield. A post-processing code for SENKIN was provided by W. Anderson at ARL.

RESULTS

Steady-State Simulations

Steady-state CFD simulations are reported for conditions corresponding to shot 27 of the ARL 120-mm ram accelerator.¹ The accelerator tube was filled with the standard gaseous mixture of $3\text{CH}_4 + 2\text{O}_2 + 10\text{N}_2$ (molar) at 300 K and pressurized to 750 psi (50 atm). This mixture has a sound speed of 361 m/s, a Chapman-Jouget detonation speed of 1448 m/s, and a pre-combustion γ of 1.379. The projectile fins were neglected so that axisymmetric simulations could be used. The flowfield equations (Eq. 1) were then marched in a time-accurate fashion until steady-state was achieved for a fixed projectile velocity. The presence of the obturator was neglected. Comparison between CFD simulation and measured tube wall pressure data, for a variety of conditions, have been reported by Nusca.¹⁷

Figure 2 shows the computed temperature contours for projectile velocity of 1195 m/s (Mach No. = 3.3, $V/V_{CJ} = .83$); the mixture was restrained to be chemically frozen. The projectile nose shock reflects from the tube wall, heating the mixture to 410K, and then from the projectile surface, further heating the mixture to 480K. On the projectile surface, gas temperatures approach the stagnation temperature (950K). For results shown in Figure 3, the mixture was allowed to chemically react. Ignition of the mixture is indicated by the sudden appearance of H_2O , a major reaction product. Chemical reactions start both in the forebody boundary layer and at the point of shock reflection from the tube wall. Reactions engulf the entire projectile afterbody surface and continue in the tube wall boundary layer downstream of the projectile. The projectile wake contains reaction products as well (not shown in Figure 3, see Reference 2). Figure 4 shows the comparison of measured and computed tube wall pressures for these conditions (see Reference 17 for additional comparisons between computed and measured tube wall pressures).

Figures 5 and 6 show computed results for projectile velocities corresponding to Mach numbers of 4.3 and 5.3, all other conditions the same as for Figure 3. The shock and boundary-layer induced reactions produce more water near the projectile, which begins to diffuse further out into the flowfield on the projectile forebody. A small region of ignition on the projectile nose occurs at the flow stagnation point. Figure 5 indicates the "high Mach number unstart" phenomena³ as a wave of combustion now travels ahead of the projectile, starting at the nosetip. More intense combustion (i.e., large amounts of H_2O) are observed at the forebody-afterbody junction. The computed projectile thrust values (force normalized by fill pressure and tube cross sectional area, F/PA) corresponding to Figures 2, 3, 5 and 6 are -.61 (for the non-reacting case), 2.5, 2.3, and -.21, respectively. Negative values indicate a projectile drag force. Thrust was determined by numerical integration of pressure and shear stress on the projectile surface. The initial gas pressure also influences projectile performance.²

The results of Figures 3, 5, and 6 demonstrate that increasing projectile velocity, while decreasing the characteristic flow time, increases the gas temperature (through shock and boundary layer heating) which decreases the characteristic chemical time. Figure 7 shows the results of several SENKIN calculations for the standard mixture at constant pressures of 50 and 100 atm, and initial temperatures of 1250 and 1350K. These temperatures are typical of those achieved by the shock waves (bow and reflected) and stagnation in the wall boundary

layer (CFD simulations show for flow velocity from 1200 to 2000 m/s pre-combustion temperatures are 700 to 1200K in the forebody shock layer and 1000 to 1800K in the afterbody flow field). The value 1350K was chosen as an average over the velocity range 1200-2000 m/s and since this temperature leads to ignition times of the same order of magnitude as the flow time over the ARL projectile ($L=0.522\text{m}$, $U=1200\text{-}2000\text{m/s}$, $L/U=0.435\text{-}0.261\text{ ms}$). The ignition delay time (see Fig. 7) is linearly dependent on pressure (for this mechanism, mixture, and temperature range) while the effect of initial temperature on ignition time is more dramatic; hotter initial temperatures produce shorter times. The Damkohler number (ratio of flow time to chemistry time) can be computed using,¹⁸

$$\text{Da} = \frac{\rho^\epsilon L}{U \exp(-T)} \quad (21)$$

where ϵ is 1 for two-body collisions and 2 for collisions involving three bodies. Thus the flow time is L/U and the chemical time is $\exp(-T)/\rho^\epsilon$. The chemical time decreases with increasing temperature and increasing pressure (density). For $\text{Da} \gg 1$ the flow approaches chemical equilibrium (i.e., no ignition delay); for $\text{Da} \ll 1$ the flow approaches chemically frozen conditions (i.e., infinite ignition delay); for $\text{Da} \simeq 1$ the flow is in chemical nonequilibrium. Increases in Da with increasing gas dynamic flow temperature (exponential effect) causes chemical ignition of the mixture closer to the nosetip as observed in Figures 3, 5, and 6. Relying solely on the heat released by the mixture, $Q/c_p T$, to judge mixture performance does not show this effect since $Q/c_p T$ is a constant 3.64 for this mixture (c_p and T are the initial fill specific heat and temperature of the mixture). Flow temperature can also increase (decreasing the ignition time) due to the type of chemical diluent used, as discussed below.

Figure 8 shows the results of several SENKIN calculations for 5 different gas mixtures, a constant pressure of 50 atm, and an initial temperature of 1350K. The standard mixture (STD) is $3\text{CH}_4+2\text{O}_2+10\text{N}_2$. The mixtures 34/1 and 36/1 (shot number/stage number) are slight variations, $2.6\text{CH}_4+2.1\text{O}_2+10.4\text{N}_2$ and $2.7\text{CH}_4+2.1\text{O}_2+9.67\text{N}_2$, respectively. The mixtures 34/2 and 36/2 contain different amount of diluent (N_2) or helium as a diluent, $2.5\text{CH}_4+2.1\text{O}_2+6.5\text{N}_2$ and $5\text{CH}_4+2\text{O}_2+4\text{He}$, respectively. The values of heat released by these mixtures, $Q/c_p T$ (i.e., the area under the curves), are STD: 3.64, 34/1: 3.78, 36/1: 3.81, 34/2: 5.15, and 36/2: 4.08. The standard mixture, usually the intended content of the first stage of the ARL ram accelerator, has been shown to yield good projectile acceleration.¹ The mixture in these exact molar proportions is not always achieved after filling, with typical variations represented by mixtures 34/1 and 36/1. However, these variations reduce the chemical ignition time noticeably, and increase $Q/c_p T$. Even greater reduction in ignition time and increase in $Q/c_p T$ is achieved by reducing the amount of N_2 or replacing N_2 with helium. For mixture 34 it is expected that more ignition may occur on the forebody (reducing thrust) due to reduced ignition time; however, this is balanced by greater heat release and pressure levels on the afterbody (resulting in an increased net thrust) due to the greater $Q/c_p T$. Using the typical temperature of 1350K (as in the 34 case) for the mixture with helium diluent (36/2) was found not to be appropriate since helium yields a higher gas temperature as an atomic species (with two energy degrees of freedom) compared to diatomic nitrogen (with five energy degrees of freedom). The higher gas temperature for helium occurs despite its higher sound speed that yields a lower projectile Mach number (weaker shocks) for the same projectile velocity. The curve marked (36/2)* in Figure 8 was generated using 1400K (i.e., a temperature higher than 1350K) and thus suggests that shot 36 will perform

less satisfactorily that shot 34 due to the significantly shorter ignition time for stage 2 (in fact shot 36 produced a gas dynamic unstart after entering the second stage¹⁹). It should be cautioned that Figures 7 and 8 be used to compare mixture ignition times and that the actual times not be used in an absolute sense. Performance results for these mixtures are discussed in the next section.

Time-Accurate Simulations

Time-accurate CFD simulations are reported for conditions corresponding to shots 27, 34, and 36 of the ARL 120-mm ram accelerator.¹ For shot 27 the accelerator tube is filled with the standard mixture. For shots 34 and 36 the first tube is filled the 34/1 and 36/1 mixtures, respectively, while the second (and third) tubes were filled with the 34/2 and 36/2 mixtures. The initial pressure and temperature of all tubes was 50 atm and 300K, respectively. The tubes for stages 1, 2, and 3 were each 4.7m long. Doppler radar was used to obtain a continuous in-bore velocity-time history of the projectile. The shot 27 CFD simulation was started with entrance of the projectile/obturator combination into the first accelerator tube at $t = 20.05$ ms with specified velocity (1256.4 m/s) and obturator back pressure (4000 psi). The projectile fins were neglected so that axisymmetric simulations could be used. The flowfield equations (Eq. 1) were then solved in a time-accurate fashion along with a force computation for the projectile and obturator, individually. The velocity of the projectile and the relative separation between the projectile base and obturator were updated for each time step (0.2 ms) using the computed, time-dependent force and given masses. The backpressure on the obturator due to the conventional charge was assumed to be nonexistent after 20.45 ms. Since the obturator is greater than five projectile lengths downstream of the projectile base after this time, its influence on the projectile flowfield is negligible. A downstream outflow condition is then prescribed one projectile body length behind the projectile. Although the tubes are sealed with PVC diaphragms, projectile transition between accelerator tubes was simulated assuming no physical barrier.

Figure 9 shows the measured projectile velocity-time history. The projectile velocity was measured using a Doppler radar positioned outside the accelerator and beamed into the tube using a sacrificial mirror. The computer simulation shows overprediction by about 2.3% with respect to measurements. Obturator tilting (i.e., the obturator length is such that the obturator can spin within the tube cross-section) was observed using a clear tube section in the test.¹ Thus pressure is relieved from behind the projectile and thrust is decreased.

Figure 10 shows the computed time sequence of projectile obturator separation in terms of gas H_2O mass fraction. Water is a major product for the reaction given by Equation 17, thus illustrating regions of significant combustion activity. For Figure 10, white corresponds to the absence of H_2O in the flowfield, while dark grey corresponds to a water mass fraction of 0.1. Reference 2 shows the Mach number contours for this time sequence. Flow stagnation on the obturator, when in close proximity to the projectile, causes both a normal shock and a combustion front to occur on the projectile. The combustion front is located on the projectile forebody while the normal shock is located on the afterbody (see Ref. 2). Flow between the combustion front and the normal shock is slightly supersonic. As the obturator is pushed further back from the projectile (the last frame of Figure 10 corresponds to an obturator location of 1.47 m, 2.81 projectile lengths, behind the projectile base), the normal shock moves rearward and is eventually positioned behind the projectile. At

this point the projectile is in fully supersonic flight. Combustion occurs at the projectile-afterbody junction, due to shock heating, in the projectile and tube wall boundary layers due to stagnation heating, and behind the normal shock traveling behind the projectile. This normal shock, which also initiates combustion, is now driven by the obturator (i.e., a piston). Due to the high combustion pressures on the side toward the projectile and the relieved backpressure, the obturator is moving slower than the projectile.

Figure 11 shows three frames from a transient CFD simulation for shot 34 during passage from stage 1 to 2. Stage 1 was simulated as shot 27, described previously. Frame 1 of the figure shows H_2O mass fractions for the end of stage 1 with mixture 34/1 and projectile velocity of 1435m/s (measured value was 1405m/s). In comparison to the standard mixture at the same Mach number (see Figure 3), which has a longer chemical ignition time (see Figure 8), predictably more ignition is observed in the forebody boundary layer in Figure 11. The computed thrust coefficient (F/PA) for this case is 2.0 (-0.61 for the forebody component). Frame 2 of the figure shows the start of stage 2 with the same projectile velocity but with mixture 34/2. Since this mixture has a shorter chemical time more ignition is observed in the forebody boundary layer, but more intense combustion on the afterbody (due to the higher mixture heat release) resulting in higher thrust and positive projectile acceleration. The computed thrust coefficient for this case is 2.33 with a higher drag for the forebody (-0.72 for the forebody component). The last frame of the figure represents the end of the combined stage 2 and 3 (both filled identically) where the projectile velocity is 1680m/s (measured value was 1648m/s). More combustion is observed on the forebody since increased flow temperature (due to increased projectile velocity) has increased Da (note the exponential effect of temperature and the linear effect of velocity in Eq. 21). The computed thrust coefficient for this case is 2.18 (-0.75 for the forebody component). This shot was a success but with an unusually large amount of light on the projectile forebody observed at shot exit.¹⁹

Figure 12 shows three frames from a transient CFD simulation for shot 36 during passage from stage 1 to 2. Frame 1 of the figure shows H_2O mass fractions for the end of stage 1 with mixture 36/1 and projectile velocity of 1400m/s (measured value was 1357m/s). Frame 2 of the figure shows the start of stage 2 with the same projectile velocity but with mixture 36/2. Since this mixture has slightly longer chemical time (Fig. 8) combustion is observed on the forebody but to a lesser extent than for entrance into stage 2 of shot 34. Mixture 36/2 has a larger sound speed than mixture 34/2 (484 and 356m/s, respectively) and thus the Mach number and nose shock strength are decreased in stage 2 of shot 36. This lesser combustion on the forebody could be attributed to reduced gas temperatures due to a weaker nose shock. However, the helium diluent used in mixture 36/2 will contribute to higher gas temperatures, for the same energy, due to reduced energy degrees of freedom as compared to nitrogen (as discussed previously). The last frame of Figure 12 represents a position further into the second stage where the projectile has decelerated to 1275m/s (measured value was 1250m/s). In the CFD simulation, the projectile thrust suddenly reduces to negative values (i.e., drag) as a combustion wave moved up onto the projectile forebody, as shown in this frame, and produced high pressure forces there (note that a normal shock does not appear in this flow field in contrast to that shown in Fig. 10). The simulation shows the unstart originating behind the projectile and moving forward. This type of unstart has been observed experimentally.²⁰ Shot 36 produced a gas dynamic unstart in the second stage as determined

from radar data measured during the firing.¹⁹

CONCLUSIONS

Numerical simulations show that stagnation of the combustible gas on the projectile obturator causes the formation of both a normal shock and a combustion wave in the flowfield. As the obturator is gasdynamically discarded, the normal shock trails behind the projectile and the combustion wave collapses into shock-induced combustion on the projectile. With the obturator sufficiently downstream, the projectile accelerates at supersonic speeds. Projectile transition from stage 1 to 2 (i.e., into a mixture with lower nitrogen diluent content) resulted in increased projectile forebody ignition due to the smaller chemical ignition time in stage 2, but increased projectile acceleration due to increased heat release on the projectile afterbody. The use of helium diluent resulted in a smaller chemical ignition time (compared to nitrogen) and higher flow temperatures, despite the higher sound speed, and thus caused a gas dynamic unstart in stage 2.

ACKNOWLEDGEMENTS

Mr. D. Kruczynski, Mr. A. Horst, and Dr. T. Minor provided support for numerical simulation for the HIRAM project and have contributed to this work through various technical discussions. Drs. W. Anderson and A. Miziolek provided technical guidance for SENKIN.

REFERENCES

1. Kruczynski, D.L., Liberatore, F., and Kiwan, M., "Flow Visualization of Steady and Transient Combustion in a 120-MM Ram Accelerator," AIAA Paper No. 94-3344, June 1994.
2. Nusca, M.J., "Reacting Flow Simulation for a Large Scale Ram Accelerator," AIAA Paper No. 94-2963, June 1994.
3. Hertzberg, A., Bruckner, A.P., and Bogdanoff, D.W., "Ram Accelerator: A New Chemical Method for Accelerating Projectiles to Ultrahigh Velocities," AIAA Journal, Vol. 26, No. 2, Feb. 1988, pp. 195-203.
4. Smeets, G., Seiler, F., Patz, G., and Srulijes, J., "First Results in a 30-mm-Caliber Scram Accelerator Using a Rail Tube for Cylindrical Projectiles," 25th International Symposium on Combustion, Irvine CA, July 1994.
5. Giraud, M., Legendre, J.F., and Simon, G., "Ram Accelerator in 90 MM Caliber or RAMAC 90 Experimental Results Concerning the Transdetonative Combustion Mode," 14th International Symposium on Ballistics, Quebec, Canada, Sept. 1993, pp. 95-104.
6. Chakravarthy, S.R., Szema, K.Y., Goldberg, U.C., Gorski, J.J., and Osher, S., "Application of a New Class of High Accuracy TVD Schemes to the Navier-Stokes Equations," AIAA Paper No. 85-0165, January 1985.
7. Palaniswamy, S., and Chakravarthy, S.R., "Finite Rate Chemistry for USA Series Codes: Formulation and Applications," AIAA Paper No. 89-0200, January 1989.

8. Palaniswamy, S., Ota, D.K., and Chakravarthy, S.R., "Some Reacting-Flow Validation Results for USA-Series Codes," AIAA Paper No. 91-0583, January 1991.
9. Roe, P.L., "Approximate Riemann Solvers, Parameter Vectors, and Difference Schemes," Journal of Computational Physics, Vol. 43, 1981, pp. 357-372.
10. Stull, D.R., and Prophet, H., "JANNAF Thermochemical Tables," 2nd ed., National Bureau of Standards, NSRDS-Rept. 37, June 1971.
11. Wilke, C.R., "A Viscosity Equation for Gas Mixtures," Journal of Chemistry and Physics, Vol. 18, No. 4, pp. 517-519, 1950.
12. Drummond, J.P., Rogers, C., and Hussaini, M.Y., "A Numerical Model for Supersonic Reacting Mixing Layer," Computer Methods in Applied Mechanics and Engineering, Vol. 64, 1987.
13. Hirschfelder, J.O., Curtiss, C.F., and Bird, R., Molecular Theory of Gases and Liquids, John Wiley & Sons, 1954.
14. Anderson, W.R., and Kotlar, A.J., "Detailed Modeling of CH₄/O₂ Combustion for Hybrid In-Bore Ram Propulsion (HIRAM) Application," 28th JANNAF Combustion Meeting, CPIA Pub. No. 573, Vol. 2, Oct. 1991, pp. 417-426.
15. Frenklach, M., Wang, H., Goldenberg, M., Smith, G.P., Golden, D.M., Bowman, C.T., Hanson, R.K., Gardiner, W.C., and Lissianski, V., Gas Research Institute, Chicago, Illinois, report in press, 1995.
16. Lutz, A.E., Kee, R.J., Miller, J.A., "SENKIN: A Fortran Program for Predicting Homogeneous Gas Phase Chemical Kinetics with Sensitivity Analysis," Sandia, SAND 87-8248, Feb. 1991.
17. Nusca, M.J., "Numerical Simulation of Fluid Dynamics with Finite-Rate and Equilibrium Combustion Kinetics for the 120-MM Ram Accelerator," AIAA Paper No. 93-2182, June 1993.
18. Anderson, G., Kumar, A., Erdos, J., "Progress in Hypersonic Combustion Technology with Computation and Experiment," AIAA Paper No. 90-5254, Oct. 1990.
19. Kruczynski, D.L., Liberatore, F., "Ram Accelerator Experiments with Unique Projectile Geometries," AIAA Paper No. 95-2490, July 1995.
20. Knowlen, C., Higgins, A.J., and Bruckner, A.P., "Investigation of Operational Limits to the Ram Accelerator," AIAA Paper No. 94-2967, June 1994.

Table 2. GRI Methane/Air Reaction Set (M is a third body)

$2O+M \rightleftharpoons O_2+M$ $O+HO_2 \rightleftharpoons OH+O_2$ $O+CH_2 \rightleftharpoons H+HCO$ $O+CH_3 \rightleftharpoons H+CH_2O$ $O+HCO \rightleftharpoons OH+CO$ $O+CH_2OH \rightleftharpoons OH+CH_2O$ $O+CH_3OH \rightleftharpoons OH+CH_3O$ $O+C_2H_2 \rightleftharpoons OH+C_2H$ $O+C_2H_4 \rightleftharpoons CH_3+HCO$ $O+HCCO \rightleftharpoons H+2CO$ $O_2+CO \rightleftharpoons O+CO_2$	$O+H+M \rightleftharpoons OH+M$ $O+H_2O_2 \rightleftharpoons OH+HO_2$ $O+CH_2^* \rightleftharpoons H_2+CO$ $O+CH_4 \rightleftharpoons OH+CH_3$ $O+HCO \rightleftharpoons H+CO_2$ $O+CH_3O \rightleftharpoons OH+CH_2O$ $O+C_2H \rightleftharpoons CH+CO$ $O+C_2H_2 \rightleftharpoons CO+CH_2$ $O+C_2H_5 \rightleftharpoons CH_3+CH_2O$ $O+CH_2CO \rightleftharpoons OH+HCCO$ $O_2+CH_2O \rightleftharpoons HO_2+HCO$	$O+H_2 \rightleftharpoons H+OH$ $O+CH \rightleftharpoons H+CO$ $O+CH_2^* \rightleftharpoons H+HCO$ $O+CO+M \rightleftharpoons CO_2+M$ $O+CH_2O \rightleftharpoons OH+HCO$ $O+CH_3OH \rightleftharpoons OH+CH_2OH$ $O+C_2H_2 \rightleftharpoons H+HCCO$ $O+C_2H_3 \rightleftharpoons H+CH_2CO$ $O+C_2H_6 \rightleftharpoons OH+C_2H_5$ $O+CH_2CO \rightleftharpoons CH_2+CO_2$
$H+O_2+M \rightleftharpoons HO_2+M$ $H+O_2+N_2 \rightleftharpoons HO_2+N_2$ $2H+M \rightleftharpoons H_2+M$ $2H+CO_2 \rightleftharpoons H_2+CO_2$ $H+HO_2 \rightleftharpoons O_2+H_2$ $H+H_2O_2 \rightleftharpoons OH+H_2O$ $H+CH_2^* \rightleftharpoons CH+H_2$ $H+HCO(+M) \rightleftharpoons CH_2O(+M)$ $H+CH_2O(+M) \rightleftharpoons CH_3O(+M)$ $H+CH_2OH \rightleftharpoons H_2+CH_2O$ $H+CH_3O(+M) \rightleftharpoons CH_3OH(+M)$ $H+CH_3O \rightleftharpoons OH+CH_3$ $H+CH_3OH \rightleftharpoons CH_3O+H_2$ $H+C_2H_3(+M) \rightleftharpoons C_2H_4(+M)$ $H+C_2H_4 \rightleftharpoons C_2H_3+H_2$ $H+C_2H_6 \rightleftharpoons C_2H_5+H_2$ $H+CH_2CO \rightleftharpoons CH_3+CO$	$H+2O_2 \rightleftharpoons HO_2+O_2$ $H+O_2+AR \rightleftharpoons HO_2+AR$ $2H+H_2 \rightleftharpoons 2H_2$ $H+OH+M \rightleftharpoons H_2O+M$ $H+HO_2 \rightleftharpoons 2OH$ $H+CH \rightleftharpoons C+H_2$ $H+CH_3(+M) \rightleftharpoons CH_4(+M)$ $H+HCO \rightleftharpoons H_2+CO$ $H+CH_2O \rightleftharpoons HCO+H_2$ $H+CH_2OH \rightleftharpoons OH+CH_3$ $H+CH_3O \rightleftharpoons H+CH_2OH$ $H+CH_3O \rightleftharpoons CH_2^*+H_2O$ $H+C_2H(+M) \rightleftharpoons C_2H_2(+M)$ $H+C_2H_3 \rightleftharpoons H_2+C_2H_2$ $H+C_2H_5(+M) \rightleftharpoons C_2H_6(+M)$ $H+HCCO \rightleftharpoons CH_2^*+CO$ $H+HCCOH \rightleftharpoons H+CH_2CO$	$H+O_2+H_2O \rightleftharpoons HO_2+H_2O$ $H+O_2 \rightleftharpoons O+OH$ $2H+H_2O \rightleftharpoons H_2+H_2O$ $H+HO_2 \rightleftharpoons O+H_2O$ $H+H_2O_2 \rightleftharpoons HO_2+H_2$ $H+CH_2(+M) \rightleftharpoons CH_3(+M)$ $H+CH_4 \rightleftharpoons CH_3+H_2$ $H+CH_2O(+M) \rightleftharpoons CH_2OH(+M)$ $H+CH_2OH(+M) \rightleftharpoons CH_3OH(+M)$ $H+CH_2OH \rightleftharpoons CH_2^*+H_2O$ $H+CH_3O \rightleftharpoons H_2+CH_2O$ $H+CH_3OH \rightleftharpoons CH_2OH+H_2$ $H+C_2H_2(+M) \rightleftharpoons C_2H_3(+M)$ $H+C_2H_4(+M) \rightleftharpoons C_2H_5(+M)$ $H+C_2H_5 \rightleftharpoons H_2+C_2H_4$ $H+CH_2CO \rightleftharpoons HCCO+H_2$ $H_2+CO(+M) \rightleftharpoons CH_2O(+M)$
$OH+H_2 \rightleftharpoons H+H_2O$ $OH+HO_2 \rightleftharpoons O_2+H_2O$ $OH+CH \rightleftharpoons H+HCO$ $OH+CH_2^* \rightleftharpoons H+CH_2O$ $OH+CH_3 \rightleftharpoons CH_2^*+H_2O$ $OH+HCO \rightleftharpoons H_2O+CO$ $OH+CH_3O \rightleftharpoons H_2O+CH_2O$ $OH+C_2H \rightleftharpoons H+HCCO$ $OH+C_2H_2 \rightleftharpoons C_2H+H_2O$ $OH+C_2H_4 \rightleftharpoons C_2H_3+H_2O$	$2OH(+M) \rightleftharpoons H_2O_2(+M)$ $OH+H_2O_2 \rightleftharpoons HO_2+H_2O$ $OH+CH_2 \rightleftharpoons H+CH_2O$ $OH+CH_3(+M) \rightleftharpoons CH_3OH(+M)$ $OH+CH_4 \rightleftharpoons CH_3+H_2O$ $OH+CH_2O \rightleftharpoons HCO+H_2O$ $OH+CH_3OH \rightleftharpoons CH_2OH+H_2O$ $OH+C_2H_2 \rightleftharpoons H+CH_2CO$ $OH+C_2H_2 \rightleftharpoons CH_3+CO$ $OH+C_2H_6 \rightleftharpoons C_2H_5+H_2O$	$2OH \rightleftharpoons O+H_2O$ $OH+C \rightleftharpoons H+CO$ $OH+CH_2 \rightleftharpoons CH+H_2O$ $OH+CH_3 \rightleftharpoons CH_2+H_2O$ $OH+CO \rightleftharpoons H+CO_2$ $OH+CH_2OH \rightleftharpoons H_2O+CH_2O$ $OH+CH_3OH \rightleftharpoons CH_3O+H_2O$ $OH+C_2H_2 \rightleftharpoons H+HCCOH$ $OH+C_2H_3 \rightleftharpoons H_2O+C_2H_2$ $OH+CH_2CO \rightleftharpoons HCCO+H_2O$
$2HO_2 \rightleftharpoons O_2+H_2O_2$ $HO_2+CH_3 \rightleftharpoons O_2+CH_4$ $HO_2+CH_2O \rightleftharpoons HCO+H_2O_2$ $C+CH_3 \rightleftharpoons H+C_2H_2$ $CH+H_2O \rightleftharpoons H+CH_2O$ $CH+CH_4 \rightleftharpoons H+C_2H_4$ $CH+CH_2O \rightleftharpoons H+CH_2CO$ $CH_2+H_2 \rightleftharpoons H+CH_3$ $CH_2+CH_4 \rightleftharpoons 2CH_3$ $CH_2^*+N_2 \rightleftharpoons CH_2+N_2$ $CH_2^*+O_2 \rightleftharpoons CO+H_2O$ $CH_2^*+H_2O \rightleftharpoons CH_2+H_2O$ $CH_2^*+CO \rightleftharpoons CH_2+CO$ $CH_2^*+C_2H_6 \rightleftharpoons CH_3+C_2H_5$ $CH_3+H_2O_2 \rightleftharpoons HO_2+CH_4$ $CH_3+HCO \rightleftharpoons CH_4+CO$ $CH_3+CH_3OH \rightleftharpoons CH_3O+CH_4$ $HCO+H_2O \rightleftharpoons H+CO+H_2O$ $CH_2OH+O_2 \rightleftharpoons HO_2+CH_2O$ $C_2H+H_2 \rightleftharpoons H+C_2H_2$ $C_2H_5+O_2 \rightleftharpoons HO_2+C_2H_4$	$2HO_2 \rightleftharpoons O_2+H_2O_2$ $HO_2+CH_3 \rightleftharpoons OH+CH_3O$ $C+O_2 \rightleftharpoons O+CO$ $CH+O_2 \rightleftharpoons O+HCO$ $CH+CH_2 \rightleftharpoons H+C_2H_2$ $CH+CO(+M) \rightleftharpoons HCCO(+M)$ $CH+HCCO \rightleftharpoons CO+C_2H_2$ $2CH_2 \rightleftharpoons H_2+C_2H_2$ $CH_2+CO(+M) \rightleftharpoons CH_2CO(+M)$ $CH_2^*+AR \rightleftharpoons CH_2+AR$ $CH_2^*+H_2 \rightleftharpoons CH_3+H$ $CH_2^*+CH_3 \rightleftharpoons H+C_2H_4$ $CH_2^*+CO_2 \rightleftharpoons CH_2+CO_2$ $CH_3+O_2 \rightleftharpoons O+CH_3O$ $2CH_3(+M) \rightleftharpoons C_2H_6(+M)$ $CH_3+CH_2O \rightleftharpoons HCO+CH_4$ $CH_3+C_2H_4 \rightleftharpoons C_2H_3+CH_4$ $HCO+M \rightleftharpoons H+CO+M$ $CH_3O+O_2 \rightleftharpoons HO_2+CH_2O$ $C_2H_3+O_2 \rightleftharpoons HCO+CH_2O$ $HCCO+O_2 \rightleftharpoons OH+2CO$	$HO_2+CH_2 \rightleftharpoons OH+CH_2O$ $HO_2+CO \rightleftharpoons OH+CO_2$ $C+CH_2 \rightleftharpoons H+C_2H$ $CH+H_2 \rightleftharpoons H+CH_2$ $CH+CH_3 \rightleftharpoons H+C_2H_3$ $CH+CO_2 \rightleftharpoons HCO+CO$ $CH_2+O_2 \rightleftharpoons OH+HCO$ $CH_2+CH_3 \rightleftharpoons H+C_2H_4$ $CH_2+HCCO \rightleftharpoons C_2H_3+CO$ $CH_2^*+O_2 \rightleftharpoons H+OH+CO$ $CH_2^*+H_2O(+M) \rightleftharpoons CH_3OH(+M)$ $CH_2^*+CH_4 \rightleftharpoons 2CH_3$ $CH_2^*+CO_2 \rightleftharpoons CO+CH_2O$ $CH_3+O_2 \rightleftharpoons OH+CH_2O$ $2CH_3 \rightleftharpoons H+C_2H_5$ $CH_3+CH_3OH \rightleftharpoons CH_2OH+CH_4$ $CH_3+C_2H_6 \rightleftharpoons C_2H_5+CH_4$ $HCO+O_2 \rightleftharpoons HO_2+CO$ $C_2H+O_2 \rightleftharpoons HCO+CO$ $C_2H_4(+M) \rightleftharpoons H_2+C_2H_2(+M)$ $2HCCO \rightleftharpoons 2CO+C_2H_2$

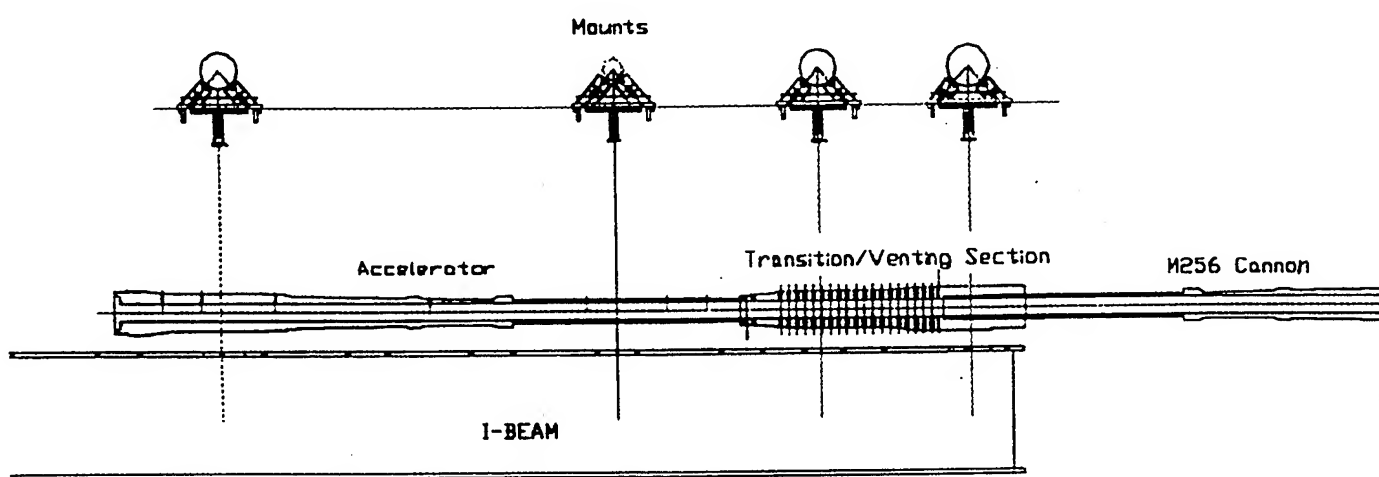
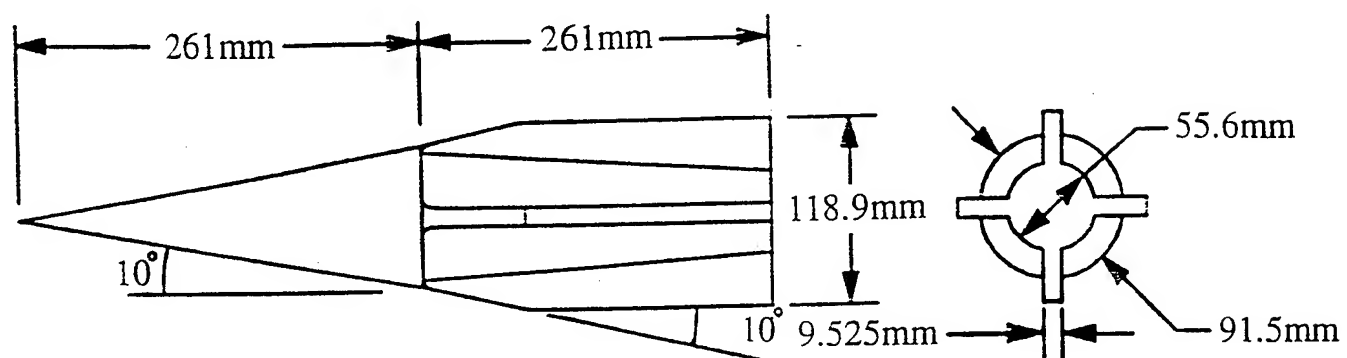


Figure 1: Schematic of projectile and gun assembly for 120-mm ram accelerator.

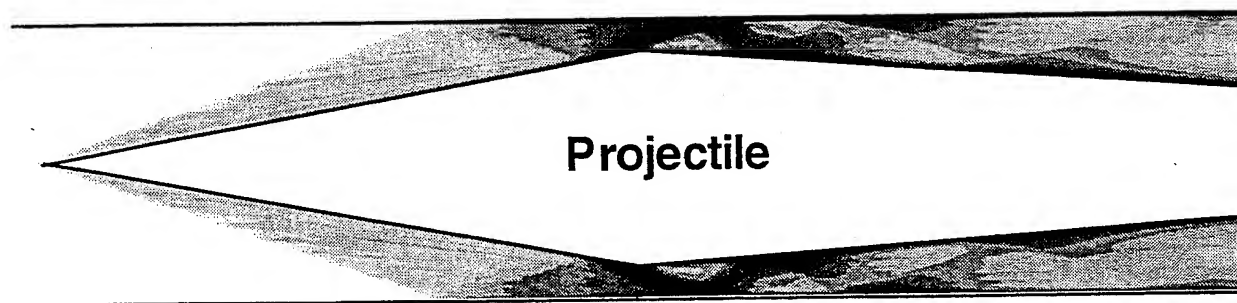


Figure 2: Non-reacting flowfield temperature contours ($300 \leq T \leq 480 + K$, white to dark black). Standard mixture at 50 atm. Velocity = 1195 m/s, $V/V_{CJ} = .83$. Mach No. = 3.3

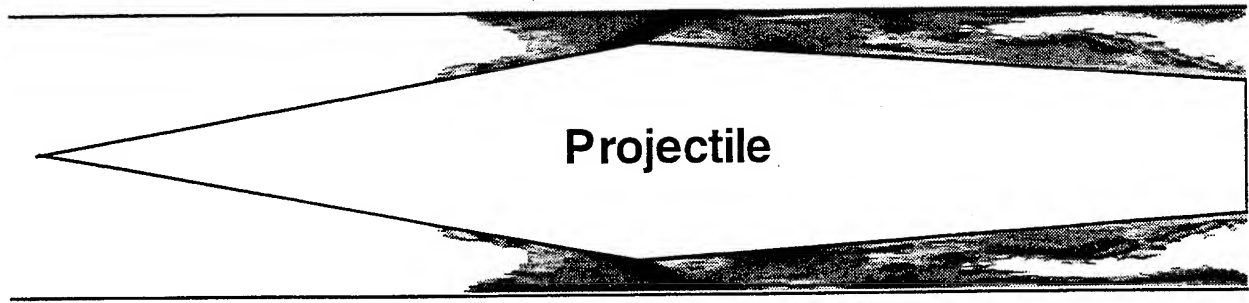


Figure 3: Flowfield H_2O mass fraction contours ($0 \leq c \leq 0.08$ in white, $0.08 < c \leq 0.1$ in grey to dark black). Standard mixture at 50 atm. Velocity = 1195 m/s, $V/V_{CJ} = .83$, Mach No. = 3.3

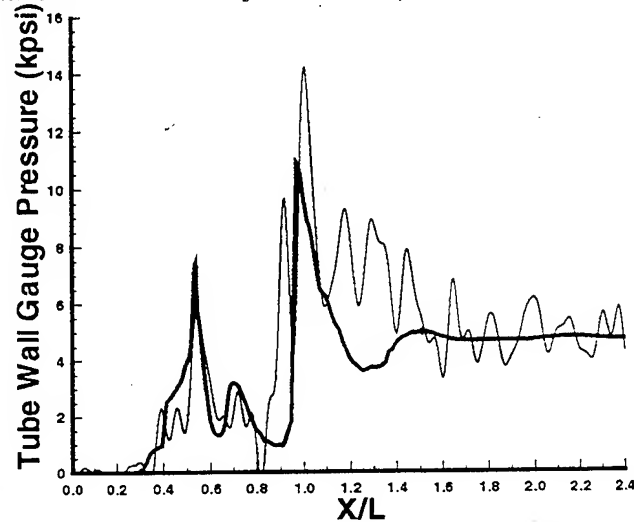


Figure 4: Computed (thick line) and measured (thin line) tube wall pressure distributions for conditions of Figure 3 ($L = .522\text{m}$ projectile length).

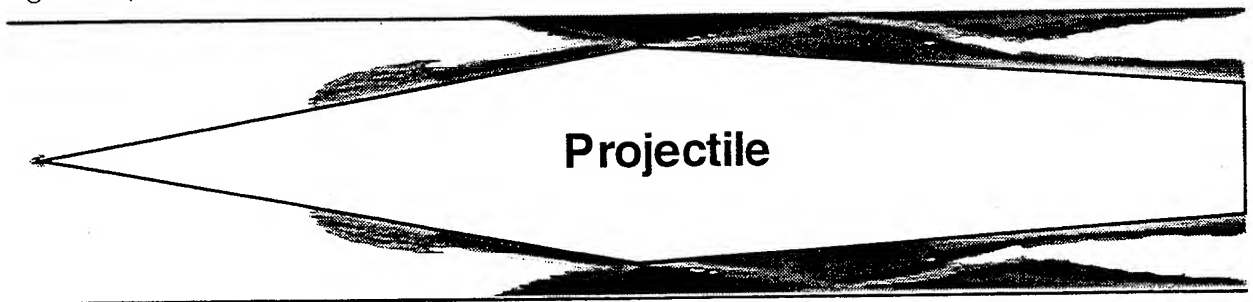


Figure 5: Flowfield H_2O mass fraction contours ($0 \leq c \leq 0.08$ in white, $0.08 < c \leq 0.1$ in grey to dark black). Standard mixture at 50 atm. Velocity = 1557 m/s, $V/V_{CJ} = 1.08$, Mach No. = 4.3

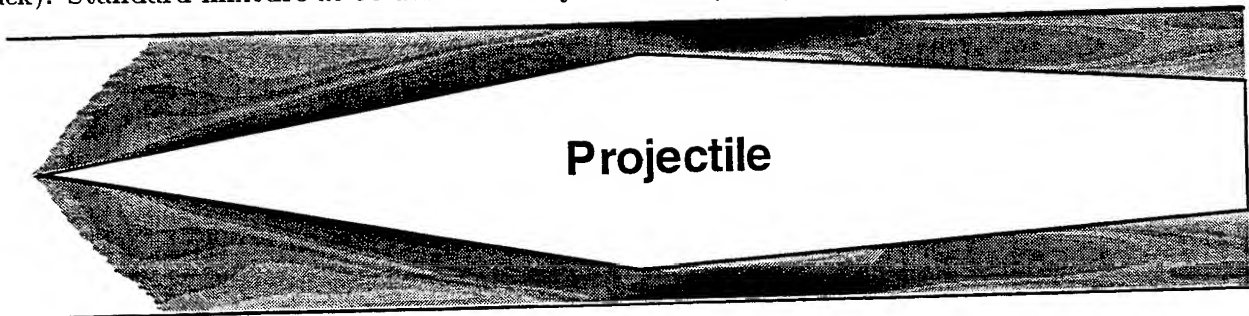


Figure 6: Flowfield H_2O mass fraction contours ($0 \leq c \leq 0.08$ in white, $0.08 < c \leq 0.1$ in grey to dark black). Standard mixture at 50 atm. Velocity = 1919 m/s, $V/V_{CJ} = 1.33$, Mach No. = 5.3

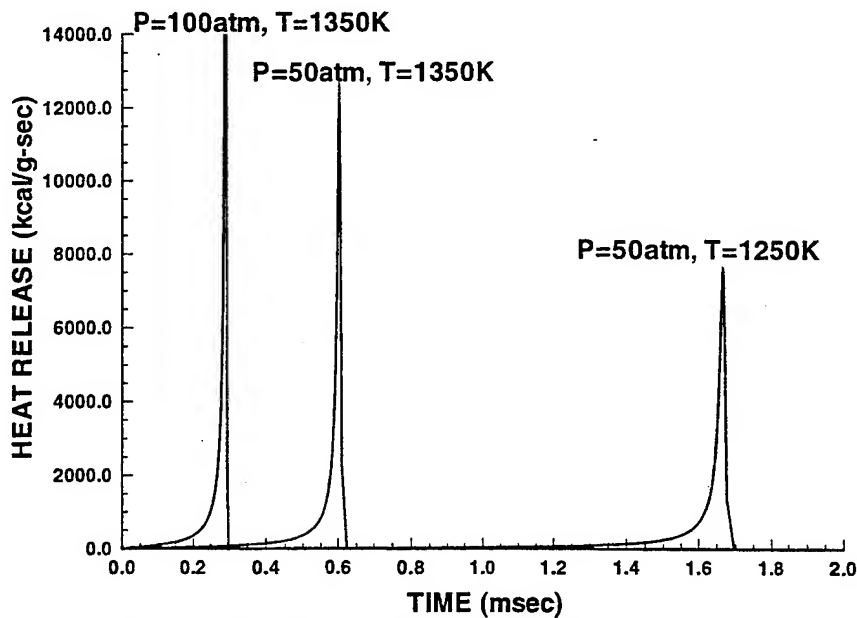


Figure 7: SENKIN results for the standard mixture.

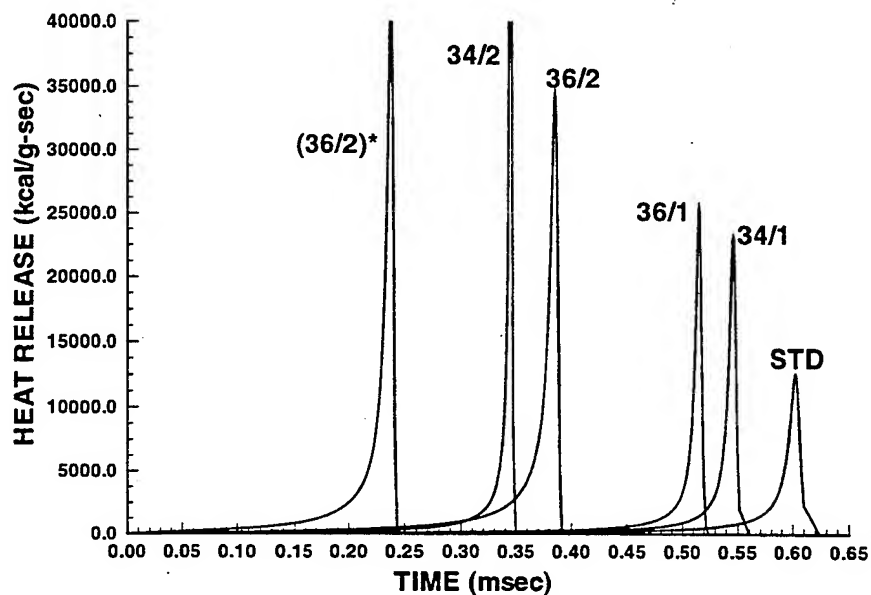


Figure 8: SENKIN results for $P = 50 \text{ atm}$, $T = 1350\text{K}$ (* $T = 1400\text{K}$), five different mixtures (see text for designations).

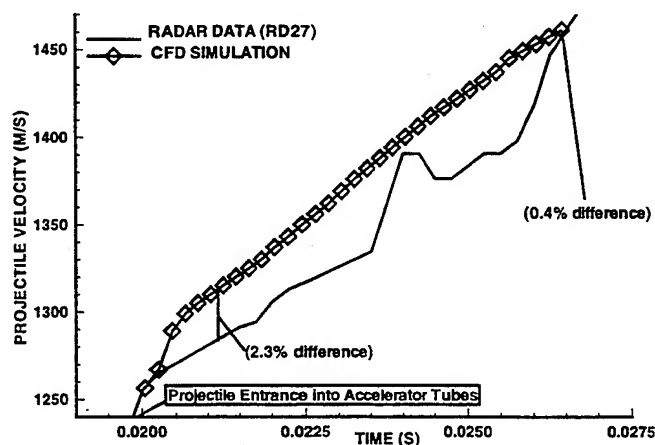


Figure 9: Computed and measured projectile velocity vs. time of flight for shot 27, standard mixture at 50 atm and 300 K fill conditions.

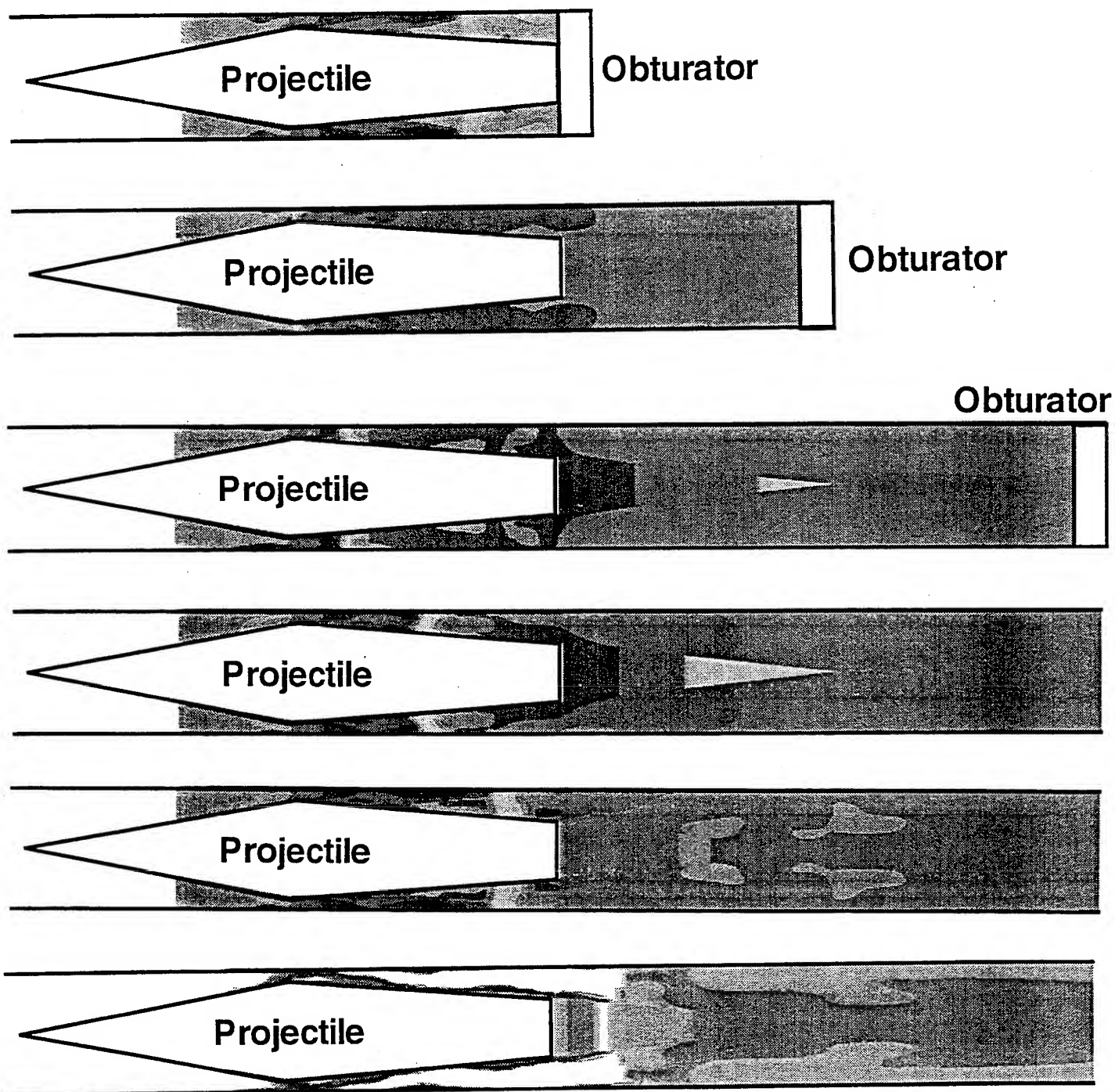


Figure 10: Flowfield H_2O mass fraction contours ($0 \leq c \leq 0.1$ for white to dark black) for shot 27. Time sequence from 20.05 ms to 21.05 ms, 0.2 ms interval. Computed projectile velocities: 1256, 1267, 1289, 1299, 1305, 1310 m/s. Computed obturator locations: 0, .443, .961, 1.51, 2.1, 2.81 L from projectile base.

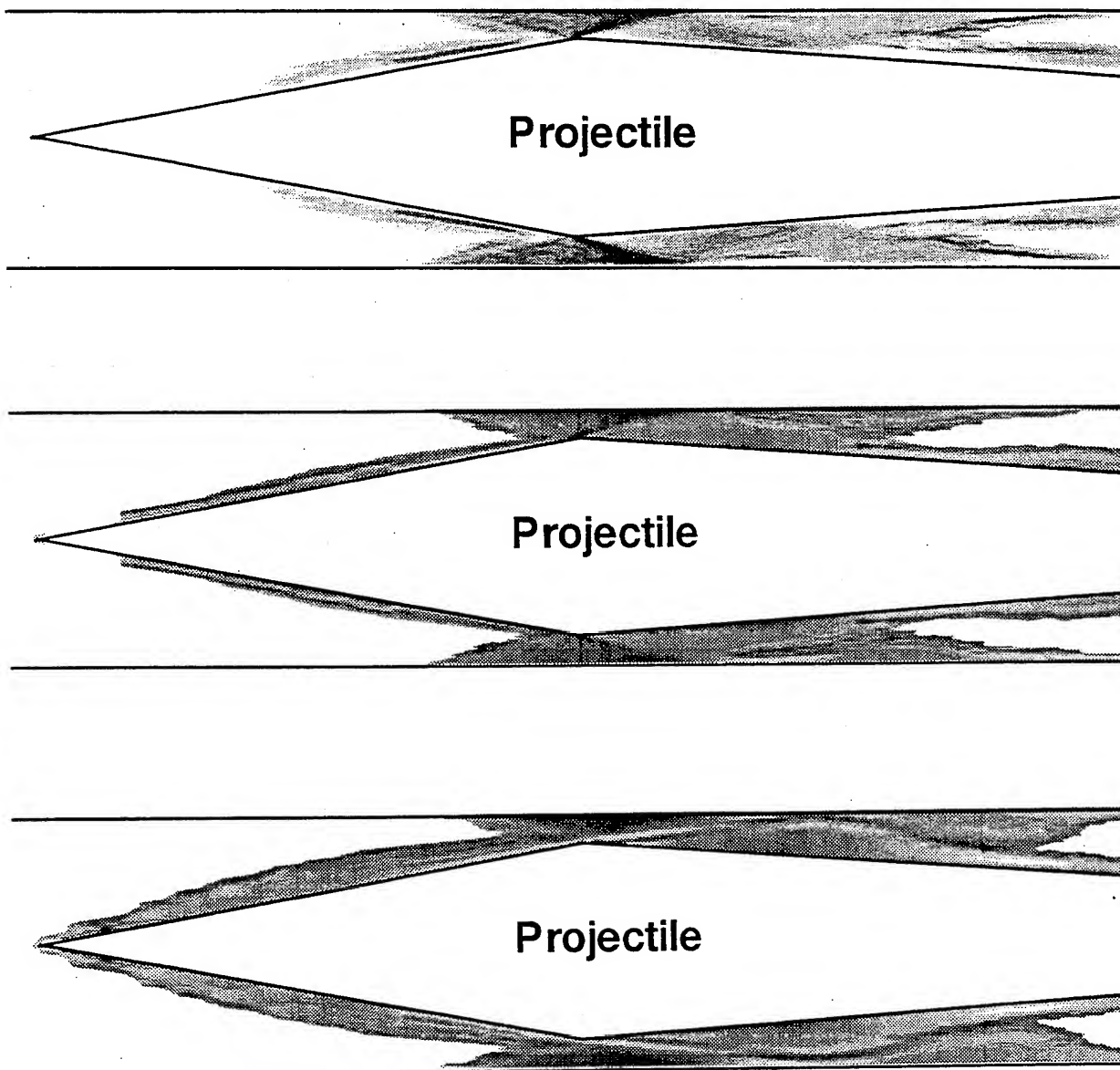


Figure 11: Flowfield H_2O mass fraction contours for shot 34. Frame 1: end of stage 1, mixture 34/1, projectile vel. = 1435 m/s ($0 \leq c \leq 0.092$ in white, $0.092 < c \leq 0.1$ in grey to dark black). Frame 2: start of stage 2, mixture 34/2, projectile vel. = 1435 m/s ($0 \leq c \leq 0.13$ in white, $0.13 < c \leq 0.138$ in grey to dark black). Frame 3: end of stage 3, mixture 34/2, projectile vel. = 1680 m/s ($0 \leq c \leq 0.13$ in white, $0.13 < c \leq 0.138$ in grey to dark black).

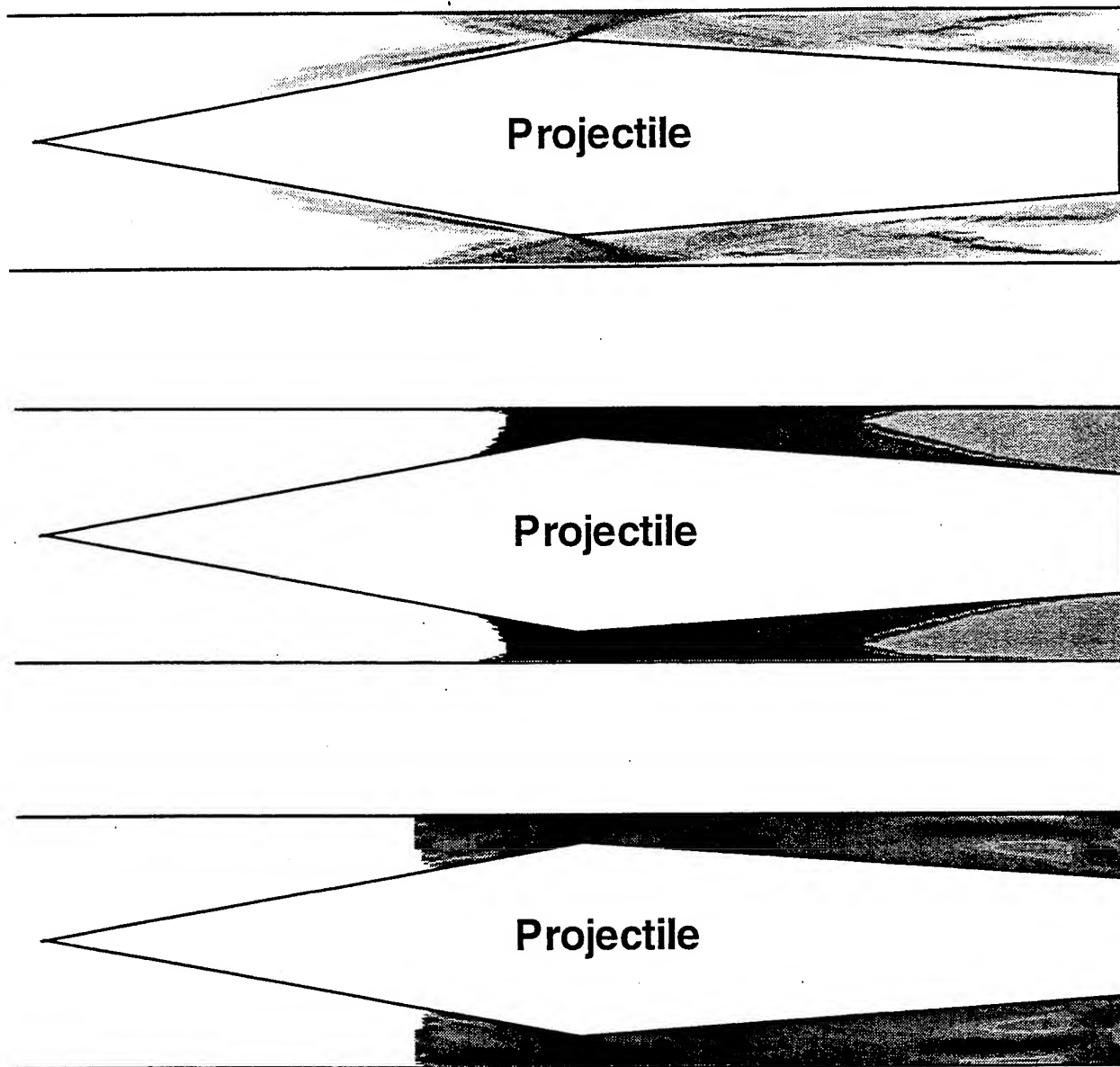


Figure 12: Flowfield H₂O mass fraction contours for shot 36. Frame 1: end of stage 1, mixture 36/1, projectile vel. = 1400 m/s ($0 \leq c \leq 0.092$ in white, $0.092 < c \leq 0.1$ in grey to dark black). Frame 2: start of stage 2, mixture 36/2, projectile vel. = 1400 m/s ($0 \leq c \leq 0.05$ in white, $0.05 < c \leq 0.1$ in grey to dark black). Frame 3: start of stage 2, mixture 36/2, projectile vel. = 1275 m/s ($0 \leq c \leq 0.09$ in white, $0.09 < c \leq 0.12$ in grey to dark black).

An Experimental and Numerical Investigation of the Three-Dimensional Flow Field About a Ram Accelerator Projectile

John B. Hinkey Jr.
Adroit Systems, Inc. (ASI)
Aeronautical and Astronautical Sciences Group
411-108th Ave. N.E., Suite 1080
Bellevue, Washington 98004, USA

ABSTRACT

An experimental and numerical investigation of the three-dimensional flow field associated with the ram accelerator projectile is presented. Experiments were performed which measured, with high spatial and temporal resolution, the tube wall pressure induced by a sub-caliber projectile as it travels supersonically through a tube containing a methane-based, pre-mixed combustible gas mixture. These experiments were performed in the sub-, trans-, and superdetonative regimes of a single-stage ram accelerator and reveal the three-dimensional nature of the projectile flow field as affected by the projectile fins, various combustion phenomena, and the phenomena of projectile canting. Numerical simulations of the non-reacting, three-dimensional flow field using a finite-volume based, inviscid, second-order spatial accurate computational fluid dynamics (CFD) code have helped to reveal the structure of the flow field between the projectile and the tube wall and have been compared to experimental results. It was found that the flow field is highly influenced by the projectile fins and that the non-reacting, inviscid simulations agree well with experimental results. Canting of the projectile was experimentally observed and numerically verified. It is hypothesized that the phenomenon of projectile canting has a significant link the physics of projectile unstarts.

INTRODUCTION

The ram accelerator is a ramjet-in-tube propulsion concept developed at the University of Washington (Hertzberg, Bruckner, and Bogdanoff, 1988) which operates in a manner similar to a conventional ramjet or scramjet, as shown in Fig. 1. A sub-caliber projectile similar in shape to the centerbody of a conventional ramjet travels supersonically through a tube filled with a gaseous combustible mixture, with the tube wall acting as an outer cowling. Combustion on and behind the projectile produces a pressure rise which results in a net positive thrust. A typical projectile, as shown in Fig. 2, has four fins which extend from the sides of the body and serve to center the projectile in the tube. Projectiles are typically fabricated from high strength aluminum or magnesium alloys into hollow segments, the nose cone and body, which are threaded together to form the complete projectile.

Previous to the study of Hinkey, Burnham, and Bruckner (1992), the influence of the projectile fins on the flow field between the projectile surface and tube wall were thought to be negligible and hence did not have a significant effect on projectile performance (i.e., acceleration and/or maximum velocity). Previous numerical studies were forced to assume the flow around the projectile to be completely axisymmetric in nature mainly due to the difficulties of modeling compressible, three-dimensional flows and also due to the belief that three-dimensional effects were not significant in regards to performance. Recently, with the availability of higher performance computers and enhanced diagnostics, experimental and numerical studies have begun the investigation of the full three-dimensional flow field about the ram accelerator projectile. These

studies have taken into account the fins on the afterbody of the projectile which have a significant effect on the flow field and projectile performance.

EXPERIMENTAL AND NUMERICAL RESULTS

The measurement of the tube wall pressure distribution created by the passage of a projectile is severely hampered by the standard distribution of instrumentation ports in the ram accelerator facility (Knowlen et al., 1991). As shown in Fig. 3, the distance between successive transducers is 40 cm which is quite large compared to the length of a projectile. In addition, at each transducer location the transducer ports are separated by either 90 or 120 degrees, making high spatial resolution measurements very difficult. As shown in Fig. 4, two types of short tube sections, which are inserted between the standard ram accelerator facility tube sections, were constructed. Both designs have greatly increased axial and circumferential transducer port density. The highly instrumented tube section (HITS) and tube "inserts" were utilized to measure the tube wall pressure distribution of various projectiles in the sub-, trans-, and superdetonative velocity regimes (Hertzberg, Bruckner, and Knowlen, 1991) in the "standard" first stage mixture of $2.7\text{CH}_4 + 2\text{O}_2 + 5.8\text{N}_2$ which has a Chapman-Jouguet (C-J) detonation velocity of 1750 m/s.

Results from a typical experiment utilizing the HITS are shown in Fig. 5 for a standard four-fin projectile in the subdetonative mode (Hertzberg, Bruckner, and Knowlen, 1991). The large pressure spikes found in traces 2, 4, 6, and 8 were found to be caused by the passage of the projectile fins directly over the transducers whose locations are denoted relative to the projectile fins in the small diagram at the top of Fig. 5. These pressures are never seen in axisymmetric calculations due to the absence of the projectile fins. Further evidence as to the effect of the projectile fins on the flow field between the projectile surface and the tube wall is illustrated in Fig. 6 which presents a comparison between an axisymmetric calculation of tube wall pressure and a typical experimental tube wall pressure trace taken along a circumferential position halfway between two adjacent fins. The initial pressure variation is nearly identical, but beginning at the 70 μsec mark, the two plots appear quite different with the experimental plot exhibiting a large pressure rise which is absent in the calculation. It was found that this pressure rise was a result of the convergence and reflection of the shock waves created by the leading surface of the projectile fins (Hinkey, Burnham, and Bruckner, 1992). The calculated tube wall distribution at several circumferential angles is shown in Fig. 7 and is shown to be quite different from the axisymmetric calculation. It has been shown that projectiles with a different number of fins (i.e., five fins as opposed to four) show significant differences in performance (Hinkey, Burnham, and Bruckner, 1993).

The phenomenon of projectile "canting" has also been observed (Hinkey, Burnham, and Bruckner, 1993). Projectile canting is defined as a projectile whose axis is not co-linear with the tube axis while it is being accelerated down the tube, i.e., it is either simply translated to one side or has a non-zero angle of attack relative to the tube axis. Typical data utilizing the HITS showing the effects of projectile canting is illustrated in Fig. 8. Note the differences in arrival time and initial shock amplitude between transducers. A line connecting the arrival times of the initial shock for each probe has been constructed to illustrate the characteristic "S" shape that is produced by a canted projectile. The effect is illustrated conceptually in Fig. 9 where an axisymmetric projectile has a non-zero angle of attack relative to the tube axis. The "upper" wall pressure distribution has a characteristic large initial pressure rise which is nearly always of much larger magnitude than the "lower" wall pressure distribution which arrives earlier and is much weaker. A three-dimensional calculation utilizing an axisymmetric projectile was performed in an attempt to determine the extent of projectile canting for select experiments. A method was developed which was utilized to obtain a close guess as to the extent of the projectile canting (Hinkey, Burnham, and Bruckner, 1993). Figure 10 presents the resulting numerical simulation as compared to the experimental pressure

traces previously shown in Fig. 9. The numerical and experimental results match qualitatively quite well and as a result the angle of attack of the projectile was estimated to be approximately 4.5 degrees and the nose tip of the projectile was translated approximately 7.5 mm from the centerline axis of the tube. A corresponding three-dimensional calculation including the effects of projectile fins is shown in Fig. 11. Note the wide variation in the character of the tube wall pressure distribution for the different circumferential locations. The widely varying nature of the pressure distribution may have serious consequences regarding high speed (superdetonative) operation of a ram accelerator projectile, i.e., the phenomena of high speed unstarts (Hinkey, 1994).

REFERENCES

- Hertzberg, A., Bruckner, A.P., and Bogdanoff, D.W., 1988. "Ram Accelerator: A New Chemical Method for Accelerating Projectiles to Ultrahigh Velocities," *AIAA Journal*, Vol. 26, pp. 195-203.
- Hertzberg, A., Bruckner, A.P., and Knowlen, C., 1991. "Experimental Investigation of Ram Accelerator Propulsion Modes," *Shock Waves*, Vol. 1, pp. 17-25.
- Hinkey, J.B., 1994. "An Experimental and Numerical Investigation of the Three-Dimensional Flow Field About a Ram Accelerator Projectile," Ph.D. Dissertation, University of Washington.
- Hinkey, J.B., Burnham, E.A., and Bruckner, A.P., 1993. "Investigation of Ram Accelerator Flow Fields Induced by Canted Projectiles," AIAA Paper 93-2186.
- Hinkey, J.B., Burnham, E.A., and Bruckner, A.P., 1992. "High Spatial Resolution Measurements of Ram Accelerator Phenomena," AIAA Paper 92-3244.
- Knowlen, C., Li, J.G., Hinkey, J.B., and Dunmire, B., 1991. "University of Washington Ram Accelerator Facility," 42nd Meeting of the Aeroballistic Range Association.

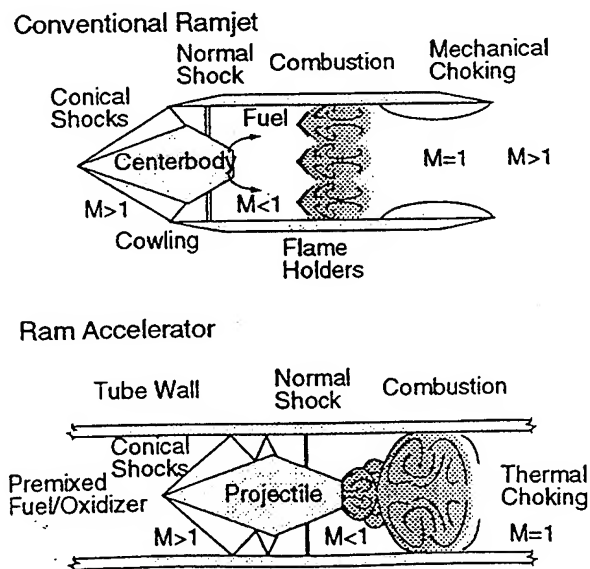


Fig. 1 Comparison of the ram accelerator to a conventional ramjet.

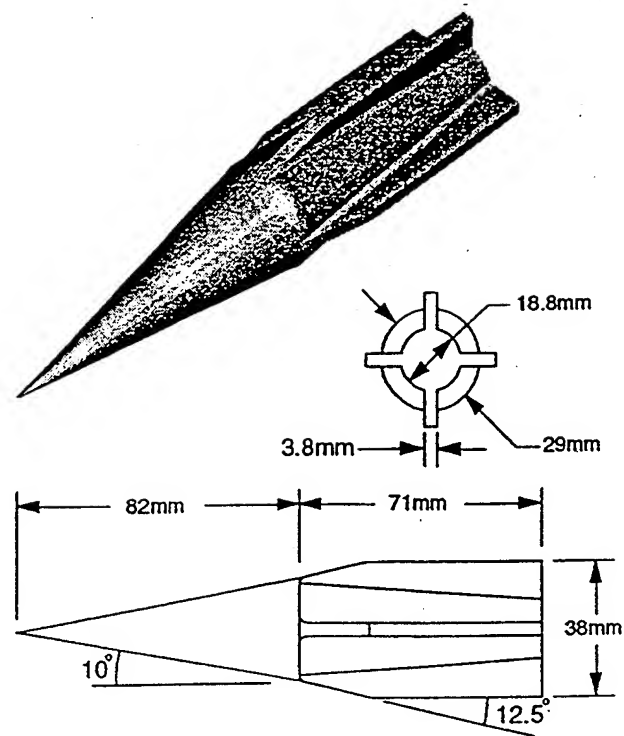


Fig. 2 Geometry of a standard ram accelerator projectile used for experiments.

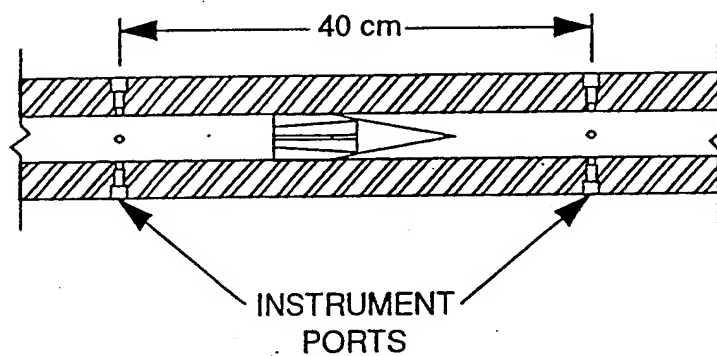


Fig. 3 Illustration of the distance between instrumentation stations relative to the length of a projectile for the standard ram accelerator facility.

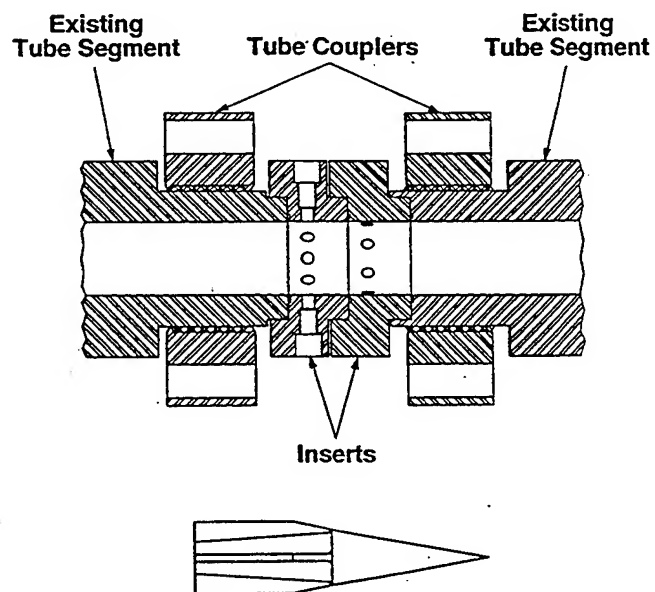
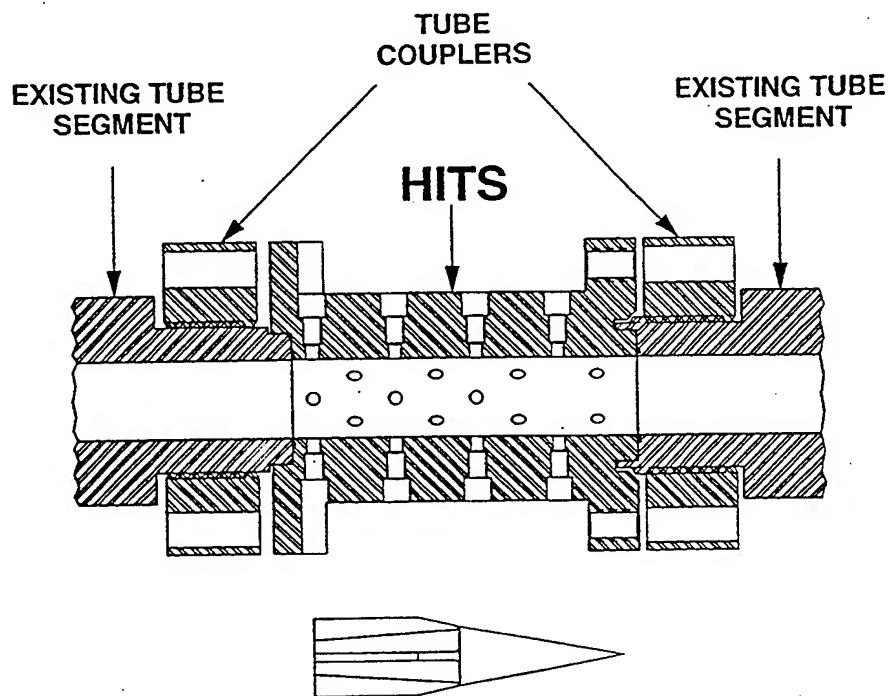


Fig. 4 Schematics of the highly instrumented tube section (HITS) and tube "inserts" as installed between two sections of ram accelerator tubes. Projectiles shown for scale.

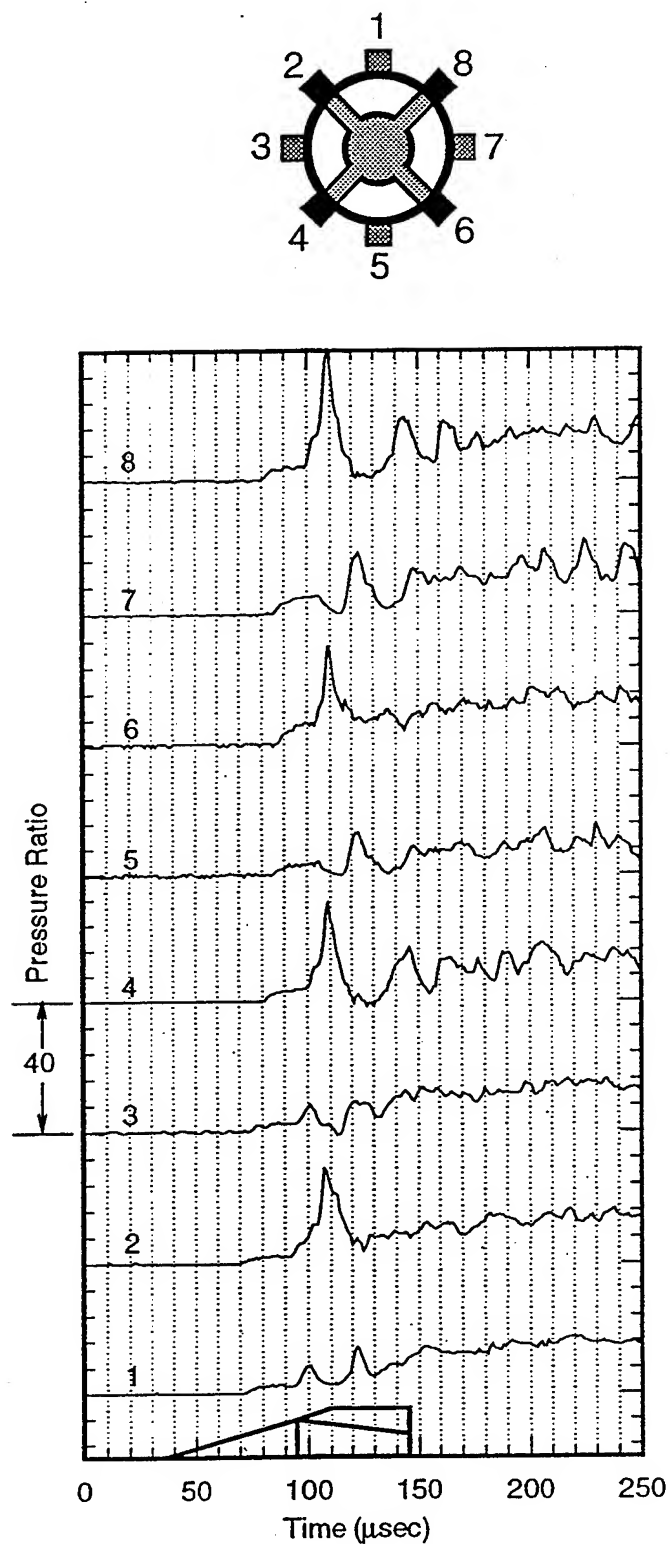


Fig. 5 Tube wall pressure distribution of a 4-fin projectile showing the influence of the fins on the flow field. Subdetonative regime, 1440 m/s (Mach 4.0) or 82% of the C-J detonation speed. Gas Mixture of $2.7\text{CH}_4 + 2\text{O}_2 + 5.8\text{N}_2$.

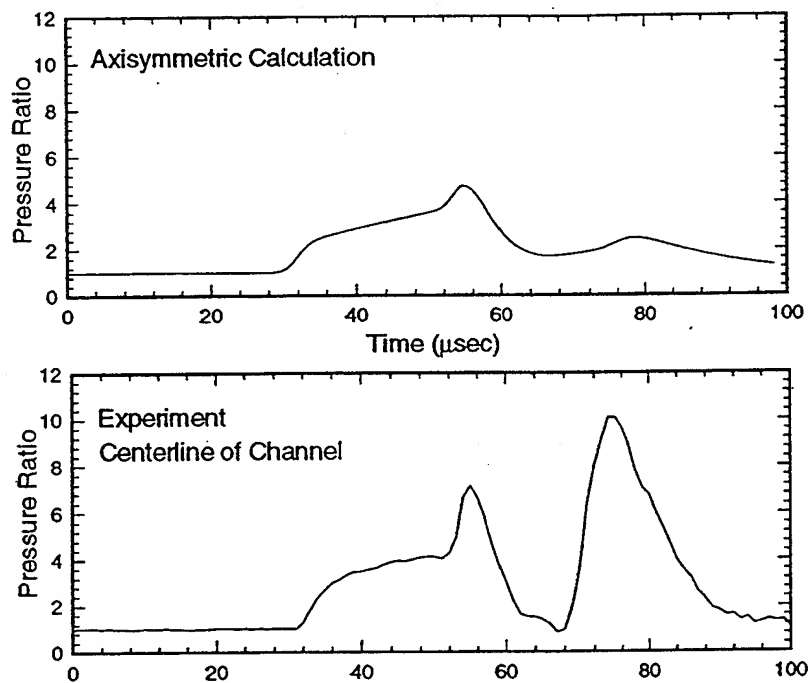


Fig. 6 Comparison of the experimental tube wall pressure along the centerline of a channel (directly between two adjacent fins) with the results from an axisymmetric simulation.

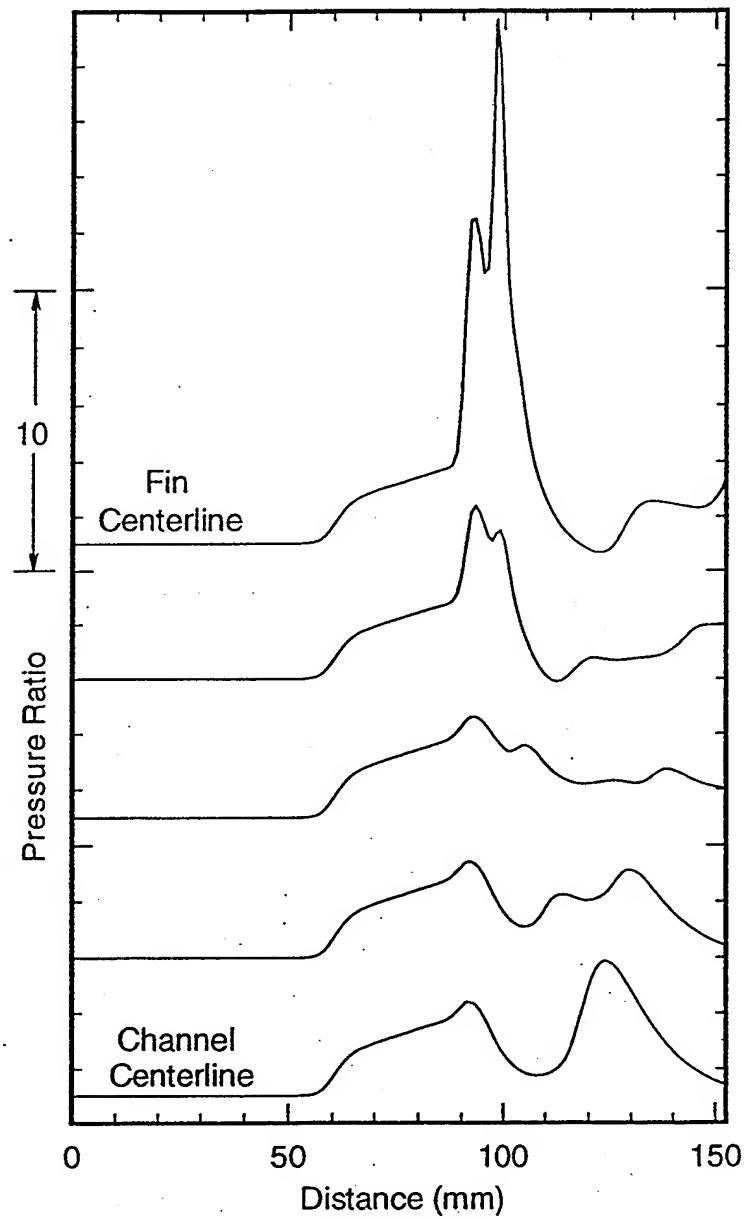


Fig. 7 Line plots of the calculated tube wall pressure of a 4-fin projectile as a function of distance at 5 different circumferential angles from the centerline of a fin to the centerline of a channel. Projectile velocity of 1440 m/s (Mach 4.0) in a non-reacting mixture of $2.7\text{CH}_4 + 2\text{O}_2 + 5.8\text{N}_2$.

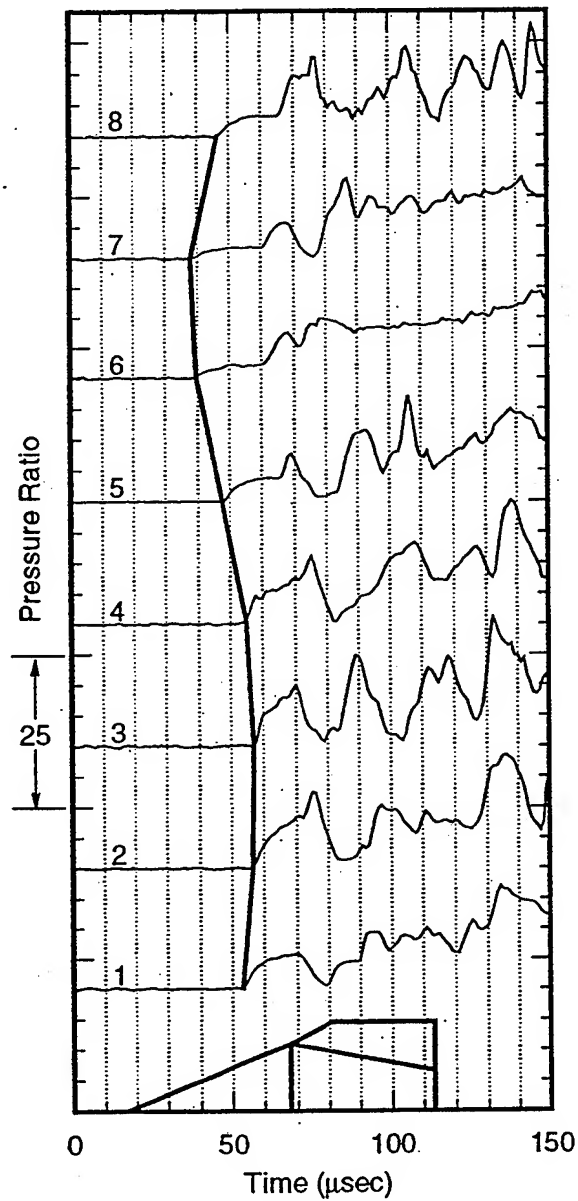


Fig. 8 Tube wall pressure traces using the HITS illustrating a canted projectile. The arrival times of the initial shock wave has been connected by lines to show the characteristic "S" shape. Subdetonative regime, 1560 m/s (Mach 4.3) or 89% of the C-J detonation speed. Gas Mixture of $2.7\text{CH}_4 + 2\text{O}_2 + 5.8\text{N}_2$.

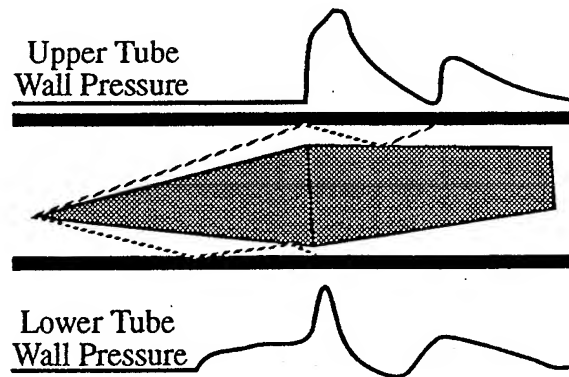


Fig. 9 Illustration of the difference in arrival position of the initial shock wave and the magnitude of the reflection at opposite sides of a tube for a canted projectile.

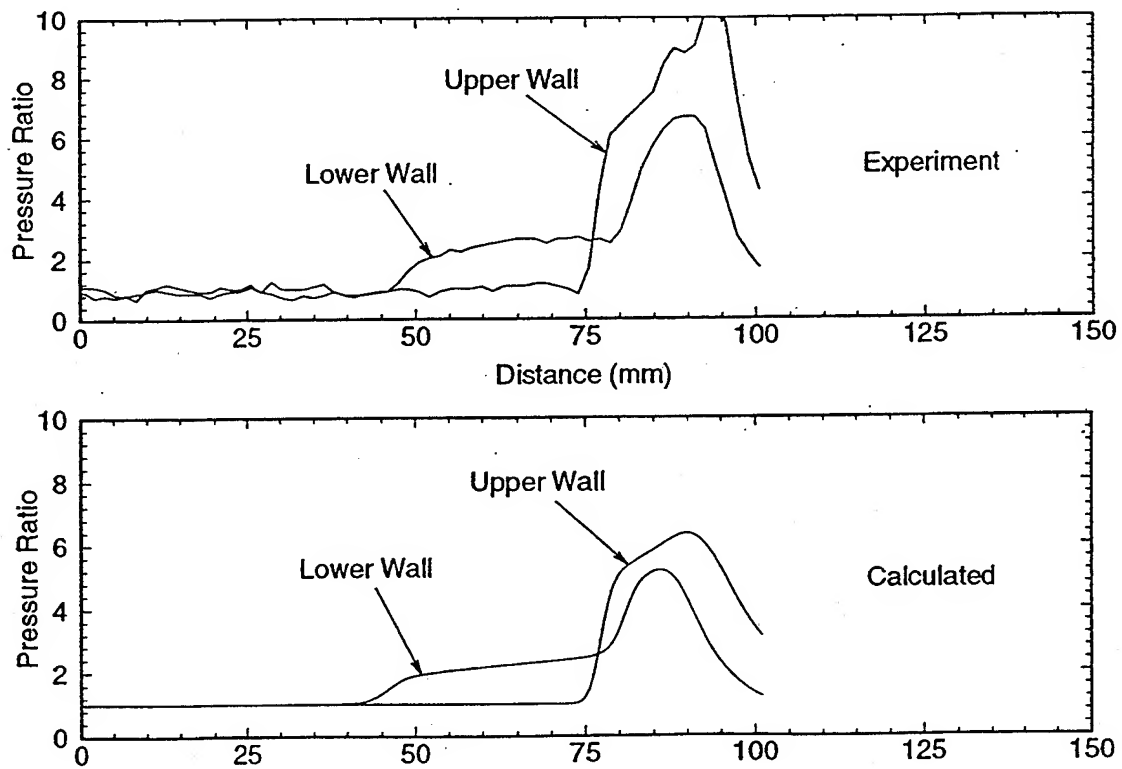


Fig. 10 Comparison of calculated (bottom) to experiment (top) tube wall pressure traces for a canted projectile with an estimated angle of attack of 4.5 degrees and a nose tip translation of 7.5 mm. Subdetonative regime, 1560 m/s (Mach 4.3) or 89% of the C-J detonation speed.

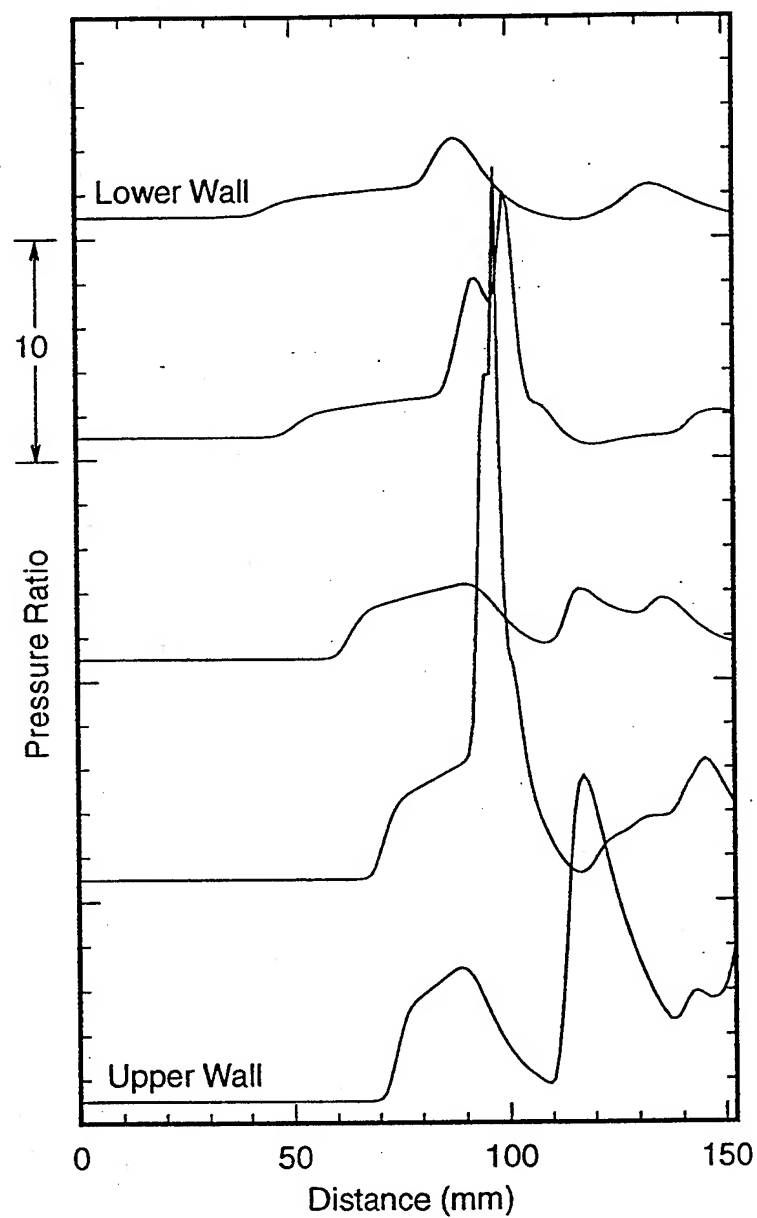


Fig. 11 Line plots of the calculated tube wall pressure distribution of a canted projectile with fins which has an angle of attack of 4.5 degrees and a nose tip translation of 7.5 mm. Subdetonative regime, 1560 m/s (Mach 4.3) or 89% of the C-J detonation speed. These 5 traces correspond to 45 degree increments in circumferential angle from the "upper" to "lower" wall.

Introduction

Previous work

- **Experiments:**
 - Record low spatial resolution tube wall pressure and luminosity profiles in all regimes of operation
 - Experimentally determine operational limits
 - Benchmark for theoretical performance calculations
 - Generally more advanced than numerical simulations
- **1-D Calculations (control volume approach):**
 - Gives theoretical subdetonative acceleration performance and maximum velocity of projectile
 - Does not predict observed trans- or superdetonative performance
- **2-D Axisymmetric Calculations:**
 - Navier-Stokes with chemical reaction
 - Predicts observed trans- and superdetonative performance “fairly well”
- **3-D Calculations:**
 - None prior to the start of this research
 - Numerous experiments and simple 3-D calculations performed herein have “inspired” others to perform the initial 3-D chemically reacting, Navier-Stokes calculations

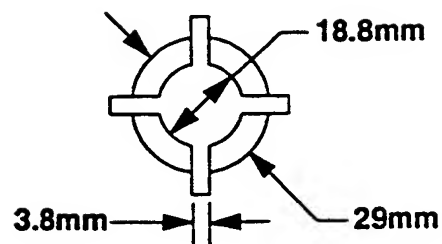
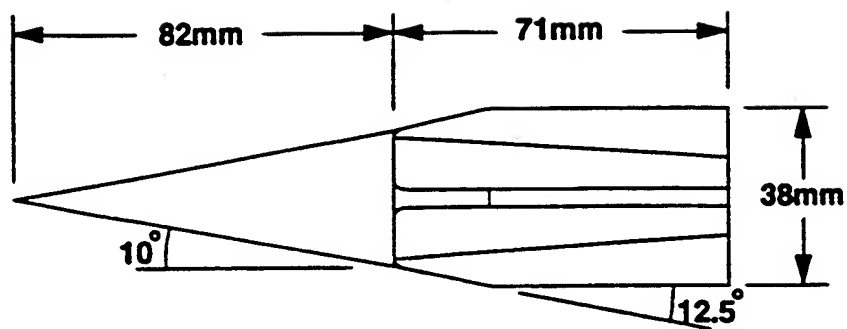
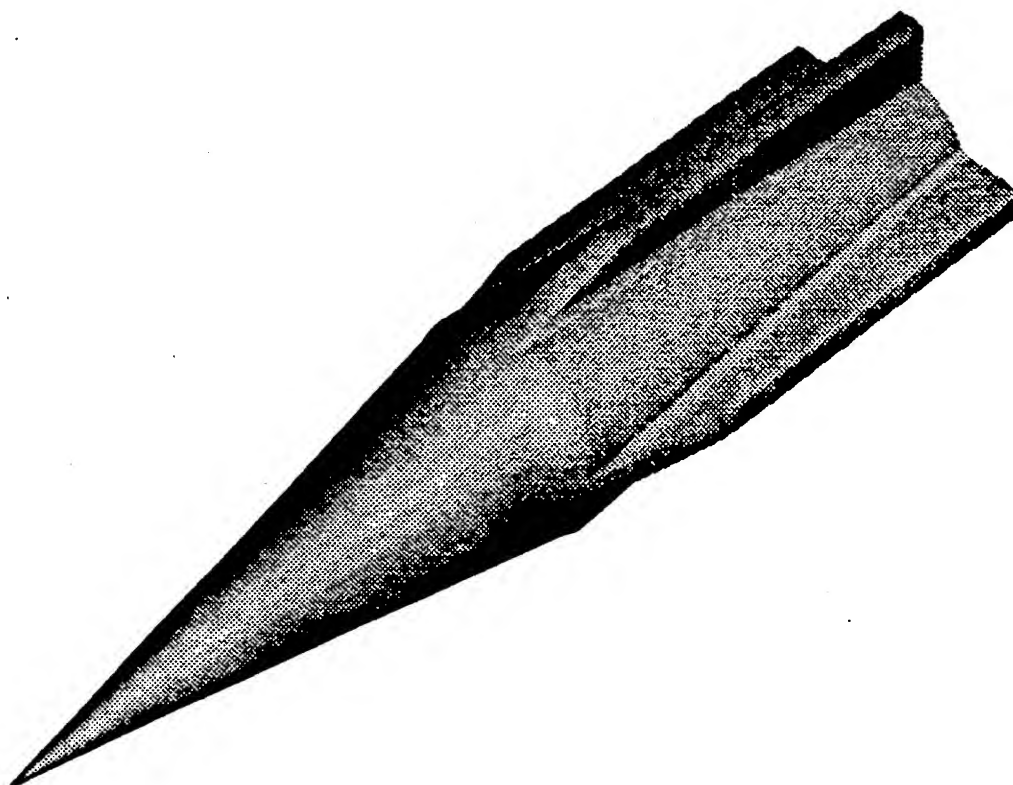
Introduction

(con't)

Why investigate the 3-D flow field?

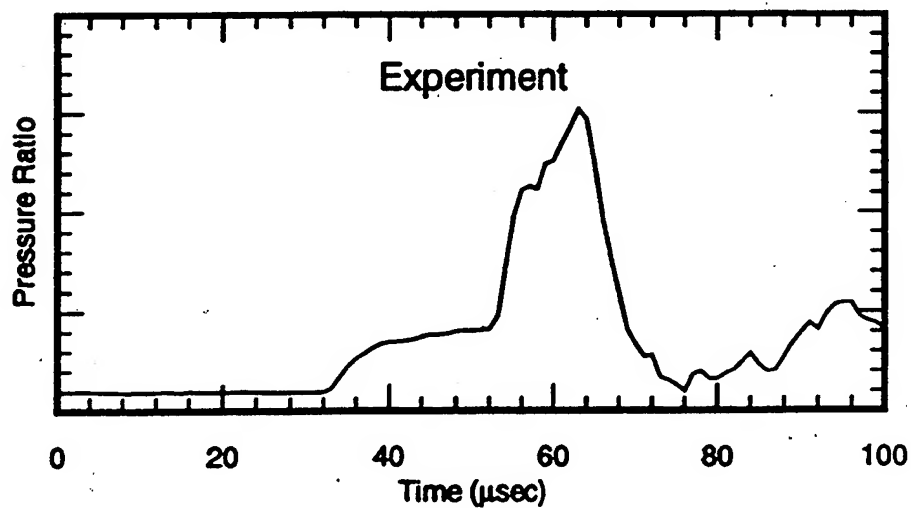
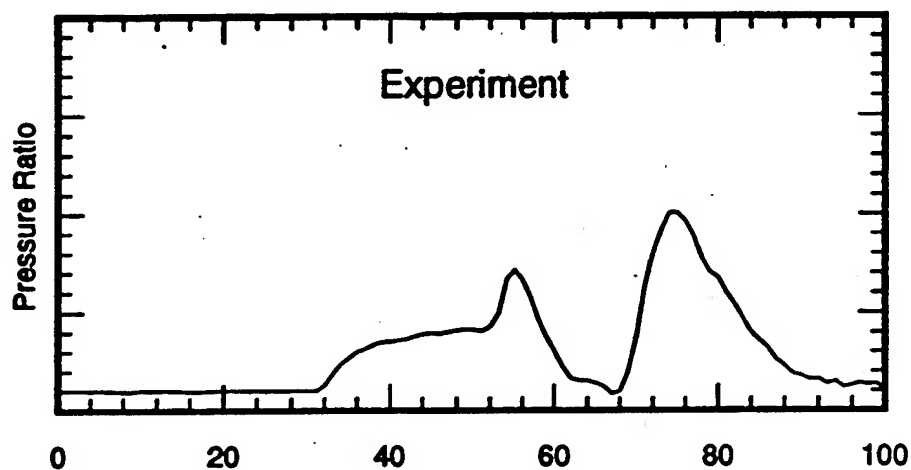
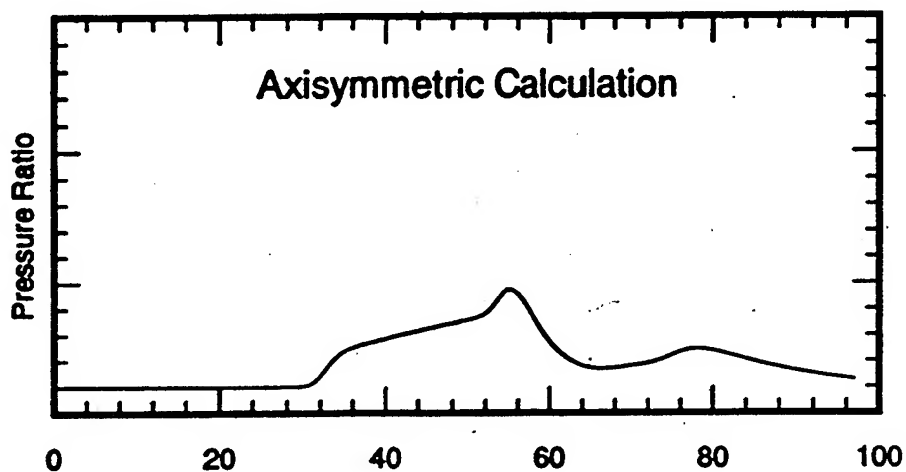
- There are several phenomena which are not predicted by 1-D or 2-D calculations:
 - Anomalous tube wall pressure recordings
 - Deviations from predicted sub-, trans-, and superdetonative projectile acceleration performance
 - Projectile unstarts (high velocity limits)
- Determine the 3-D aspects of the flow field to:
 - Determine the cause of anomalous tube wall pressure recordings
 - Increase projectile acceleration performance in all regimes
 - Determine what limits the maximum velocity of a particular projectile geometry in a particular mixture
 - GO FASTER!

Ram Accelerator Projectile

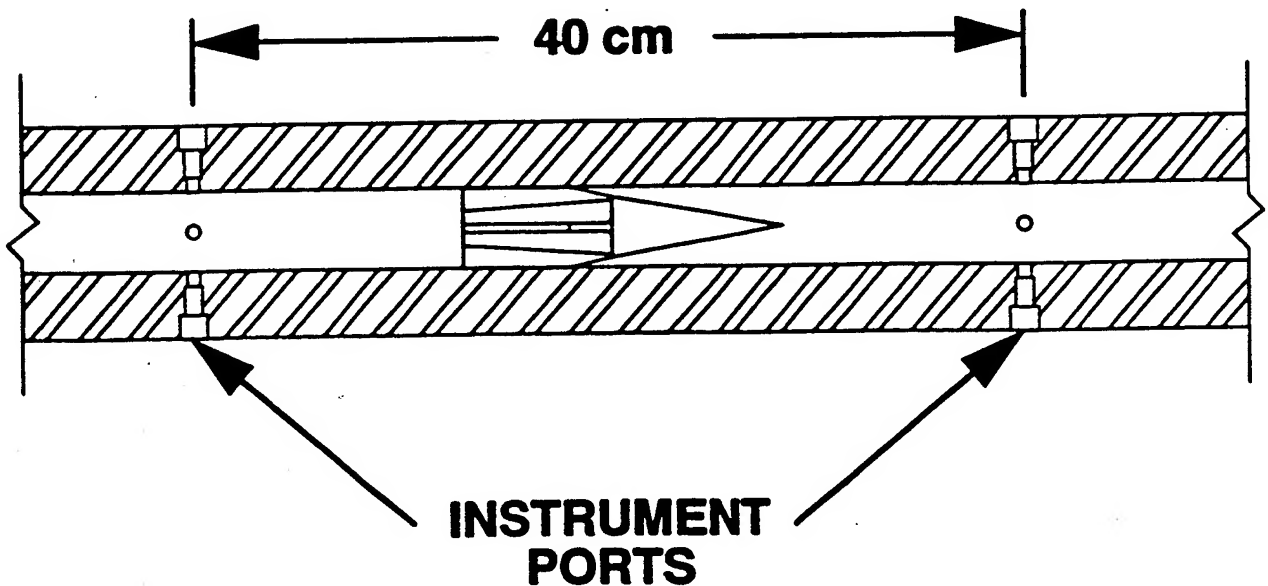
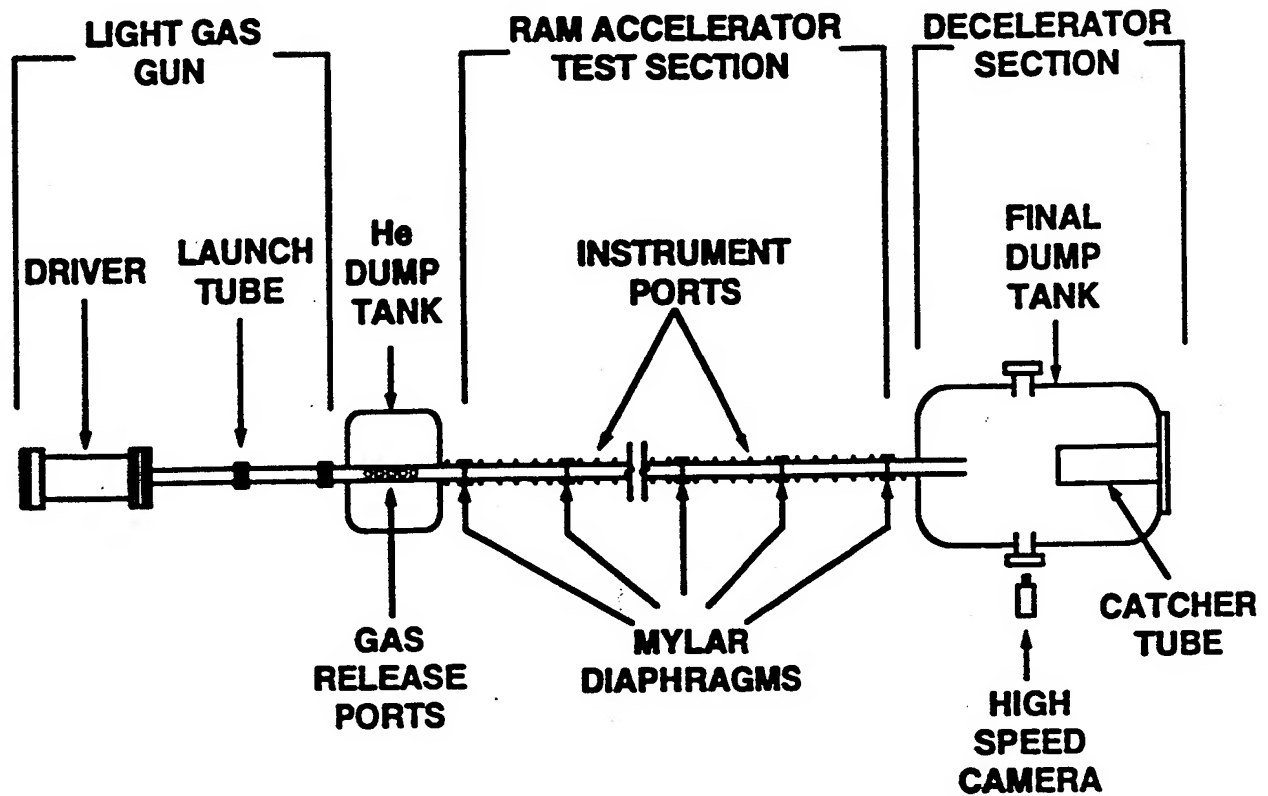


Axisymmetric Simulations and Experiments

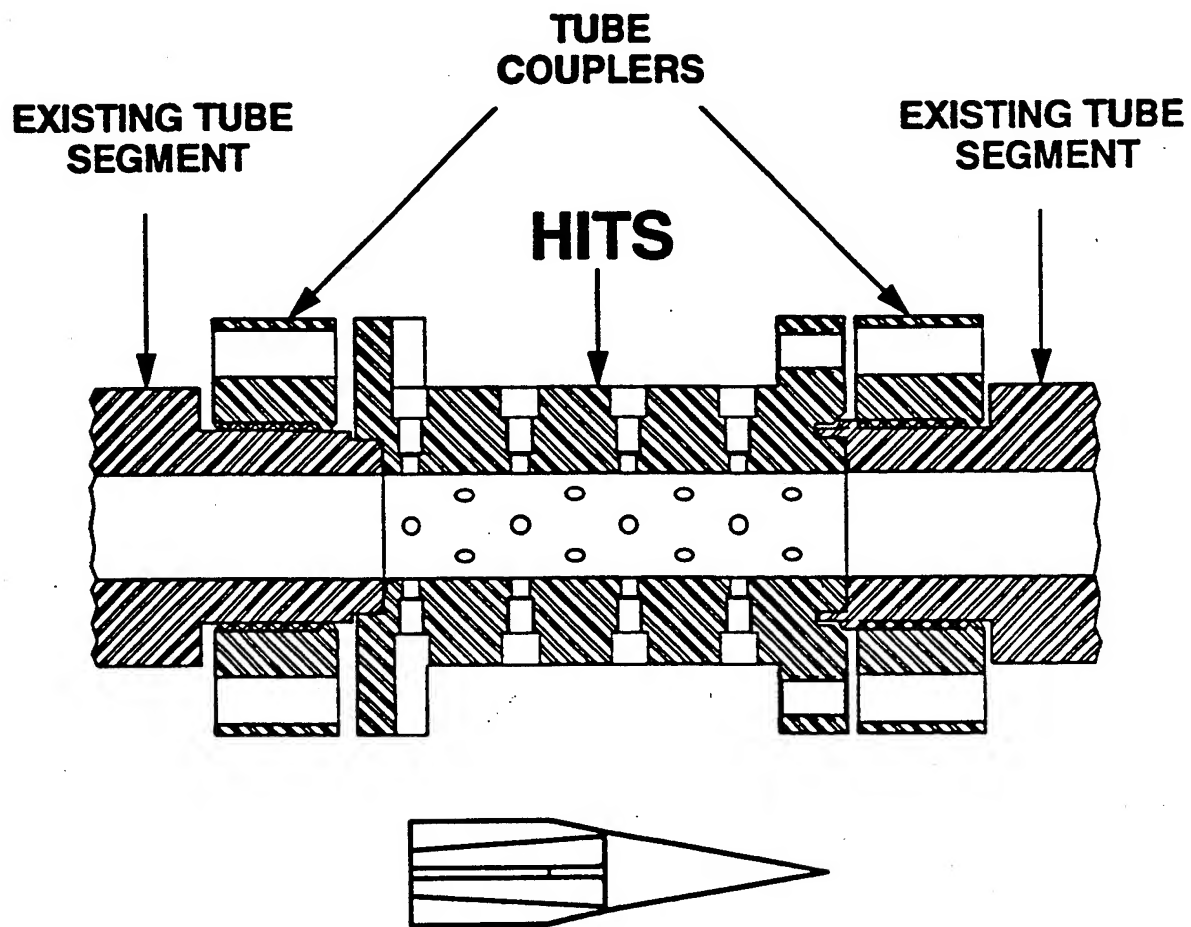
Tube Wall Pressure



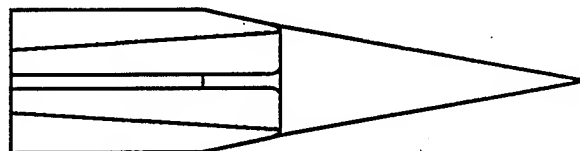
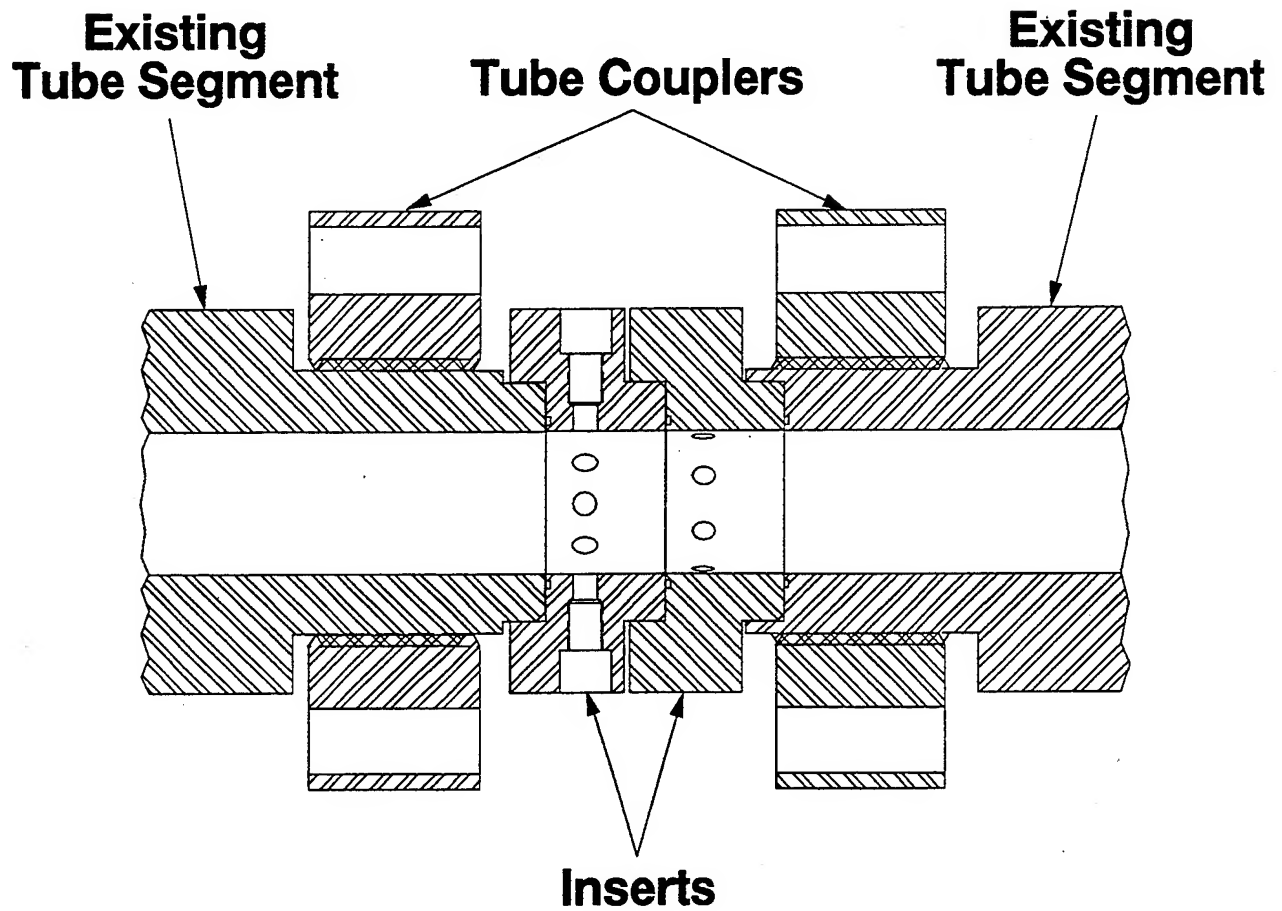
Ram Accelerator Facility



Highly Instrumented Tube Section (HITS)



Inserts



Experiments

Single-stage experiments

- Reacting gas mixture of $2.7\text{CH}_4 + 2\text{O}_2 + 5.8\text{N}_2$
- Non-reacting gas mixture of $2.7\text{CH}_4 + 7.8\text{N}_2$
- Initial tube fill pressures from 18 to 35 atm

Projectiles

- CNC manufactured (high dimensional repeatability)
- High strength aluminum alloy (7075-T651)
- 4-fin or 5-fin projectiles

High instrument density tube sections

- Placed where projectile would have desired velocity
- Used fin orientation sensors
- Mostly pressure and magnetic transducers (very few experiments performed with luminosity probes)

Numerical Simulation Method

Three-dimensional finite-volume formulation

- Ideal, calorically perfect gas
- Non-reacting
- Inviscid (Euler flow)

Spatial accuracy

- MUSCL differencing
- 2nd-order accurate in regions of smooth flow
- 1st-order accurate in regions of steep gradients

Approximate Riemann solver

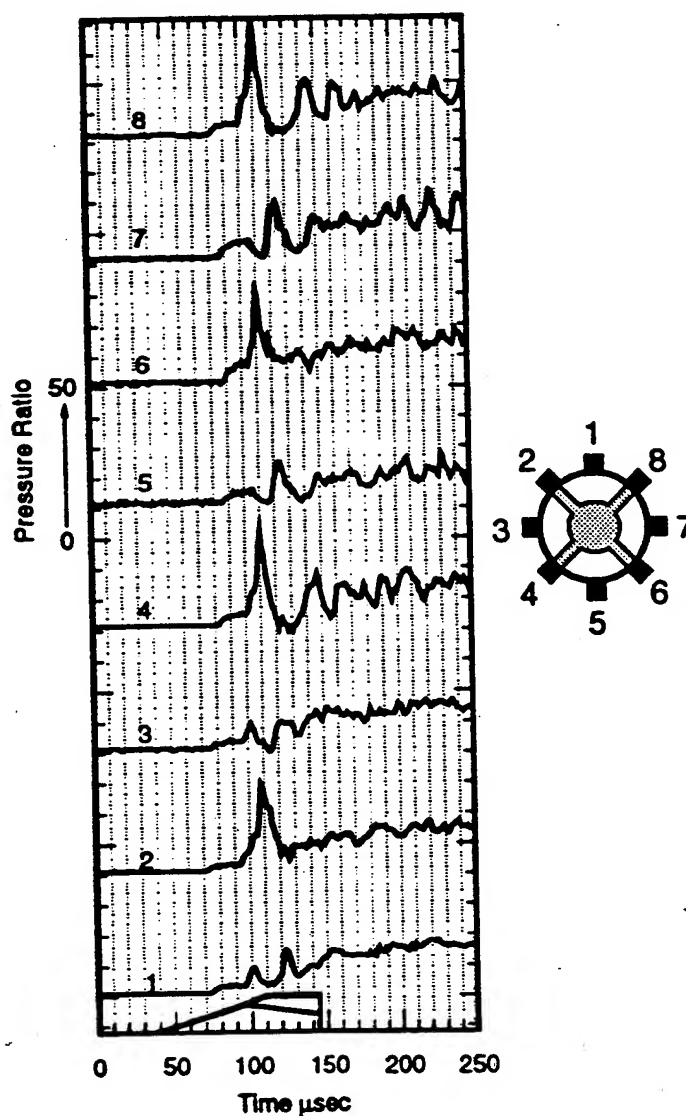
- Riemann solver used to get fluxes at cell interfaces
- Approximate Riemann solver of Harten, Lax, and van Leer (HLL)
- Non-dissipative, resolves discontinuities well

Explicit time integration to steady-state

- Local time stepping (not time accurate)
- Residual smoothing (increased CFL numbers)

Subdetonative HITS Pressure Profiles

4-Fin Projectile
 $2.7\text{CH}_4 + 2\text{O}_2 + 5.8\text{N}_2$
Mach 4.0
1440 m/s (82% C-J)

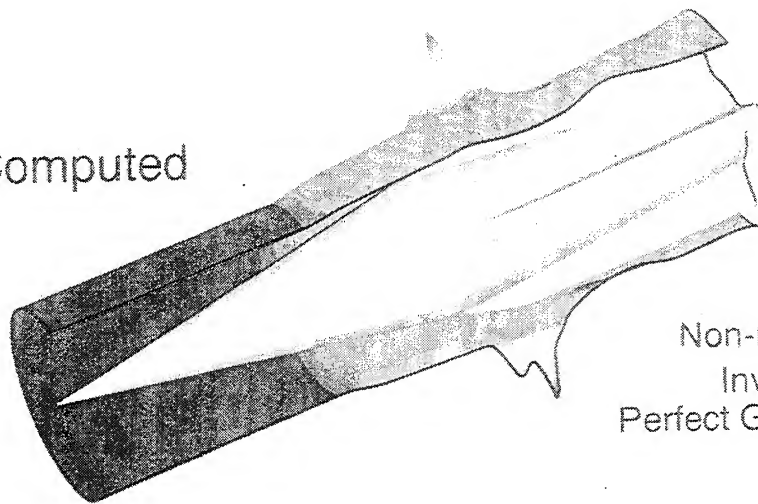


Experimental and Computed Tube Wall Pressure Distribution

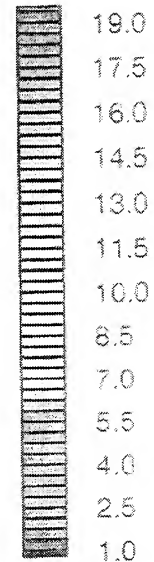
Mach 4, 1440 m/s (82% C-J)



Computed

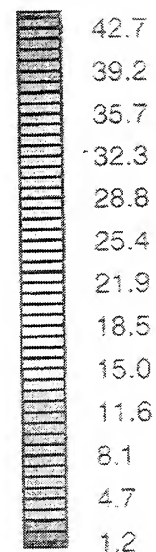
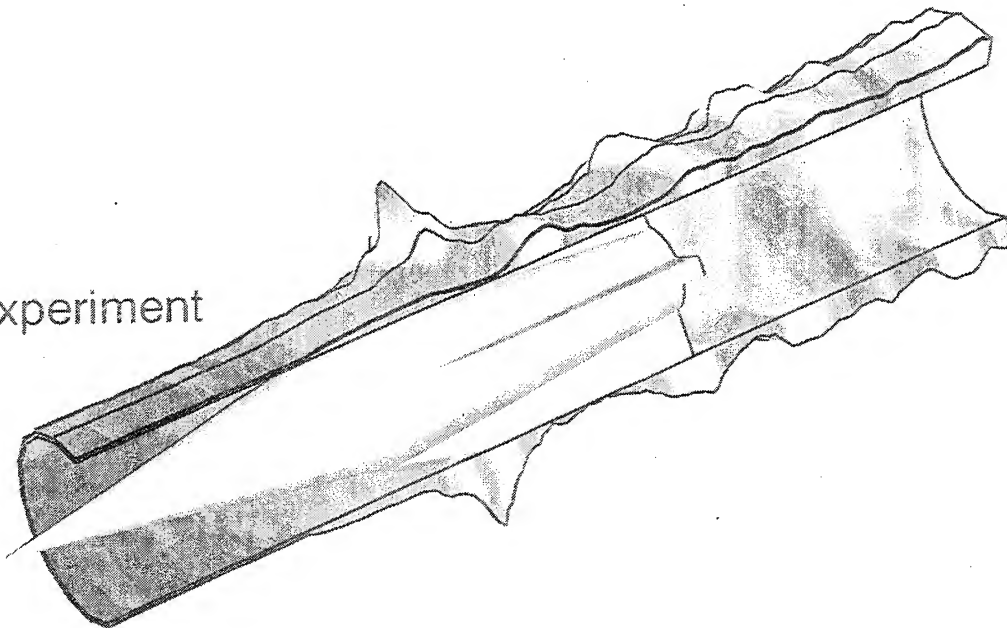


Non-reacting
Inviscid
Perfect Gas, $\gamma=1.365$



Pressure Ratio

Experiment



Pressure Ratio

Computed Pressure Distributions

4-Fin Projectile

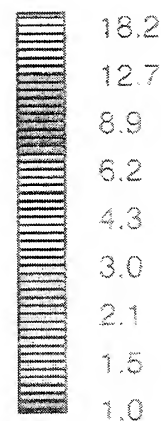
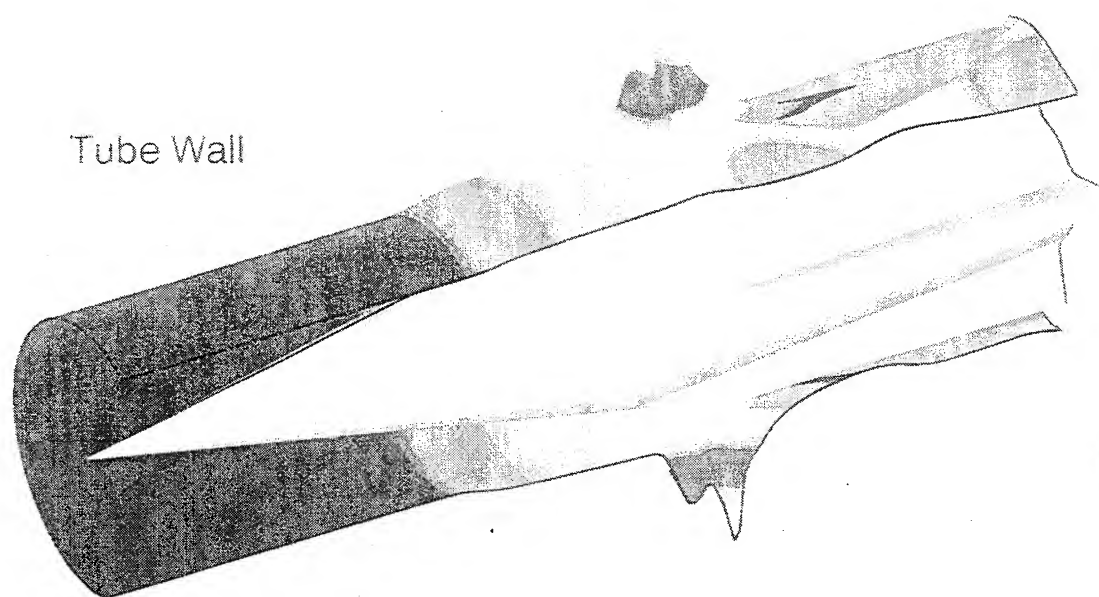
Non-Reacting, Inviscid

Mach 4.0

1440 m/s (82% C-J)

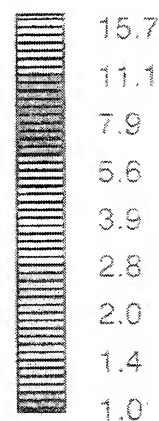
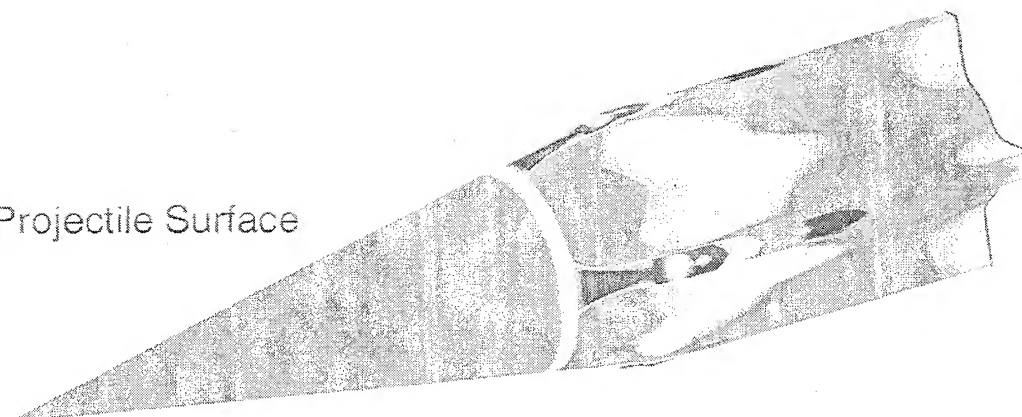
$2.7\text{CH}_4 + 2\text{O}_2 + 5.8\text{N}_2$

Tube Wall



Pressure Ratio

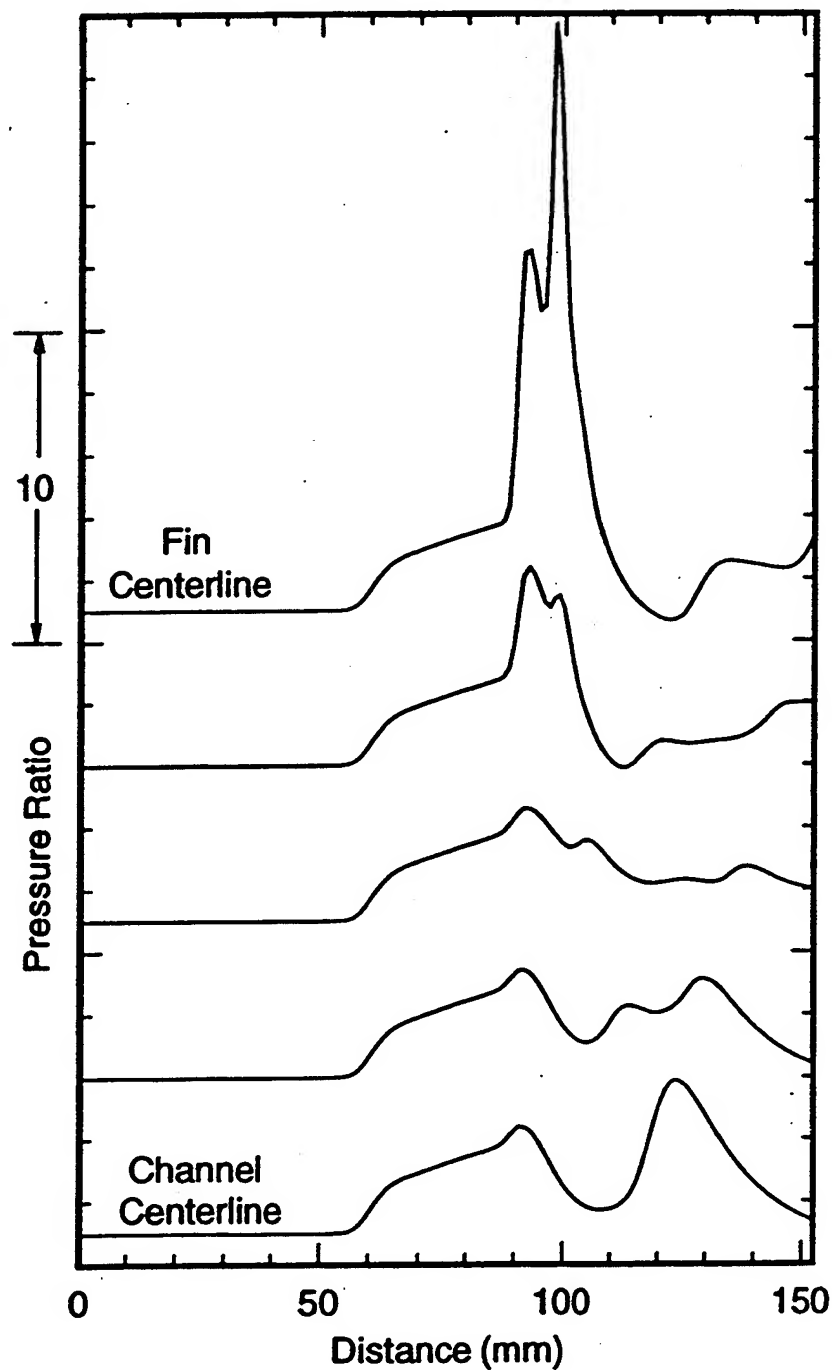
Projectile Surface



Pressure Ratio

Line Plots of Calculated Tube Wall Pressure 4-Fin Projectile

1400 m/s (Mach 4.0), 80% C-J
Non-Reacting, Inviscid

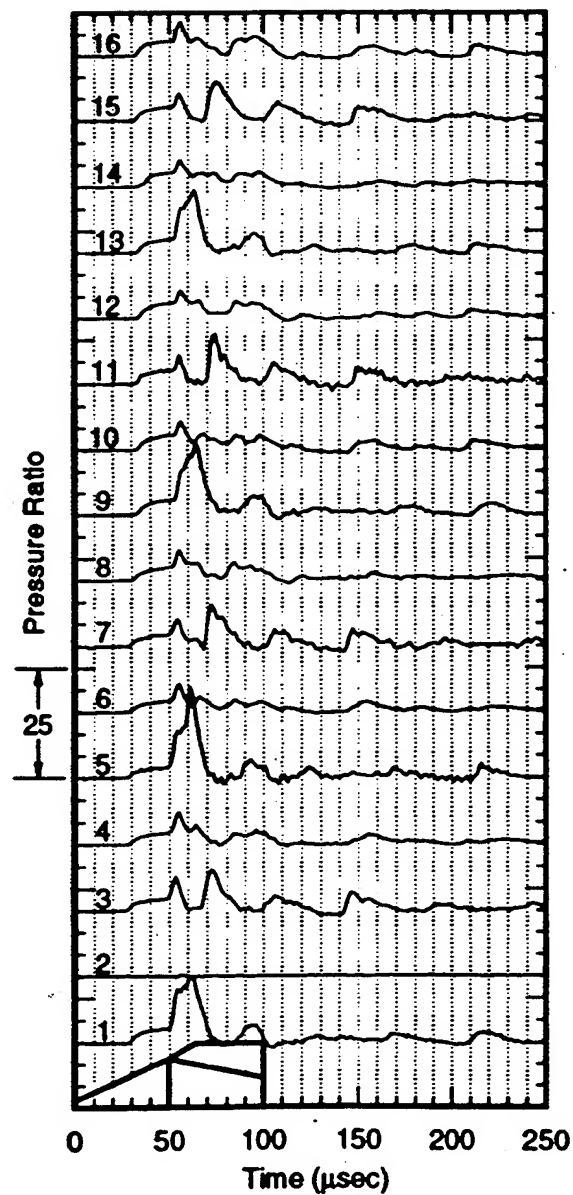
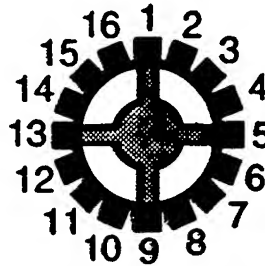


Centered Projectile

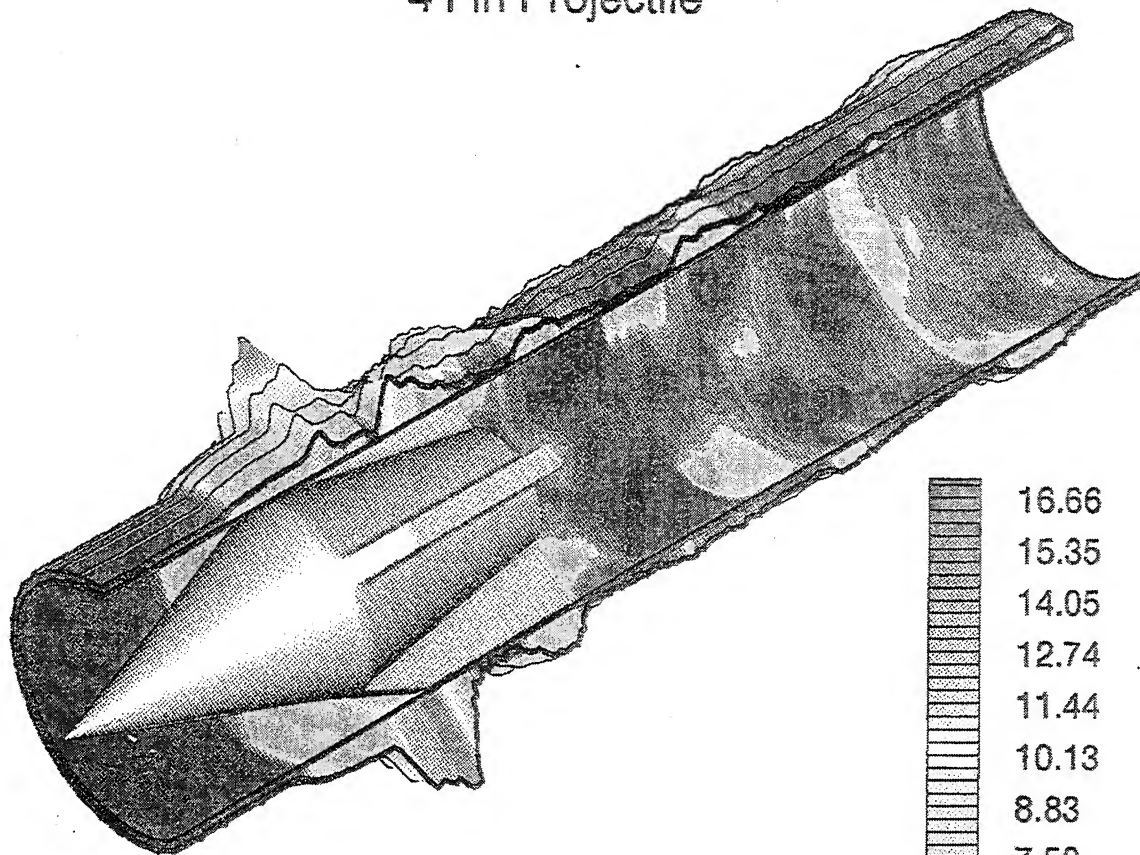
Subdetonative Regime

1410 m/s (Mach 3.9)

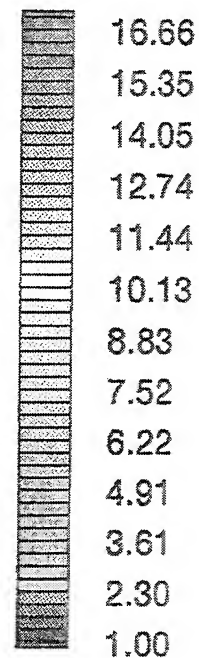
$2.7\text{CH}_4 + 7.8\text{N}_2$



Tube Wall Pressure Distribution Non-Reacting Mixture 4 Fin Projectile



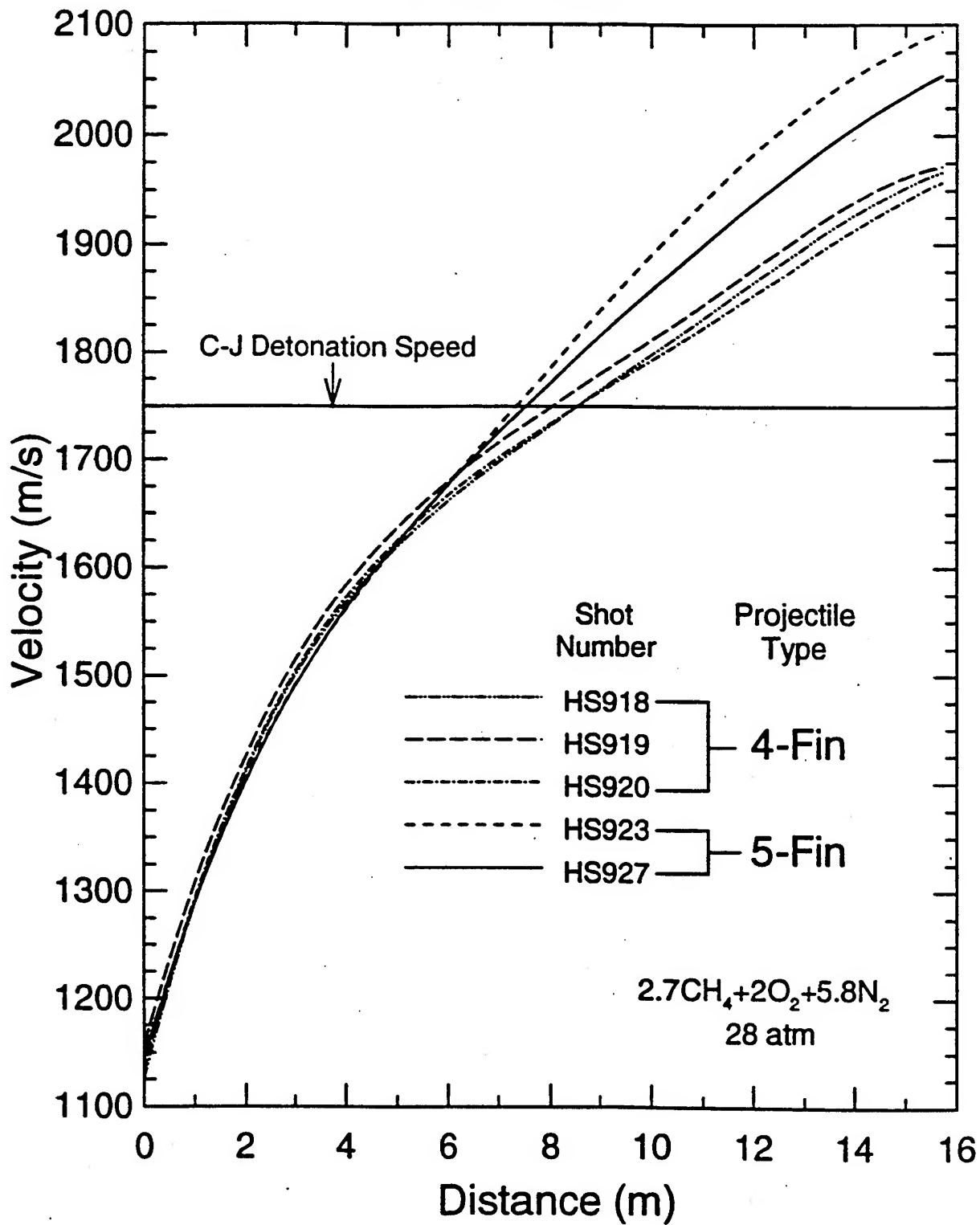
1410 m/s
Mach 3.9
81% of C-J Detonation Speed
 $2.7\text{CH}_4 + 7.8\text{N}_2$



Pressure Ratio

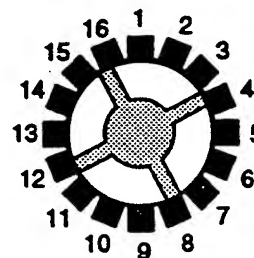
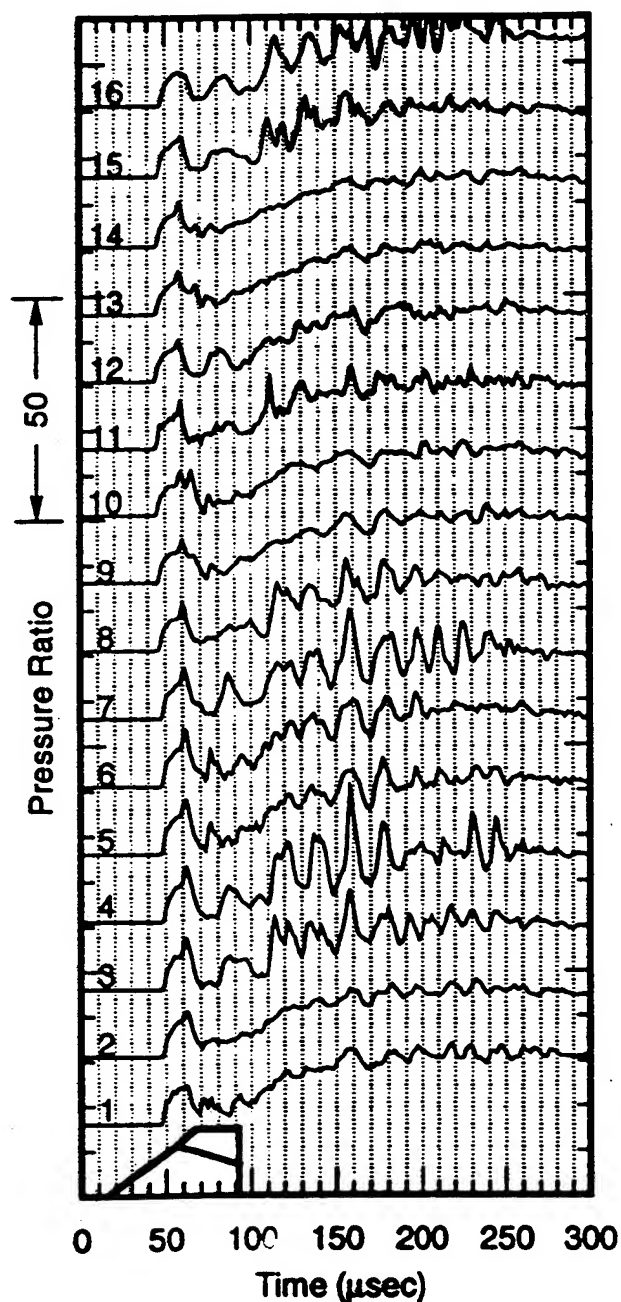
Velocity Profiles

4-Fin and 5-Fin Projectiles
Single Stage



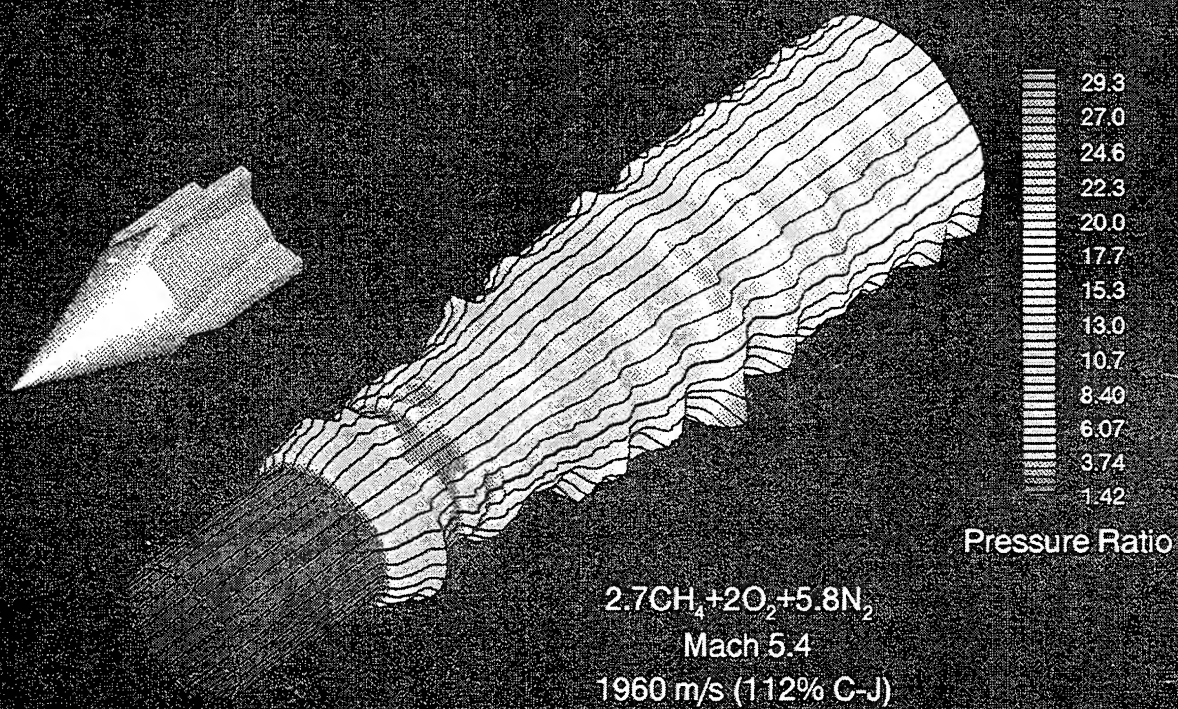
Superdetonative Insert Pressure Profiles

4-Fin Projectile
 $2.7\text{CH}_4 + 2\text{O}_2 + 5.8\text{N}_2$
Mach 5.4
1960 m/s (112% C-J)



Experimental Pressure Distribution

Tube Wall
4-Fin Projectile



Non-ideal 3-D Projectile Flow Field

Combustion phenomena

- Pressure variations in flow field behind projectile
- Shock induced combustion in diffuser

Projectile canting

- Experimental evidence
- Estimation of position of the projectile in the tube

Numerical simulations

- Confirmation of estimated projectile position
- Simulations of canted projectiles with fins

High Mach number unstarts

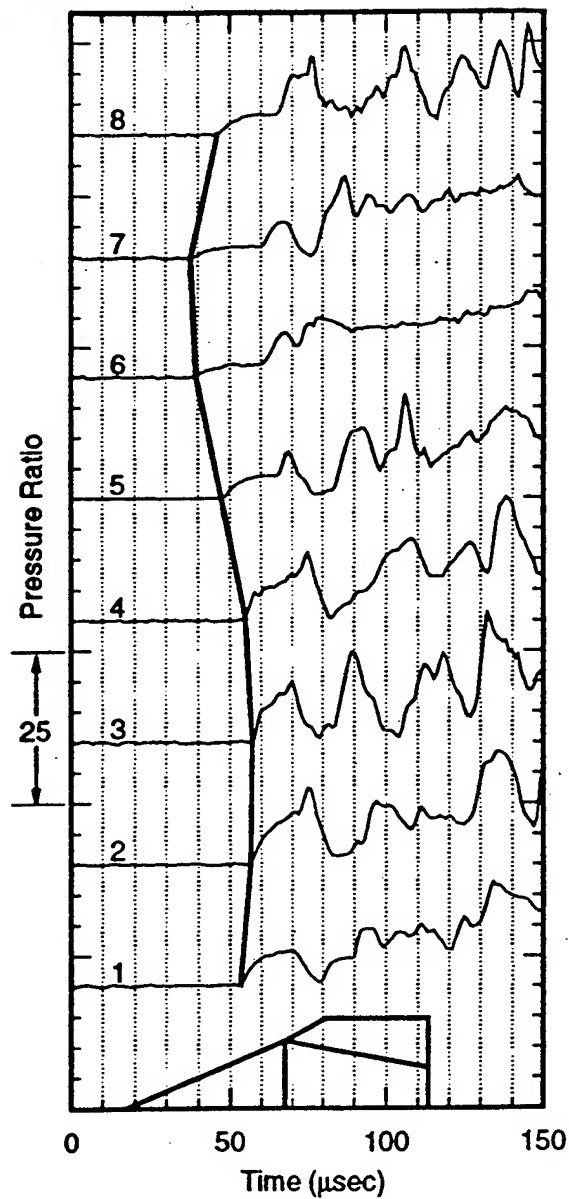
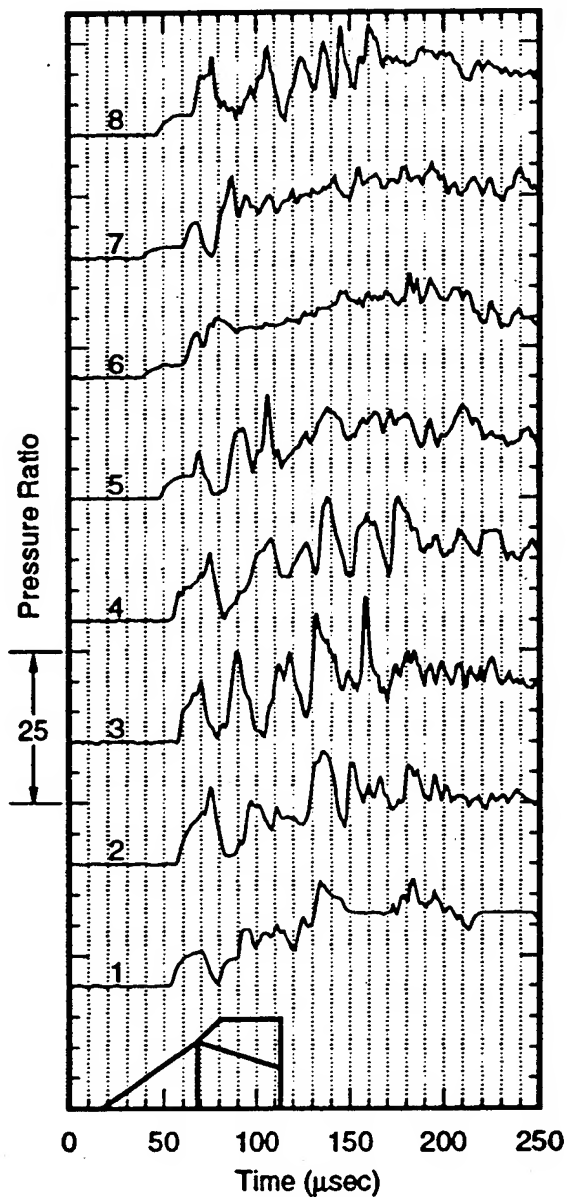
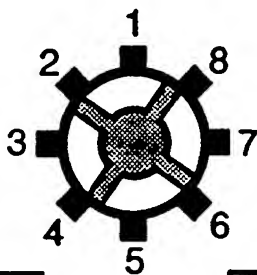
- Experimental data and numerical simulations of others
- Link to canting

Canted Projectile

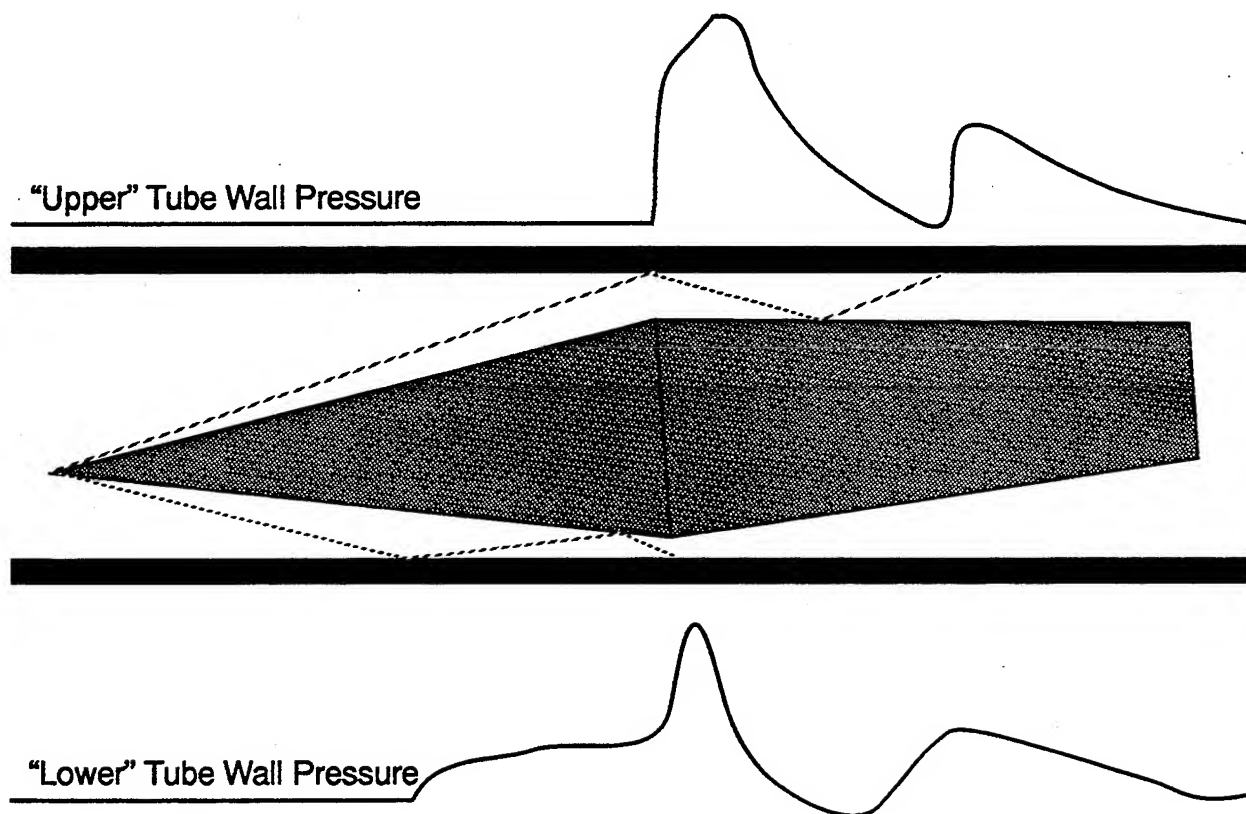
Subdetonative Regime

1560 m/s (Mach 4.3)

$2.7\text{CH}_4 + 2\text{O}_2 + 5.8\text{N}_2$

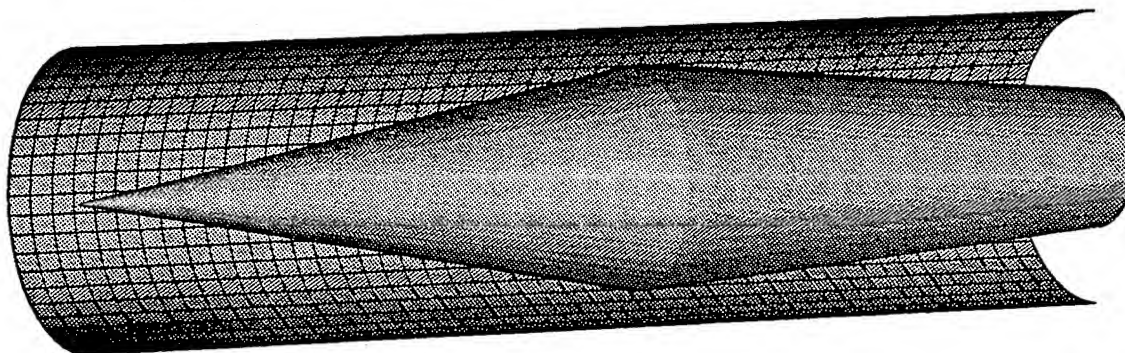


Tube Wall Pressure Distribution Induced by Projectile Canting

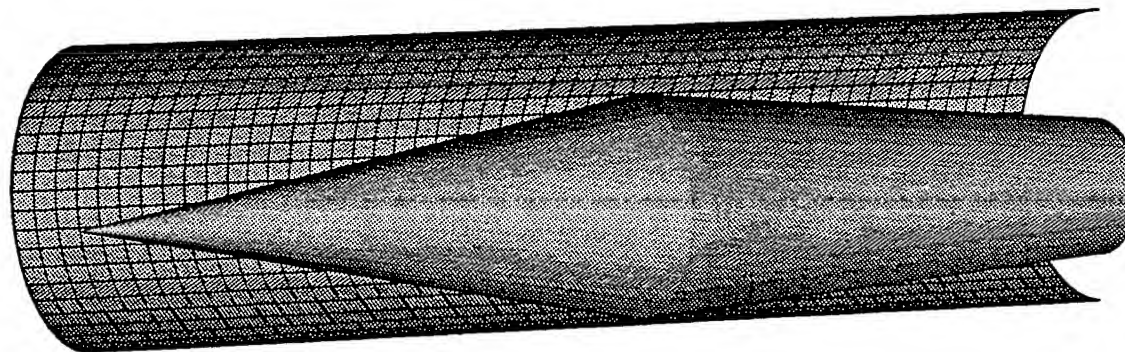


Possible Projectile Orientations

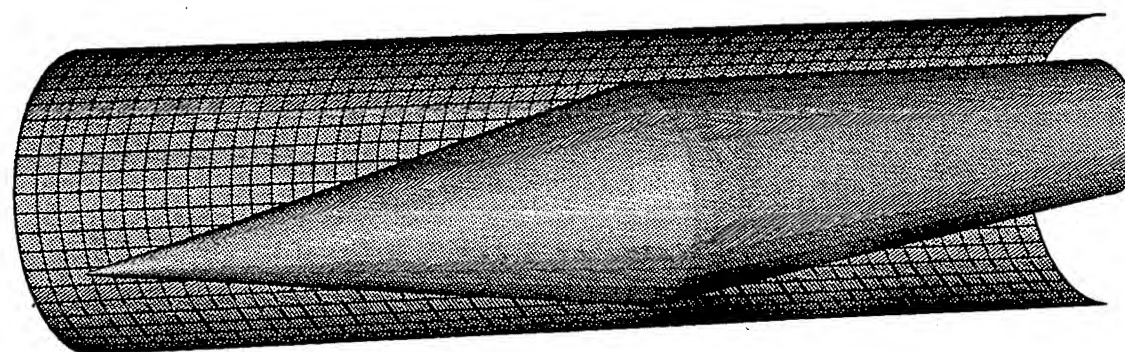
Axisymmetric Projectile



Colinear
Axes



Translated



Translated
and Rotated

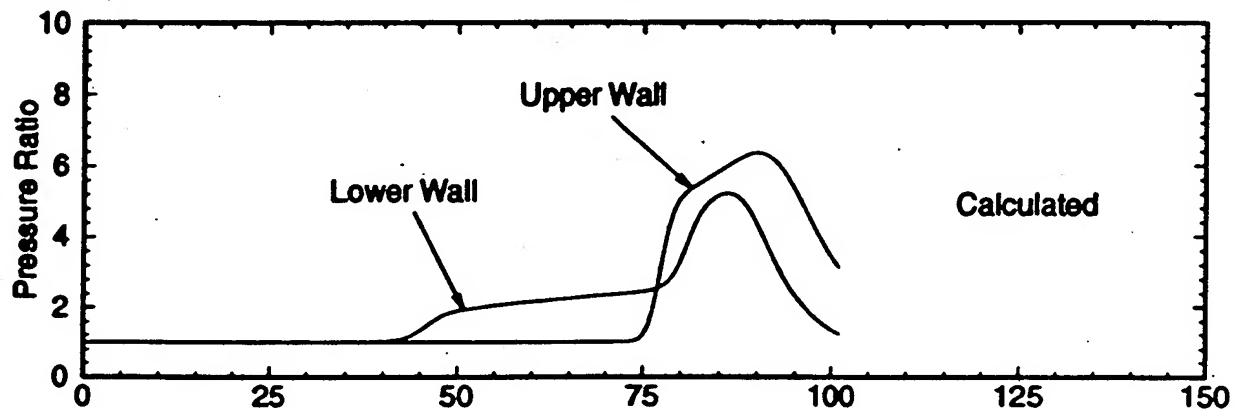
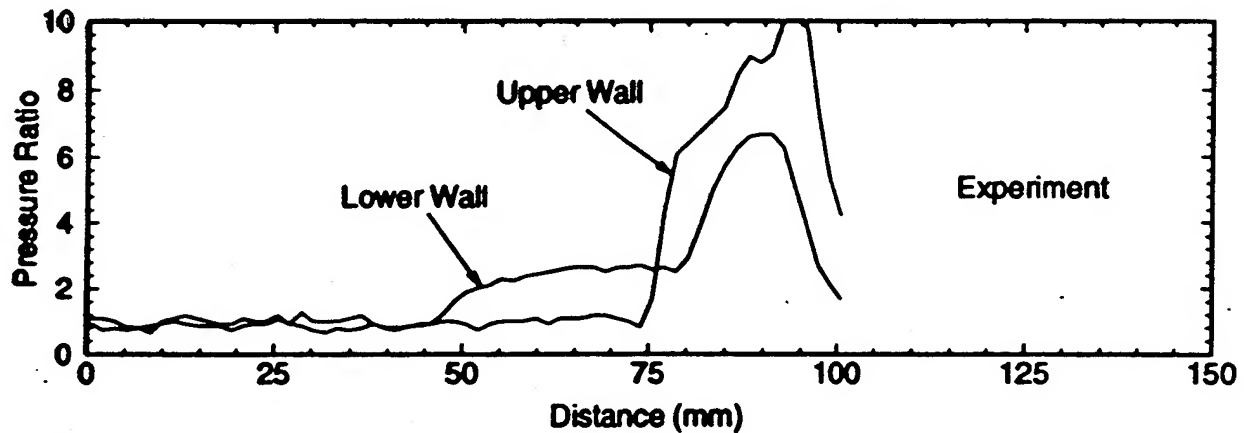
Computed and Experimental Pressure Distribution Canted Projectile

Subdetonative Regime (89% C-J)

1560 m/s (Mach 4.3)

4.5° Angle of Attack

7.5mm Nose Tip Translation



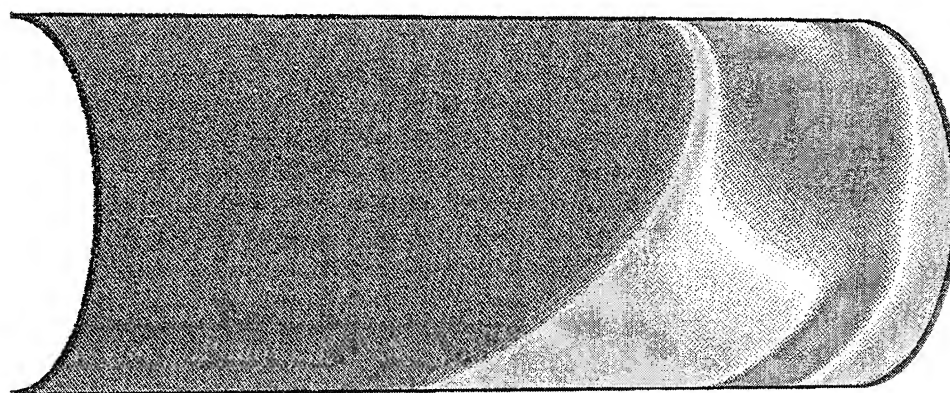
Computed Pressure Distributions Canted Projectile

Subdetonative Regime

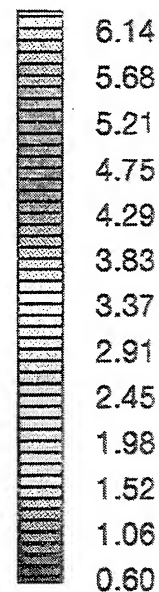
1560 m/s (Mach 4.3)

Non-Reacting

$\alpha=4.5^\circ$, $\Delta y=7.5$ mm

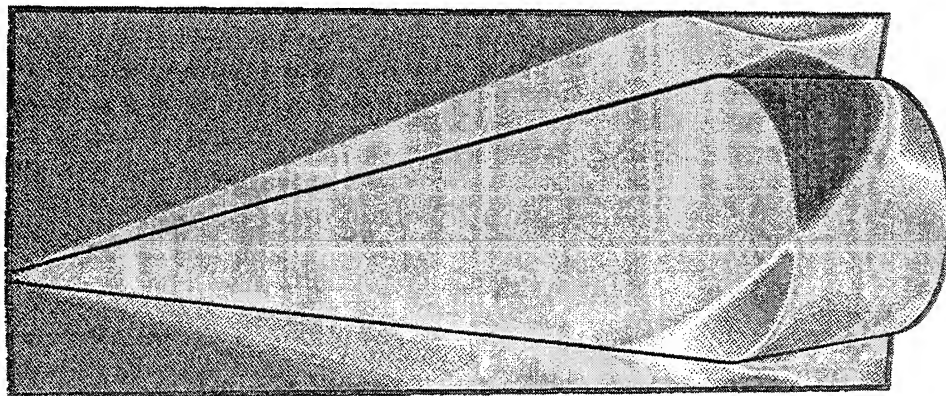


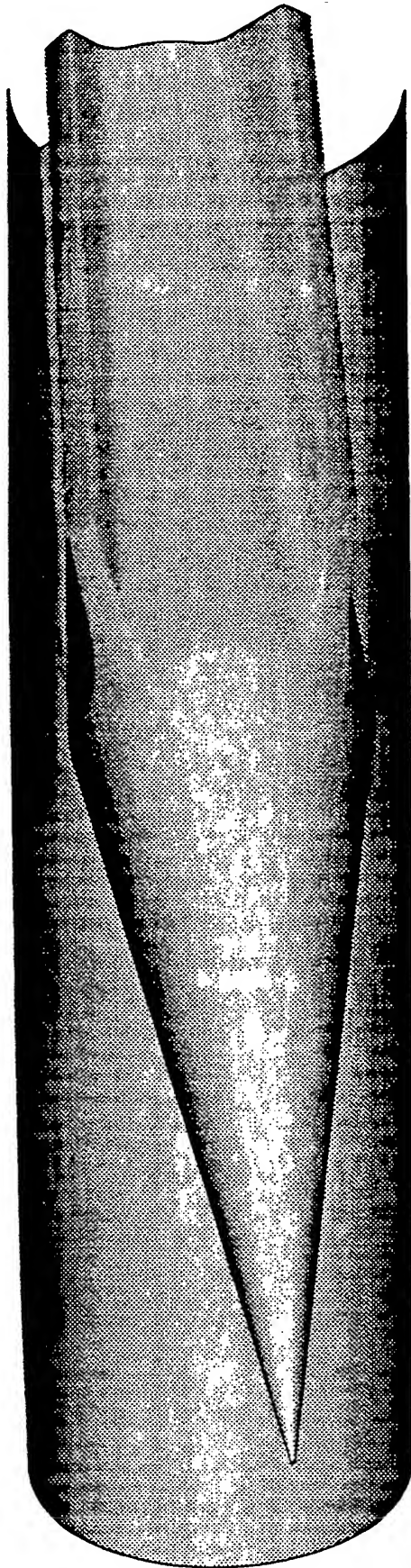
Tube Wall



Pressure Ratio

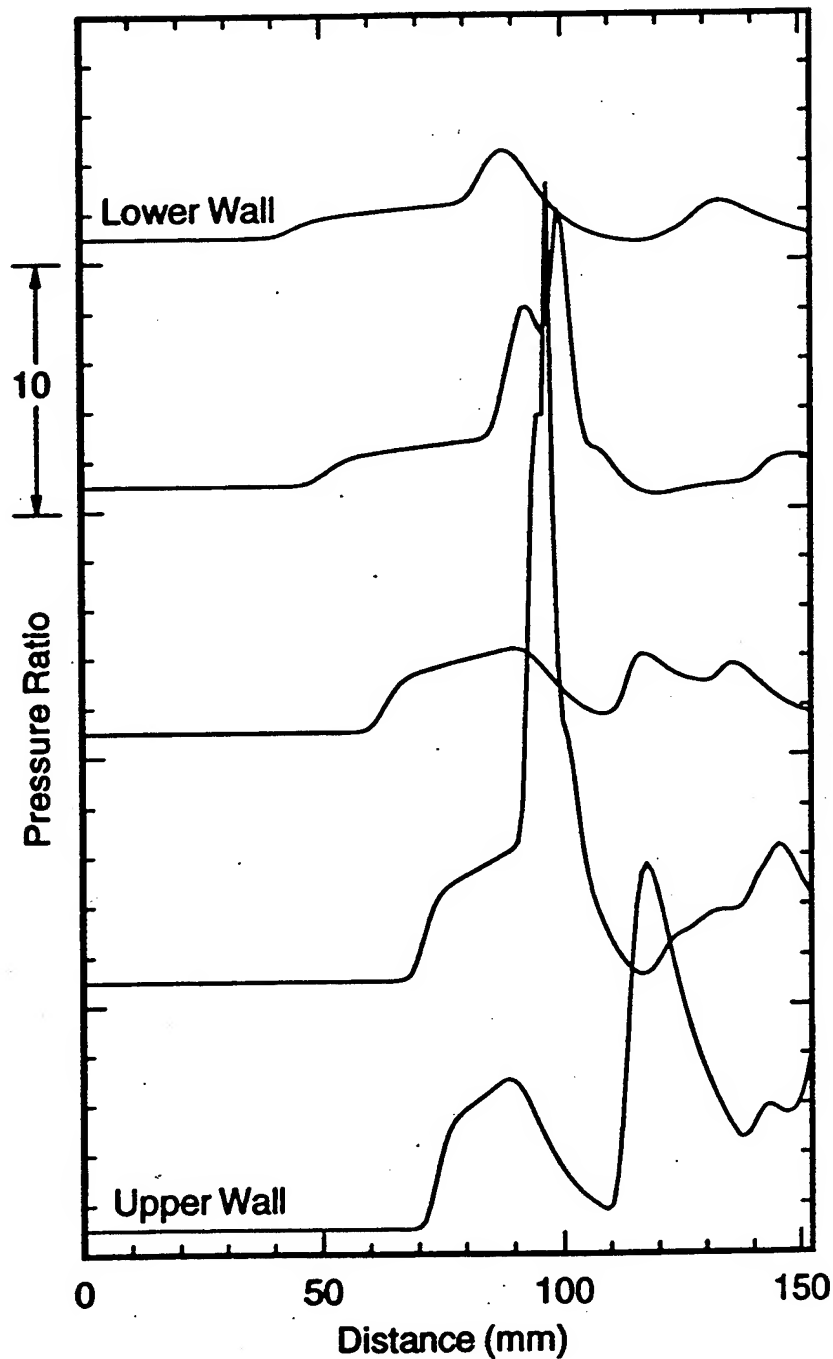
Projectile and Symmetry Plane





Line Plots of Calculated Tube Wall Pressure Canted 4-Fin Projectile

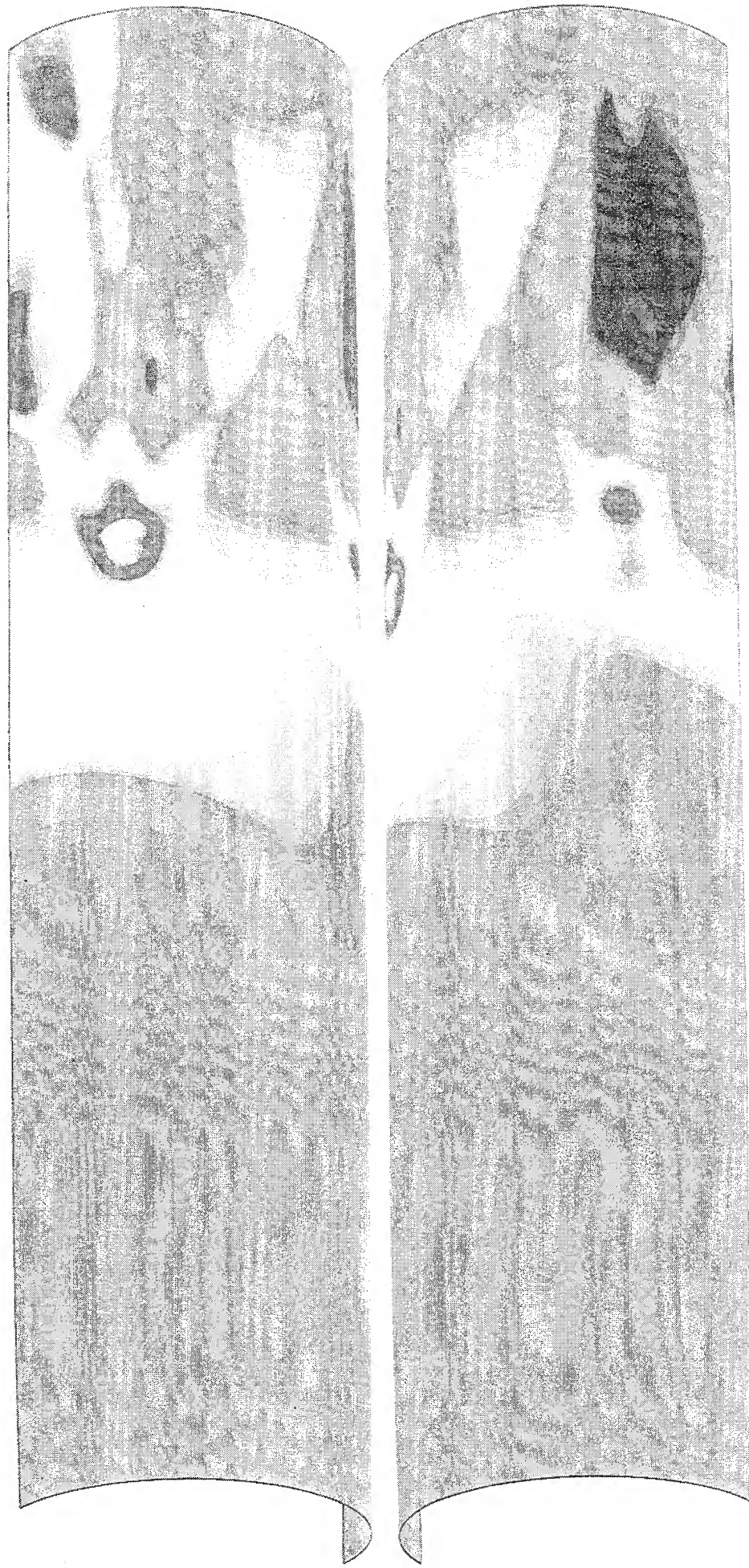
1560 m/s (Mach 4.3), 89% C-J
Non-Reacting, Inviscid



Simulated Tube Wall Pressure Distribution Canted 4-fin Projectile

$M_\infty = 4.3$ (1560 m/s), $\alpha = 4.5^\circ$, $\Delta y = 7.5$ mm

Non-Reacting, Inviscid



0.82 1.28 2.02 3.17 4.97 7.80 12.25 19.22 30.18

Pressure Ratio

Simulated Projectile Surface Pressure Distribution

Canted 4-fin Projectile

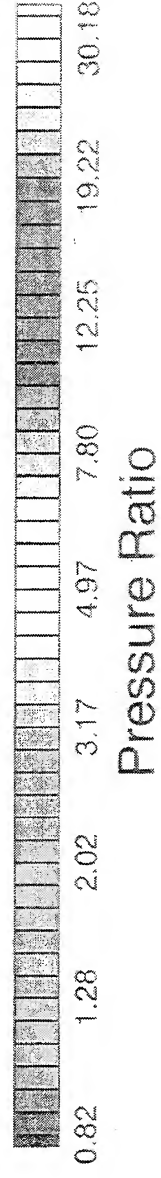
$M_x = 4.3$ (1560 m/s), $\alpha = 4.5^\circ$, $\Delta y = 7.5$ mm

Non-Reacting, Inviscid

Upper Symmetry
Plane



Lower Symmetry
Plane



Summary

Projectile flow field

- Flow field is highly 3-D in nature due to fins
- Presence of fins significantly affect performance
- Fins need to be taken into account to accurately model performance (# of fins as well as their geometry)

Combustion phenomena

- Pressure variations exist and are not probe artifacts
- Shock induced combustion in diffuser has been observed at high Mach numbers and qualitatively correlated with numerical simulations of others
- Pressure imbalances between channels exist

Projectile canting

- Experimentally and numerically confirmed
- Strongly linked to high Mach number unstarts
- Significant problem
- Fin erosion/deformation is significant

High Mach number unstarts

- Experimental data and numerical simulations of others
- Linked to canting

PRESSURE DISTRIBUTIONS ON RAM-ACCELERATOR PROJECTILES

Chiping Li, K. Kailasanath, Elaine S. Oran, and Jay P. Boris

Laboratory for Computational Physics
Naval Research Laboratory, Washington, DC 20375

In the ram accelerator, the pressure distribution on the projectile is a crucial element in the projectile acceleration and stability. In this work, we use time-accurate simulations to study the pressure distribution on the ram-accelerator projectile. The pressure on the inner wall of the ram-accelerator tube has been routinely measured in experiments. However, the pressure distribution on the projectile is difficult to obtain from experiments. The numerical simulations can be used to provide the needed pressure information on the projectile to complement the experiments.

In this presentation, the following results related to the pressure distribution on the projectile are shown. (1)*Pressure distributions on a ram-accelerator projectile from the simulations of two different resolutions:* The results show that nearly identical pressure distributions from two simulations. (2)*A pressure trace on the wall of the launch tube from a simulation:* This pressure trace is compared to the experimental data and shows similar major features such as the reflected shocks and the normal shock generated by the thermally choked combustion. (3)*Stability analysis of the projectile based on pressure distributions obtained from the simulations:* The analysis show the normal shock generated by the thermally choked combustion plays a crucial role in projectile stability. When the center of projectile mass is in the middle of the projectile, the projectile is stable if the normal shock is maintained on the rear of projectile. The projectile is unstable if this normal shock is absent. (4)*Pressure profiles on projectiles in ram accelerator operating in the oblique detonation mode:* The results show detailed detonation structures on projectile. The detonation can be stabilized during acceleration and generate high pressures on the rear part of projectile body.

Pressure Distributions on Ram-Accelerator Projectiles

Chiping Li, K. Kailasanath, E. S. Oran, and J. P. Boris

**Laboratory for Computational Physics and Fluid Dynamics
Naval Research Laboratory
Washington, DC 20375**

Surpported by AFOSR and NRL

Issues in Ram-Accelerator Development

Combustion Mechanism

- thermally choked combustion ($V_p < V_{cj}$)
- oblique detonation ($V_p > V_{cj}$)
- transitional combustion mechanisms ($V_p \sim V_{cj}$)

Unsteady Flow Features

- motion of the normal shock in the thermally choked mode
- starting process
- large-scale flow structure

Boundary Layer Effects

- shock strengthening and viscous heating

High Temperature and Pressure Effects

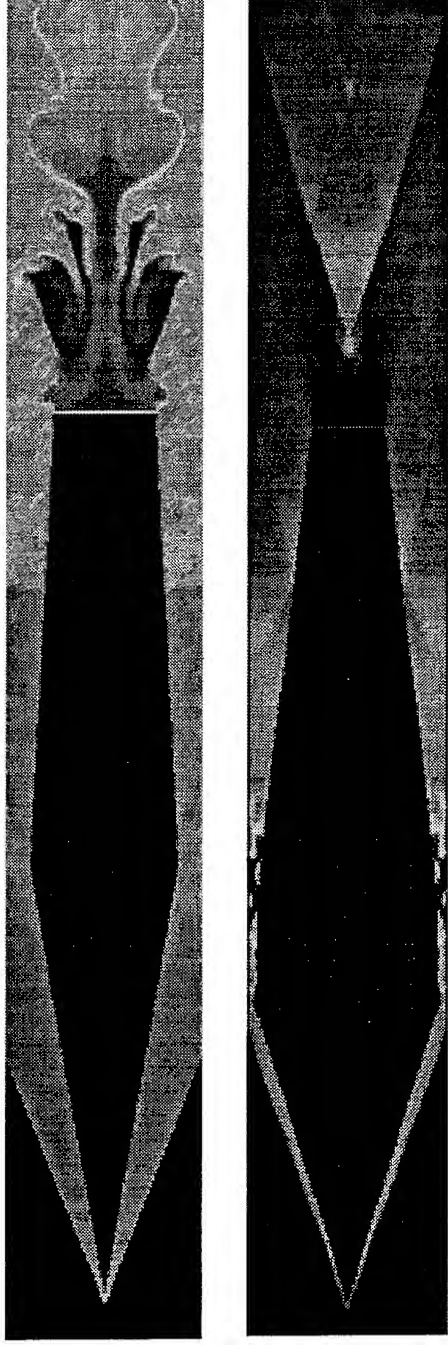
- equations of states and chemical reaction rates

Projectile Geometry and Performance

- pressure distribution
- acceleration and stability
- three-dimensional effects on combustion

Research Approach:

- Using the numerical simulation to study basic issues in ram accelerators operating in the thermally choked mode and the oblique detonation mode.



Research focuses:

- Pressure distribution on the projectile
- Pressure trace on the wall
- Projectile stability and canting
- Detonation structure on the projectile

Pressure Distributions on the Projectile from Simulations of Two different Resolutions

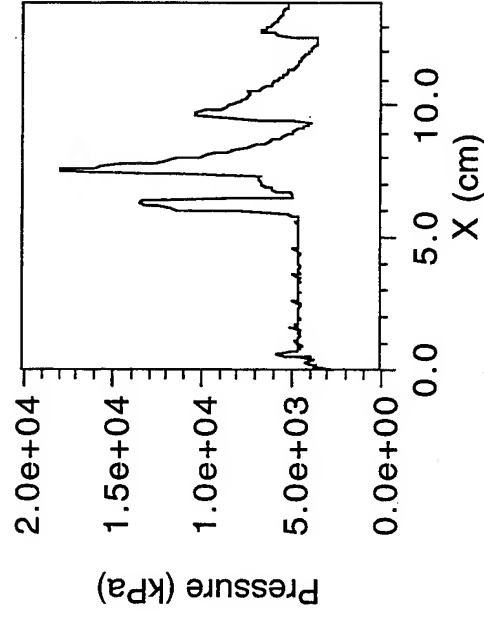


500 x 76

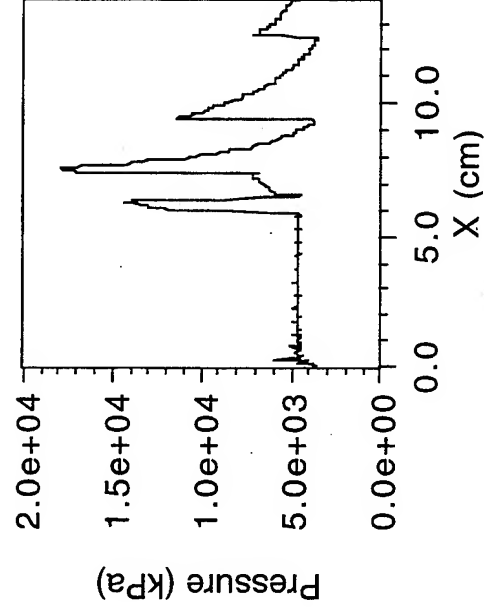


1000 x 152

500X76

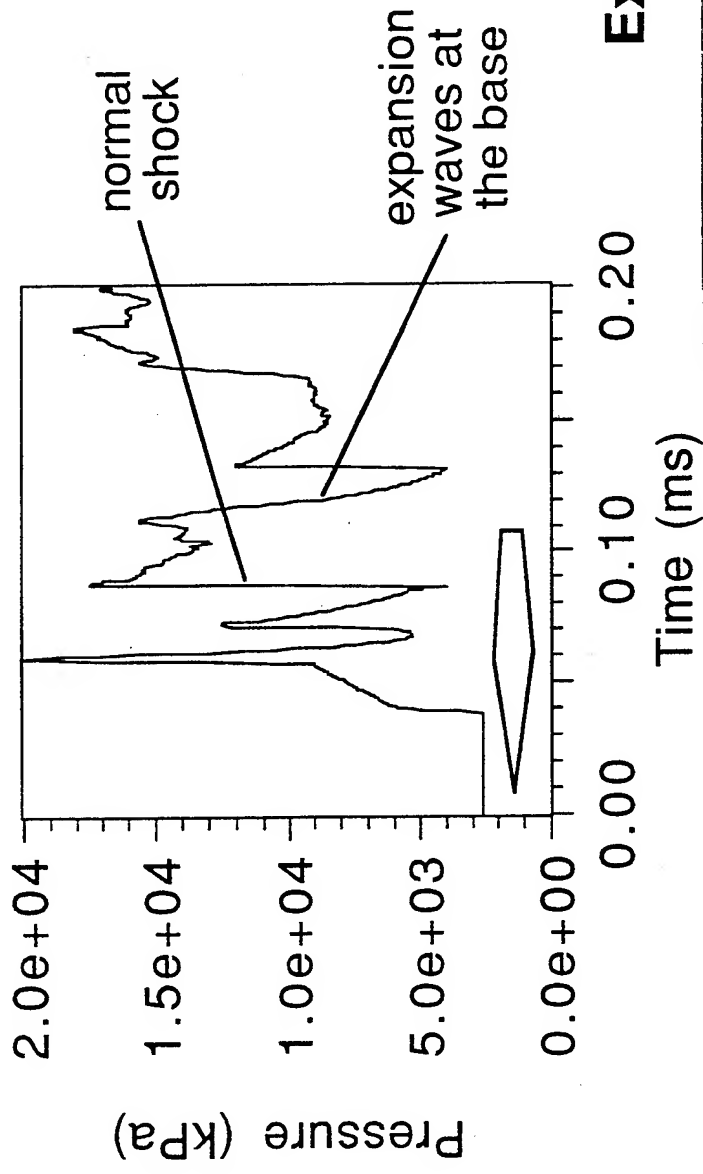


1000X152

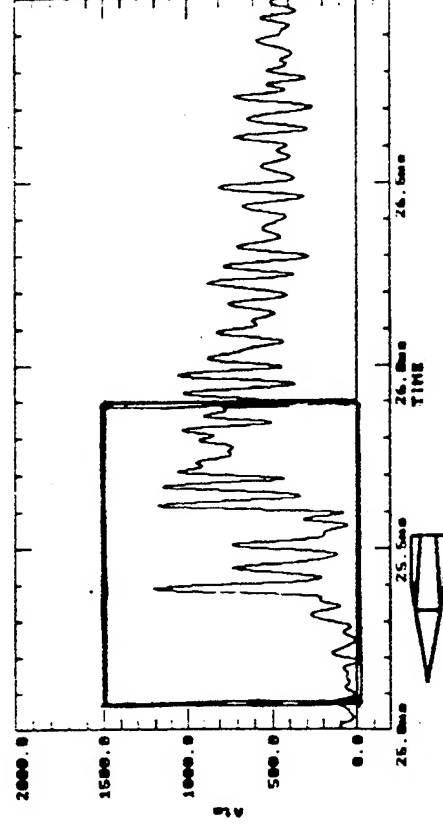


Pressure Trace on the Wall

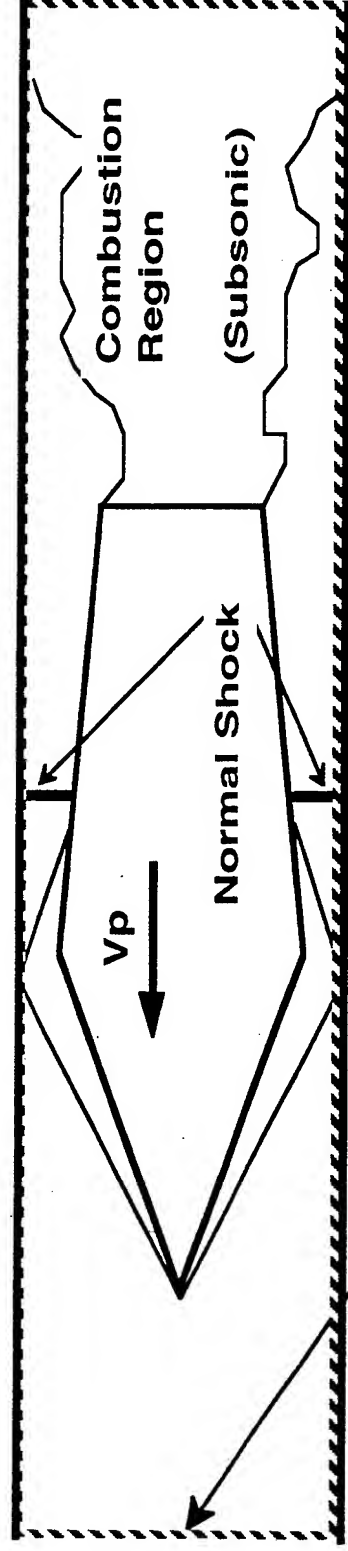
Simulation



Experiment

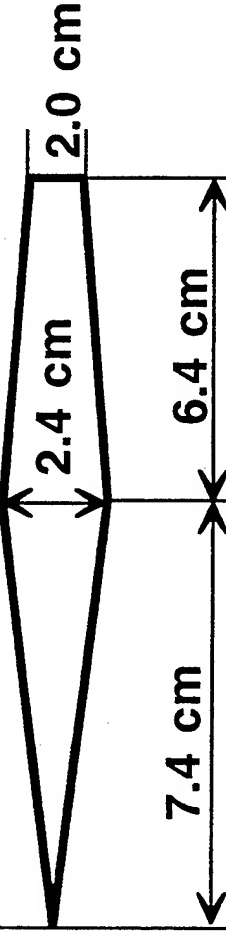


Projectile Stability and Canting



computational domain (dotted enclosure)

centered



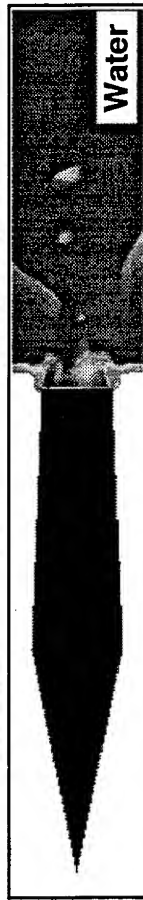
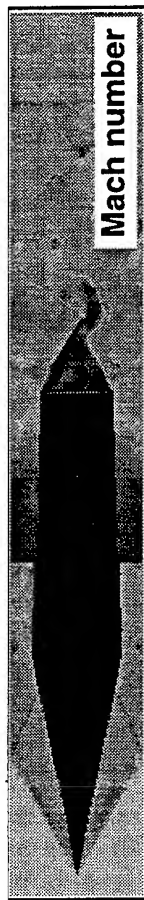
translated



rotated



centered projectile



1.9

Y(cm)

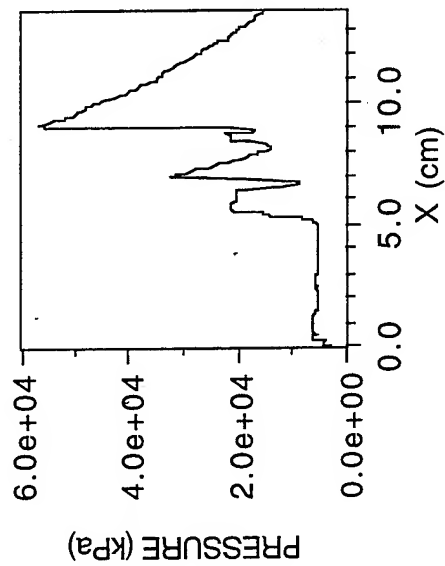
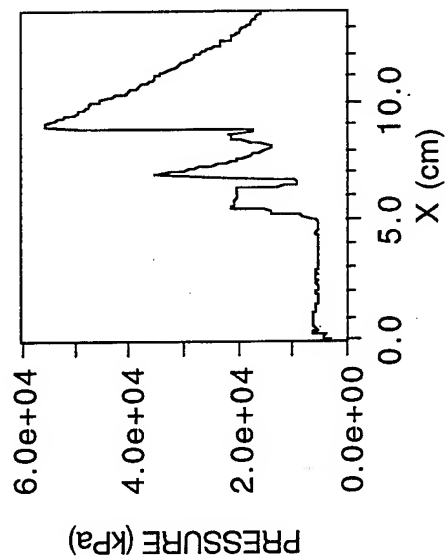
-1.9

X(cm)

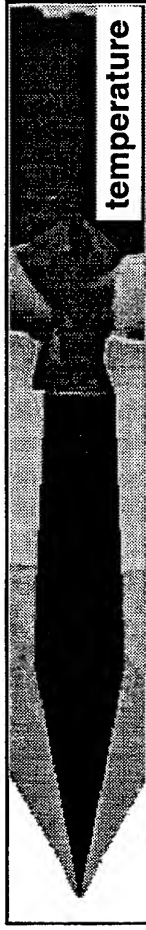
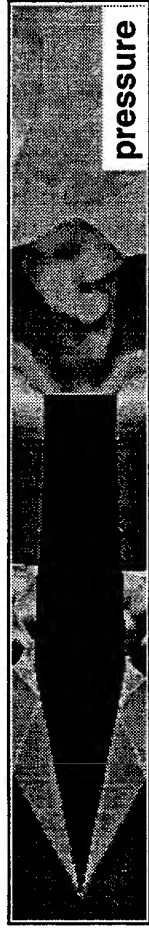
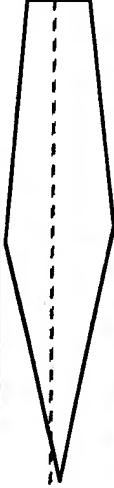
25.0

LOWER SURFACE

UPPER SURFACE



translated projectile



1.9

Y(cm)

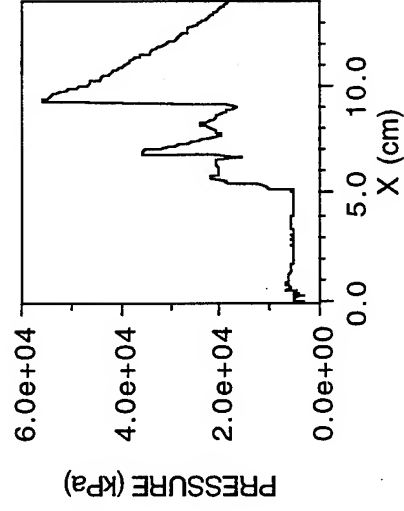
-1.9

0.0

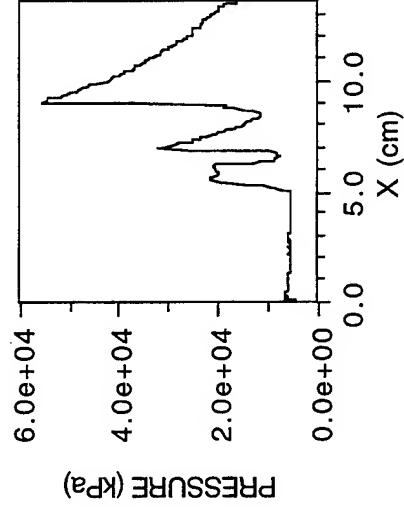
X(cm)

25.0

LOWER SURFACE



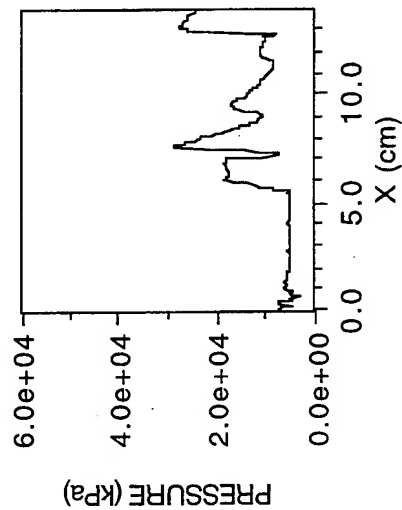
UPPER SURFACE



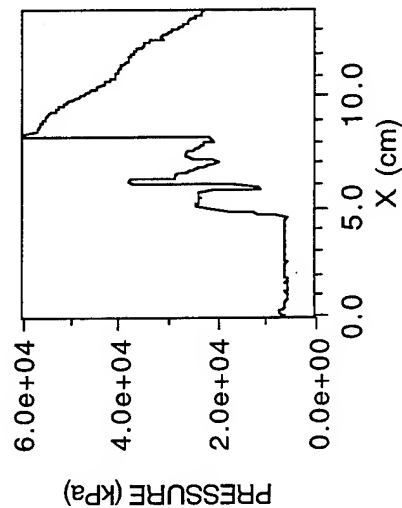
rotated projectile



LOWER SURFACE



UPPER SURFACE



Torque on the Projectile with the Normal Shock

Projectile Axis	Location of Center-of-Mass		
	3.4 cm	7.4 cm	11.4 cm
Centered	-4.0 to 3.0	-6.0 to 14.0	-40.0 to 30.0
Translated	2.6 to 5.0×10^3	3.0 to 5.4×10^2	-2.3 to -1.4×10^2
Rotated	-2.2 to -1.5×10^4	-9.0 to -5.5×10^3	2.8 to 3.2×10^3

Torque on the Projectile without the Normal Shock

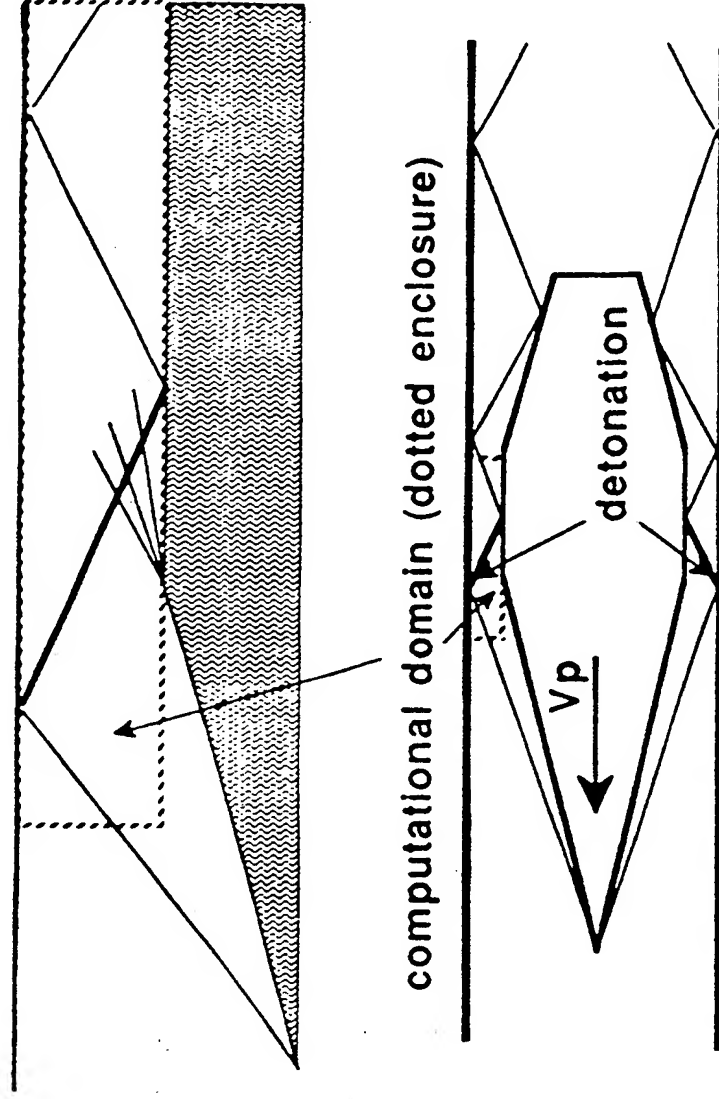
Projectile Axis	Location of Center-of-Mass		
	3.4 cm	7.4 cm	11.4 cm
Centered	-18.0 to 24.0	-2.0 to 10.0	-3.5 to 2.0
Translated	1.8 to 2.4×10^3	3.2 to 4.5×10^2	-2.8 to -1.2×10^3
Rotated	-5.2 to -3.5×10^3	2.3 to 8.5×10^3	1.0 to 1.6×10^3

Summary of the Projectile-Stability Study

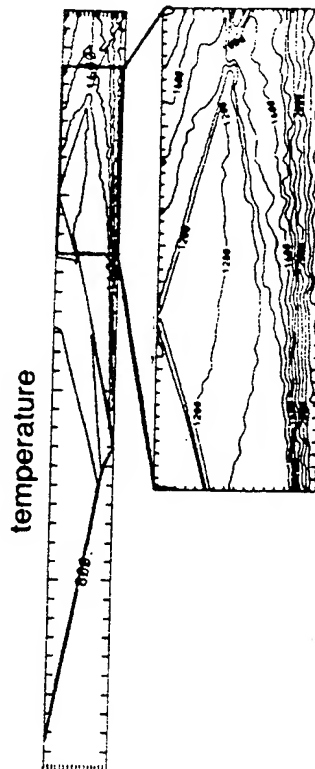
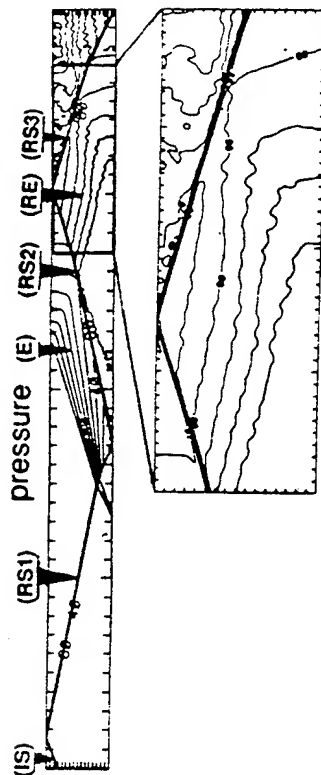
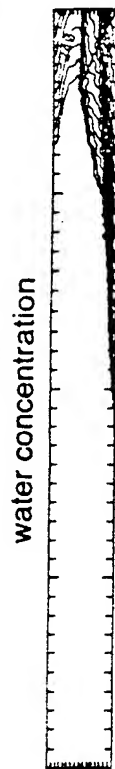
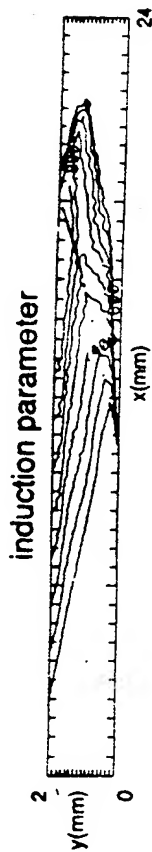
The normal shock is the crucial element in the projectile stability. For the projectile with its center of mass located in the middle part of projectile, similar to the projectile used in the experiments, the aerodynamic torque stabilizes the projectile if a normal shock is maintained on the rear part of the projectile by the thermally choked combustion and destabilizes the projectile if this normal shock is absent.

Since this thermally choked shock tends to stabilize the projectile, projectile canting could possibly be more serious in a failed launch process in which no thermally choked normal shocks are maintained on the rear part of the projectile.

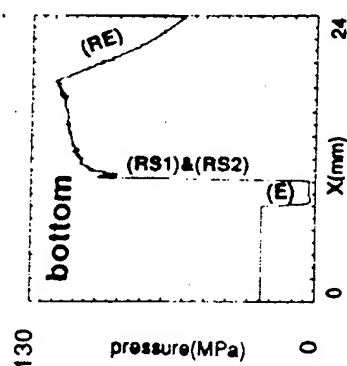
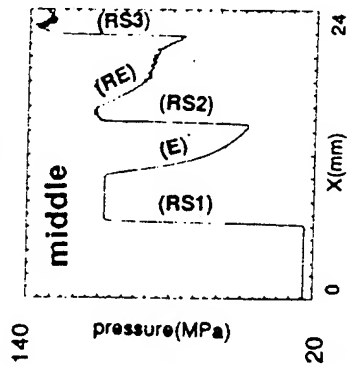
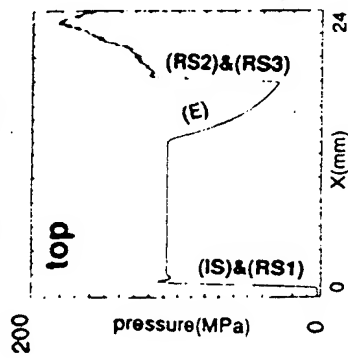
Detonation Structure on the Projectile



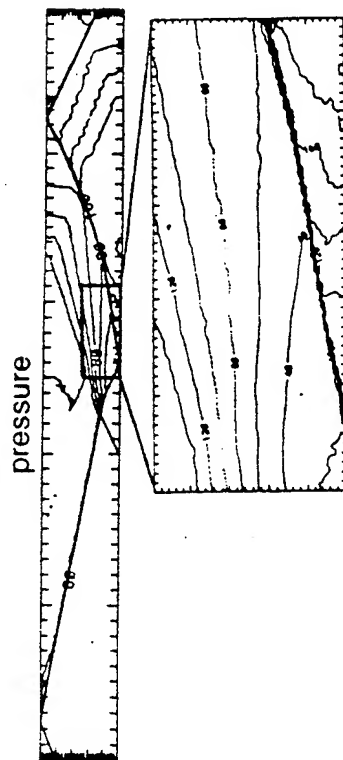
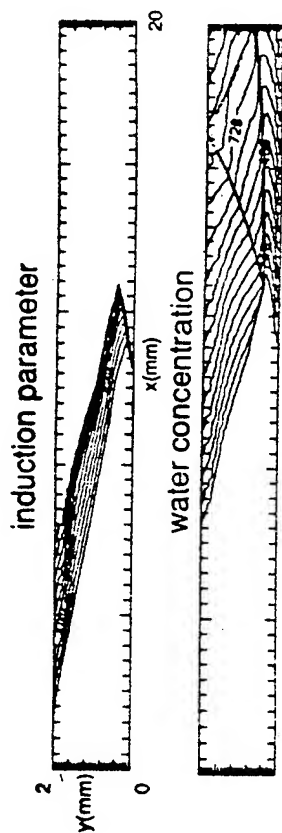
$M = 7.6$



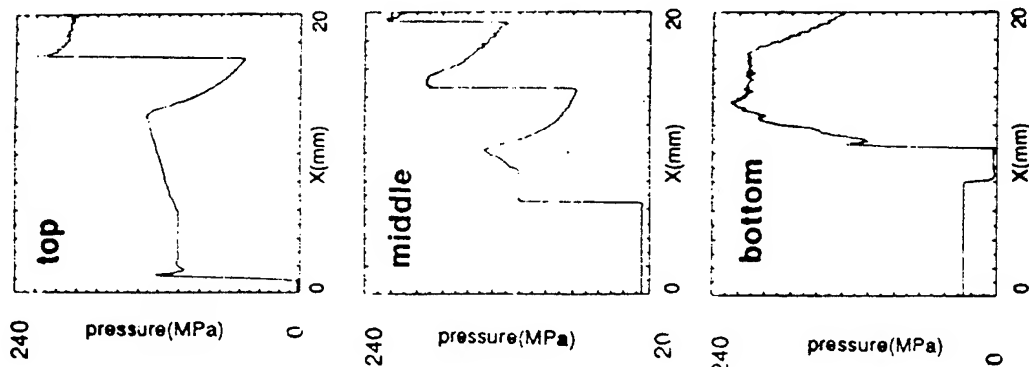
$M = 7.6$



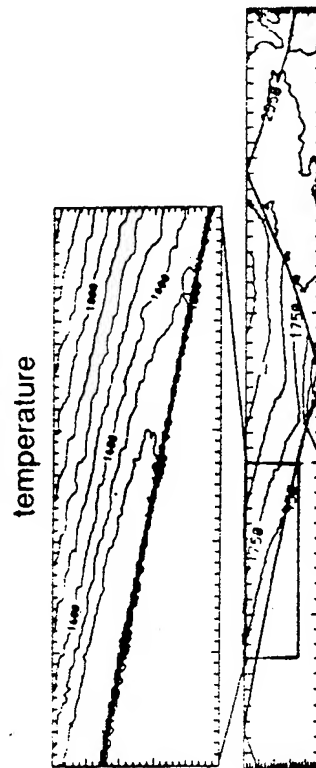
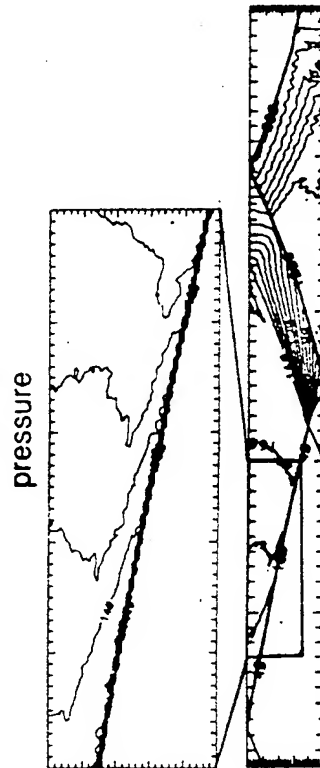
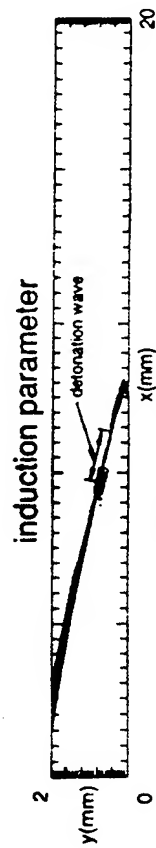
$M = 8.0$



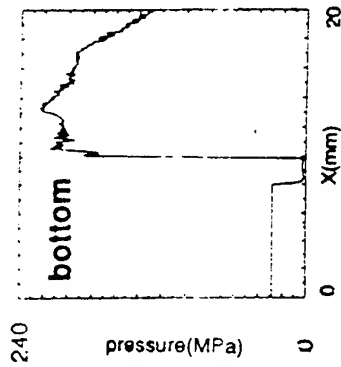
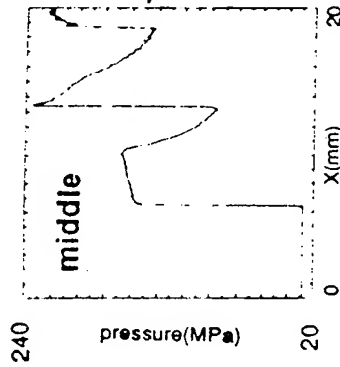
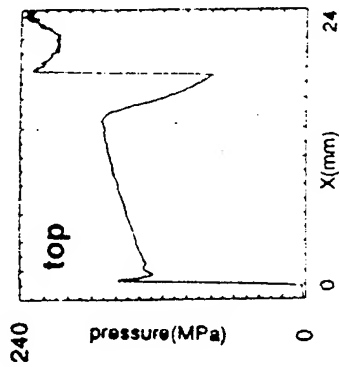
$M = 8.0$



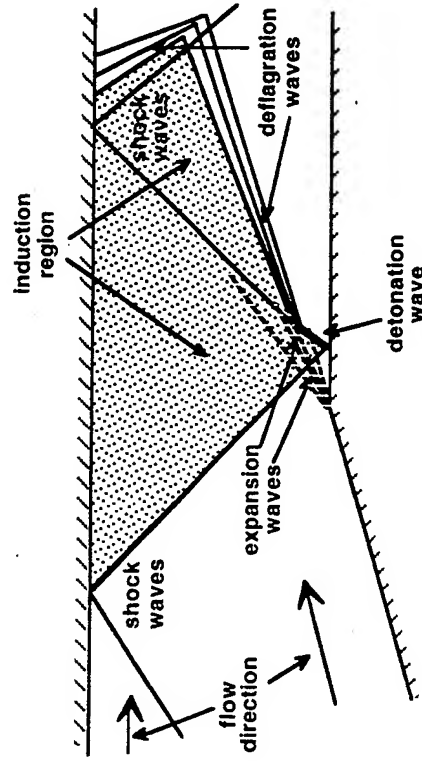
M = 8.4



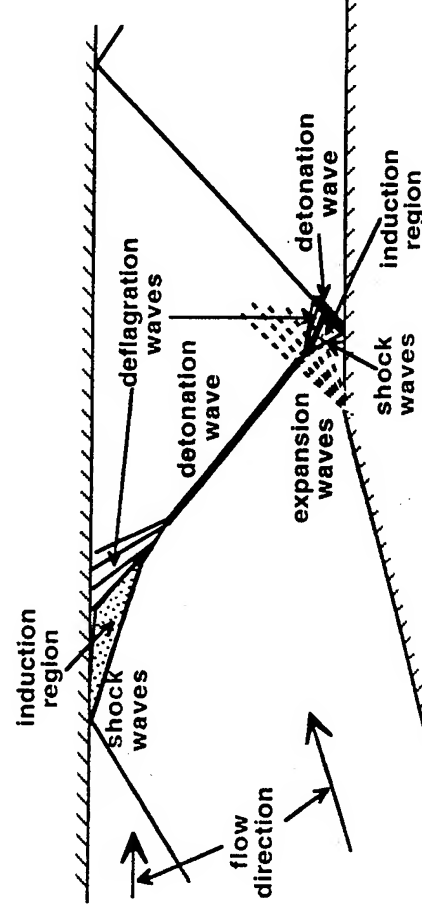
M = 8.4



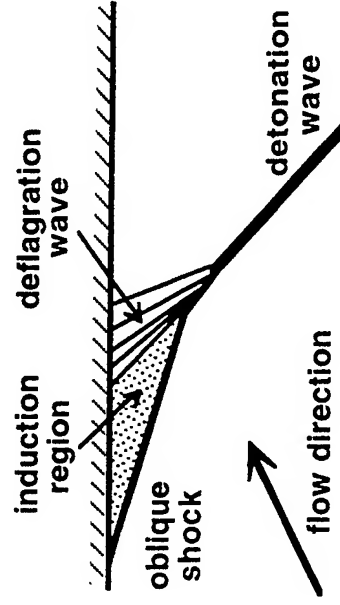
Detonation tructure on
a projectile at $M=7.6$



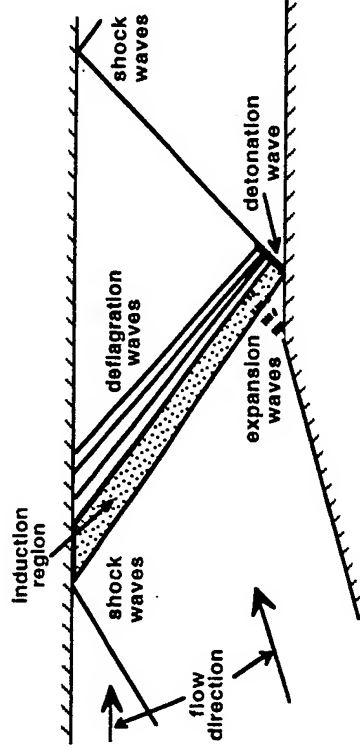
Detonation tructure on
a projectile at $M=8.4$



Detonation structure generated
by a single, oblique shock



Detonation tructure on
a projectile at $M=8.0$



Summary of the Detonation-Structure Study

Detonation structures can be generated by multiple shock reflections at different locations and in various configurations on the projectile, depending on the flow conditions. These detonation structures have the same basic elements as those in wedge-induced detonation structures.

For example, at $M = 8.4$, the induction region is primarily associated with the first reflected shock and the detonation structure is very similar to that of a wedge-induced detonation.

However, at $M = 8.0$ and at $M = 7.6$, the induction region extends across the first and second reflected shocks and the overall detonation structure is significantly complicated by these shocks.

A paper based on the above results has been submitted to *Combustion and Flame*.

PERSPECTIVES AND REMAINING ISSUES

Thermally Choked Mode:

The normal shock on the projectile is the key element in the projectile acceleration and stability. This shock is transient and strongly depends on the starting process. The effect of the starting process is currently under investigation. Also, the projectile stability will be further studied using three-dimensional simulations.

Oblique Detonation mode:

The oblique detonation provides a reliable combustion mechanism and generates the high pressure needed to accelerate the projectile. However, different methods to achieve the velocity condition under which oblique detonations can be generated and stabilized remain to be explored. The projectile stability under these conditions also needs to be studied.

FUNDAMENTAL STUDIES OF HYPERSONIC COMBUSTION WAVES FOR RAM ACCELERATORS

T. Endo, J. E. Leblanc, J. Kasahara and T. Fujiwara
Nagoya University,
Chikusa-ku, Nagoya 464-01, Japan

ABSTRACT

Two-dimensional hypersonic shock-induced combustion waves were numerically investigated using an elementary-reaction model. The stoichiometric hydrogen-air mixture impinged on blunt-nosed flat plates. Varied as parameters were the inflow Mach number ($M_0=4.91-9.82$) and the nose radius ($R=1-16$ [mm]). In this parameter region, four modes of combustion were observed. It has been found that oblique detonation waves ignite only for nose radii larger than a critical one. By analyses using detonation polars, it has been shown that the combustion waves are significantly in non-equilibrium. And also, it has been shown that the oblique detonation waves close to the border between the weak and strong ones are unstable against disturbances. The obtained critical (minimum) nose radius for the oblique-detonation ignition is explainable with an analytical $D(\text{velocity})-\kappa(\text{curvature})$ relation of expanding detonation waves.

INTRODUCTION

Hypersonic shock-induced combustion waves have been attractive for many years. They are not only interesting in themselves but also important fundamental issues for hypersonic propulsion applications. The well-known applications are the ram accelerator and the oblique detonation wave engine.¹ Especially, the advent of the ram-accelerator concept renewed interests in hypersonic combustion waves.² Hypersonic shock-induced combustion waves play important roles in the ram accelerator. Therefore, it is indispensable for stable accelerator operations to understand well the properties of the combustion waves in the ram accelerator. The influential fundamental issues on hypersonic combustion waves are conditions for ignition and steady solutions, and stability of steady solutions. In the hypersonic propulsion applications, the ambient conditions are often complicated. Hence, necessary are investigations of hypersonic combustion waves not only in the practical devices but also in simpler geometries.¹ From such points of view, we have been doing fundamental studies of hypersonic combustion waves especially in simplified geometries.

In this paper, we present numerical results on combustion in hypersonic reactive flows impinging on projectiles. The geometry we treated was mainly Cartesian two-dimensional. The projectiles were blunt-nosed flat plates. The reactive gas was the stoichiometric hydrogen-air mixture. The inflow Mach number of the reactive gas (M_0) and nose radius of the projectile (R) were varied as parameters. The parameter region we investigated was that $M_0=4.91-9.82$ and

$R=1-16$ [mm]. The flowfield was calculated using Euler conservation equations including chemical reactions. The hydrodynamic conservation equations were solved by an explicit upwind TVD algorithm. The chemical reactions were treated by an elementary-reaction model, where the reaction rates were implicitly integrated.

In the numerical experiments, the following four combustion modes were observed; (1) stable combustion in the vicinity of the nose, which was decoupled with the bow shock wave, (2) stable combustion which was partially coupled with the bow shock wave only in the vicinity of the nose, (3) stable combustion which was entirely coupled with the bow shock wave, and (4) unstable combustion which was entirely coupled with the bow shock wave. It has been shown by the numerical experiments that a minimum nose radius for the oblique-detonation ignition exists. Analyses were focused on thermodynamic properties of the reactive gas, stability of the oblique detonation waves, and conditions for the oblique-detonation ignition. They were discussed using detonation polars and an analytical solution of expanding detonation waves. In the following, the numerical model and the arrangement of the numerical experiments are described in the beginning. After that, we give an overview of the numerical results. And then, the details of the numerical results are discussed using detonation polars and an analytical $D(\text{velocity})-\kappa(\text{curvature})$ relation of expanding detonation waves.

NUMERICAL MODEL

The simulation code we used was developed by Matsuo³ and extended by Lefebvre.⁴ Details of the simulation code have been described in Ref. 4. The governing equations were the Euler conservation equations, including chemical-reaction source terms, in a time-invariant general coordinate frame. We used the equations of state for a thermally perfect gas, but for a calorically imperfect gas, namely, the specific heat was a function of temperature. The internal energy consisted of internal energy of formation and sensible internal energy. The heat release was dealt with integrating a detailed set of chemical reaction rates. The set of chemical reactions and rate constants was the one developed by Wilson and MacCormack and modified by Jachimowski. However, the code we used did not take into account the species from the reactions of nitrogen. We treated 8 reactive species and their 19 reactions, which are shown in Table I. The hydrogen-oxygen kinetic mechanism we used has been tested and compared with experimental data.³

For the integration of the fluid-dynamics conservation equations, we used a second-order accurate in both time and space explicit upwind TVD algorithm adopting flux extrapolation and Roe's averaging method. The stiff chemical source terms were implicitly integrated using a splitting technique.

ARRANGEMENT OF THE NUMERICAL EXPERIMENTS

Figure 1 shows the arrangement of the numerical experiments we carried out. The right boundary imposed the permanent inflow conditions which gave the pressure P_0 , temperature T_0 , gas-mixture ratio (molar ratio is shown in Fig. 1), and velocity U_0 . At the inflow conditions shown in Fig. 1, the Chapman-Jouguet

Table I. Chemical reactions included in the simulation code.

No	Chemical Reaction
(1)	$H_2 + O_2 \rightleftharpoons HO_2 + H$
(2)	$H + O_2 \rightleftharpoons OH + O$
(3)	$O + H_2 \rightleftharpoons OH + H$
(4)	$OH + H_2 \rightleftharpoons H + H_2O$
(5)	$OH + OH \rightleftharpoons O + H_2O$
(6)	$H + OH \rightleftharpoons H_2O$
(7)	$H + H \rightleftharpoons H_2$
(8)	$H + O \rightleftharpoons OH$
(9)	$H + O_2 \rightleftharpoons HO_2$
(10)	$O + O \rightleftharpoons O_2$
(11)	$HO_2 + H \rightleftharpoons OH + OH$
(12)	$HO_2 + H \rightleftharpoons H_2O + O$
(13)	$HO_2 + O \rightleftharpoons O_2 + OH$
(14)	$HO_2 + OH \rightleftharpoons H_2O + O_2$
(15)	$HO_2 + HO_2 \rightleftharpoons H_2O_2 + O_2$
(16)	$H + H_2O_2 \rightleftharpoons H_2 + HO_2$
(17)	$O + H_2O_2 \rightleftharpoons OH + HO_2$
(18)	$OH + H_2O_2 \rightleftharpoons H_2O + HO_2$
(19)	$H_2O_2 \rightleftharpoons OH + OH$

detonation velocity (D_{C-J}) is $D_{C-J}=1980$ [m/s]. The upper and left boundaries were treated as the outflow condition. The outflow condition was characterized by equal physical quantities through one guard cell. The projectile surface was characterized by a slip and adiabatic condition. The projectiles were blunt-nosed flat plates, that is, the geometry was Cartesian two-dimensional. As parameters, we varied the inflow velocity U_0 , identical to the inflow Mach number M_0 , and the nose radius R . The parameter region was that $U_0=2000-4000$ [m/s] ($M_0=4.91-9.82$) and $R=1-16$ [mm].

The general coordinate system $\xi - \eta$ was so that ξ and η coordinates were along and normal to the projectile surface, respectively. All the calculations but $R=16$ [mm] cases were carried out on 90×90 grids in ξ and η directions. The calculations for $R=16$ [mm] cases were carried out on 120×180 or 180×180 grids.

OVERVIEW OF THE RESULTS

Figure 2 shows an overview of the simulation results in $U_0(M_0)-R$ plane. In the parameter region we investigated, four modes of combustion were observed. We call them hereafter (1) decoupled, (2) partially-coupled, (3) entirely-coupled (stable), and (4) entirely-coupled (unstable) combustions. Figure 3 shows examples of the flowfields of the decoupled, partially-coupled, and entirely-coupled (stable) combustions, which are all numerically-converged flowfields.

As shown in Fig. 3(a), the decoupled combustion is such that the combustion occurs only on the surface of the projectile nose. This case corresponds to that the bow shock wave is too weak to initiate the combustion. Figure 3(b) shows a partially-coupled combustion. This case is such that the combustion is coupled with the bow shock wave only in the vicinity of the nose. As shown in Fig. 2, it is remarkable that the combustions are still partially-coupled even if the highest-Mach-number cases when $R \leq 4$ [mm]. Figure 3(c) shows an entirely-coupled (stable) combustion. This mode is such that the combustion is coupled with the bow shock wave in the entire region, and in

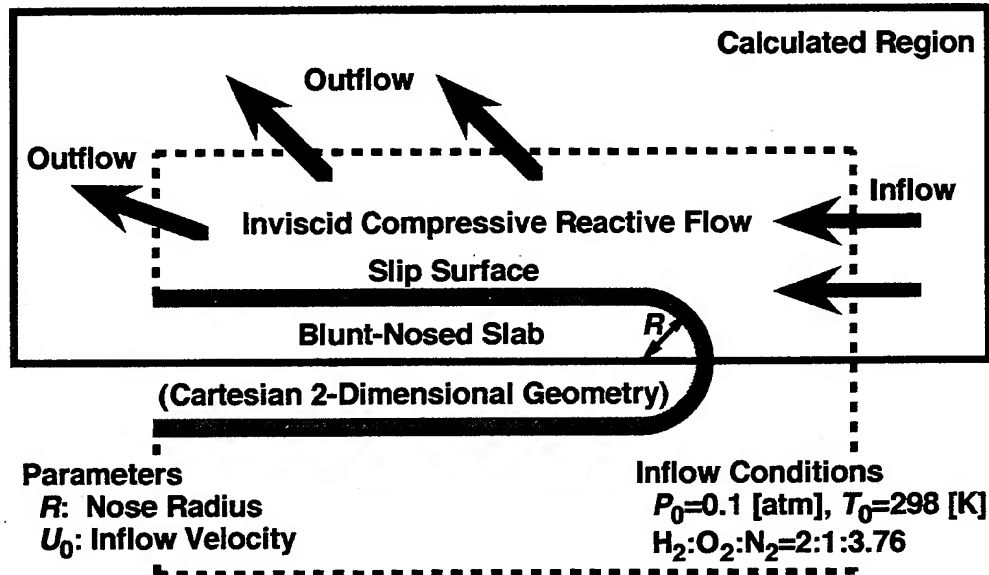


Fig. 1 Arrangement of the numerical experiments.

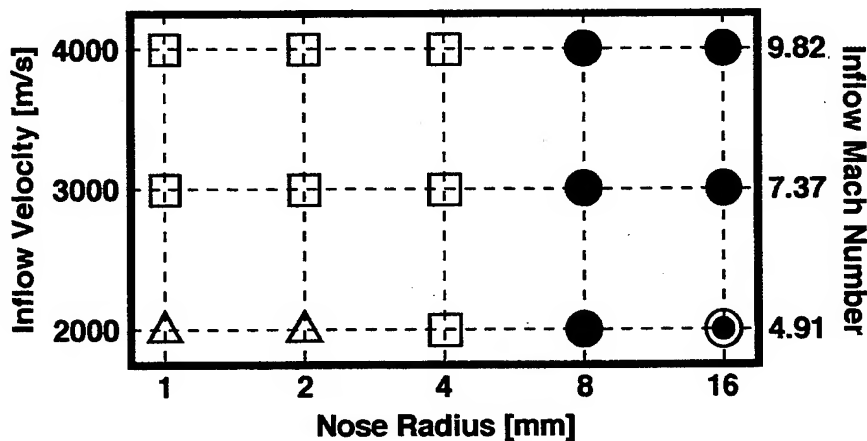


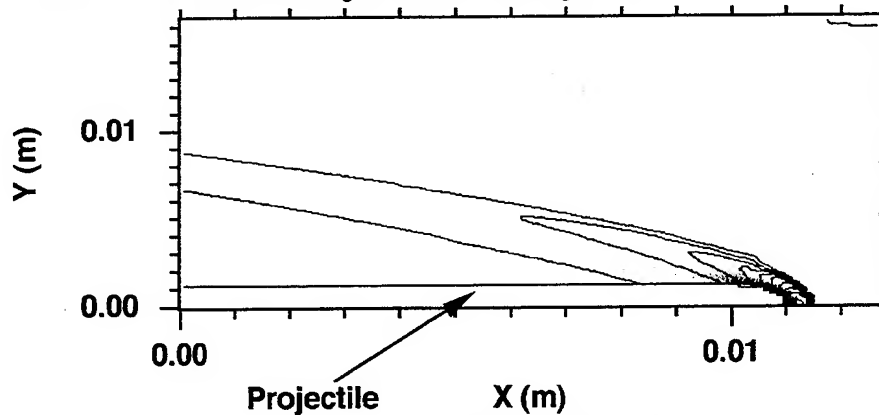
Fig. 2 Overview of the results of the numerical experiments. Four modes of the combustion were observed. The meanings of the symbols are that Δ : Decoupled, \square : Partially coupled, \bullet : Entirely coupled (Stable), \odot : Entirely coupled (Unstable).

H₂O Production Rate [kg/(m³·s)]

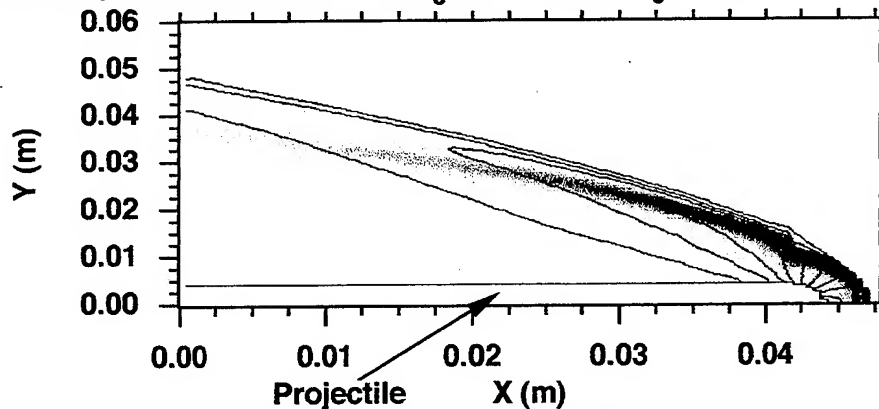
0.0x10⁰⁰ 5.0x10⁰³

Isocontour: Pressure (every 3x10⁴ [Pa])

(a) Decoupled: $R=1$ [mm], $U_0=2000$ [m/s] ($M_0=4.91$)



(b) Partially Coupled: $R=4$ [mm], $U_0=2000$ [m/s] ($M_0=4.91$)



(c) Entirely Coupled (Stable): $R=8$ [mm], $U_0=2000$ [m/s] ($M_0=4.91$)

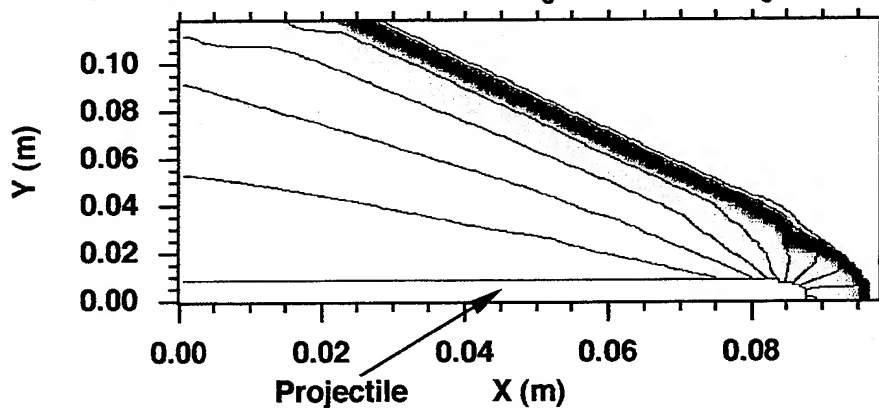


Fig. 3 Examples of the flowfields. (a) Decoupled combustion. (b) Partially-coupled combustion. (c) Entirely-coupled (stable) combustion.

steady state. By coupling between the combustion and the bow shock wave, the straight-shape oblique detonation wave is generated. As shown in Fig. 2, entirely-coupled combustions were observed at all investigated Mach numbers when $R \geq 8$ [mm]. Directly from the results of the numerical experiments shown in Fig. 2, it is concluded that a minimum nose radius for the generation of the entirely-coupled combustions exists.

About the entirely-coupled (unstable) combustion, development of the flowfield is shown in Fig. 4. Figure 4(a) shows the flowfield at the time when the residual is minimum. This flowfield is very similar to that of the entirely-coupled (stable) combustion shown in Fig. 3(c). It is noteworthy that the breakdown of the flowfield shown in Fig. 4(a) is initiated at the left boundary which is characterized by the outflow condition. This is physically strange. Since the outflow condition was given by the 0-th-order extrapolation, the left and upper boundaries could be sources of small disturbances. Therefore this observed unsteadiness may not be intrinsic but be due to disturbance growth of the oblique detonation wave.

ANALYSES WITH DETONATION POLARS

As shown in Fig. 3(c), the entirely-coupled (stable) combustion clearly includes a straight-shape steady-state oblique detonation wave. For understanding properties of the observed combustion waves, comparison of the simulation results with Rankine-Hugoniot relations is of great value. Rankine-Hugoniot relations for a straight-shape steady-state oblique detonation wave are obtained from the two-dimensional steady-state reactive Euler equations.⁵ In the geometrical arrangement shown in Fig. 1, an expansion wave exists attaching down the oblique detonation wave. Hence we first have to define the end surface of the detonation wave. Figure 5 shows a magnified flowfield around the straight-shape steady-state oblique detonation wave. By comparison between Figs. 5(a) and 5(b), it is found that positions at which strong chemical reaction ends are almost identical with those at which pressure is maximum. At such positions, the flow was found to be supersonic in the simulation results. Considering a Rayleigh flow, pressure increases when a supersonic flow is heated. On the other hand, pressure decreases in an expansion wave attaching down the oblique detonation wave. Therefore, we can reasonably define the end surface of the detonation wave as a surface on which pressure is maximum.

The β (shock-wave angle)- θ (deflection angle) detonation polar is written as follows.

$$x = \frac{[(1 - \varepsilon - C)y^2 - \varepsilon] \pm \sqrt{[y^2 - \varepsilon(y^2 + 1)]^2 - C(\gamma + 1)y^2(y^2 + 1)}}{y[(C + 2\varepsilon + \gamma - 1)y^2 + (2\varepsilon + \gamma + 1)]},$$

where

$\text{H}_2\text{O Production Rate [kg/(m}^3\cdot\text{s)]}$
 0.0×10^{00}
 5.0×10^{03}

Isocontour: Pressure (every 2.5×10^4 [Pa])

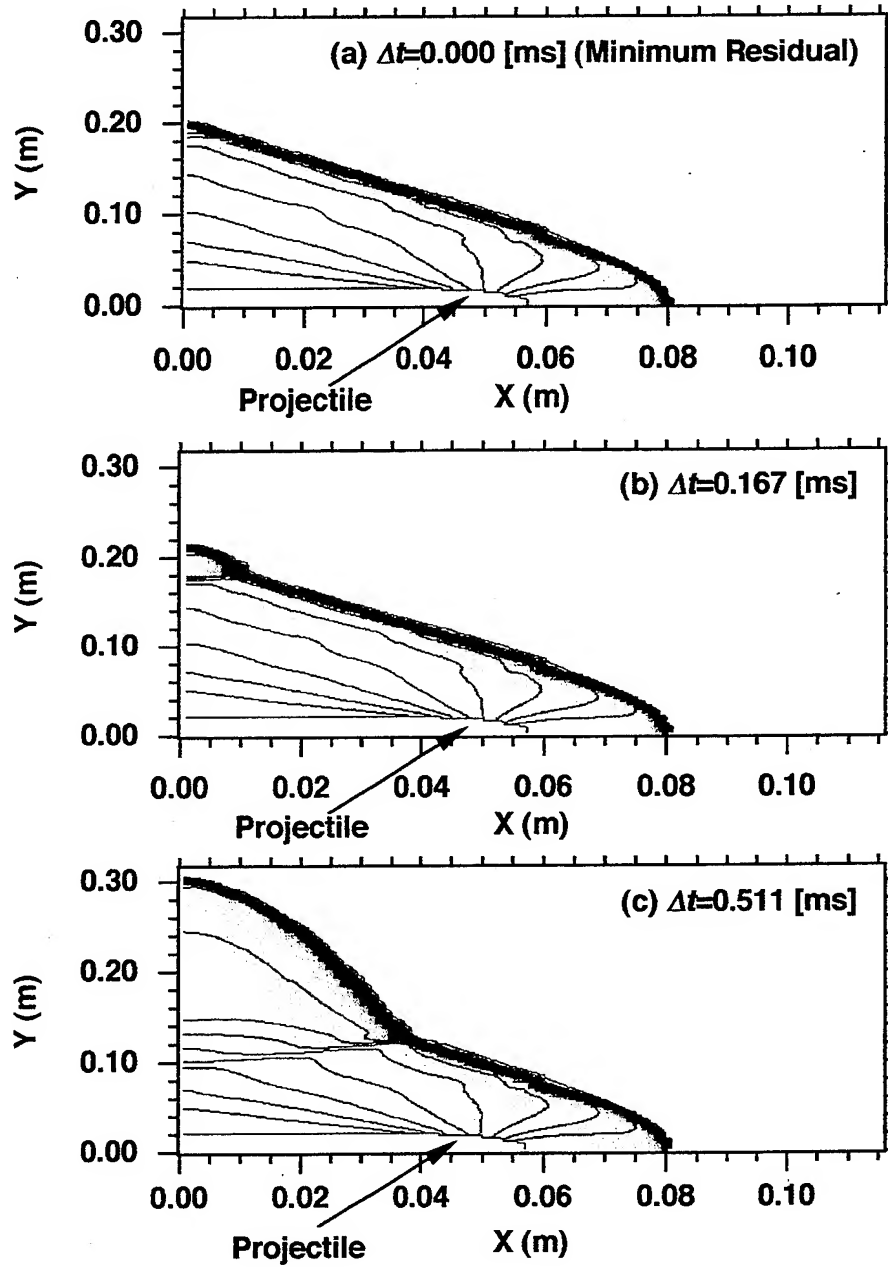


Fig. 4 Development of the flowfield for the entirely-coupled (unstable) case; $R=16$ [mm] and $U_0=2000$ [m/s] ($M_0=4.91$). Relative time (Δt) is defined so that $\Delta t=0$ corresponds to the minimum residual.

$$x = \tan \theta, \quad y = \tan \beta, \quad \varepsilon = \frac{1}{M_0^2}, \quad C = 2\varepsilon \frac{\gamma - 1}{\gamma} q\lambda, \quad q = \frac{q_*}{P_0/\rho_0},$$

M_0 is the inflow Mach number, γ is the specific heat ratio, λ is the common reaction progress variable ($\lambda=0$ before reaction and $\lambda=1$ after complete reaction), q_* is the heat of reaction (released energy per unit mass of the mixture gas in the case of complete reaction, that is, $\lambda=1$), P_0 is the inflow pressure, and ρ_0 is the inflow mass density.

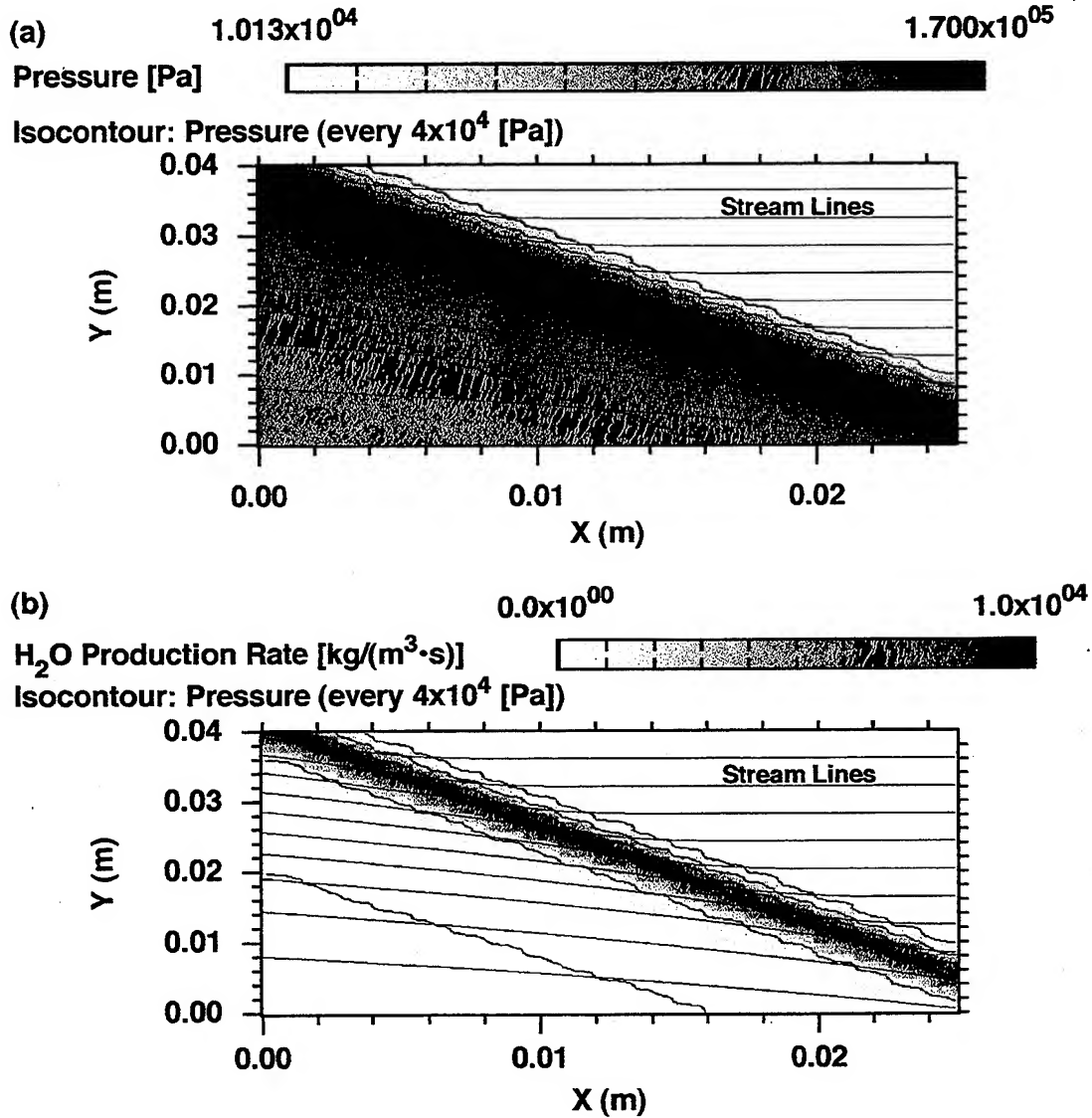


Fig. 5 Magnified plots of the flowfield around the steady oblique detonation wave; $R=8$ [mm], $U_0=2000$ [m/s] ($M_0=4.91$). (a) Pressure. (b) H₂O production rate.

Figure 6 shows the β - θ detonation polars for $M_0=4.91$, 7.37 and 9.82, and for $\lambda=0$, 0.18 and 0.36. The detonation polars for $\lambda=0$ correspond to the inert-shock polars. In the calculation of the detonation polars, we used $\gamma=1.4$. As shown in Fig. 6, all the simulation results are almost on the detonation polars for $\lambda=0.18$ and correspond to the weak overdriven oblique detonation waves.⁶ For plotting the simulation results in Fig. 6, we determined β and θ of them as follows. The shock-wave angle β was determined by tracing positions at which pressure was a half of the maximum pressure of the detonation wave. The deflection angle θ was determined by the velocity ratio between parallel and perpendicular to the inflow velocity at the end surface of the detonation wave. For the entirely-coupled (unstable) combustion which was observed at $M_0=4.91$ and $R=16$ [mm], we determined β and θ from the flowfield at the time of minimum residual which was shown in Fig. 4(a).

The common reaction progress variable λ is to be directly derived from the simulation results. The mass fraction of H_2O , $Y(H_2O)$, can be known at arbitrary positions in the simulation results. Since $Y(H_2O)$ should be $Y(H_2O)=0$ when $\lambda=0$ and $Y(H_2O)=0.255$ when $\lambda=1$ in the conditions shown in Fig. 1, λ is to be calculated by $\lambda(H_2O)=Y(H_2O)/0.255$ at arbitrary positions. It was found by the simulation results that $\lambda(H_2O)=0.619\pm0.034$ at the end surface of the detonation wave. This is significantly larger than $\lambda=0.18$ which was derived from the comparison shown in Fig. 6. Assuming the one-step reaction, λ is to be derived by another way. Since the mass fraction of H_2 , $Y(H_2)$, should be $Y(H_2)=0.0283$ when $\lambda=0$ and $Y(H_2)=0$ when $\lambda=1$ in the conditions shown in Fig. 1, λ is to be calculated by $\lambda(H_2)=1-Y(H_2)/0.0283$ at arbitrary positions. It was found by the simulation results that $\lambda(H_2)=0.780\pm0.027$ at the end surface of the detonation wave. This disagrees with both $\lambda(H_2O)=0.619\pm0.034$ derived from $Y(H_2O)$ and $\lambda=0.18$ derived from the β - θ detonation polars. Because the simulation code we used adopted an elementary-reaction model for H_2 - O_2 combustion, the fact that $\lambda(H_2)>\lambda(H_2O)$ stands for that the reactive gas contains a considerable amount of activated complex. About 16% of the whole hydrogen atoms are included in the activated complex at the end surface of the detonation wave. Formation of activated complex is endothermic. Therefore, the effective common reaction progress variable λ , which is proportionally related to the net released energy and is derived from detonation polars, should be smaller than both $\lambda(H_2O)$ and $\lambda(H_2)$.

We discuss the stability of oblique detonation waves using a detonation polar assuming quasi-steady state. As described above, the entirely-coupled (unstable) combustion may be due to growth of small-disturbances whose source is a boundary of the computer simulation. Figure 7 shows a P (pressure)- θ (deflection angle) detonation polar for $M_0=4.91$ and $\lambda=0.18$. An oblique detonation wave, at the end surface of which the flow is subsonic, is called a strong oblique detonation wave. On the other hand, when supersonic, it is called a weak one. About the entirely-coupled combustions in the simulation results, the flow at the end surface of the oblique detonation wave was unambiguously supersonic except for the case of the unstable combustion, namely, the case of $M_0=4.91$ and $R=16$ [mm]. Only in the case of $M_0=4.91$ and $R=16$ [mm], the flow at the end surface of the oblique detonation wave was almost sonic (the Mach

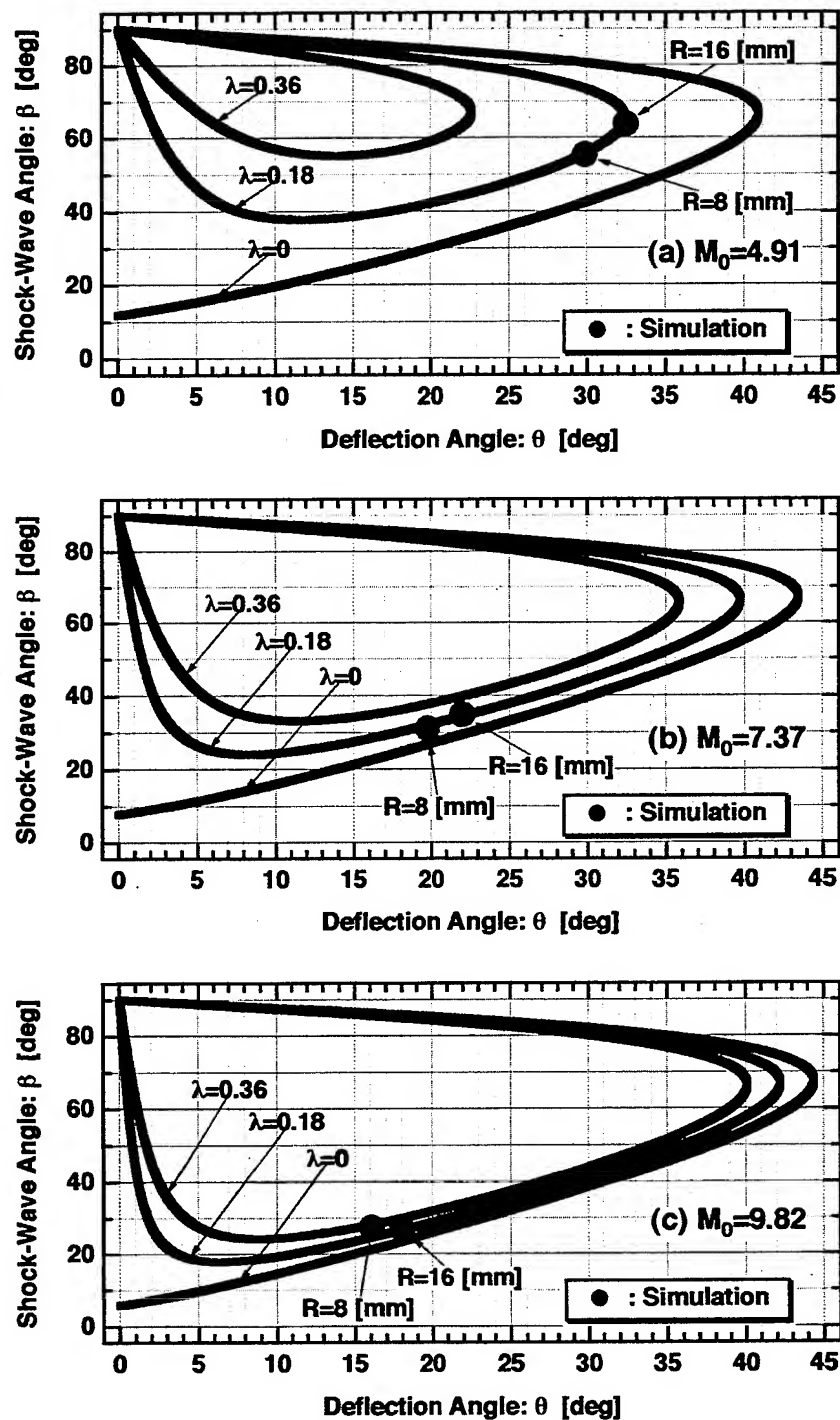


Fig. 6 Comparison between the simulation results and the β - θ detonation polars.

number was 1.04 in the simulation result).

Let ΔP stand for the small pressure disturbance at a position on the end surface of the detonation wave. And let $\Delta\theta$ stand for the small deflection-angle disturbance induced by the pressure disturbance ΔP . The source of the disturbance is the left or upper boundary as stated above. Therefore in the geometrical situation shown in Fig. 1, it is enough to discuss the influence of the pressure disturbance ΔP on the region between the projectile and the stream line which passes through the position of ΔP . If the flow at the end surface of the detonation wave is unambiguously supersonic, there is no influence. If the flow at the end surface of the detonation wave is subsonic, there are some influences. In the case that the flow at the end surface of the detonation wave is supersonic but almost sonic, there are some influences if the pressure disturbance ΔP is so large that the flow is forced to be subsonic.

When the flow at the end surface of the detonation wave is subsonic, $\Delta\theta/\Delta P < 0$ because $dP/d\theta < 0$ as is shown in Fig. 7. Therefore, $\Delta\theta < 0$ if $\Delta P > 0$, and $\Delta\theta > 0$ if $\Delta P < 0$. If $\Delta P < 0$, the flow at the end surface of the detonation wave, which is supersonic but almost sonic, can not be forced to be subsonic as is shown in Fig. 7. Hence it is enough to discuss the case of $\Delta P > 0$. Let $\Delta(P_d)$ stand for the small pressure disturbance at a position which is slightly downstream from the position of ΔP . If $\Delta\theta < 0$, stream lines, which are slightly on the projectile side of the stream line which passes through the position of ΔP , converge. Therefore, $\Delta(P_d) > 0$ if $\Delta\theta < 0$, that is, $\Delta(P_d) > 0$ if $\Delta P > 0$. When the flow between the positions of $\Delta(P_d)$ and ΔP is subsonic, weak pressure waves propagate from the position of $\Delta(P_d)$ to the position of ΔP . Consequently, the

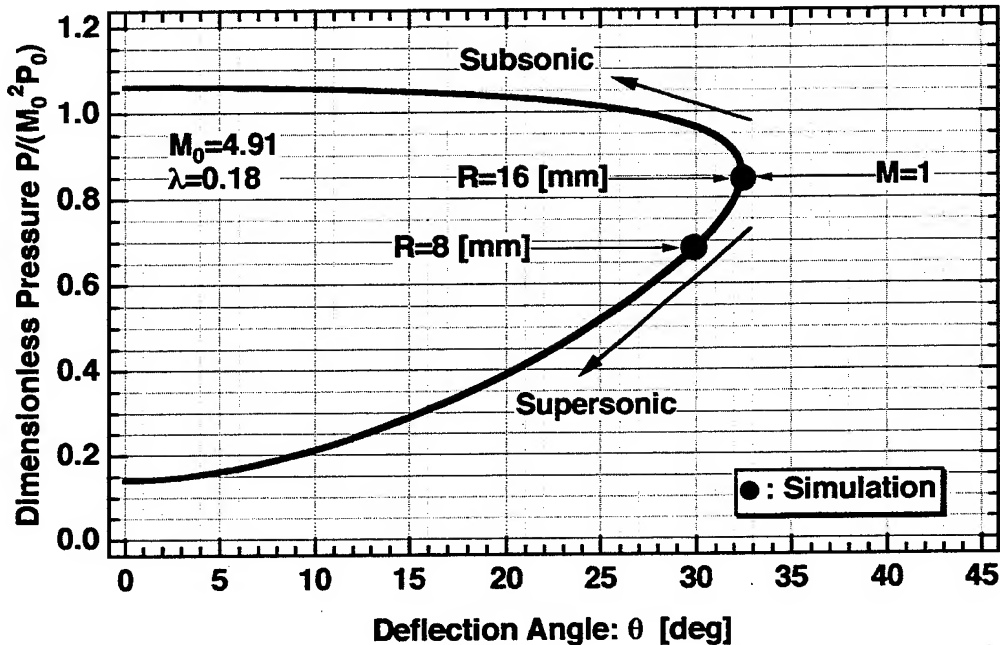


Fig. 7 P (pressure)- θ (deflection angle) detonation polar.

pressure disturbance ΔP is forced to become large. Namely, the pressure disturbance ΔP grows if the initial value of ΔP is large enough to force the flow to be subsonic.

For further investigation of the unstable combustion, we carried out calculations for the nose radius of $R=16$ [mm] and the inflow Mach numbers of $M_0=6.14, 5.52, 5.22, 5.07$, and 4.99 . When $M_0=6.14-5.07$, the entirely-coupled (stable) combustions were obtained. About the case of $M_0=4.99$, the entirely coupled combustion was stable when the oblique detonation wave was incident on the left boundary, although unstable when the oblique detonation wave was incident on the upper boundary. This is an evidence of that the observed unsteadiness is not intrinsic but due to disturbance growth of the oblique detonation wave.

ANALYSIS OF THE IGNITION CONDITION WITH D - κ RELATION

As shown in Fig. 2, a minimum nose radius for generation of the entirely-coupled combustions exists. In other words, an oblique detonation wave ignites when the nose radius is larger than the minimum nose radius. Figures 8 and 9 show developments of the flowfields for the cases of $R=8$ and 4 [mm], respectively, where the inflow Mach number was $M_0=4.91$ in both cases. Figures 8 and 9 correspond to the entirely-coupled (stable) and partially-coupled combustions, respectively. As shown in Figs. 8 and 9, the development of the flowfield before the numerical convergence looks like that of an expanding detonation wave from the projectile nose.

Recently, Yao and Stewart⁷ derived an explicit relation between the detonation-wave velocity, D , and the detonation-wave curvature, κ . When the derivation, they assumed that the detonation wave was quasi-one-dimensional and quasi-stationary. The D - κ relation derived by Yao and Stewart is the following.

$$\kappa = \frac{1}{\ell} \frac{\exp\left[b\theta\left(\frac{D}{D_{C-J}} - 1\right)\right]}{d\theta} \left\{ 1 - \exp\left[a\theta\left(\frac{D}{D_{C-J}} - 1\right)\right] \right\},$$

where κ is the detonation-wave curvature, which should be defined as $1/R_c$ for cylindrical expansion and as $2/R_c$ for spherical expansion in terms of the curvature radius R_c , D is the detonation-wave velocity,

$$a = \frac{(1+\delta)(\gamma-1)(\gamma+1)^2}{(\gamma+\delta)(2\gamma-\gamma\delta+\delta)^2}, \quad b = \frac{(\gamma-1)(\gamma+1)^3(3\gamma-1+3\delta-\gamma\delta)}{(\gamma+\delta)(\gamma-1+2\delta)^2(2\gamma-\gamma\delta+\delta)^2},$$

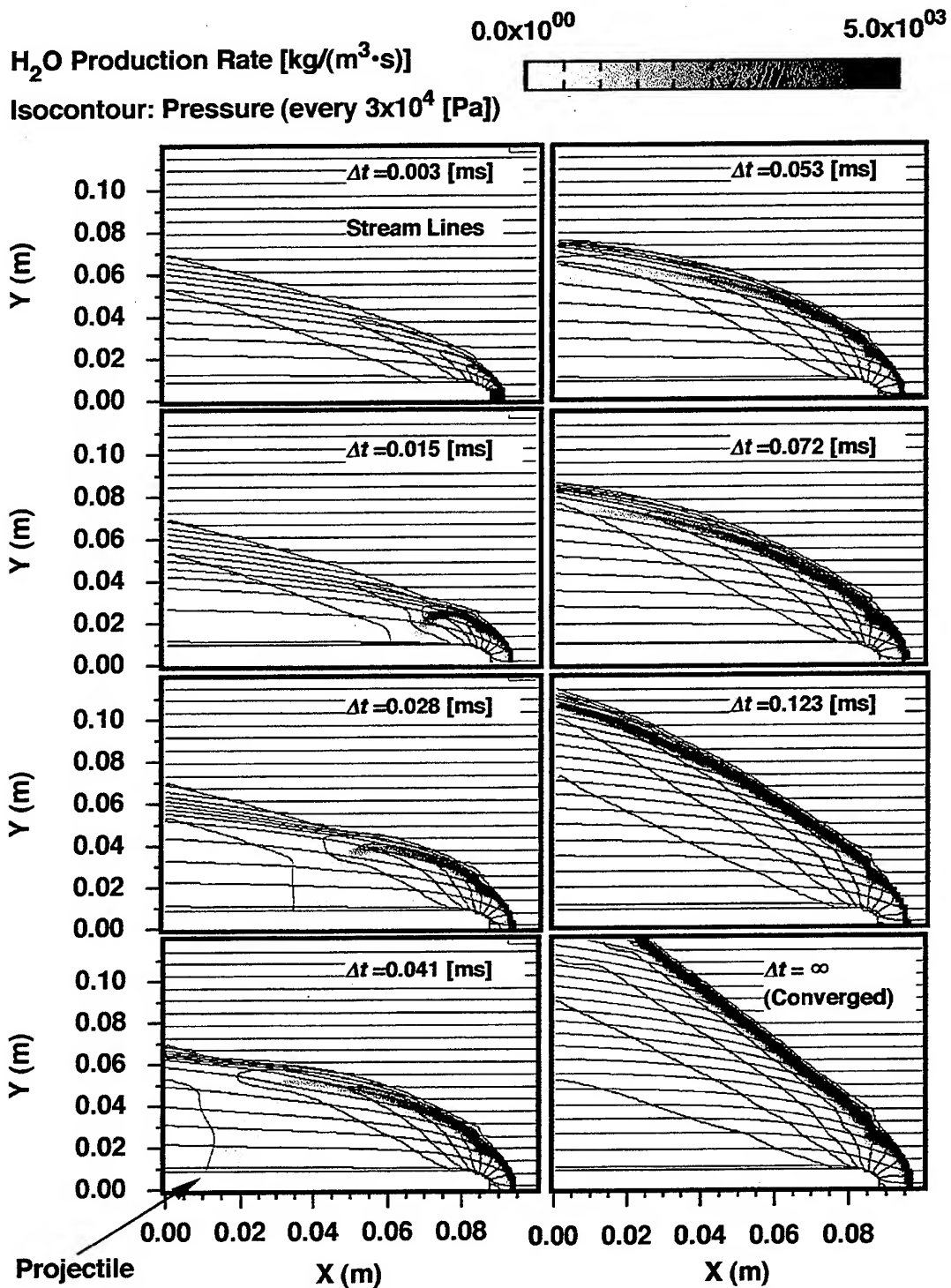


Fig. 8 Development of the flowfield for the entirely-coupled (stable) case; $R=8$ [mm] and $U_0=2000$ [m/s] ($M_0=4.91$). Chemical reaction was turned on at $\Delta t=0$. Before $\Delta t=0$, the flow was inert and numerically converged.

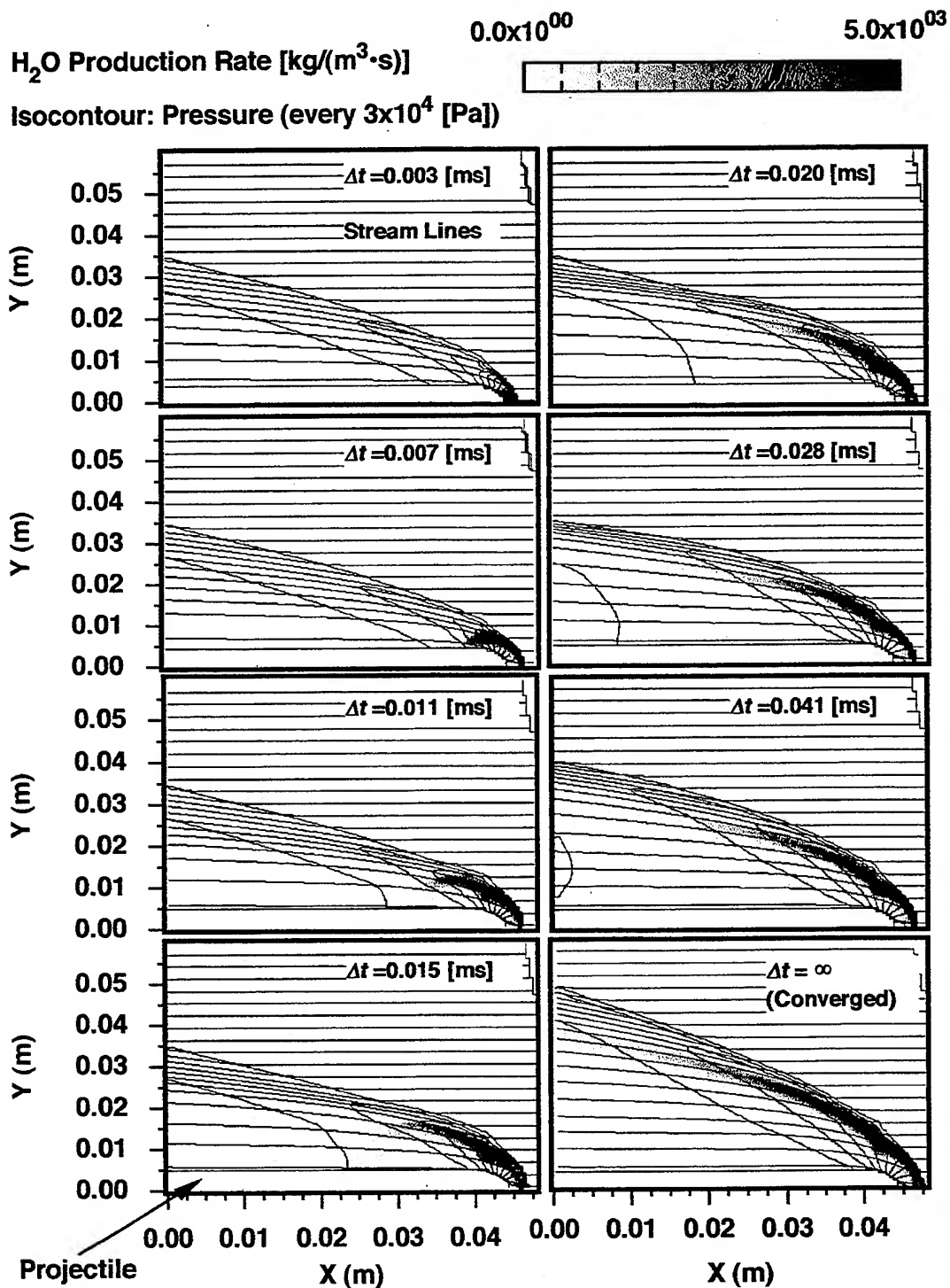


Fig. 9 Development of the flowfield for the partially-coupled case; $R=4$ [mm] and $U_0=2000$ [m/s] ($M_0=4.91$). Chemical reaction was turned on at $\Delta t=0$. Before $\Delta t=0$, the flow was inert and numerically converged.

$$d = \frac{4(\gamma - 1)(\gamma - 1 + 2\delta)^2(2\gamma - \gamma\delta + \delta)}{(1 - \delta)(\gamma + 1)^2(3\gamma - \gamma^2 - 3\gamma\delta + \delta)}, \quad \delta = \frac{\gamma P_0 / \rho_0}{D_{C-J}^2}, \quad \theta = \frac{\gamma E}{D_{C-J}^2},$$

$$\ell = \frac{D_{C-J}}{k\theta} \exp\left(\frac{\theta}{C_s^2}\right), \quad C_s^2 = \frac{(\gamma - 1 + 2\delta)(2\gamma - \gamma\delta + \delta)}{(\gamma + 1)^2},$$

ℓ is the scale length of the induction zone, γ is the specific heat ratio, D_{C-J} is the C-J detonation velocity, P_0 and ρ_0 are respectively the initial pressure and mass density, and k and E are respectively the collision-frequency factor and the activation energy of the Arrhenius equation.

For the calculation of the D - κ relation, we use that $\gamma=1.4$ and $D_{C-J}=1980$ [m/s] which have already been stated. We assume that P_0 and ρ_0 are the same as the inflow conditions shown in Fig. 1. About k and E , it is important that these constants well express the induction zone, because Yao and Stewart derived the above formula by analyzing the induction zone. We use that $k=1.88 \times 10^8$ [s⁻¹] and $E=3.90 \times 10^6$ [J/kg]. These constants were determined by using the constants which were obtained for the molar ratio of H₂:O₂:Diluent=2:1:7 by Fujiwara and Reddy⁸ to express well the induction reaction of the Korobeinikov's two-step reaction model,⁹ and using the induction-time conversion formula between different dilutions obtained by Oran and Boris.¹⁰ The calculated D - κ relation for cylindrical expanding detonation waves is shown in Fig. 10.

As shown in Fig. 10, the maximum curvature κ_{\max} for quasi-stationary solutions exists. That is, there is no quasi-stationary solution when the curvature radius R_c is smaller than the minimum curvature radius $(R_c)_{\min}=1/\kappa_{\max}$. This means that an expanding detonation wave possibly becomes extinguished when the initial radius of it is smaller than $(R_c)_{\min}$. By analogy between the flowfield development shown in Figs. 8 and 9 and a cylindrical expanding detonation wave, the initial radius of the corresponding expanding detonation wave should be of the order of the nose radius. The calculated minimum curvature radius is $(R_c)_{\min}=32$ [mm] as is shown in Fig. 10, and the minimum nose radius for the oblique-detonation ignition is between 4 and 8 [mm] as is shown in Fig. 2. These are in considerable agreement taking into account that the situations are not exactly the same. Therefore, we conclude that the essential physics included in the existence of the minimum nose radius for the oblique-detonation ignition is the decay, during the induction time, of a detonation wave expanding from the vicinity of the projectile nose.

In order to verify the above conclusion, we carried out calculations of the axisymmetric three-dimensional cases. When the geometry becomes three-dimensional, the decay effect of the expanding detonation wave should be emphasized. On the basis of the quasi-one-dimensional quasi-stationary expanding-detonation-wave theory, the minimum nose radius for the oblique-detonation ignition should become twice as large as that for the two-dimensional

case. The simulation results are summarized in Fig. 11 and the minimum radius became large as was expected. Indeed the minimum nose radius became more than twice as large as that for the two-dimensional case. However taking into consideration the difference of the situations, this qualitative agreement between the numerical results and the analytical expectation is meaningful.

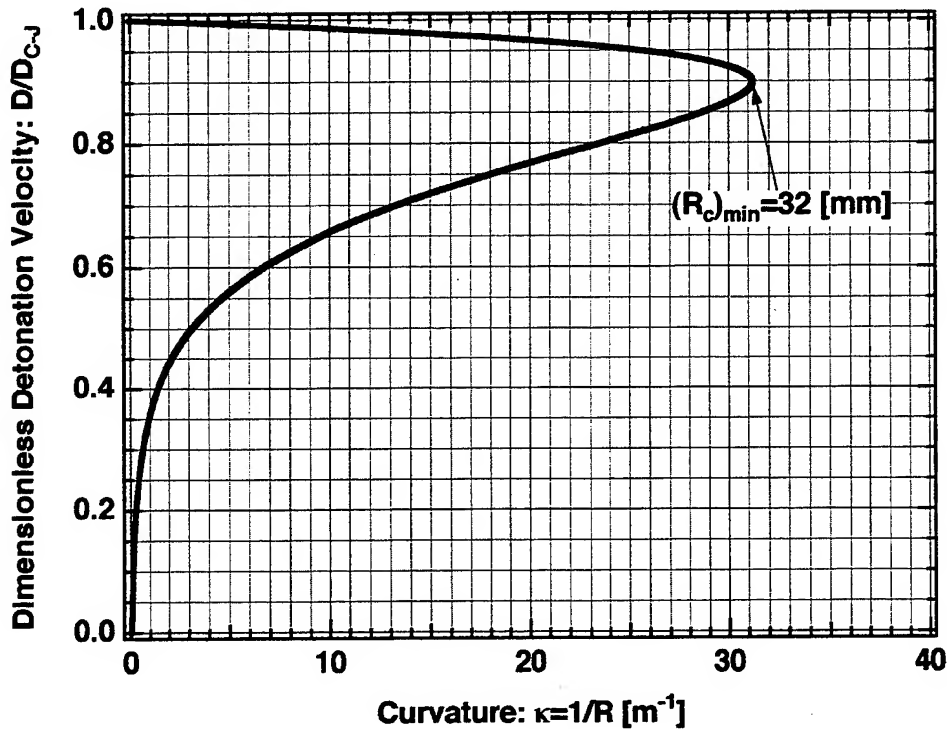


Fig. 10 $D(\text{velocity})-\kappa(\text{curvature})$ relation.
When the curvature radius R_c is $R_c < (R_c)_{\min}$, there is no quasi-stationary solution.

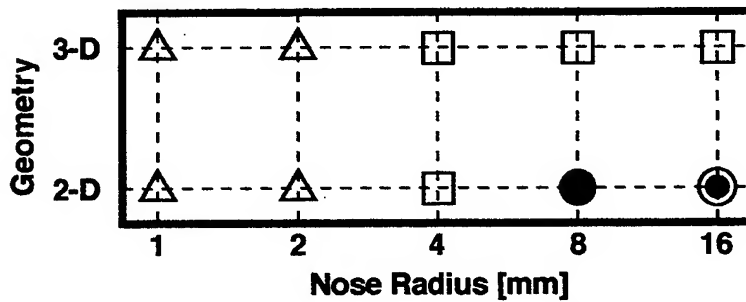


Fig. 11 Effect of the geometry on the modes of combustion. The meanings of the symbols are that Δ : Decoupled, \square : Partially coupled, \bullet : Entirely coupled (Stable), \odot : Entirely coupled (Unstable). 3-D and 2-D stand for axisymmetric three-dimensional and Cartesian two-dimensional geometries, respectively.

CONCLUSION

We numerically investigated two-dimensional hypersonic shock-induced combustion waves using an elementary-reaction model. The stoichiometric hydrogen-air mixture impinged on blunt-nosed flat plates. As parameters, we varied the inflow Mach number ($M_0=4.91-9.82$) and the nose radius ($R=1-16$ [mm]). In this parameter region, four modes of combustion were observed. They were (1) stable combustion in the vicinity of the nose, which was decoupled with the bow shock wave, (2) stable combustion which was partially coupled with the bow shock wave only in the vicinity of the nose, (3) stable combustion which was entirely coupled with the bow shock wave, and (4) unstable combustion which was entirely coupled with the bow shock wave. The combustion modes (3) and (4) included straight-shape oblique detonation waves. It has been found that a minimum nose radius for the oblique-detonation ignition exists. By comparison of the numerical results with detonation polars, it has been shown that the combustion waves are significantly in non-equilibrium. And it has also been shown that the oblique detonation waves close to the border between the weak and strong ones are unstable against disturbances. The observed minimum nose radius for the oblique-detonation ignition is explainable with an analytical $D(\text{velocity})-\kappa(\text{curvature})$ relation of cylindrical expanding detonation waves. The interpretation of the minimum nose radius has been numerically supported by comparison between the two- and three-dimensional cases.

ACKNOWLEDGMENT

We would like to acknowledge valuable discussions with Prof. N. Yoshikawa and Mr. M. Hishida. All of the computations were carried out on a Fujitsu-VP2600 supercomputer of Nagoya University.

REFERENCES

1. Powers, J.M., "Oblique Detonations: Theory and Propulsion Applications," *Combustion in High-Speed Flows* (Kluwer Academic Publishers), 1994, pp. 345-371.
2. Hertzberg, A., Bruckner, A.P., and Bogdanoff, D.W., "Ram Accelerator: A New Chemical Method for Accelerating Projectiles to Ultrahigh Velocities," *AIAA Journal*, Vol. 26, 1988, pp. 195-203.
3. Matsuo, A., "Characteristics of the Standing Oblique Detonation Supported by a Two-Dimensional Blunted Wedge and an Axisymmetric Blunt Body," PhD dissertation, Nagoya University, Japan, 1993.
4. Lefebvre, M.H. and Fujiwara, T., "Robust Euler Codes for Hypersonic Reactive Flows," *Memoirs of the School of Engineering, Nagoya University*, Vol. 46, 1994, pp. 1-54.

5. Powers, J.M. and Stewart D.S., "Approximate Solutions for Oblique Detonations in the Hypersonic Limit," AIAA Journal, Vol. 30, 1992, pp. 726-736.
6. Powers, J.M. and Gonthier, K.A., "Reaction zone structure for strong, weak overdriven, and weak underdriven oblique detonations," Phys. Fluids A, Vol. 4, 1992, pp. 2082-2089.
7. Yao, J. and Stewart, D.S., "On the Normal Detonation Shock Velocity-Curvature Relationship for Materials with Large Activation Energy," Combust. Flame, Vol. 100, 1995, pp. 519-528.
8. Fujiwara, T. and Reddy, K.V., "Propagation Mechanism of Detonation -Three-Dimensional Phenomena," Memoirs of the Faculty of Engineering, Nagoya University, Vol. 41, 1989, pp. 93-111.
9. Korobeinikov, V.P., Levin, V.A., Markov, V.V., and Chernyi, G.G., "Propagation of Blast Waves in a Combustible Gas," Astronautica Acta, Vol. 17, 1972, pp. 529-537.
10. Oran, E.S. and Boris, J.P., "Weak and Strong Ignition. II. Sensitivity of the Hydrogen-Oxygen System," Combust. Flame, Vol. 48, 1982, pp. 149-161.

Ramac II
July 17-20, 1995

Modeling of Unstarts in Ram Accelerator

M.H. Lefebvre

Department of Chemistry
Polytechnique Institute - Royal Military Academy
1040 Brussels - Belgium

Ramac II
July 17-20, 1995

Abstract

The structure of the detonation wave around the throat of a ram-accelerator device is investigated numerically. The mixture studied is stoichiometric hydrogen-oxygen, diluted with nitrogen, at low initial pressure (0.1 bar). The projectile is a conical forebody connected to a conoid afterbody. The tube bore diameter is 4.0 cm.

The numerical simulation is based on the compressible Euler conservation equations. Neither mass diffusion nor viscosity effect have been taken into account. The code consists of a shock-capturing, upwind-TVD algorithm, solved explicitly to second order in time and space. The chemical source terms are solved implicitly and integrate a full set of chemical reaction rates.

The study focuses on flowfields which result in the unstart phenomenon, i.e. the phenomenon whereby a normal detonation is disgorged from the throat (shoulder of the projectile) and outruns the projectile. Unstarts have been observed experimentally. The exact reasons for failure by unstart are not clear yet and the experimental conditions to observe it are not readily predictable. The aim of the work is to investigate possible reasons causing the unstart.

Simulations are performed for various inflow velocities, ranging from 2000 to 3000 m/s. We calculate first the steady flowfield of a non reactive flow; then, turning the chemistry on, we analyse the combustion process occurring behind the shoulder. For certain inflow velocities, chemical reactions, stemming from a vortex behind the shoulder develop and expand. In a limited range of incoming Mach numbers, we do observe the unstart phenomenon: the chemical reaction does not stabilize behind the shoulder and passes through the throat. As a result, a very strong normal detonation outruns the projectile. Analysis of the flowfields indicates the importance of the projectile geometry near and behind the shoulder. Whether or not the chemical reaction is going to be disgorged upstream seems to be controlled by an expansion fan stemming from the shoulder.

In a second set of simulations, we thus investigate the influence of the geometry. We change the forecone angle and we insert a finite-length constant-diameter section between the forebody and the afterbody. Analysis of non reactive and reactive flowfields shows major influence of the geometry on the flow characteristics and on the combustion process. Modification to the projectile design causes or prevents unstart. Relatively minor changes in the shock structure trigger unstart. As a conclusion, canting or translation of the projectile might modify the shock structure near the shoulder to a sufficient extent and cause unstart.

Ramac II
July 17-20, 1995

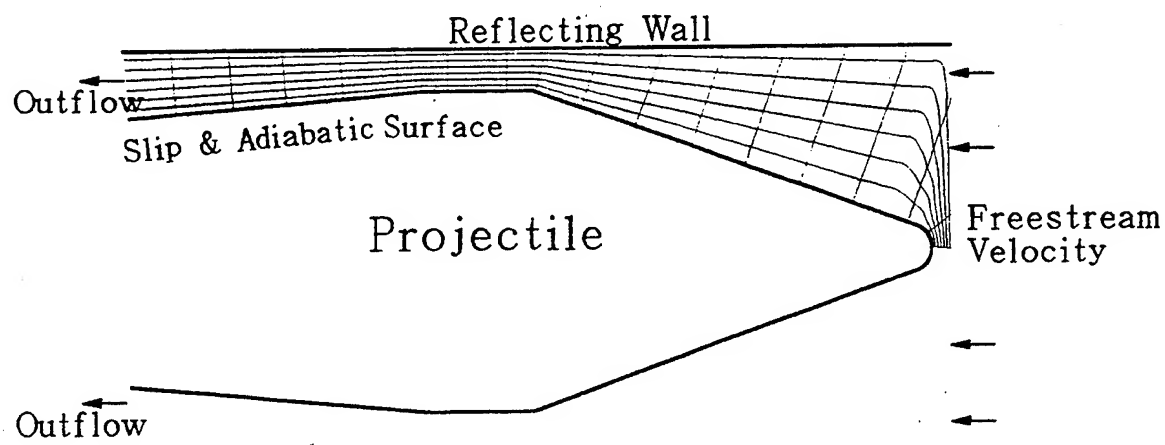
- **Physical Model**
- **Equations and Numerical Analysis**
- **Unstart event**
- **Nonreactive Simulations**
- **Reactive Simulations**

Inflow Velocity
Projectile Geometry

- **Comments**

Ramac II
July 17-20, 1995

Physical Model



Physical parameters

Mixture:

H₂ 2

O₂ 1

N₂ 3 - 3.76 - 5

Inflow velocity:

2000 to 3000 m/s

Initial pressure

0.1 bar

Initial temperature

298 K

Geometry

Tip radius:

1.5 - 2.0 - 2.5 mm

Cone half angle:

20 - 15 - 10 degrees

Aft angle:

5 - 7.5 - 10 degrees

Tube diameter:

4.0 cm

Projectile diameter:

3.2 cm

Isolator:

none - 1.0 cm

Total projectile length:

8.0 cm

Ramac II
July 17-20, 1995

Equations and Numerical Method

- **Fluid dynamics: Euler equations, Axisymmetric**

$$\frac{\partial Q}{\partial t} = -\frac{\partial E}{\partial \xi} - \frac{\partial F}{\partial \eta} - H + S$$

- **Chemistry**

Full set of chemical reaction rates; Arrhenius type;
C.J. Jachimowski's mechanism (19 reactions).

- **Ideal gases**
- **Numerical approach**

Conservation eqs.:

explicit, 2d order in time and space, upwind TVD scheme,
Roe's averaging method.

Chemistry term:

Implicit scheme.

Computational parameters:

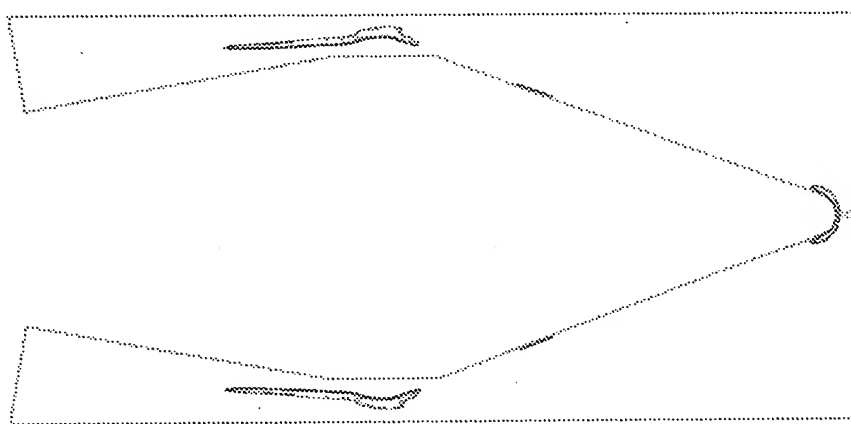
Stability: CFL = 0.5

Convergence: residual < exp(-05) or exp(-06)

- **Boundary conditions**

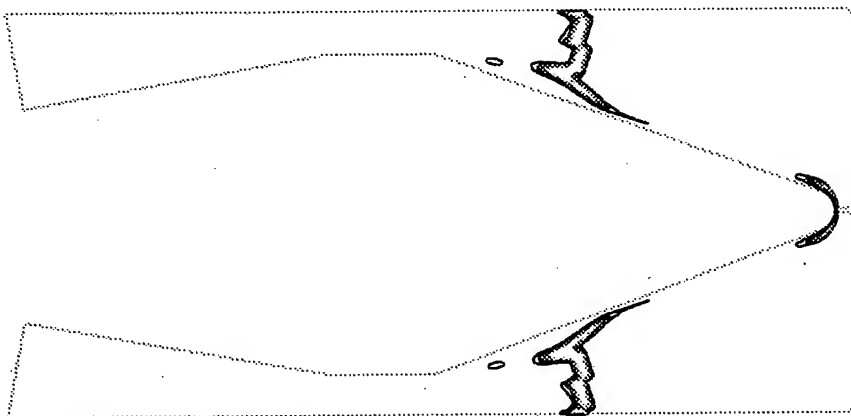
Ramac II
July 17-20, 1995

LOCATION OF REACTION ZONE



NO UNSTART

← 2200 m/s



UNSTART

← 2500 m/s

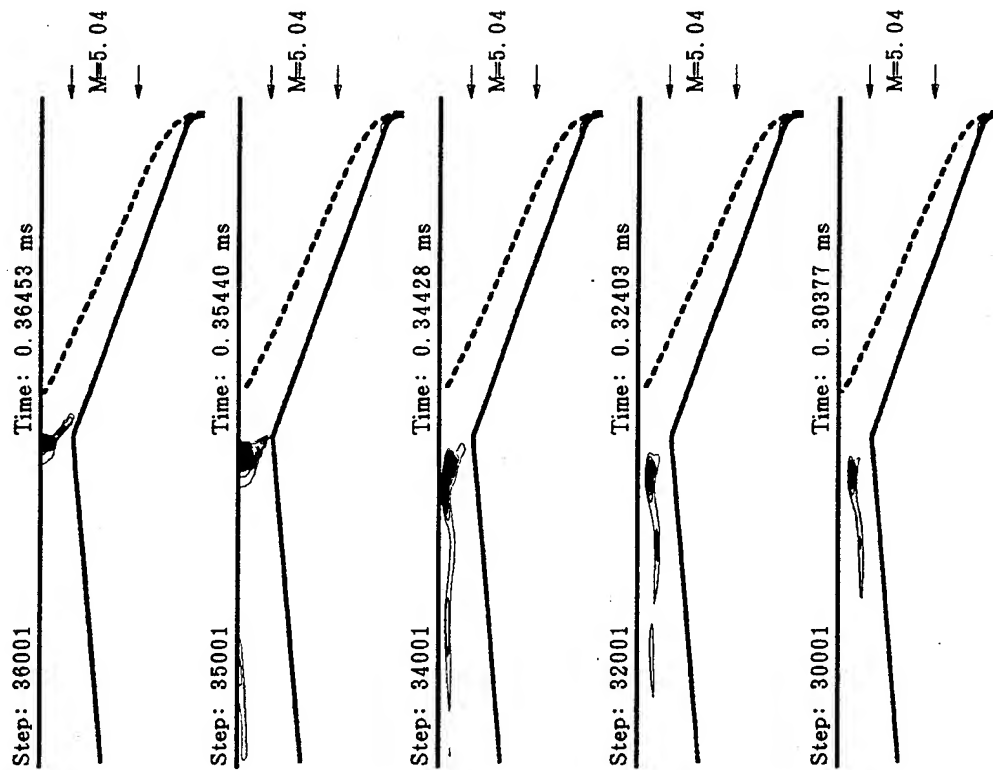
$P_o = 0.1 \text{ bar}$

$T_o = 298 \text{ K}$

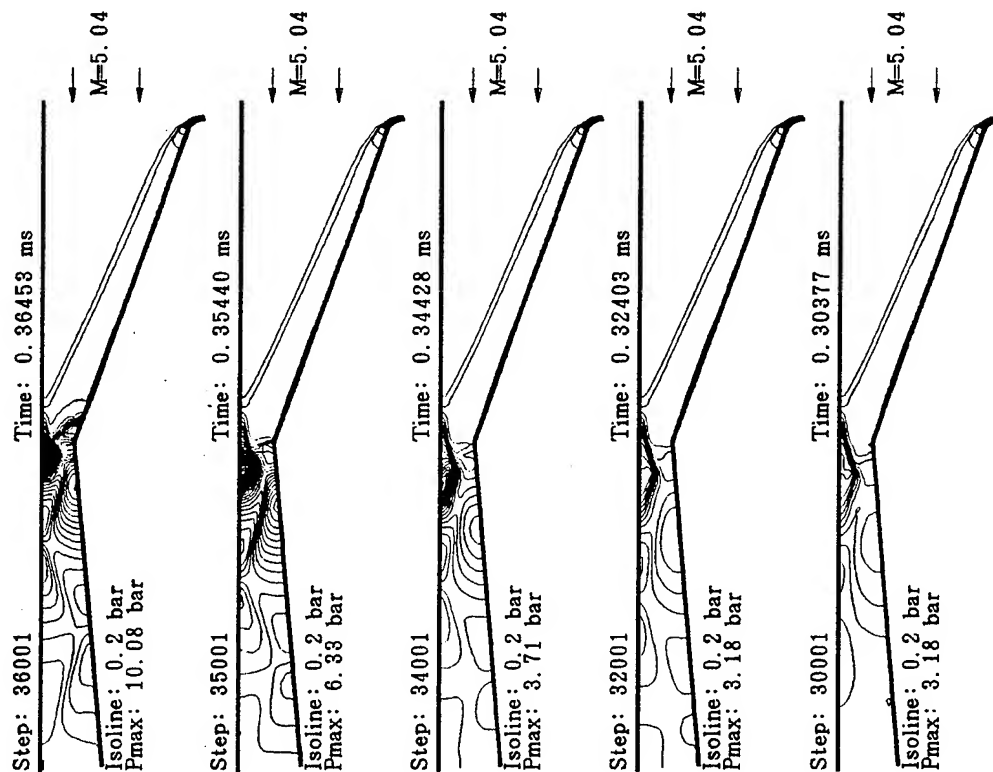
$\text{H}_2/\text{O}_2/\text{N}_2 = 2/1/3$

Ramac II
July 17-20, 1995

H2O PRODUCTION RATE



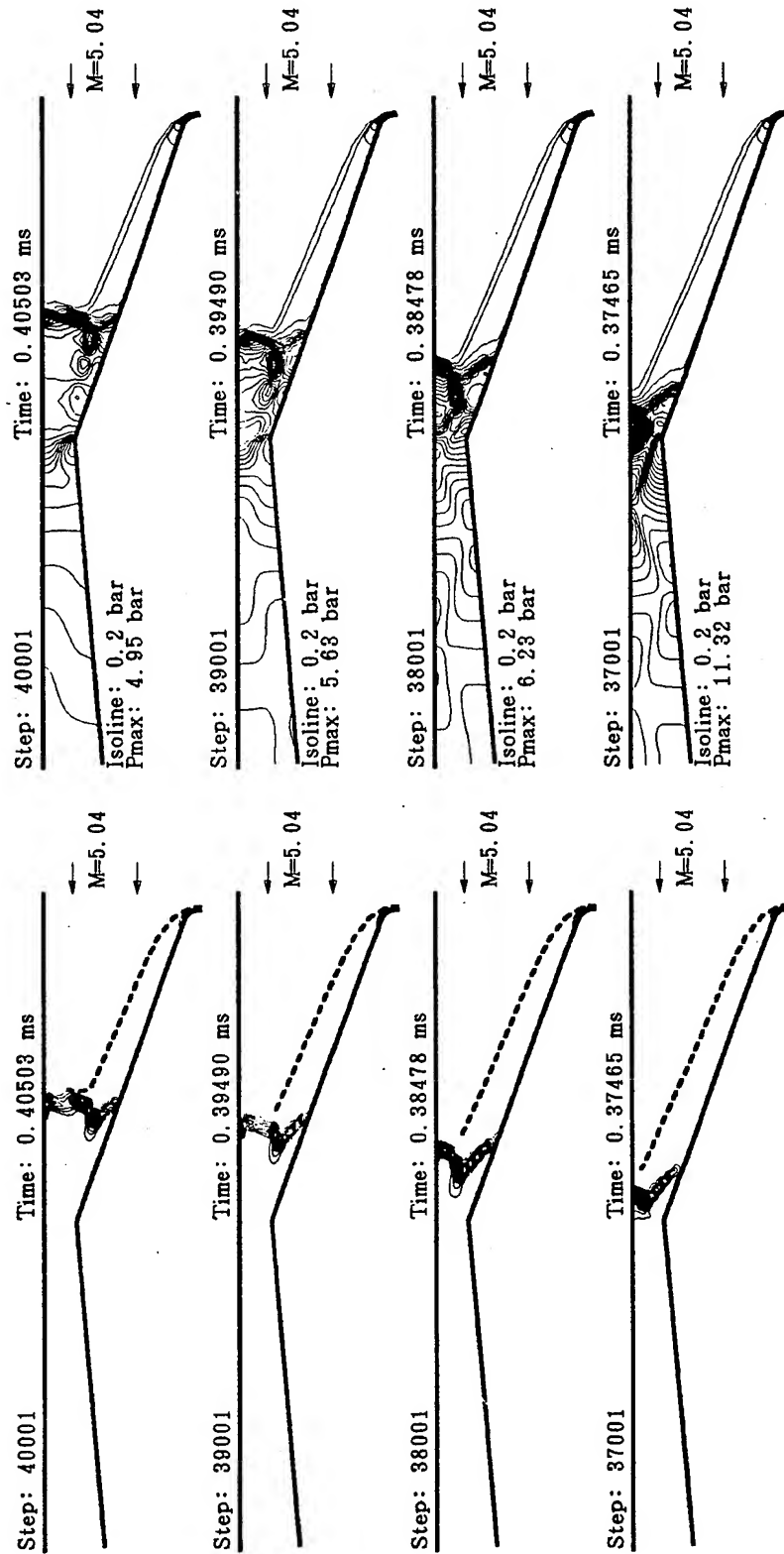
PRESSURE



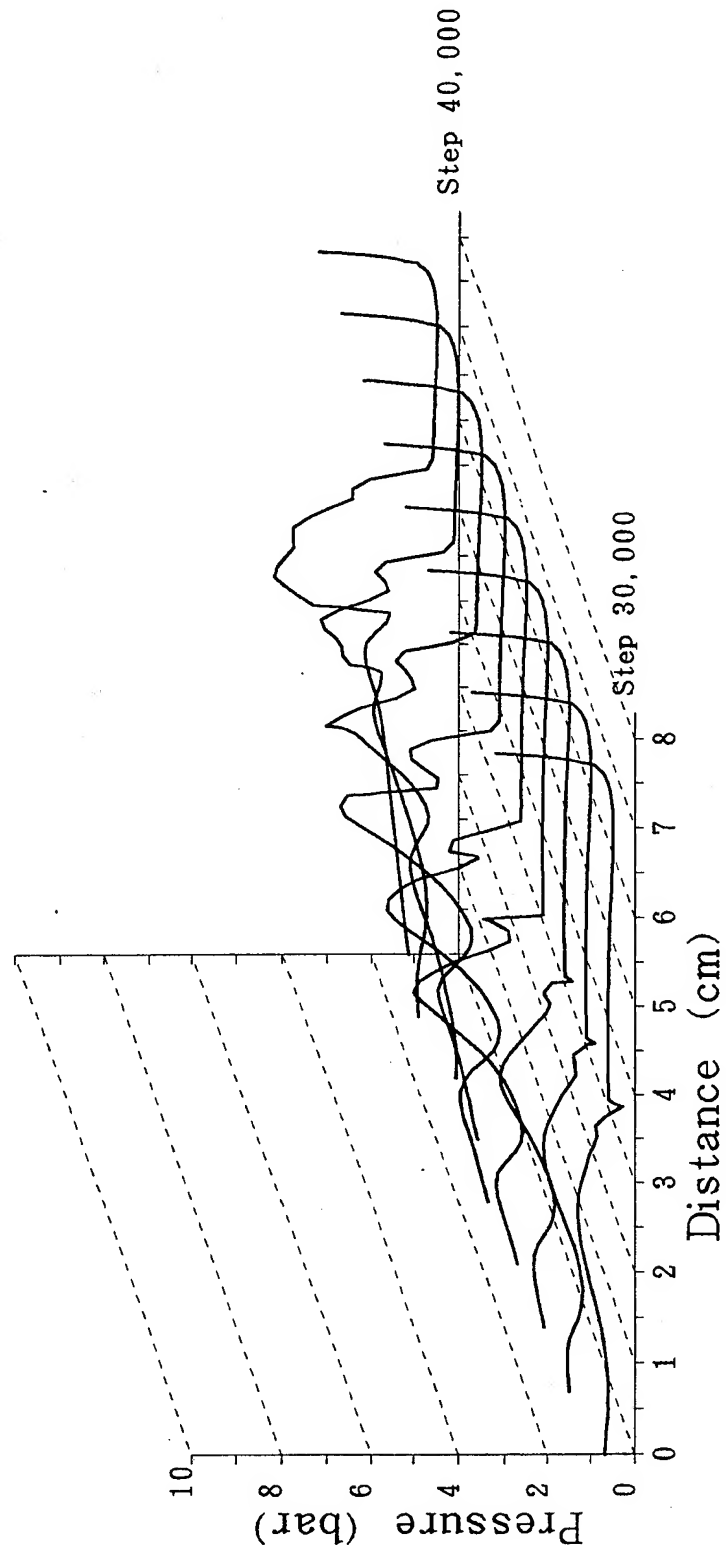
Ramac II
July 17-20, 1995

PRESSURE

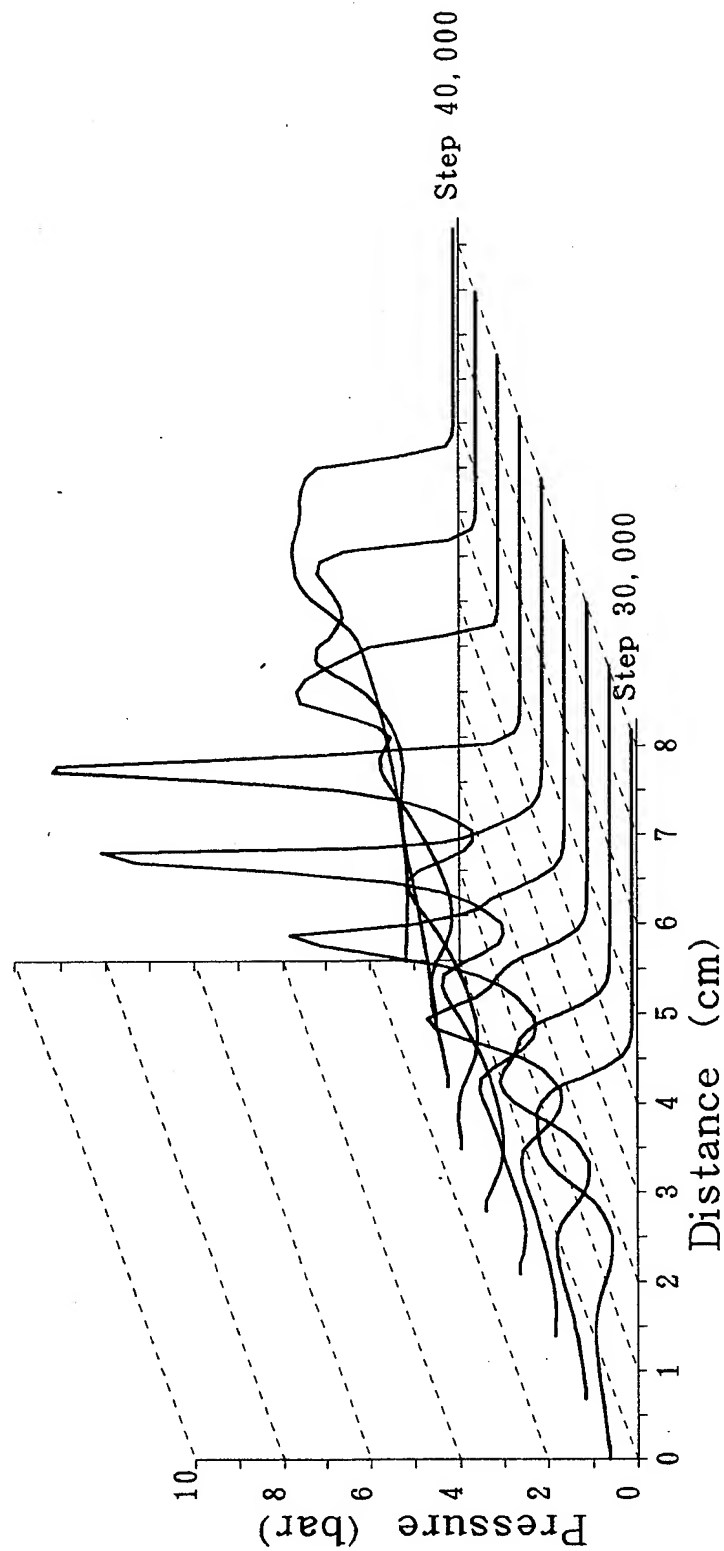
H2O PRODUCTION RATE



Pressure on Projectile – Unstart



Pressure on the Wall - Unstart



Ramac II
July 17-20, 1995

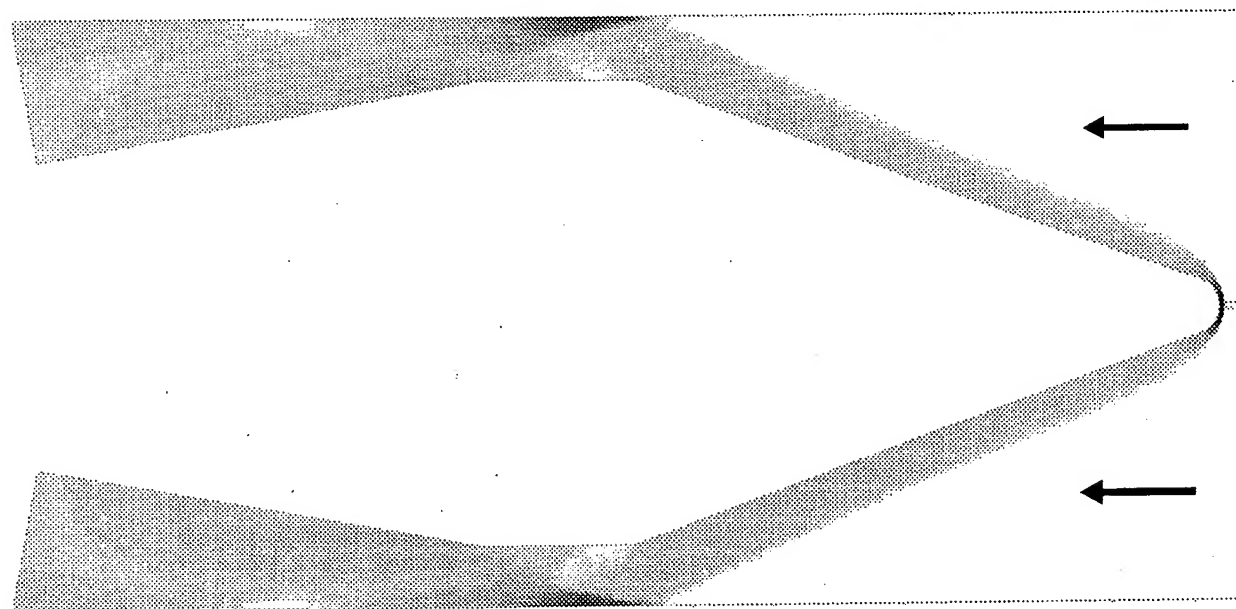
NON REACTIVE FLOW (Pressure field)

$P_o = 0.1 \text{ bar}$

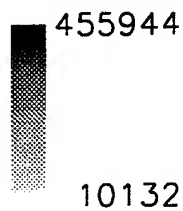
$T_o = 298 \text{ K}$

$\text{H}_2/\text{O}_2/\text{N}_2 = 2/1/3$

Inflow vel. = 2500 m/s



$P \text{ (Pa)}$



Ramac II
July 17-20, 1995

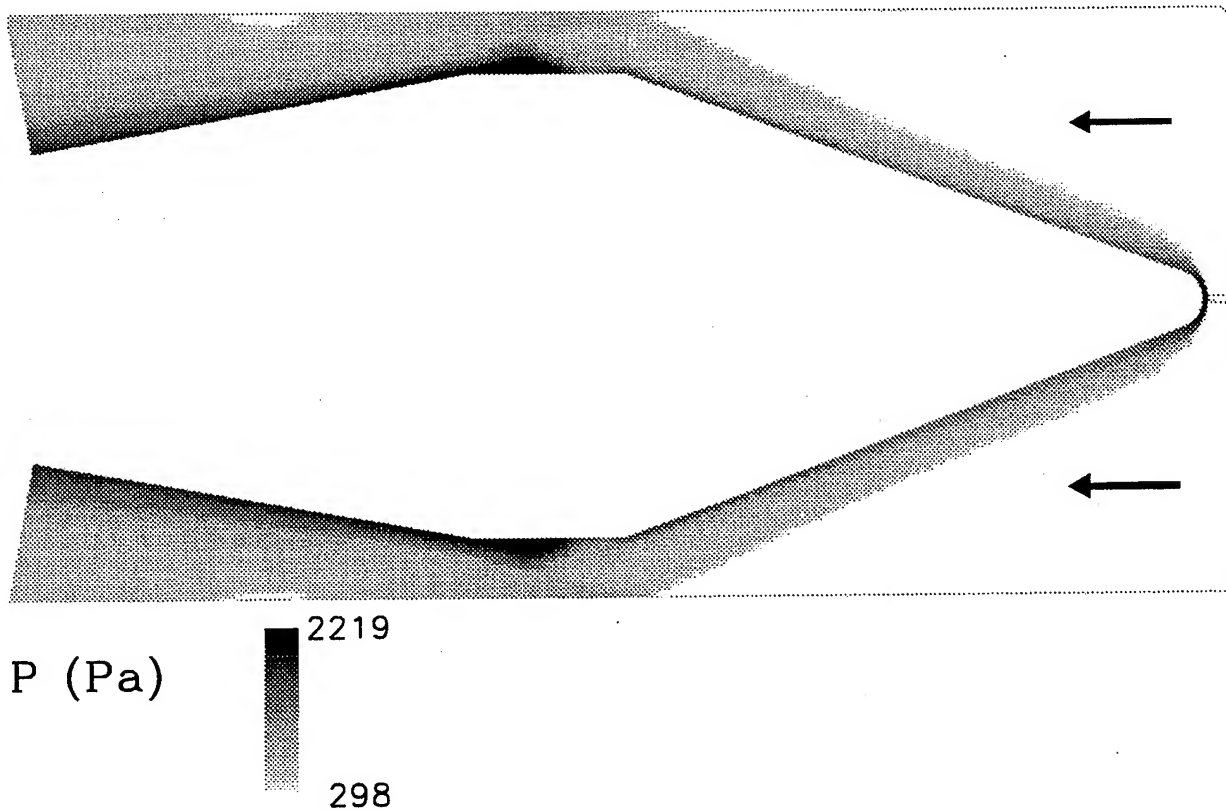
NON REACTIVE FLOW (Pressure field)

$P_o = 0.1 \text{ bar}$

$T_o = 298 \text{ K}$

$\text{H}_2/\text{O}_2/\text{N}_2 = 2/1/3$

Inflow vel. = 2500 m/s



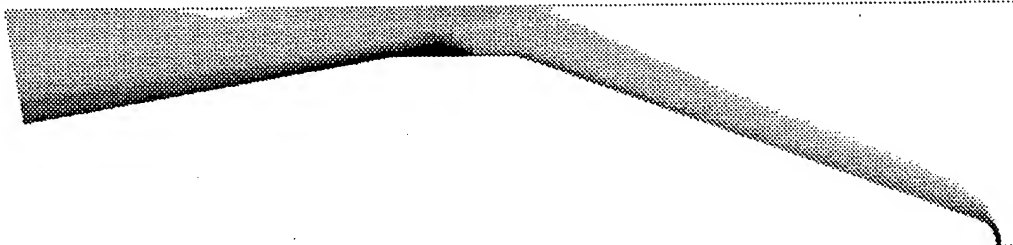
Ramac II
July 17-20, 1995

NON REACTIVE FLOW

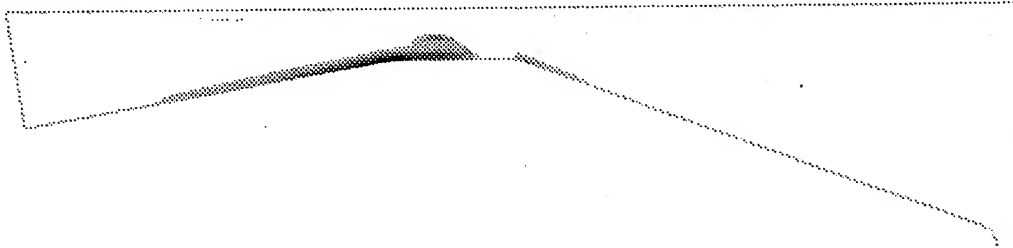
PRESSURE



TEMPERATURE



VORTICITY



$P_o = 0.1 \text{ bar}$

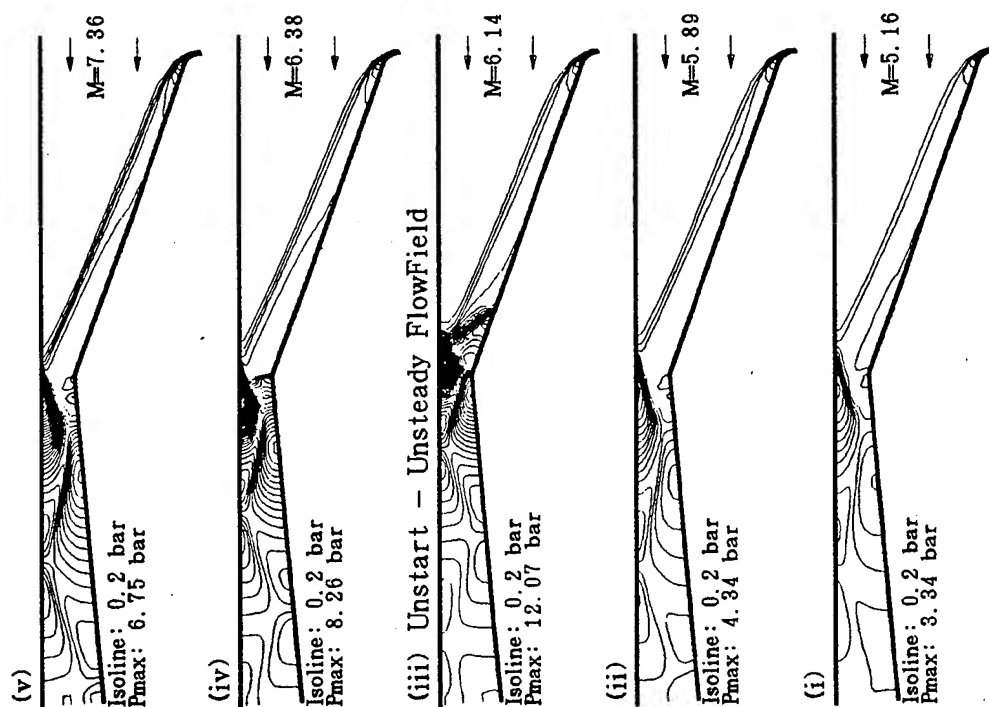
$T_o = 298 \text{ K}$

Inflow vel. = 2500 m/s

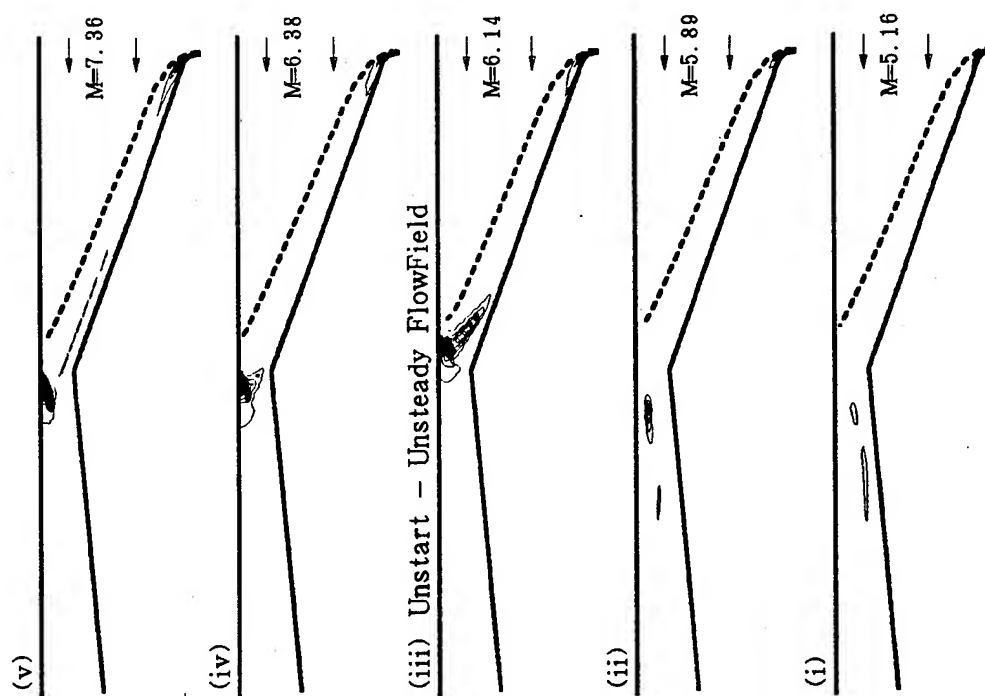
Cone angle = 20 deg.

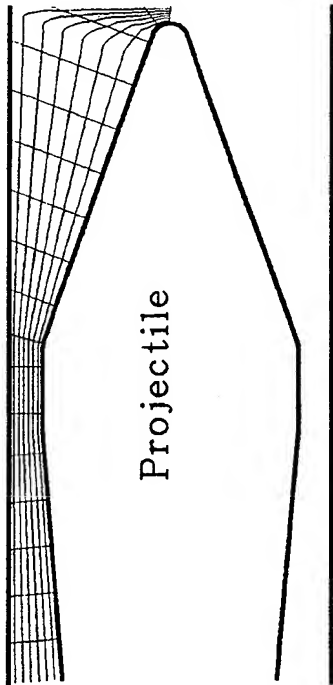
Ramac II
July 17-20, 1995

PRESSURE



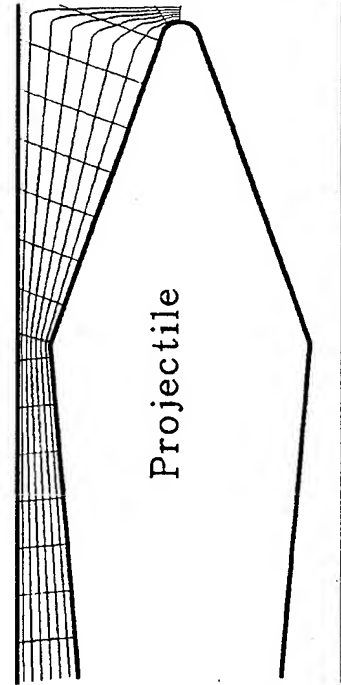
H2O PRODUCTION RATE





$M = 5.89$
Aft Angle: -5 deg.
Cyl. Portion: 1.06 cm

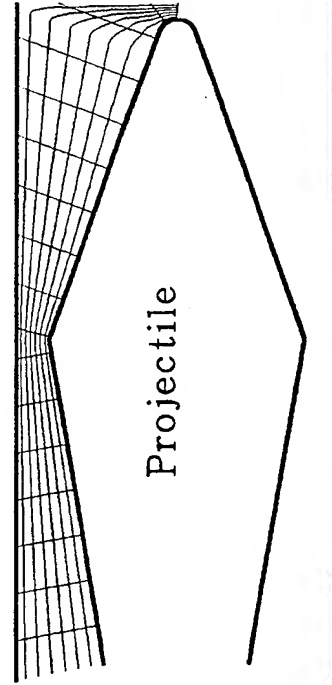
↑ ? Trigger Unstart ?



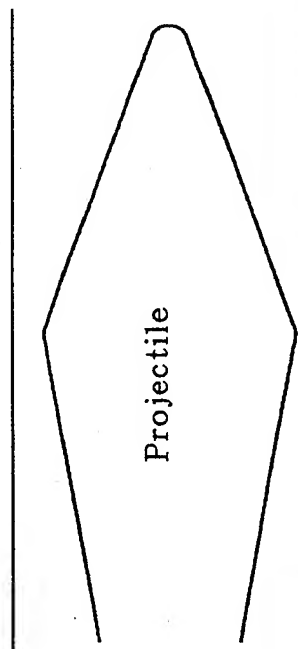
NoUnstart
 $M = 5.89$
Aft Angle: -5 deg.

$M = 6.14$
Aft Angle: -5 deg.
Unstart

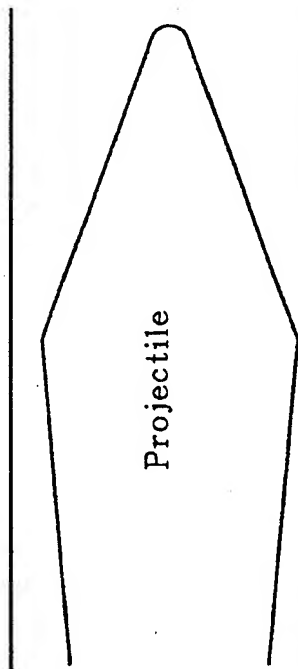
↓ ? Prevent Unstart ?



$M = 6.14$
Aft Angle: -10 deg.

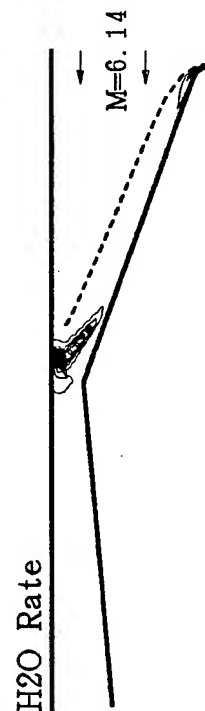
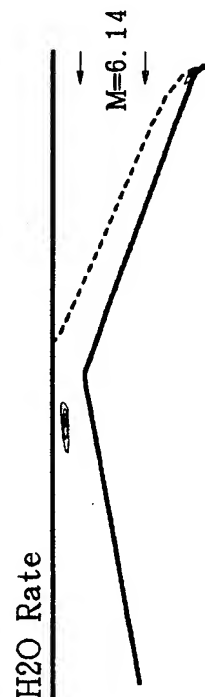
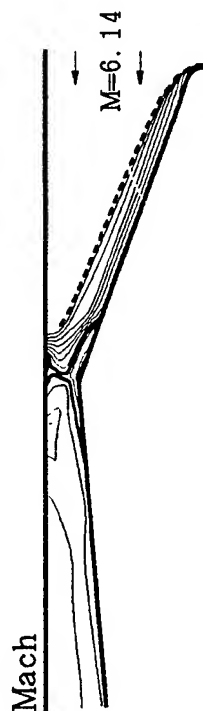
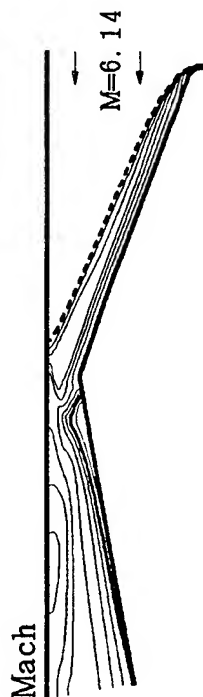
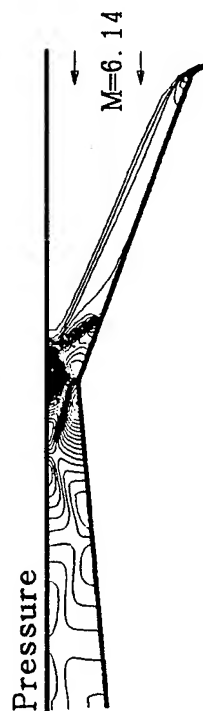
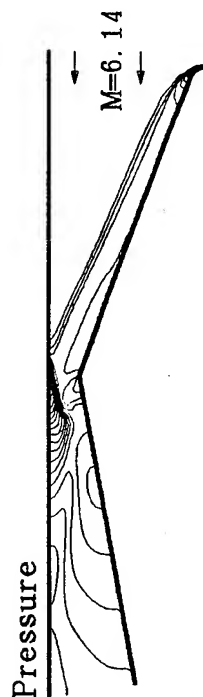


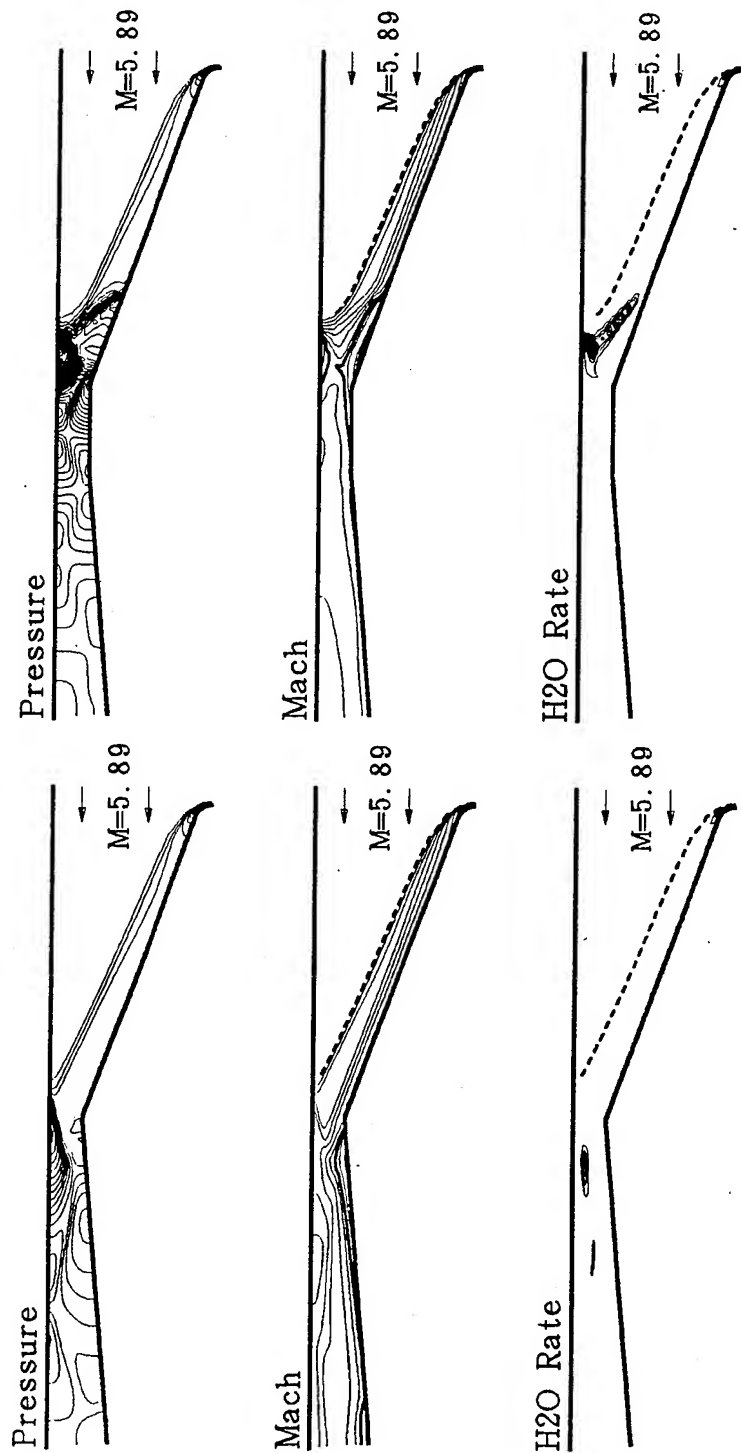
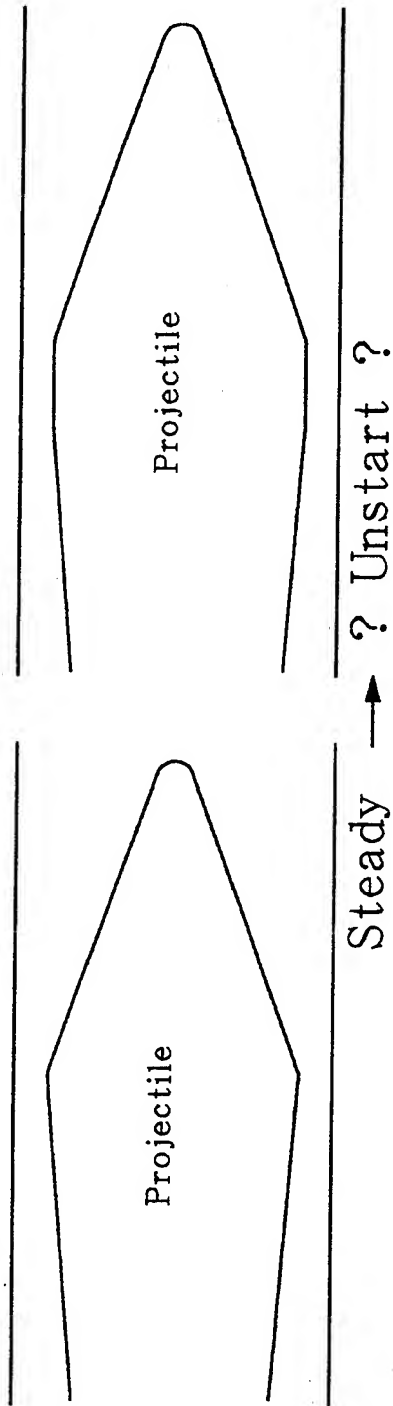
Projectile



Projectile

Unstart → ? Steady ?





Ramac II
July 17-20, 1995

Discussion

- **No chemical reaction along the streamlines.**
- **Chemical reaction stems from a vortex zone behind the shoulder.**
- **Scanning freestream velocities:**
 - Slight heat release behind the reflected shocks.**
 - Stabilized reaction close to the shoulder.**
 - Outrunning detonation.**
 - Oblique detonation induced by the tip.**
- **Isolator causes unstart to occur sooner.**
- **Larger aft angle prevents unstart.**
- **Similar qualitative behavior for various tip radii and forebody angles.**

Ramac II
July 17-20, 1995

References

1. Lefebvre, M.H. and Fujiwara, T., *Trans. Japan Soc. Aero. Space Sciences*, (in press).
2. Wilson, G.J. and MacCormack, R.W., American Institute of Aeronautics and Astronautics, 1990, Paper AIAA-90-2307.
3. Jachimowski, C.J., NASA-TP-2791, 1988.
4. Lefebvre, M.H. and Fujiwara, T., *Memoirs of the School of Engineering, Nagoya University*, 46:2, 1994.
5. Yee, H.C., NASA-TM-89464, 1987.
6. Yee, H.C. and Shinn, J.L., American Institute of Aeronautics and Astronautics, 1987, Paper AIAA-87-1116.
7. Lefebvre, M.H., Oran, E.S., Kailasanath, K., and Van Tiggelen, P.J., in *Prog. Aeronaut. Astronaut.*, 153, pp. 64-73 (1993).
8. Oran, E.S., Young, T.R., and Boris, J.P., *Combust. Flame*, 48:135 (1982).
9. Lefebvre, M.H. and Fujiwara, T., Nineteenth International Symposium on Space Technology and Science, Yokohama, 1994, pp. 371-376.

Session 7

HEAT TRANSFER

BOUNDARY LAYER MODEL FOR CALCULATING THE HEAT TRANSFER INTO A RAM PROJECTILE FIRED IN A RAM ACCELERATOR

F. Seiler, G. Mathieu

French-German Research Institute of Saint-Louis (ISL)
F-68301 Saint-Louis, France

ABSTRACT

In a ram accelerator a sharp-nosed-body flies at supersonic velocity through a tube initially filled with a highly compressed combustible gas mixture. By shock compression, i.e., bow wave and its reflections at the tube wall, the gas mixture is heated progressively so that it becomes ignited in subdetonative combustion mode at the body's back and in superdetonative mode in the slit between the projectile surface and the tube wall giving a forward thrust to the ram-projectile. Due to the transfer of heat from gas to projectile, the latter's surface temperature increases on the one hand in the nose region (no ignition desired) and on the other hand at the body contour with ignition in superdetonative combustion mode. This temperature rise can lead to melting processes at the nose and the body region. Then ablation of surface material begins which is naturally undesirable not only at the sharp nose but also at the fins and the body of the ram projectile, especially when combustion is localized at the body of the projectile in superdetonative mode. The control of the heating at the nose and the body is necessary for successful ram accelerator operation, therefore a prediction of the heat flux becomes needful. For this reason a **boundary layer and ablation model** has been developed by which the heating of the projectile and its ablation at nose, fins and body can be estimated for an optimal choice of projectile material at a desired velocity range.

INTRODUCTION

For vehicle acceleration to super speeds, several possibilities are known to this date, e.g., electromagnetic acceleration and light gas gun. In the last years a new type of mass accelerator, called ram accelerator, was built and successfully tested by HERTZBERG et al. [1]. Following their publications, the ram accelerator can be used as an in-tube mass driver for velocities higher than 10 km/s with the gasdynamic principles well known from Ramjet- and Scramjet-engines. Fig. 1, e.g., shows the superdetonative combustion mode for ram accelerator operation in supersonic flow.

Owing to ISL's need for a hypersonic mass accelerator facility, the decision was taken to build two ram accelerators: a 30-mm-tube, called RAMAC 30 and a 90-mm-one, RAMAC 90 [12]. As described by HERTZBERG et al. [1] the ram-tube is filled with a high-pressured combustible gas mixture containing, e.g., methane, oxygen and some inert gases as diluent. By pre-acceleration a subcaliber test projectile is fired supersonically with 1 km/s up to 2 km/s into the ram-tube, closed initially by membranes. By further acceleration for example in the ISL 30-mm-caliber ram accelerator it is planned with a ram-tube length of 12 m and initial gas pressures of 20 bars up to 50

bars that projectiles of, e.g., 60 g - 200 g may be brought to about 3000 m/s. To date the RAMAC 30 has been tested in two versions: (a) the rail tube concept [2] with no-fin and no-sabot projectiles and (b) the smooth bore concept [3] with fin stabilized projectiles. With pre-acceleration by a powder gun to about 1800 m/s - 1900 m/s the projectiles are fired at moment in the RAMAC 30 directly into the superdetonative combustion mode (scram accelerator). A schematic set-up of the RAMAC 30 accelerator device is shown in Fig. 2a. The main facility parts are: Powder gun, two dump tanks, ram-tube (see photography in Fig. 2b) and decelerator tube.

At these high gas pressures and high mass velocities, surface heating during the in-tube flight of the projectile will be excessively high. Since no large surface deformation by ablation can be tolerated, the surface temperature during in-bore movement has to be kept lower than the melting temperature so that melting processes at the projectile surface can be suppressed (or limited) in order to avoid, e.g., preignition of the combustible gas mixture at the nose followed by a ram unstart. Furthermore chemical reactions between projectile material and the oxygen as well as the diluent may occur, especially in case the surface is heated and melted by a high heat flux into the projectile surface. But chemical reactions, i.e., burning of the projectile material, are not treated herein and are not included in the ablation model.

MODELING OF HEATING AND ABLATION

Heating model

Assumptions

For calculating the temperature distribution at the surface and inside of the ram-projectile as shown in Fig. 3a, b, a flow model was developed in the reference frame of the projectile (a) for the rail tube guided smooth cylindrical projectile [2] and (b) the fin stabilized projectile [3]. It is assumed that compressible and turbulent boundary layers develop at the following projectile surface regions:

- (I) at the cylindrical nose cone,
- (II) in the combustion zone between projectile and tube wall,
- (II_f) at the guiding fins in case of the smooth bore [3], and
- (III) in the expansion zone.

The flow between conical bow wave and projectile in region (I) is assumed parallel to its surface as well as in regions (II), (II_f) and (III). It is also assumed that at these surfaces a compressible and turbulent boundary layer develops similar to that at a flat plate that will be simulated as two-dimensional in the flow model. This assumption is justified as long as the boundary layer thickness at the surface is much smaller than the radius of the projectile. Although this assumption fails near the cone's tip, this small error is tolerated for obtaining an analytical solution for the description of the whole ram projectile heating.

Solution of boundary layer equation

Beginning with Prandtl's boundary layer equations, the same differential equation was analytically found for regions (I, II, II_f, III) that satisfies the given boundary conditions. As an

analytical solution, for the prediction of surface and in-tube temperature distribution the heat flux \dot{q}_w along the coordinate x at the surface at $y = 0$ is given:

$$\dot{q}_w(x) = a_f \left(\frac{n+1}{n+3} \right)^{\frac{2}{n+3}} (B(n)\varphi)^{\frac{n+1}{n+3}} c_p (T_r - T_w) Pr^{-\frac{2}{3}} \rho_e \left(\frac{\delta^{**}}{\delta} \right)^{\frac{2}{n+3}} u_e^{\frac{n+1}{n+3}} \left(\frac{v_e}{x} \right)^{\frac{2}{n+3}} \quad (1)$$

The parameter u_e in equation (1) is the flow velocity parallel to the surface in regions (I), (II), (II_f) and (III), outside of the boundary layer. The other quantities used, as n , $B(n)$, φ , δ , δ^{**} , T_r , T_w , c_p , ρ_e and v_e are explained by HEISER et al. [4].

Solution of heat conduction equation

For taking into account the heat flux \dot{q}_w to the sharp-cone geometry of the ram-projectile-nose in zone (I) the calculated flat-plate heat flux of equation (1) is transformed using the analogy factor a_f well known for this transformation. For the determination of the factor a_f the calculated heat flux \dot{q}_w of (1) is fitted to the experimental heat transfer results of CHIEN [5] on a 5 degree sharp-cone. The best agreement, see Fig. 4, is found with $a_f = 1.07$ using $n = 9$ for the exponent of the u -velocity profile normal to the surface inside the turbulent boundary layer with thickness δ . In zone (II), (II_f) and (III) the constant a_f is set equal to 1. The u -profile chosen is the following one:

$$\frac{u}{u_\infty} = \left(\frac{y}{\delta} \right)^{\frac{1}{n}} \quad (2)$$

Owing to small variations in the calculated heat flux $\dot{q}_w(x)$ tangentially along the x -coordinates at the surfaces, the heat conduction was considered one-dimensional in y -direction, i.e., depth. Therefore, the one-dimensional heat-conduction equation could be applied inside the wall region. Thus, an analytical solution can be found for the temperature distribution ΔT_w inside the ram-projectile material as a function of the heat flux $\dot{q}_w(x)$ at the surface at $y = 0$. The instationary, time-dependent acceleration process was taken into account by a time-step-procedure as shown in Fig. 5. The real acceleration cycle expected in our RAMAC 30 is approached by successive time intervals $\Delta t_1, \Delta t_2, \dots, \Delta t_n, \dots$ with constant flow quantities during these steps, but changing with ongoing time. In this procedure the heat flux $\dot{q}_w(x)$ becomes additionally a function of time: $\dot{q}_w(x, t)$. Thus, from OERTEL [6], the temperature distribution $T_w(x, y, t)$ is found in the regions (I), (II) and (III) for each time-step as follows:

$$\Delta T_w(x, y, t) = \frac{1}{\sqrt{\pi \rho_w c_w \lambda_w}} \int_0^t \frac{\dot{q}_w(x, \tau)}{\sqrt{t - \tau}} \exp\left(-\frac{\rho_w c_w y^2}{4 \lambda_w (t - \tau)}\right) d\tau \quad (3a)$$

By a summarizing procedure taking into account the temperature rise $\Delta T_{w,n}$ in each time-step n according to equation (3), the total wall temperature distribution is found:

$$\Delta T_{w, \text{total}} = \sum_n \Delta T_{w,n}(x, y, t) \quad (3b)$$

The equations (3a,b) are also applied for the fin heating (II_f) with the assumption that the fins are thick enough to avoid the heat from arriving at the middle of the fin's width during heating cycle.

Analytical ablation model

Assumptions

It is assumed that ablation occurs only by melting erosion with no evaporation. Melting erosion often takes place when hot gas flows with a high stagnation temperature are in contact with colder walls. This process is extensively treated by many authors, see ADAMS [7]. In this paper an analytical ablation model for the ablation of a ram-projectile is described, see SEILER [8] and SEILER and NAUMANN [9]. A similar theory using a numerical model was developed by NAUMANN [10]. In the analytical model herein it is assumed that the sharp-cone geometry (I), the body and fin contours (II, II_f) and the back contour (III) remain approximately unchanged by heating and ablation (= small amount of ablation). Therefore, the boundary layer formation is considered to be uninfluenced. Due to strong shear stress it is assumed that the melting is whipped away from the cone surface, as soon as it is produced by heat input when the wall temperature exceeds the melting temperature. This means that no liquid layer develops on the solid surface. Heat addition from melt to gas flow is not considered.

Ablation equations

Heating and melting ablation are decoupled during time interval Δt_n at each point x along the x -coordinate in each zone: (I), (II), (II_f) and (III). For $t < t_n$ the wall temperature $T_{w,n-1}(x, y, t < t_n)$ is lower than the melting temperature T_{melt} , see Fig. 6. For $t = t_n$ the wall temperature $T_{w,n}(x, y, t)$ exceeds the melting temperature T_{melt} by the heat input $\dot{q}_{w,n}(x, t)$ of equation (1). Now melting occurs in the layer Δy_j ($j = 1, \dots, m$) at time interval $\Delta t_n = t_{n+1} - t_n$ and the melting heat h_{melt} of the projectile material has to be taken into account. The total heat flux input $\dot{q}_{w,n}$ must be divided into one part $\dot{q}_{c,n}(x, t)$ for heat conduction and one part for heat of melting:

$$\dot{q}_{w,n}(x) \Delta t_n = \dot{q}_{c,n}(x) \Delta t_n + \rho h_{\text{melt}} \Delta y_j, \quad j = 1, \dots, m. \quad (4)$$

For obtaining the molten layer Δy_j equation (4) can be solved with equation (3) and the additional assumption

$$T_{w,n}(x, y = y_{n+1}) = T_{\text{melt}}. \quad (5)$$

At the end of time interval Δt_n the molten layer Δy_j is whipped away by the shearing forces exerted by the strong wall shear stress τ_w . The described processes of melting and shearing are continued during the whole ram acceleration cycle, as:

$$\begin{aligned} t < t_n: T_{w,n-1} &< T_m \\ t = t_n: T_{w,n} &> T_m & \xrightarrow{\Delta y_1 = y_{n+1} - y_n} & T_{w,n+1} = T_m, \\ t > t_n: T_{w,n+1} &> T_m & \xrightarrow{\Delta y_2 = y_{n+2} - y_{n+1}} & T_{w,n+2} = T_m, \\ & & & \xrightarrow{\Delta y_m = y_{n+m} - y_{n+m-1}} & T_{w,n+m} = T_m. \end{aligned} \quad (6)$$

Then, the total erosion e at position x is: $e(x) = \sum_{j=1}^m \Delta y_j(x)$, $j=1, \dots, m$. (7)

RESULTS CALCULATED WITH THE HEATING AND THE ABLATION MODEL

Nose cone (I)

Results for the heating of the ram projectile nose are given for the acceleration cycle of Fig. 5 expected for the operation of the ISL 30-mm-caliber ram accelerator RAMAC 30. The calculation are carried out for fin guided projectiles of aluminum and titanium accelerated in the smooth bore version [3]. The actual experimental results are shown in Fig. 7 obtained with stoichiometric hydrogen based gas mixtures: $2H_2 + O_2 + 5.7CO_2$ (shot no. 136, aluminum) and $2H_2 + O_2 + 6.3CO_2$ (shot no. 138, titanium). At the moment RAMAC 30 is operated with only one stage with a tube length of 6 m. The data of density ρ , specific heat c_p , heat conduction λ and melting temperature T_{melt} for the aluminum and titanium used are the following ones:

	ρ [Kg/m ³]	c_p [J/Kg K]	λ [J/m s K]	T_{melt} [K]
aluminum	2700	945	238	933
titanium	4540	522	16	1941

Initially in shots no. 136 and no. 138 the gas fill pressure was 20 bars. The projectile had a half cone angle of 16 degrees and a cone length of 35 mm, see Fig. 8. The constant diameter combustor region was 50 mm long and the divergent back part 25 mm. In these firings the initial velocity at the beginning of the ram-tube was $u_p = 1779$ m/s (shot no. 136) and $u_p = 1768$ m/s (shot no. 138).

Acceleration was achieved for both firings along the first 3 - 4 m inside of the ram-tube, see Fig. 7, for shot no. 136 to $u_{p,max} = 1866$ m/s and for no. 138 to $u_{p,max} = 1823$ m/s. Then the acceleration turns to deceleration: in case of aluminum (no. 136) the velocity drop is much stronger as for titanium (no. 138). In both firings the impact onto the steel plates arranged inside of a piston housing which is placed in the decelerator tube of Fig. 2 is weak. These weak impacts indicate that the projectiles have been damaged inside of the ram-tube with an extraordinary mass loss during the ram accelerator cycle.

An impression of the distribution of surface heat flux \dot{q}_w calculated with equation (1) along the x_I -coordinate at the cone surface is given in Fig. 9 for an aluminium cone (shot no. 136) and for a titanium one (shot no. 138). The heat flux develops during flight in the pre-accelerator up to $u_p < 1800$ m/s very small. Only in the ram accelerator flight the heat flux becomes important for the heating of the cone with $u_p \geq 1800$ m/s. Towards the tip of the cone the heat flux increases as expected for the boundary layer development.

The surface temperature T_w for $y = 0$ as determined with relations (3a,b) is shown in Fig. 10a for $u_p = 2000$ m/s and in Fig. 10b for $u_p = 3000$ m/s. In case of Fig. 10a the surface temperature does not reach neither with aluminum nor with titanium the melting temperatures. That means that in the experiments no. 136 and no. 138 with maximal projectile velocities of 1866 m/s, resp., 1823 m/s melting at the cone surface is not predicted. Looking at the x-ray photography in Fig. 11a the

nose cone, loosed from projectile by other reasons, is well shaped, i.e., no ablation occurs supporting the theoretical prediction. For $u_p = 3000$ m/s (Fig. 10b) surface melting is present for aluminum as well as for titanium.

The total erosion e predicted with the sum procedure (7) is given in Fig. 12 for $u_p = 3000$ m/s. With the use of a titanium nose the ablation by melting is much smaller than with aluminum. A titanium nose should be preferred in the velocity range of $u_p \geq 3000$ m/s.

Projectile body region (II)

The flow conditions in region (II) are determined by the combustion of the gas mixture. Therefore in zone (II) the gas conditions after combustion have to be used as core flow conditions for solving the boundary layer equations. These data are available from the one-dimensional model of SMEETS et al. [11] for describing the flow formation, inclusive combustion, around a ram projectile. That calculation was carried out beginning with the following starting conditions in front of the projectile: gas temperature $T = 293$ K, initial projectile velocity $u_p = 1800$ m/s and gas mixture $2H_2 + O_2 + 6CO_2$ used for both shots no. 136 and no. 138 and a cross-section ratio $A_{\text{projectile}}/A_{\text{tube}} = 0.53$. The gas pressure in the combustion region (II) was deduced from experiments [3] to about 1000 bars. As a result the gas conditions after combustion in region (II) are: gas temperature $T = 1823$ K, gas density $\rho = 248$ Kg/m³ and flow velocity $u = 1543$ m/s. For calculating further parameters for zone (II) the reacted gas mixture must be considered: $2H_2 + O_2 + 6CO_2 \Rightarrow 2H_2O + 6CO_2$.

With equations (1) and (3) the surface temperature along the body coordinate x_{II} was calculated. The temperature solution obtained is drawn in Fig. 13. The melting temperature is already reached for $u_p = 2000$ m/s and proceeds up to $u_p = 3000$ m/s.

The total surface erosion e given by equation (7) is $e = 0.2$ mm for the aluminum projectile body at $x_{II} = 10$ mm off the beginning of the combustor zone (II) and $u_p = 2000$ m/s, Fig. 14a. The x-ray image of Fig. 11b shows an extreme diameter reduction from 20 mm to less than 15 mm in the projectile body region (II). The erosion predicted by the heating and ablation model is smaller than the diameter reduction seen on the x-ray photography of Fig. 11b. It can be supposed that besides melting erosion chemical reactions, i.e., burning of the aluminum with the oxygen are additionally present giving as result the diameter loss seen in Fig. 11b in region (II). For $u_p = 3000$ m/s the ablation induced by surface melting increases dramatically as given in Fig. 14b.

The mass loss by melting and burning of projectile material produces, besides gas combustion, an additional undesired heat release inside the combustor channel which contribute to projectile acceleration shown in Fig. 7.

Expansion region (III)

In the x-ray Figure 11a,b nearly no erosion is seen in the divergent region (III). Here, the gas expands strongly, followed by a drop in temperature and pressure and consequently by lower surface temperatures.

Projectile fins (IIf)

At the projectile fins (IIf) the same ablation as for the body (II) is expected and calculated. Therefore, the results presented in Fig. 14a,b for the body region (II) can be extended to the erosion e along the x_{IIf} -coordinate at the fin's surface (IIf). For $u_p = 2000$ m/s the erosion is for aluminum material as mentioned above $e = 0.2$ mm at $x_{IIf} = 10$ mm downstream of the beginning edge of the fins. For titanium material the erosion e is much smaller at the same position. Because melting acts at both sides of the fins, the erosion data drawn in Fig. 14 must be doubled to define the minimal thickness of the guiding fins required for surviving the shot cycle when melting erosion is present. It came out that the fin thickness in experiment no. 136 and no. 138, 2.5 resp. 2 mm, is enough to survive the acceleration along the first 3 - 4 m in the ram-tube to 1866 m/s, resp., 1823 m/s. Nevertheless, these firings fail and the fins vanishes. Melting of surface material by heating seems therefore not to be the only process ablating the fins and also the body of the ram-projectile. As discussed above, burning of aluminum and maybe also titanium, i.e., reactions between surface material and oxygen (supported by surface melting), may play an important role in the failure of shot no. 136 and no. 138.

CONCLUSIONS

Analytical methods have been developed for calculating the heating and the ablation of a sharp-nosed body flying at hypersonic speed in a tube filled with high-compressed gas, i.e., in a so-called ram accelerator. The heat flux from gas to solid is calculated beginning with Prandtl's boundary layer equations. With an analytical solution of the one-dimensional heat conduction equation for surface temperature evaluation and an ablation model, the melting erosion was calculated for projectiles of aluminum and titanium used in the RAMC 30 experiment in the smooth bore version [3]. In subdividing the projectile contour in four regions, i.e., the cone (I), the body (II), the fins (IIf) and the back part (III), the following results are important:

Cone (I): With aluminum and titanium the heating and melting up to $u_p = 3000$ m/s is small. No significant deformation is expected.

Body (II): Ablation by melting in case of aluminum and titanium projectiles is calculated to be much higher than at the cone (I) due to the high gas temperature and gas pressure produced by combustion.

Fin (IIf): Ablation at the fins is of the same order as at the body (II). The calculated erosion e for shot no. 136 (aluminum) and shot no. 138 (titanium) is smaller than the fin width in the velocity range of up to 2000 m/s. Nevertheless, the projectiles have lost their fins during ram firing as depicted with x-ray photos. That means other erosion mechanisms must be additionally present. It is supposed that chemical reactions between fin material and the oxygen as well as the diluent (here CO_2) are considered for metals as aluminum and titanium, which easily form aluminum oxide as well as titanium dioxide, especially at high temperatures as present in the combustion region. Such chemical reactions, if possible, are also present in the body region (II).

Chemical reactions of projectile material with the oxygen and the diluent CO_2 have been found in previous RAMAC 30 experiments [13], done with projectiles of magnesium. Magnesium reacts well with oxygen by burning. The same tendency is present for aluminum and for titanium.

Therefore pure magnesium, aluminum or titanium should not be brought in contact with the hot combusted gas mixture, especially in case of melting processes and in case of CO_2 as diluent.

To avoid melting and burning other materials than magnesium, aluminum or titanium should be used, maybe steel. An advantage could be the possibility of coating in order to protect the ground material against high temperatures and also against burning reactions.

The results obtained with aluminum projectiles coated with zirconium oxide (ZrO_2) and aluminum oxide (Al_2O_3) are given in Fig. 15. In these two firings the aluminum seems to be protected against the heat influence for about 4 - 5 m flight, but no velocity increase is detected. It seems that the thrust originated by combustion just balances the high-pressure flow drag and the mechanical friction forces of the fins at the tube wall. With calculations done with the model of SMEETS et al. [11] the velocity increase for shot no. 136 is about 100 m/s on 6 m projectile travel. This velocity rise seems to be compensated by the forces mentioned. For example in shot 144 no combustion occurred and the projectile velocity dropped by an amount of $-\Delta u = 89$ m/s. Therewith the effects of flow drag and tube friction on projectile velocity are made visible with Fig. 16. If that hypothesis is true, the acceleration present in Fig. 7 is caused by burning of the projectile body and its fins forming a second heat source besides the heat release by gas combustion. The consequence is a undesired velocity gain by burning of the projectile material.

REFERENCES

1. HERTZBERG A., BRUCKNER A. P., BOGDANOFF D. W., The Ram Accelerator: A New Chemical Method of Achieving Ultra-high Velocities, 37th ARA-Meeting, Quebec, Canada
2. SEILER, F., PATZ, G., SMEETS, G., SRULIJES, J., The Rail Tube in Ram Acceleration: Feasibility Study with ISL's RAMAC 30, Second International Workshop on Ram Accelerator, RAMAC II, University of Washington, Seattle, USA, 1995
3. PATZ, G., SEILER, F., SMEETS, G., SRULIJES, J., Status of ISL's RAMAC 30 With Fin Guided Projectiles Accelerated in a Smooth Bore, Second International Workshop on Ram Accelerator, RAMAC II, University of Washington, Seattle, USA, 1995
4. HEISER, R., SEILER, F., ZIMMERMANN, K., Experimental and theoretical investigation of heat transfer in a gun barrel, 13th International Symposium on Ballistics, Stockholm, 1992
5. CHIEN, K.-Y., Hypersonic, Turbulent Skin-Friction and Heat-Transfer Measurements on a Sharp-Cone, AIAA Journal, Vol. 12, No. 11, 1974
6. OERTEL, H., Messungen im Hyperschallstoßrohr, "Kurzzeitphysik", Springer-Verlag, 1967
7. ADAMS, Mac C., Recent Advances in Ablation, ARS Journal, 1959
8. SEILER, F., Heating and ablation of a sharp-nosed body flying at hypersonic velocity through a tube filled with highly compressed gas mixture, IUTAM Symp. on Aerothermochemistry and Associated Hypersonic Flows, Marseille, 1992
9. SEILER, F., NAUMANN, K.W., Bow shock wave heating and ablation of a sharp-nosed projectile flying at supersonic velocity inside of a ram accelerator, 19th International Symposium on Shock Waves, Marseille, July 26-30, 1993
10. NAUMANN, K. W., Heating and ablation of projectiles during acceleration in a ram accelerator tube, AIAA/SAE/ASME/ASEE 29th Joint Propulsion Conference and Exhibit, Monterey, Ca., USA, 1993
11. SMEETS, G., GATAU, F., SRULIJES, J., Rechenprogramm für Abschätzungen zur Ram-Rohrbeschleunigung, ISL-Report RT 507/92, 1992

12. GIRAUD, M., LEGENDRE, J.-F., SIMON, G., RAM Accelerator in 90 mm Caliber or RAMAC 90; Experimental Results Concerning the Transdetonative Combustion Mode, 14th International Symposium on Ballistics, Québec, Canada, 26-29 September 1993
13. SEILER, F., PATZ, G., SMEETS, G., SRULIJES, J., Status of ISL's RAMAC 30 with Rail Stabilized Projectiles, First Int. Workshop on Ram Accelerator, RAMAC I, ISL, France, 1993

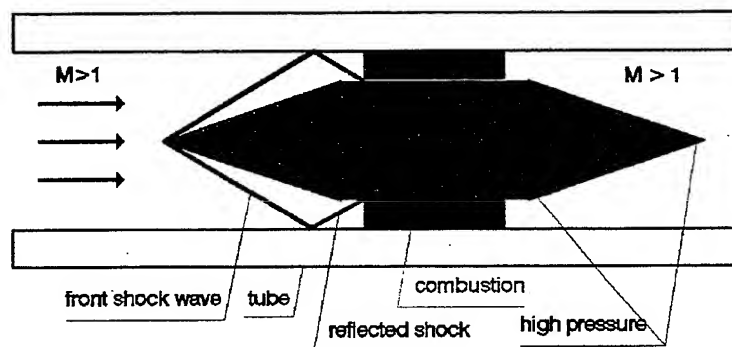


Fig. 1. Principle of the scram accelerator process

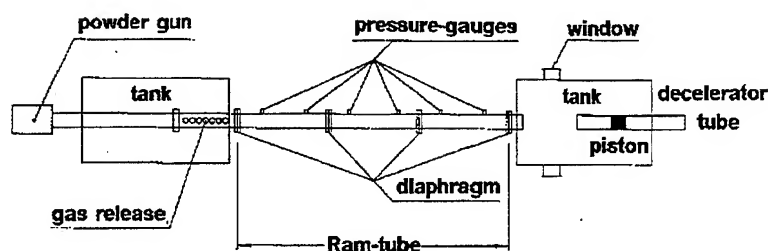


Fig. 2a. Set-up of ISL's ram accelerator



Fig. 2b. Smooth bore 6 m ram tube (left) and 1.5 m sabot stripper tube (right)

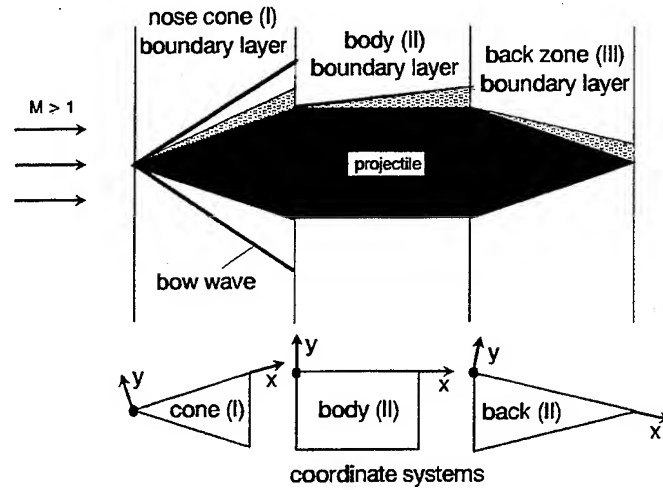


Fig. 3a. Boundary layer formation at the smooth cylindrical projectile

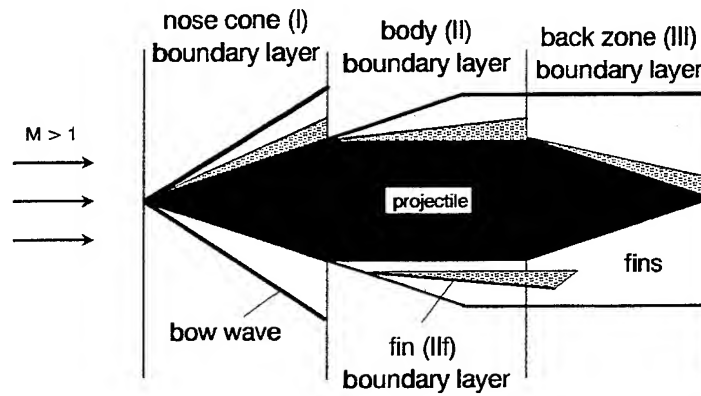


Fig. 3b. Boundary layer formation at the fin stabilized projectile

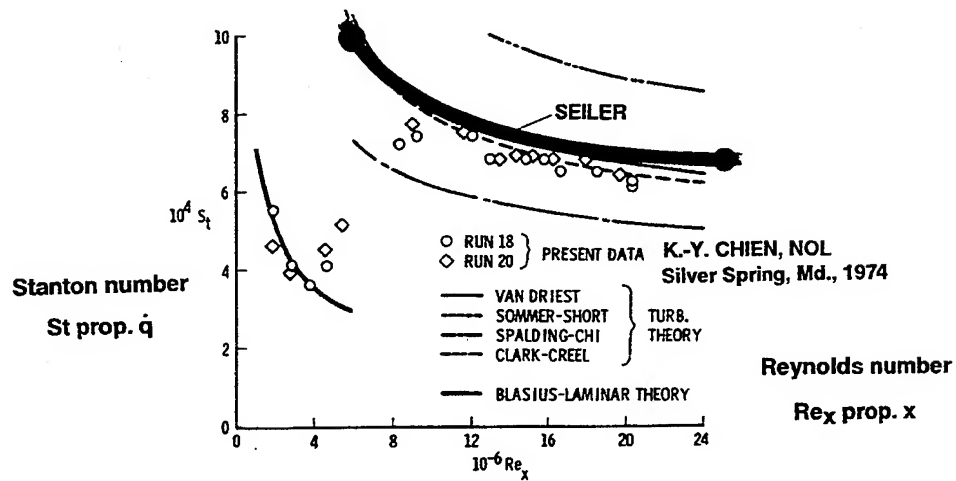


Fig. 4. Comparison of heat flux with CHIEN (1974)

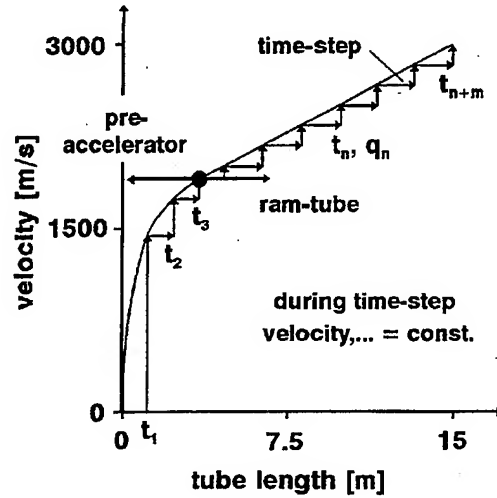


Fig. 5. Velocity cycle and time-step approach for actual and future RAMAC 30 operation

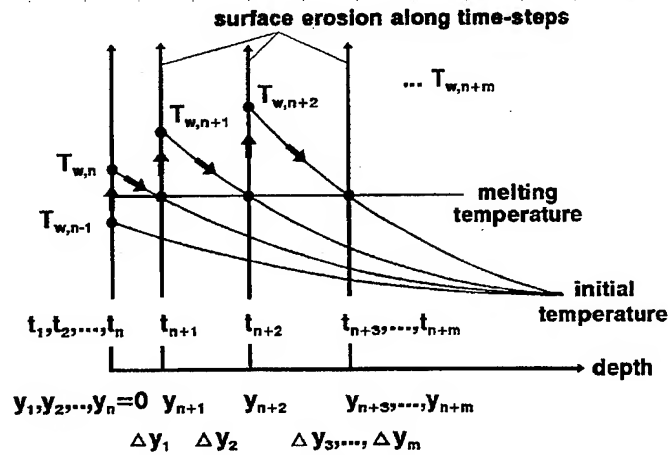


Fig. 6. Temperature $T_{w,1} \dots T_{w,n+m}$ and ablation $\Delta y_1 \dots \Delta y_m$ along time-step-procedure

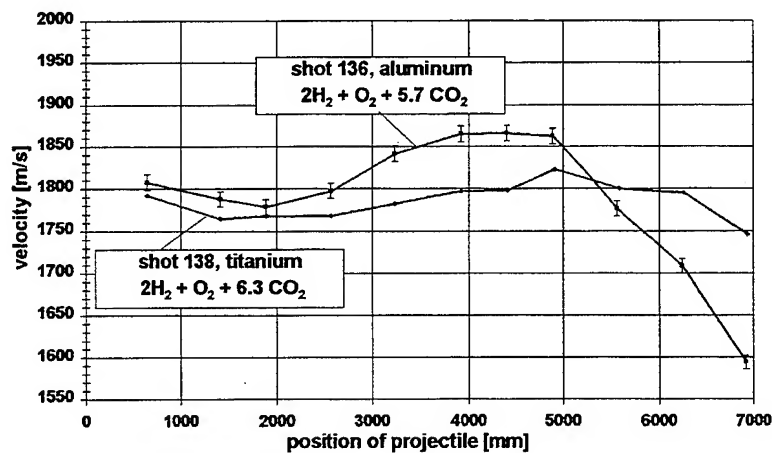


Fig. 7. Velocity increase with projectiles made of aluminum and titanium

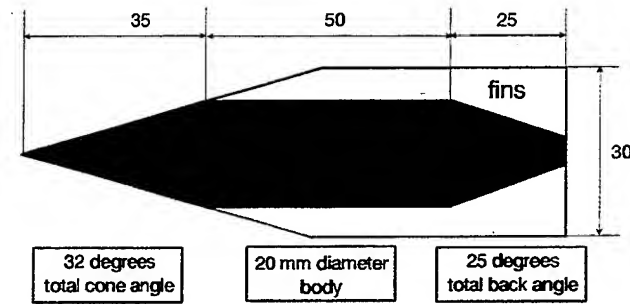


Fig. 8. Geometry of actual fin stabilized projectile (June 1995)

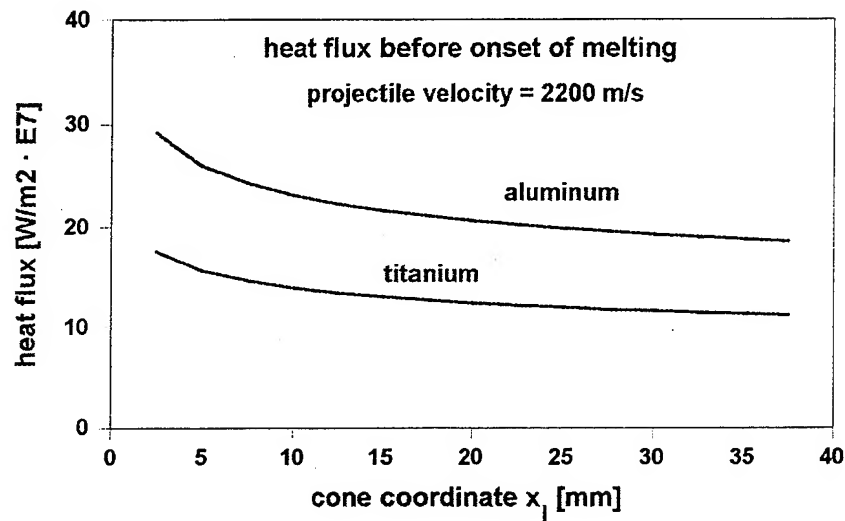


Fig.9. Aluminum and titanium cone surface heat flux

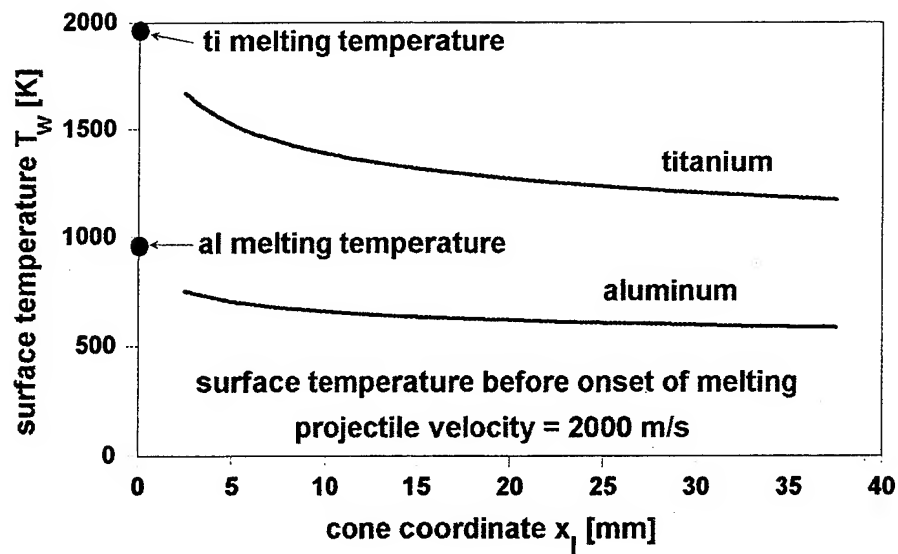


Fig. 10a. Cone (I) surface temperature for aluminum and titanium projectiles at $u_p = 2000$ m/s

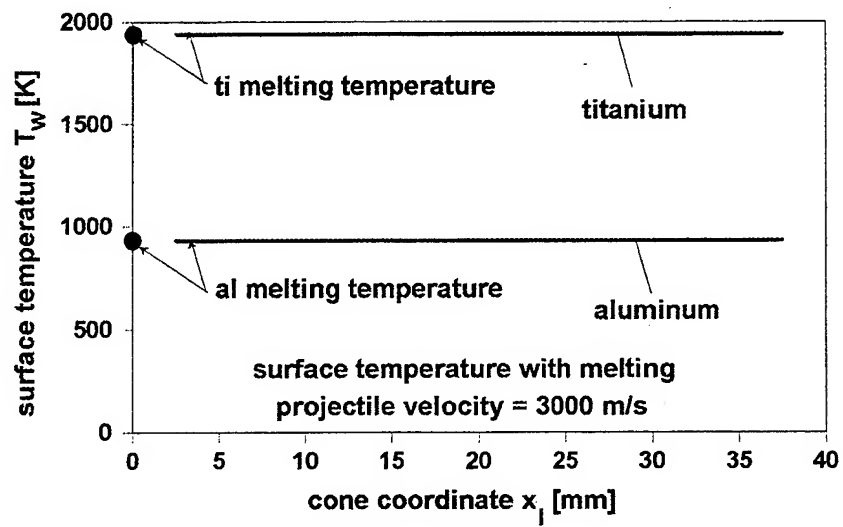


Fig. 10b. Cone (I) surface temperature for aluminum and titanium projectiles at $u_p = 3000$ m/s

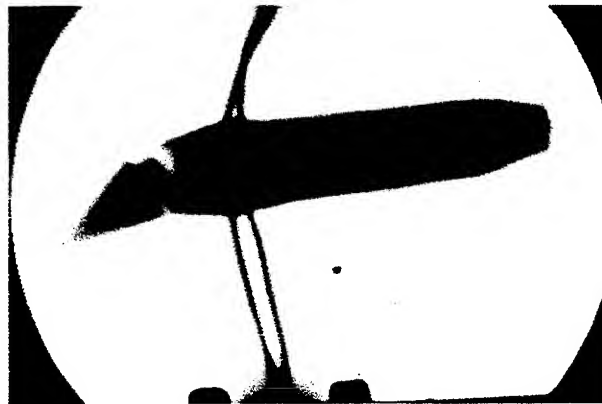


Fig. 11a. x-ray image for shot no. 134 after 3m projectile path with a mixture as for no. 136



Fig. 11b. x-ray photo for shot no. 139 after 6m projectile path

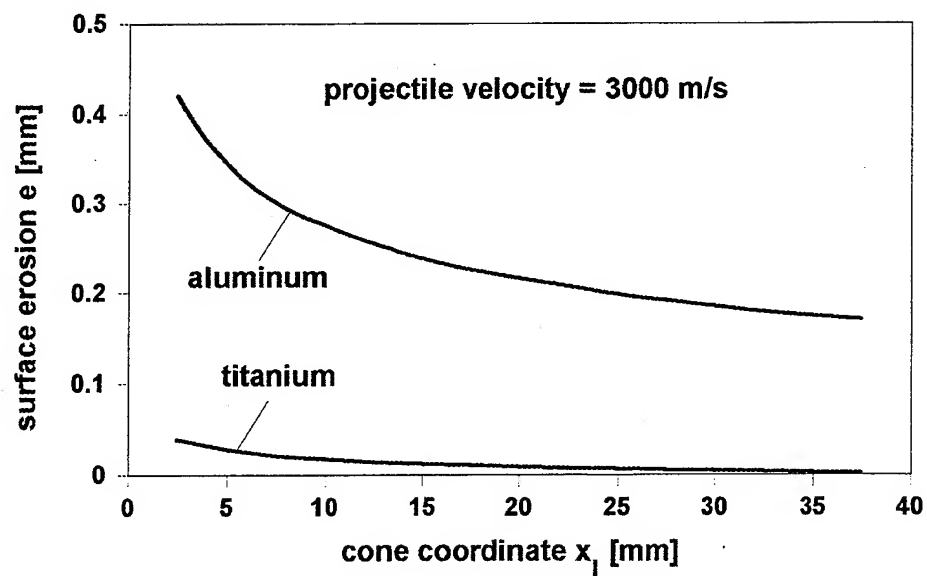


Fig. 12. Cone (I) surface erosion with aluminum and titanium projectiles at $u_p = 3000$ m/s

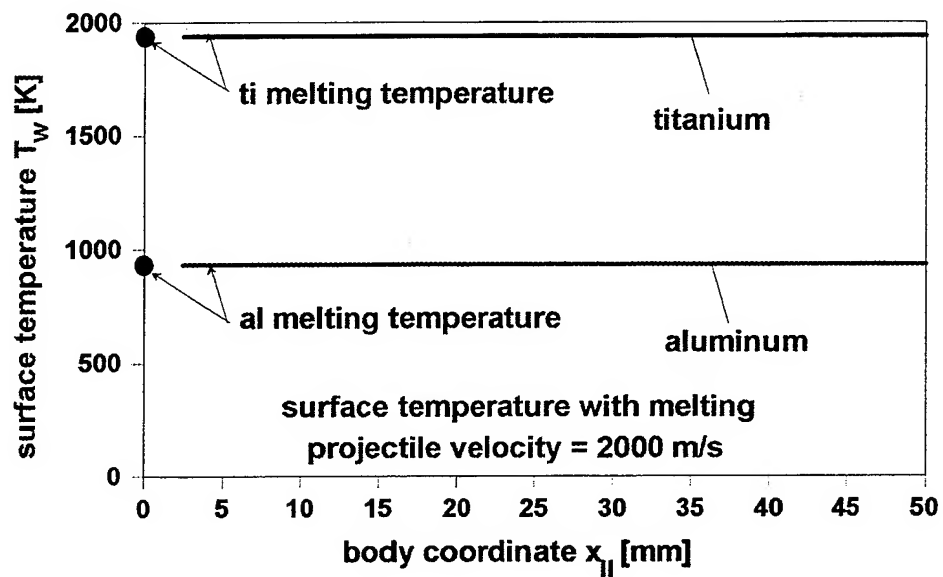


Fig. 13. Body (II) as well as fin (II_f) surface temperature for aluminum and titanium projectiles

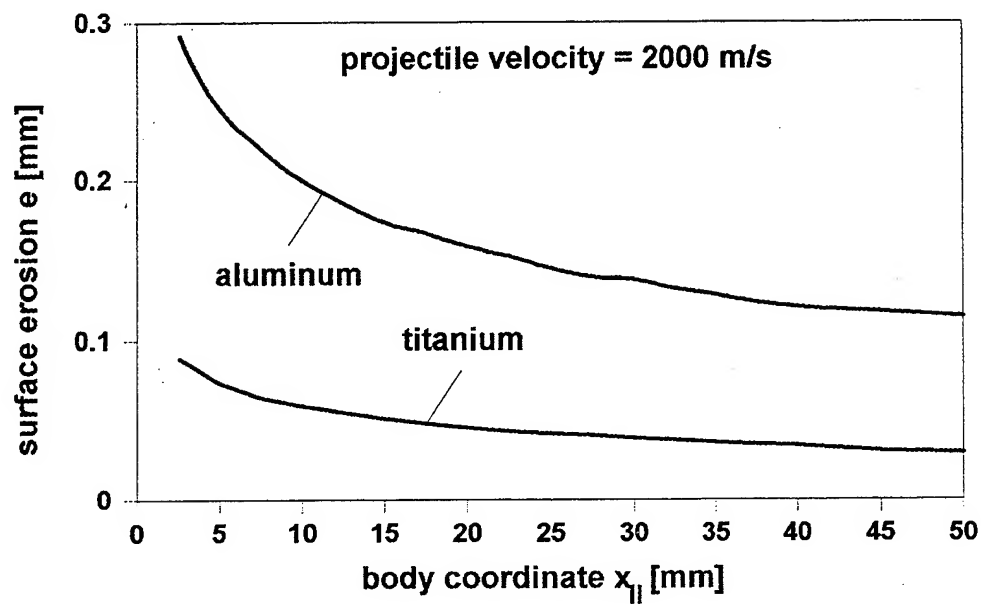


Fig. 14a. Body (II) as well as fin (II_f) surface erosion for aluminum and titanium

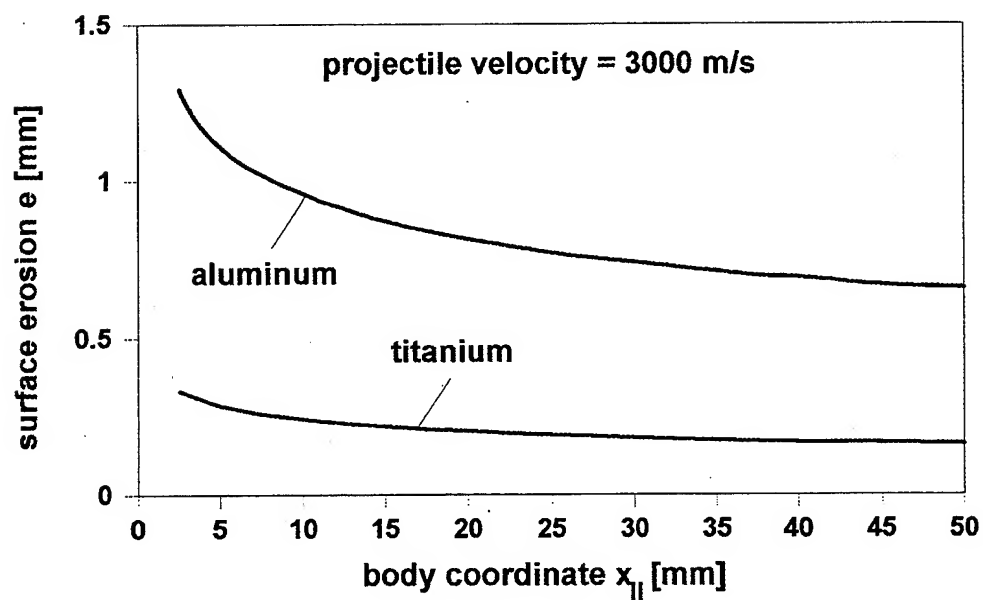


Fig. 14b. Body (II) and fin (II_f) surface erosion obtained for aluminum and titanium projectiles

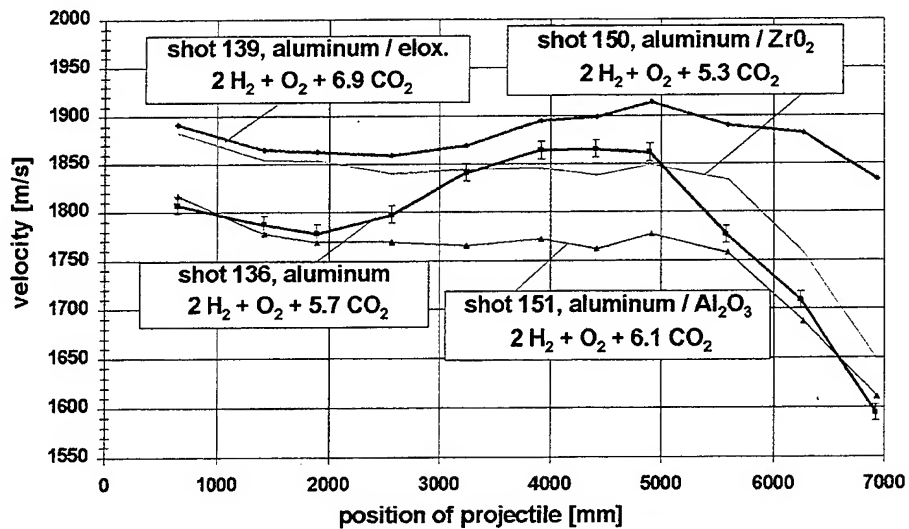


Fig. 15. Velocity increase with projectiles made of aluminum (no. 136), eloxadized aluminum (no. 139), aluminum with zirconium oxide coating (no. 150) and aluminum oxide layer on aluminum (no. 151)

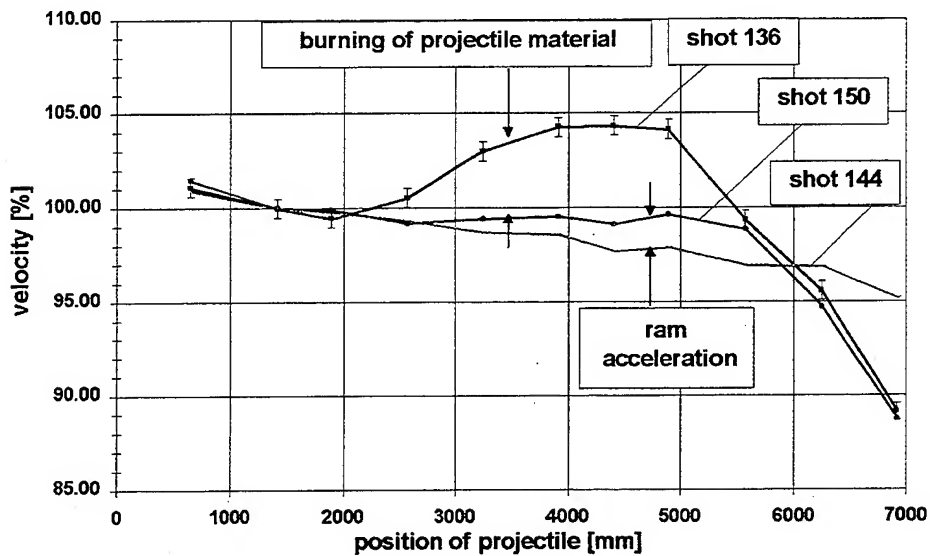


Fig. 16. Flow drag and friction forces balanced by ram acceleration in no. 150 (ram combustion) compared with shot no. 144 (no combustion) and no. 136 (ram combustion and aluminum burning)

THERMAL STRESS DUE TO AERODYNAMIC HEATING OF PROJECTILES DURING ACCELERATION IN A RAM ACCELERATOR TUBE

K. W. Naumann

*French-German Research Institute of Saint-Louis
5, rue du Général-Cassagnou, 68301 Saint-Louis, France*

Paper presented to the
2nd Int. Workshop on Ram Accelerators, Seattle, July 17-20, 1995

INTRODUCTION

During the acceleration in a ram accelerator tube the projectiles move through the dense propellant gas at very high velocity. The high density and the high velocity cause very heavy aerodynamic heating, even within the short time of some milliseconds of acceleration. This may cause even ablation of light metal alloys, or mechanical weakening of thin structures like fins or thin walls¹. Using suitable materials or material combinations can delay the onset of ablation, or prevent it over all of the acceleration process². Nevertheless, an other effect can affect the mechanical stability of the projectile: thermal stress, which is caused by the almost inevitable strong temperature gradients in the projectile wall, and the associated thermal expansion. This thermal compression stress acts coincident with the external pressure of the flow around the ram projectile, which tends to compress the projectile as well. Hence these conditions differ e. g. from those inside of a gun breech. There similar wall heating conditions creating thermal expansion combine with tensile stress at the inner wall due to internal pressure. Inside of the gun breech both effects eliminate each other at least partially.

Fortunately for the heated surface of such a ram projectile the peak stress due to external pressure occurs at the inner surface of the projectile wall, or at the centreline, if the projectile is massive³. Figure 1 shows a simplified sketch of the basic effects. In accordance with the fluid dynamic notion the pressure stresses are positive, the tensions negative. The formulae for the stresses at any radial coordinate r inside the projectile wall are, for an ideal cylindrical body of infinite length³

$$\sigma_t = \frac{p_{w,e} \eta^2 - p_{w,i}}{\eta^2 - 1} + \frac{(p_{w,e} - p_{w,i})}{\eta^2 - 1} \cdot \frac{r_{w,e}^2}{r^2} \quad (1)$$

$$\sigma_r = \frac{p_{w,e} \eta^2 - p_{w,i}}{\eta^2 - 1} - \frac{(p_{w,e} - p_{w,i})}{\eta^2 - 1} \cdot \frac{r_{w,e}^2}{r^2} \quad (2)$$

σ_t is the stress tangential to the surface, σ_r acts in radial direction, and η is the ratio of the outer and inner radius of the wall, i. e. $\eta = r_{w,e}/r_{w,i}$. The external pressure is $p_{w,e}$, and the internal pressure $p_{w,i}$. At the inner wall surface, i. e. $r = r_{w,i}$ we get

$$\sigma_t = \frac{2\eta^2 p_{w,e} - p_{w,i}(\eta^2 + 1)}{\eta^2 - 1} \quad (3)$$

$$\sigma_r = p_{w,i} \quad (4)$$

Formula (3) shows that for a massive body, where η is infinite and $p_{w,i} = 0$, the maximum permitted external pressure is

$$p_{w,e,per} = \sigma_{t,per}/2 \quad (5)$$

At the exterior wall surface we obtain

$$\sigma_t = \frac{p_{w,e}(\eta^2 + 1) - 2p_{w,i}}{\eta^2 - 1} \quad (6)$$

$$\sigma_r = p_{w,e} \quad (7)$$

Here for a massive body we get the straightforward result

$$\sigma_t = \sigma_r = p_{w,e} \quad (8)$$

At a rough estimate the pure pressure load would not have been considered to pose serious problems in view of the matter of fact that guns can hold thousands of atmospheres. However, external pressure is the much more adverse case, because the tolerable external pressure is utmost half of the permitted pressure stress of the body material. As stated above, the maximum load due to external pressure affects the least heated inner wall, or axis, of the ram projectile. Notwithstanding, we need to keep in mind that the external pressure contributes significantly to the mechanical load of the ram projectile, and that any consideration on thermal stress has to account for this. Experiments on the superdetonative propulsion mode yield peak pressures after the reflected conical shock (for a sketch see Fig. 2) of about 100 MPa or more⁴. Pressure of this order of magnitude alone can cause the disintegration of projectiles made of some light alloys.

GENERAL CONSIDERATIONS

The effects caused by thermal expansion depend strongly on temperature gradient, wall thickness, and properties of the materials used. Two limiting cases can be characterized: 'thick' walls and 'thin' walls (see Fig. 3). Bodies of ram accelerator projectiles generally have thick walls because of the considerable external pressure, as is outlined just above. If the projectile has fins, these are in general thinner, and have two heated sides. It can happen, that the wall is not 'thick' but 'intermediate', necessitating the use of a different approach. On the other hand, the fins are subjected to roughly equal pressure from both sides, if the combustion-flow-field develops ideally.

At a thick wall heating affects just a thin layer underneath the surface, the surface layer (SL). The most of the structure, designated deep wall (DW), remains cold. This is the case, if the

thermal conductivity λ_b is not sufficient to transfer a significant amount of heat into the interior of the wall within the duration of the heat flux. A rapid estimate whether a wall under consideration is rather 'thick' or 'thin' is explained in ref. 5: For the distance z of an isothermal with temperature T from the wall surface after time t of exposure to a laminar shock boundary layer, the analytical solution given by ref. 6 is

$$y = K_T \cdot [(\lambda_w / \rho_w c_w) t]^{1/2} \quad (9)$$

$K_T = f\{(T-T_1)/(T_{w,e}-T_1)\}$, with T_1 being the starting temperature, can be taken from Fig. 4. If $y = f\{(T-T_1)/(T_{w,e}-T_1)\} \approx 0.1$ or 0.2 is significantly less than the wall thickness S_w then the 'thick' wall approximation is valid, and the main of the structure is not affected by heating for the duration t considered. If $S_w \approx y = f\{(T-T_1)/(T_{w,e}-T_1)\} \approx 0.1$ to 0.7 , then all of the wall thickness is affected by heating, and we have the 'intermediate' case. Notice that for fins heated from both surfaces $S_w/2$ has to be used for this estimation. 'Thin' walls which heat almost uniformly will not appear in the frame of this consideration.

In general the projectile structures are three-dimensional and the temperature gradients not uniform. This creates a three-dimensional stress situation, which depends strongly on the shape and the structure of the wall. In the frame of this paper we start the general investigation by considering mainly the stress σ_t acting parallel to the surface. The approximation of the projectile body by a cylinder is roughly correct in the case of a ram accelerator with a rail tube⁴. The fins are approximated by flat plates.

Several measures can be taken in order to minimize the thermal stress:

- 1 The structure can be made from material with a low thermal coefficient of expansion α_e , for example steel with 36% of nickel.
- 2 Intermediate walls of uniform temperature gradient can be made from layers of different materials, whose α_e is chosen to obtain uniform thermal expansion $\alpha_e T$ over the wall thickness.
- 3 A suitable composition of layers of different materials can also be developed for thin walls with non-uniform temperature gradient, if in addition to $\alpha_e T$ the moduli of elasticity E are chosen to keep $\sigma(s) < \sigma_{per}$.
- 4 At thick walls the material of the thin SL can be chosen to obtain $\sigma_{p,per} > \sigma_p$ for the acceleration process considered, whereas the material of DW does not affect the aerothermal properties of the structure.
- 5 The material of SL can be chosen to ablate, before σ_p

approaches $\sigma_{p,per}$, if the corresponding degree of ablation can be tolerated.

We notice that the selection of the right material is not straightforward. This holds particularly for the case of a 'thick' wall. Moreover, in addition to the very different approaches to stress minimization, the level of the wall heat flux q_w and its duration t_q have to be taken into account as well.

In the following this paper will present an approach, which allows to determine the aerothermal suitability of materials for the use with 'thick' walls by similarity parameters, dependent on q_w , t_q , and the material properties. Extensions allow to express q_w in terms of readily available flow parameters.

THERMAL STRESS AND EXTERNAL PRESSURE

In the thin heated surface layer thermal pressure $\sigma_{t,WL}$ is much larger than the balancing strain $-\sigma_{t,DW}$ of the deep wall (see Fig. 3). If σ_t exceeds the permitted $\sigma_{t,per}$ of the material, mechanical destruction or degradation of the SL can happen.

For our considerations we assume:

- ▷ Hooke's law, i. e. $\sigma = \epsilon E$. E is assumed not to vary with T . ϵ is the variation in length, i. e. $\epsilon = \alpha_e \Delta T$. Since in general α_e increases with increasing T , and E decreases, the change of $\alpha_e \Delta T \cdot E$ with T is moderate.
- ▷ The tension in the cold DW, with $T = T_{DW}$, and its change in length are neglected.
- ▷ Only tensions orientated parallel to the surface are considered.

Each layer in SL is subjected to a pressure tension, which has to balance the thermal expansion,

$$\sigma_t/E = \epsilon = \alpha_e \Delta T = \alpha_e (T - T_{DW}) \quad (10)$$

and the maximum permitted temperature rise of this layer is

$$\Delta T_{per} = \sigma_{t,per} / (\alpha_e E) \quad (11)$$

For the thin outer layer of a cylindrical body the contribution of the external pressure $\sigma_{t,p}$ can readily be evaluated using equ.

(6), to yield

$$\Delta T_{per} = (\sigma_{t,per} - \sigma_{t,p}) / (\alpha_e E) \quad (12)$$

and for a massive body

$$\Delta T_{\text{per}} = (\sigma_{t,\text{per}} - p_{w,e}) / (\alpha_e E) \quad (13)$$

Let us consider a brief example: A University of Washington, Seattle projectile⁷ made from aluminum alloy (Data see Tab. 1) is subjected to $p_{w,e} \approx 7.5$ MPa at the end of shot #833, and to $p_{w,e} \approx 8$ MPa at the end of shot #944¹. The cone is hollow, and at the point investigated $r_{w,e} = 4.24$ mm and $r_{w,i} = 2.21$ mm, which give $\eta = 1.92$. The maximum permitted temperature rise of the surface layer from (11) is $\Delta T_{\text{per}} = 325$ K. In this case external pressure contributes little: According to (6), and for $p_{w,i} = 0$ we obtain $\sigma_{t,p,e} = 13$ MPa, and with this in (12) we get $\Delta T_{\text{per}} = 317$ K. The maximum permitted absolute temperature, calculated with an assumed laboratory temperature of 295 K, is: $T_{\text{per}} = 620$ K for $p_{w,e} = 0$; $T_{\text{per}} = 612$ K for $p_{w,e} = 7.5$ MPa. Figure 5 shows the wall temperatures of 4 shots performed at the University of Washington, Seattle⁷ (for more details on these cases see ref. 1). We see that with a maximum surface temperature of 650 K the projectile of shot #883 keeps roughly within the calculated limits (it survived the acceleration procedure), whereas the projectiles of the other shots reach about the melting temperature, before they unstart.

The fact that the wall temperature can exceed the above calculated temperature limit to some extent or for a limited time before failure is not surprising. After all, each well-performing technical device can bear some overload. Figure 6 shows¹ that in all three cases at the time of unstart the 620 K - isothermal had penetrated the wall by about 0.3 mm, i. e. 0.11 of the wall thickness. Of course other, more effective reasons may have provoked these unstarts, what is discussed in ref. 1. Nevertheless, the criterion of permitted maximum temperature rise too yields in these cases consistent results.

HOMOGENOUS WALLS

Similarity Considerations on Thermal Relations

For the calculation of the example above we used data taken from detailed investigations. The rough judgement in advance, how a surface will perform in view of a given heating rate - exposure time history, or which material does better, can be carried out by normalization of ΔT_{per} by the difference between wall surface temperature $T_{w,e}$ and internal temperature T_{DW} . The increase of $T_{w,e}$ of a homogenous 'thick' wall due to aerothermal heating can be written according to Smeets⁸

$$[T_{w,e}(t) - T_1] / [T_r - T_1] = f\{[4\dot{q}_{w,\text{max}}^2 t] / [\pi \rho_w c_w \lambda_w (T_r - T_1)^2]\} \quad (14)$$

$$[T_{w,e}(t) - T_1] = [T_r - T_1] f\{\varphi\} \quad (15)$$

T_r is the recovery temperature, $\dot{q}_{w,\text{max}}$ the cold-wall heat flux, and $\rho_w c_w \lambda_w$ are density, specific heat capacity and thermal conductivity of the solid wall. T_1 is the starting temperature,

and usually $T_1 = T_{DW}$. Division of (11) by (15) yields

$$\mathcal{P} = \Delta T_{\text{per}} / [T_w(t) - T_1] = [\sigma_{t,\text{per}} / (\alpha_e E)] / (T_r - T_1) f\{\mathcal{P}\} \quad (16)$$

and division of (12) by (15), for the case with $\sigma_{t,p} \neq 0$

$$\mathcal{P} = \Delta T_{\text{per}} / [T_w(t) - T_1] = [(\sigma_{t,\text{per}} - \sigma_{t,p}) / (\alpha_e E)] / (T_r - T_1) f\{\mathcal{P}\} \quad (17)$$

$f\{\mathcal{P}\}$ can be taken readily from Fig. 7⁸. It is as well possible to use \mathcal{P} directly as a similarity parameter by writing

$$Q = [\sigma_{t,\text{per}} / (\alpha_e E)] / [T_r - T_1] \mathcal{P} \quad (18)$$

or, respectively

$$Q = [(\sigma_{t,\text{per}} - \sigma_{t,p}) / (\alpha_e E)] / [T_r - T_1] \mathcal{P} \quad (19)$$

The difference is that Q is easier to be obtained, but \mathcal{P} gives more straightforward information:

- ▷ $\mathcal{P} < 1$ indicates that mechanical destruction or degradation of the wall surface can happen.
- ▷ $\mathcal{P} > 1$ indicates a safe structure for the conditions considered.

At the right hand side of equ. (18) and (19) the material properties, and for convenience the constants, can be combined to form

$$M = [\sigma_{p,\text{per}} / (\alpha_e E)] [\rho_w c_w \lambda_w \pi / 4] \quad (20)$$

with the dimensions $[J^2/m^4 s K]$.

The sense of M is that a high value indicates a suitable material for the use as a thin SL of a 'thick' wall: As well high ΔT_{per} as high heat sink capacity $\rho_w c_w$ and good heat conductivity λ_w tend to lessen the risk of destruction of the surface layer due to thermal stress. Fig. 8 shows M over the melting temperature T_m . Notice that the widely used Al- and Mg-alloys show reasonable good values of M , which are better than that of Ti, Ir, or Zr. A deficit of Al- and Mg-alloys is the rapid decrease of mechanical strength with increasing temperature. The latter materials have a higher melting temperature, but the relative mechanical load of SL due to thermal expansion is higher. A very good performance shows Invar[®], a steel with 36% of Ni. The extremely low α_e overrules the poor heat conductivity. The equally good performance of well hardened and tempered steel is due to its high σ_{per} , which favourably is greatest in the SL. In addition steel generally offers good mechanical properties. Other good and readily available materials are Waspalloy[®] and CuZn40Pb2 F68. Alloys based on Mo (i. e. TZM), W, Re and Rh offer good heat resistance in combination with excellent values of M , which is due to their good λ . Since the λ of ceramics differs significantly they show great differences as well: ZrO₂ performs worse than most metals, Sialon[®] and borium nitride match very good ordinary metals, Shapal[®] is

excellent, and SiC the best of the band. In addition we should keep in mind, that ceramics keep their mechanical strength up to temperatures of 1200 K or more. If lightweight construction is the necessary, ceramics offer superior performance. The properties of Kevlar reinforced resin are bad because of its extremely low λ . In the next paragraph we will see that it is an excellent material for protective layers.

An other question is, whether a material will first melt, soften or decomposit, or rather crack under thermal stress, and external pressure. This can be answered by normalizing ΔT_{per} by $\Delta T_{\text{max}} = (T_{\text{max}} - T_{\text{DW}})$ which yields an other parameter M ,

$$M = \Delta T_{\text{per}} / \Delta T_{\text{max}} = [(\sigma_{t,\text{per}} - \sigma_{t,p}) / (\alpha_e E)] / (T_{\text{max}} - T_{\text{DW}}) \quad (21)$$

For materials with strong dependence of $\sigma_{t,\text{per}}$ on T , as for example metals with $\sigma_{p,\text{per}} \rightarrow 0$ as $T \rightarrow T_m$, the temperature T_{max} is less than T_m . $M < 1$ indicates that mechanical degradation due to thermal stress occurs before melting, softening or decomposition, $M > 1$ indicates that the latter make the limiting effect, which qualifies a material for use as an ablative layer. Figure 9 gives M of some materials. Values for metals are calculated with the lowest T_m , those for ceramics with the maximum temperature of continuous use. Hence the given values for metals represent the lower limit.

We see readily that many of the metals with high T_m have very small M , as for example Ir, Rh, TZM, Densimet[®], Ta, Re, Zr, and W75Re25. As a matter of fact these metals have not sufficient strength to allow heating up to temperatures which are about T_m . The surface will disintegrate at much lower temperatures *if just a SL of these materials is heated*. These materials can nevertheless be well used for 'thin' and 'thin intermediate' walls, because in this case the thermal stress is less important. They can as well be used for 'thick' walls, if layers of different materials with correctly tuned factor $\alpha_e E$ are used. Metals with a somewhat balanced behaviour are the alloys based on Al, Mg, Ni, Ti, and steel, mainly because of their lower T_m . Densimet[®] performs excellent because of its extreme $\sigma_{p,\text{per}}$, and has in addition a very high high T_m . However, for use with ablative layers only polymeric or ceramic materials seem to be appropriate. The best of the ceramics is ZrO₂ because of its little λ . Also very good is Sialon[®], whose λ is not yet too high. Borium nitride, Shapal[®], and SiC can effectively not be used because of too high λ . The best of all is Kevlar reinforced resin, with $M = 5$ to 10 for $\sigma_{p,\text{per}} = 500$ MPa, and $\lambda = 0,2$ W/mK. The disadvantage is the little T_{ab} , which means that the heat flux which has to be absorbed is comparatively high, as is in consequence the flux of mass lost due to ablation. An other advantage is the combination of little density and high heat capacity.

Examples

Let us again have a look to an example, calculated using the UW shots mentioned above⁷ (for more details on thermal data see again ref. 1): At the end of the acceleration process $T_{w,e} = 640$ K for shot #883 and $T_{w,e} = 850$ K for the others. Using the roughly estimated and over t averaged recovery temperatures of 1000 K and 1350 K, respectively, yields

$$\begin{array}{lll} f(\mathcal{P}) = 0.4894; & \mathcal{P} = 0.68; & \text{shot \#883} \\ f(\mathcal{P}) = 0.5261; & \mathcal{P} = 0.85; & \text{shot \#944} \end{array}$$

For the aluminum alloy used, $\rho_w c_w \lambda_w = 333 \cdot M [J^2/m^4 s K^2]$. Replacement of these aluminum data by those of titanium or magnesium (see Tab. 1), i. e. $\rho_w c_w \lambda_w = 13.84 \cdot M [J^2/m^4 s K^2]$ and $141 M [J^2/m^4 s K^2]$, respectively, gives for similar cones of titanium and magnesium, and the same flow conditions,

$$\begin{array}{lll} \mathcal{P} = 16.36; & f(\mathcal{P}) = 0.865; & \text{shot \#883/Ti} \\ \mathcal{P} = 20.46; & f(\mathcal{P}) = 0.880; & \text{shot \#944/Ti} \\ \mathcal{P} = 1.606; & f(\mathcal{P}) = 0.622; & \text{shot \#883/Mg} \\ \mathcal{P} = 2.008; & f(\mathcal{P}) = 0.644; & \text{shot \#944/Mg} \end{array}$$

Using this, and neglecting the comparatively small contribution of external pressure we obtain for \mathcal{P} the following data:

$$\begin{array}{ll} \mathcal{P} = 0.968 & \text{shot \#883/Al-cone} \\ \mathcal{P} = 0.602 & \text{shot \#944/Al-cone} \\ \mathcal{P} = 2.237 & \text{shot \#883/Ti-cone} \\ \mathcal{P} = 1.469 & \text{shot \#944/Ti-cone} \\ \mathcal{P} = 0.598 & \text{shot \#883/Mg-cone} \\ \mathcal{P} = 0.386 & \text{shot \#944/Mg-cone} \end{array}$$

We see clearly that the aluminum alloy is noticeably too weak for the heating conditions of shot #944, whereas it is about at the brink with shot #883. The titanium alloy performs better, but not to that extent as would have been expected from aerothermal reasonings which take into consideration just the melting temperature. As a matter of fact $T_{w,e}(t)$ depends strongly on T_r at such high \mathcal{P} - values as they occur with the titanium walls, and because T_r goes up to 1800 K at the end of the acceleration process of shot #944, the value $\mathcal{P} = 1.469$, which is estimated using a mean recovery temperature is rather optimistic. Magnesium performs worst and is well below $\mathcal{P} = 1$ even for the conditions of shot #883. This agrees with experimental observations: the projectile of shot #842 had a magnesium cone and unstirred just before the surface reached the melting temperature. Using from ref. 1 $T_{w,e} = 840$ K, and the roughly estimated and over t averaged recovery temperature of 1250 K, we obtain

$$f(S) = 0.5707 \Rightarrow \mathcal{P} = 0.4807$$

which is a little bit lower than the \mathcal{P} - value calculated for the Al-cone of shot #944.

In spite of the good agreement these calculations do not allow to definitely fix the value of \mathcal{P} , at which the structures fail. According to the findings in ref. 1 in all these cases the

time of unstart coincides as well with the time of onset of ablation at large areas of the surface of the projectiles.

An other example can be calculated using shot #8 of ISL RAMAC 30 (for general information see ref. 4 and the references cited therein, for calculations on heating see ref. 2). The conditions of this shot are characterized by a very high and roughly constant heating rate and a very short time till the unstart. Former calculations showed that a front cone of magnesium should not ablate². With the flow data of Tab. 2 we get for a 'thick' cone of

MgAl8Zn:	$\mathcal{P} = 0.1200 \Rightarrow$	$f(\mathcal{P}) = 0.2703 \Rightarrow$	$\mathcal{P} = 0,549$
AlCu4MgSi	$\mathcal{P} = 0.0492 \Rightarrow$	$f(\mathcal{P}) = 0.1660 \Rightarrow$	$\mathcal{P} = 0,812$
TiAl6V4:	$\mathcal{P} = 1.223 \Rightarrow$	$f(\mathcal{P}) = 0.5753 \Rightarrow$	$\mathcal{P} = 1.395$

These findings correspond with the observed results that the magnesium projectile failed and the aluminum projectile survived. The titanium data are for comparison. No Ti-projectiles have been used with the rail tube. For the sake of completeness we should mention that very heavy ablation from almost the beginning was calculated for the corner between the projectile cone and the tube rails. Since in this case the 473-K-isothermal preceeds the ablation front by just 0.2 mm, the zone of tensional overload is thin². Till the time of unstart there is no indication that this local ablation affects the acceleration process². Another reasonable cause for the observed unstarts of the magnesium projectile could have been burning of the surface, which could have choked the bypass due to excessive heat production.

Concluding this set of examples we once more have to emphasize that the thin SL certainly will not disintegrate to a noteworthy amount immediately when the outermost layer of wall surface molecules attains the value $\mathcal{P} = 1$. Since real structures can tolerate some overload, the criterion $\mathcal{P} = 1$ should not mark a sharp limit, but indicate a safe construction. The examples indicate that effective failure occurred at about $0.4 < \mathcal{P} < 0.7$.

Similarity Considerations Including Heat Transfer Analysis

Let us now turn over to the heat transfer term of \mathcal{P} or Q , respectively: At ram acceleration conditions the convective heat transfer caused by the turbulent boundary layer (BL) is by far dominant, with the exception of some spots with shock/BL interaction^{1,2}. The heat transfer coefficient α_h is defined by

$$\alpha_h = \dot{q}_w / (T_{ref} - T_w) \quad (22)$$

T_{ref} is the significant temperature inside the BL for \dot{q}_w . For the cold wall we can assume

$$T_w = T_1 = T_\infty \quad (23)$$

which holds in most cases. With this, for $\dot{q}_w = \dot{q}_{w,max}$, i. e. at a cold wall, and for a turbulent boundary layer we can approximate^{5,9}

$$T_{ref} = T_{max,BL} \cong T_\infty (1 + 0.24 \cdot Ma^2 / f) \quad (24)$$

with f being the number of the internal degrees of freedom of the gas. Using

$$A = (\pi/4) \rho_w C_w \lambda_w \quad (25)$$

and putting (22), (24) and (25) into (14) and (15):

$$\varphi = (\dot{q}_{w,\max}^2 t) / [A (T_r - T_1)^2] \quad (26)$$

gives

$$\varphi = \alpha_{h,\max}^2 t (T_\infty \cdot 0.24 Ma^2 / f)^2 / [A (T_r - T_1)^2] \quad (27)$$

For the heat transfer coefficient we use Reynolds analogy with the extension of Prandtl and Taylor (for details see refs. 10, 5, 9). This can be written as

$$Nu = \frac{Pr \cdot Re \cdot (C_f / 2)}{1 + \frac{W_{lam}}{W_\infty} (Pr - 1)} \quad (28)$$

Here C_f is the local turbulent friction coefficient, W_{lam} is the velocity at the edge of the laminar boundary layer, and the Nusselt-number $Nu = Sta / (Re \cdot Pr)$. λ_f is the heat conductivity of the fluid, i. e. the propellant gas, and l is the length of BL flow. With this α_h becomes

$$\alpha_h = Nu \cdot \frac{\lambda_f}{l} = \frac{Pr \cdot Re_l \cdot (C_f / 2) \cdot \frac{\lambda_f}{l}}{1 + \frac{W_{lam}}{W_\infty} (Pr - 1)} \quad (29)$$

Since for hypersonic flow conditions with a cold wall W_{lam} / W_∞ is very small⁵, the denominator is less than 1.05 for $0.5 < Pr < 1.5$, and we can approximate for Pr being about unity

$$\alpha_h = Re_l (C_f / 2) (\lambda_f / l) \quad (30)$$

Now putting in from ref. 10

$$C_f = 0.0592 Re^{0.2} \quad (31)$$

and from (refs. 10 and 5)

$$C_{f,\text{compr}} / C_{f,\text{incompr}} = (1 + Ma^2 / f)^{-1/2} \quad (32)$$

we obtain

$$\varphi = \frac{0.0296^2 \cdot Re_l^{1.6} \cdot t \left[\frac{\lambda_f}{l} \cdot T_\infty \cdot 0.24 \frac{Ma^2}{f} \right]^2}{A (T_r - T_\infty)^2 \left(1 + \frac{Ma^2}{f} \right)^{1/2}} \quad (33)$$

Combining the temperature and Mach number terms to

$$\mathcal{T} = \frac{(T_{\infty} \cdot 0.24 Ma^2 / f)^2}{(T_r - T_{\infty})^2 (1 + Ma^2 / f)^{1/2}} \quad (34)$$

and putting this into (34) yields

$$\mathcal{P} = 0.0296^2 Re_1^{1.6} \cdot t(\lambda_F / l)^2 \cdot \mathcal{T} / A \quad (35)$$

and this in (17)

$$\mathcal{P} = \frac{(\sigma_{t,per} - \sigma_{t,p})}{\alpha_e \cdot E \cdot (T_r - T_{\infty}) \cdot f \{ \mathcal{T} \cdot 0.0296^2 Re_1^{1.6} \cdot t(\lambda_F / l)^2 / A \}} \quad (36)$$

This formula consists of well available parameters. It allows an immediate estimate of the stability of the surface of a specific 'thick' wall, which is subjected to aerothermal stress caused by a compressible turbulent boundary layer at specific acceleration conditions, and the comparison of different structures made of different materials. For equations (16) and (18), (19) on Q the corresponding expression can be formulated as well. Since the deductions from (26) onwards assume inherently that $\dot{q}_{w,max}^2$ is constant over t , the accuracy is best for moderate variations, or saw-tooth histories of $\dot{q}_{w,max}^2$, as they are typical for staged ram acceleration processes.

INHOMOGENOUS WALLS

Inhomogenous walls are made of layers of different materials, as is shown in Fig. 10. This can be protective layers (PL) of especially heat-resistant or non-oxidizing metals, ceramics, surface treatments, or varnishes, which shield the inner wall (IW). Other possibilities include two or more wall layers (WL) of different materials chosen to obtain a specific temperature gradient, or to save expensive materials where they are not essential, or to minimize thermal stress (see Fig. 10). In the frame of this paper the last application is the dominant one.

Protecting Layers

The demands on the material of a PL depend on its function, and can be expressed in those terms as we have developed them above. Depending on the type of the protecting layer, these are as follows:

1 Thin PL against oxidation of the IW material

Necessary requirements are:

- ▷ $\mathcal{P}_{IW} \geq 1$; tolerable thermal load of IW.
- ▷ $T_{m,PL} > T_{w,e}$; no melting, decomposition, etc., of PL.
- ▷ Whether it is essential that $\alpha_{e,PL} \approx \alpha_{e,IW}$ depends on the thickness and the structure of PL.

Of secondary importance are, dependent on thickness and structure of the PL, E and $\sigma_{t,per}$.

2 Thermally isolating PL

Necessary requirements are:

- ▷ Little $\lambda_{PL}/\rho_{PL}c_{PL}$. Because of the very high heat transfer rates, the necessary thickness of those PL can be surprisingly high.
- ▷ High $T_{m,PL} \geq T_r$, because the surface of good isolators heats rapidly. Otherwise ablation will take place, then: high M .
- ▷ Either little $\alpha_{e,PL}$ or high $[\sigma_{t,per}/(\alpha_e E)]_{PL}$; the conditions are the same as those of a SL.

Little important are the relations $\alpha_{e,PL}/\alpha_{e,IW}$ or $(\alpha_e E)_{PL}/(\alpha_e E)_{IW}$ if the temperature at the inner side of the PL is low.

3 Ablating PL

Here the term ablation summarizes all processes which cause material loss, like melting, erosion, oxidation, sublimation, decomposition, etc. Necessary requirements are:

- ▷ High specific heat of ablation $q_{ab,PL}$.
- ▷ If mass doesn't matter: high $\rho q_{ab,PL}$.
- ▷ Little λ_{PL} . This allows to use up a great part of PL, with $T_{w,i,PL}$ remaining low.
- ▷ $M > 1$ in order not to loose PL due to mechanical overload.

Wall Made of Different Wall Layers

This kind of wall cannot be sharply divided from the walls with protective layers, because the outermost layer will certainly be chosen in order to have the necessary protective qualities. The distinction is more evident from the mechanical point of view, because protective layers usually have not to fulfill mechanical functions, as has each WL in the cases under consideration in this chapter.

For the outermost wall layer, designated WL1 (see Fig. 10), the material should be heat resistant. If it tends to react chemically with the gas, a PL against oxidation can be used. Necessary requirements are:

- ▷ High T_{max} .
- ▷ High $(\rho c)_{WL1}$, i. e. high M .

Secondary requirements are either little $\alpha_{e,WL1}$, or high $[\sigma_{t,per}/(\alpha_e E)]_{WL1}$. These requirements can be dropped if the $(\alpha_e E)$ of the different WLs are matched appropriately. If for example $(\alpha_e E)_{WL1} = (\alpha_e E)_{WL2}$ there is no jump of σ_t at the boundary between WL1 and WL2. On the other hand, combinations of WLs with different $(\alpha_e E)$ can help to distribute the thermal stress over wider parts of the structure. Hence for the interior WLs the requirements are:

- ▷ Those WLs which heat little should have higher α_e , ideally:

$$\alpha_e \{WLi\} \cdot \Delta T \{t, WLi\} = \text{const.} \quad (37)$$

This kind of optimization necessitates a detailed numerical analysis of the history of the temperature gradient.

- ▷ With equ. (21), and the use of $\Delta T \{t, WLi\}$ in the place of ΔT_{\max} we can set up

$$Mi' = \Delta T_{\text{per}} \{WLi\} / \Delta T \{t, WLi\} \quad (38)$$

and the requirement for each WL is $Mi' \ll 1$. The mechanical loads originating e. g. from external pressure or forces due to acceleration can be incorporated into $\Delta T_{\text{per}} \{WLi\}$ as is shown above. In general $\Delta T \{t, WLi\}$ needs to be evaluated by a numerical procedure.

CONCLUSION

The considerations presented above show that the choice of the right materials or of suitable combinations of these is not straightforward, and that the use of just one material property as a parameter can lead to suboptimal solutions. Since the mechanical load on ram projectiles results from a combination of external pressure and thermal stress, useful parameters have to take into account both effects. Because of the complexity of the physical effect, almost all mechanical and thermal parameters need to be incorporated. The parameters evaluated allow to qualify the materials according to the selected application, and give some insight, why specific materials perform well or wrong.

For the case with about constant heat flux into homogeneous walls an extension allows an immediate estimate whether a given structure should fail or survive. Calculations with data of shots performed in different laboratories, with different flow conditions and different materials, show for $0.4 < P < 0.7$ failure of the projectiles. But, because other effects may have caused these unstarts as well, this observation cannot be taken as a proof.

Further considerations on the heat transfer term of the parameter allow to qualify generally the thermomechanical behaviour of generic projectile structure, without detailed calculations on the flow field.

The considerations on inhomogenous walls give an overview on the relevant criteria for the choice of the right material. The parameters which are evaluated for homogenous walls, and modifications of these, can also be used for the material selection in these cases.

After all it should be emphasized that some progress can also be achieved with very elementary reasoning: the mechanical load on the ram projectiles can be alleviated significantly, if it is hollow, and the cavity is pressurized by a connection to

those parts of the projectile surface, where the external pressure attains a suitable level. This can be the base for subdetonative projectiles, or the side of the body for those fired in the superdetonative mode.

REFERENCES

- 1 Naumann, K. W., "Heating and Ablation of Projectiles During Acceleration in a Ram Accelerator Tube", AIAA 93-2184, 29th Joint Prop. Conf., Monterey, 1993
- 2 Naumann, K. W., "Structural Heating and Ablation of Projectiles During Acceleration in a Ram Accelerator Tube", 1st Int. Workshop on Ram Acceleration, ISL, Saint-Louis, France, 1993
- 3 Dubbel, "Taschenbuch für den Maschinenbau", Vol. 1, 13th Ed., Springer Berlin Heidelberg New York, 1974
- 4 Smeets, G., Seiler, F., Patz, G., Srulijes, J., "First Results Obtained in a 30-mm-Caliber Scram Accelerator Using a Rail Tube for Cylindrical Projectiles", 25th Int. Symp. on Combustion, Irvine, CA, USA, July 31 - Aug. 5, 1994
- 5 Naumann, K. W., Smeets, G., "Die Durchwärmung von dünnen Körpern im hyperrasanten Flug", ISL R 126/89, 1989 (German and French)
- 6 Oertel, H., "Shock Tubes", Springer Wien New York, 1966 (German)
- 7 Bruckner, A. P., Knowlen C., University of Washington, Seattle, WA, USA, private communication, 1993
- 8 Smeets, G., "Abschätzungen zur Aufheizung schneller Flugkörper", ISL N 603/87, 1987
- 9 Naumann, K. W., Smeets, G., "Aerodynamic Heating of KE- and Hypervelocity Projectile Structures", Proc. 12th Int. Symp. Ballistics, San Antonio, TX, 1990
- 10 Schlichting, H. "Grenzschicht-Theorie", Braun Karlsruhe, Germany, 1982

Table 1

Material	ρ kg/m ³	c J/kgK	λ W/mK	α 1/10 ⁶	E GPa
AlZn6MgCu	2800	915	130	23,5	72
AlCu4MgSi	2790	920	134	23	74
MgAl8Zn	1800	1047	75	27	47
Ti90Al6V4	4420	540 ¹	5,8	8	110

Tab. 1 Data of some materials

Table 2

p_{cone}	6 MPa
$\dot{q}_{w,\text{max,cone}}$	160 MW/m ²
\bar{T}_r	2000 K
t	1.5 ms

Tab. 2 Data of ISL shot #8

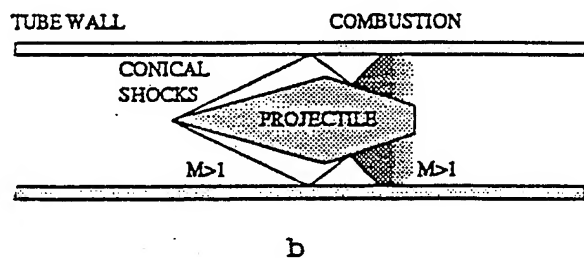
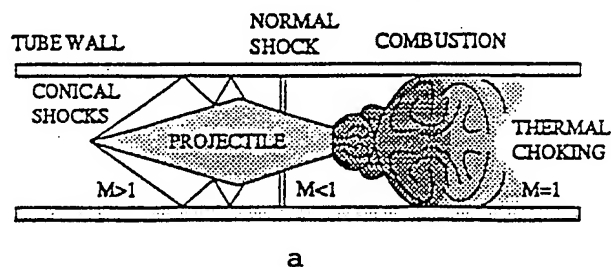


Fig. 2 Ram accelerator propulsion modes a) subdetonative, b) superdetonative

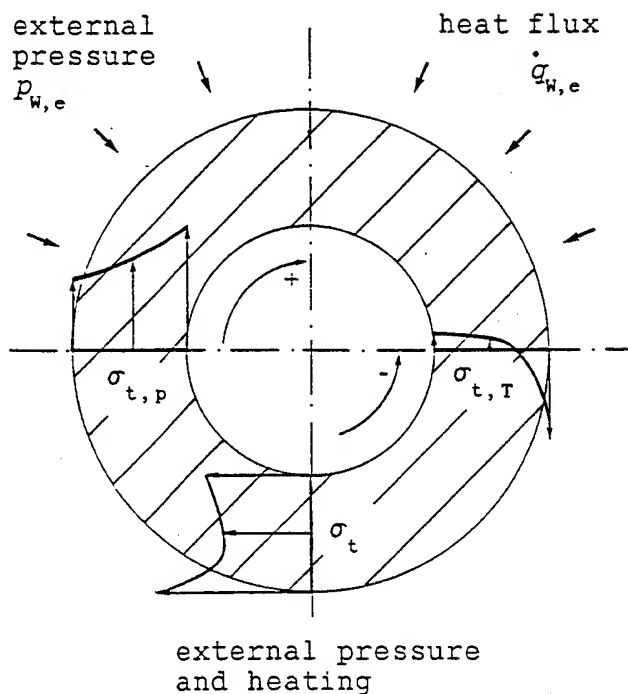


Fig. 1 Sketch of a body under combined pressure and thermal load.

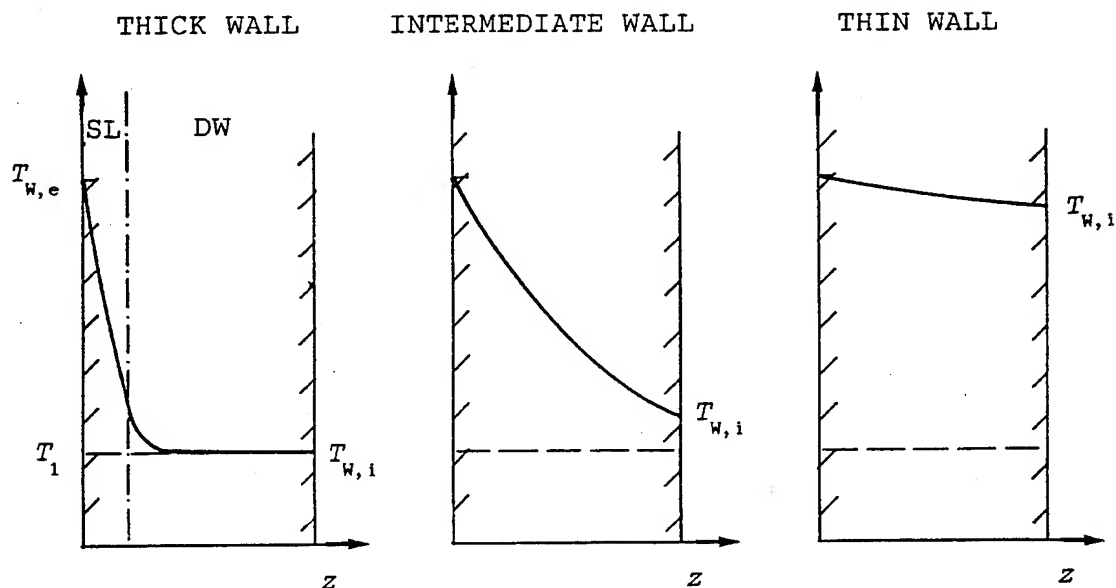


Fig. 3 'Thick', 'intermediate' and 'thin' walls.

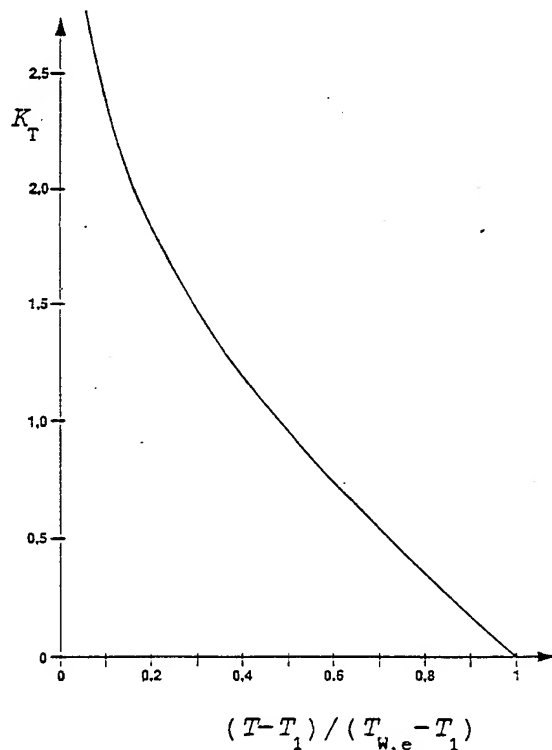


Fig. 4 K_T over $(T-T_1)/(T_{w,e}-T_1)$.

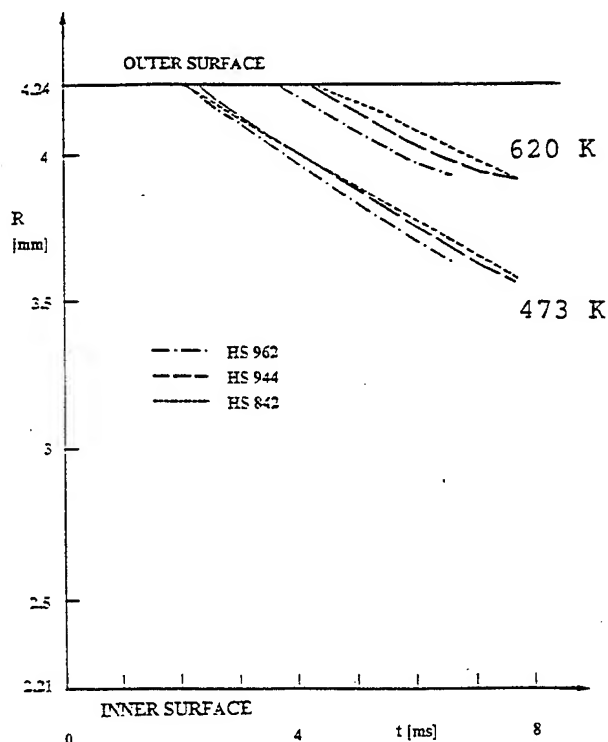


Fig. 6 Calculated isothermals for UW shots at point CA.

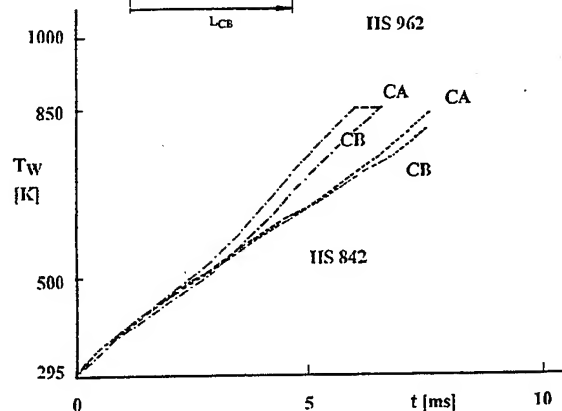
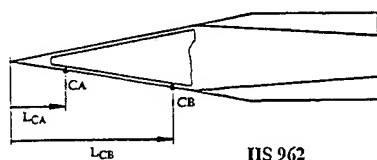
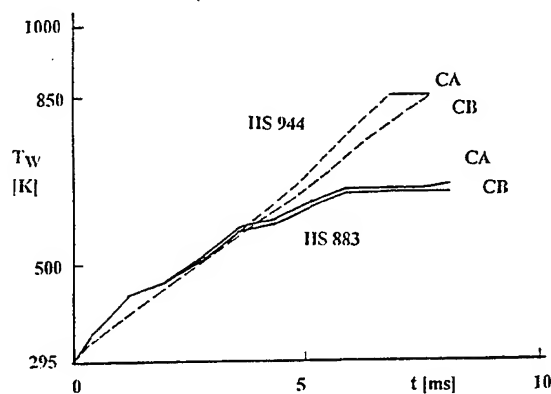


Fig. 5 Calculated surface temperature histories of UW shots.

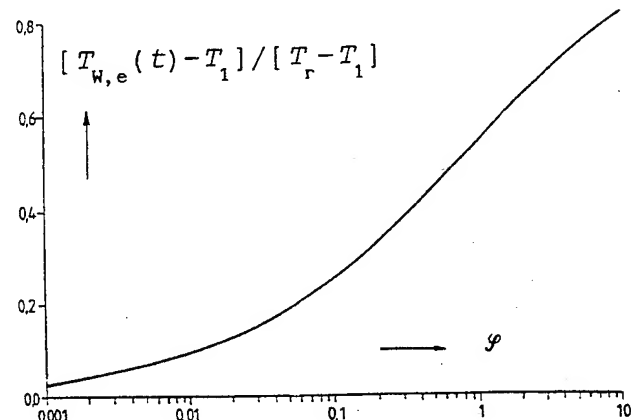


Fig. 7 The function $f\{P\}$.

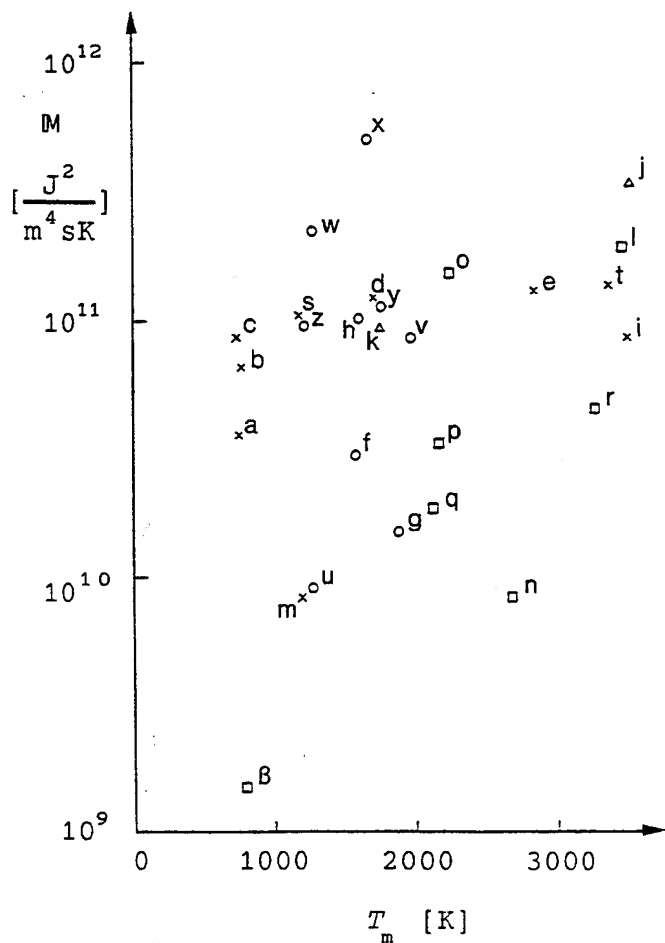


Fig. 8 M over T_m .

Materials in Figs. 8 and 9: a) MgAl8Zn, b) AlCu4MgSi,[®] c) AlZn6MgCu, d) Invar[®], e) TZM, f) Ni55/Ti45, g) Ti90AL6V4, h) Waspalloy[®], i) Densimet[®] tension, j) densimet[®] pressure, k) hardened steel, l) Re, m) Pr, n) Ir, o) Rh, p) V, q) Zr, r) Ta, s) CuZn40Pb2 F68, t) W75/Re25, u) ZrO₂, v) Al₂O₃, w) Shapal[®], x) SiC, y) Sialon[®], z) PBN 200[®], B) Kevlar.

Symbols in Fig. 8:

x exact
o estimated
□ averaged
Δ maximum value
▽ minimum value

Symbols in Fig. 9:

Δ calc. with max. T of use
▽ calc. with T_m

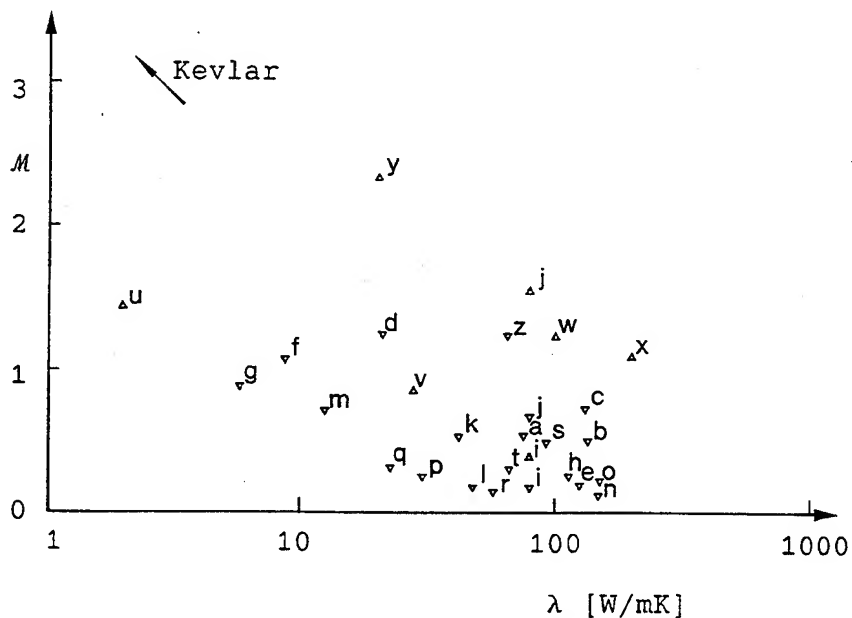


Fig. 9 M over λ .

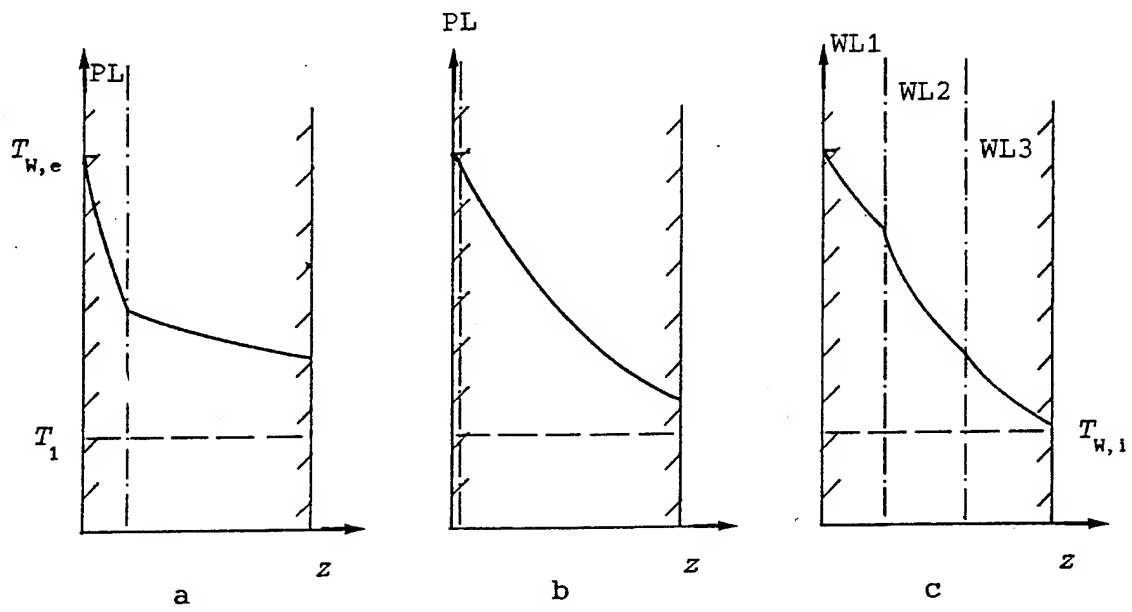


Fig. 10 Different kinds of inhomogeneous walls a) heat protecting layer b) oxidation protecting layer c) layered wall.

COMPUTATIONAL STUDY OF PROJECTILE NOSE HEATING IN A RAM ACCELERATOR

G. Chew and A.P. Bruckner
Aerospace and Energetics Research Program
University of Washington, FL-10
Seattle, WA, USA, 98195

EXTENDED ABSTRACT

Introduction

For nearly a decade, research has been conducted at the University of Washington on the ram accelerator,¹⁻³ a ramjet-in-tube device that propels projectiles to high velocities. In a ram accelerator, a projectile travels supersonically through a combustible mixture of gases within a sealed tube. The accompanying shock system compresses the gas flow, which combusts in a zone that travels with the projectile. The resulting pressure distribution generates thrust that accelerates the projectile. In spite of the extensive research performed on the ram accelerator, its maximum demonstrated velocity has been limited by a lack of detailed understanding of the involved processes. In particular, the effects of supersonic aerodynamic heating on ram accelerator projectiles are potentially significant, but have not yet been studied with any detail. However, recent experimental and numerical research sheds new light on this topic. To aid in this endeavor, a new numerical code has been developed, which couples the flow of gases around the projectile to the conduction of heat within the nose alloy. The current study involves both experimental and computational research on the effects of aerodynamic heating on ram accelerator projectiles.

Motivation

Although ram accelerator research has sparked much interest, many of the processes involved are not well understood, such as the effects of localized aerodynamic heating of the projectile and associated blunting of the nose. This problem may limit the velocity capability of ram accelerators, as the aerodynamic heating at high Mach numbers weakens, and even melts, the surface of the projectile.

An examination of the heat flux to the surface of spheres in supersonic flow⁴ shows that the stagnation point heat flux is inversely proportional to the square root of the radius of curvature. Thus, a sharp nose with an attached conical shock can melt quickly into a blunt nose with a detached bow shock. This blunting may have deleterious effects on the flow, stemming from the presence of the entropy layer,⁵ the streamtubes of gas next to the projectile that must pass through the strong (normal to near-normal) shock around the centerline. The hot entropy

layer may induce combustion in the flow earlier than in flow over sharp cones. The effects of early ignition include movement of the combustion zone through the subsonic boundary layer from behind the projectile up onto the projectile itself, and possibly to the nose. While combustion on the body has been speculated as producing thrust at velocities greater than the Chapman-Jouguet detonation speed of the gas mixture,⁶ combustion on the nose may lead to choking of the flow at the throat and an undesired unstart. (In ram accelerator experiments testing the limits of operation, the experiment often ends with the cessation of projectile acceleration within the tube, and the formation of a normal shock ahead of the projectile. The situation is analogous to ramjet engine unstarts, and hence the term is also used in conjunction with ram accelerators. The causes of unstarts are not yet completely understood.) Consequently, aerodynamic heating can have a twofold effect: it can weaken the nose cone and it can change the aerodynamics of the flow, possibly adversely affecting overall ram accelerator performance. In order to design for these detrimental effects and minimize them, aerodynamic heating of ram accelerator projectiles needs to be better quantified.

Research Methodology

A series of laboratory experiments compare projectiles with identical external projectile configurations, but made of different alloys, operating under similar conditions. Any differences in velocity history would be expected to result mainly from the differences in the thermal and mechanical properties of the alloys. The experimental data consist of a series of experiments to compare the maximum velocity attained by nearly identical projectiles, differing mainly in the alloy used to construct the nose. These experiments provide a controlled study of the effects of projectile material on overall performance.

Because of the limitations in the available instrumentation in the ram accelerator facility at the University of Washington, computational methods are needed for more in-depth study of aerodynamic heating. Thus, to complement the experimental effort, a more general computer program has been written that simulates laboratory experiments. In this program, the Yee-Klopfer-Montagne algorithm⁷ solves the Navier-Stokes equations; the Baldwin-Lomax model⁸ is used to simulate turbulence effects. Heat conduction within the projectile is solved using a standard Alternating Direction Implicit method⁹ on the unsteady heat equation. The program couples solutions of the gas flow around the projectile to solutions of the heat flow within the projectile through a finite-volume formulation of the energy conservation equation on the gas-solid interface. Typical material properties and velocity histories from laboratory experiments are used in the simulations. Using this computer program, the extent of heat transfer to ram accelerator projectiles in simulated experiments is investigated.

Results

In the laboratory experiments, projectiles with titanium alloy noses generally attain a higher peak velocity, and survive for longer periods of time at high velocity, than standard projectiles with aluminum alloy noses. Since the major variation in parameters is the nose alloy,

the implication is that the inherent differences in properties of the alloys, particularly mechanical strength, heat capacity, density, and thermal conductivity, are major factors in limiting the maximum velocity of the projectile. The data indicate that the more refractory noses endure the harsh conditions of high-velocity ram acceleration better than the standard aluminum noses.

Using the computer simulation program, the temperature histories of projectiles were reconstructed from the velocity histories of the experiments. Analyses of the state of stress in the projectiles confirm that the aluminum projectile nose tips are likely melting, eroding into a blunt configuration, while the titanium nose tips do not melt and thus are much less likely to erode, remaining sharp. Further simulations with blunt nose tips indicate that, although blunting reduces the heat flux to leading edges of hypersonic bodies, melting temperatures are still reached in these noses. Projectile noses with larger cone half-angles are shown to likely experience even worse tip erosion than standard noses, due to the higher temperatures and pressures behind steeper conical shocks. A simulation of a high-strength steel nose indicates that steel is somewhat resistant to heat, much like titanium. Thus, nose cones made of more refractory alloys are predicted to retain structural integrity, and thus attain higher maximum speeds.

A goal of these simulations is to design a nose that both resists erosion due to aerodynamic heating and is low in mass. The most promising projectile nose configuration seems to be one with a basic aluminum structure, but coated with a refractory material. The simulation of a titanium-clad aluminum nose indicated that such a nose would combine the better properties of the two materials; namely, the low thermal diffusivity, high strength, and high melting temperature of titanium, with the relatively low density and good strength-to-weight ratio of aluminum. Such a projectile nose would be lightweight, yet shielded from the deleterious effects of aerodynamic heating.

References

1. Hertzberg, A., Bruckner, A.P., and Bogdanoff, D.W., "Ram Accelerator: A New Chemical Method for Accelerating Projectiles to Ultrahigh Velocities," AIAA Journal, Vol. 26, No. 2, 1988, pp. 195-203.
2. Bruckner, A.P., Knowlen, C., Hertzberg, A., and Bogdanoff, D.W., "Operational Characteristics of the Thermally Choked Ram Accelerator," Journal of Propulsion and Power, vol.7, 1991, pp. 828-836.
3. Bruckner, A.P. and Knowlen, C., "Overview of Ram Accelerator Technology," National Shock Wave Symposium, Sendai, Japan, January 14-16, 1993.
4. Anderson, J.D., Hypersonic and High Temperature Gas Dynamics, McGraw-Hill, New York, 1989, pp. 250-256.
5. Ibid, pp. 14, 295-297.
6. Soetrisno, M., Imlay, S.T., and Roberts, D.W., "Numerical Simulations of the Transdetonative Ram Accelerator Combusting Flow Field on a Parallel Computer," AIAA Paper 92-3249, July 6-8, 1992.
7. Yee, H.C., Klopfer, G.H., and Montagne, J.-L., "High-Resolution Shock-Capturing Schemes for Inviscid and Viscous Hypersonic Flows," NASA-TM-100097, April 1988.
8. White, F.M., Viscous Fluid Flow, McGraw-Hill, New York, 1991, pp. 442.
9. Anderson, D.A., Tannehill, J.C., Pletcher, R.H., Computational Fluid Mechanics and Heat Transfer, McGraw-Hill, 1984, p. 117.

MOTIVATION

Hypersonic aerodynamic heating:

$$q_w \approx \frac{1}{2} \rho_\infty V_\infty^3 C_H$$

Stagnation-point heat transfer to a sphere

$$q_w = 0.763 \text{ Pr}^{-0.6} \sqrt{\frac{\rho_e \mu_e}{R}} \left(\frac{2(p_e - p_\infty)}{\rho_e} \right)^{\frac{1}{4}} (h_{aw} - h_w)$$

Ram accelerator projectiles have sharp noses and approach hypersonic Mach numbers.

Aerodynamic heating is a potential problem (recovery temperature can exceed melting temperature)

Effects

- Weakening or melting of the nose cone
- Changing of the aerodynamics of the flow

In order to minimize detrimental effects, aerodynamic heating of ram accelerator projectiles needs to be quantified.

PROJECTILE ALLOYS

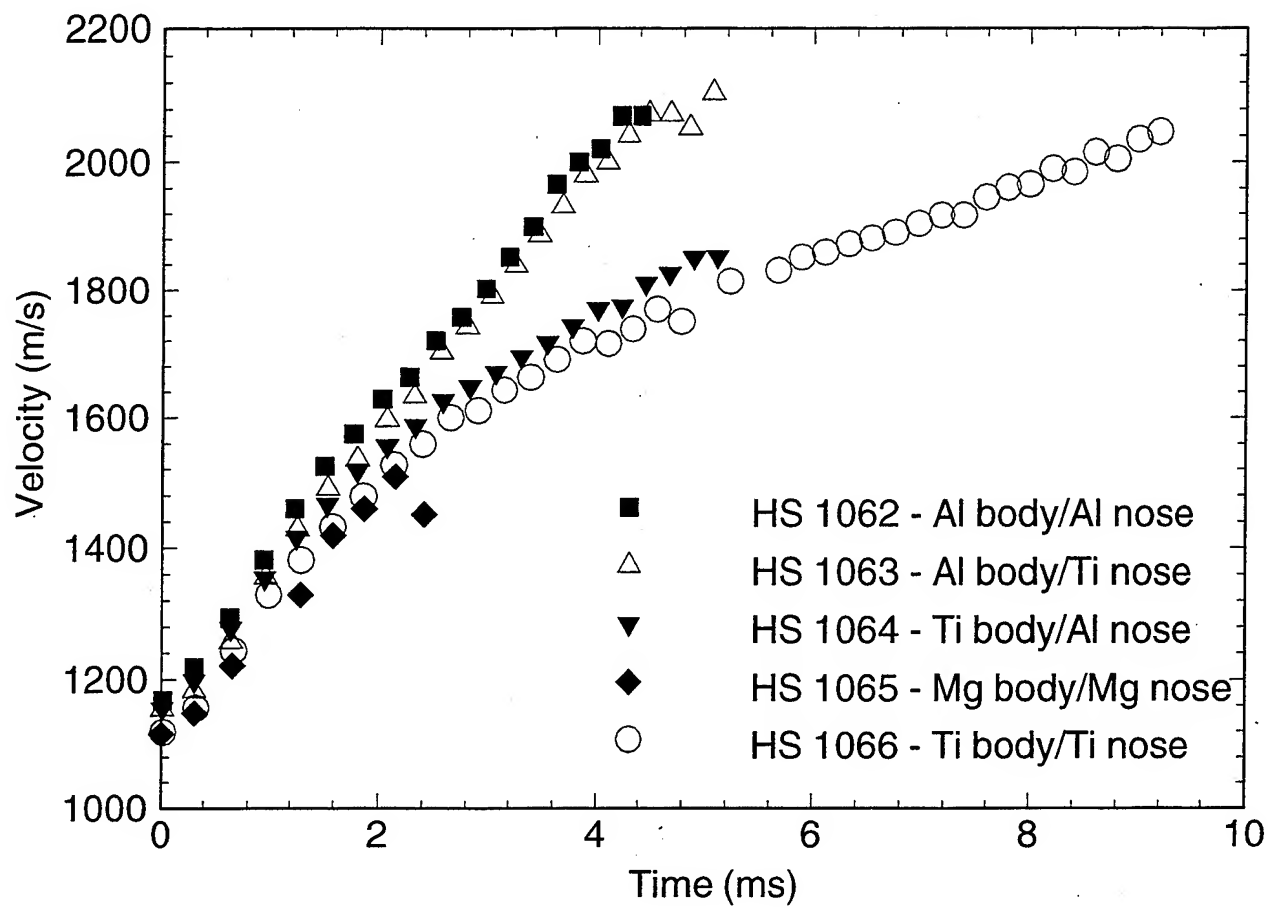
Property	Aluminum 7075-T6	Magnesium ZK60A	Titanium 6Al-4V
Melting Temperature (K)	750-910	795-910	1810-1920
Density (kg/m ³)	2800	1830	4470
Thermal Conductivity (W/m-K)	121-182 (280-590K)	121-132 (310-560K)	7-18 (310-1140K)
Specific Heat (J/kg-K)	835-1045 (300-590K)	1045-1340 (370-750K)	565-837 (310-1030K)
Yield Tensile Strength (10 ⁸ Pa)	4.8 (310 K) 0.5 (590 K)	3.6 (293K) 1.0 (500K)	10.2 (310 K) 1.8 (1140K)

ALLOY VARIATION EXPERIMENTS

EXPERIMENT NO.	HS 1062	HS 1063	HS 1064	HS 1065	HS 1066
Body alloy	Al	Al	Ti	Mg	Ti
Nose alloy	Al	Ti	Al	Mg	Ti
Total Mass (g)	76.85	86.63	100.95	107.16	108.70
Tube Fill Pressure (Pa)	$5.0(10^6)$	$5.1(10^6)$	$5.1(10^6)$	$5.2(10^6)$	$5.1(10^6)$
Max. Velocity (m/s)	2070	2100	1850	1510	2046
Unstart?	Yes	Yes	Yes	Yes	No

VELOCITY HISTORIES

Single-Stage Ram Accelerator



FLUID DYNAMICS SOLVER

Yee-Klopfer-Montagne Scheme

- Implicit
- 2-D or Axisymmetric Unsteady Navier-Stokes Equations
- Second-Order Accuracy in Space and Time

Polynomial Model of Enthalpy (Non-calorically perfect)

Baldwin-Lomax Turbulence Model (Eddy viscosity)

$$\mu = \mu_L + \mu_T$$

$$k = k_L + k_T$$

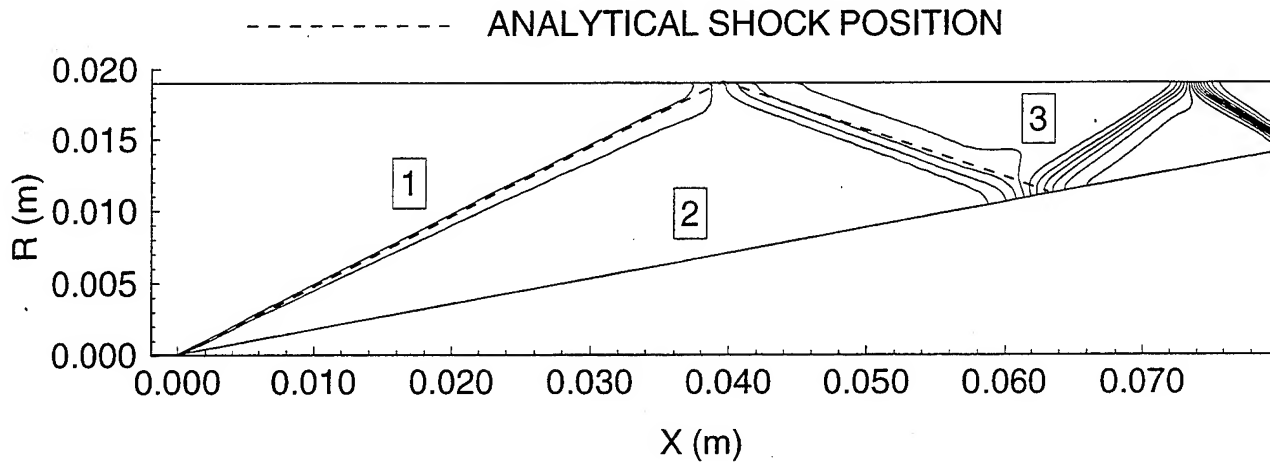
HEAT CONDUCTION SOLVER

Alternating Direction Implicit Scheme

- Implicit
- 2-D or Axisymmetric Unsteady Heat Equation
- Second-Order Accuracy in Space and Time

SUPERSONIC CONVERGING DUCT

Pressure contours

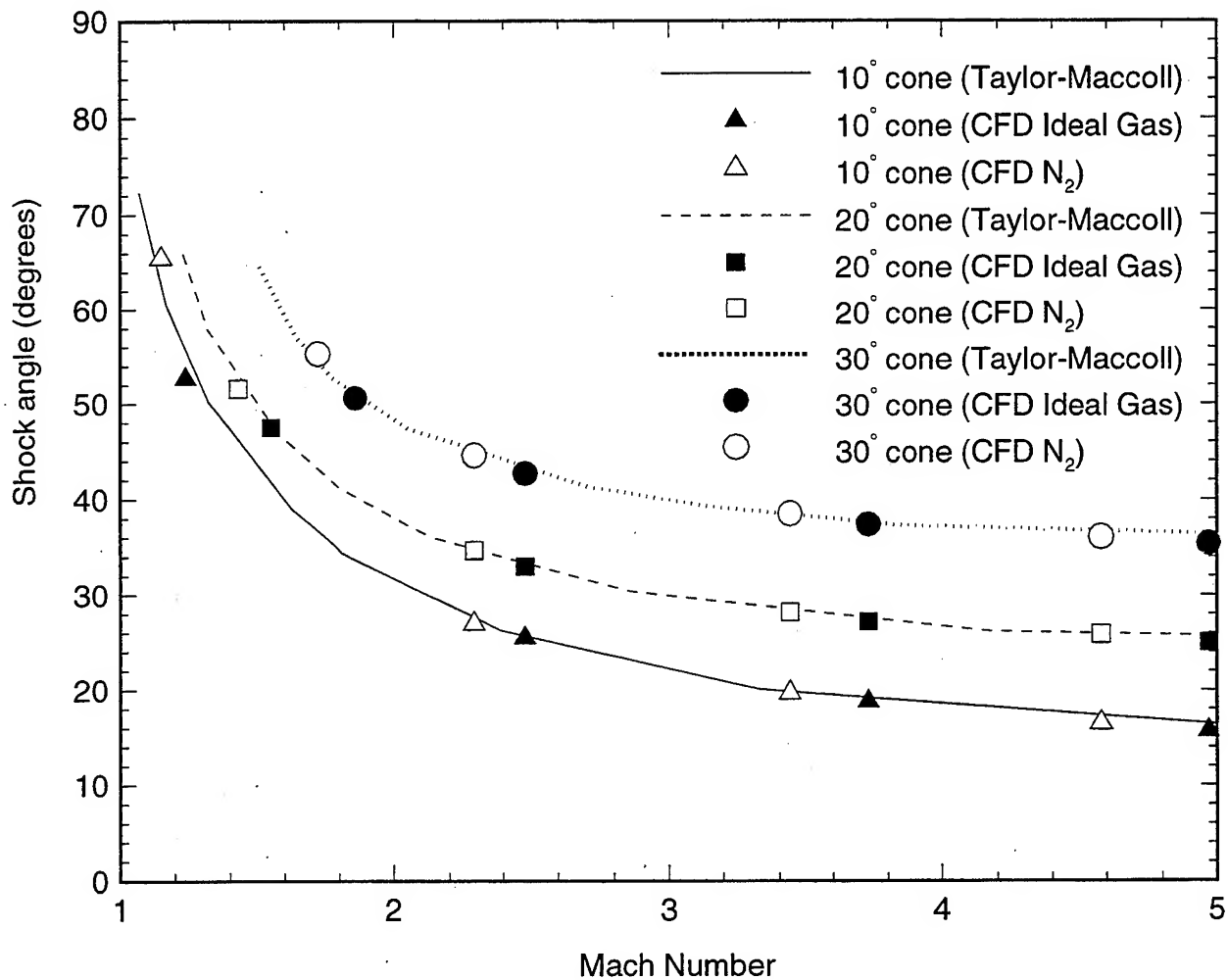


CFD vs. Analytic Solution

Region	Parameter	Analytical Solution (constant c_p)	CFD Solution (thermally perfect gas)
2	Mach Number	2.743	2.739
	Pressure (Pa)	$1.103(10^7)$	$1.100(10^7)$
	Density (kg/m^3)	100.1	99.59
	Temperature (K)	371	372
3	Mach Number	2.293	2.292
	Pressure (Pa)	$2.154(10^7)$	$2.145(10^7)$
	Density (kg/m^3)	160.1	159.2
	Temperature (K)	453	454

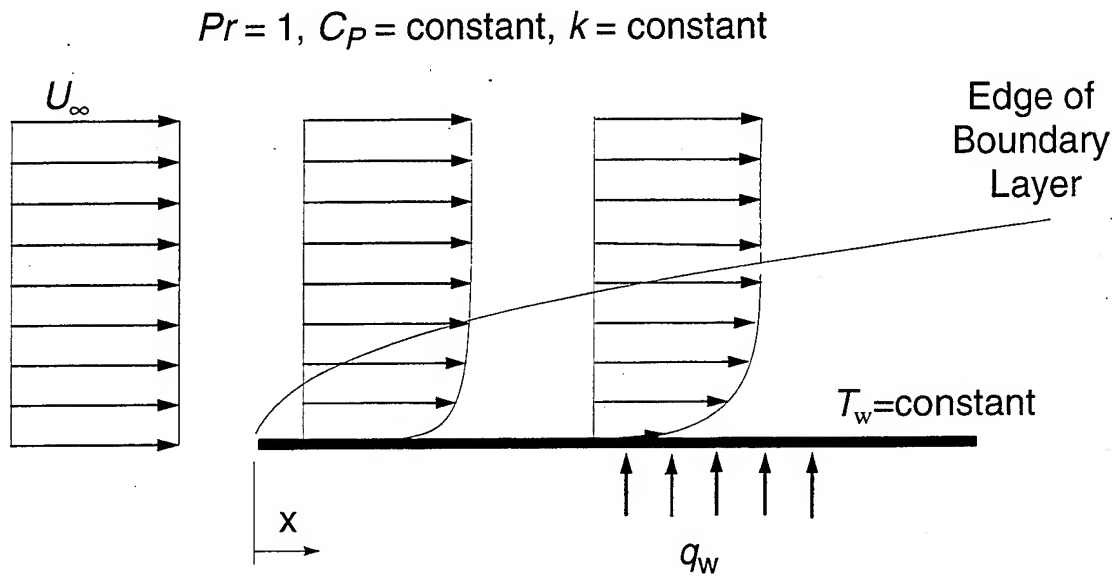
SUPERSONIC CONICAL FLOW

Comparison of conical shock angles



ISOTHERMAL FLAT PLATE

Schematic of Test Configuration



Laminar Flow Test Case

Gas = air

$T_{\text{plate}} = 586.4 \text{ K}$

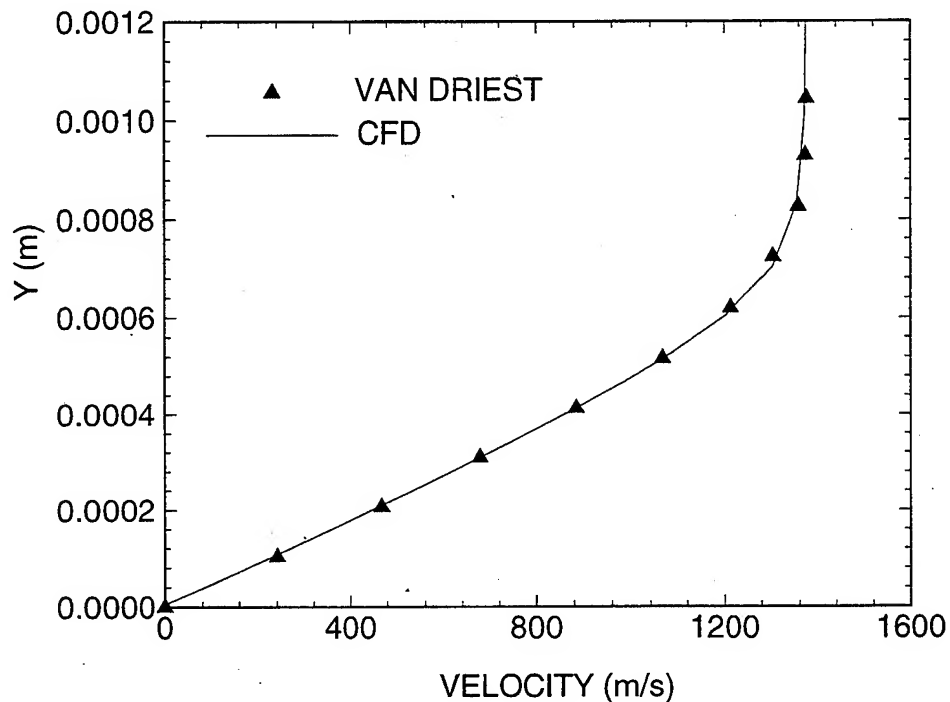
$T_\infty = 293.2 \text{ K}$

$V_\infty = 1376 \text{ m/s (Mach 4)}$

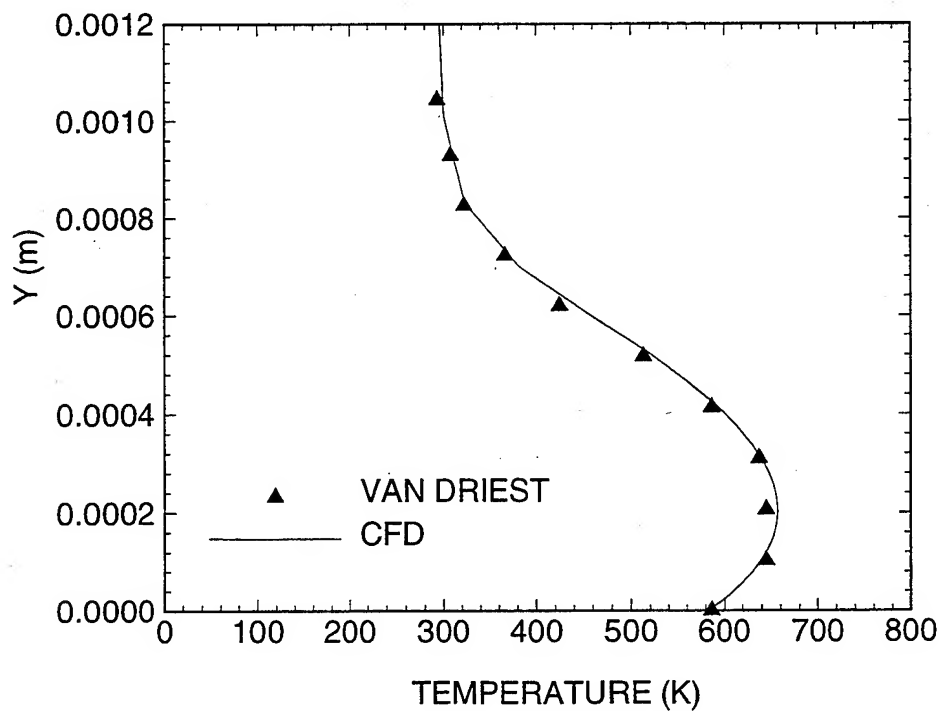
ISOTHERMAL FLAT PLATE

CFD and Van Driest Solutions - Laminar Flow

Velocity profile (0.5 m from front of plate)



Temperature profile (0.5 m from front of plate)



ISOTHERMAL FLAT PLATE

CFD Solution vs. Pappas Data - Turbulent Flow

Test Conditions

Gas = air

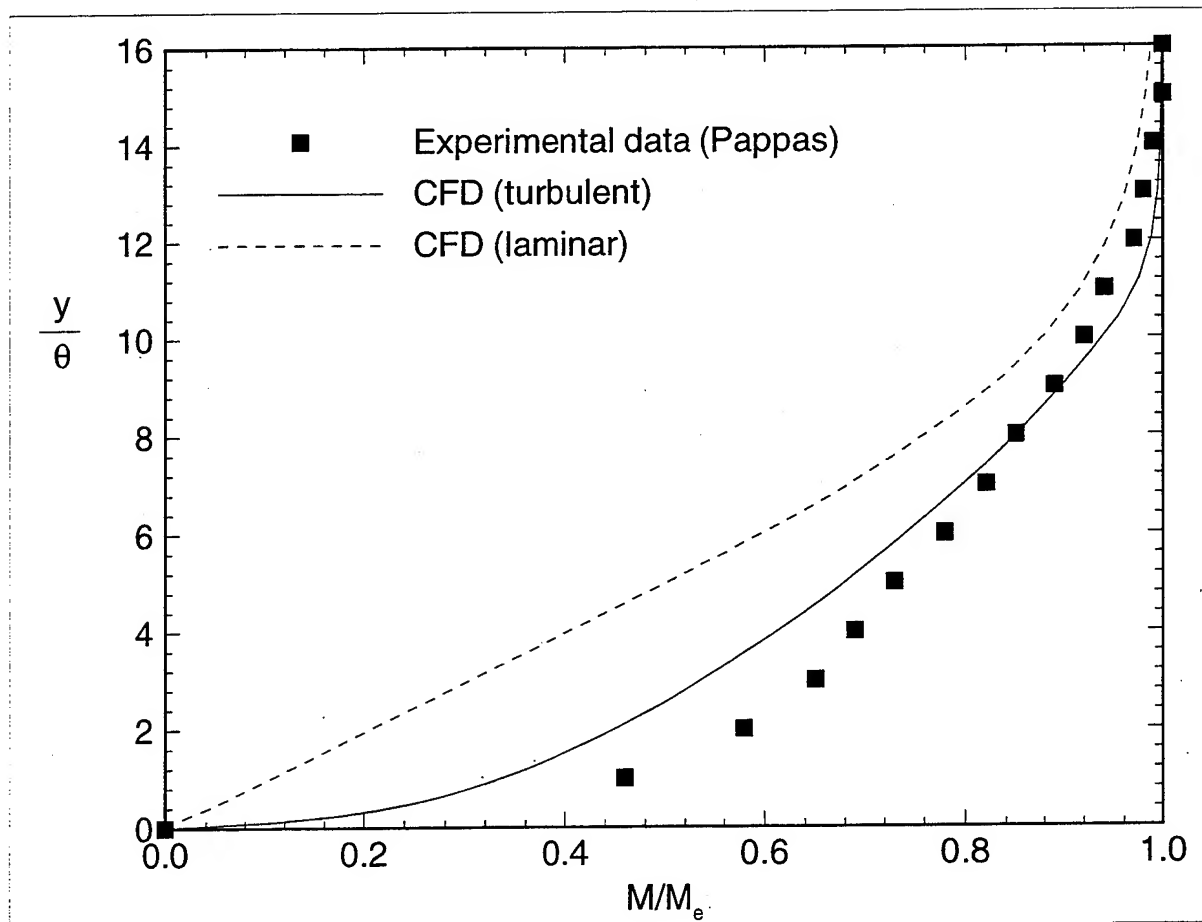
Mach 2.27

$T_0 = 118^\circ \text{ F (320.9 K)}$

$T_w/T_e = 2.19$

$P_0 = 30 \text{ psia (2.069} \times 10^5 \text{ Pa)}$

Mach Number Profile in Turbulent Boundary Layer



UNSTEADY HEAT CONDUCTION

Test Case - Semi-Infinite Slab

$$T_{\text{wall}} = 600 \text{ K}$$

$$T_{\text{initial}} = 100 \text{ K}$$

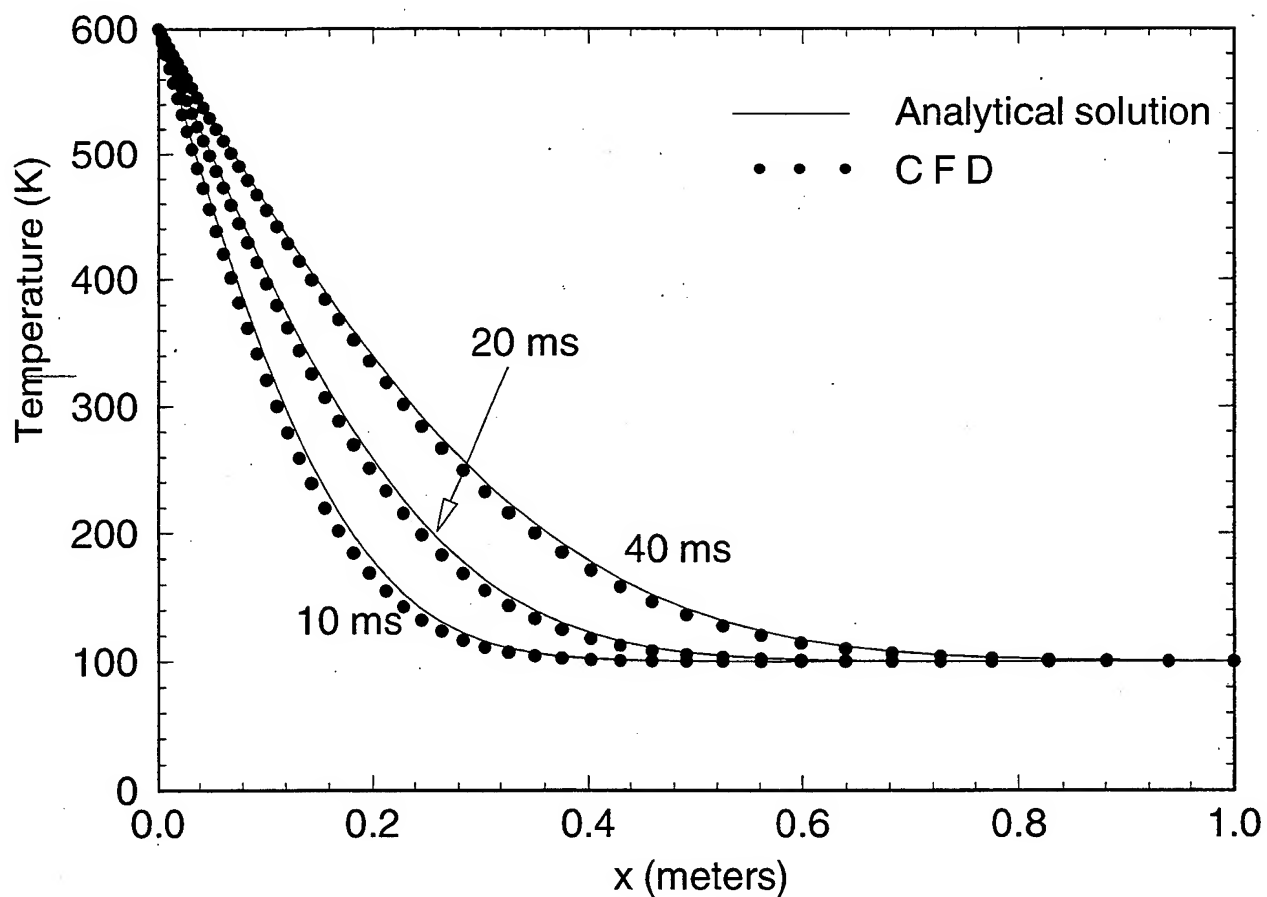
$$k = 1 \text{ W/m}^2\text{-s}$$

$$\rho = 1 \text{ kg/m}^3$$

$$C = 1 \text{ J/kg-}^\circ\text{s}$$

$$\alpha = 1 \text{ m}^2/\text{s}$$

Comparison of Analytic and Computed Temperatures



ANALYSIS OF STRUCTURAL INTEGRITY

FRED Finite Element Program

Inputs

External pressure distribution

Temperature distribution

Output

Principal stresses

Von Mises Yield Criterion

$$(\sigma_1 - \sigma_2)^2 + (\sigma_2 - \sigma_3)^2 + (\sigma_3 - \sigma_1)^2 = 2\sigma_{\text{yield}}^2$$

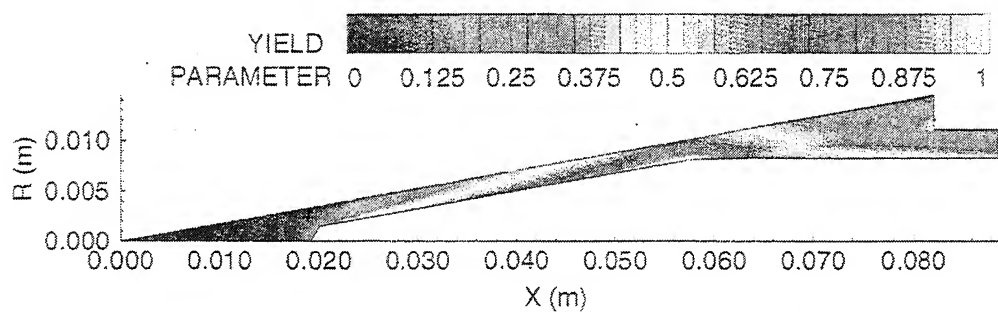
Nondimensional Yield Parameter

$$\frac{\sqrt{(\sigma_1 - \sigma_2)^2 + (\sigma_2 - \sigma_3)^2 + (\sigma_3 - \sigma_1)^2}}{\sqrt{2}\sigma_{\text{yield}}} = \text{"Yield Parameter"}$$

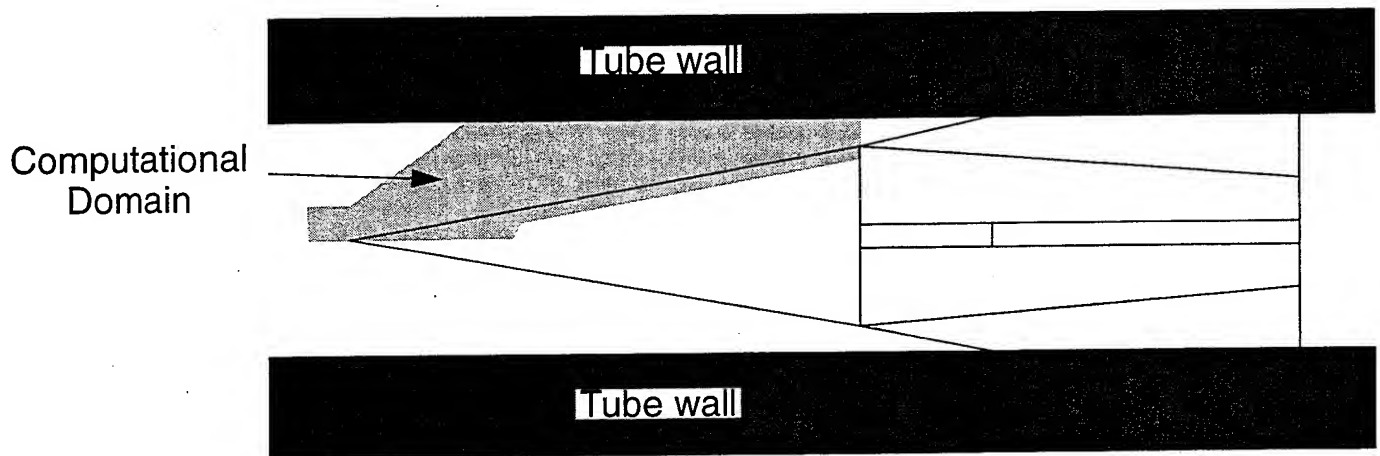
HYDROSTATIC PRESSURE TEST

Standard Machinist Magnesium Nose

P = 8800 psi

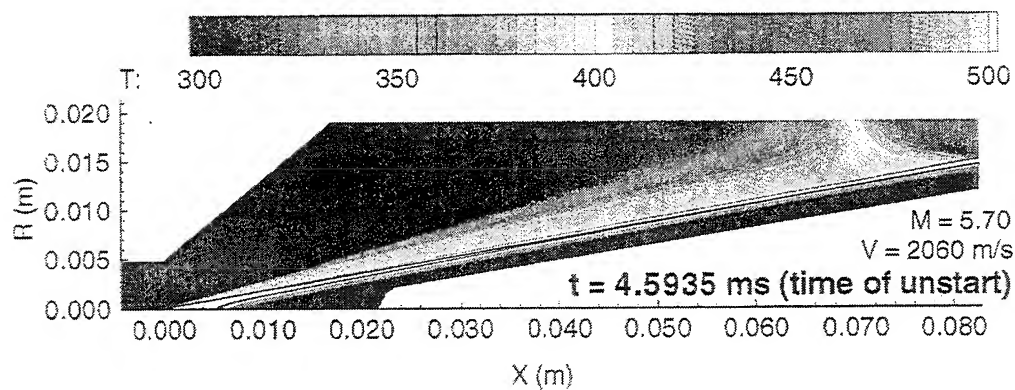
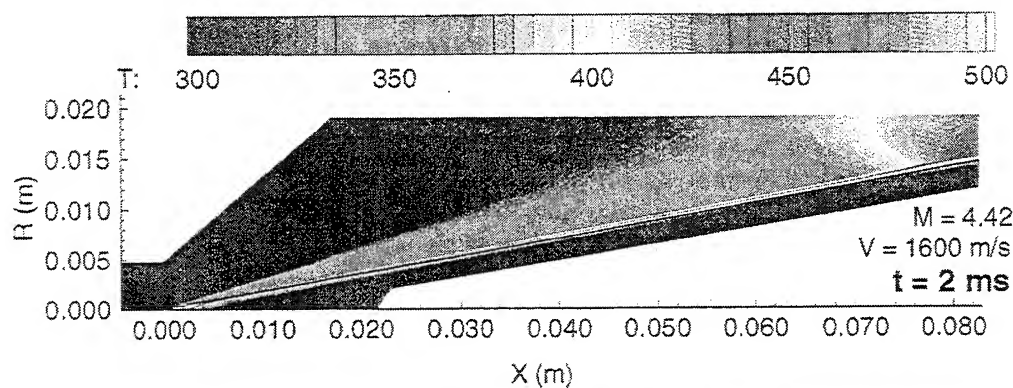
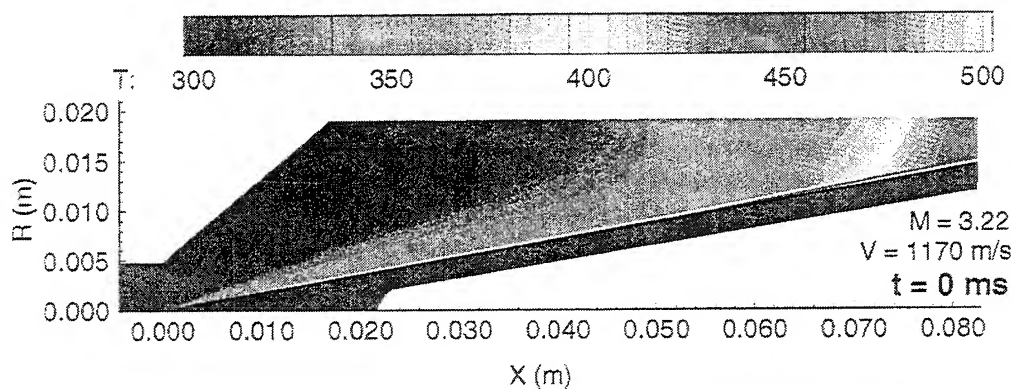


PHYSICAL REGION OF COMPUTATIONAL DOMAIN



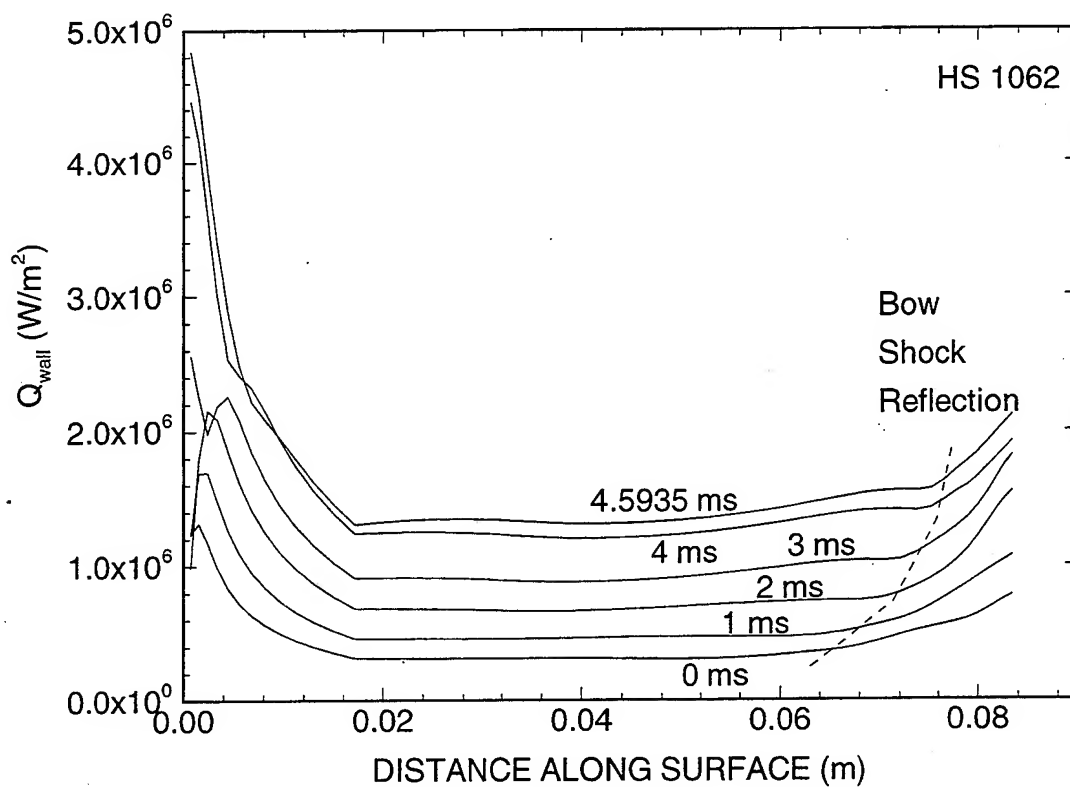
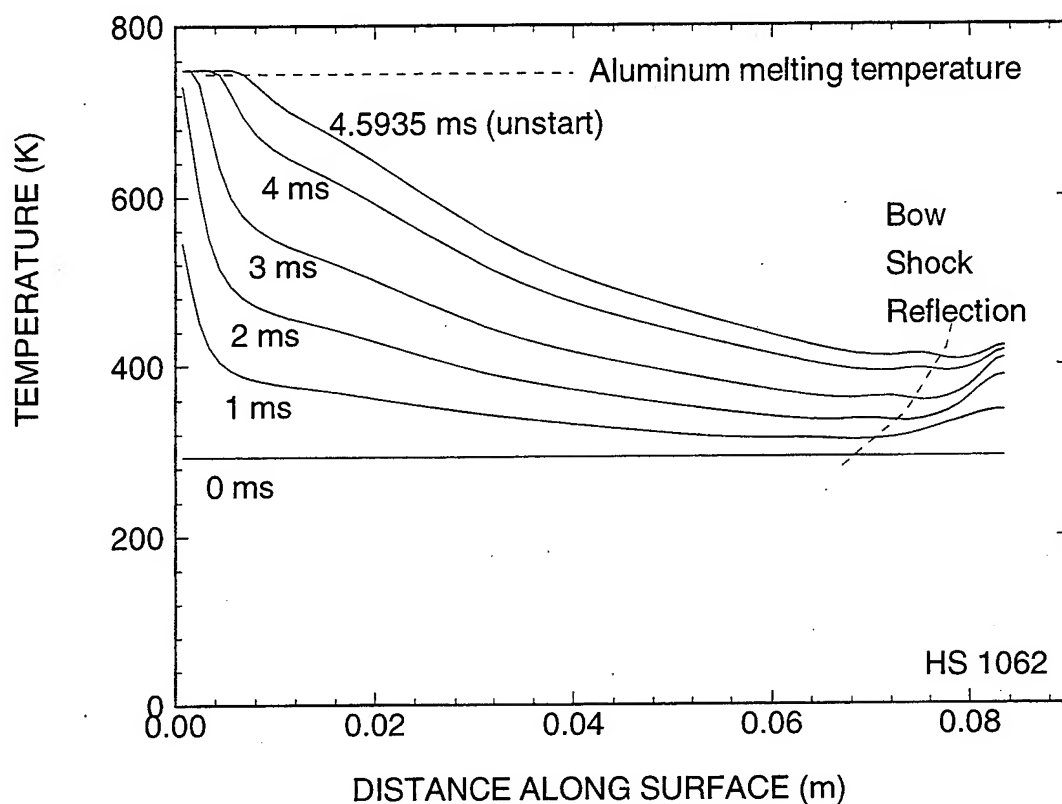
TEMPERATURE DISTRIBUTION

HS 1062 (Al nose, Al body)



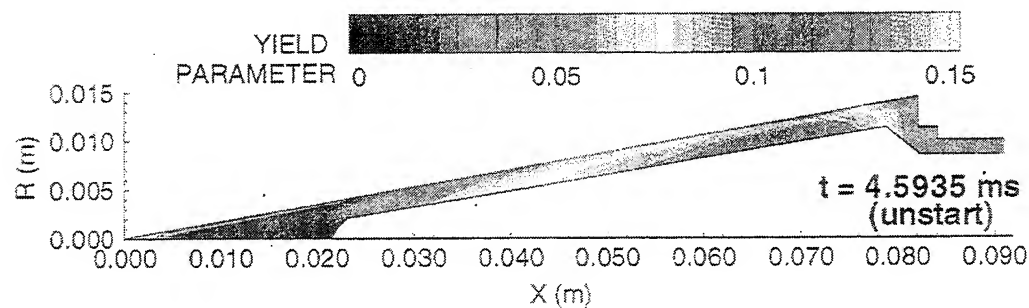
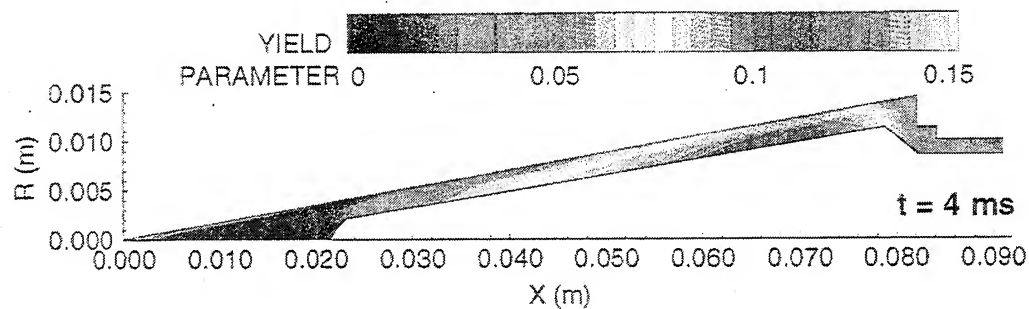
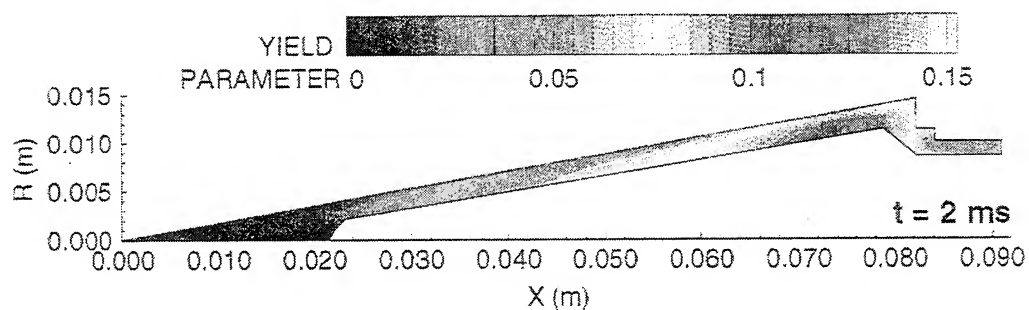
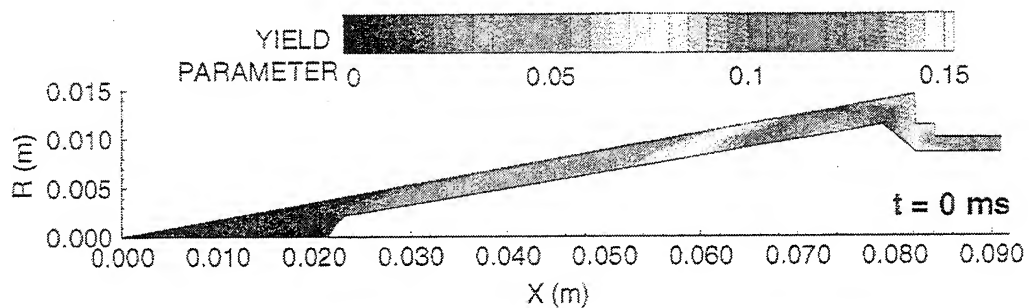
SURFACE TEMPERATURE AND NORMAL HEAT FLUX

HS 1062 (Al nose, Al body)



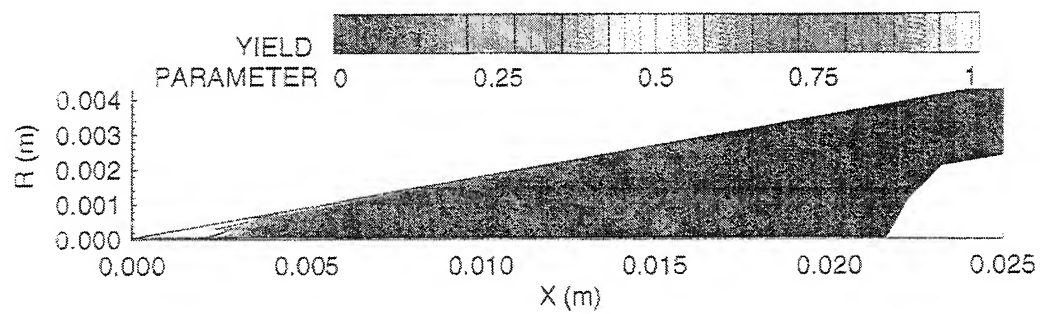
YIELD PARAMETER DISTRIBUTION

HS 1062 (Al nose, Al body)



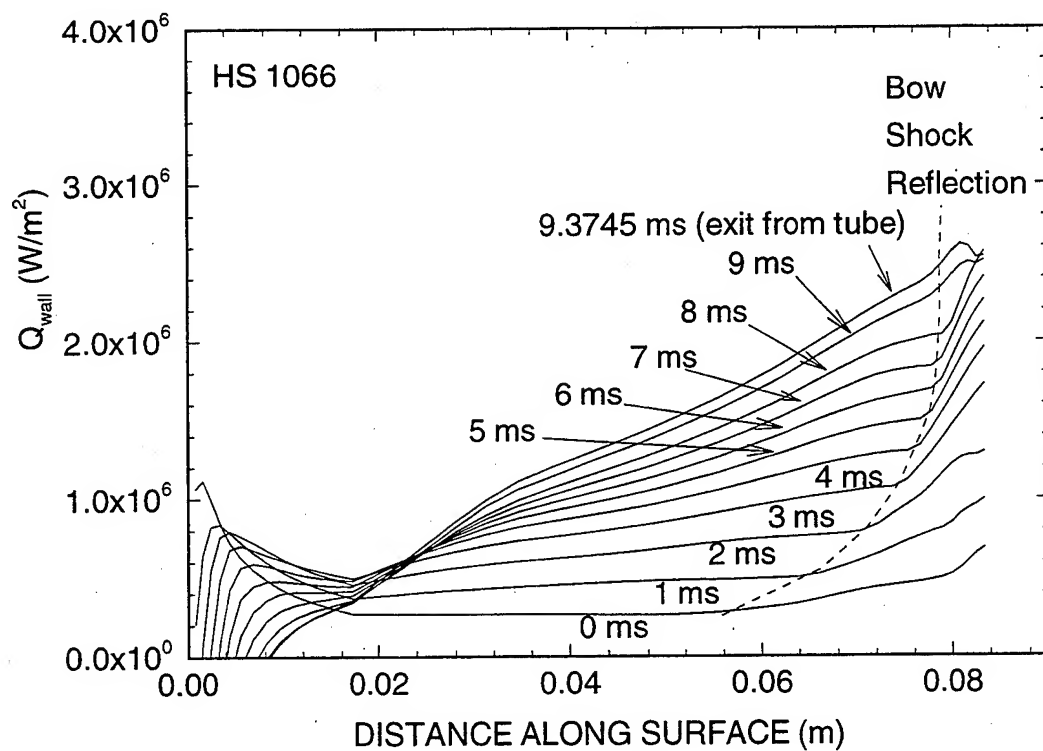
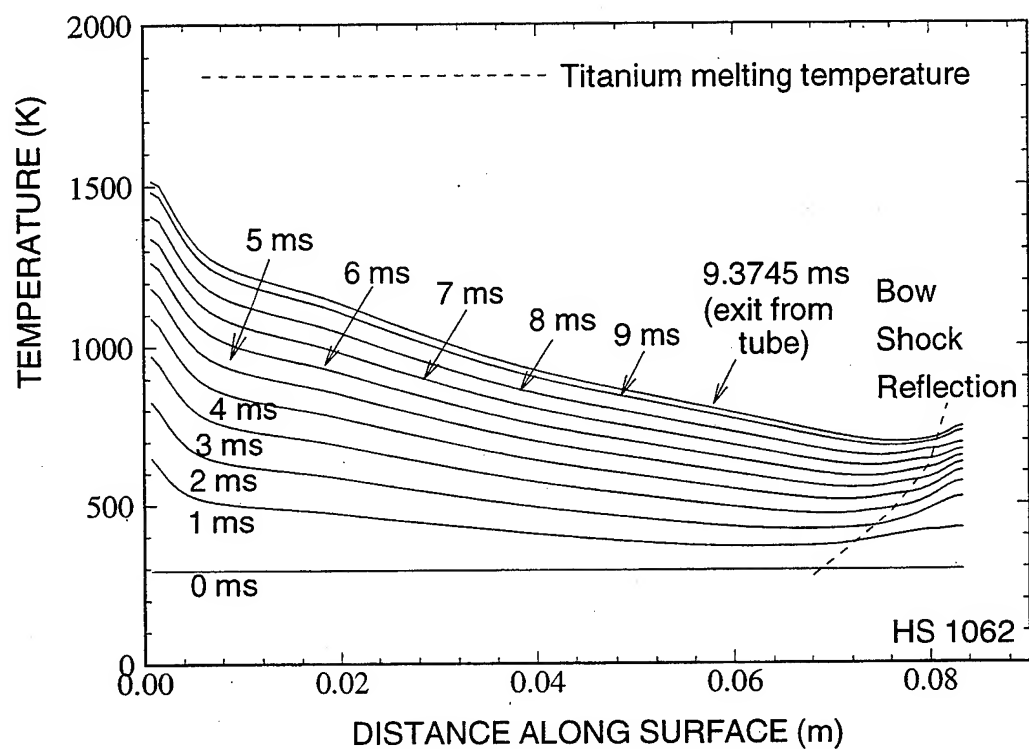
YIELD PARAMETER DISTRIBUTION

Tip of Nose at End of Simulation of HS 1062



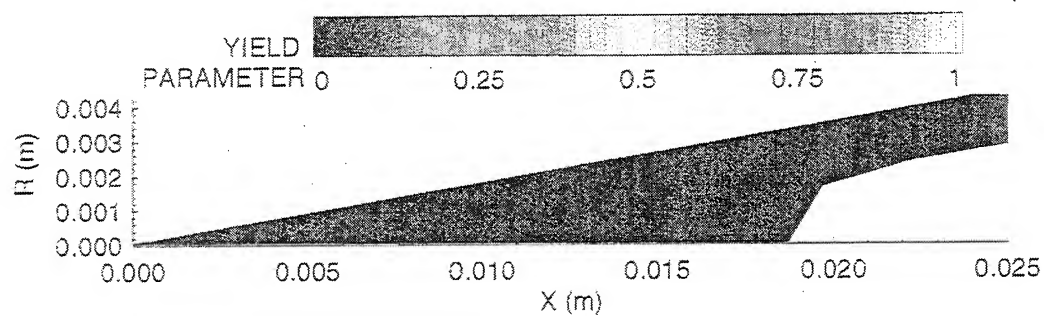
SURFACE TEMPERATURE AND NORMAL HEAT FLUX

HS 1066 (Ti nose, Ti body)



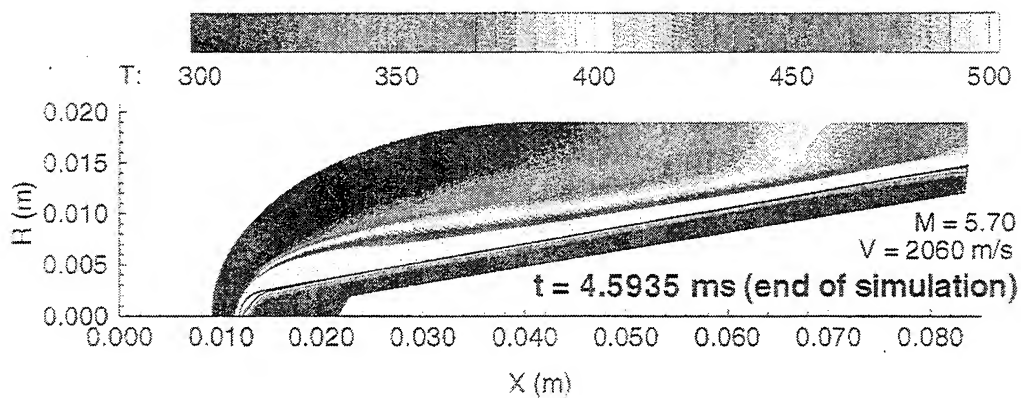
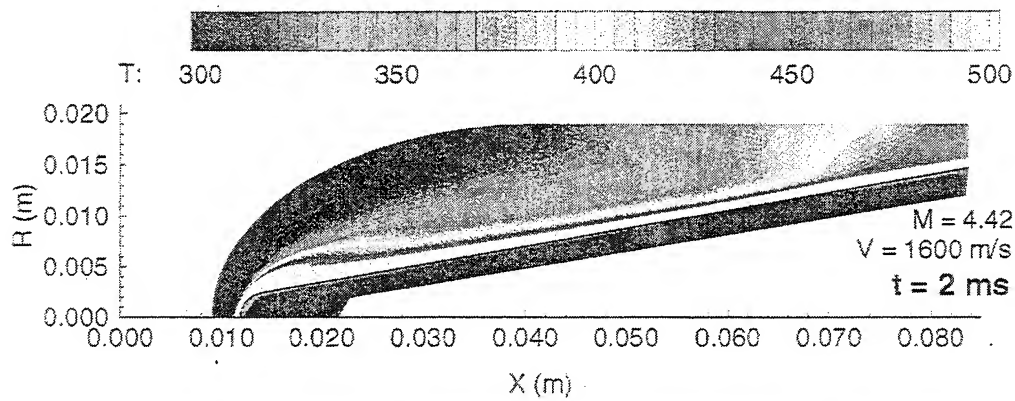
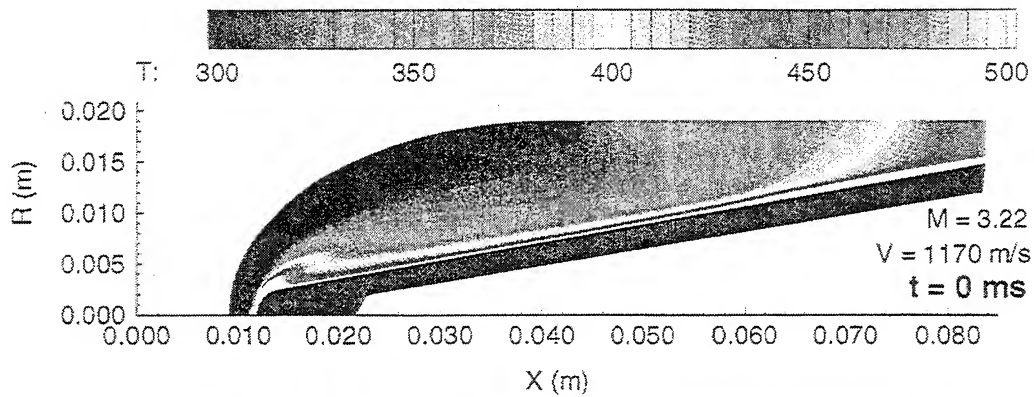
YIELD PARAMETER DISTRIBUTION

Tip of Nose at End of Simulation of HS 1066



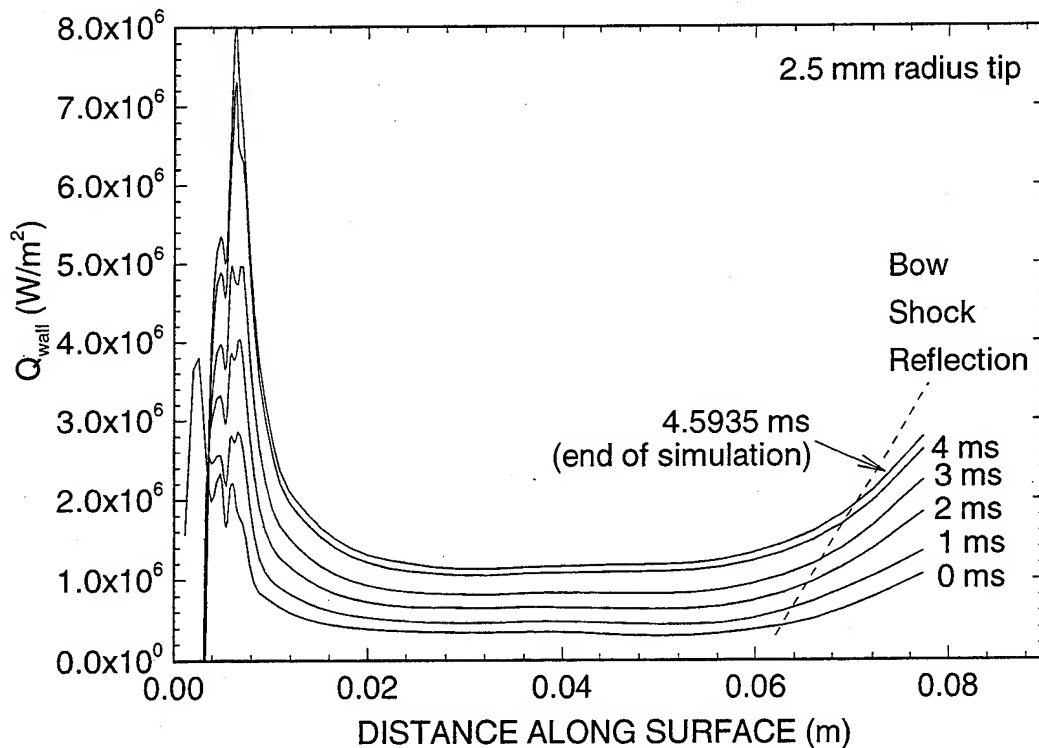
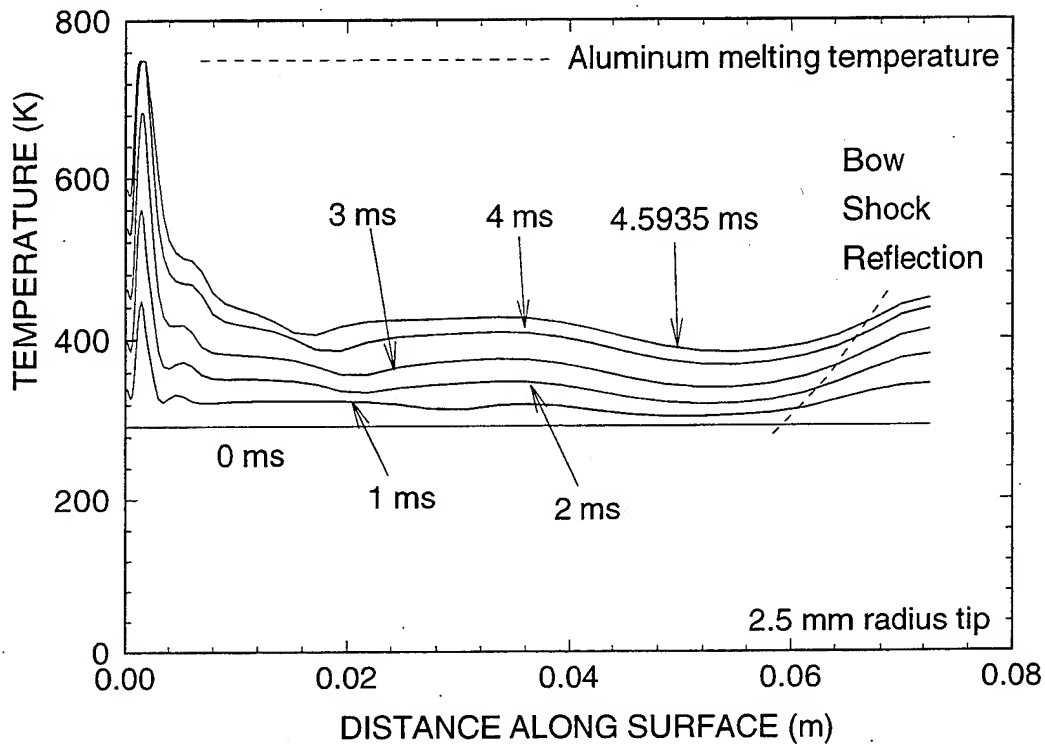
TEMPERATURE DISTRIBUTION

2.5 mm Radius Nose Tip



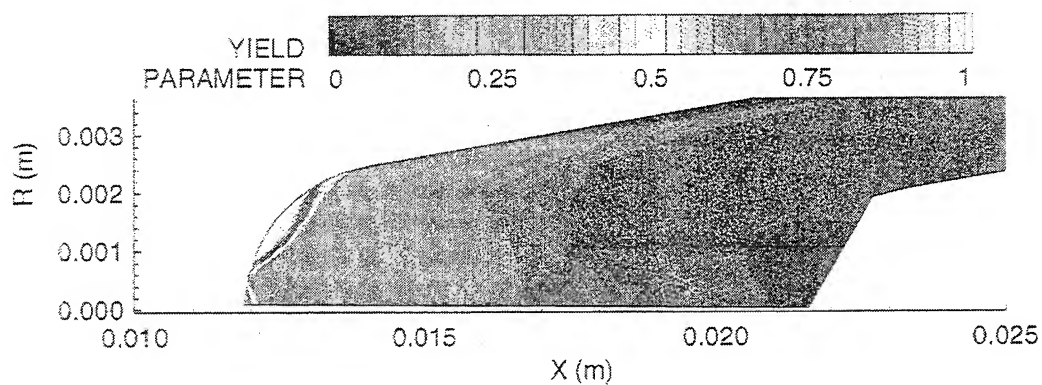
SURFACE TEMPERATURE AND NORMAL HEAT FLUX

2.5 mm Radius Nose Tip



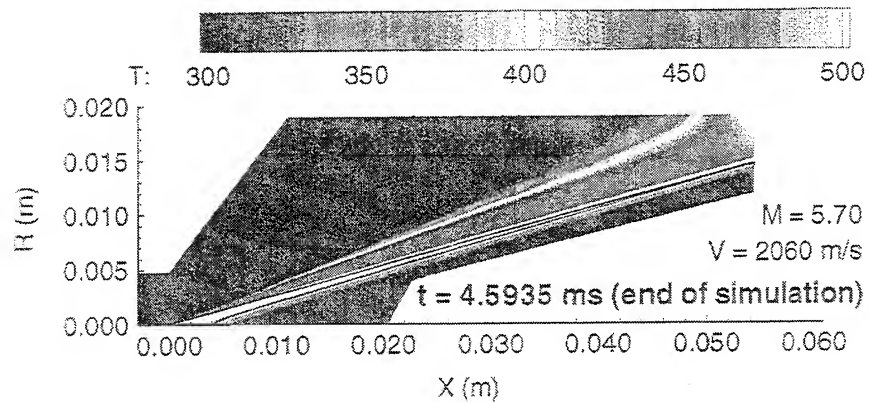
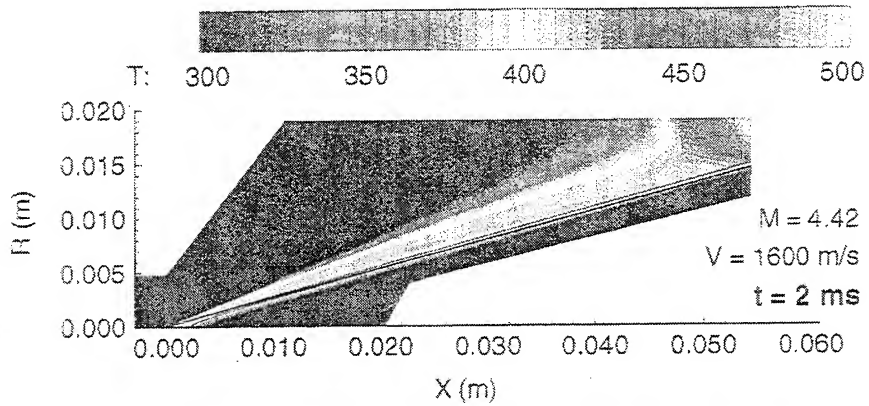
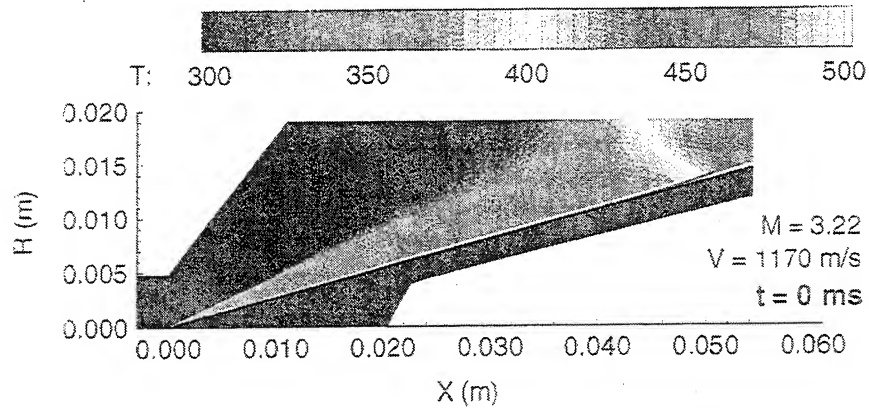
YIELD PARAMETER DISTRIBUTION

2.5 mm Radius Nose Tip at End of Simulation



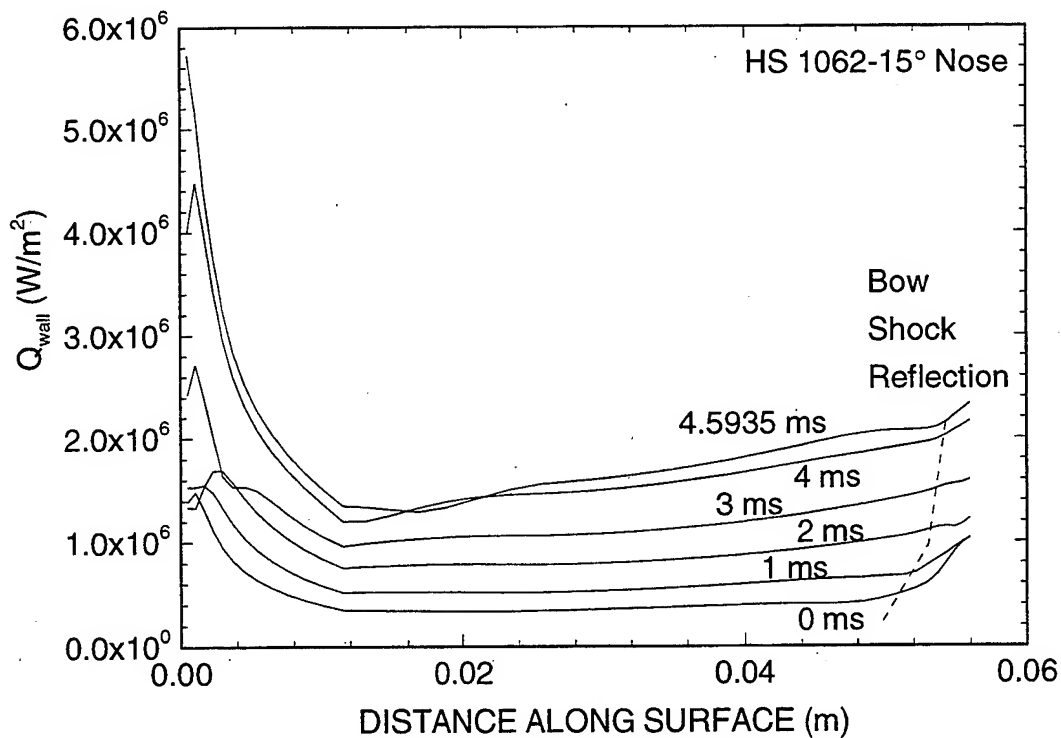
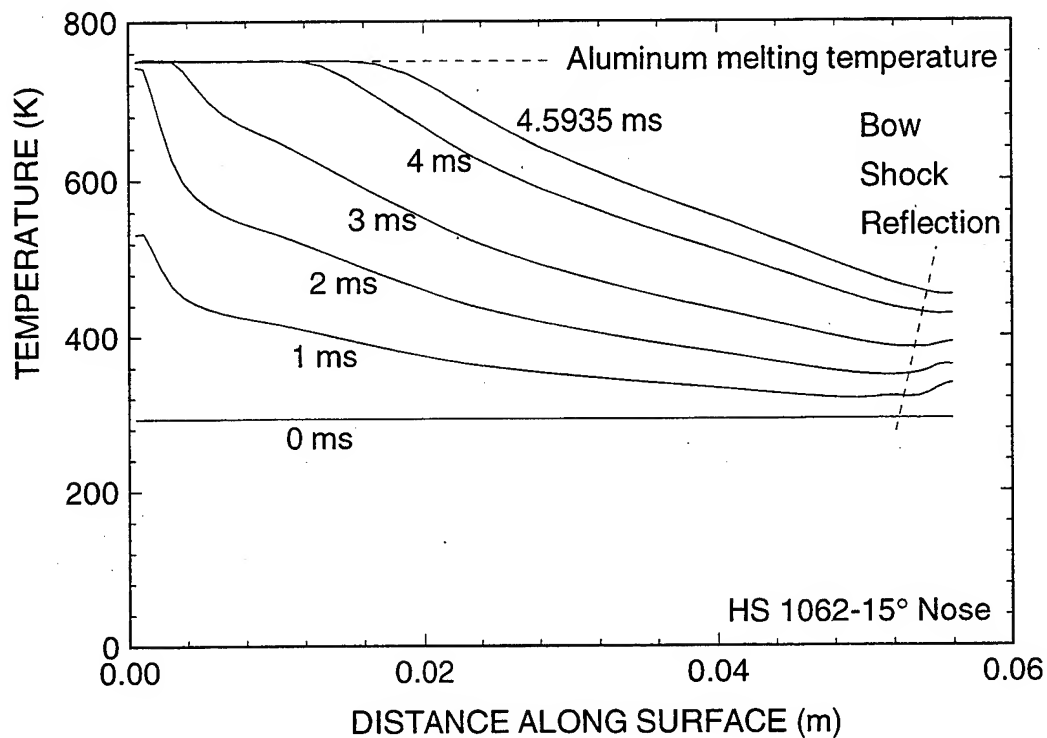
TEMPERATURE DISTRIBUTION

15°-angle nose



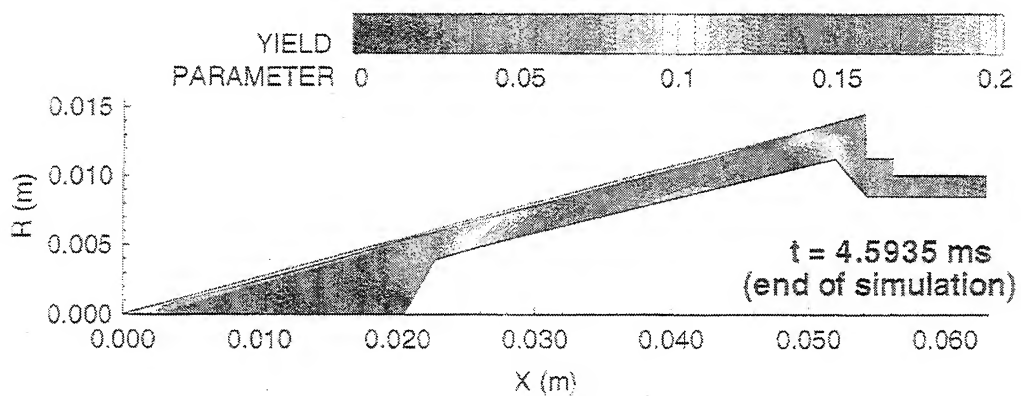
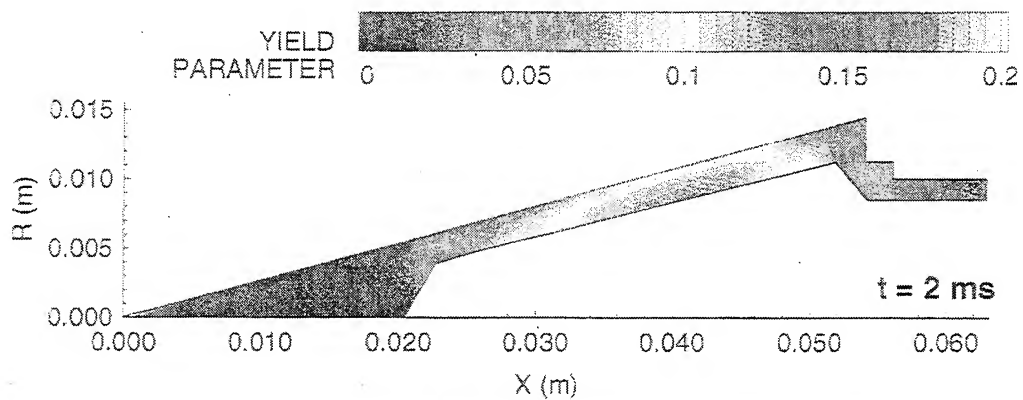
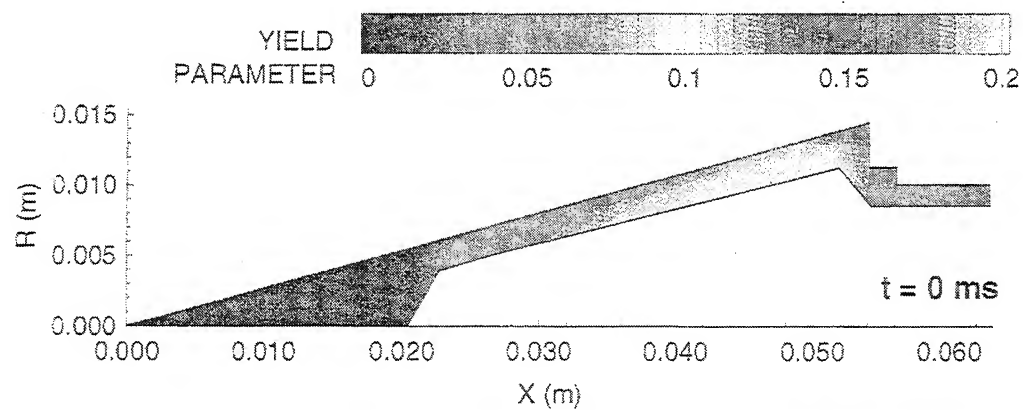
SURFACE TEMPERATURE AND NORMAL HEAT FLUX

15°-Angle Nose



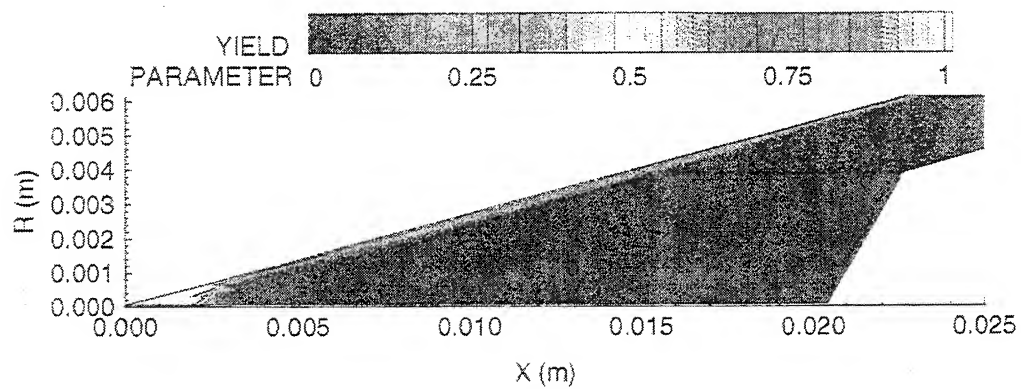
YIELD PARAMETER DISTRIBUTION

15°-angle nose



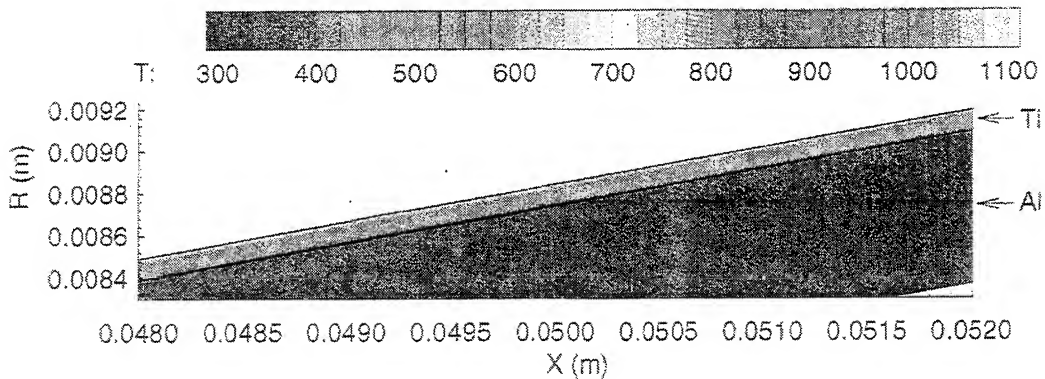
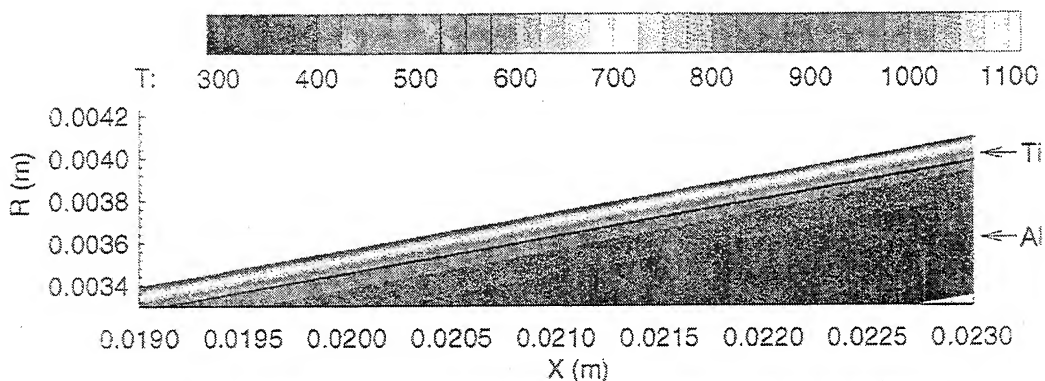
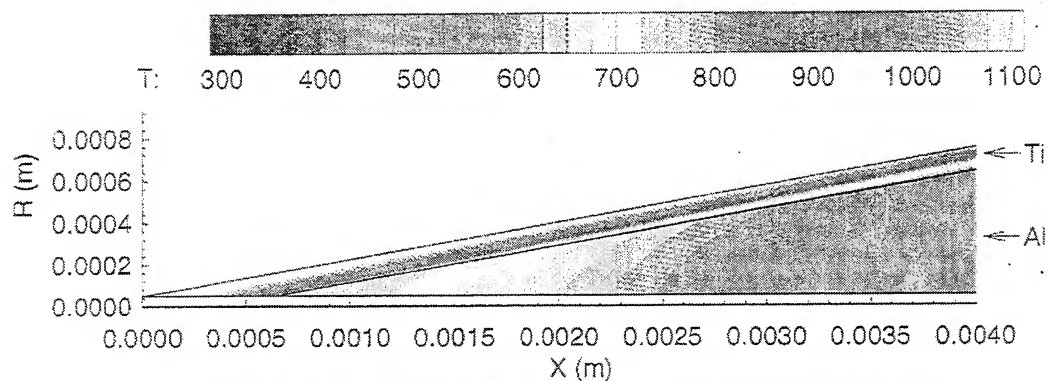
YIELD PARAMETER DISTRIBUTION

Tip of 15°-Angle Nose at End of Simulation



TEMPERATURE DISTRIBUTION

Expanded View of Titanium-Coated Aluminum Nose



TEMPERATURE DISTRIBUTION

Tip of Uncoated Aluminum Nose at End of Simulation

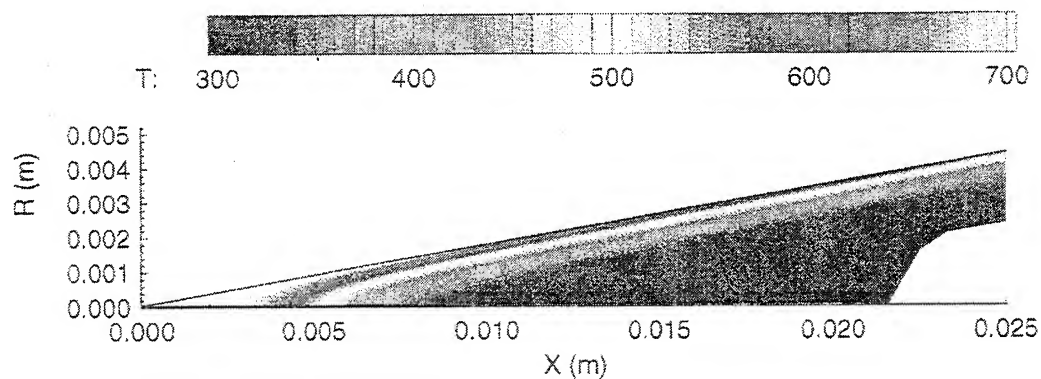
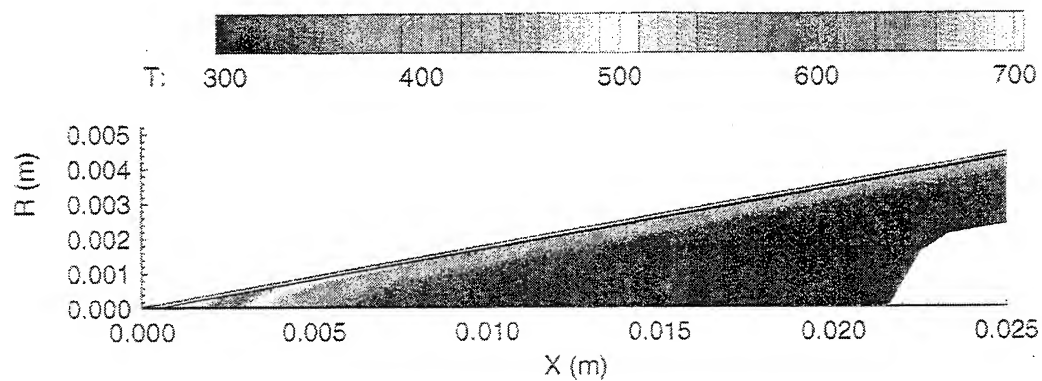
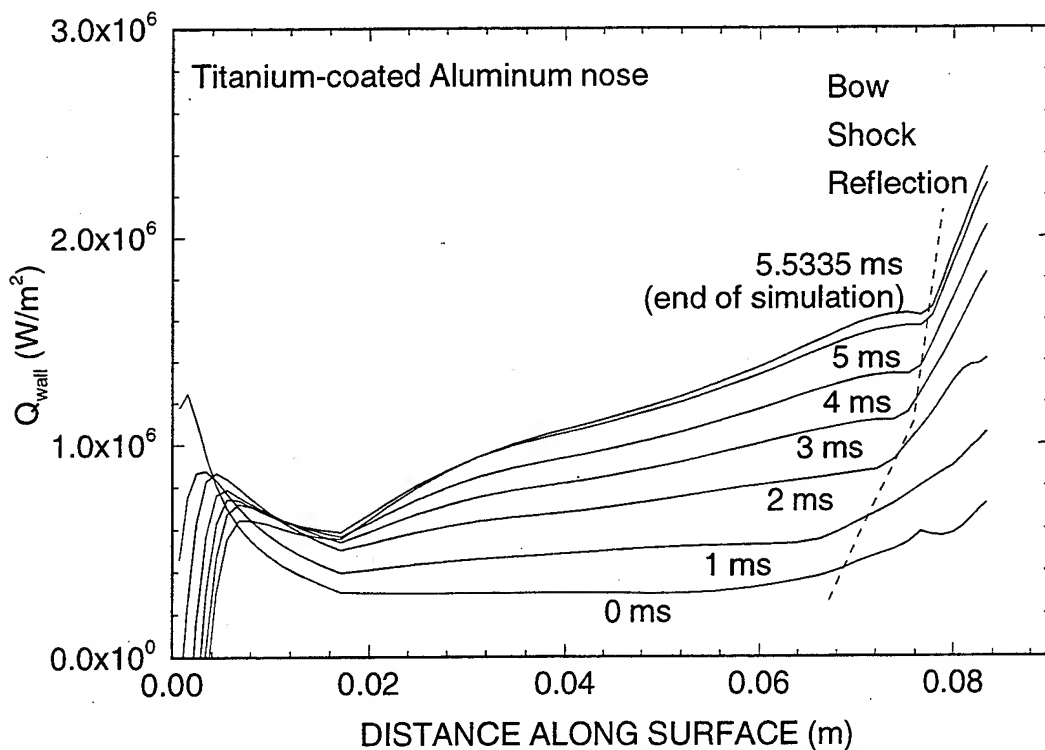


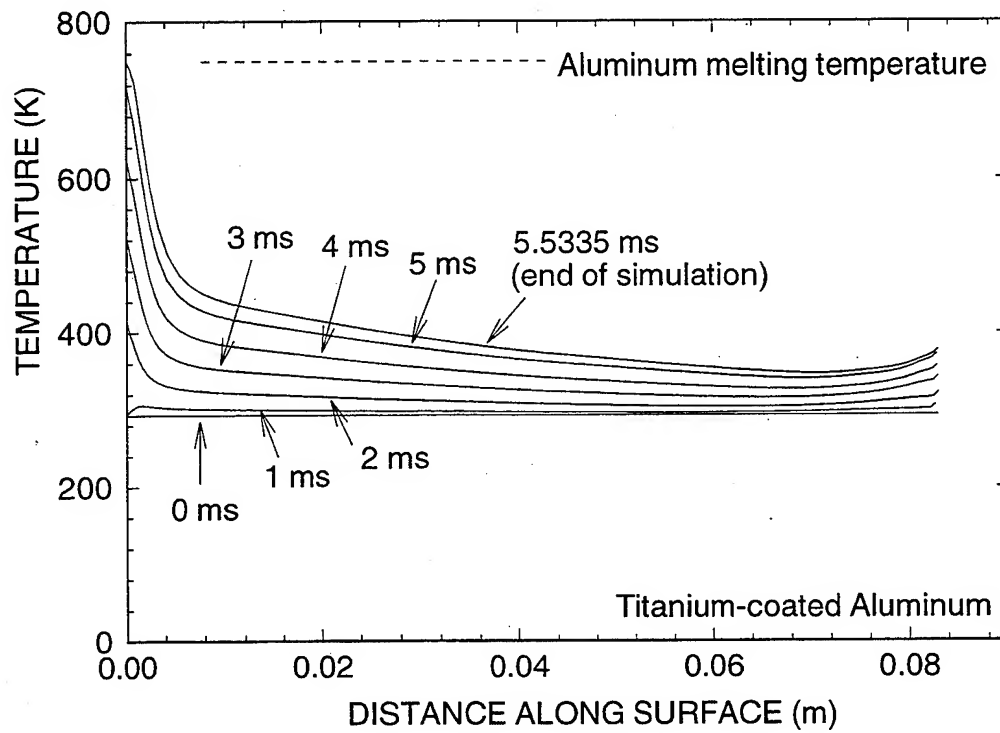
Figure 83. Temperature contours in tip of uncoated nose of aluminum projectile 5.5335 ms after start of simulation (time of unstart of HS 1064).



Titanium-Coated Aluminum Nose

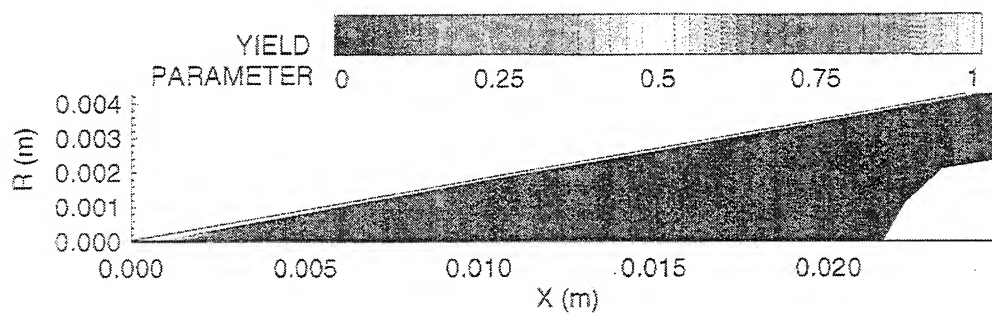


Titanium-Coated Aluminum Nose



YIELD PARAMETER DISTRIBUTION

Tip of Titanium-Coated Aluminum Nose at End of Simulation



SUMMARY

Experimental Data

- Series of pairs of experiments compare projectiles with different nose alloys
- Projectiles with titanium alloy noses generally attain a higher peak velocity, and survive for longer periods of time at high velocity, than standard projectiles with aluminum alloy noses.
- Results imply that maximum attainable velocity is greatly influenced by differences in alloy properties

Numerical Simulations

- Computer program combines turbulent viscous flow solver and heat conduction solver to couple solutions of flow in gas and temperature in solid
- Temperature histories of projectiles were reconstructed from velocity histories of laboratory experiments
- Aluminum projectile nose tips reach melting point and probably erode into a blunt configuration
- Even blunted aluminum noses reach the melting point.
- Titanium nose tips do not reach melting point and thus are much less likely to erode, remaining sharp
- Projectile noses with larger cone half-angles are shown to likely experience even worse tip erosion than standard noses
- Steel noses would resist heat better than aluminum noses, but may be too massive
- Titanium-clad aluminum noses would be lightweight and resistant to melting

Session 8

UNIQUE CONCEPTS

Ram Accelerator Operation With Hollow Projectiles

A. Sasoh^{*}, A. J. Higgins[†], C. Knowlen[‡] and A. P. Bruckner[§]

Aerospace and Energetics Research Program
University of Washington
Seattle, Washington 98195

A ram accelerator is characterized by its potential of launching a heavy payload at high speeds. This potential is basically owing to the fact that pressure is always highest immediately behind a projectile, and encourages one to apply this technology to a space launcher,^{[1]-[4]} a hypersonic ground test facility^[5] and hypervelocity impact experiment, etc. The concept of a ram accelerator was developed and experimentally validated by University of Washington^[6], being experimentally followed by ARL^[7] and ISL^{[8],[9]}, who showed that the scaling-up of a ram accelerator was feasible. However, in order to realize the above applications, the performance of the apparatus needs to be further improved.

A key for the further improvement is to better understand the flow field in a ram accelerator. With a conventional center-body projectile, due to the existence of fins, the flow field around the projectile is three dimensional and, being combined with combustion and turbulence etc., is considerably complicated. So far neither experimental diagnostics nor computational fluid dynamics has not yet become successful in thoroughly understanding the relevant flow field. If possible, simplification of the flow field will promote the understandings to a large extent. ISL^[9] tested ram accelerator operation with an axisymmetric projectile supported by rails installed on the tube. Although the configuration of the projectile itself was axisymmetric, the flow field with the rails was still three dimensional.

One way to obtain axisymmetric flow passage is to use a hollow projectile; supporting the projectile by its cylindrical body, it does not need fins. Recently, a hollow projectile attracts attention also in developing an oblique detonation wave engine (ODWE).^{[10]-[13]} In

^{*}Visiting Scholar; currently Associate Professor, Shock Wave Research Center, Institute of Fluid Science, Tohoku University, 2-1-1 Katahira, Aoba-ku, Sendai 980-77, Japan, Member AIAA

[†]Graduate Student, Student Member AIAA

[‡]Research Associate, Member AIAA

[§]Professor, Associate Fellow, AIAA

an ODWE, the motion of a projectile produces a thrust in free space. The projectile should coast at speeds higher than the detonation speed of the mixture. Because a projectile flies in an open space, hollow configuration is suitable for producing a large thrust. In spite of the above-mentioned differences between a ram accelerator and an oblique detonation wave engine, technologies developed in hollow projectile ram accelerator operation are transferable to those for an oblique detonation wave engine. Also, the relevant phenomena are closely related to ram/scramjet studies. In this study, ram accelerator operation with hollow projectiles are experimentally investigated.

Experimental Apparatus

The hollow projectiles shown in Figs. 1a and b were used in this study. They are made of 7075T061 aluminum alloy. The outer diameter of the projectiles is 38.0 mm, which is 0.1 mm smaller than the tube diameter. The projectiles have a 10-degree inverse cone section upstream. In order to avoid damage from rupturing diaphragms, the apex angle of the inverse cone at the lip is made large – 30 degrees. The cross-sectional area ratio of a throat to the tube is 0.41, equaling that for a conventional center-body projectile.^[14] The downstream section is a diverging inverse cone which is truncated by a base. The cross-sectional area ratio of the flow passage at the base to the tube also equals that for the conventional projectile with fins being taken into account. A magnetized plastic ring is installed into the groove on the side of the projectiles. The Projectile A and B weigh 0.105 kg and 0.095 kg, respectively.

The experiments were conducted using the ram accelerator at Aerospace and Energetics Research Program, University of Washington.^{[6],[15]} It has a 38.1-mm-bore ram acceleration tubes. In this study, the total length of the ram acceleration test section was 8 m. A projectile is pre-launched by a single stage Helium gun up to a speed ranging from 1000 m/s to 1250 m/s. The projectile speed was measured through the time of flight method by sensing magnetic inductions produced by the movement of the magnetized ring on the projectile. The pressure histories on the tube were measured by pressure transducers (PCB 119M44). Both the magnetic sensors and pressure transducers were installed respectively by a separation of 0.4 m from each other. The luminosity of light emitting from high temperature chemically reacting gas was measured through optical fibers and photo diodes.

Results and Discussion

Operation conditions and resulting ΔU_p are summarized in Table 1. As is seen in the data from No. 5 to 7 and 9 to 11, there exist appropriate range of U_{p0} for obtaining a positive acceleration. For a high-Q mixture, an excessively high transition speed resulted in immediate unstart (No. 1 and 11). The combination of a low-Q and a low U_{p0} yielded supersonic coasting without combustion (No. 4 and 5).

Figure 2 shows the example of the projectile velocity histories of the shots No. 1, 2 and 4 in Table 1. For $Y = 3.0$ (No. 2 in Table 1), when the projectile enters the ram acceleration section,

the mixture is ignited behind the projectile, producing high pressure of the order of 30 MPa. The combustion region is well identified by the history of luminosity and agrees well with that identified with the pressure history. The projectile is accelerated up to $x = 2.6$ m. A velocity gain ΔU_p of 108 m/s was obtained. At $x = 3.0$ and further, the pressure histories indicates the occurrence of unstart – a shock wave discharges over the projectile, which is decelerated by the high pressure behind the shock wave.

For $Y = 4.0$ (No. 4 in Table 1), the mixture is not ignited. After entering the ram acceleration section, the supersonic diffuser operation is made – the projectile coasts with supersonic flow passing through. The drag over the projectile is relatively small. At about 900 m/s, a normal shock appears in front of the projectile. Behind the shock wave the flow becomes subsonic, resulting in failure of the supersonic diffuser operation.^[16] After this gasdynamic unstart, the drag increased. The kink at $x = 4.6$ in Fig. 2 corresponds to this transition of the operation mode. For $X = 2.5$ (No. 1 in Table 1), due to rapid heat release by combustion, unstart occurs immediately after entering the ram acceleration section.

For the operation condition of No. 2 in Table 1, from the ram accelerator Hugoniot theory,^{[17],[18]} the non-dimensional thrusts $F/(p_1 A_t)$ are estimated to be 3.5 and 2.7 for $U_{p0} = 1170$ m/s and 1270 m/s, respectively. However, the mean value of the measured non-dimensional thrust is 2.0 – much smaller than the theoretical value. A simple calculation shows that if a pressure of 30 MPa is exerted only on the inside of the projectile its outer diameter increases by 0.15 mm, which is comparable with the clearance between the projectile and the tube wall. Therefore, under such high pressure, friction force against the tube wall due to this expansion is not negligible in thrust production. Moreover, it is seen from No. 5 to 7 and 9 to 11 that the peak velocity depends on U_{p0} . In the clearance between the projectile and the tube wall the effect of viscosity is so large that the static temperature is increased due to the viscosity and the mixture can be ignited there.

In order to solve these problems associated with the clearance, it is preferable to increase the clearance. However, increasing the clearance makes the projectile attitude unstable. Further study should be focused on solving this problem.

Summary

In this study, with the hollow projectiles positive acceleration is obtained. This encourages further study on improving the performance of the hollow projectile ram accelerator along with that on the development of an oblique detonation wave engine. In accelerating hollow projectiles, one needs to solve gasdynamic and structural problems. The gasdynamic problems are based on the fact that with the same apex angle a shock wave generated at the leading edge is stronger for a hollow projectile than for a center-body one. This makes the operational regime for a hollow projectile narrow. The mixture and the entry speed must be carefully determined. The design of the projectile tip must be carefully made in order both to maintain

the integrity of the leading edge of the hollow projectile against diaphragm rupture and to keep the shock wave weak enough to obtain ram acceleration.

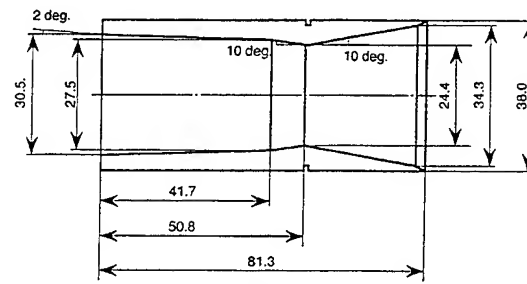
Acknowledgment

The authors would like to appreciate valuable suggestions and encouragements made by Professor Abraham Hertzberg. Also the authors thank considerable helps made by Gilbert Chew in designing the hollow projectiles through CFD computation and those made by Messers Tom Imrich and Josh Elvander in the experiment.

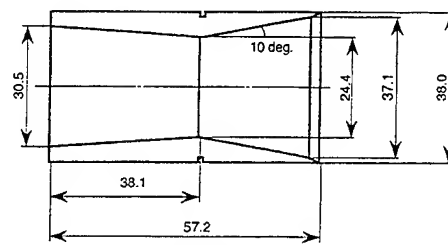
References

- [1] Bruckner, A. P. and Hertzberg, A., "Ram Accelerator Direct Launch System for Space Cargo," IAF-87-211, 1987.
- [2] Kaloupis, P. and Bruckner, A. P., "The Ram Accelerator: A Chemically Driven Mass Launcher," AIAA-88-2968, 1988.
- [3] Bogdanoff, D. W., "Ram Accelerator Direct Space Launch System: New Concept," J. Propulsion and Power, Vol. 8, No. 2, 1992, pp.481-490.
- [4] Sekino, N. and Shimada, T., "An Assessment of Future Low-Cost, High-Acceleration Launching to LEO," IAF-93-V.5.636, 1993.
- [5] Naumann K. W. and Bruckner A. P., "Ram Accelerator Ballistic Range Concept for Softly Accelerating Hypersonic Free-Flying Models," J. Aircraft, Vol. 31, No. 6, 1994, pp. 1310-1316.
- [6] Hertzberg, A., Bruckner, A. P. and Bogdanoff, D. W., "Ram Accelerator: A New Chemical Method for Accelerating Projectiles to Ultrahigh Velocities," AIAA J., Vol. 26, No. 1, 1988, pp. 195-203.
- [7] Kruczynski, D. L., "New Experiments in a 120-mm Ram Accelerator at High Pressures," AIAA paper, 93-2589, 1993.
- [8] Giraud, M., Legendre, J. F., Simon, G. and Catoire, L., "Ram accelerator in 90 mm caliber. First results concerning the scale effects in the thermally choked propulsion mode," 13th International Symposium on Ballistics, Stockholm, also ISL Report CO 210/92, 1992.
- [9] Seiler, F., Patz, G., Smeets, G. and Srulijes, J., "Status of ISL's RAMAC 30 with Rail Stabilized Projectiles," Proceedings of the first ram accelerator workshop, Saint-Louis, France, September 1993.

- [10] Dunlap, R., Brehm, R. L. and Nicholls, J. A., "A Preliminary Study of the Application of Steady State Detonative Combustion to a Reaction Engine," *Jet Propulsion*, Vol. 28, 1958, pp. 451-456.
- [11] Pratt, D. T., Humphrey, J. W. and Glenn, D. E., "Morphology of Standing Oblique Detonation Waves," *J. Propulsion and Power*, Vol. 7, No. 5, 1991, pp. 837-845.
- [12] Heiser, W. H. and Pratt, D. T., *Hypersonic Airbreathing Propulsion*, AIAA Educational Series, 1994, pp. 546-551.
- [13] Lee, J. H. S., Zhang, F. and Chue, R. S., "Some Fundamental Problems of Detonation Instabilities and its Relation to Engine Operation," 2nd ICASE/NASA LaRC Meeting on Combustion, Newport News, VA, Oct. 12-14.
- [14] Knowlen, C., Higgins A. J. and Bruckner A. P., "Investigation of Operational Limits to the Ram Accelerator," AIAA Paper AIAA-94-2967, 1994.
- [15] Bruckner, A. P., Knowlen, C., Hertzberg, A. and Bogdanoff, D. W., "Operational Characteristics of the Thermally Choked Ram Accelerator," *J. Propulsion and Power*, Vol. 7, No. 5, 1991, pp. 828-836.
- [16] Kantrowitz A. and Donaldson C. duP., "Preliminary Investigation of Supersonic Diffusers," NACA ACR No. L5D20, 1945.
- [17] Knowlen C. and Bruckner A. P., "Hugoniot analysis of the ram accelerator," *Shock Waves*, Proceedings of the 18th International Symposium on Shock Waves, Vol. I, Springer-Verlag, Heidelberg, pp. 617-622, 1992.
- [18] Knowlen C., *Theoretical and Experimental Investigation of the Thermodynamics of the Thermally Choked Ram Accelerator*, Ph.D Dissertation, University of Washington, 1991.



Type A



Type B

Fig. 1 Hollow projectiles, dimensions in mm.

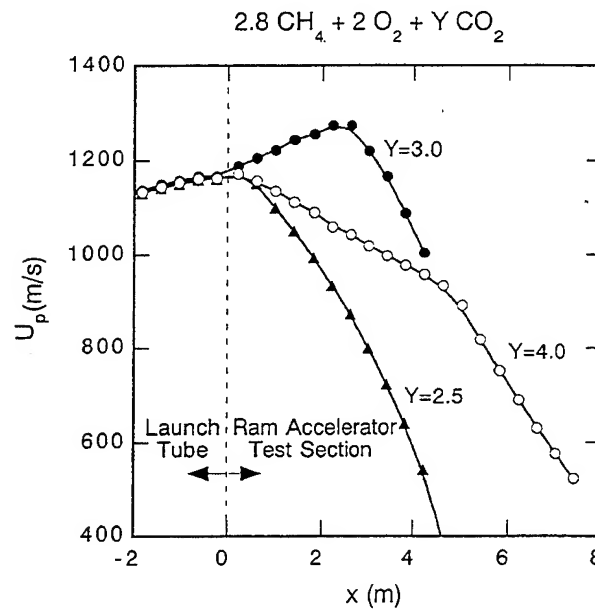


Fig. 2 U_p v.s. x , $X=2.8$, No. 1, 2 and 4 in Table 1

Table 1 Operation conditions and resulting ΔU_p in the experiment;
 $XCH_4+2O_2+YCO_2$, $p_1=2.5\text{MPa}$, -; no positive acceleration

No.	X	Y	Projectile	U_{p0} (m/s)	ΔU_p (m/s)
1	2.8	2.5	A	1160	-
2	2.8	3.0	A	1166	108
3	2.8	3.0	B	1174	62
4	2.8	4.0	A	1162	-
5	1.5	4.5	B	1013	-
6	1.5	4.5	B	1090	59
7	1.5	4.5	B	1177	71
8	1.5	4.5	A	1163	15
9	1.5	4.0	B	1020	67
10	1.5	4.0	B	1088	44
11	1.5	4.0	B	1184	-

SECOND INTERNATIONAL WORKSHOP ON RAM ACCELERATORS
July 17-20, 1995, Seattle WA

RECENT DEVELOPMENTS IN THE RESEARCH ON EXTERNAL PROPULSION ACCELERATOR

J. Rom¹, M.J. Nusca², D. Kruczynski³, M.J. Lewis⁴, A.K. Gupta⁵ and J. Sabean⁶

ABSTRACT

The present paper presents the results of recent developments in the research on the External Propulsion Accelerator (EPA). This research is motivated by the fact that the chemical propellants are about three order of magnitude more compact in weight and size than electromagnetic energy production and storage systems. Therefore, there is great interest in developing accelerators of hypervelocity projectiles using chemical propellants. There are two methods for in-tube chemical accelerators utilizing premixed gaseous detonative mixtures; the Ram Accelerator (RA) and the External Propulsion Accelerator (EPA). These in-tube chemical launchers for accelerating projectiles to hypervelocity utilize, in the superdetonative mode of operation, the possibilities of generating continuous thrust by initiating detonation in the premixed fuel/oxidizer mixture by shock wave interactions. The first method proposed for an in-tube chemical launcher was the Ram Accelerator (RA), originated and developed by A. Hertzberg and his colleagues at the University of Washington. The second method for operating the chemical in-tube accelerator is based on the utilization of the external propulsion cycle, proposed by J. Rom at the Technion-Israel Institute of Technology. In the External Propulsion Accelerator (EPA) the projectile is fired into the launcher tube which is filled with premixed fuel/oxidizer mixture, however, here the projectile diameter is much smaller than the tube diameter (about 25%) so that there is no interaction between the flow over the projectile and the tube wall over the complete length of the projectile. In this case the detonation is established by aerodynamic means on the projectile, such as a forward facing step on the projectile shoulder or by the blunt leading edge of a ring wing positioned on the center/rear part of the projectile. By the interactions of the detonation wave with the nose shock wave an "external combustion chamber" is produced. This aerodynamically confined region which is filled with the hot chemical reaction products is then expanded on the rear part and into the base region of the projectile, producing thrust on the projectile. In this paper we present some investigations of the operational performance limits of the Ram and the External Propulsion Accelerators using an energy balance analysis. The energy balance analysis is applied to evaluate the maximum velocity which can be achieved in the in-tube accelerators when the available chemical reaction energy is utilized. It is shown that the maximum velocity of the projectile in the RA is limited, due to the high drag caused by the choking, to about 1.3 the detonation velocity while the maximum velocity of the projectile in the EPA can reach up to 6 times the detonation velocity. Then the results of numerical simulation of the flow over projectile configurations and some performance parameters of the EPA are presented. The applications of the EPA to ground test facilities such as a launcher for a hypersonic range and as a facility for combustion research in scramjet engines are discussed. The use of the EPA as a single stage to orbit launcher is also considered.

¹ Professor, Lady Davis Chair, Faculty of Aerospace Engineering, Technion - Israel Institute of Technology, Visiting Professor, Department of Mechanical Engineering, University of Maryland, Fellow AIAA.

² Aerospace Engineer, Weapons Technology Directorate, Aberdeen Proving Ground, Army Research Laboratory.

³ Aerospace Engineer, Weapons Technology Directorate, Aberdeen Proving Ground, Army Research Laboratory.

⁴ Associate Professor, Department of Aerospace Engineering, University of Maryland.

⁵ Professor, Department of Mechanical Engineering, University of Maryland, Fellow AIAA.

⁶ Graduate student, Department of Aerospace Engineering, University of Maryland.

INTRODUCTION

The present paper presents the results of recent developments in the research on the External Propulsion Accelerator (EPA). This research is motivated by the fact that the chemical propellants are about three order of magnitude more compact in weight and size than electromagnetic energy production and storage systems. Therefore, there is great interest in developing accelerators of hypervelocity projectiles using chemical propellants. There are two methods for in-tube chemical accelerators utilizing premixed gaseous detonative mixtures; the Ram Accelerator and the External Propulsion Accelerator. These in-tube chemical launchers for accelerating projectiles to hypervelocity utilize, in the superdetonative mode of operation, the possibilities of generating continuous thrust by initiating detonation in the premixed fuel/oxidizer mixture by shock wave interactions. The first method proposed for an in-tube chemical launcher was the Ram Accelerator, originated and developed by A. Hertzberg and his colleagues at the University of Washington (Ref. 1). The concept of the Ram Accelerator, operating in the superdetonative mode, is based on utilization of the scramjet cycle, where the projectile acts as a free centerbody and the tube as an extended cowl (Fig. 1). The sharp nosed projectile diameter is slightly less (typically 70% to 80%) than the tube diameter, therefore, the nose shock wave is reflected from the tube wall into the projectile centerbody. Under proper conditions this reflected shock wave initiates a detonation process so that when the products of the chemical reactions are expanded on the rear part of the projectile, thrust is generated.

Another method for operating the chemical in-tube accelerator is based on the utilization of the external propulsion cycle, proposed by Rom (Ref. 2). In the External Propulsion Accelerator the projectile is fired into the launcher tube which is filled with premixed fuel/oxidizer mixture, however, here the projectile diameter is much smaller than the tube diameter (about 25%) so that there is no interaction between the flow over the projectile and the tube wall over the complete length of the projectile (Fig. 2). In this case the detonation is established by aerodynamic means on the projectile, such as a forward facing step on the projectile shoulder or by the blunt leading edge of a ring wing positioned on the center/rear part of the projectile. By the interactions of the detonation wave with the nose shock wave an "external combustion chamber" is produced. This aerodynamically confined region which is filled with the hot chemical reaction products is then expanded on the rear part and into the base region of the projectile, producing thrust on the projectile.

Some characteristics of the EPA and various applications are discussed in Refs. 3, 4, and 5. The CFD calculations indicate that it is possible to establish and stabilize a combustion-detonation front on projectiles of various geometry flying at hypersonic speeds in detonable gas mixtures. The characteristics of the hypersonic combustion-detonation on the projectiles in the External Propulsion Accelerator are also relevant to the Oblique Detonation Wave engine, the Ram Accelerator and various scramjet engines. Certain characteristics of the EPA were presented in Refs. 6, and 7. Some analytical investigations, based on many simplifying assumptions, for the establishment of combustion front ahead of the forward facing step and on spherical nosed blunt bodies in hypersonic flows of detonable mixtures, including the studies of the oscillations that may occur were investigated by Tivanov and Rom (Ref. 8, 9 and 10).

In this paper we present some investigations of the operational performance limits of the Ram and the External Propulsion Accelerators using an energy balance analysis. The energy balance analysis is applied to evaluate the maximum velocity which can be achieved in the in-tube accelerators when the available chemical reaction energy is utilized. It is shown that the maximum velocity of the projectile in the RA is limited due to the high drag caused by the choking, to about 1.3 the detonation velocity while the maximum velocity of the projectile in the EPA can reach up to 6 times the detonation velocity. Then the results of numerical simulation of the flow over projectile configurations and some performance parameters of the External Propulsion Accelerator are presented. The applications of the EPA to ground test facilities such as a launcher for a hypersonic range and as a facility for combustion research in scramjet engines are discussed.

AN ENERGY BALANCE ANALYSIS FOR THE DETONATION DRIVEN PROJECTILE IN THE IN-TUBE CHEMICAL ACCELERATORS

The performance limits of the in-tube chemical accelerators, the RA and EPA, can be evaluated using an energy balance analysis. In this analysis we equate the energy of the chemical reaction with the drag work of

the flying projectile. Using the energy required to initiate detonation is used to determine the minimum projectile velocity which is needed to initiate the detonation. While utilizing the total energy available in the mixture will determine the maximum velocity of the projectile.

A. The Minimum Projectile Velocity Required to Initiate Detonation

The minimum velocity of the projectile flying in the Ram Accelerator (RA) or in the External Propulsion Accelerator (EPA) needed to initiate detonation can be evaluated by equating the energy required to initiate detonation in the fuel/oxidizer mixture with the drag work of the flying projectile, as presented in Ref. 12. The energy for the initiation of detonation by the hypervelocity projectile is evaluated by the use of the blast wave analogy (Ref. 12). It is shown in Ref. 12 that for the flow of the fuel/oxidizer mixture at hypersonic velocity over the projectile in the EPA, as illustrated in Fig. 2, the minimum Mach number for the initiation of detonation on a projectile with a forward facing step can be evaluated by

$$\frac{V_{\infty}^2}{D^2} = 2.504 \frac{H}{d} \left(\frac{D \tau_r}{H} \right)^2 \frac{1}{C_{D_{step}}} \quad (1)$$

Where d is the projectile diameter, the step height is H (where $H/d \ll 1$), D is the Chapman-Jouguet detonation speed and τ_r is the reaction time. Since typical H/d values can be $1/30$ and smaller, $D \tau_r / H$ should be less than 1 (probably in the range of $1/3$ to $1/5$) for detonation to occur and $C_{D_{step}}$, the drag coefficient for a forward facing step is about 1. Therefore, introducing these values into Eq. 1, the minimum projectile velocity that produces energy to balance the critical initiation energy for detonation is evaluated to be much below the detonation velocity. Since the projectile in the EPA is expected to fly well above the detonation speed then there is no problem of securing the energy required to initiate the detonation both in the step and also the ring wing configurations.

This energy balance, presented in Eq. 1, is also applicable to the projectile in the RA. In this case, the drag coefficient is equated with that of the drag of the projectile including the effects of the interaction between the projectile and the tube wall and the reference area is the cross section of the projectile body. As the projectile speed increases the drag force on the projectile increases so as to provide the energy for initiation of the detonation. At the lower initial speeds the required drag is provided by the perforated piston or butrator which is used in the RA for initiation of the process.

B. The Maximum Projectile Velocity in the In-Tube Chemical Accelerators.

It is obvious that the flow as well as the combustion process are very different in the cases of the RA and in the EPA, however, in both cases the work done by the drag force acting on the hypervelocity projectile is balanced by the energy released by the detonating gas mixture.

1. Maximum velocity of the projectile in the EPA.

Following the discussion in Ref. 12, the maximum velocity is

$$\frac{V_{\infty_{max}}^2}{D^2} = \frac{\beta^2 \eta_c}{C_D (\gamma^2 - 1)} \quad (2)$$

and following Lee (Ref. 13), we can assume a value of $2/3$ for η_c (assuming high combustion temperature of 3000°K and low temperature of 1000°K). In Eq. 2, β is defined as the ratio of the outside diameter of the external combustion zone to the projectile diameter. In the EPA the thickness of the external combustion layer varies as a function of the flow Mach number. It was found from the numerical calculations, which are reported in part in Refs. 3, 11 that for the 32 mm diameter projectile with a 1 mm step the combustion layer thickness varies from 3 step heights at Mach number 5 to 5.5 step heights at Mach number 6 and to 17 step heights at Mach number 10. The value of C_D for the cone with the 1 mm step is about 0.26-0.28 for Mach

numbers above 5 (for cone-cylinder without the step the drag coefficient is about 0.07-0.08). Then, using Eq. 2, the maximum projectile velocity can be about 1.9 times the detonation velocity at Mach number 5, about 2.1 times the detonation velocity at Mach number 6 and about 3.3 times the detonation velocity at Mach number 10. At higher flight Mach numbers the combustion may extend to the tube wall, then for the 120 mm tube with the 32 mm projectile the maximum velocity is about 6 times the detonation velocity, which is well above the escape velocity to orbit into space. Therefore, when the projectile is injected at initial velocity between Mach 5 to 6, only about 21% to 28% of the energy of combustion is used to overcome the drag, so that about 72% to 79% of the combustion energy is available for accelerating the projectile. Actually the available combustion energy increases as the Mach number increases, reaching to about 90% at Mach number 10 and will be even higher as the Mach number is increased further. In this case of accelerating the projectile in the EPA we can conclude that only a small fraction of the available combustion energy which can be released in the detonation process is needed to overcome the drag of the hypervelocity projectile and this available energy can be used for accelerating the projectile to higher hypervelocity. Of course as the projectile velocity increases the problems of heating and ablation of the projectile surfaces and the aerodynamic and acceleration loads on the projectile structure become more critical.

2. Maximum Velocity of the Projectile in the RA

The maximum velocity of the projectile in the RA is evaluated using a similar analysis (Ref. 12). Such evaluation was first done by Lee in Ref. 13. Lee assumes a value of the drag coefficient for the projectile flying in the RA tube to be of order 1, $C_D = O(1)$, which is equal to the drag coefficient of a blunt body at hypersonic speeds. So, using Eq. 2 with $\gamma = 1.4$ and $\beta = 1.5$, he estimates the value of the maximum projectile velocity to be about 1.3 times the detonation velocity. He then concludes that when the projectile velocity is equal to the detonation velocity about 75% of the available energy is used to overcome the drag so that only a small fraction of the energy is available for additional acceleration of the projectile. This result is in agreement with the experimental data on projectiles obtained in the RA of the University of Washington. The projectiles tested at the University of Washington and ARL, as presented in Refs. 1 and 11, have a drag coefficient of about 0.2 -0.25 at Mach numbers above 5 in free flight without the tube wall interference. However, the multiple shock wave reflections from the tube wall to the projectile center-section and the blunt leading edges of the fins which may initiate detonation increase the drag coefficient of the projectile considerably in its flight in the accelerator tube. At these conditions the assumption of a drag coefficient of about 1, which is the value for a blunt body, seems reasonable. As the projectile velocity increases the strength of the reflected oblique shock waves increase and the total pressure loss in the shock interference region on one hand provides energy for the initiation of the detonation but on the other hand due to the extremely high drag consumes an increasing portion of the available reaction energy until the energy required to overcome the drag force will be larger than the available energy from the chemical reaction and we will face the conditions of "unstart" if the projectile will deform and disintegrate or it will exit the tube at this maximum velocity. The fact that the "unstart" is obtained at about 1.15 to 1.2 the detonation velocity is shown in Figs. 3a and 3b, based on the data of Ref. 14, for aluminum projectiles. Using a titanium projectile, which did not deform, the maximum velocity is obtained and the projectile flies at this maximum velocity for the last 3 meters of the tube, as shown in Fig. 4. This maximum velocity is 1.2 the detonation velocity and is in very good agreement with the energy analysis value.

THE PERFORMANCE OF PROJECTILES FLYING AT HYPERSONIC SPEED IN THE EXTERNAL PROPULSION ACCELERATOR

A. Description of the External Propulsion Accelerator (EPA)

An outline of an EPA facility is presented in Fig. 5. The first stage of the EPA facility can be a large caliber smooth bore conventional powder gun for the initial acceleration of the sabot-projectile/missile payload. Since the projectile/missile must be accelerated to velocities higher than the detonation velocity of the

fuel/oxidizer mixture in the accelerator tube (detonation speeds of 1000 m/sec to 1500 m/sec), we require muzzle exit velocities of 1300 m/sec to 1800 m/sec in order to accommodate various mixture compositions. These muzzle velocities can be achieved in large caliber powder guns with barrel lengths of 6 m to 10 m.

The second stage must be a sabot separation section. There are various methods used for sabot separation, mechanical and/or aerodynamic methods, which can be utilized in this design. In Fig. 5 a sabot stripper plate is used. The "clean" projectile/missile flies through the sabot stripper and enters at a velocity which is higher than the detonation velocity into the fuel/oxidizer mixture in the accelerator tube.

The third stage is the accelerator section. This section is a large tube, its diameter should be in the order of 4 times the projectile/missile maximum diameter, which is filled with various premixed gaseous fuel and oxidizer mixtures. Both ends of the accelerator tube must be sealed, either by diaphragms which are pierced by the flying missile or by quick acting valves which are opened in synchronization with the flying missile. This tube can be divided into sections closed by separating diaphragms, so that different mixtures can be filled into each of these subsections. In this way mixtures of increasing detonation speeds can be matched to the projectile/missile velocity as this velocity increases due to the acceleration of the projectile/missile as it flies down the tube through these sub-sections.

The tube, in this case, acts only as a containing vessel for the premixed fuel/oxidizer atmosphere through which the projectile/missile flies. The tube structure must be designed to withstand the initial mixture pressure which can be of the order of 20 atm. to 200 atm., if we wish to use the tube for a single shot operation, or it can be made to withstand the peak pressures experienced after the passage of the gun blast and the explosion of the remaining mixture after the passage of the projectile/missile.

At the exit of the accelerator section the projectile/missile emerges, after piercing the exit diaphragm, at its highest velocity. The exit velocity is determined by the thrust which is generated on the projectile/missile and the length of the accelerator section. The calculations reported in Ref. 3 indicate that thrust levels of F/pA (where F is the thrust force, p is the initial pressure in the tube and A is the maximum cross section of the projectile/missile) of about 3 can be achieved. This thrust level can be increased by using more energetic fuels and by optimizing the projectile/missile design. This thrust level is sufficient to accelerate reasonable size projectile/missile to above 50,000 g's. We use this acceleration level since there are guidance and control systems as well as telemetering units hardened to operate at this 50 Kg's level. The added velocity at the exit of the accelerator tube as a function of the tube length is shown in Fig. 6. Thus, assuming initial velocity of 1500 m/sec., the exit velocity for a 8 m long accelerator tube will be 3500 m/sec. and for 32 m long tube the exit velocity will be 5500 m/sec. It was shown in Ref. 12, using an energy balance analysis, that it is possible to reach in the EPA a maximum velocity of about 6 times the detonation velocity of the mixture used in the tube. Therefore, using mixtures with detonation speeds of 2,500 m/sec. and up to 3,000 m/sec. enable the utilization of the EPA to reach about 18,000 m/sec., well beyond escape velocity from earth. This may be a very promising method to obtain a "single stage to orbit" mission.

The diameter of the acceleration section is about 1 m for a 25 cm diameter projectile/missile and 40 cm. for a 10 cm. diameter projectile/missile, or smaller or larger for smaller or larger projectile/missiles.

B. Aerodynamic design of the EPA projectile.

After being stripped from its sabot and upon entering the acceleration tube section the projectile flies freely in the gas mixture which is in the tube. The projectile is aimed to pierce the entrance diaphragm near its center and should fly near the tube center. Therefore, the projectile is designed to be aerodynamically stable, both statically and dynamically. In order to insure stability over the range of flight Mach numbers the basic configuration needed for external propulsion, i.e. the cone, forward facing step - cylindrical with boattail aft section, is fitted with small elongated fins at the end of the boattail section. At first, a design with fins with a span equal to the maximum body diameter is investigated. This configuration with 6 fins is shown in Fig. 7. In order to stabilize the flight trajectory in the center of the tube the possibility of imparting a slow spin by canting the fins is also tested. In Fig. 7 the fins are canted to 3° to the model axis while the tail with parallel fins is also shown. The aerodynamic coefficients are measured in the supersonic wind tunnel of the Aerodynamic Laboratory in the Technion. The aerodynamic coefficients are measured at $M = 3.4$ and these values are extrapolated to the hypersonic flight Mach number using slender body analysis methods. Preliminary wind tunnel results indicate that the aerodynamic center of the 6 fins configuration is positioned so as to obtain some stability margin for the positions of the center of gravity of the projectile. In order to

ascertain larger stability margin larger span trapezoidal fins are used in a new design shown in Fig. 8. This configuration is also tested in the wind tunnel at Mach number 3.4 for the determination of the aerodynamic coefficients. The aerodynamic coefficients evaluated from the wind tunnel results are used to evaluate the flight trajectory by a six degrees of freedom program. This work is currently underway and will be included in future report. In parallel, a firing test is being planned using the Ram Accelerator facility at the Army Research Laboratories of the US Army at Aberdeen Proving Grounds in Maryland, USA. Following this investigation on the aerodynamic stabilization and flight trajectory it is planned to study the heat transfer rates to the projectile surfaces and determine a practical method for thermal protection at the hypersonic speeds that can be achieved by projectiles in the EPA.

C. Evaluation of the combustion characteristics on the projectile using the ARL Navier-Stokes program.

The performance characteristics of the projectile flight in the accelerator tube is evaluated by the use of the computer code which is based on the solution of the Navier-Stokes equations for flows with chemical processes. This computer code was developed for the Ram Accelerator calculations at ARL by Nusca (Refs. 16, 17). This program uses the Rockwell Science Center USA-RG (Unified Solution Algorithm Real Gas) code written by Chakravarthy et al (Refs. 18, 19). This CFD code includes the full 3D unsteady Reynolds-Averaged Navier-Stokes (RANS) equations including equations for chemical kinetics (finite-rate and equilibrium). These equations are cast in conservation form and converted to algebraic equations using upwind finite-difference and finite-volume formulations. The equations are solved using a second-order TVD (total variation diminishing) scheme which is used to insure non-oscillatory numerical behavior. The flow field with the combustion generated by the forward facing step is presented in Fig. 9 and for the model with the ring wing in Fig. 10. Following these calculations, test runs of the forward facing step configurations and the ring wing projectiles are being planned in the ARL Ram Accelerator facility (Refs. 20, 21) using subcaliber models.

D. Evaluation of the combustion characteristics on the projectile using the Technion Navier-Stokes program.

A new computer code developed at the Department of Aerospace Engineering at the Technion is used for the evaluation of the combustion characteristics on the flying projectile in the EPA into a hydrogen-oxygen-nitrogen mixture. The computer code is a solution of the axisymmetric laminar Thin Layer Navier Stokes equations including chemical reactions presented in Ref. 22. The program uses an explicit TVD scheme and the chemical reaction is modeled using 7 species and 8 reactions for the $H_2 + O_2 + N_2$ mixture. The validation of the computer code is done by the calculations of the reacting flow on a hemispherical body, shown in Fig. 11. The shock capturing capability is well demonstrated in the pressure distribution calculations presented in Fig. 12. The pressure distribution on the hemisphere at Mach number 4.18 for non reacting flow is shown in Fig. 12a. The pressure distributions at Mach number 5.08 without and with chemical reactions are shown in Figs. 12b and 12c, respectively. The shock wave moves closer to the body as the Mach number increase from 4.18 to 5.08 (comparing Figs. 12a and 12b) while the chemical reactions cause the shock wave detachment distance to increase as seen from figs. 12b and 12c. The establishment of a reaction front behind the detached shock wave is seen in the temperature distribution results shown in Fig. 13b. No reaction front is seen in the non reacting case presented in Fig. 13a. The delay due to the induction time is clearly seen in the water content calculation presented in Fig. 13.c. This can be compared with experimental photograph obtained by Lehr for the hemisphere-cylinder model fired into $H_2 + O_2 + N_2$ mixture. The calculated results show that there is good agreement in the detachment distance near the stagnation point with the experimental data but the induction length is much longer in the experimental measurement. The numerical code is then applied to the conical projectile shown in Fig. 14, including the grid structure around the projectile. The projectile has a 10° half angle nose cone, then a 70° conical ramp followed by a short cylindrical section and a 5° boattail cone ending in a blunt base. The pressure distribution for non reacting flow at Mach numbers 6, 8 and 10 are shown in Fig. 15 where the detached shock wave ahead of the ramp is seen. The flow with chemical reaction is shown in Fig. 16, where the bottom figure presents the temperature distribution for non reacting flow at Mach number 8, while the temperature distribution for the flow with chemical reaction is shown in the middle figure. There the detached shock wave ignites the mixture becoming a detonation front followed by the contact surface separating the combustion region from the non reacting flow. The confinement of this

reaction region is clearly indicated in the water content distribution presented in the upper figure. An experimental verification of such flow structure on a 30° half cone with a 90° step obtained by Lehr (Ref. 23) is presented in Fig. 17.

USE OF THE EXTERNAL PROPULSION ACCELERATOR AS TEST FACILITIES

A. HYPERSONIC FLIGHT RANGE

The External Propulsion Accelerator (EPA) can be used as the launcher of aerodynamic models to hypersonic speeds in a ground test facility. The models, encased in a properly designed sabot, are accelerated in the EPA to the desired hypersonic speed and fired into an instrumented ballistic range. The EPA is theoretically capable to launch projectiles to velocities of up to 6 times the detonation velocity of the fuel-oxidizer mixture, in the order of 12,000 m/sec to 18,000 m/sec, so that it is well suited to be a launcher for the hypersonic ballistic range. The free flight range technology seems to enable the best simulation of atmospheric free flight conditions in a ground based facility. The range concept is most suitable since it uses quiescent arbitrary gas in its test sections in which the model flies at the design hypersonic speed. While in other test facilities, such as the various types of shock tunnels and gun tunnels, it is required to compress and heat the test gas to high stagnation temperatures and pressures followed by a rapid expansion in high Mach number nozzles. So that in such facilities the simulation is distorted by the effects of dissociation and ionization of the gas in the shock tunnel stagnation chamber as well as disturbances due to nozzle flow non-uniformities, effects of boundary layer disturbances, etc. The test range can be divided into sections separated by diaphragms, enabling simulation of flight at various pressure altitudes in a single shot. Therefore, such a hypersonic range with the EPA launcher can be an excellent tool for hypersonic aircraft research and development.

The requirements for a hypersonic ground based flight test range and the feasibility of the use of light-gas gun launcher was discussed by Witcofski et al (Ref. 22). In this study the use of an Electromagnetic launcher (EML) and of the Ram Accelerator (RA) were also considered. It was concluded that with the present state of technology the most suitable candidate is the two-stage light-gas gun which can be made to launch models of about 20 cm. span and length of up to 90 cm. to speeds of up to 6 km/sec. It was contemplated, that at a later stage, using more advanced launcher technology, the models can be increased to 30 cm to 45 cm in span and the velocity range will be increased to 10 km/sec to 15 km/sec.

THE TEST FACILITY

In this application, the hypersonic testing facility is basically similar to the AHAF concept presented in Ref. 24. The facility will be comprised from: 1. The Accelerator section. 2. Sabot separation section. 3. Ballistic Range for aerodynamic models free flight testing. 4. Decelerator section for model retrieval. An artist view of such facility, reproduced from Ref. 24, is shown in Fig. 18.

1. The Accelerator Section

The accelerator is comprised of two parts, an initial accelerator for accelerating the model with its sabot to the required insertion speed of 1,400 to 1,800 m/sec. (Mach number between 5 to 6.6) and the External Propulsion launcher tube which will accelerate the projectile, in which the model is inserted, into the test range. The flight Mach Number in the ballistic range can be then set to the required hypersonic speed with the possibility of reaching $M = 30$. The type of initial accelerator and the length of the External Propulsion Launcher depend on the allowable acceleration for the model. Simple aerodynamic shapes used for hypersonic flight, such as blunt reentry bodies, slender shuttle type configurations and wave riders with hardened on board instrumentation can be built to operate up to 50,000 g's acceleration level. In this case, a gun powder launcher can be used for the initial acceleration and the acceleration level of the External Propulsion launcher can be adjusted to the desired level. The gun launcher will require lengths of 5 to 20 meters. This section will be followed by the External Propulsion launcher. The lengths of the EPA section will depend on the achievable and allowable acceleration levels. Using the level of 50,000 g's, the required lengths of the EPA (Fig. 6) will be about 2 meters for $M = 7$ testing, 8 meters for $M = 11$ testing, about 18 meters for $M = 15$ testing and for Mach number 30 testing a launcher length of about 120 meters will be

required. Using the conservative evaluation for the thrust coefficient, $F/pA = 3$, the thrust generated on a 25 cm diameter projectile is nearly 300,000 Kg. for initial pressure of 50 atm. The projectile weight, including the model and sabot, is then about 58 Kg. for the 50,000 g's acceleration. This weight can be doubled if the initial pressure is increased to 100 atm. enabling robust structure for the model and sabot as well as for the onboard instrumentation. The initial accelerator as well as the EPA can be "cushioned" for lower acceleration levels. The length of this launcher varies inversely as the acceleration levels, i.e. lower acceleration will require the correspondingly longer launcher lengths.

The External Propulsion launcher diameter should be about 4 times the model maximum diameter or span. Therefore, a launcher of 1m diameter will enable launching of models of 25 cm. span encased in a projectile of comparable diameter. The launcher tube diameter can be reduced to 40 cm for 10 cm projectile diameter. Of course larger models can be considered with increase in the diameter of the accelerator.

2. Blast Chamber and Sabot Separation Section.

The blast of the combusting gas mixture as well as the blast of the gun for the initial acceleration follow the projectile and should be retained in a blast chamber at the exit of the launching tube. This chamber is followed by the sabot-model separating section, as shown in Fig. 10¹⁸

Since the projectile shape required for the initial accelerator and for the External Propulsion Accelerator should be of a specified axi-symmetric shape the aerodynamic model must be encased in a sabot. The outside shape of this sabot should be in accordance with the External Propulsion projectile design while supporting the model to withstand the acceleration levels. Upon exit from the accelerator launcher the sabot should be separated either mechanically or by special mechanism which will be initiated at the exit of the launcher and the sabot parts should be retained in this separation section while the free model flies into the test range.

3. Ballistic Range Section.

The free model can now fly in the instrumented ballistic range where its instantaneous trajectory positions and attitudes can be photographed and measured. Further offboard instrumentation may include optical instrumentation for measurements of the vibrational, translational and electron temperatures and interferometric photographs for measurements of density profiles. In addition various onboard instrumentation can be installed in the model, such as wall temperatures and pressures, accelerometers for model acceleration, strain gages for loads and stresses, and these can be monitored by telemetering system. If we consider models of 10 cm to 25 cm in diameter or span, such models are sufficiently large to include most details of the aerodynamic design, including deflected control surfaces and/or small control jets actuated by small rockets or gas supply.

The ballistic range can either be an atmospheric range or be enclosed in a large tube enabling controlled atmosphere for simulation of pressure-altitude effects and also atmospheric composition of other planets. The enclosed test range in a large tube can be divided into sections separated by diaphragms, enabling simulation of flight at various pressure altitudes and/or various gases in a single shot.

4. Deceleration Section.

The energy imparted to the model traveling at Mach 6 to 30 is very large and must be absorbed in order to stop the model. For simple models, the models can be expandable and a conventional "catcher" can be used. For more sophisticated and expansive models there may be some possibilities of some energy absorbing methods for arresting the models, at least in the lower hypersonic speed range.

B. THE HYPERSONIC SCRAMJET TEST FACILITY

The combustion-detonation phenomena in a scramjet engine as well as in an Oblique Detonation Wave Engine can be studied in the External Propulsion Accelerator. This facility provides the means to investigate the combustion-detonation process independently from the fuel mixing process. In this case, a projectile simulates the engine geometry and the combustion of the premixed fuel/oxidizer mixture is initiated in the model flying in the External Propulsion Accelerator. The scramjet combustion also provides net thrust for the

model flight in the Accelerator. Thus, this facility enables testing of the combustion characteristics as function of inlet, combustor and nozzle geometry, fuel/oxygen chemical parameters and flight velocity. The effects of various fuel/oxidizer mixtures can be studied by including sections separated by diaphragms in the accelerator tube. These sections can be filled with various mixtures to different initial pressures, so that effects of various pressure levels can also be simulated in this facility.

The scramjet model will be composed of a shallow sharp nosed cone acting as the scramjet inlet, a ring wing simulating the cowl of the scramjet around a cylindrical center body and a conical afterbody simulating the scramjet exhaust. Combustion is generated behind the shock wave established in front of the wedge shape lip of the ring wing. The flow field is illustrated in Fig. 9. The scramjet combustion in this configuration will produce high temperature high pressure combustion products resulting in significant net positive thrust.

THE SCRAMJET TEST FACILITY

In this application, the hypersonic scramjet testing facility will be comprised from: 1. The External Propulsion Accelerator section. 2. Transparent test section. 3. Decelerator section for model retrieval.

1. The External Propulsion Accelerator Section

The tests are conducted in a regular External Propulsion Accelerator using a specially designed model for the scramjet simulation. The model with its sabot are accelerated by a gun powder charge to the required insertion speed of 1,000 up to 1,900 m/sec. (Mach number between 3 to 5). In a simple configuration the projectile body will simulate the engine centerbody and a properly shaped ring wing around this centerbody will represent the engine cowl. The shapes of the engine intake and the shape of the combustion region inside the engine can be also simulated by this model. Combustion-detonation will be initiated by the shock waves generated at the intake to the ring wing and it will cause combustion in the space between the centerbody and the ring-cowl. The flow will be then expanded on the aft-body of the model, simulating the engine exhaust and nozzle flow characteristics. The operation of the scramjet will produce net thrust for the acceleration of the model. Therefore, measurements of the model acceleration-deceleration will enable the evaluation of the thrust obtained by this scramjet engine as a function of model velocity. More sophisticated measurements can be obtained using on-board instrumentation with telemetering. Models with hardened on-board instrumentation can be built to operate up to 50,000 g's acceleration level. The acceleration level in the projectile will depend on the thrust generated by the scramjet. Since the gas mixtures can be varied in the accelerator, this will be a method to study the effects of various chemical fuel compounds on the combustion and the thrust generation. Such studies can be made when the accelerator tube is divided into a number of sections separated by diaphragms. Each section of the accelerator tube can be filled with a certain fuel/oxidizer mixture at various initial pressures. So that in a single experiment the combustion characteristics of flight in various mixtures at specified initial pressures can be studied. These test sections can be positioned at the end of the basic accelerator tube in which the projectile is accelerated to the desired velocity.

The length of the facility will be determined by the acceleration of the model and the speed range for the tests. For the External Propulsion launcher at 50,000 g's, the required lengths of the EPA (Fig. 6) will be about 2 meters for $M = 7$ testing, 8 meters for $M = 11$ testing, about 18 meters for $M = 15$ testing and for Mach number 30 testing a launcher length of about 120 meters will be required. More sophisticated models requiring lower values of acceleration can be used by proper modifications to the launcher. Lower initial accelerations can be achieved by initial acceleration of either a Ram Accelerator stage initiated by a small light gas gun or a small rocket or the initial acceleration be achieved directly by a rocket motor which will separate at the entrance to the External Propulsion launcher. The length of this launcher varies inversely as the acceleration levels, i.e. lower acceleration will require the correspondingly longer lengths.

The External Propulsion launcher diameter should be about 4 times the model maximum diameter. Therefore, a launcher of 1m diameter will enable launching of models of 25 cm. diameter and the launcher tube diameter can be reduced to 40 cm for 10 cm models. Of course larger models can be considered with increase in size of the facility.

2. Transparent Test Section.

The possibility of including a transparent section into the Ram Accelerator facility was studied at ARL by Kruczynski et al. (Ref. 15). Such a transparent section at the end of the launcher tube will enable flow visualization photographs on the model, particularly, at the intake and exhaust regions.

3. Deceleration Section.

The energy imparted to the model traveling at Mach 6 to 15 is very large and must be absorbed in order to stop the model. For simple models, the models can be expandable and a conventional "catcher" can be used. For more sophisticated and expansive models there may be some possibilities of some energy absorbing methods for arresting the models, at least in the lower hypersonic speed range.

SINGLE STAGE TO ORBIT LAUNCHER

The ability of the EPA to accelerate missile-projectile to velocity of up to 6 times the detonation velocity of the mixture means that the EPA can launch payloads into space. Allowing acceleration level of 50,000 g's will enable reaching velocities of above 10 km/sec. with a 200 m long launcher tube, as seen in Fig. 6. This velocity is well beyond the escape velocity from earth into space. Therefore the missile-projectile payload can be fired into space directly as a single stage to orbit payload shot. Actually, the EPA propulsion system and all the fuel required for the launch are left on the ground and only the missile carrying the payload is fired into space.

SUMMARY AND CONCLUSIONS

The two methods for in-tube chemical accelerators utilizing premixed gaseous detonative mixtures; the Ram Accelerator (RA) and the External Propulsion Accelerator (EPA) are examined using an energy balance analysis. It is shown that the maximum velocity of the projectile in the RA is limited, due to the high drag caused by the choking, to about 1.3 the detonation velocity while the maximum velocity of the projectile in the EPA can reach up to 6 times the detonation velocity.

The results of numerical simulation of the flow over projectile configurations using a Navier-Stokes code with chemical reactions show that combustion can be generated by a small step on the shoulder of the projectile. These calculations indicate that positive thrust is obtained.

It is shown that the projectile can be stabilized aerodynamically by 6 small fins which can be canted to impart roll to the flying projectile.

The applications of the EPA to ground test facilities such as a launcher for a hypersonic flight range and as a facility for combustion research in scramjet engines are discussed.

REFERENCES

1. Hertzberg, A., Bruckner, A.P. and Bogdanoff, D.W., "Ram Accelerator: A New Chemical Method for Accelerating Projectiles to Ultrahigh Velocities", AIAA Journal, Vol. 26, No. 2, 1988, pp. 195-203.
2. Rom, J., "Method and Apparatus for Launching a Projectile at Hypersonic Velocity", U.S. Patent 4,932,306, June 12, 1990.
3. Rom, J., Nusca, M.J., Kruczynski, D., Lewis, M., Gupta, A.K. and Sabeen, J., "Investigations of the Combustion Induced by a Step on a Projectile Flying at Hypersonic Speeds in the External Propulsion Accelerator", AIAA Paper 95-0259, 1995.
4. Rom, J., Nusca, M., Lewis, M., Gupta, A.K. and Sebian, J. "Calculations of combustion in a Scramjet engine model in the External Propulsion Accelerator as a test facility" Proceedings of the 35th Israel Annual Conference on Aerospace Sciences, February 1995.

5. Rom, J., Lewis, M., Gupta, A.K. and Sebian, J., "Hypersonic aerodynamic test facility using the External Propulsion Accelerator", to be presented at the 6th International AIAA Aerospace plane and hypersonic technologies, April 1995.
6. Rom, J. and Kivity, Y., "Accelerating Projectiles up to 12 km/sec. Utilizing the Continuous Detonation Propulsion Method", AIAA Paper 88-2969, 1988.
7. Rom, J. and Avital, G., "The External Propulsion Accelerator: Scramjet Thrust Without Interaction with the Accelerator Barrel", AIAA Paper 92-3717, 1992.
8. Tivanov, G. and Rom, J., "Investigation of Hypersonic Flow of a Detonable Gas Mixture Ahead of a Forward Facing Step", AIAA Paper 93-0611, 1993.
9. Tivanov, G. and Rom, J., "Stability of Hypersonic Flow of a Detonable Gas Mixture in the Stagnation Region of a Blunt Body and a Forward Facing Step", Proceedings of the 33rd Israel Annual Conference of Aeronautics and Astronautics, Feb. 1993.
10. Tivanov, G. and Rom, J., "Analysis of the Stability Characteristics of Hypersonic Flow of a Detonable Gas Mixture in the Stagnation Region of a Blunt Body", AIAA Paper 93-1918, 1993.
11. Nusca, M.J., "Reacting Flow Simulations for Large Scale Ram Accelerator", AIAA Paper 94-2963, 1994.
12. Rom, J., "Analysis of the Initiation of Detonation on a Hypervelocity Projectile and its Maximum Velocity in the External Propulsion Accelerator", TAE Report 729, December 1994.
13. Lee, J.H.S., "On the Initiation of Detonation by a Hypervelocity Projectile", Paper presented at the Zeldovich Memorial Conference on Combustion, Sept. 12-17, 1994, Voronovo, Russia.
14. Knowlen, C., Higgins, A. and Bruckner, A., "Investigation of Operational Limits to the Ram Accelerator", AIAA Paper 94-2967, 1994.
15. Hinkey, J.B., Burnham, E.A. and Bruckner, A.P., "Investigation of Ram Accelerator Flow Fields Induced by Canted Projectiles", AIAA Paper 93-2186, 1993.
16. Nusca, M.J., "Numerical Simulation of Fluid Dynamics with Finite-Rate and Equilibrium Combustion Kinetics for the 120 mm Ram Accelerator" AIAA Paper 93-2182, 1993.
17. Nusca, M.J., "Numerical Simulation of Gas Dynamics and Combustion Kinetics for a 120 mm Ram Accelerator" First International Workshop on Ram Accelerator, ISL, France, 1993.
18. Chakravarthy, S.R., Szema, K.Y., Goldberg, U.C., Gorski, J.J. and Osher, S., "Application of a New Class of High Accuracy TVD Schemes to the Navier-Stokes Equations" AIAA Paper 85-0165, 1985.
19. Palaniswamy, S., Ota, D.K. and Chakravarthy, S.R., "Some Reacting Flow Validation Results for USA-Series Codes" AIAA Paper 91-0583, 1991.
20. Kruczynski, D.L. and Nusca, M.J., "Experimental and computational Investigation of Scaling Phenomena in a Large Caliber Ram Accelerator" AIAA Paper 92-3425, 1992.
21. Kruczynski, D.L., "New Experiments in a 120 mm Ram Accelerator at High Pressures" AIAA Paper 93-2589, 1993.
22. Avital, G., "Interaction between Detonation Waves and Shock Waves in Detonative Mixtures in Hypersonic Flow Field", Doctoral Thesis, Submitted to the Senate of the Technion, June 1995.

23. Witcofski, R., Scallion, W., Carter, D. Jr. and Courter, R., "An Advanced Hypervelocity Aerophysics Facility: A Ground-Based Flight-Test Range", AIAA Paper 91-0296, 1991

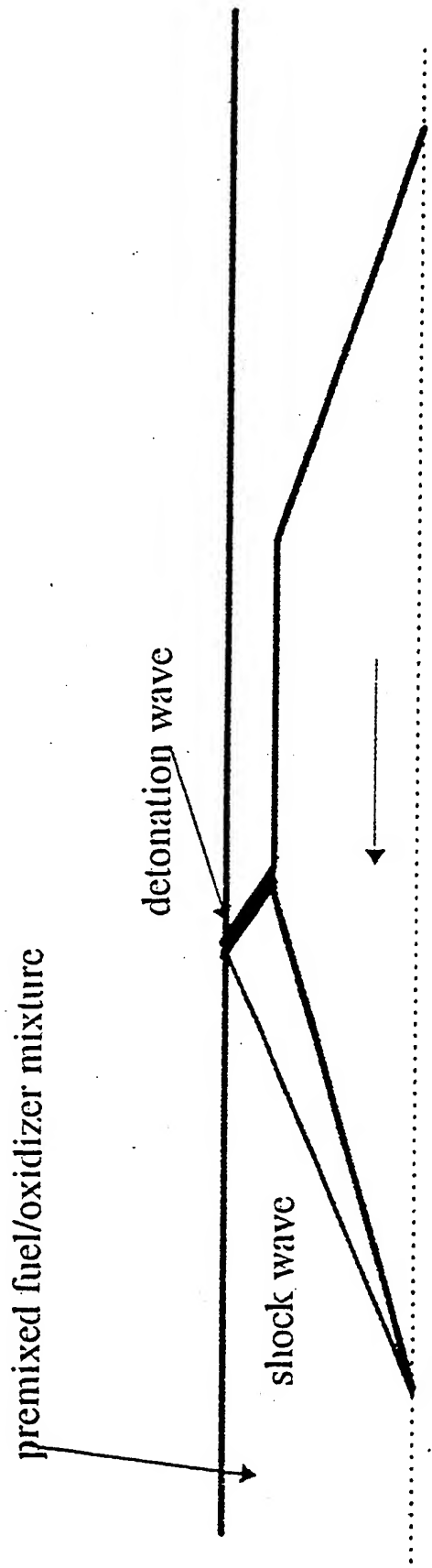


Figure 1. The Ram Accelerator projectile in the detonative mode (Ref. 1)

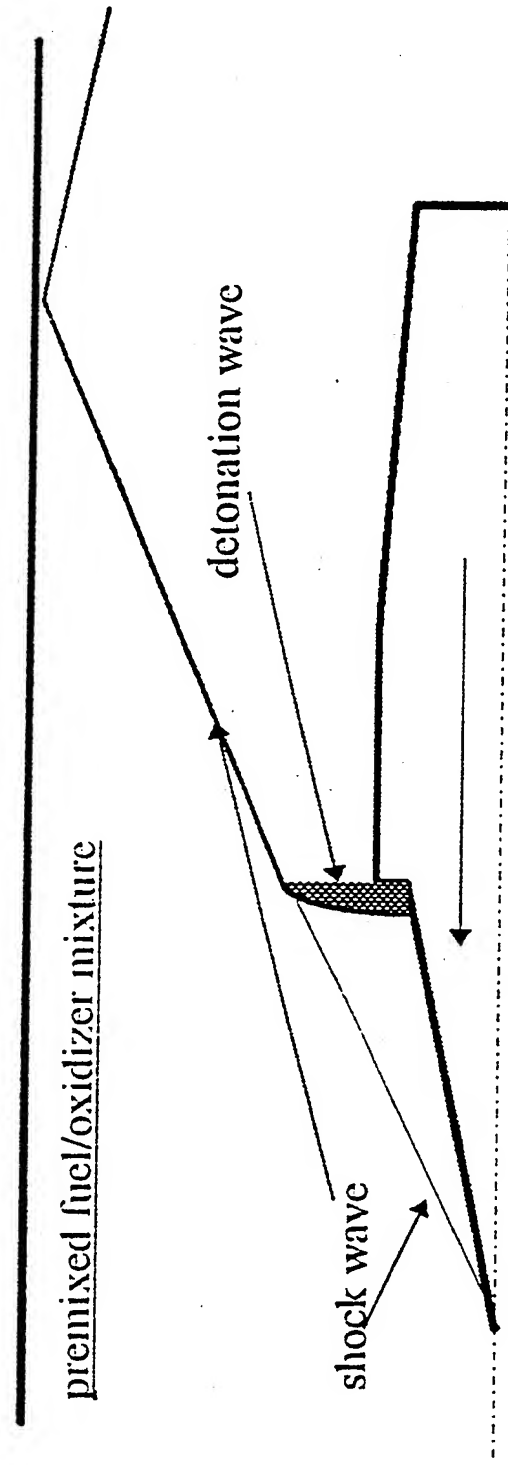


Figure 2. The External Propulsion Accelerator projectile with a forward facing sten (Ref. 2)

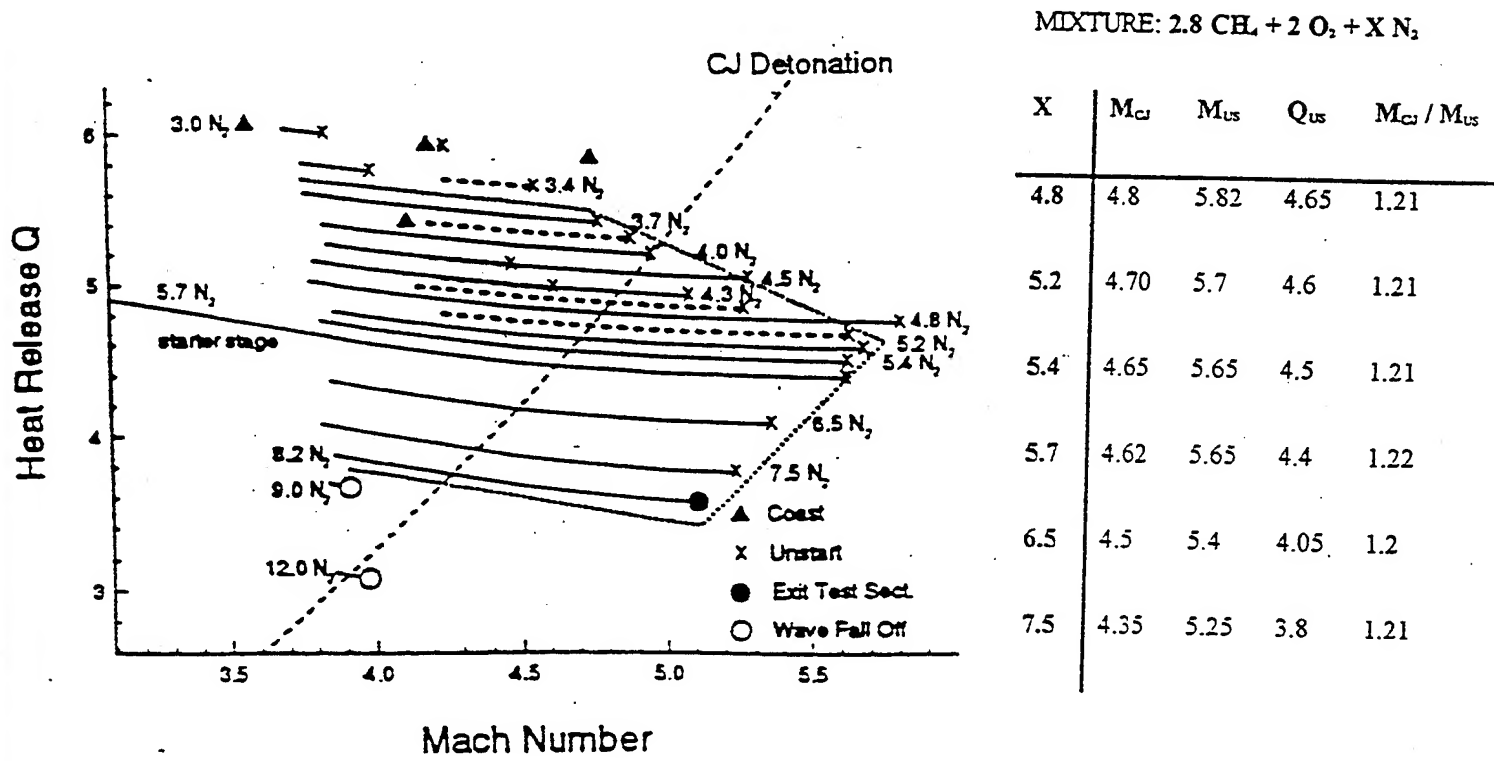


Figure 3a. Results of variable nitrogen experiments plotted as thermally choked heat release vs. flight Mach number (from Ref. 14)

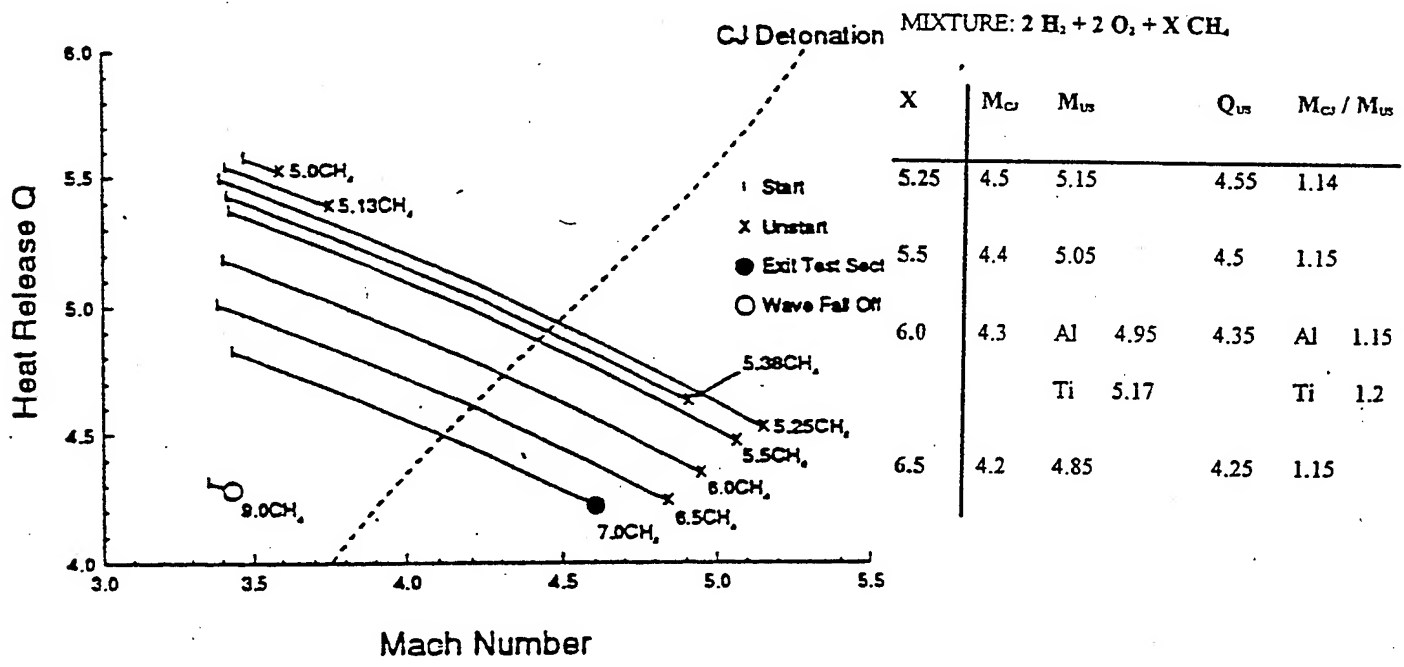
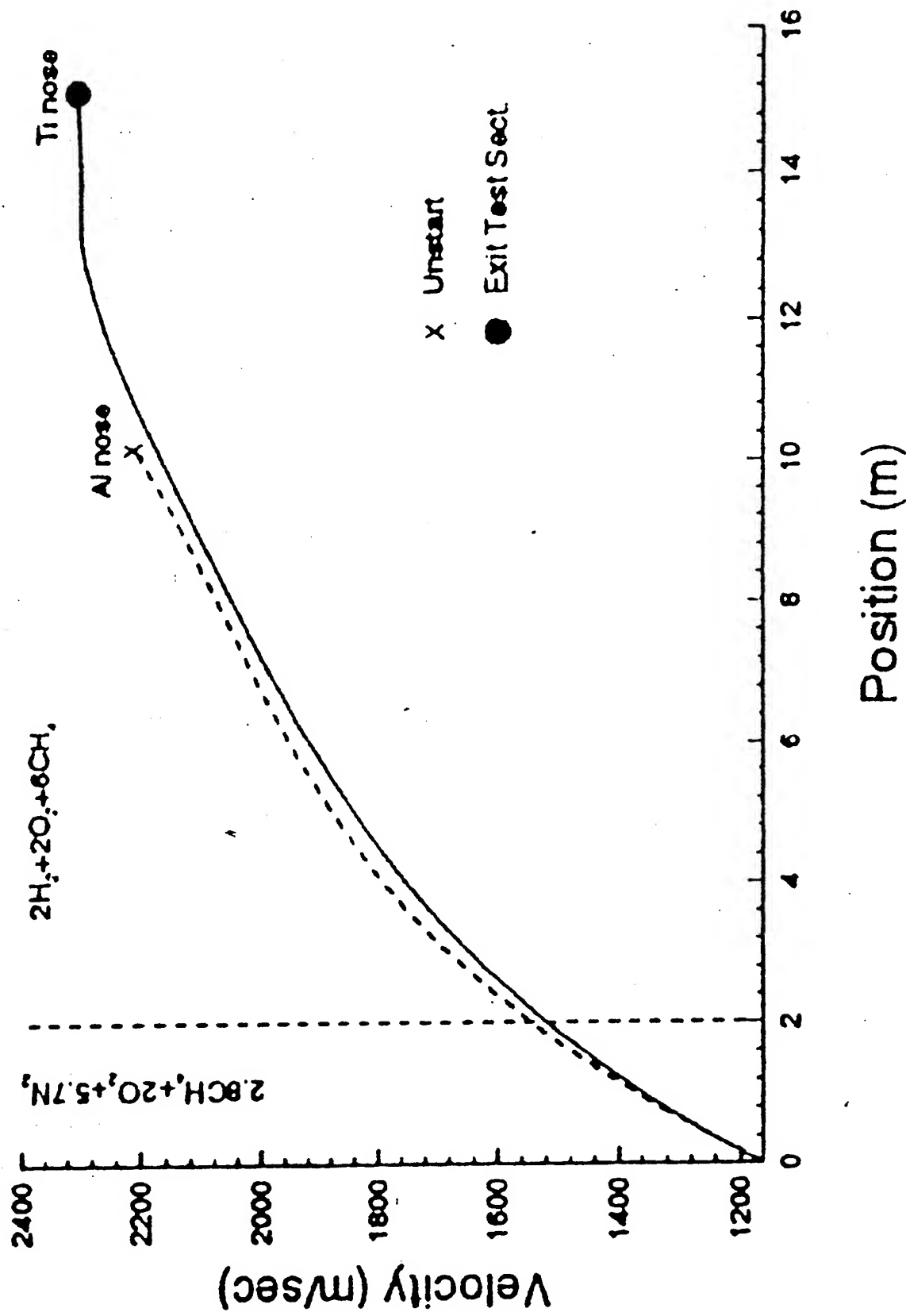


Figure 3b. Results of variable methane experiments plotted as thermally choked heat release vs. flight Mach number (from Ref. 14)



4. Velocity-distance data comparing aluminum and titanium nose projectiles (from Ref. 14).

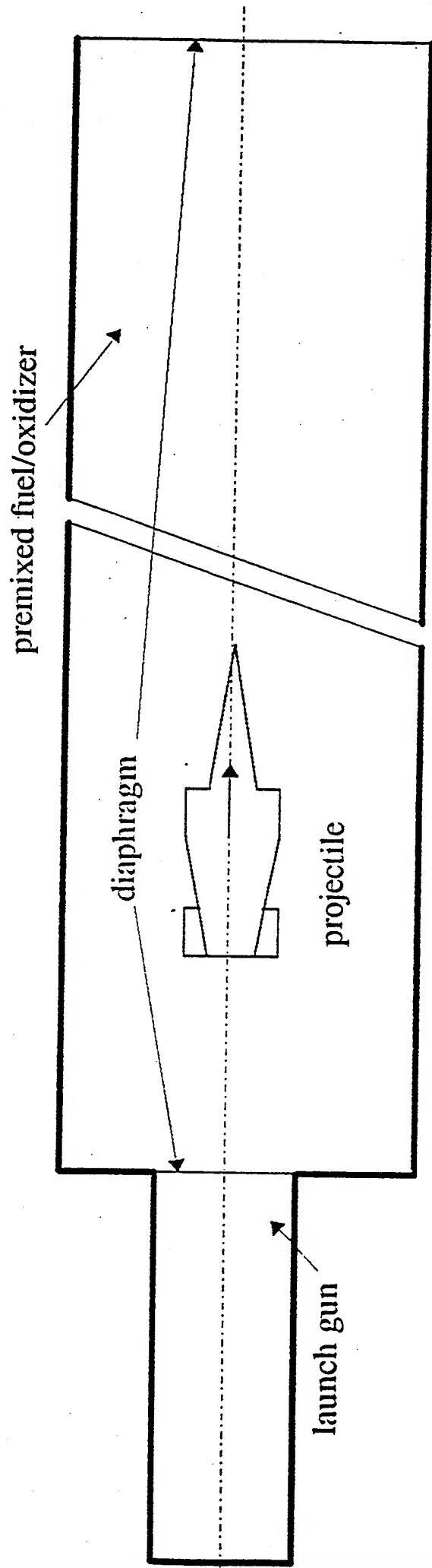


Figure 5. Schematic of the External Propulsion Accelerator facility

50,000 G

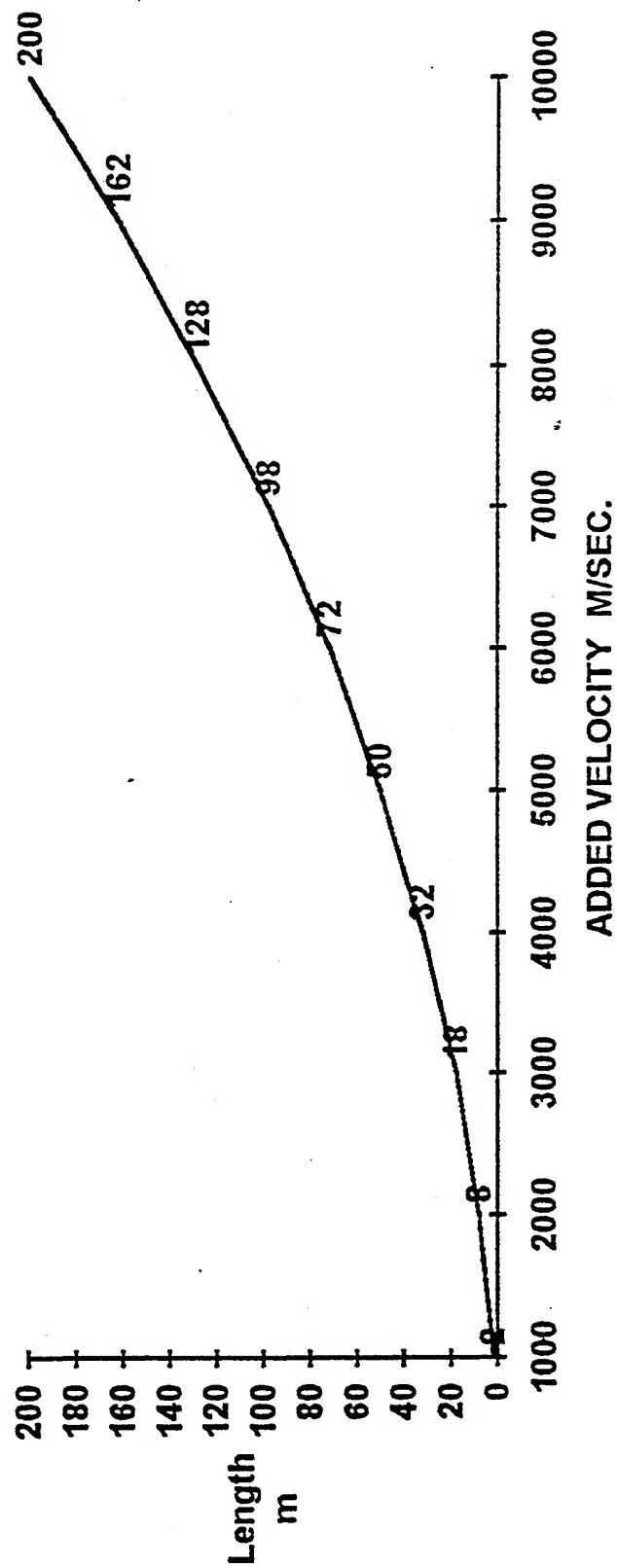


Figure 6. The added velocity as a function of accelerator tube length for 50,000 g's acceleration

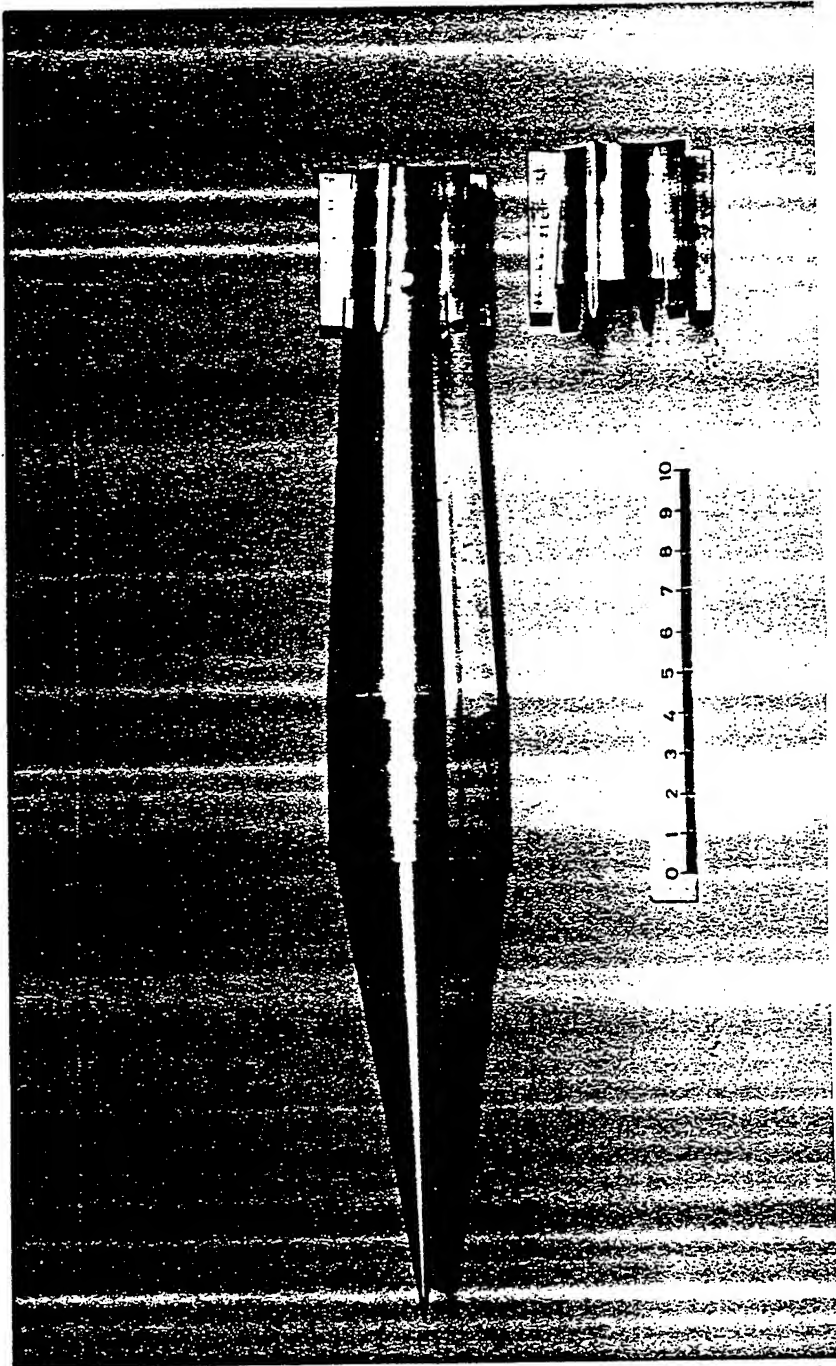


Figure 7. An External Propulsion Accelerator projectile with a 1 mm step and a tail of 6 trapezoidal fins with 32 mm span.

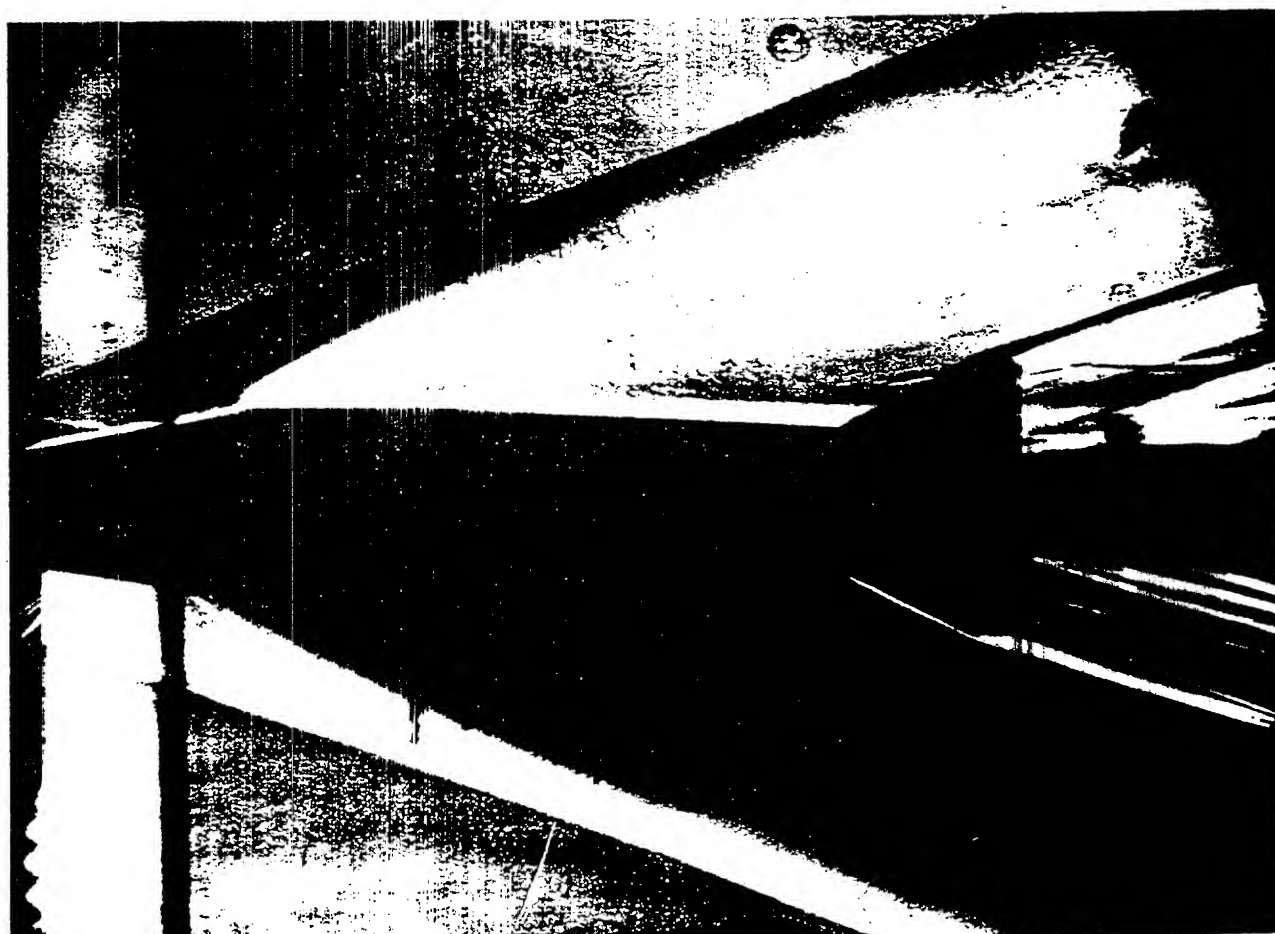
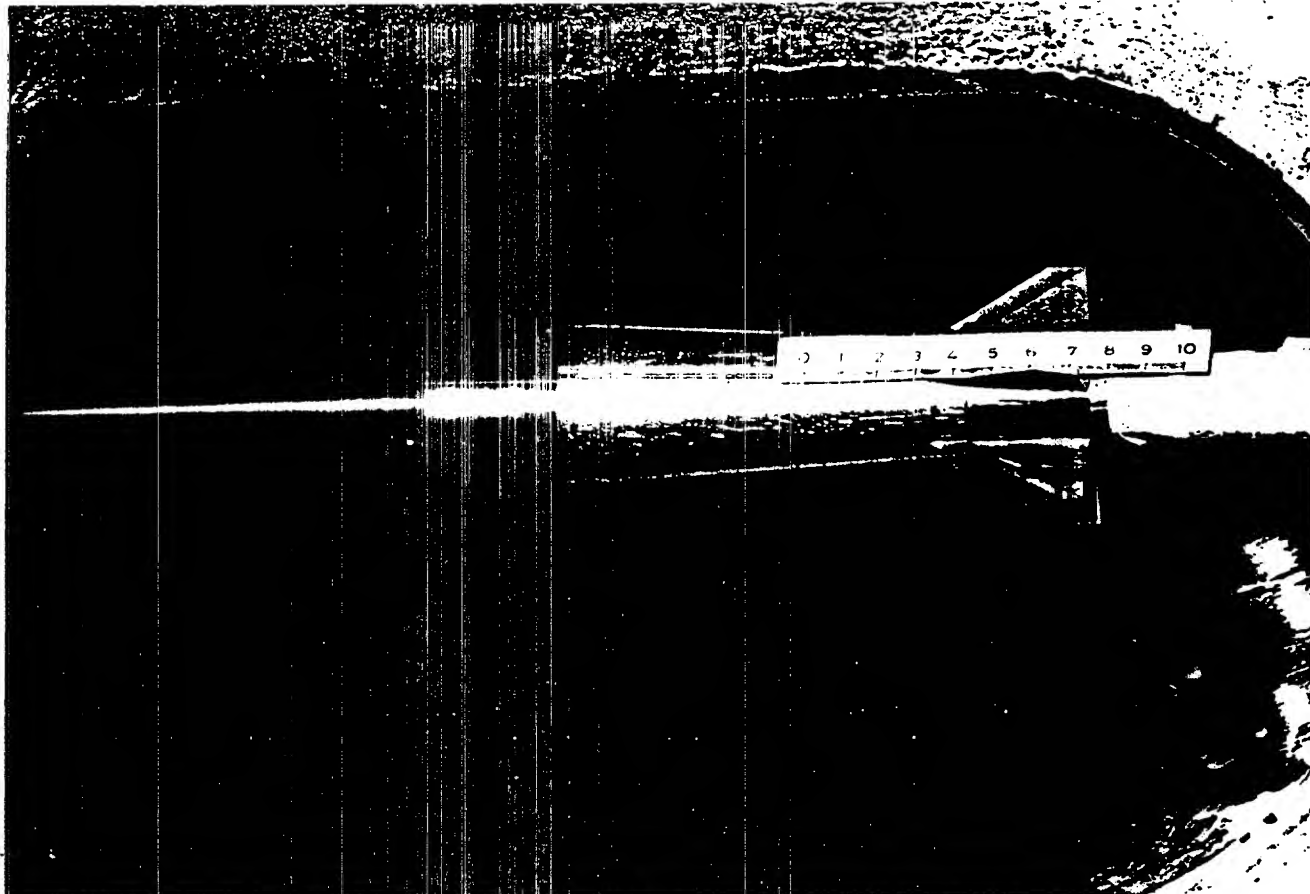


Figure 8. An External Propulsion Accelerator projectile with a 1 mm step and a tail of 6 trapezoidal fins with 51.6 mm span.

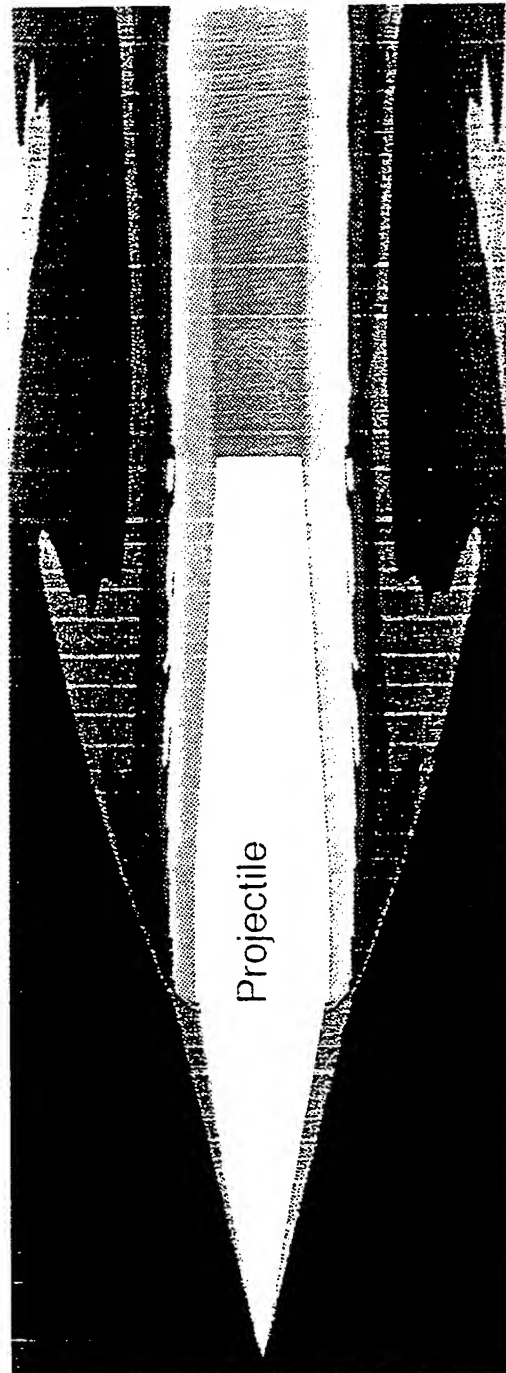
Reacting Flow Field

Velocity = 2175 m/s, Mach = 6.0, $V/V_{cj} = 1.5$

Mixture: $3CH_4 + 2O_2 + 10N_2$, $a = 361$ m/s, $\Gamma = 1.376$, $V_{cj} = 1450$ m/s

Fill Conditions: $P = 50$ atm, $T = 300$ K

1 mm Step, 3.5 deg half-angle afterbody



Tube Wall ($D=120$ mm)

T/T_{ref}

8.372
8.068
7.764
7.460
7.156
6.851
6.547
6.243
5.939
5.635
5.331
5.027
4.723
4.419
4.115
3.811
3.507
3.202
2.898
2.594
2.290
1.986
1.682
1.378
1.074

Figure 9. The temperature ratio distribution around the 1 mm step model for Mach number 6 flow with chemical reactions in the EPA.

Ring Configuration - Non-Reacting

Flow Conditions

Gamma = 1.4, Mach = 6, Velocity = 2083 m/sec

Pref = 50 atm, Tref = 300K, a = 347 m/sec

Projectile Geometry

Ring Outer Radius = 31.25 mm, Max Ring Thickness = 3.75 mm

Projectile Length = 211 mm, Max Projectile Radius = 16 mm

T/Tref
4.40934
4.22802
4.0467
3.86537
3.68405
3.50273
3.32141
3.14009
2.95876
2.77744
2.59612
2.4148
2.23348
2.05216
1.87083
1.68951
1.50819
1.32687
1.14555
0.964224

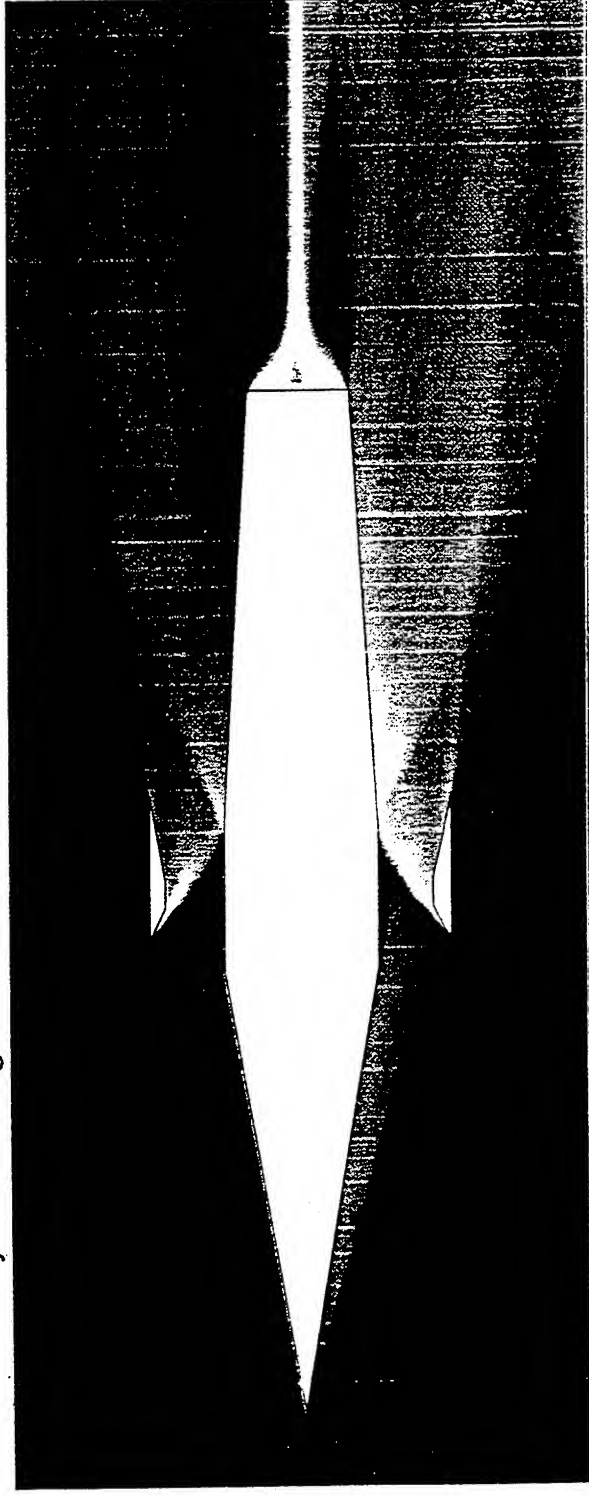


Figure 10. The temperature ratio distribution around the ring wing model for Mach number 6 flow without chemical reactions in the EPA.

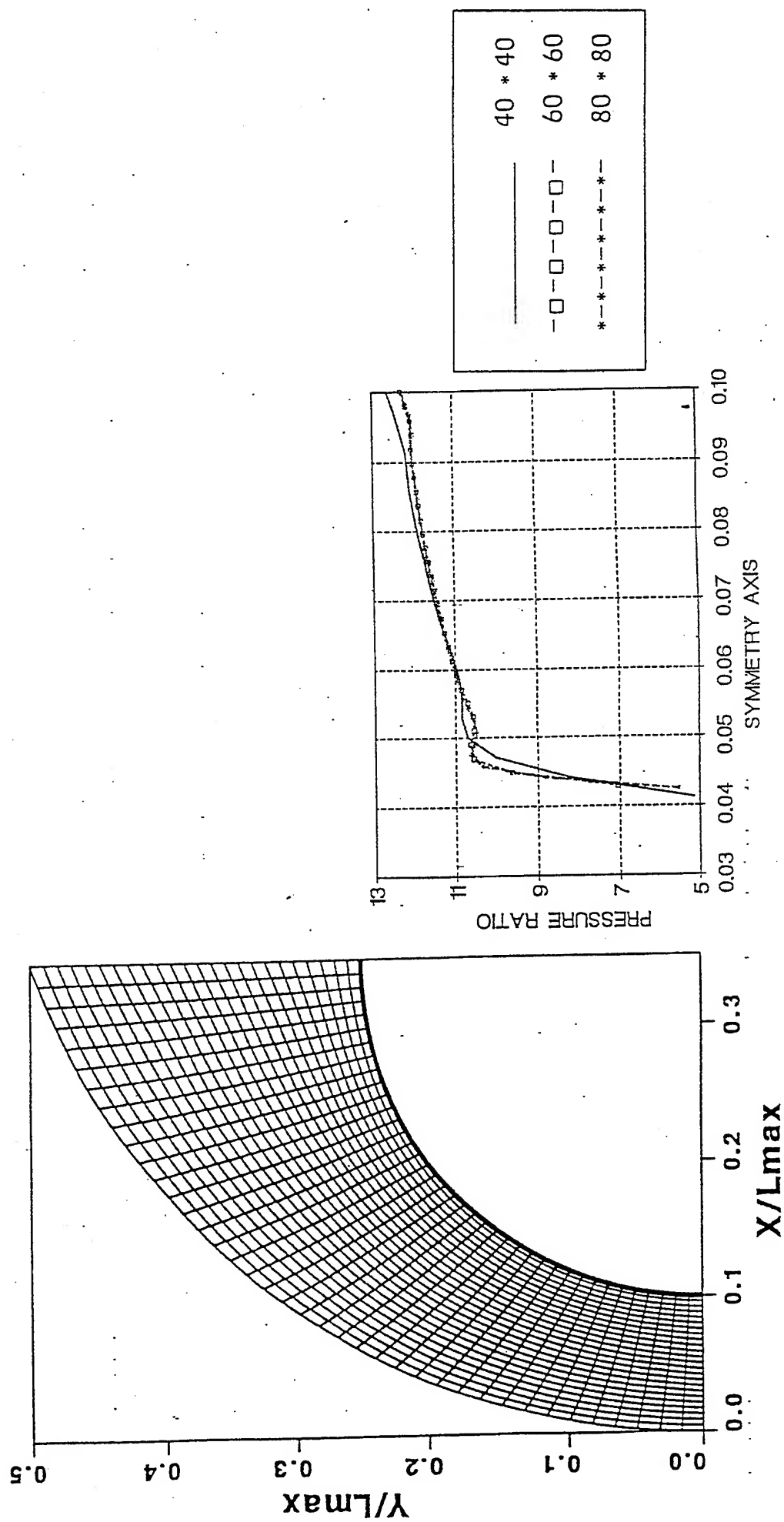


Figure 11. Schematic of the grid structure (left) and validation of grid density (right) for reacting flow calculations on a hemisphere at $M = 3$.

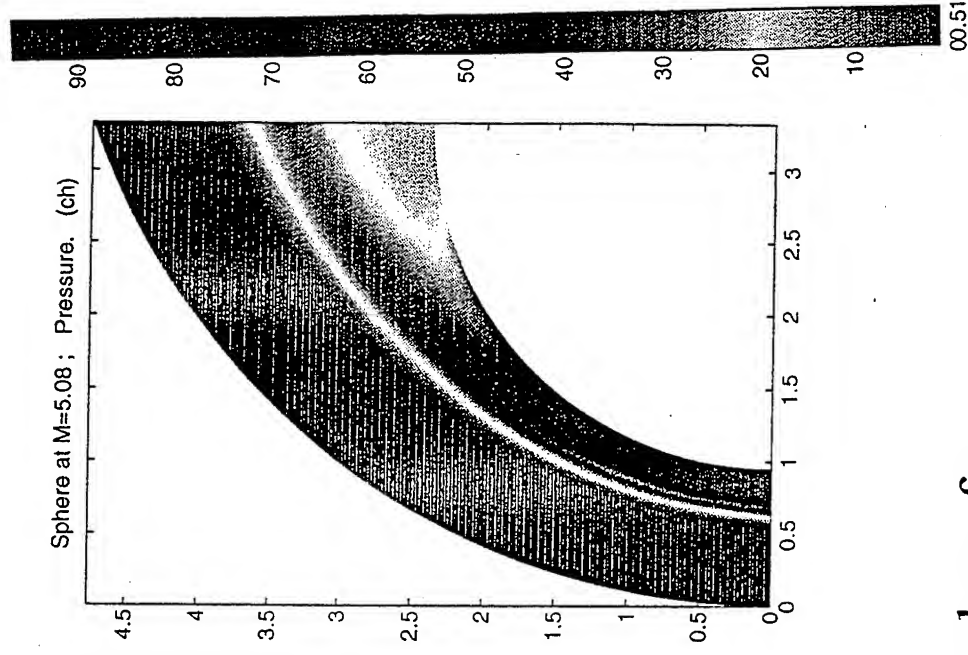
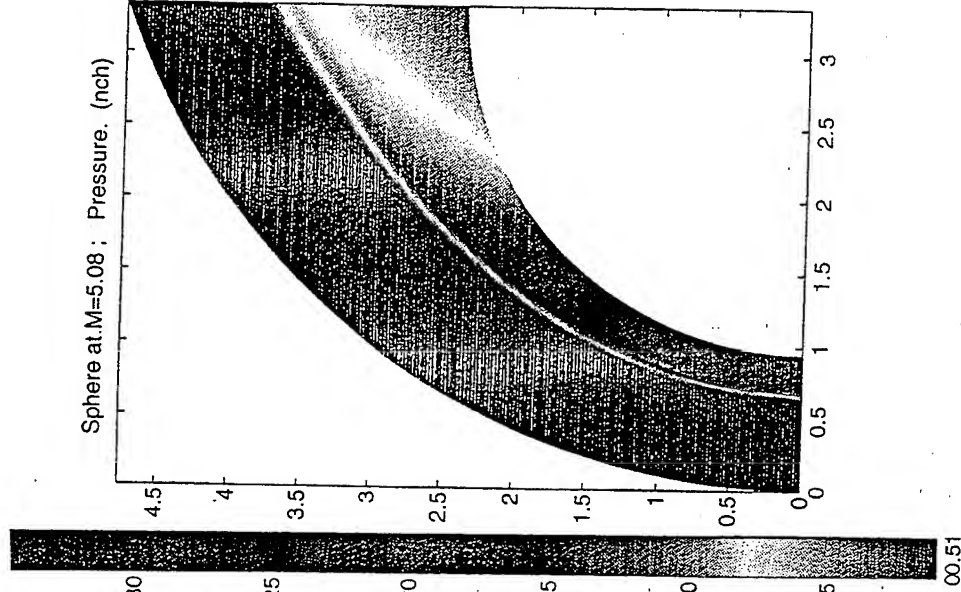
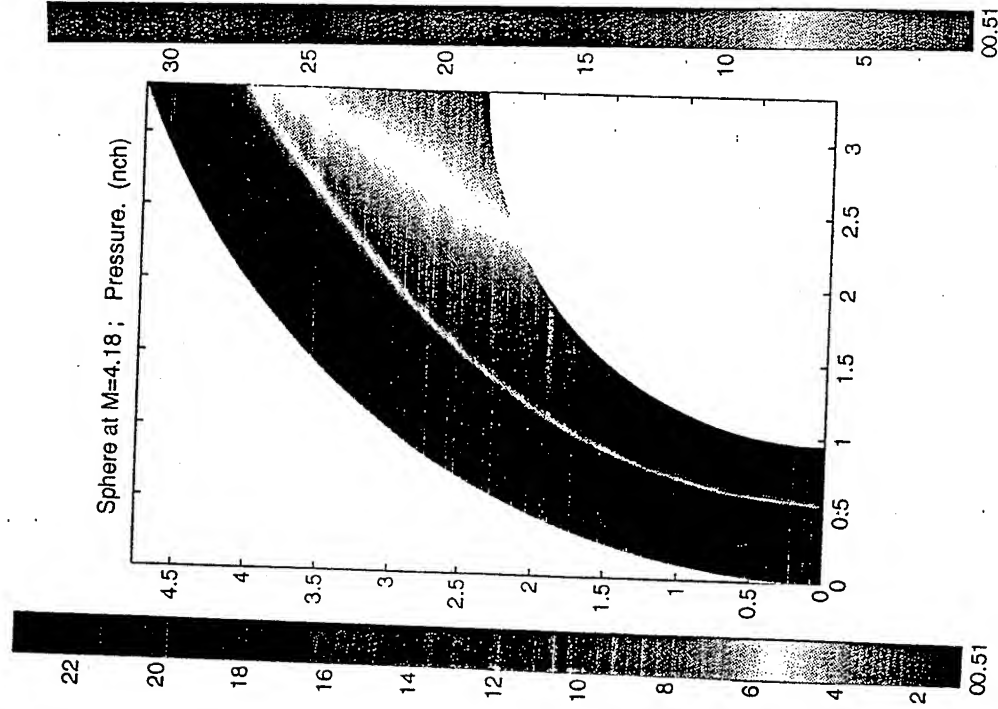


Figure 12. Pressure distribution on a hemisphere for non reacting flow at $M = 4.18$ and 5.08 and for reacting flow of $H_2 + O_2 + N_2$ mixture at $M = 5.08$ and initial

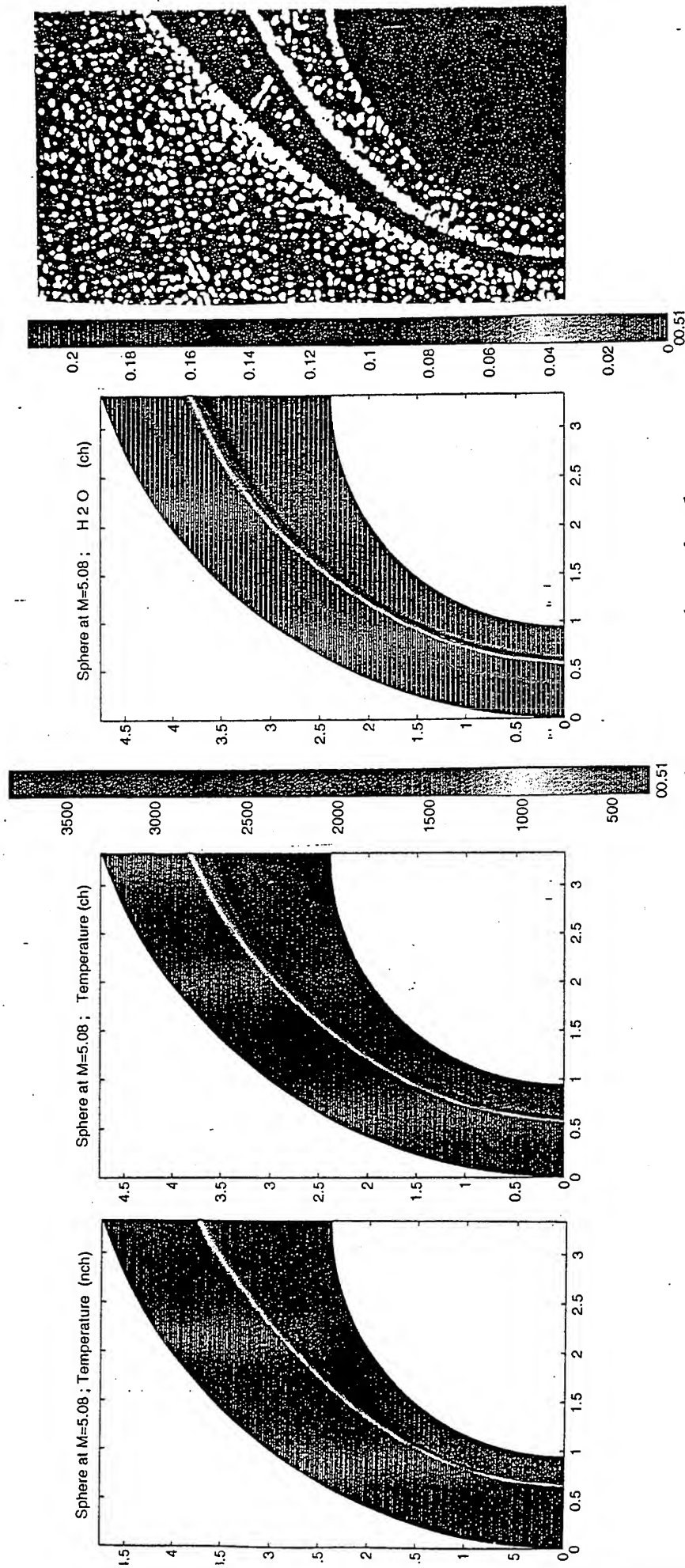


Figure 13. Temperature distribution on a hemisphere for non reacting flow at $M = 5.08$ (left), Temperature and water content distributions for reacting flow of $H_2 + O_2 + N_2$ mixture at $M = 5.08'$ and initial pressure of 1 atm. (center) and schlieren photograph of sphere shot into $H_2 + O_2 + N_2$ mixture at $M = 5.11$ and initial pressure of 0.3 atm. (right, from Lehr, Ref. 23).

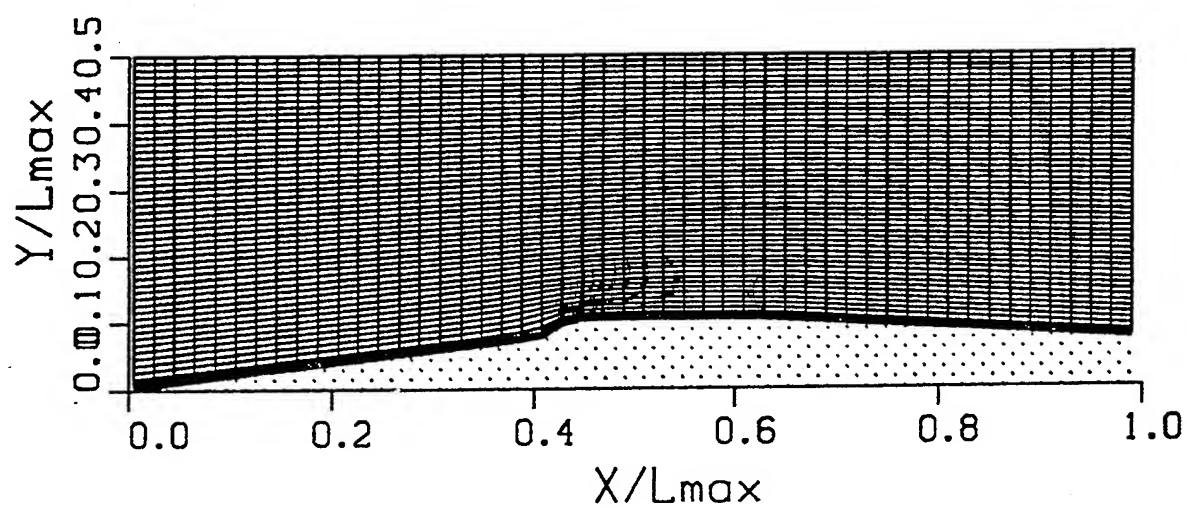


Fig. 14. Schematic of the grid structure over the projectile with the 10° half angle nose cone and a 70° conical ramp.

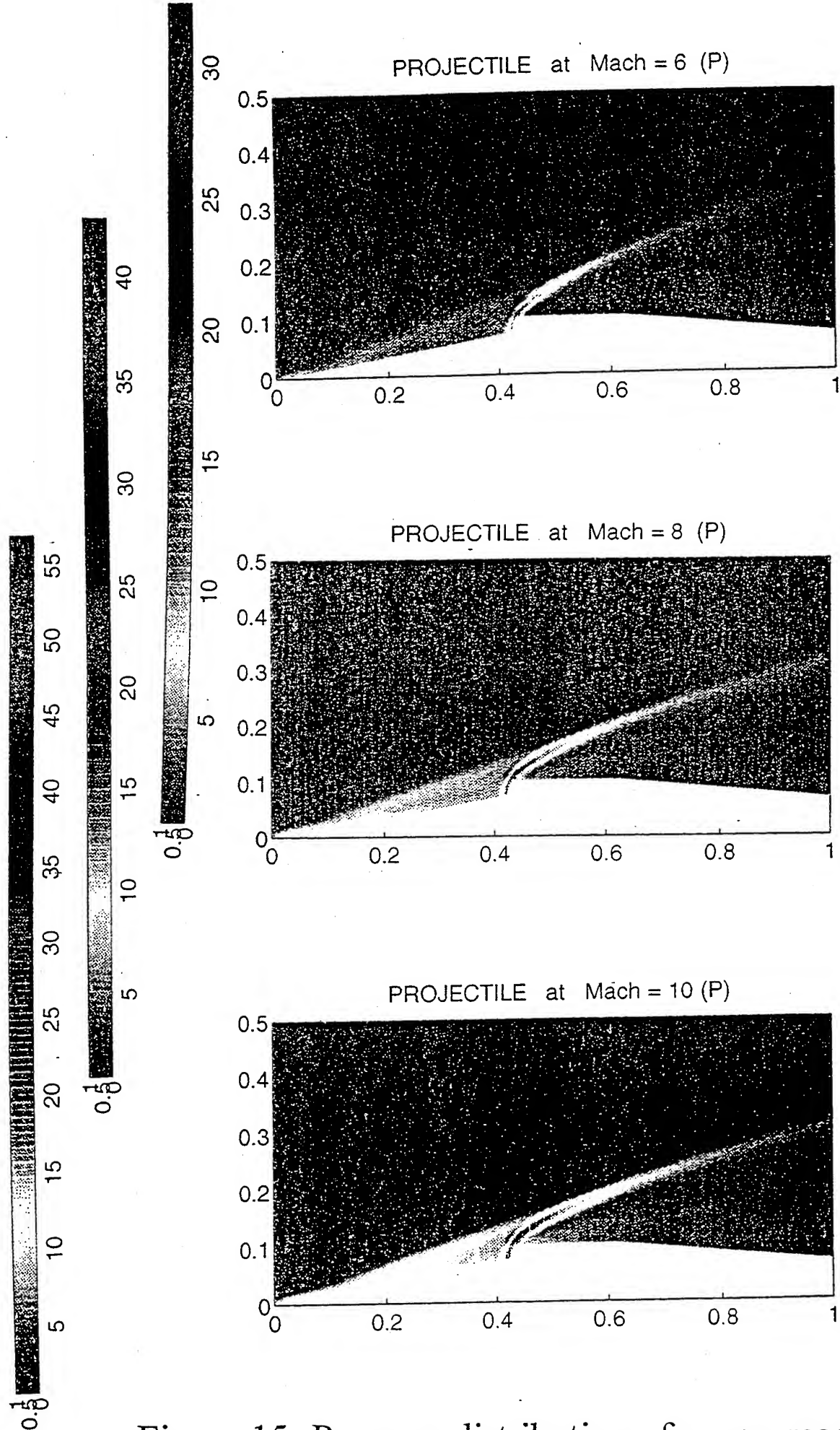


Figure 15. Pressure distributions for non reacting flow over the projectile at $M = 6, 8$ and 10 .

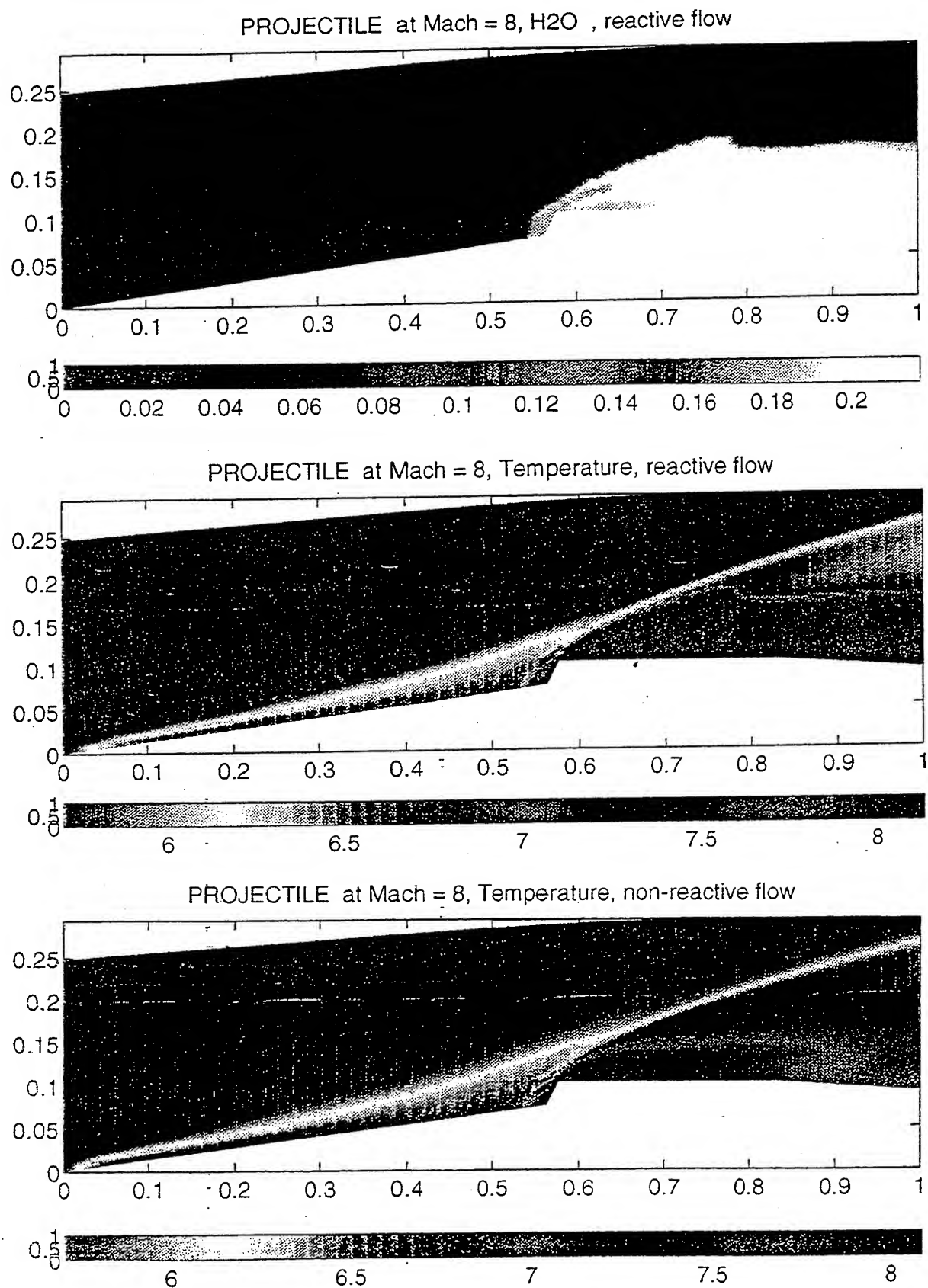


Figure 16. Temperature distribution in the front part of the projectile for non reacting flow at $M = 8$ and temperature and water content distributions for reacting flow of $H_2 + O_2 + N_2$ mixture at $M = 8$ and initial pressure of 1 atm.

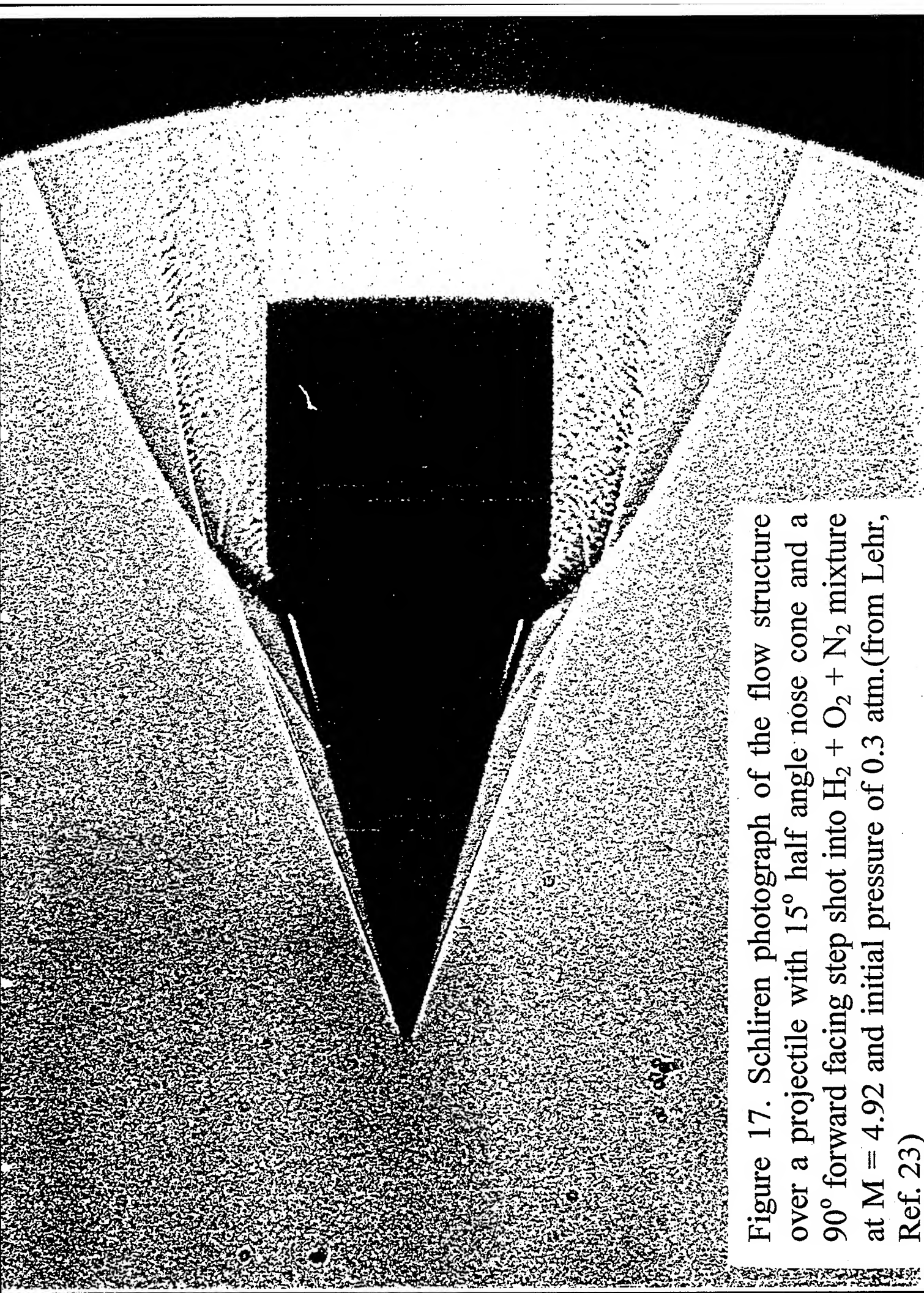


Figure 17. Schlieren photograph of the flow structure over a projectile with 15° half angle nose cone and a 90° forward facing step shot into $H_2 + O_2 + N_2$ mixture at $M = 4.92$ and initial pressure of 0.3 atm.(from Lehr, Ref. 23)



Launcher **Blast chamber**

Test section

Model-sabot separation

Figure 18. Schematic view of the hypersonic flight range facility using EPA launcher

FEASIBILITY STUDY OF JET INTERACTION FOR IGNITION IN CHEMICAL ACCELERATORS

Julius Brandeis
Ophir Oettinger

Rafael
Haifa, Israel

Introduction

This paper presents analytical and numerical results in support of the accelerator concept utilizing jet interaction for ignition, proposed earlier by Brandeis [1,2]. The main element of the proposed system that differentiates it from other published concepts, is the projectile. The projectile's external configuration depends on various factors and may not differ from other designs. Within the projectile, a chamber is provided for storing the gas under high pressure. The gas will be compressed to the necessary pressure through one of several possible means. This gas is then released as high pressure jets that by interacting with the cross-flow give rise to curved shocks just upstream of the jets. To provide a continuous shock front, the discrete jets must be distributed circumferentially in a ring around the projectile in sufficient number (6 or more). As more jets are used, the shock curtain assumes a more regular shape. Moreover, the nozzle geometry need not be circular. Rectangular slots facing the flow with the wide side could be used, and may offer the advantage of more uniform shock front. During the gun launch the projectile is enclosed within a protective sabot, which also serves to plug the jet exit ports. The high pressure from the chamber within the projectile helps to cast off the sabot, thus activating the jets.

The use of jets is essentially analogous with the initiation of combustion by use of a forward-facing step, as proposed by Rom [3]. The accelerator proposed by Rom has a barrel that is wide enough not to produce reflection of shock waves in the vicinity of the projectile, but instead, the detonation wave is produced by a shoulder portion in the form of a step. This method allows, in essence, a tube-independent propulsion mode, called "external propulsion". In all ram accelerator systems presently existing, based on the concept first demonstrated by Hertzberg et al [4], the accelerator barrel must be sufficiently narrow to produce the reflected shock (or detonation) waves. These may be called "internal propulsion" accelerators.

Hybrid Concept: Ignition Through Jet Interaction

The proposed new hybrid concept for achieving ignition and propulsion in external propulsion and ram accelerators takes advantage of the shock system established when an under expanded jet is ejected from the projectile moving at high supersonic speeds. The concept is applicable to the external propulsion system which is tube independent, as well as to the internal propulsion system. The jet interaction principle utilized here, is encountered when a jet is injected into a supersonic cross flow, see for example Spaid et al [5].

The main effect of the jet injection into a supersonic main stream is to produce a strong, curved bow shock ahead of the jet. In fact, the jet interaction shock structure and flow field are highly analogous with those due to the forward facing step proposed by Rom [3]. The strong bow shock produces sufficient heating and compression of the gas to make combustion or detonation possible along a reaction front that follows the shock and the induction zone. Both of

these modes are practical in the external and internal (tube dependent) configurations, using the proposed jet interaction scheme for ignition. Other modes of operation, such as thermally and mechanically choked modes, utilizing subsonic combustion, are possible using the present method for the internal propulsion hybrid accelerator, combining the ram or external propulsion, and the jet interaction concepts. For some combustion modes, the induction zone may be significant, while for detonation process the shock is closely coupled with the reaction (detonation) wave. The injected gas jet mixes with the ambient gas. Within this region the mixture may therefore be made locally more energetic by injecting a volatile fuel such as hydrogen, or an oxidizer, such as oxygen. The equivalence ratio is thus locally altered in such a way as to produce a more energetic reaction, allowing the use of less than optimal ambient mixture and consequently alleviating a possible cause of "unstart".

A very energetic combination of gases is the H_2/O_2 mixture with possibility of diluents. The injectant gas could then be hydrogen or oxygen. The detonation velocity of such mixture would be about 3 km/s, therefore it would be appropriate only at projectile velocities greater than that, if the detonative mode is to be used. For earlier stages of acceleration, a nitrogen delineate would be used in the ambient gas. At a still earlier phase, a hydrocarbon mixture using CH_4 (having detonation velocity <2 km/s in air), may be appropriate.

The proposed use of gas jets for inducing ignition offers several additional advantages. First, in contrast to the step, it should not (to the first order) affect the drag of the projectile because the momentum lost by the outer flow due to jet interaction is recovered as jet flow momentum turned in the direction of the free stream. In fact, by vectoring the nozzles downstream, net thrust may be obtained. As such, the jet may be the primary means for compressing and heating the gas, which would mean that the method is less dependent on the projectile's bow geometry. Therefore, slender bow shapes having low pressure drag can be utilized. Lastly, the jets could serve as an effective means of control for the projectile in free flight.

Analytical Model and Results.

Several simple phenomenological models were put together in reference 1 to establish the feasibility of using the jet interaction for ignition. In essence, the model serves to link the gas heating and compression by the shock to the parameters defining the jet that causes the shock. The simplest model used for estimating the penetration height of the jet is not sensitive to the effect of the gas' molecular weight. In reality, a light gas such as hydrogen will have an advantage in this respect over a heavier gas. The high pressure jet is assumed to be sonic at exit. The shape and location of the bow shock produced by the jet are predicted by using the blast analogy. The conditions behind the bow shock are calculated using the shock relations, once the bow shock curvature and upstream conditions are known.

Calculations with the composite model were done to estimate the variation of flow parameters such as pressure, temperature and density across the shock due to the changes in the jet parameters and the flight Mach number. In the present case, this will be done by considering only the case where the shock and the reacting flow are not coupled. The ambient atmosphere considered in these calculations is stoichiometric hydrogen-oxygen mixture at 10 atm fill pressure. The injectant gas is molecular oxygen. The gain associated with using the relatively heavy oxygen is the smaller required storage volume. This in itself is a major concern in any projectile design. Another consideration affecting the choice of the injectant gas is its effect on the reactivity of the mixture. Other parameters considered are the jet's stagnation pressure, mass flow rate and the the Mach number of the projectile.

Assuming that the bow shock due to the projectile nose heats the gas to a considerable extent, the jet bow shock needs only to contribute enough additional heat to ignite the mixture. The compression and heating ability of the shock will decrease uniformly as the shock wave curves in the direction of the surface. To facilitate comparisons, a specific value can be chosen for the minimum acceptable heating ratio for which ignition may be expected, that corresponds to a specific location along the shock. This constitutes the upper bound on that portion of the shock that can produce ignition.

During the launch phase the projectile will be accelerated through a wide range of Mach numbers. This Mach number variation has great implication in the design of the projectile and is therefore carefully examined in the next set of results. The range of Mach numbers considered (between 6 and 11) in the present ambient gas mixture is representative of the velocities 3000 m/s to 6000 m/s. The injectant gas in the forthcoming example is oxygen, and the rate of injection is 1.54 kg/s.

The jet penetration height decreases monotonously though not linearly, with Mach number. The reference point, chosen as an example of minimum heating ratio for ignition that may be required of the jet bow shock, occurs further out along the shock when the Mach number is increased, even though it corresponds to a decrease of the penetration height. Therefore, at a constant injection rate, the part of the shock wave effective in inducing reaction increases as the projectile accelerates.

Example for an Active Projectile

The method described in previous sections is now applied as an illustrative example to a typical configuration. Only the projectile characteristics are examined here and no performance calculations will be attempted. The projectile chosen has a conical forebody followed by a cylindrical shoulder section containing the jets. It is assumed that the projectile dimensions are similar to those for the Army Research Lab 120 mm ram accelerator facility [6]. The conical forebody vertex angle is chosen according to need. Larger cone angle results in stronger conical shock, thus reducing the strength of the bow shock due to the jet (and therefore the jet strength) that is required for ignition. On the other hand, for reasons of drag reduction as well as reduction of the premature ignition risk, it is desirable to have the conical forebody section as slender as possible. Therefore, a range of possible cone angles and jet injection rates will be examined parametrically. The ambient, combustible mixture in the example is again stoichiometric hydrogen-oxygen combination, and the injectant gas is oxygen. It is assumed on the basis of published data that the ambient gas mixture ignition should occur within the range of temperatures of 1300°K to 1500°K.

The amount of gas necessary is a function of many variables. The system related variables translate basically into the time the projectile requires to traverse the accelerator. This may be taken as 0.01 s as representative of accelerators several tens of meters long. The storage pressures will be between 100 and 1000 atm, depending on the ambient fill pressure and required mass flow. The stored gas will also be at an elevated temperature resulting from compression. It is reasonable that for the system discussed here the required mass will be on the order of 100 gram. The volume required to store 100 gr. of oxygen at, say, 500 atm. pressure is about 150 cc. This could be easily accommodated in a 9.15 cm diameter projectile, and the mass would be small compared to the projectile mass of 4.3 kg. The containment vessel would probably cause a greater design problem.

CFD Results

CFD simulations were carried out using the INCA code run in the inviscid (Euler) mode. These calculations were carried out in non-reactive medium where both the ambient and injected gases are

air. The model projectile discussed in the previous section having basic dimensions of the ARL projectile [6] was used in these calculations. It consists of 10 deg. fore- and aft cones, and a cylindrical midsection. Axisymmetric simulations were run on a 195x101 mesh with circumferential injection from a slot 1.5 mm wide. Grid independence was demonstrated. The 2-D results obtained are useful for parametric study, where jet pressure, temperature and exit velocity and ambient pressure are the variables investigated. The jet mass flow rate is exaggerated however, as the axisymmetric port area is an order of magnitude greater than the total area of the multiple jets in an actual configuration. For this reason comparison with analytical calculations presented earlier was not possible. The results presented show clearly that supersonic jets at high temperature are preferable in that a larger volume of the flow is heated by the shock to ignition temperature. This is largely because the speed of sound, and therefore the exit velocity for the hot jet is large, allowing greater penetration into the free stream. The penetration height is generally taken as proportional to the ratio between jet- and free stream momentum.

Three-dimensional (Euler) CFD simulations are also presented for the projectile with eight rectangular nozzles distributed circumferentially. These nozzles are 2.6 mm long in the axial direction and 6.4 mm long in the circumferential direction. Only one quarter of the configuration was modeled under the assumption of symmetry about the x-y and x-z planes. The 98x26x57 grid was distributed to assure high grid density in the vicinity of the nozzles. The grid size was close to the maximum for the available computational resources, and no further grid refinement was done. Two cases are presented, one for sonic injection and the other for Mach=2 injection, both with hot, high pressure gas. The results indicate that ignition temperature is reached within a semi-circular region projecting from each nozzle whose radius is one third of the projectile radius. The region of ignition and the gas flow rate are roughly comparable to those calculated analytically. At high Mach numbers, it appears that a larger number of nozzles will be needed to produce a uniform shock system.

Conclusions

The analytical and numerical results indicate that jet interaction is a feasible method for ignition in chemical accelerators. The amount of gas needed depends on many factors, but the analytical and numerical results show that it would be manageable. The method may be more appropriate for accelerators operating at lower fill pressures, because that would reduce the amount and pressure of the gas stored within the projectile.

References

1. Brandeis, J., "Use of Jet Interaction for Ignition in Ram- and External Propulsion Accelerators," to appear in AIAA J of Propulsion and Power.
2. Brandeis, J. "Ram Accelerator Utilizing Active Projectile," AIAA Paper 95-0288, Jan. 1995.
3. Rom, J., "Method and Apparatus for Launching Projectile at Hypersonic Velocities", US Patent No 4,932,306 June 1990. Also: Rom, J. and Avital, G., "The External Propulsion Accelerator: Scramjet Thrust Without Interaction with Accelerator Barrel," AIAA paper 92-3717, 1992.
4. Hertzberg, A., Bruckner, A.P. and Bogdanoff, D.W., "Ram Accelerator: A New Concept for Accelerating Projectiles to Ultrahigh Velocities," AIAA J V.26, No.2, Feb. 1988, pp.195-203.
5. Spaid, F.W. and Zukoski, E.E., "A Study of the Interaction of Gaseous Jets from Transverse Slots with Supersonic External Flows," AIAA J, V. 6, No. 2, Feb 1968, pp. 205-212.
6. Nusca, M.J., "Numerical Simulation of Gas Dynamics and Combustion Kinetics for a 120-mm Ram Accelerator," Proceedings, First International Workshop on Ram Accelerator, French-German Research Institute of Saint-Louis (ISL), Saint-Louis Cedex, France, 7-10 September 1993.

RAMAC II - Workshop on Ram Accelerators

July 1995

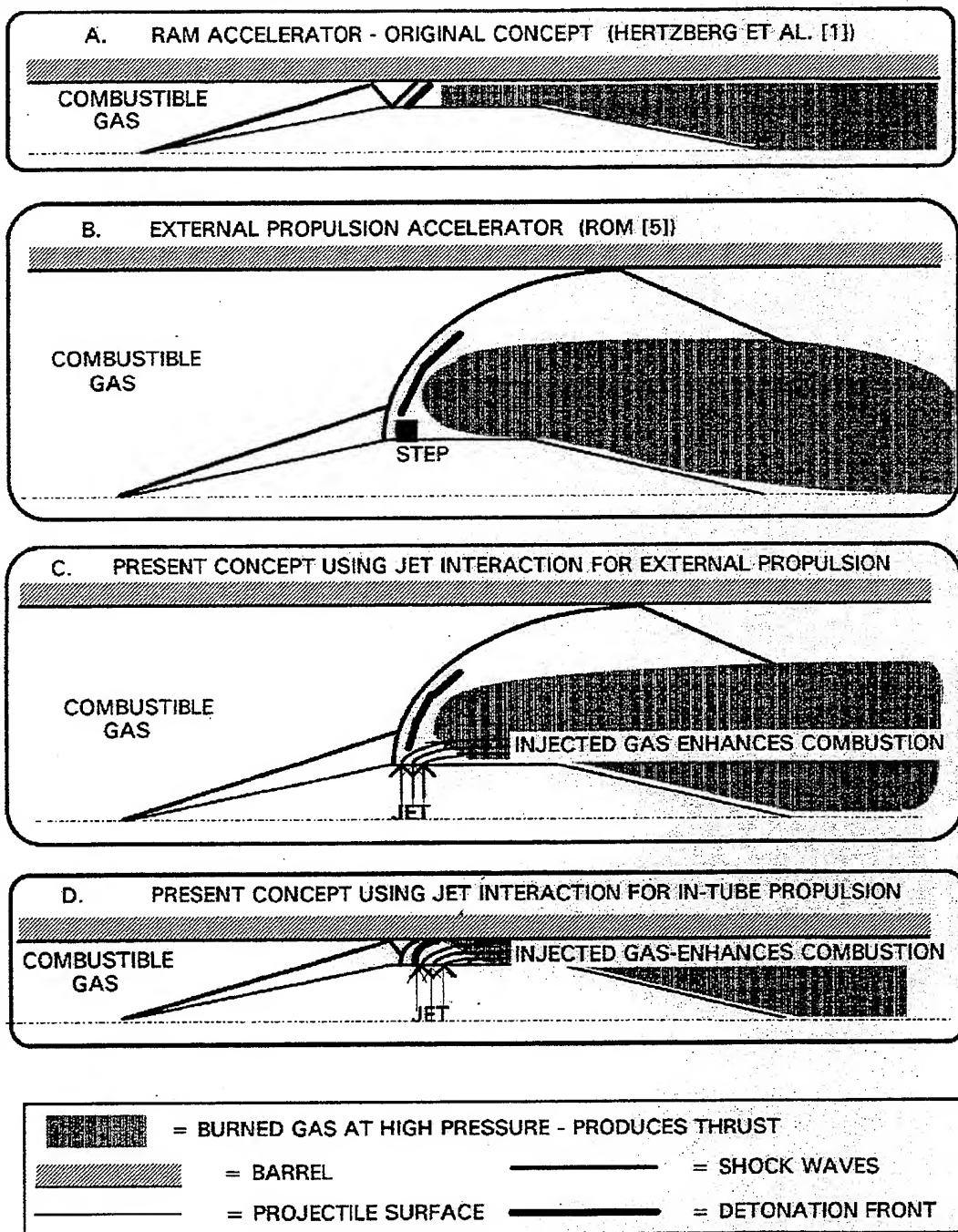
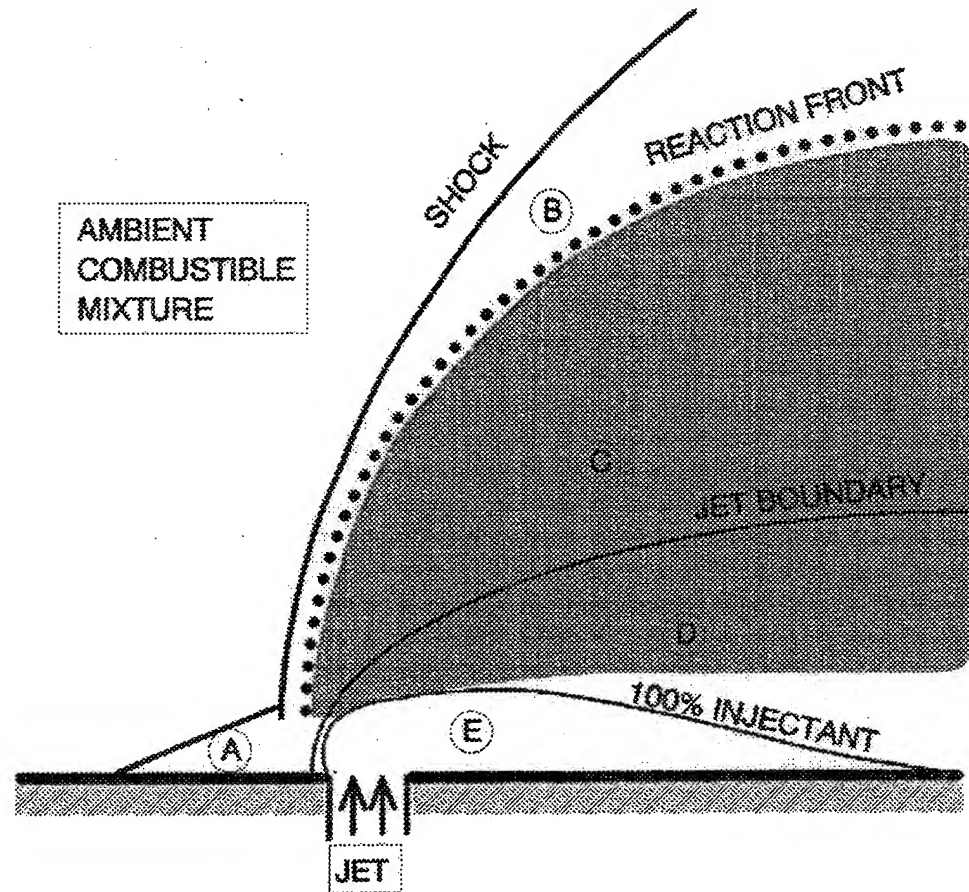


FIG. 1 EXAMPLES OF ESTABLISHED AND PROPOSED METHODS OF IGNITION FOR RAM ACCELERATOR OPERATING IN THE SUPER-DETONATIVE SPEED RANGE



- A UPSTREAM SEPARATED FLOW
- B INDUCTION ZONE
- C REGION BEYOND JET INFLUENCE
- D REGION INFLUENCED BY JET
- E REGION CONTAINING INJECTANT GAS ONLY
(NOT COMBUSTIBLE)
- REACTED REGION (DETONATION OR DEFLAGRATION)

FIG. 2 SCHEMATIC OF THE JET - INDUCED COMBUSTION

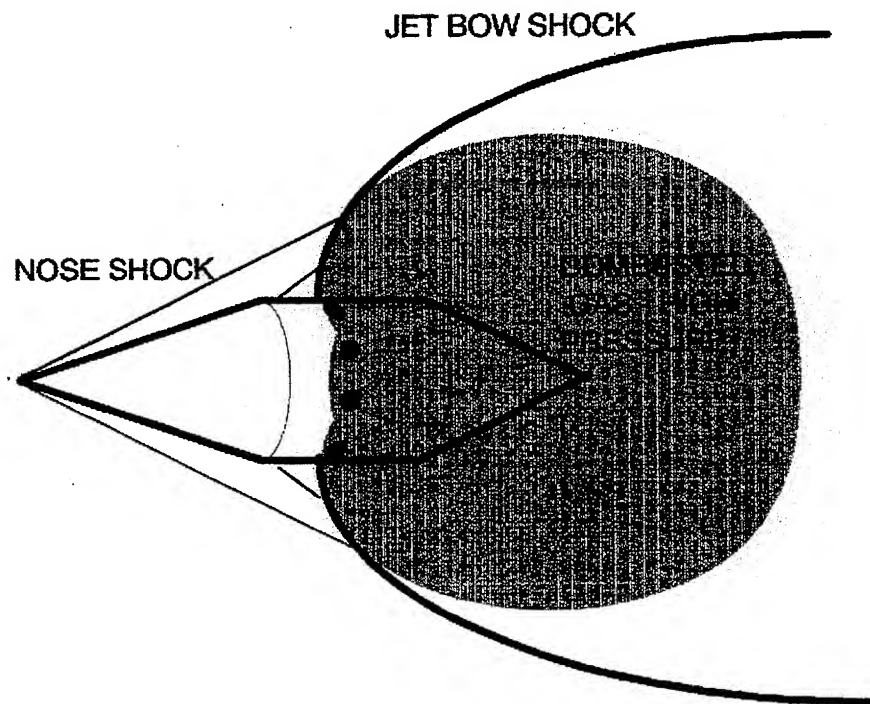
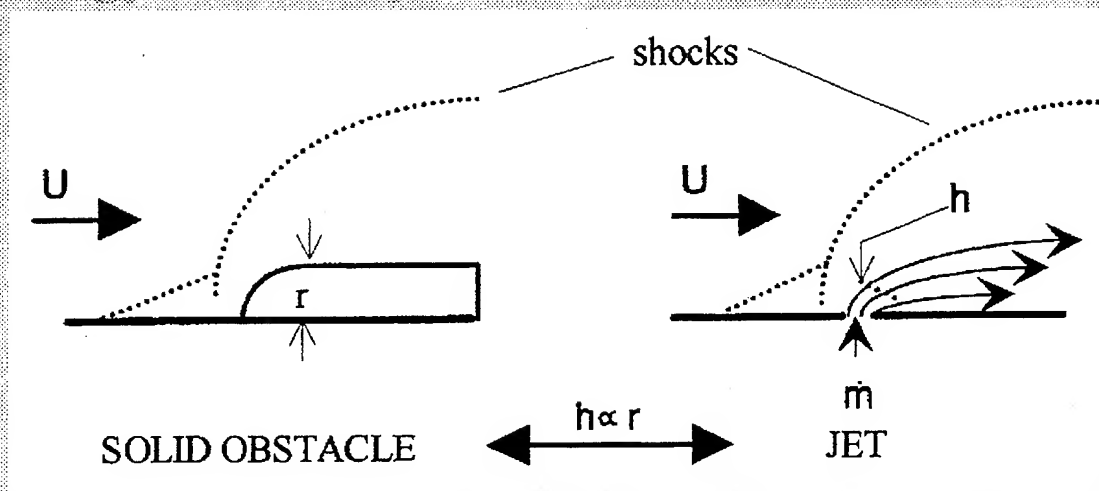


FIG. 3 SCHEMATIC OF THE PROJECTILE UNDERGOING ACCELERATION IN THE PROPOSED MODE.

ANALYTICAL MODEL

- Sonic jet
- Analogy between jet and solid obstacle



- Penetration height estimation

$$\frac{h}{d\sqrt{C}} = \frac{1}{M_\infty} \sqrt{\frac{P_{oj}\gamma_j 2}{P_\infty \gamma_\infty C_p}} \left\{ \frac{2}{\gamma_j - 1} \left(\frac{2}{\gamma_j + 1} \right)^{\frac{\gamma_j + 1}{\gamma_j - 1}} \left[1 - \left(\frac{P_\infty}{P_{oj}} \right)^{\frac{\gamma_j - 1}{\gamma_j}} \right] \right\}^{\frac{1}{4}} \quad (\text{Zukosky et al, 1964})$$

$$h = \sqrt{4 \dot{m}_j / (\pi C_D \rho U_\infty)} \quad (\text{Hsia, 1966})$$

$$h/d = 1.51 \sqrt{(\rho U^2)_j / (\rho U^2)_\infty} \quad (\text{Cohen, 1971, (empirical)})$$

● Blast analogy for computing shock shape

Lukasiewicz (1962) derived the closed form analytical relations for the resulting shock radius, R , as the function of the axial distance, x , body diameter (or thickness), z , and the equivalent body's wave drag coefficient, CD . For a blunt-nosed cylinder the second approximation form is:

$$(R/z) / (M_\infty \sqrt{C_D}) = 0.795 \sqrt{(x/z M_\infty^2 \sqrt{C_D}) [1 + 3.15(x/z M_\infty^2 \sqrt{C_D})]}$$

$CD=0.9$ for the spherical nose:.

● Shock relations for computing flow properties downstream

Density:
$$\frac{\rho_2}{\rho_1} = \frac{(\gamma + 1) M_1^2 \sin^2 \beta}{(\gamma - 1) M_1^2 \sin^2 \beta + 2}$$

Pressure:
$$\frac{P_2}{P_1} = 1 + \frac{2\gamma}{\gamma + 1} (M_1^2 \sin^2 \beta - 1)$$

Temperature:
$$\frac{T_2}{T_1} = 1 + \frac{2(\gamma - 1)}{(\gamma + 1)^2} \frac{M_1^2 \sin^2 \beta - 1}{M_1^2 \sin^2 \beta} (\gamma M_1^2 \sin^2 \beta + 1)$$

Dependence on mass flow rate

INCREASE IN JET MASS FLOW RATE LEADS TO INCREASE IN SHOCK STRENGTH...

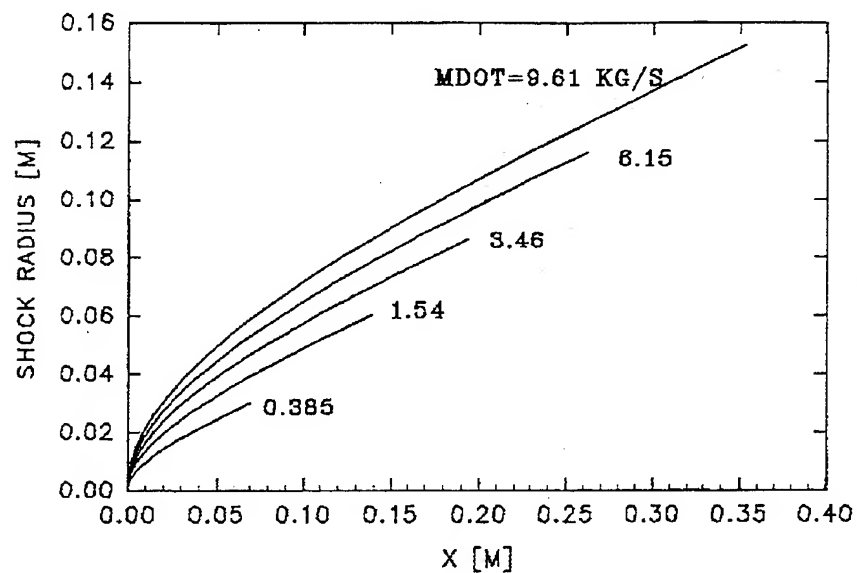


FIG. 6 SHOCK SHAPES FOR SEVERAL INJECTION RATES AT $M=6$, $P_{0j}=500$ ATM. O_2 INTO $2H_2+O_2$ MIXTURE AT 10 ATM FILL PRESSURE.

...AND TO THE CORRESPONDING INCREASE IN HEAT
ADDED TO THE FLUID CROSSING THE SHOCK.

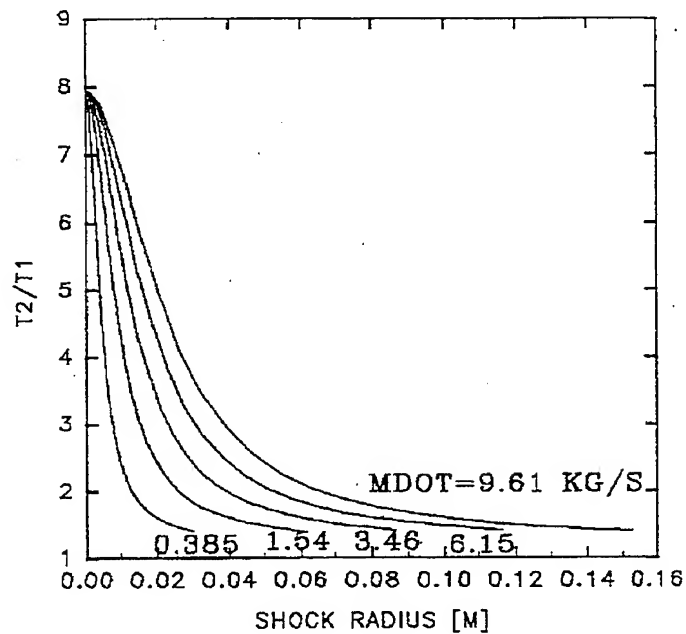


FIG. 7 TEMPERATURE RATIO ACROSS SHOCK
VS. SHOCK RADIUS FOR SEVERAL INJECTION RATES
AT $M=6$, $P_{oj}=500$ ATM. O_2 INTO $2H_2+O_2$ MIXTURE
AT 10 ATM FILL PRESSURE.

Dependence on Mach number

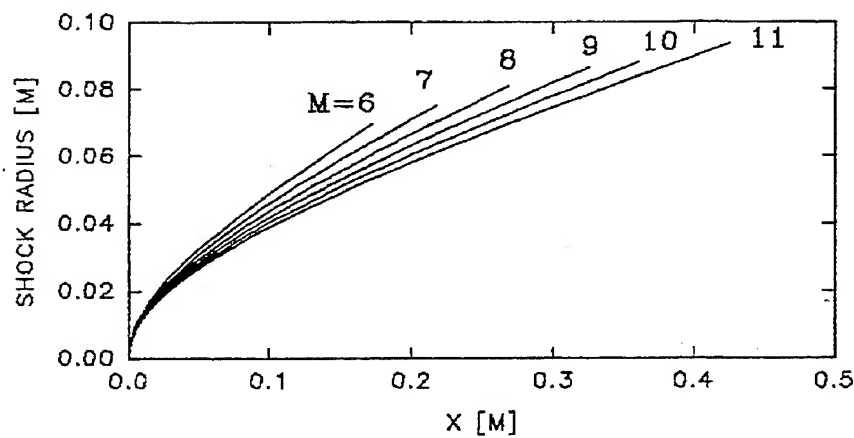


FIG. 8 SHOCK SHAPES FOR SEVERAL MACH NUMBERS
AT INJECTION RATE OF 1.54 KG/S. O₂ JET INTO
2H₂+O₂ MIXTURE.

AS EXPECTED, SHOCK HEATING INCREASES WITH MACH NUMBER.

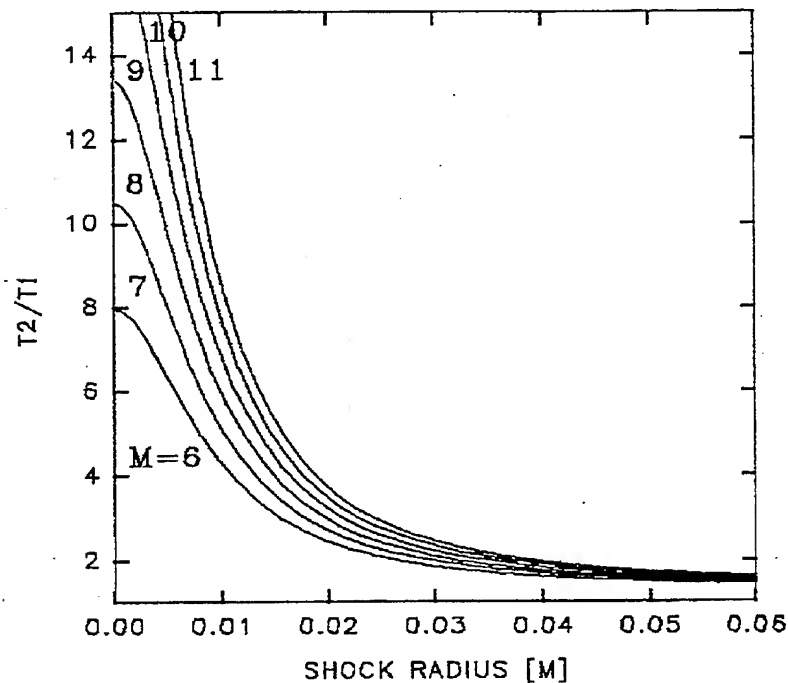


FIG. 9 SHOCK TEMPERATURE RATIO VS SHOCK RADIUS FOR SEVERAL MACH NUMBERS AT AN INJECTION RATIO OF 1.54 KG/S. O₂ JET INTO 2H₂+O₂ MIXTURE. 10 ATM FILL PRESSURE.

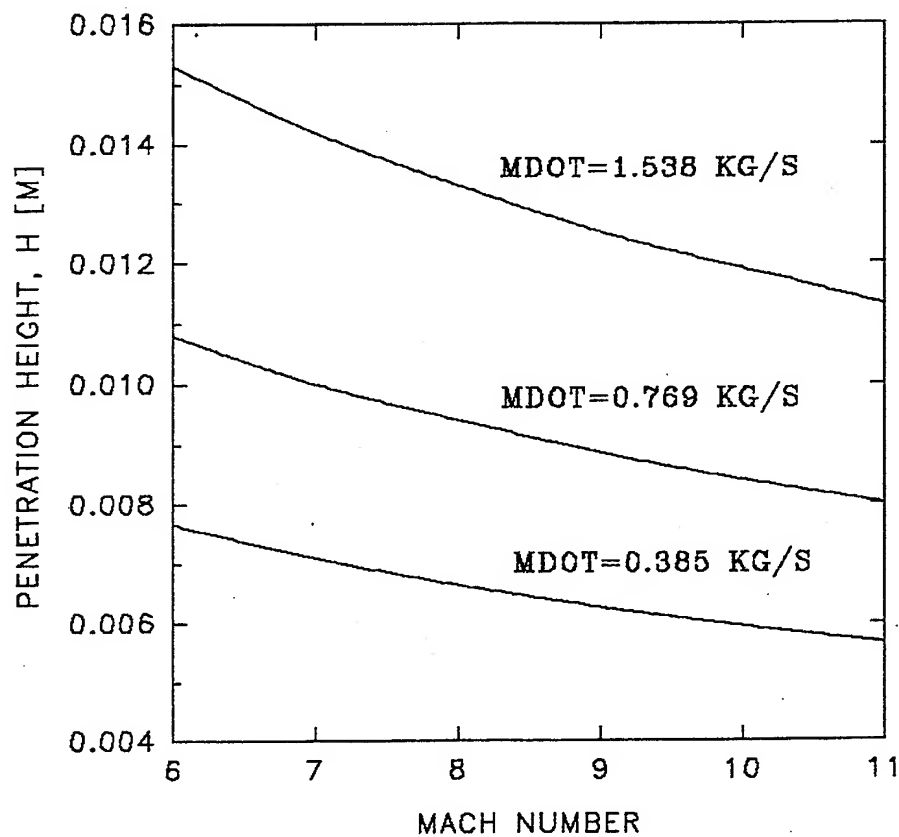


FIG. 10 JET PENETRATION HEIGHT AS FUNCTION OF MACH NUMBER FOR THREE INJECTION RATES. O₂ JET INTO 2H₂+O₂ MIXTURE, 10 ATM FILL PRESS.

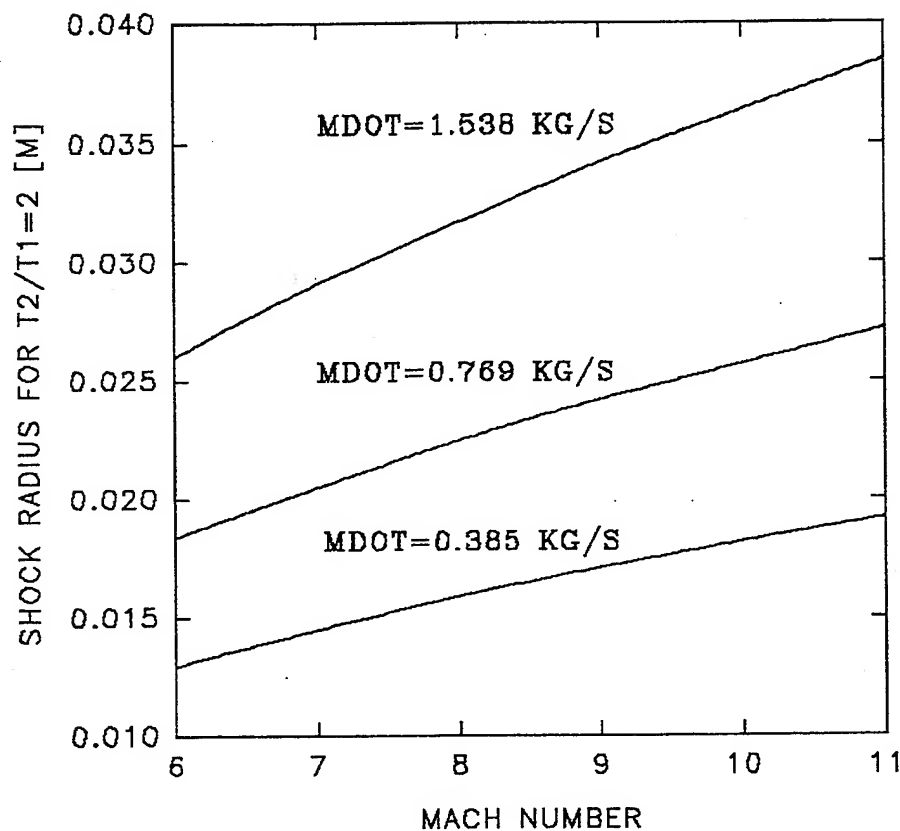


FIG 11 SHOCK RADIUS FOR TEMPERATURE RATIO 2, VS. MACH NUMBER FOR THREE INJECTION RATES. O₂ JET INTO 2H₂+O₂ MIXTURE. 10 ATM FILL PRESS.

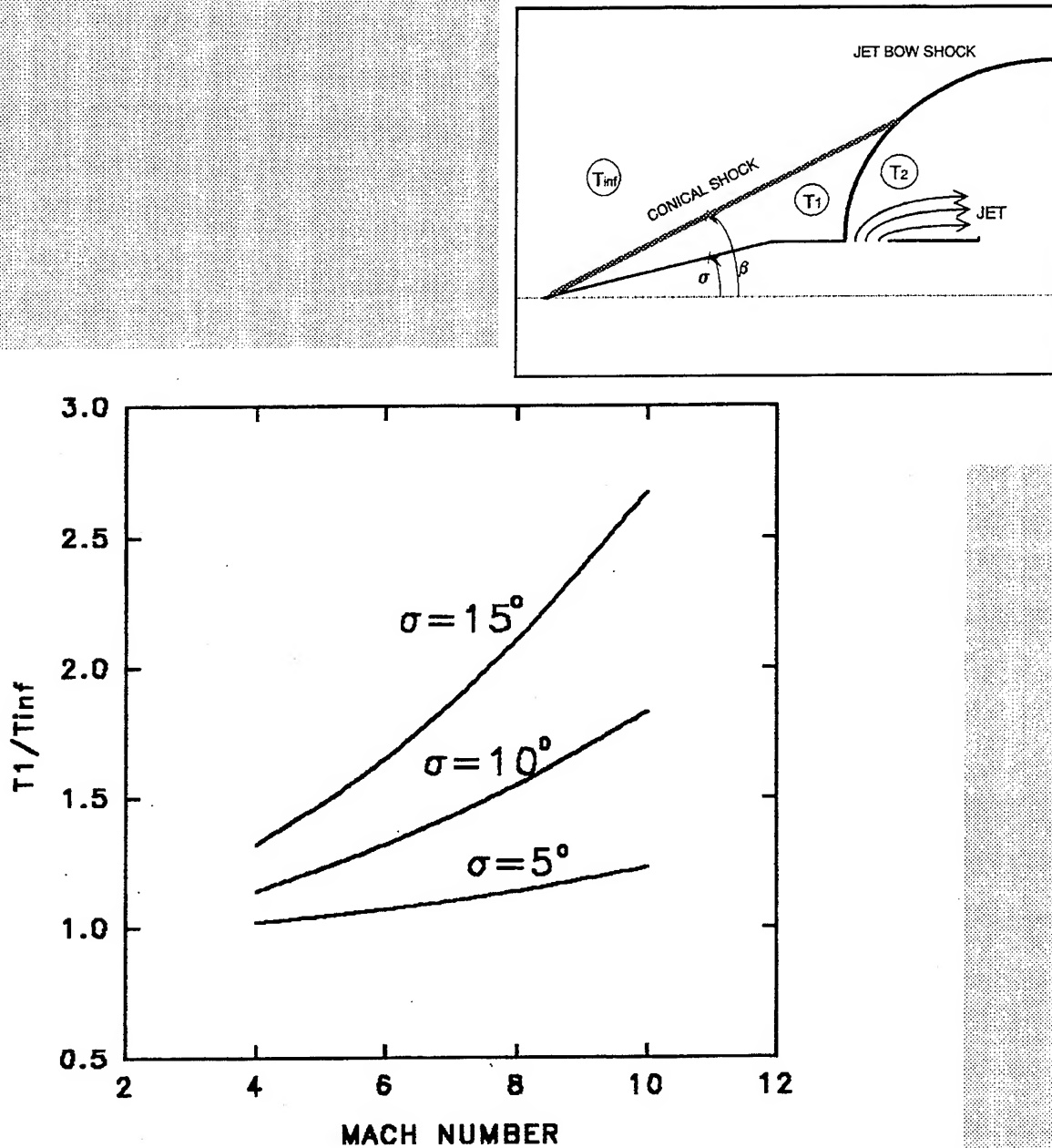


FIG. 12 TEMPERATURE RATIO ACROSS CONICAL SHOCK FOR CONES OF SEVERAL HALF-ANGLES

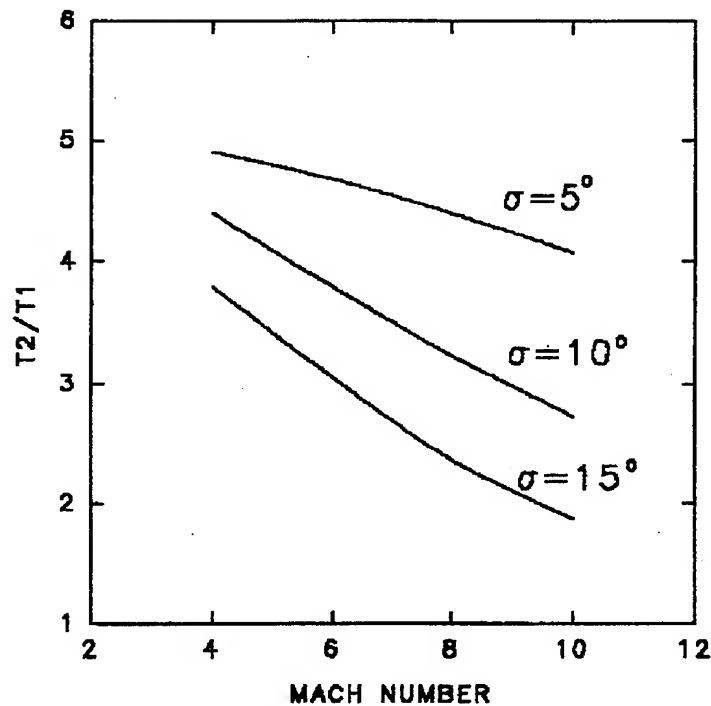
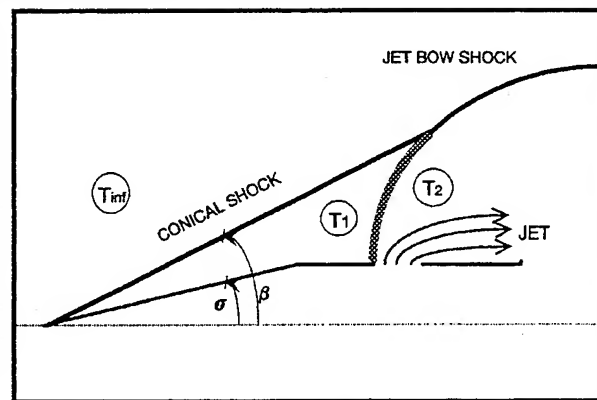


FIG. 13 MAXIMUM TEMPERATURE RATIO ACROSS JET BOW SHOCK REQUIRED FOR IGNITION FOR CONES OF SEVERAL HALF-ANGLES

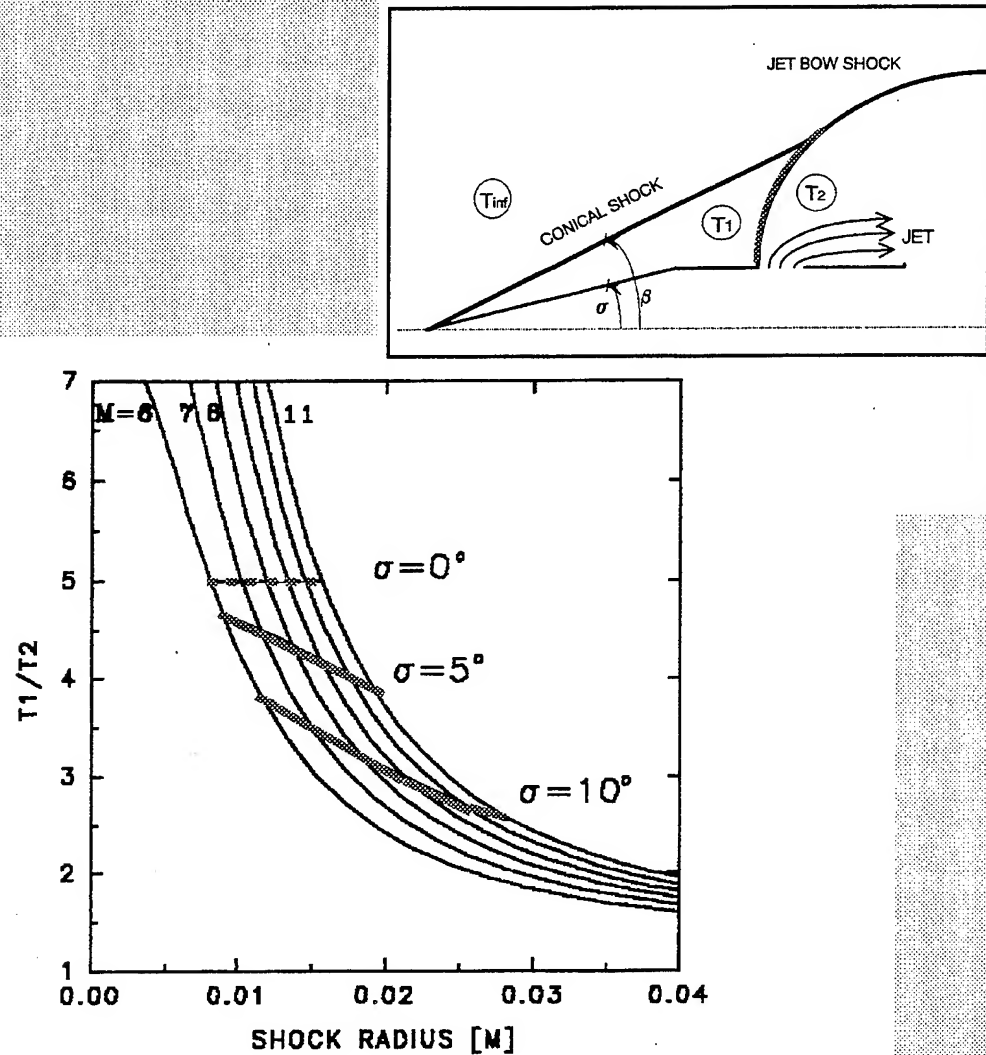


FIG. 14

MAXIMUM TEMPERATURE RATIO ACROSS JET BOW SHOCK REQUIRED FOR IGNITION FOR TWO CONE HALF-ANGLES OVERLAID ON THE SHOCK TEMPERATURE RATIO PLOTS FOR VARIOUS MACH NUMBERS. INJECTION RATE IS 1.54 KG/S. O₂ INTO 2H₂+O₂ MIXTURE. 10 ATM FILL PRESSURE.

AXISYMMETRIC PROJECTILE WITH ANNULAR JET

$M_\infty = 6$ $M_{e_{jet}} = 1$ $m\text{-dot} = 17.6 \text{ Kg/sec}$
 $P_\infty = 10 \text{ atm}$ $P_{e_{jet}} = 100 \text{ atm}$ $195 \times 101 \text{ grid}$
 $T_\infty = 300 \text{ deg K}$ $T_{e_{jet}} = 300 \text{ deg K}$

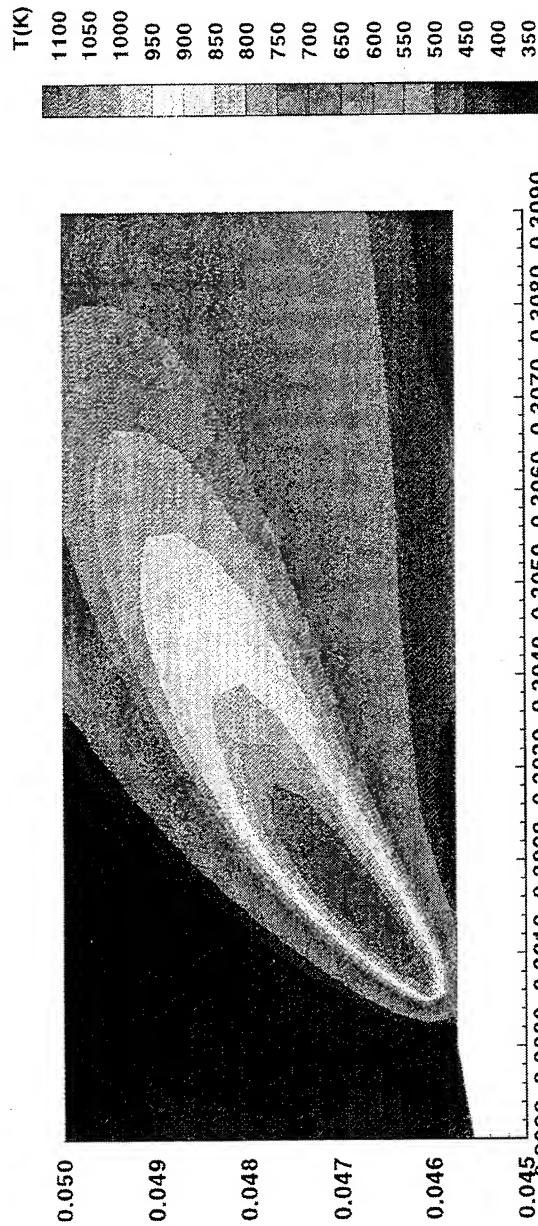
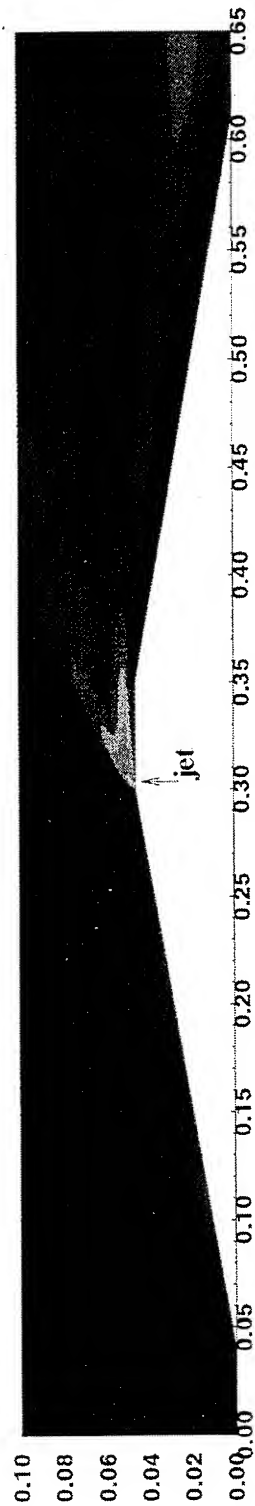


Fig. 15

AXISYMMETRIC PROJECTILE WITH ANNULAR JET

$M_\infty = 6$ $M_{e_{jet}} = 1$ $\dot{m} = 48 \text{ Kg/sec}$
 $P_\infty = 50 \text{ atm}$ $P_{e_{jet}} = 1000 \text{ atm}$ $195 \times 101 \text{ grid}$
 $T_\infty = 300 \text{ deg K}$ $T_{e_{jet}} = 1000 \text{ deg K}$

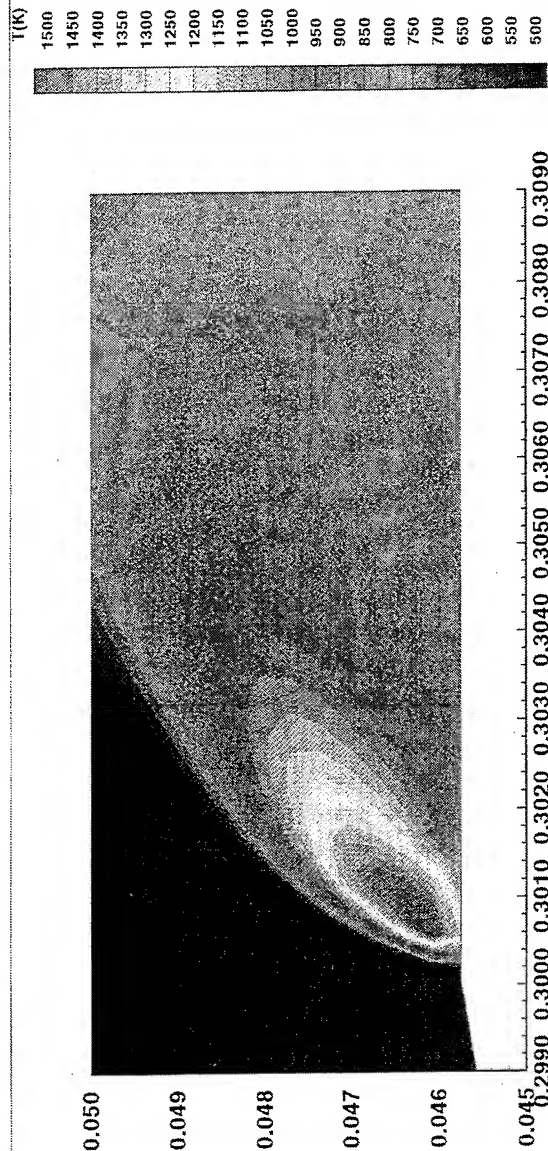
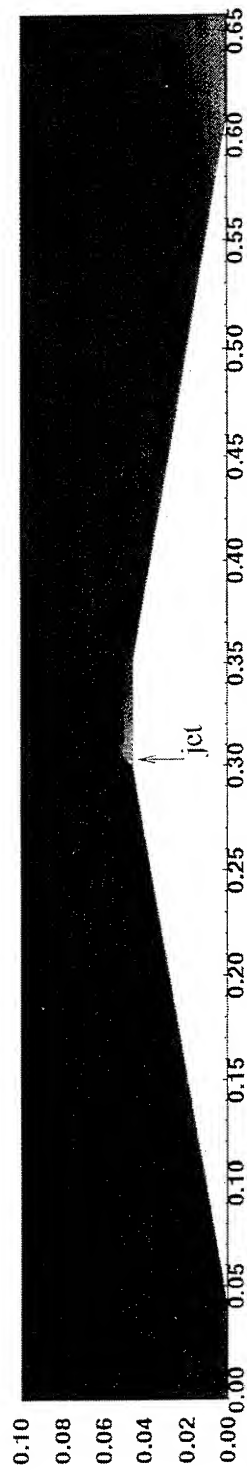


Fig. 16

AXISYMMETRIC PROJECTILE WITH ANNULAR JET

$M_\infty = 6$
 $P_\infty = 50 \text{ atm}$
 $T_\infty = 300 \text{ deg K}$
 $Me_{jet} = 1$
 $Pe_{jet} = 1000 \text{ atm}$
 $Te_{jet} = 1000 \text{ deg K}$
 $\dot{m} = 96 \text{ Kg/sec}$
 $195 \times 101 \text{ grid}$

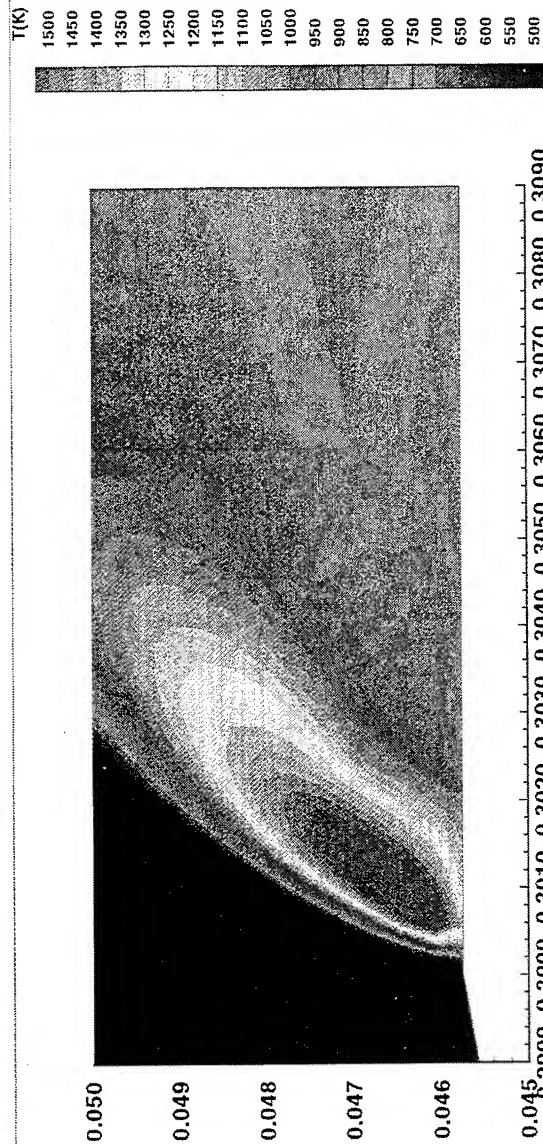
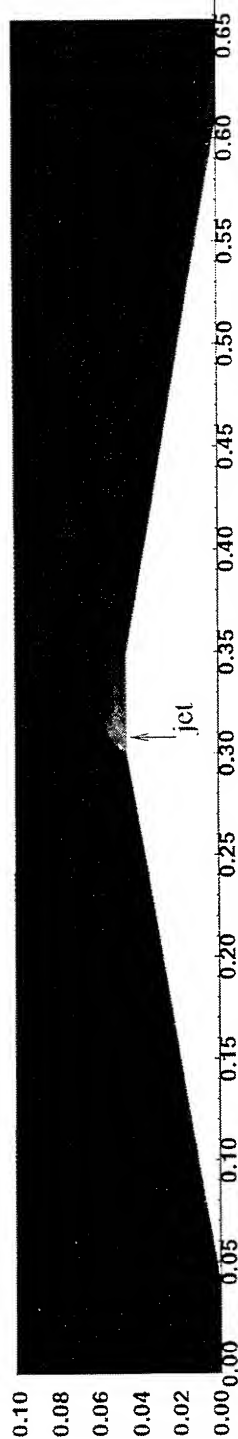
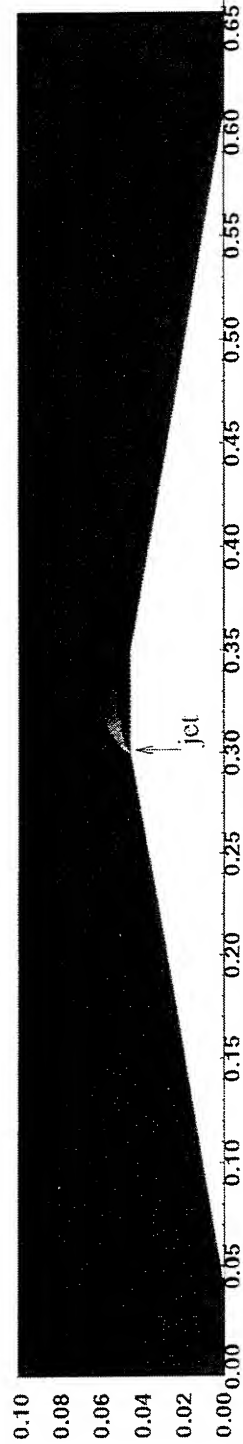


Fig. 17

AXISYMMETRIC PROJECTILE WITH ANNULAR JET

$M_\infty = 6$	$Me_{jet} = 1$	$\dot{m} = 176 \text{ Kg/sec}$
$P_\infty = 50 \text{ atm}$	$Pe_{jet} = 1000 \text{ atm}$	$195 \times 101 \text{ grid}$
$T_\infty = 300 \text{ deg K}$	$Te_{jet} = 300 \text{ deg K}$	



T(K)

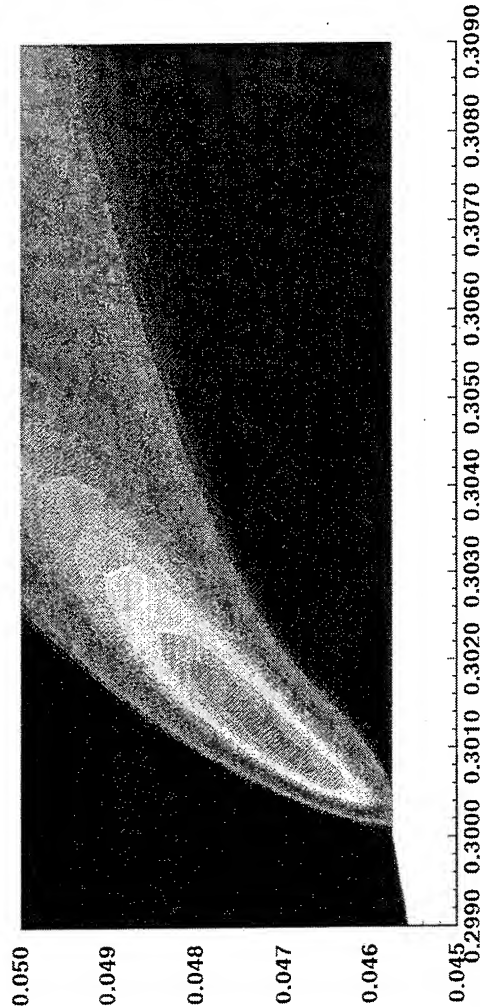
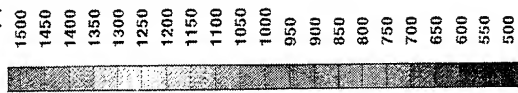


Fig. 18

AXISYMMETRIC PROJECTILE WITH ANNULAR JET

$M_\infty = 6$
 $P_\infty = 50 \text{ atm}$
 $T_\infty = 300 \text{ deg K}$
 $M_{e_{jet}} = 2$
 $P_{e_{jet}} = 1000 \text{ atm}$
 $T_{e_{jet}} = 1000 \text{ deg K}$
 $\dot{m} = 193 \text{ Kg/sec}$
 $195 \times 101 \text{ grid}$

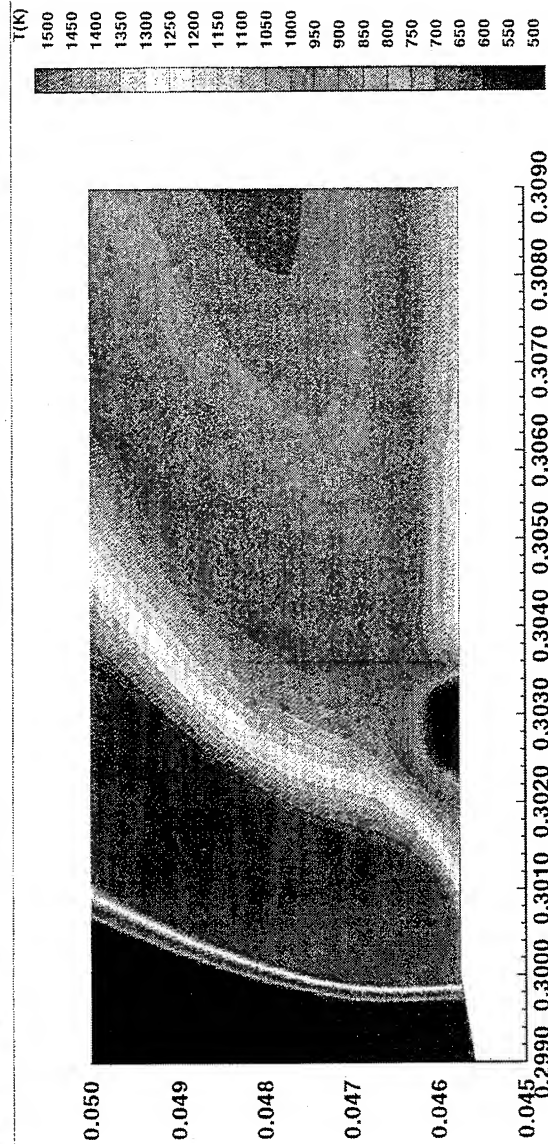
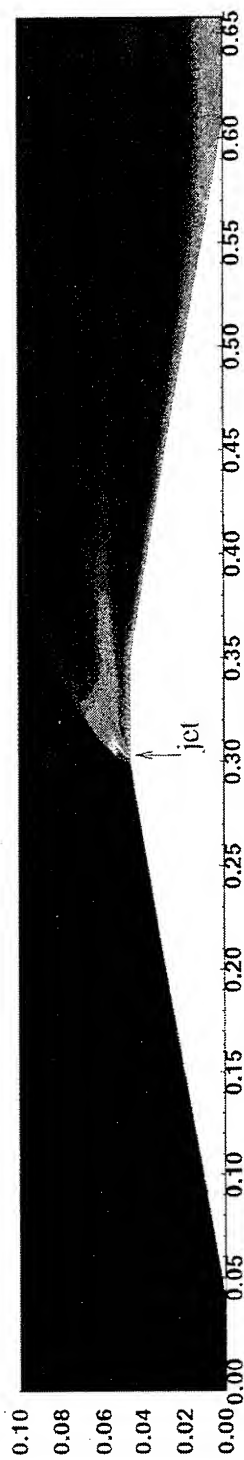
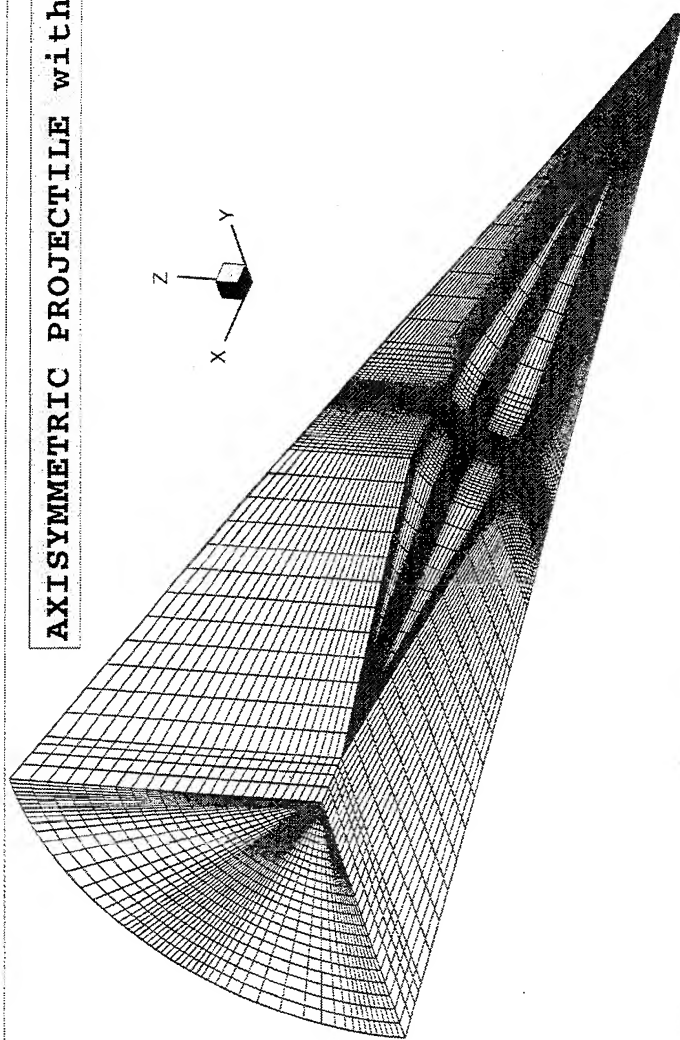


Fig. 19

AXISYMMETRIC PROJECTILE WITH EIGHT DISCRETE JETS



$M_\infty = 6$
$P_\infty = 20 \text{ atm}$
$T_\infty = 300 \text{ deg K}$
$Me_{jet} = 1$
$Pe_{jet} = 1000 \text{ atm}$
$Te_{jet} = 1000 \text{ deg K}$
$m\text{-dot} = 30 \text{ Kg/sec}$
Projectile Radius = 45.75 mm
Each Nozzle 2.6x6.4 mm
98x25x57 grid

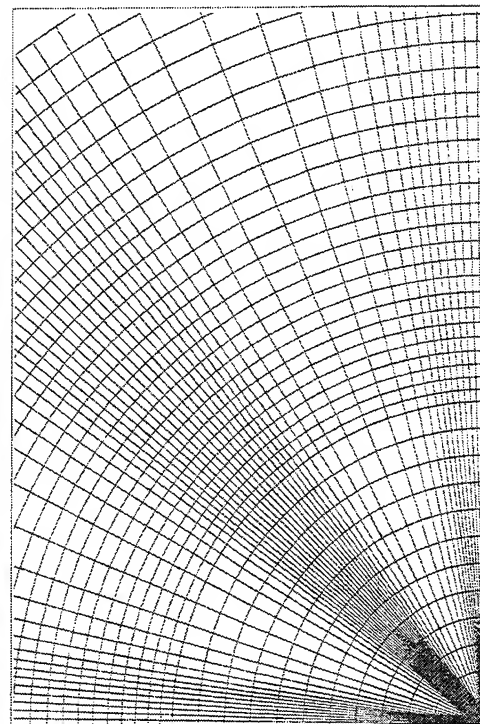
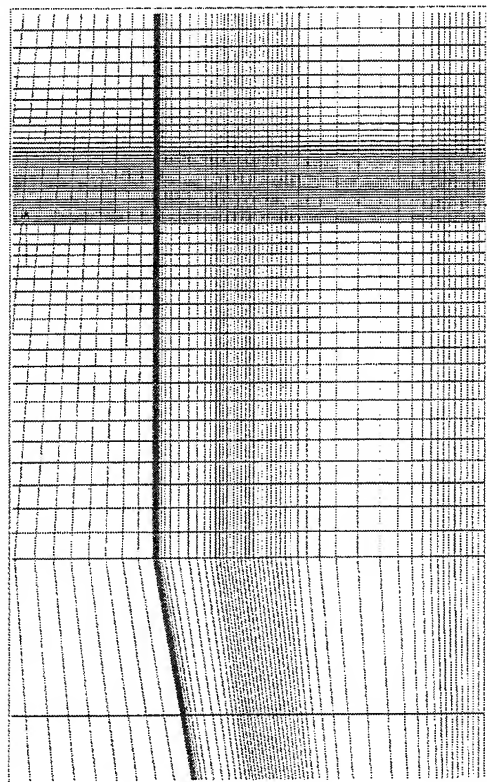


Fig. 20

AXISYMMETRIC PROJECTILE WITH EIGHT DISCRETE JETS

$M_\infty = 6$
 $P_\infty = 20 \text{ atm}$
 $T_\infty = 300 \text{ deg K}$
 $Me_{jet} = 1$
 $Pe_{jet} = 1000 \text{ atm}$
 $Te_{jet} = 1000 \text{ deg K}$
 $m\text{-dot} = 30 \text{ Kg/sec}$
 Projectile Radius = 45.75 mm
 Each Nozzle $2.6 \times 6.4 \text{ mm}$
 $98 \times 25 \times 57 \text{ grid}$

T(K)

1200
1100
1000
900
800
700
600
500
400
300

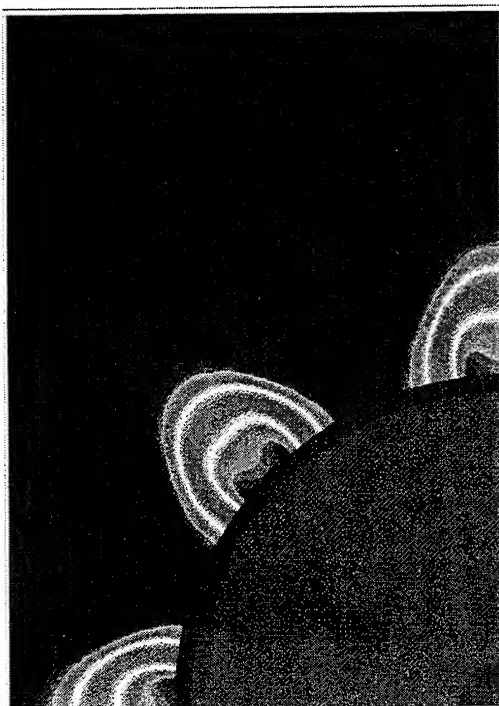
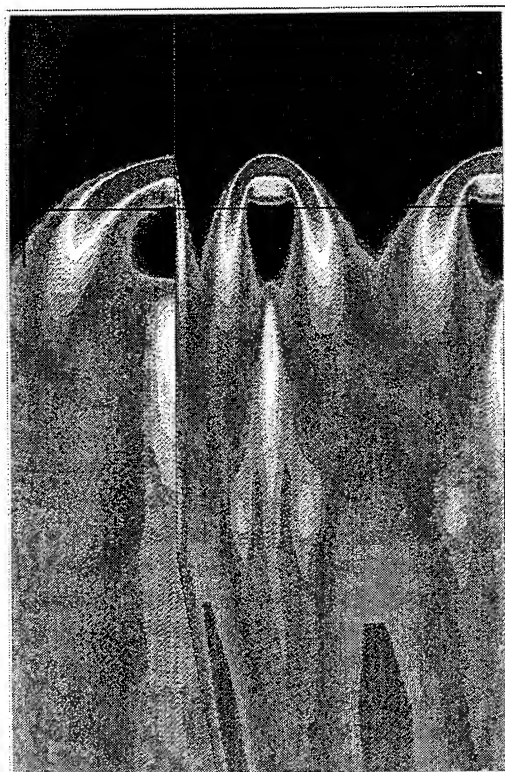
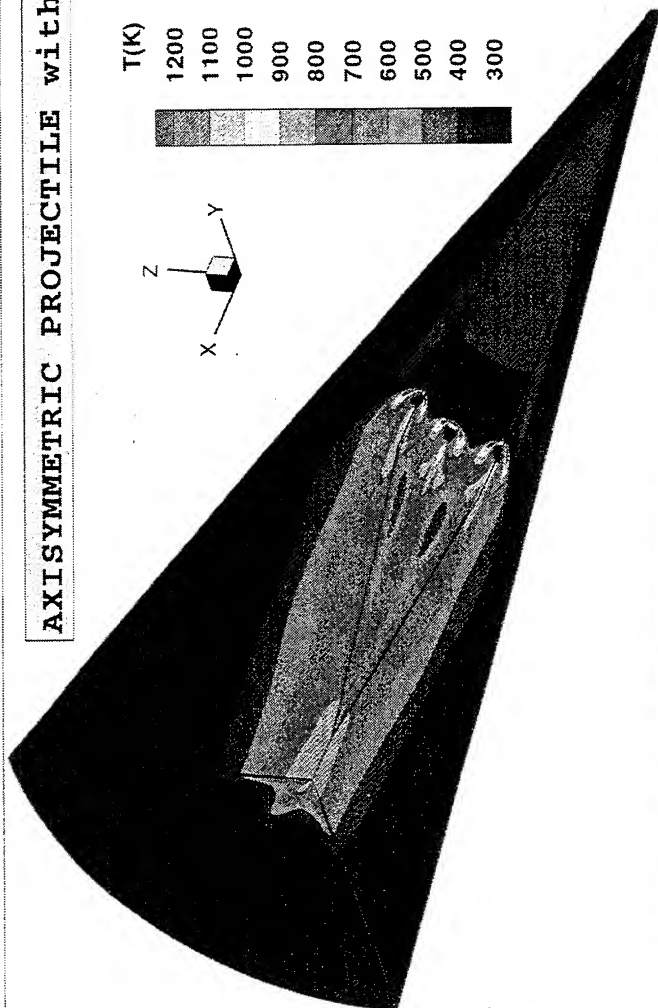
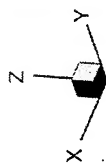


Fig. 21

AXISYMMETRIC PROJECTILE WITH EIGHT DISCRETE JETS

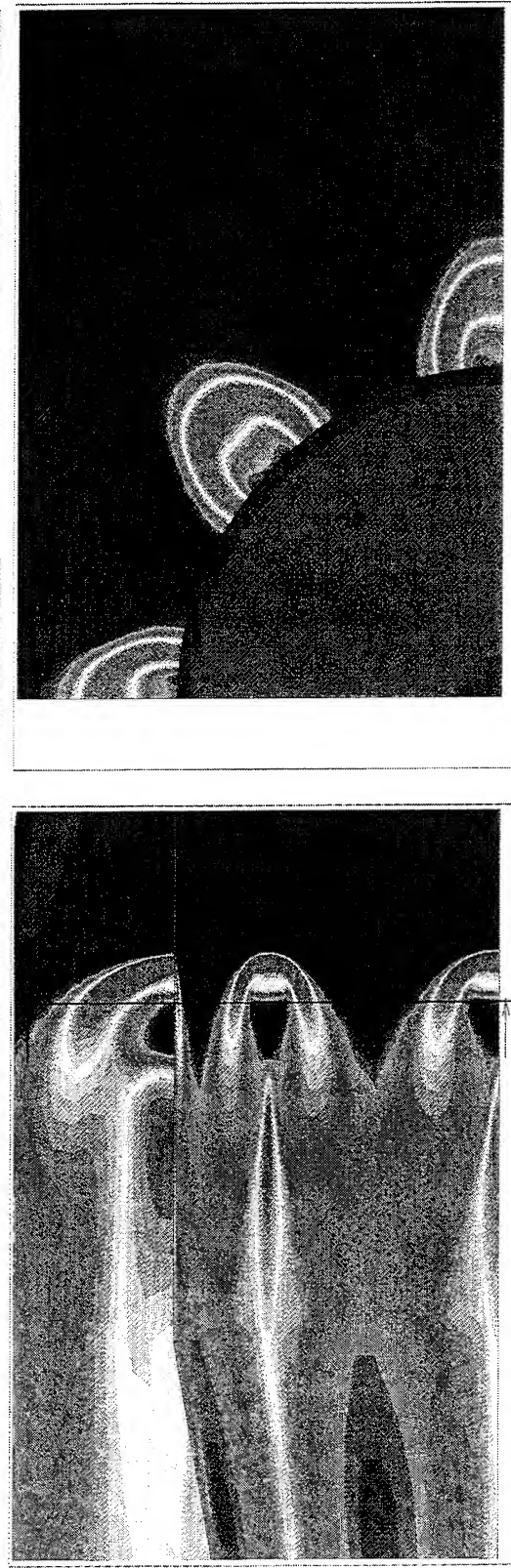
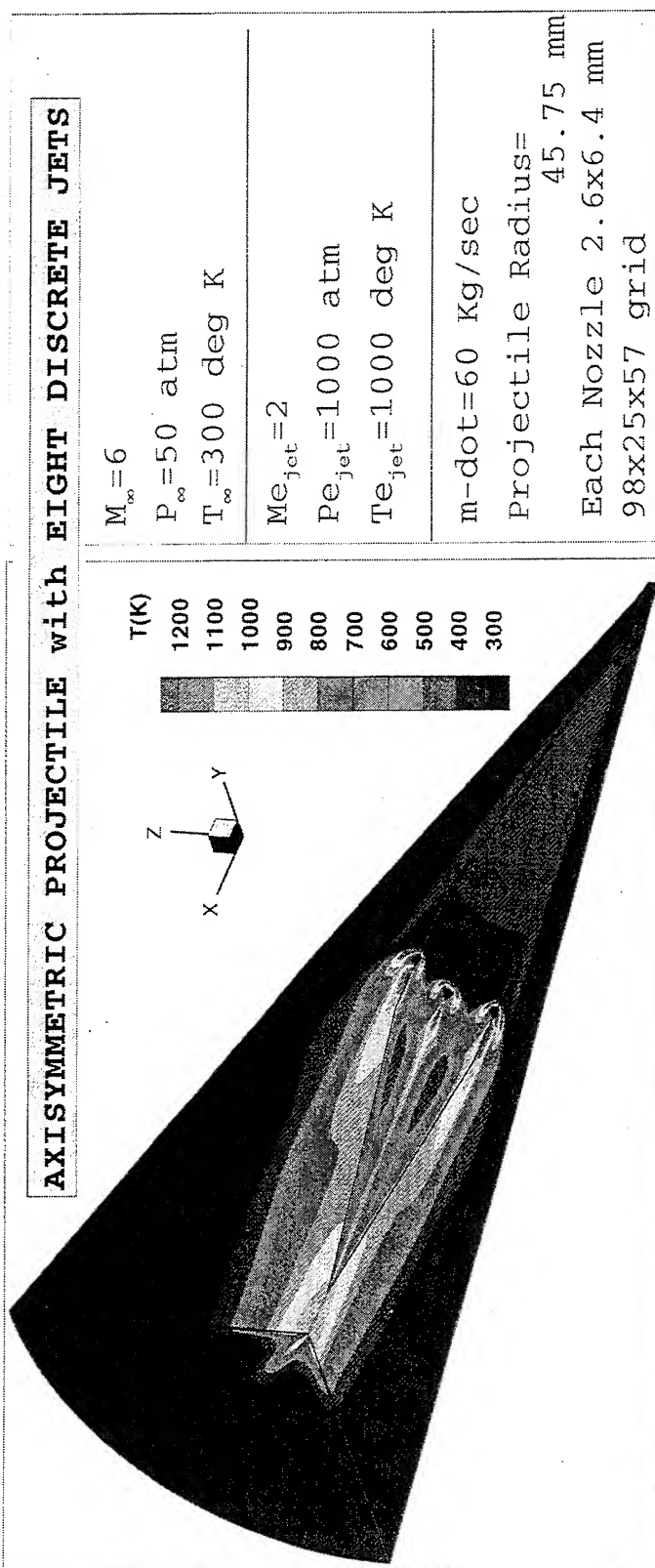


Fig. 22

THEORETICAL MODELING OF DETONATION PULSE ENGINE WITH APPLICATION TO RAM ACCELERATOR

V.P.Korobeinikov*, S.Wojcicki**

*Institute for Computer Aided Design, RAS, 19/18, 2nd
Brestskaya, Moscow 123865, Russia

**Washington State University, Pullman WA 99164-2920

ABSTRACT

One of the new types of internal combustion engines is an electrochemical pulse jet. The new scheme of the thrust creation includes electrodischarge in combustion chamber, when flame front passes special electrodes. The ring-type discharge is recommended to create converging shock in combustion mixture, which leads to a fast burning process with detonation stage. The reflection in central part of the chamber and interaction of the shocks with walls lead to fast complete mixture burning during a pulse. The analytical estimations of the converging shocks and detonation waves parameters are made. Numerical simulation of two-dimensional combustible gas flow in the chamber and engine tubes is performed. An estimate of impulse and thrust values and efficiency of the engine system are considered. The pulse engine propulsion scheme can be used for improvement of ram accelerator operation in different modes. Three pulsation regimes are considered. The converging shocks and detonation combustion take place during the pulses. Estimations of thrust increments for the regimes are presented.

INTRODUCTION

The creation of new types of internal combustion engines is of significant interest both for theory and practice. One of relatively new schemes is an electrochemical pulse jet. The

scheme was previously studied by S.Wojcickii.¹ To produce an effective conversion of thermal energy into mechanical one by increasing of compression ratio, electrodischarge in combustion chamber can be used. By this way we can convert combustion into detonation and explosion and use these processes to generate high pressure, increase the engine trust and have good efficiency of the engine system. The new scheme of the trust creation includes electrodischarge in combustion chamber, when flame front passes special electrodes. The "collar" (ring-type) discharge is recommended to create converging shock in combustion mixture, which leads to a fast burning process with detonation stage. The reflections in central part of the chamber and interaction of the shocks with walls lead to a fast complete mixture burning during a pulse. The energy of combustion of one pulse have to be much higher than electrodischarge energy. The analytical estimations of the converging shocks and detonation waves parameters are made. Numerical stimulation of two-dimensional combustible gas flow in chamber and engine tubes is performed. The chemical kinetics, wall friction and heat losses are taken into account. The Godunov's finite difference methods was adapted for the numerical solution. The calculations are made² for several initial data, system parameters and types of mixture. The estimate of impulse and thrust values and efficiency of the engine system are considered.

The pulse engine propulsion scheme can be used for improvement of ram accelerator^{3,4} operation in different modes. The three main pulsation regimes are considered: a) the electrodischarges (or laser sparks) in the vicinity of a projectile base; b) combustible mixture breathing pulse ramjet engine using a chamber inside of the projectile; c) a total pulsating regime with discharging in combustion region behind of the projectile. It is assumed that total energy of electrodischarges is significantly less than that of combustion heat released during acceleration. The converging shocks and detonation combustion take place during the pulses. The

estimations of trust increments for the pulsating regimes are presented. We used here the analytical results of works ³⁻⁵

The numerical modeling is based on equations for quasi-one-dimensional and two-dimensional unsteady flows of the combustible gaseous mixtures.

GOVERNING EQUATIONS AND NUMERICAL METHODS

Quasi-one-dimensional Approach

The model are based on the equations for quasi-one-dimensional nonsteady flow of gas mixture in tube of variable cross section. The combustion processes, the wall friction and heat losses are approximately taken into account. The following governing equations were used.

a) Gas motion

$$\frac{\partial}{\partial t} (\rho A) = - \frac{\partial}{\partial x} (\rho u A)$$

$$\frac{\partial}{\partial t} (\rho u A) = - \frac{\partial}{\partial x} (\rho u^2 A + p A) + p \frac{dA}{dx} - \rho A F$$

$$\frac{\partial (E \rho A)}{\partial t} = - \frac{\partial}{\partial x} [u (\rho E + p) A] + \rho A q_T + \rho A q$$

$$p = R \rho T, \quad E = \frac{p}{\rho(\gamma-1)} + \frac{u^2}{2}, \quad F = \frac{4f}{L} \frac{u^2}{2} \frac{u}{|u|} \quad (\text{friction})$$

b) Combustion and heat releasing

$$q = Q \beta_r \quad (\text{heat releasing rate})$$

$$\frac{dc}{dt} = -K p^{n_1} \rho^{n_2} \exp\left[-\frac{E_1 \rho}{p}\right] \quad (\text{induction period, } 0 < c \leq 1)$$

$$\beta_r = -\beta^m \rho^m K_b \exp\left[-\frac{E_1 \rho}{p}\right] \quad (\text{burning after the induction period})$$

$$\frac{\partial A \beta}{\partial t} = -A U \frac{\partial \beta}{\partial x} + A \alpha(x, t) + A \beta_r + \frac{\partial}{\partial x} \left(\rho A D_\beta \frac{\partial \beta}{\partial x} \right) \quad (\text{diffusion})$$

L is a tube diameter, q_T heat losses, $A = A(x)$ cross-section area, Q combustion heat; E_1 , E_2 , K , K_b are constants, D_β is turbulent diffusion coefficient, α source of the matter.

Two-dimensional model

The models are based on the equations for two-dimensional nonsteady flow of gas mixture in a tube of variable cross-section. The combustion processes, the walls friction and heat losses are taken into account. The following governing equations were used.

a) Gas motion

$$\frac{\partial a}{\partial t} + \frac{\partial b}{\partial x} + \frac{\partial c}{\partial r} = -\frac{1}{r} f_0 + f$$

$$a = \begin{bmatrix} \rho \\ \rho u \\ \rho v \\ e \end{bmatrix}, \quad b = \begin{bmatrix} \rho u \\ p + \rho u^2 \\ \rho u v \\ (e+p)u \end{bmatrix}, \quad c = \begin{bmatrix} \rho v \\ \rho u v \\ p + \rho v^2 \\ (e+p)v \end{bmatrix}, \quad f_0 = \begin{bmatrix} \rho v \\ \rho u v \\ \rho v^2 \\ (e+p)v \end{bmatrix}$$

$$f = \begin{pmatrix} 0 \\ -\rho F_x \\ -\rho F_r \\ \rho(q_t + q + q_{el}) \end{pmatrix}, \quad p = (\gamma - 1)\rho\varepsilon, \quad \varepsilon = c_v T, \quad e = \rho(\varepsilon + V^2/2),$$

$$F_x = 2fV^2 \frac{u}{|V|}, \quad F_r = 2fV^2 \frac{v}{|V|}$$

b) Combustion and heat releasing

$$q = Q \frac{d\beta}{dt} \quad (\text{heat releasing rate})$$

$$\frac{d\beta}{dt} = -\beta^m \rho^n K_2 \exp \left[-\frac{E_1 \rho}{P} \right] \quad (\text{burning})$$

where ρ is density, p is pressure, u and v are components of velocity vector \vec{V} , ε is internal energy, $q_t = K_1(T_{in} - T)$ is heat losses, Q combustion heat; m, n, E_1, K_1, K_2 are constants, f is friction coefficient ($f \neq 0$ near walls only), T is temperature, T_{in} is temperature of environment, q_{el} is electrodischarge energy and β is combustion mixture concentration. The method of integral relation and Godunov's finite difference method⁵ were used for numerical solution of the problems. Nonuniform computing meshes were used. A special procedure was worked out to calculate combustion kinetic equation and find concentration β .

PROBLEMS AND RESULTS

We shall consider the processes in an engine that include four essential parts: mixture inlet, combustion chamber, electric discharge, outlet of combustion products. A simple models (problems) for these operation units are considered below.

Problem 1. Combustible Gas Flow in a Combustion Chamber and Engine Tubes.

The pattern of the flow in the combustion chamber ¹ is shown in Fig.1 (a,b). Here BM is combustion mixture, CP product of burning, F flam, C_{ch} the combustion chamber, ED place of electrodischarge. Numbers at Fig.1 (b) correspond to the sizes in mm for calculated example. The numerical solution was made for the following data. Pulse frequencies: 200Hz, 148Hz, 139Hz, 167Hz. Mass deposit rate of combustion mixture 15.4 g/s, mean rate of combustion heat releasing $q = 26 \cdot 10^3 \text{ J/s}$, (C_2H_2 and C_3H_8 + air mixtures), $f = 0.01$, $h = 5 \cdot 10 \text{ W/m}^2\text{K}$ ($q_T = h \cdot \Delta T$), electrical discharge energy: 30J/cycle. The results of computation are shown at the Figs.2,3. The Fig.3 corresponds to the propane case with mean temperature $T = 2,000\text{K}$, pulse frequencies 167 Hz, with electric discharges. The results of Figs.2,3 were obtained by the Godunov's method for the one-dimensional model.

The experimental results are presented in Fig.4 for the same chamber configuration. The theoretical results are qualitatively close to the experiment.

The estimation of efficiency showed:

a) Mean mechanical thrust of the engine is increased by 40% with the discharge if relative additional energy by the discharges input is about 23%. Ratio of kinetic energy generated by the engine to the energy input (thermal energy plus electrical energy) may increase to 5% for the case of the electrodischarge. These estimations depend on the wall losses.

b) As usual the point of operation of the electrochemical pulsejet at maximum efficiency will not coincide with the maximum specific thrust point (the thrust per cross section area of the engine). A variation of the operation by electrodischarge, heat conduction, combustible mixture selection can allow us to set the engine with the efficiency close to that for supersonic ramjet air-breathing aircraft engines.

We also note that inlet problems were studied in works.⁷⁻⁹

To study the two-dimensional flow picture we considered the case of discharge when electrode situated along the combustion chamber axis with length of discharge energy release zone equal to $n\Delta x$, where Δx is computing cell size, $n=1,2$ (cylindrical explosion). The discharge energy was 30J/cycle (as adopted above). The results of two-dimensional unsteady calculations made by A.Gavrilov are shown in Figs.5,6. It is appeared that after reflection of detonation wave from the chamber wall the implosion stage of gas flow begins. The converging shock at the center of chamber implodes at time about 15 μ sec after discharged moment ($t=t_d$). Everybody can see high pressure region near center of the chamber. The complicate flow arises which promote to fast burning of combustible mixture (propane case). It leads to conception of special type of discharge to obtain primary employing wave, considered in the next section.

The outlet velocity from the tube is increased by 20% comparatively with ordinary discharge stream. The flow velocity field inside the chamber is shown in Fig.7.

Problem 2. New Detonation Pulse Engine.

New variants of Pulse Engine may be developed using detonation process in the combustion chamber. The "collar" (ring-type) discharge is recommended to create converging shock in combustible mixture which leads to a fast burning process with detonation stage (see Fig.9). A cylindrical gas shell with high pressure and temperature arises during the discharge of the electrodes system. The implosion process begins and converging overdriven detonation will propagate to the centre of the combustion chamber (as in Fig.7). The specific energy of the shell explosion can be estimated as:

$$E_* = \frac{E_d + E_c}{2\pi h l r_0}.$$

Here $r_0 = R - h$, l size of electrodes surface along the tube, h is

length of electrodes, E_d discharge energy, E_c is energy released during combustion. The pressure of initial stage will be close to that for an equivalent plane "point" explosion and estimated by formula:⁵

$$E_* = (E_d + E_c) / 2\pi h r_0,$$

$$\frac{\Delta p_s}{p_0} = \frac{4\gamma}{(\gamma+1)[-1+(1+9\gamma\alpha\frac{E_0}{p_0}(r_0-r_s))^{1/2}]}, \quad (1)$$

$$0.1 < (1 - \frac{r_s}{r_0}) < 0.5, \quad 2E_0 = E_*, \quad E_c < E_*$$

Where $\Delta p_s = p_s - p_0$, r_s is shock wave radius, E_c combustion energy in shocked zone α is known constant (for $\gamma=1.4$, $\gamma\alpha \approx 1.5$) For dependence of radius r_s on time we have approximate relation:

$$t = t_* \left[B_0 \left(\frac{x_s}{r_0} \right)^{3/2} \left[1 - B_1 x_s \right] \right], \quad (2)$$

$$x_s = \frac{r_0 - r_s}{r_0}, \quad 0.1 < x_s < 0.5,$$

$$t_*^2 = \frac{2\pi p_0 r_0^4}{2E_0}, \quad B_0 = 1.04, B_1 = 0.184, \text{ (for } \gamma = 1.4\text{)}.$$

Because the gas is combustible mixture we can take $\Delta p_s = p_{C.J.} - p_0$ instead of calculated by (1), if we find $p_s < p_{C.J.}$ ($p_{C.J.}$ is pressure in Chapman-Jouset detonation wave). Near central parts of the combustion chamber shock pressure will follow asymptotic of Guderley-Landau-Stanyukovitch,¹⁰ namely $p_s \sim r_s^{-0.393}$

($\gamma=1.4$). See also graphs in Fig.10, obtained using numerical results of paper.¹¹ After the reflection the pressure will increase in 17 times in the center vicinity.

Then $E_c \geq E_*$ we have to take into account combustion

influence on the flow parameters.

According to R. Cheret results¹² we can use the following dependences to find overpressure Δp_s :

$$\frac{D-D_0}{D} = \frac{c_*}{4m^2} \left[\left(\frac{r_0}{r} \right)^m - 1 \right]^2 \quad (3)$$

$$\frac{\Delta p_s}{p_0} = \frac{\rho_0}{p_0} \frac{D^2}{\gamma+1} \left(1 - \frac{a_0^2}{D^2} \right)$$

Where D is detonation wave front velocity, $D_0=D(r_0)$, r is distance from the tube center, $m=m(\gamma)$, and $m=0.1868$ ($\gamma=4/3$),

$m=0.1973$ ($\gamma=1.4$), $c_* = \frac{\Gamma_*^2}{2(\Gamma_*+1)(2\Gamma_*-G_*)}$, where Γ_* is adiabatic exponent near Ch-J point, G_* Grunisen coefficient for the product of combustion, a_0 sound speed in the mixture. The relations (2), (3) take into account effects of both combustion and convergence. Thus this simple estimation shows that we have in the problem the case of high pressure and high temperature combustions. The arising shocks will interact with chamber walls. It leads to very fast and complete combustion of the mixture.

To simulate the parameters we can also use methods and results of two-dimensional calculations considered above.

We propose to use this new scheme not only in internal engine, but also for the body acceleration by gas motions in tubes.

RAM ACCELERATOR APPLICATION

Pulse Modes

Ram accelerator is a device for acceleration of a projectile

to hypersonic velocities.^{3,4} The general scheme of the accelerator is given in Fig.11. There are three modes of acceleration: (a)Subsonic combustion thermally choked ram accelerator mode; (b)Oblique detonation ram accelerator mode; (c)Superdetonative ram accelerator operation.

The results of A.Hertzberg and his coworkers (see for example ⁴) show that the projectile velocity about 3 km/c can be easily obtained by the ram accelerator.

According to our consideration this type accelerator can be supplied by additional devices which allow to use the pulse engine modes to increase the projectile velocities.

Let consider separately three main types of operations of pulse modes:

- 1)Electrical or laser sparks ignition near the projectile back wall.
- 2)Pulse detonation combustion inside of the projectile.
- 3)Imploding mode using laser beam pulses of a ring configuration or the belt-type electric discharge.

To study the new applications of pulse engine approach the developed above theory can be used. The acceleration schemes of Fig.10 and pulse engine patterns of Fig.1 have the similar parts: inlets, combustion domains and outlet streams. It gives for us possibility to get the thrust increasing using combustion in the ram acceleration modes together with detonation pulse engine methods of the thrust creation

Sparks Ignition near base of the projectile

Let we have electrical discharge across tube using two electrode origin from opposite side of the accelerator tube behind projectile (see Fig.1(a)). To find the arising shock pressure we used empirical relation:⁵

$$\frac{p_s}{p_0} - 1 = \frac{\Delta p_s}{p_0} = \frac{0.24}{R_s^2} + \frac{0.48}{R_s^{3/4}} \quad (4)$$

$$R_s = r_s / \left(\frac{E_0}{p_0} \right)^{1/2}$$

E_0 is specific energy, r_s cylindrical shock front distance from the discharge line. Let energy of a discharge be $E_* = 30\text{J} = 3 \cdot 10^8 \text{erg}$, diameter of the tube $2R = 3.8\text{cm}$. We have $E_0 = \frac{E_*}{2R} = 7.895 \cdot 10^7 \frac{\text{erg}}{\text{cm}}$. An estimation by formula (4) shows that due to the discharge overpressure on the basement of projectile increased in range 36bar-240bar (for initial pressure of mixture $p_0 = 20\text{bar}$). During a pulse the combustion process take place in very short period because of high mixture pressure and temperature. The trust and velocity of the projectile will be increased by about 20%, (for frequency 150Hz) and the lower p_0 the better trust increment for the same electrodischarge energy. Instead of electric discharge we can use laser explosion near projectile base. It is known that for $p_0 = 1\text{bar}$ a specific impulse of overpressure can have value of $J_{sp} = 50 \frac{\text{dyne} \cdot \text{s}}{\text{J}}^{13}$ if laser pulse energy is about $E_* = 30\text{J}$. For the small projectile $J_{sp} = \frac{J}{E_*}$, (J is mechanical impulse of pressure during laser pulse action.) Thus using the laser "explosion" we also can improve the ram accelerator characteristic.

Pulse Detonation Combustion Inside of Projectile

Suppose now that we prepare the projectile as gas-breathing pulse engine. If initial pressure is high ($p_0 \approx 20\text{bar}$) and pressure inside of the body p_i relatively small ($p_i/p_0 < 1$) the inlet flow velocity can be supersonic and bow shock arises ahead of fuel stream which can lead to combustion and local detonation inside the chamber: a small increment of the trust can be obtained by used pulse engine scheme (see Fig.1 and ¹⁴). Application of electrical discharge technique is difficult for the small projectile which is usually used in experiments. By using a converging profile of the wall it is possible to obtain high pressure and high stream velocity in nozzle outlet (exit) (Fig.1).

Implosions Near Projectile Base

The implosion by using ring-type laser beam or collar-type (belt-type) electric discharge (see Fig.7(b)) in the tube near bottom parts of the projectile can lead to very high pressure at the projectile bottom. The result of calculation¹⁵ of ring type laser beam action on the plane surface (projectile bottom) is shown in Fig.11. It was found, that very high pressure arose in central part of the projectile bottom. The significant trust will occur during arising plasma flow. The detonation of gas gives near base high background pressure P_* . Thus we will have acceleration effect which leads to higher velocity of projectile.

Example: Let we have ram acceleration tube diameter of 4cm, tube pressure $p_0=20\text{bar}$, methan-oxygen mixture with projectile of mass 100g and cross section diameter of base 3cm. The projectile entered the ram accelerator tube with velocity 1200m/sec. We have discharge devices each 6 meters and a tube longer than 18 meters. The energy of a discharge is $E_d=100\text{J}$. We also supposed that the discharge domain is $h \times l \times 2\pi r_0$ (a "belt" of combustion mixture near wall tube) r_0 is inner radius of the belt, h its thickness and l its length along tube, $l=4\text{cm}$. The arising mean overpressure due to the discharge can be find by expression:

$$\Delta p_* = (\gamma - 1) \frac{E_d}{V} \quad (5)$$

where V is the volume of the belt. Using the results described above, Chishell method, analytical approach in book⁵ and formulas (1)-(3) we can find dependance of overpressure on the distance from tube center. The result is presented in Fig.13. for the case $E_d=100\text{J}$, $\gamma=1.4$ during converging process. Because of high initial pressure and low the energy of discharge the relative initial overpressure is $\frac{\Delta p_*}{p_0} < 1$, namely for the example we have: $\Delta p_* = p_* - p_0 = 10\text{bar}$, then $\Delta r = 0.4\text{cm}$, $\Delta p_*/p_0 = 0.5$. Because of

converging flow the shock pressure after small decreasing begins to grow and reach near center the value higher than 500bar. The overdriven detonation waves occurs near projectile during reflection process of the shock. The reflections of the detonation waves from the tube wall projectile base and axis of symmetry will preserve high pressure until 18μsec or more. During this period the projectile gets pressure impulse of about $5.1 \cdot 10^{-2} \text{ bar} \cdot \text{sec}$. It gives possibility to obtain the velocity increment of $5 \frac{\text{m}}{\text{sec}} - 10 \frac{\text{m}}{\text{sec}}$ for one cycle with the discharge (for mass projectile 100g). It has to be noted that the discharge and imploding process does not influence significantly on general picture of the flow (small disturbance) but change dramatically the combustion process near the projectile base.

The electrical discharge can be replaced by laser pulse action near the back wall of the projectile.

It is also known that the electrical energy of amount 500KJ and powerful discharges were used for acceleration of projectile to velocity of 5km/sec and more.^{16,17}

CONCLUSION

The results of numerical and analytical calculations showed that using pulse electrochemical engine conception leads to higher trust than ordinary combustion pulse engine. The numerical method for two-dimensional flows was developed. It was shown the results for pulse engine with detonation stage of combustion can be used for improvement of ram accelerator technique. The estimates of trust and pressure levels in internal combustion pulse engine and accelerating devices were obtained. The projectile acceleration problem needs for detail numerical simulation which can be fulfilled on the base of developed methods.

Acknowledgments

The authors are grateful to A.N.Gavrilov for his assistance in numerical modelling.

The support of Department of Mechanical and Material Engineering of Washington State University was important for the authors.

REFERENCES

1. Ponizy D., Wojcicki S, "On Modeling of Pulse Combustor", Archivum Combustionis, v.4, #3/4, 1984, pp.161-170.
2. Korobeinikov V.P., Gavrilov A.N., Wojcicki S. "Theoretical Analysis of Combustion and Detonation Wave Propagation in Pulse Engine", Book of Abstracts, 13th ICDERS, Nagoya, 1991, p.53.
3. Bruckner, A.P., Knowlen C., Hertzberg A., Bogdanoff D.W., "Operation Characteristics of the Thermally Choked Ram Accelerator", J.Prop. and Power, v.7, #5, 1991, pp.828-836.
4. Hertzberg A., Bruckner A.P., Knowlen C., "Experimental Investigation of Ram Accelerator Propulsion Modes", Shock Waves, v.1, 1991, pp.17-25.
5. Korobeinikov V.P., Problems of Point Blast Theory, Am.In.Ph., New York, 1991.
6. Godunov S.K., Raznostnyi Metod Chislennogo Rascheta Razryivnykh Reshenii Uravnenii Gidrodinamiki (in Russian), Matem. Sbornik, v.47, #3, 1959, pp.271-280.
7. Zakharov N.S., Korobeinikov V.P., "Similarity Motion of A Gas in the Case of Local Supply of Mass and Energy in a Fuel Mixture", (Transl. from Russian, 1980), Mekhanika Zhidkosti i Gasa, #4, 1979, pp.70-77.
8. Gavrilov A.N., Korobeinikov V.P., "Dvizhenie dvukhfaznykh Sred v Trubkakh Peremennogo Setcheniya pri Lokal'nom Podvode

Massyi i Energii" (in Russian), Zhurn. Prikl. Mekhan. Tekh. Fiziki, #2, 1992, pp.89-94.

9. Dwyer H. et al., "On Modeling of Pulse Combustors", in book: Numerical Approach to Combustion Modeling, ed. by Oran E., Boris J., 1991, pp.693-701.
10. Baum F.A. et al., Fizika Vzryiva , Nauka, Moscow, 1975.
11. Korobeinikov V.P., Markov V.V., Putjatin B.V., "O Raschete Skhodjatshikhsja Tehenii Gazov", in book: Dynamika Sploshnoi Sredyi v Cosmose i na Zemle, Acad. Nauk SSSR, Moscow, 1978, pp.87-94.
12. Cheret R., Detonation of Condensed Explosives, Springer-Verlag, Hong Kong, 1992.
13. Prokhorov A.M., et al., Vzaimodeistvie Lazernogo Izlutcheniya s Metallami (in Russian), Nauka, Moscow and Editura Academiei, Bucuresti, 1988.
14. Eidelman S., Grossman W., Lottati I., A Propulsion Device Driven by Reflected Shock Waves, Preprint, Sci.Appl. Internat. Corporation, Mc Lean, USA, 1991.
15. Zakharov N.S., Korobeinikov V.P., "Nestatsionarnyie Tehenija Errozionnoi Plasmyi pri Oblutchenii Tverdikh Mishenei Kol'tzevyimi Luchami"(in Russian), Mechanika Zhidkosti i Gasa, #3, 1989, pp.179-182.
16. Lecomte C.I. "Hypervelocity Launcher", in book: High Speed Physics, Springer-Verlag, Wien, 1967, pp.247-275.
17. Brode H.L. Theoretical Description of the Perfomance of The UTIAS Hypervelocity Launcher, RAND Corporation, RM-6298 PR, 1970.

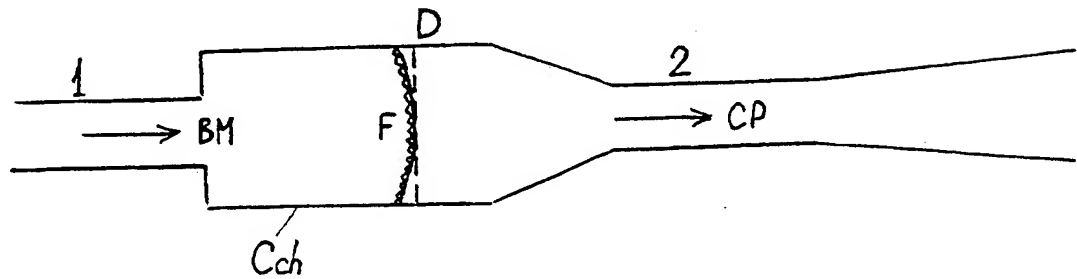


Fig.1 (a). Pattern of the flow in combustion chamber and the tubes system.
1 inlet, 2 outlet, Cch combustion.

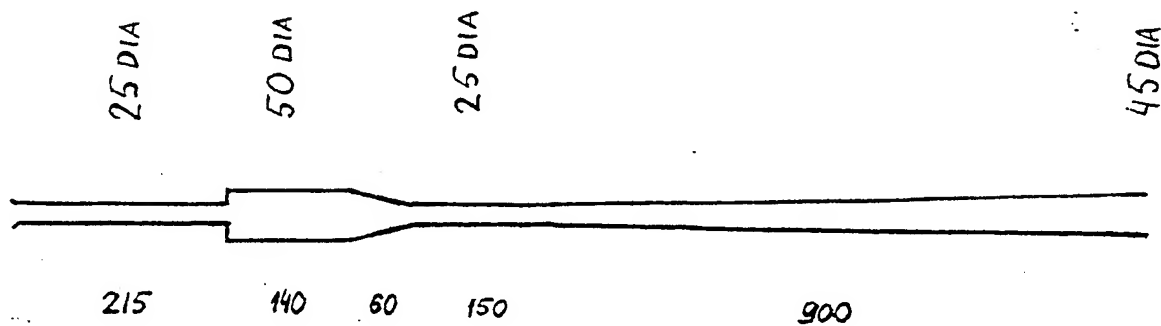


Fig.1 (b). Pattern of flow in combustion chamber and the tubes system.
The model for experiment and calculation; numbers are tubes dimension in mm.

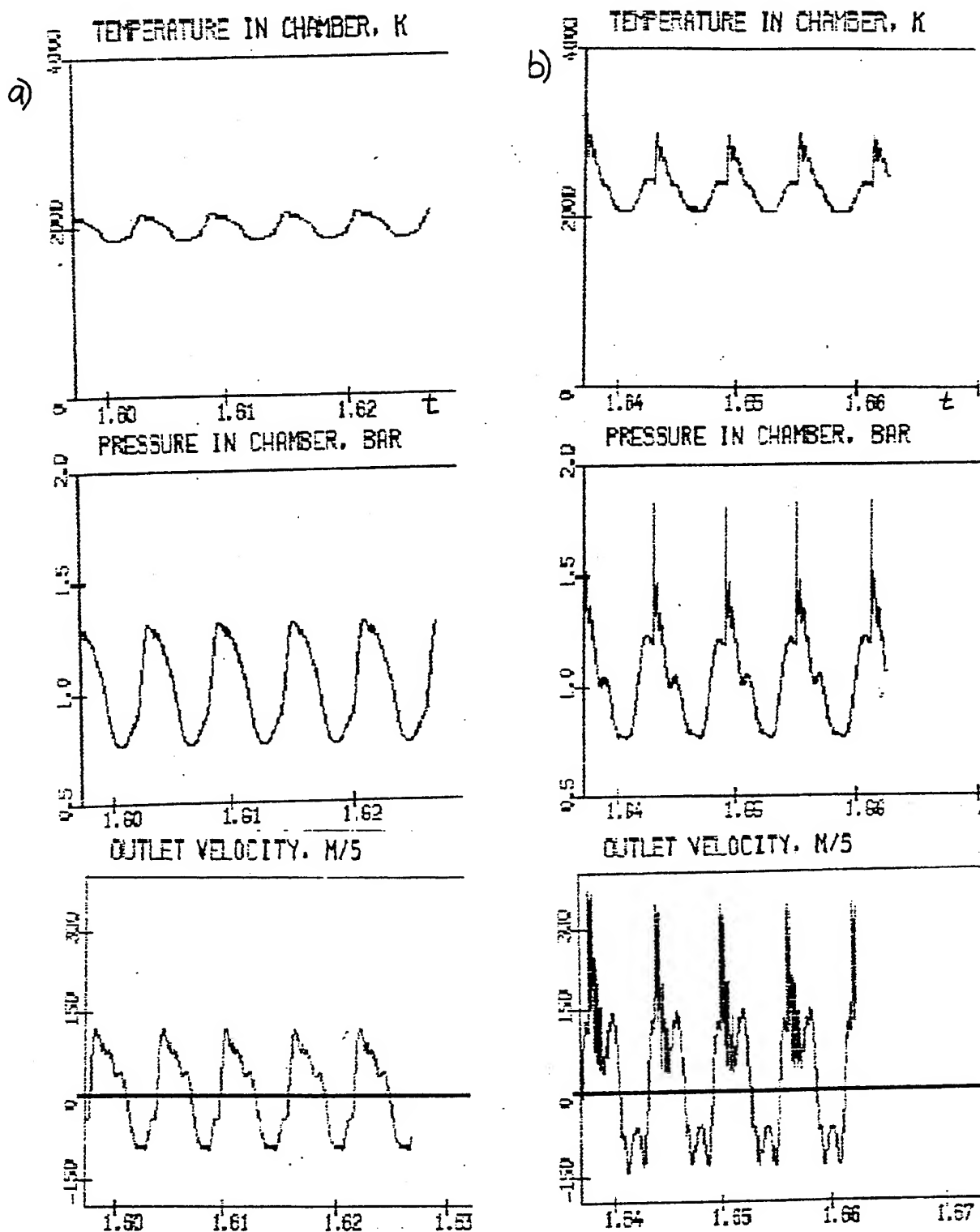


Fig 2. Pulse engine operation; Fuel: acetylene + air, Frequency: $F=167$ Hz;
 a) operation without discharge, thrust is 1.385N;
 b) operation with electrodischarge, thrust 1.936N.

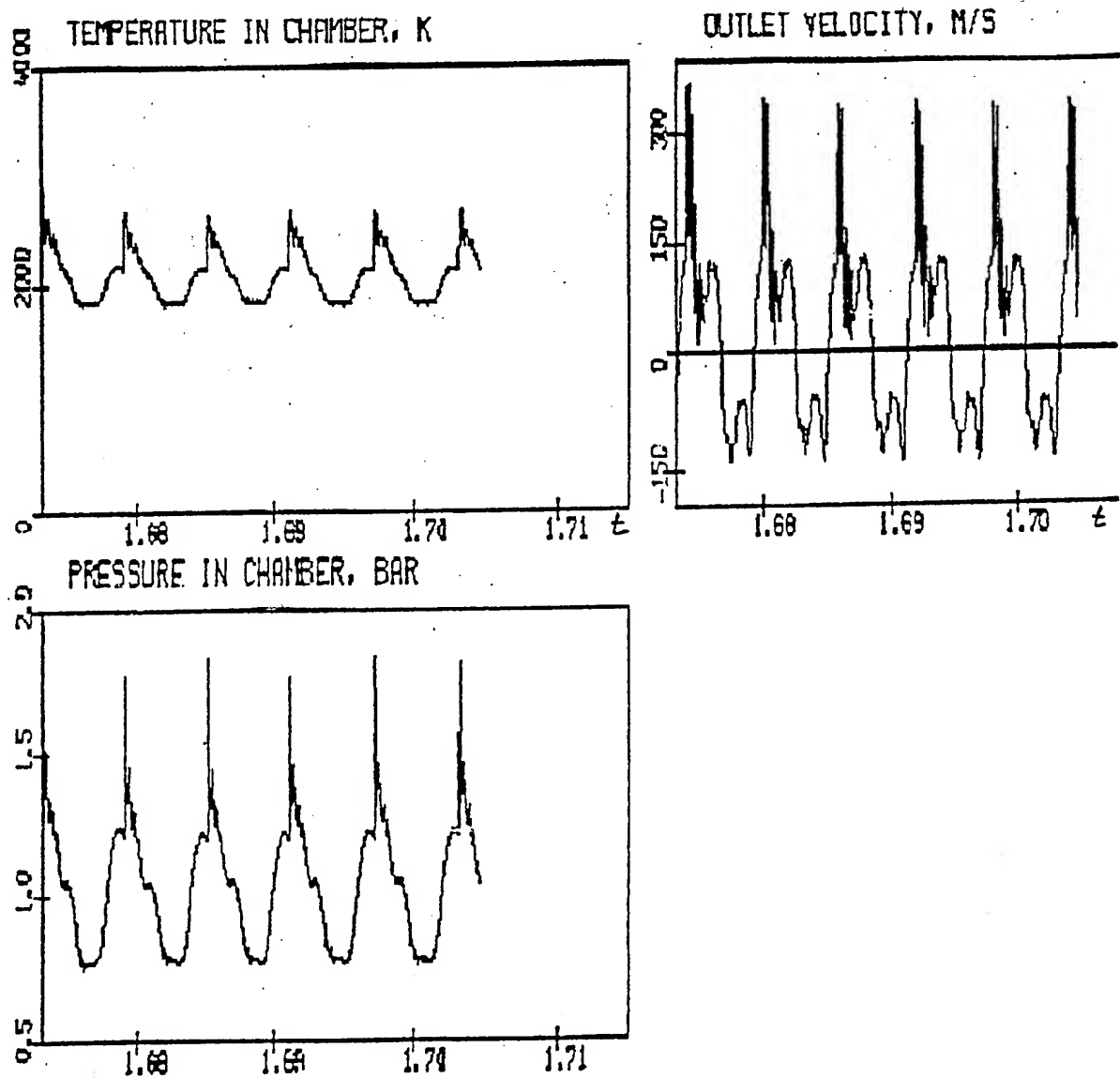


Fig. 3. Operation with discharge
Fuel: propane + air, Frequency: 167 Hz, Thrust: 2.058 N.

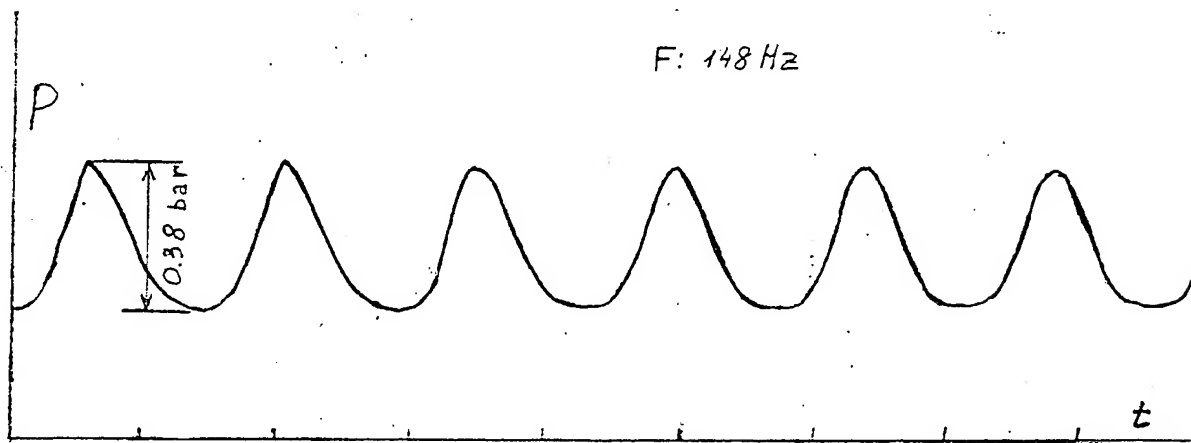


Fig.4 (a). Operation without electrical discharge, experimental pressure in centre of the chamber.

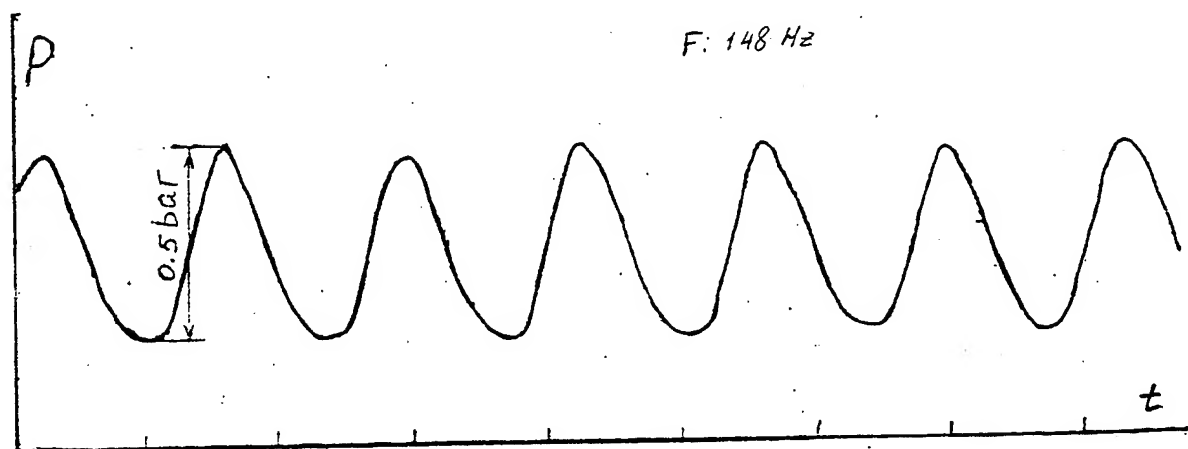


Fig.4 (b). Operation with electrical discharge, experimental pressure in centre of the chamber.

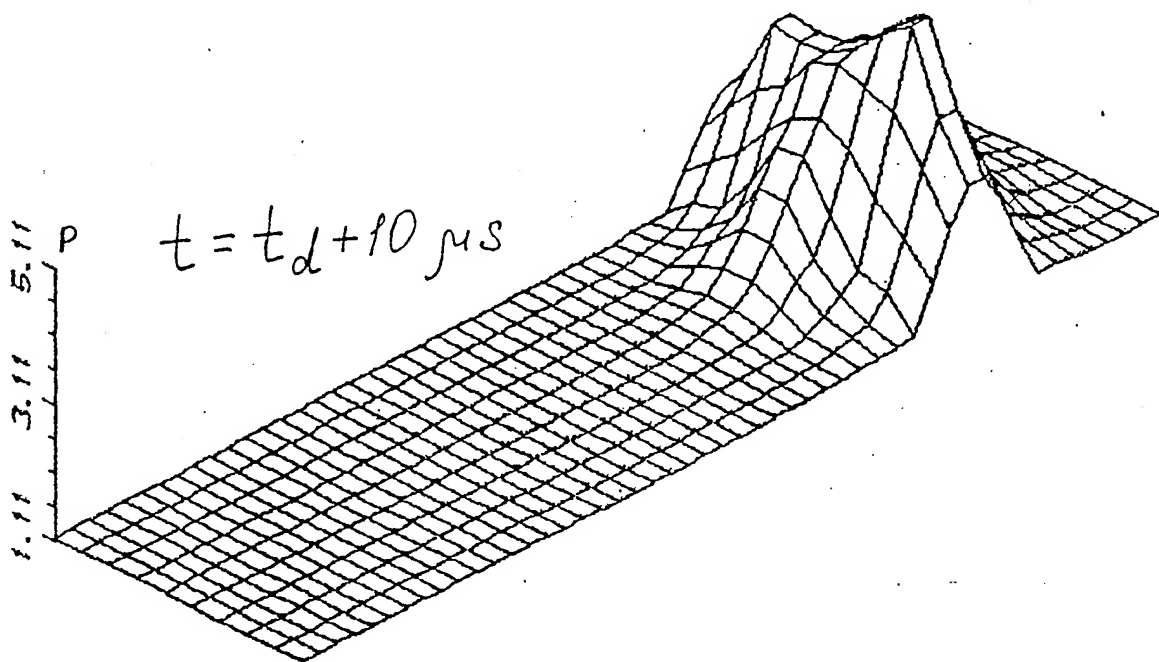
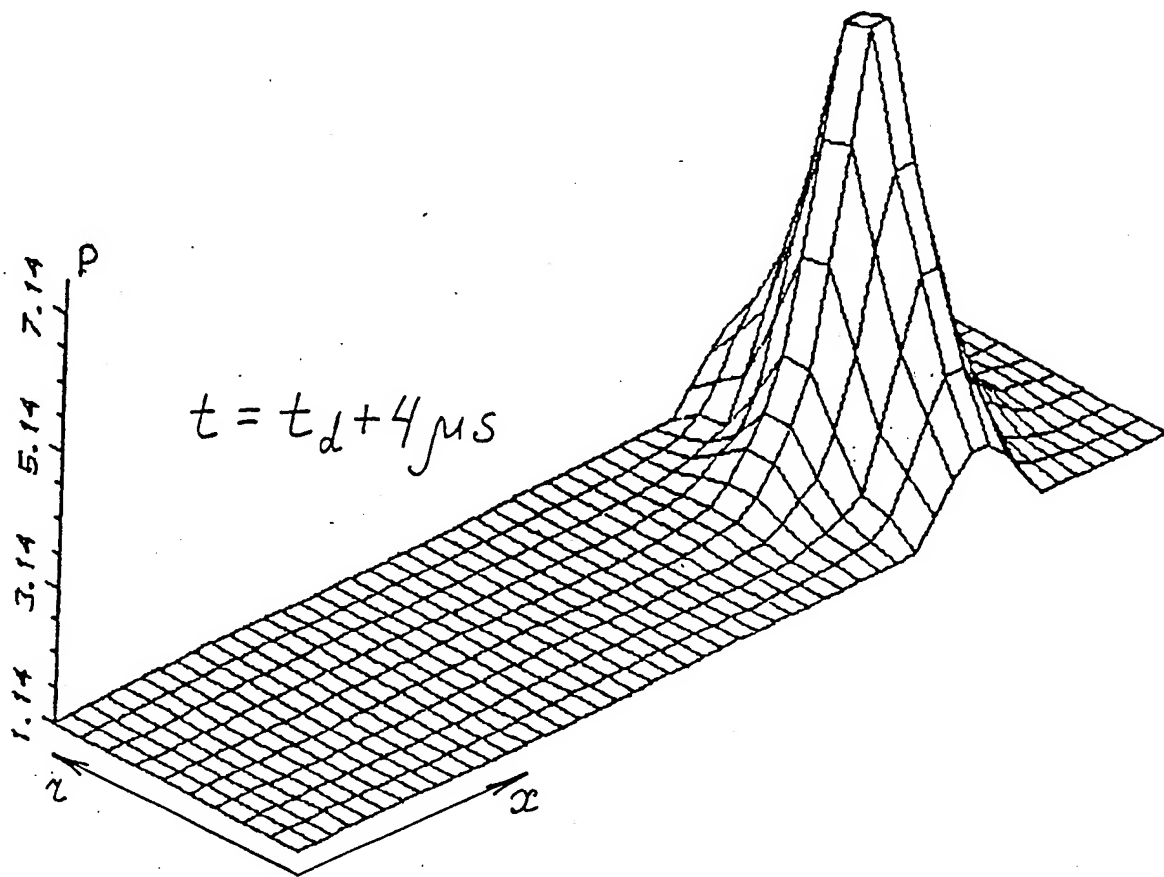


Fig. 5. Pressure distribution in the chamber, t_d is discharge time; r, x cylindrical coordinate.

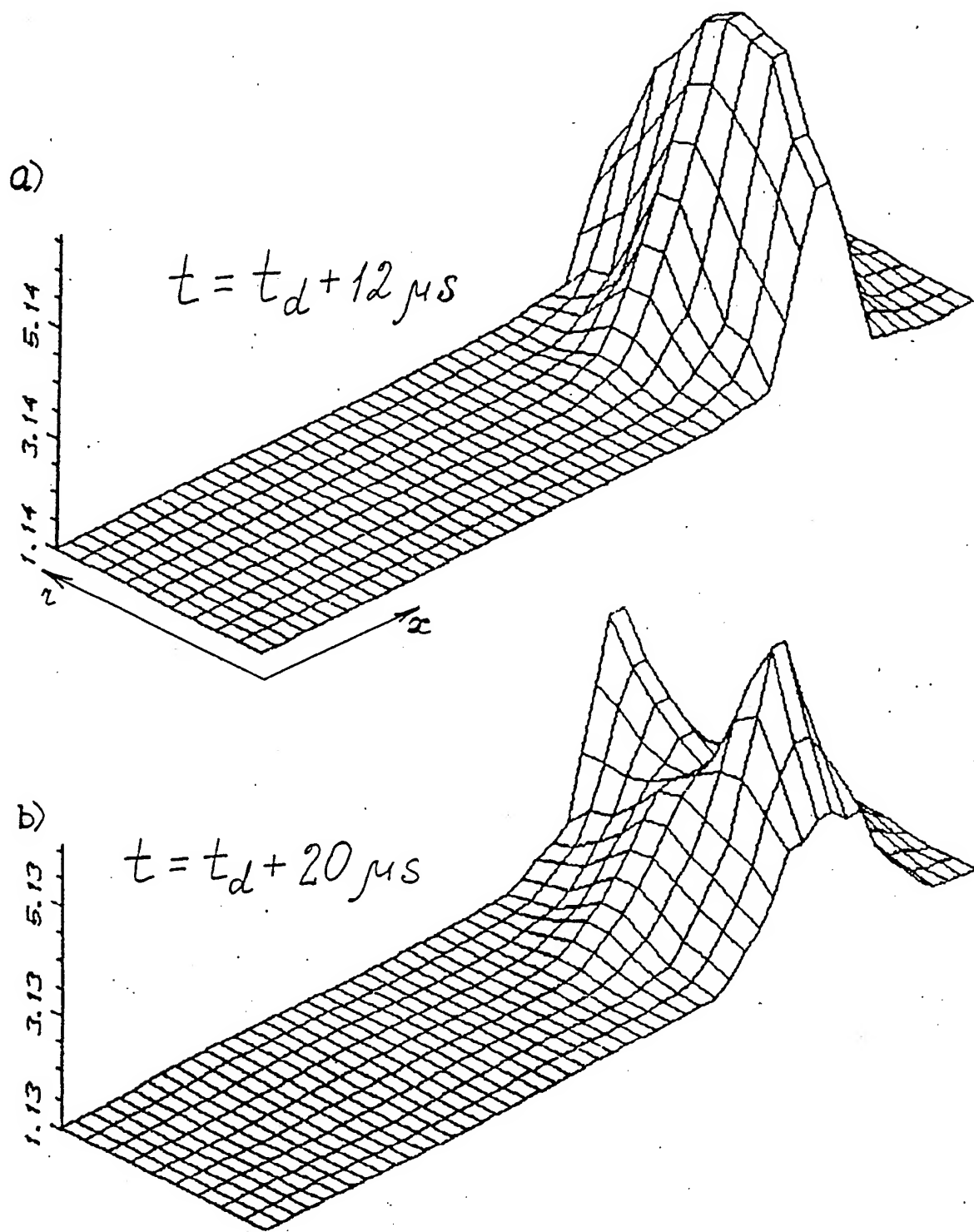
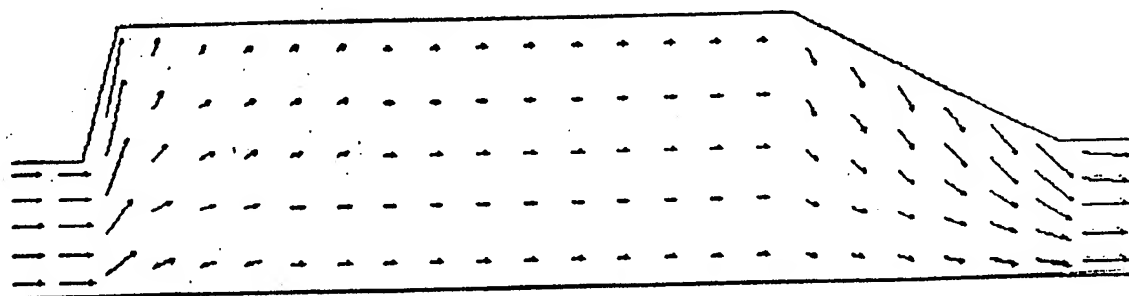

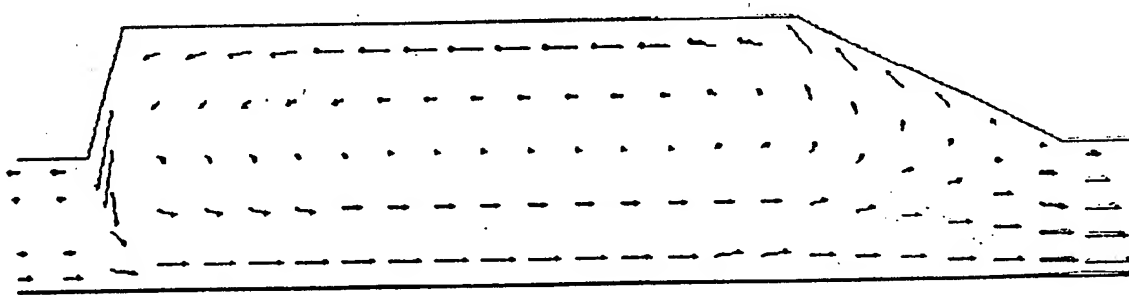


Fig. 6. Pressure distribution in the chamber for two time moments (a)converging stage; b)diverging flow after implosion).



$$t = t_b + 0.2 t_c$$

30 m/s




$$t = t_b + 0.5 t_c$$

Fig.7. Velocity fields inside the chamber;
 t_b is beginning of cycle, t_c duration of cycle.

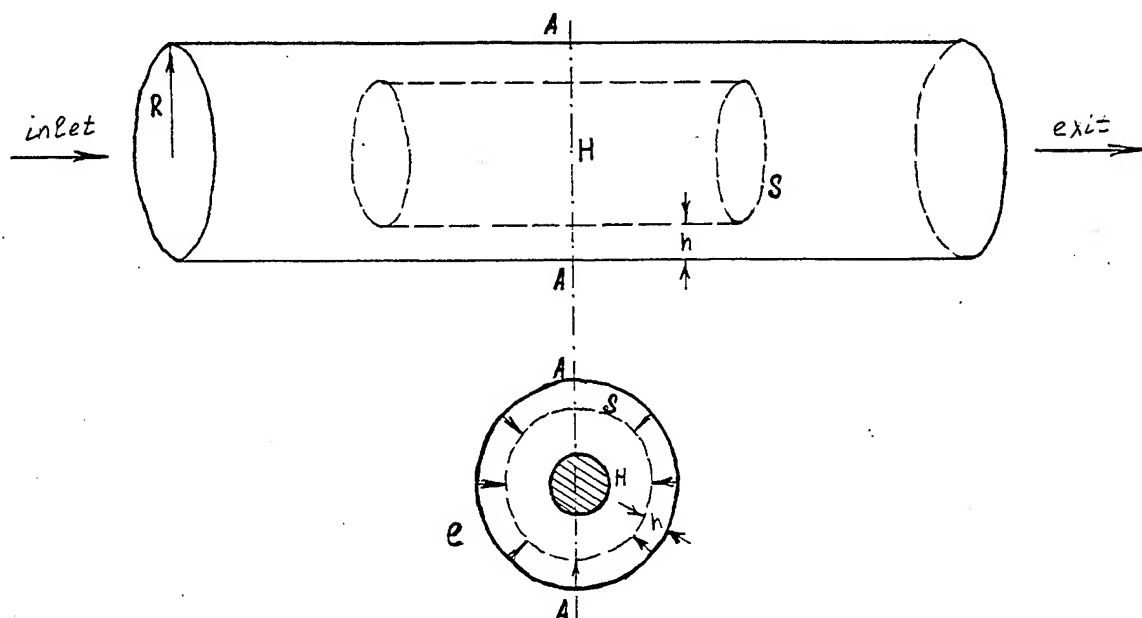


Fig. 8. Scheme of the implosion process.
 a) Combustion chamber; S is electrodes surface;
 b) A-A is section of the chamber; e an electrode, h its length ($h \approx 0.1R$); H high pressure zone due to implosion

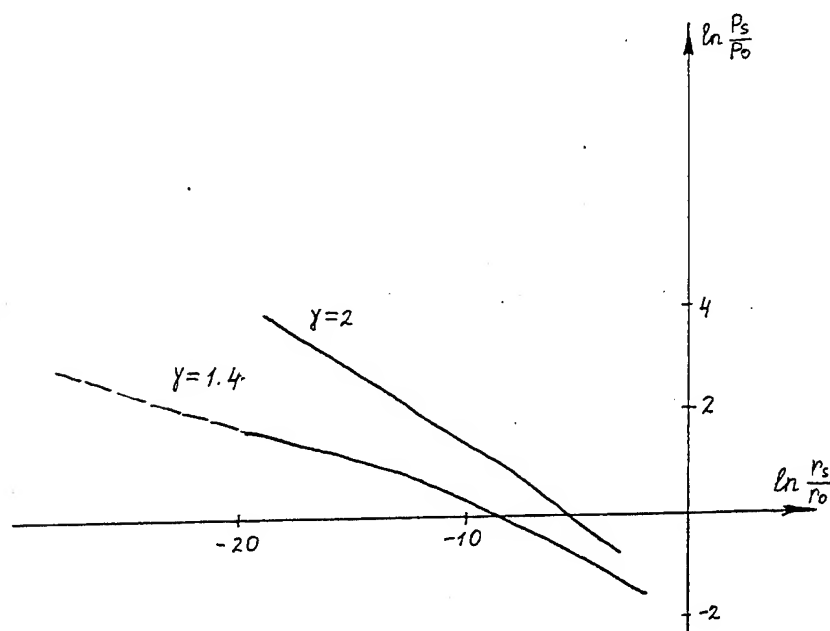


Fig. 9. Shock pressure near center of symmetry; $\frac{\Delta P_S}{P_0} \sim r_S^{-0.394}$,
 cylindrical implosion, $\gamma=1.4$, $\gamma=2$.

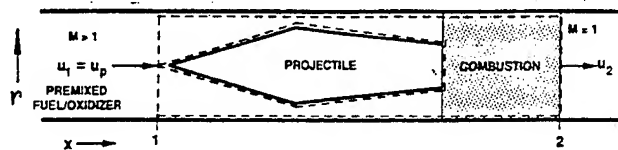


Fig. 10. Thermally choked (subsonic) combustion ram accelerator scheme;
frame of reference moves with projectile,
--- control volume boundary,
1 is "inlet" place, 2 "outlet" position.

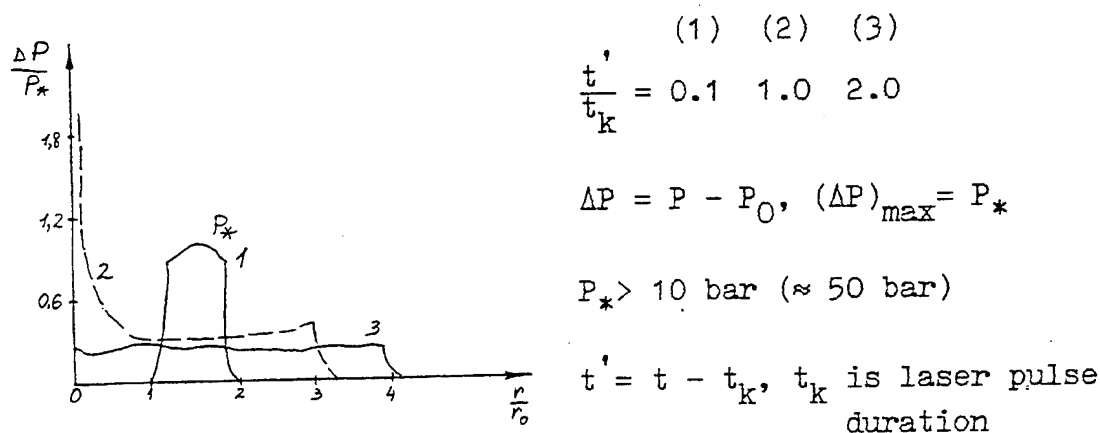


Fig. 11. Overpressure on plane target.

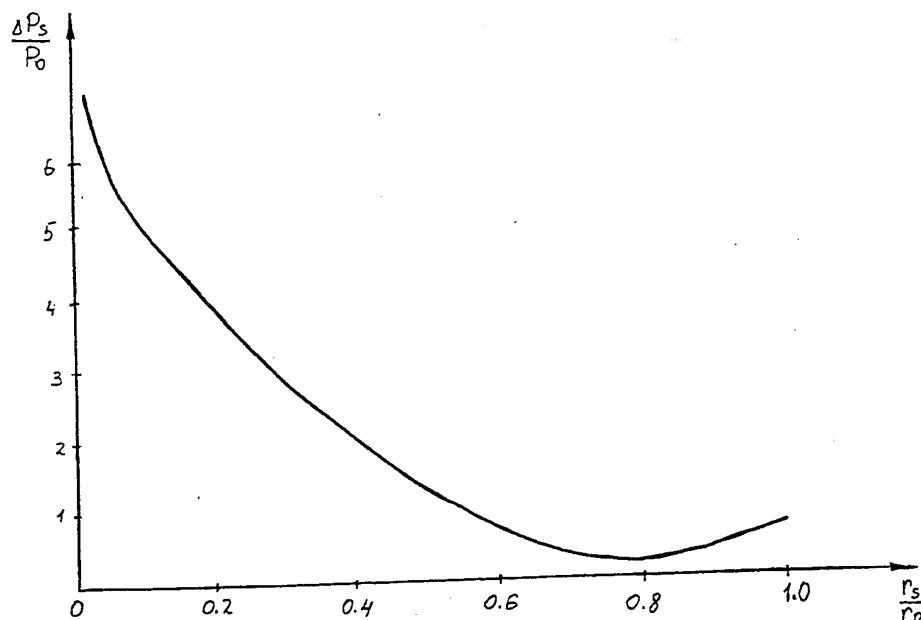


Fig. 12. Overpressure at the front of cylindrical converging detonation wave.

BALSAD – BALLISTIC SYSTEM FOR ANTI-ASTEROID DEFENSE

Pavel V. Kryukov
Ballistic Technology Scientific Venture
(TsNIIMASH)
Kaliningrad, Moscow Region, P.O. Box 92
RUSSIA 141070
E-mail: kryukov@baltec.msk.su

ABSTRACT

Any collision of a kilometer-size asteroid with the Earth constitutes a grave threat to the whole of mankind. This paper reflects an attempt to build an economically feasible concept of anti-asteroid defense using a gasdynamic ballistic system capable of delivering thermonuclear projectiles to the desired zone of intercept with their subsequent detonation resulting from their high speed impacts on the asteroid's surface. Both the design of the gasdynamic ballistic system for direct injection of projectiles into Outer Space and some issues concerning hypervelocity projectile transit through the dense atmospheric layers are discussed in this paper.

INTRODUCTION

In recent years the world community as well as various scientific teams have evinced a growing interest in the problem of preventing collisions of huge heavenly bodies (asteroids and comets) with Earth¹. Such collisions, depending on the scale of event, may lead to either local catastrophic demolitions or a global holocaust. An encounter between Earth and another Tunguska-size meteorite may result in millions of casualties, if one takes into account the proliferation of hazardous industries nowadays. Collision with a kilometer-size asteroid constitutes a grave threat to the whole of mankind. Although the probability of an asteroid collision is fairly low, the conditional probability of any human being to be killed during such a catastrophe is on a par with the probability of dying in an aircraft accident or after nuclear power station burst. In other words, if we are not concerned with this pressing problem now, we may be overtaken by such an event. Hence, the threat of heavenly bodies to Planet Earth as well as the research of cost-effective countermeasures require appropriate consideration.

This paper reflects our attempt to build an economically feasible concept of an anti-asteroid defense on the basis of a gasdynamic ballistic system capable of delivering thermonuclear projectiles to the desired zone of intercept with their subsequent detonation resulting from their high speed impacts on the asteroid's surface. The design of this type of a thermonuclear device precludes the need for fissionable materials. Command guidance from Earth is used to steer a projectile to its target. The projectile maneuvers by exploiting the kinetic energy stored in its rotational motion, i.e. the projectile spinning around its longitudinal axis. Collision of an asteroid with Earth is avoided by changing the incoming asteroid's trajectory, which change is forced by a series of thermonuclear detonations on its surface. In addition, these explosions disperse and

partially evaporate the asteroid's body: its scattered fragments are substantially less hazardous should they hit Earth.

The enclosed figures illustrate various elements of the antiasteroid defense concept based on gasdynamic throwers. More detailed analysis of these issues is the subject of another paper which is now being prepared. The present paper is aimed at describing both the design of a gasdynamic ballistic system for the direct injection of projectiles into Outer Space as well as some issues concerning hypervelocity projectile transit through the dense atmospheric layers.

THE BALLISTIC SYSTEM

The main part of the throwing system for directly launching projectiles into Outer Space is a ballistic bore which consists of a thick-wall tube pointing to the sky with a reloadable liner inserted into it. A powder gun with a rifled bore is mounted at the bottom for projectile injection. The bore is attached at its muzzle to a pontoon and hangs precisely vertically in a protective cylindrical canister which is also fixed to the pontoon and which prevents any disturbances of the subsurface ocean flows from reaching the ballistic bore. The suspension-type design of the thrower system helps to stabilize the ballistic bore after a shot thus ensuring a high linear accuracy. Deployment of the ballistic system in the ocean allows its relocation to practically any latitude which, coupled with the Earth rotation, provides the capability to hit any region of Outer Space within 1 million kilometers of the Earth. An ocean-based thrower system has some other advantages: (a) the recoil pulse dissipates effectively in the surrounding waters, (b) the excessive heat is easily transferred into the water, and (c) the requirements to reduce the acoustic impact on the environment are not as stringent in this case. Evacuation of air from the bore is done with ejection pumps fed by compressed air. To soften the impact of the projectile as it is injected into the dense atmosphere and to avoid its possible demolition, a smooth increase of pressure at the upper part of the ballistic bore near the muzzle is also provided by these ejection pumps.

Loading of the explosive charge is planned to be executed from the muzzle down the bore. First, pyropowder packs are loaded, and then the projectile is lowered. It is mounted in a sabot with a hexagonal driving band to steer it along the rifled gun barrel. This band makes it possible to load the powder gun from its muzzle. Then a distributed layer of explosive compound is inserted into the bore along its full length. This compound is a 5-mm thick plasticized PETN sheet. Strips of this sheet several centimeters wide are stitched in a regular pattern to paper cardboard sheets with not less than 1-mm gap (it should be noticed that gluing the strips with adhesives may substantially alter the parameters of the explosive compound). Then each cardboard sheet is rolled into a tube and wooden rings are slipped on it along its full length. The external diameter of these rings is equal to the internal diameter of the ballistic bore with an allowance made for the plastic deformation of the bore's walls under the shock loads generated by each shot. The sections thus assembled with an explosive charge are loaded one by one down the ballistic bore. This type of the ballistic tube design does not require any precision metal-cutting operations. Gaps between the PETN strips prevent axial detonation of the distributed charge. The thickness of the wooden rings between the explosive layer and deformable liner in the ballistic bore is selected to dampen the shock wave to the point where it will not cause the mechanical

destruction of the liner in which the rest of the shock wave energy is absorbed. The remnants of cardboard and wood, if any, are blown out of the ballistic bore with the powerful gasdynamic jet.

A preliminary boost of the sabot-equipped projectile to a speed of 1.5 km/s is carried out by a powder gun with a rifled bore. Both the projectile and its sabot gain translational and rotational motion simultaneously. After the pre-boost the rapidly spinning projectile enters the evacuated ballistic bore with the explosives on its walls. The internal diameter of the bore is greater than the projectile caliber, hence the latter proceeds without any mechanical contact with the walls. Additional speed is transferred to the projectile by the successive detonation of the explosive strips as the projectile flies by. As the detonations begin, the sabot is discarded and starts to lag behind. Synchronous detonation is achieved because liquid, stored in the projectile, is sprayed out of the projectile side wall under the centrifugal force. Drops of the liquid hit the surface of explosive layers at a grazing angle which initiates detonation due to viscous friction and shock compression. At this time, gaseous products of detonation expand at a high speed towards the tube axis and collide on the cone aft of the projectile pushing it ahead. The translational motion of the projectile without any mechanical contact with the ballistic bore walls is accomplished by gyro-stabilization of its attitude and by the centering effect in the bore of the detonation products expanding towards the bore axis. Parameters of the full-scale ballistic system for anti-asteroid defense are given in the figure.

Exploratory development of the high speed throwing technology is being conducted at the TsNIIMASH large-scale ballistic facility. By now 60 meters of the bore of the experimental 100-mm ballistic system have been manufactured. The final version of the experimental ballistic system will have the following parameters:

Ballistic bore length:	150 m
Weight of the distributed explosive charge:	up to 150 kg
Projectile caliber:	85 mm
Projectile weight:	1.5 kg
Projectile muzzle velocity:	up to 12 km/s
Pre-boost muzzle velocity:	up to 5 km/s
Projectile angular rate:	up to 1600 rps

Upgrades of the experimental ballistic system are planned for the future to test an ocean-based version. In this case the length of the bore could be extended to 1 km. The pre-boost to 1.5 km/s will be executed with a powder pre-booster. The energetic capabilities of the ocean-based experimental ballistic system will allow it to launch into Outer Space projectiles weighing 3 to 5 kg.

Experiments to investigate detonation phenomena of the PETN explosive were carried out using a 1.5-gram plastic projectile of 12.7-mm caliber which was fired into a flat PETN specimen from a two-stage light-gas gun at velocities ranging from 1.2 km/s to 3 km/s and at impact angles of 30 and 90 degrees. The specimen was fixed with the same technology which is to be used in the design of the experimental ballistic system. It was revealed that initiation of detonation in the

explosive layer occurred throughout the full velocity range when the impact angle equaled 30 degrees. On the other hand, at the normal angle of impact, the explosive did not detonate even at 3 km/s. This can possibly be explained by the additional heating which the explosive surface experiences caused by the high-speed tangential flow of the projectile material along the specimen layer in the 30 degree case.

Ten explosive tests were carried out to assess the lifetime of the 100-mm bore of the experimental ballistic system. A 1.8-mm PETN layer was inserted into the tube section in compliance with the technique described above. Then the section was hermetically sealed from both sides with endcaps. The explosive detonation was initiated with an electrical detonator. Inner and outer diameters of the steel tube at various cross-sections were measured before and after the test series. It was established experimentally that after 10 tests the inner diameter of the tube incremented to not more than 0.2 mm. The computed efficiency of the thrower using this approach matches the results published in Russian journals.^{2,3}

PROJECTILE HYPERVELOCITY ATMOSPHERIC TRANSIT

In order to achieve the projectile's transit of the dense atmospheric layers at 13 km/s, the nose cone taper angle was selected to obtain a drag factor not greater than 10^{-2} . In this case the speed loss due to atmospheric drag is not more than 2 km/s assuming that this drag has a constant value. The sharp taper angle of the projectile can be sustained during the atmospheric transit because the projectile is fired vertically and the total duration of this transit lasts around one second. This permits the active heat protection design of the aerodynamic cone of the projectile to be accomplished with intensive coolant depletion. The ballistic cone itself is manufactured from a hard carbon-based material, monocrystalline graphite, a modification with curled-up atomic layers which form a macrocylinder, was selected to build the cone. Ordinary monocrystalline graphite possesses flat atomic layers. The strength of monocrystalline graphite along the atomic layers is enormous (200,000 atm), and it withstands temperatures up to 2600 C. It is true that graphite atomic layers have weak interlayer bonds, and it can be easily sliced like mica. However, should one manage to curl the atomic layers into a cylinder, this shortcoming will be removed. Because of graphite two-dimensional crystalline structure when the stress overcomes the rupture limit destruction proceeds according to the viscous mechanism, i.e. some additional work must be expended prior to rupture. In contrast to graphite, most of high-strength materials with three-dimensional crystalline structure demonstrate a brittle mechanism of destruction: the propagation of a crack is momentary and additional energy is not needed. The high mechanical strength of graphite together with its moderate density (2.26 g/cm^3) make it possible to spin a projectile made of this graphite so rapidly that the linear speed at its periphery can reach 3 km/s. At such angular rates cone ablation will proceed axisymmetrically, thus decreasing projectile deviation from the local vertical, and this substantial gyroscopic moment will stabilize its motion in the atmosphere. Another useful and important feature of monocrystalline graphite is its record heat conductivity along atomic layers (2,000 W/m-K), which is five times better than that of silver at a room temperature. The high heat conductivity provides protection for the graphite surface against overheating and sublimation in the high-speed air flow. However, above 600 C graphite readily interacts with atmospheric oxygen and the design of the heat protection means should be considered to block oxygen access to the graphite surface.

Graphite oxidization can be overcome with the help of a layer of atomic lithium over the cone surface. The weak interlayer bonds of graphite permit substantial doping with lithium, up to one lithium atom per eight carbon atoms. The dopant atoms form bonds between the graphite's atomic layers without markedly altering graphite crystalline lattice due to the small atomic radius of lithium. Above 1500 C, as the heat wave proceeds in depth, the lithium interlayer bonds disintegrate violently liberating lithium atoms which will rise to the surface through the intact graphite crystalline lattice and yield intensive degassing. The atomic lithium flow provides active heat protection of the surface and it readily reacts with atmospheric oxygen thus impeding its access to carbon atoms on the surface. The high speed of heat propagation in graphite supports the needed level of lithium degassing per unit area. The thermal energy released during lithium oxidization is partially absorbed by endothermic disintegration of lithium interlayer bonds. This is the approach chosen to provide heat protection for the side surface of the projectile ballistic cone. The relatively short time of atmospheric ascent, the high heat and temperature conductivity of monocrystalline graphite, together with its ability to store large amounts of lithium make this a solid basis for the design.

Unfortunately lithium doping is not enough to protect a tip of the cone. Indeed, if a 12 km/s projectile enters the lower atmosphere, which is known to have a density 1.23 kg/m^3 , then a powerful shock wave originates at its tip with a pressure behind the shock front of 2,000 atm and the temperature above 15,000 K. At this temperature the major component of heat transferred to the projectile surface is in the near-UV. To protect the tip, a substantial gas flow is pumped through its outside. This gas must be inert with respect to graphite, have good absorption of near-UV radiation and be cool enough not to sublime the graphite. The use of the gaseous products of some type of solid propellant combustion has been proposed. To implement this, an axial cavity is drilled in the projectile and filled with propellant powder. As the projectile enters the lower atmosphere, propellant combustion is initiated. The rate of protective gas depletion is an exponential function of the shock layer pressure. While the projectile rises, the pressure decreases and combustion slows down. The initial solid propellant mass is calculated, with these functions in mind, to provide heat protection along the whole path of the projectile in the atmosphere and amounts to about 10% of the total projectile mass.

At present research is being conducted to explore approaches to synthesize monocrystalline graphite. In particular, a technique of forced spatial orientation of its atomic layer planes has been found. This technique is applicable for layer orientation both in the process of graphite crystal growth and during high temperature annealing of the ready-made crystal. Proof-of-concept experiments have confirmed the feasibility of the key concept underlying the technique. In these experiments the crystalline planes of the pyrolytic graphite polycrystal have been aligned to better than 0.1 angular degree under the proposed force factors, the initial polycrystal having a misalignment on the order of 20 degrees. Near-term plans include commissioning of a technological installation for graphite monocrystal synthesis which will be capable of putting into practice controlled growth of graphite crystals with a three-dimensional order to their structure. The major criterion for the crystal quality acceptance tests is the tensile strength in the direction parallel to its atomic plane.

Exploratory development of the active heat protection means of the projectile is planned to be carried out at the TsNIIMASH large-scale ballistic facility which after special upgrades will be capable of generating hypersonic flows of cool air at Mach numbers between 30 to 40. Such flows are possible due to a tenfold radial compression of an air vortex which has an initial speed of rotation about 1000 m/s. The energetic capabilities of the facility makes it possible to obtain high-speed jets lasting for up to 100 ms during which time the air jet density decreases from its nominal value to zero, thus providing conditions for projectile atmospheric transit which simulate the real environment.

ACKNOWLEDGEMENTS

The author wish to appreciate the support of International Science and Technology Center, Prof. Adam Bruckner, Mr. David Kruczynski, Dr. Roy Reichenbach, Ms. Stephanie Strom and the others who make this presentation possible. The efforts of Dr. Boris Goncharov on the translation of this paper into English and Ms. Sarah Kirby's editing are also gratefully acknowledged.

REFERENCES

1. Materials of the International Conference on Space Protection of Earth SPE-94, Chelyabinsk-70, September, 1994.
2. A.E. Voitenko, "Major energetic characteristics of the linear jet motor", In: *Zurnal Prikladnoi Mechanic i Tekhnicheskoi Fiziki*, 1990, #2, pp. 118-120. (In Russian).
3. V.I. Tarjanov, "On the acceleration of the massive body upon the front of detonation wave", In: *Fizika Goreniya i Vzryva*, 1991, #1, pp. 136-138. (In Russian).

BALLISTIC SYSTEM FOR ANTI-ASTEROID DEFENSE

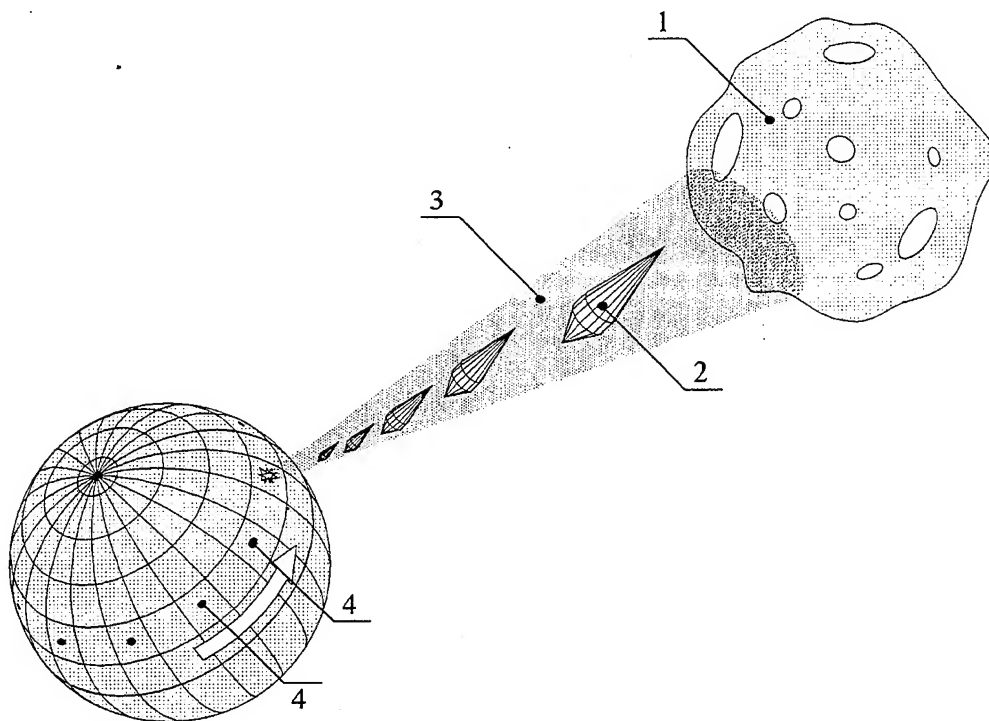


Fig. 1

1 - asteroid, 2 - BALSAD projectile, 3 - pointing beam, 4 - BALSAD launchers

Principles of BALSAD functioning

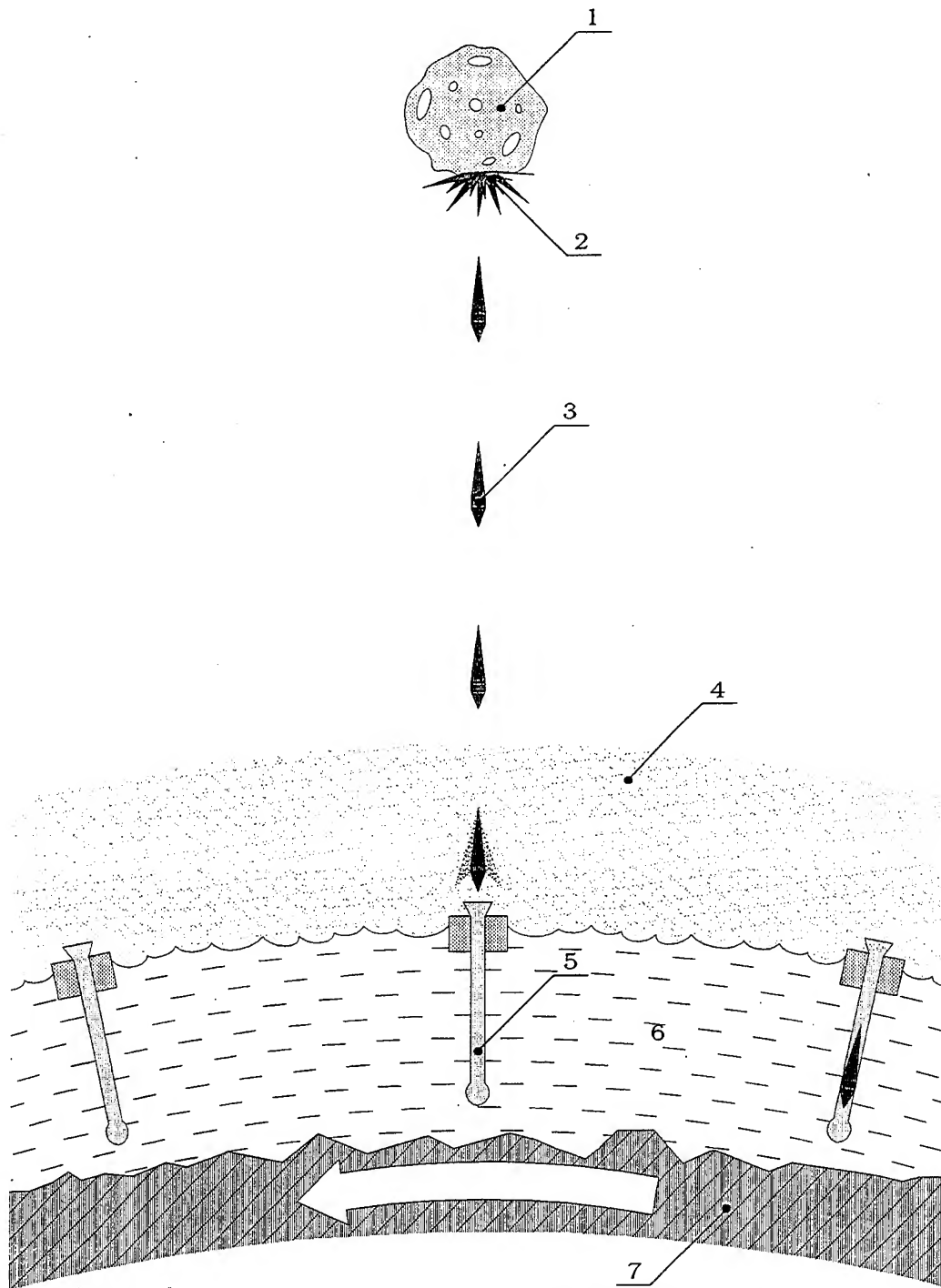


Fig. 2 1 - asteroid, 2 - thermonuclear detonation, 3 - BALSAD projectile, 4 - atmosphere, 5 - BALSAD launcher, 6 - ocean, 7 - Earth

Estimated Parameters of the Ballistic System for Antiasteroid Defence (BALSAD)

Radius of sphere for positioning of BALSAD projectiles.....	about 1M km
Total quantity of BALSAD projectiles	up to 10^5
Time for defense deployment.....	less than 3 months
Energetic capability of a single BALSAD projectile	up to 0.1MT TNT
Total energetic capability of the antiasteriod defense (ANASDEF) ...	up to 10 GT TNT
Type of projectile guidance to an asteroid	active
Usage of fission and radioactive materials in BALSAD projectiles	avoided
Total quantity of BALSAD launchers for ANASDEF deployment.....	up to 1000
Cost assessment to build ANASDEF	4÷5 billion USD

Figure 3

Ocean-based ballistic launcher

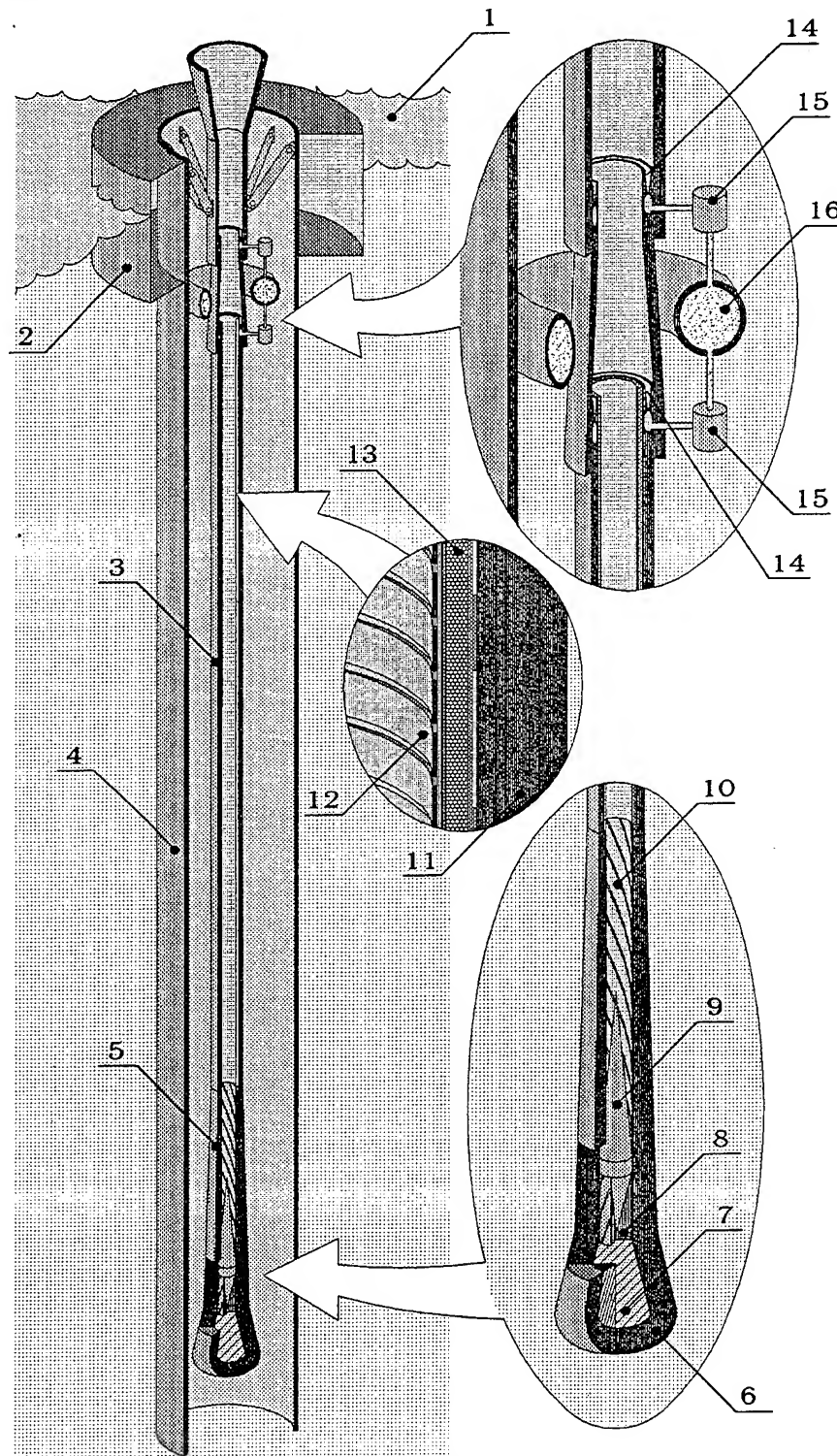


Fig. 4 1 - ocean surface, 2 - pontoon, 3 - gascumulative stage, 4 - outer casing, 5 - cannon powder stage, 6 - powder chamber, 7 - powder charge, 8 - sabot, 9 - projectile, 10 - rifled bore, 11 - launcher barrel, 12 - high explosive, 13 - deformable liner, 14 - ejector pump, 15 - pipe fitting, 16 - compressed air tank

Principles of the ballistic launcher

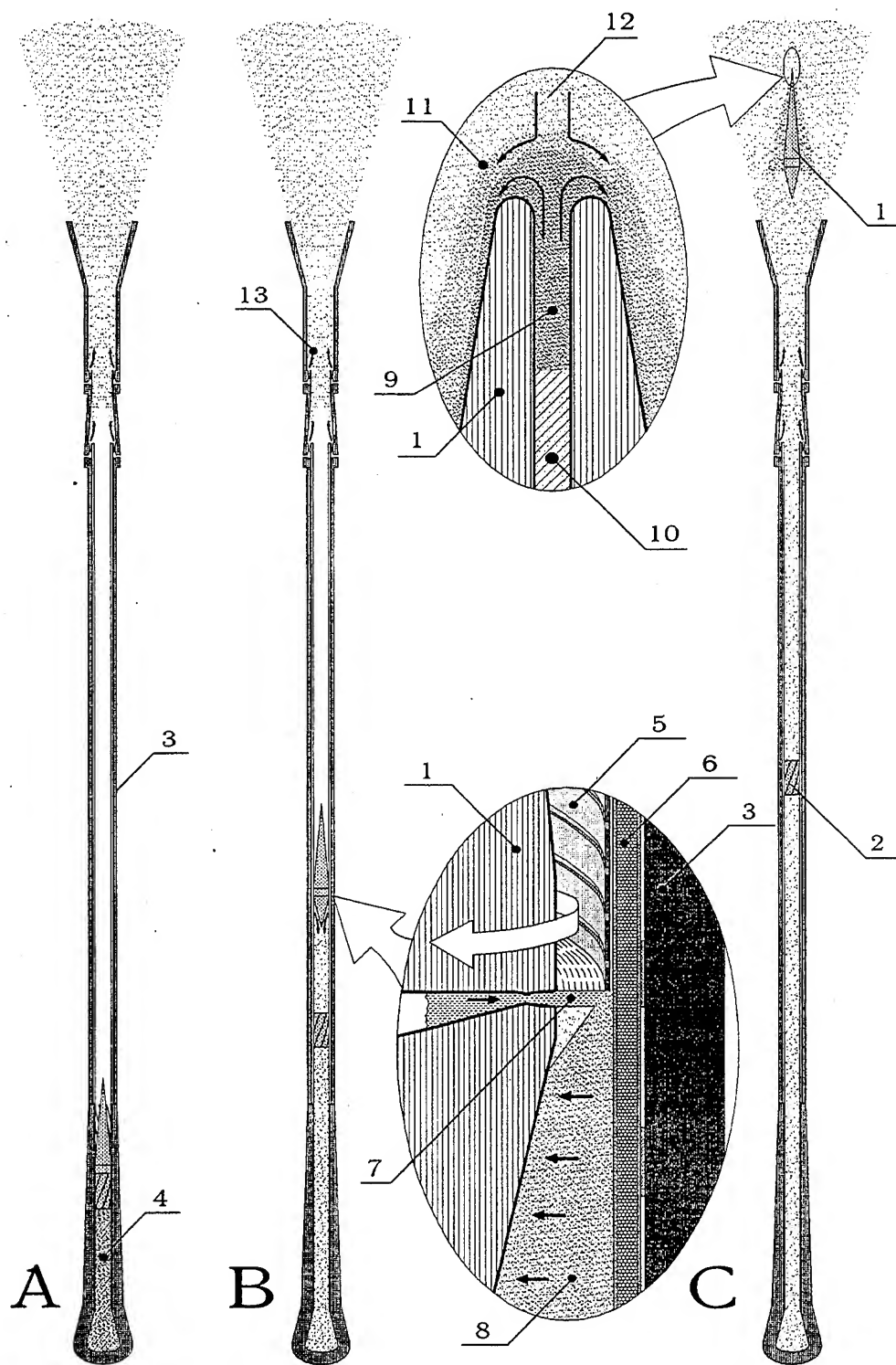


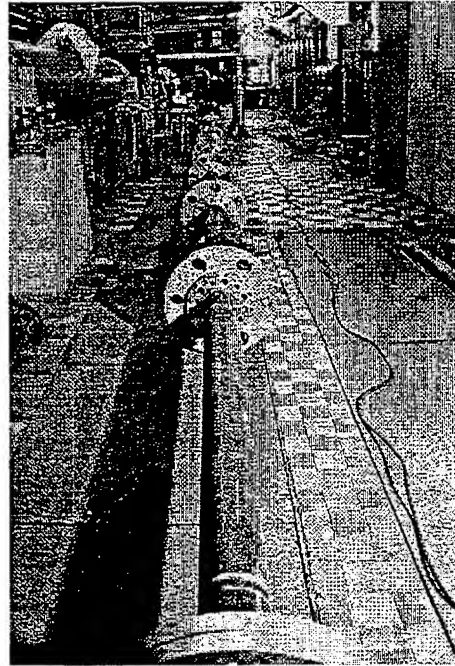
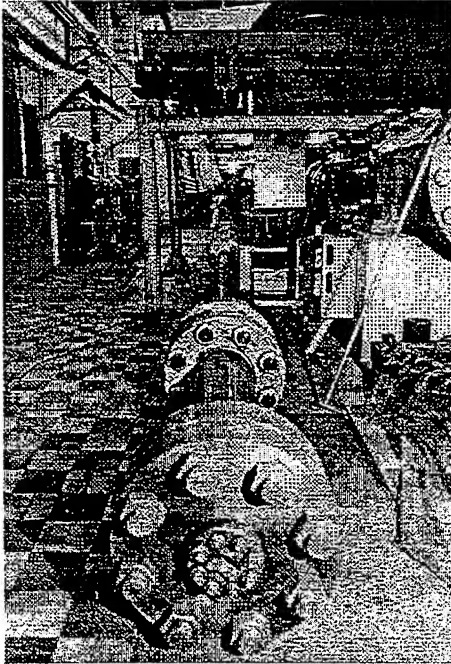
Fig. 5 A - cannon powder pre-boost B - gascumulative acceleration C - motion in atmosphere
 1 - projectile, 2 - sabot, 3 - launcher barrel, 4 - powder combustion products, 5 - high explosive,
 6 - deformable liner, 7 - liquid jet, 8 - explosion products, 9 - powder gas jet, 10 - cannon powder
 charge, 11 - shock wave, 12 - atmosphere, 13 - ejector pumping-out

Expected Parameters of the BALSAD Submersible Launcher for Injection of Projectiles into Outer Space

Shooting position	precisely vertical
Bore caliber.....	0.5 m
Preliminary evacuation of gas from the bore	0.1 torr
Launcher length.....	about 1000 m
Launcher weight	less than 4000 ton
Weight of distributed explosive charge.....	up to 50 ton
Weight of solid propellant charge	about 1 ton
Firing rate.....	1 shot per day
Launcher life cycle (with changeable bore) ..	10,000 shots
Assessed cost of the launcher.....	about 2M USD

Figure 6

100-mm ballistic gascumulative facility



Projectile

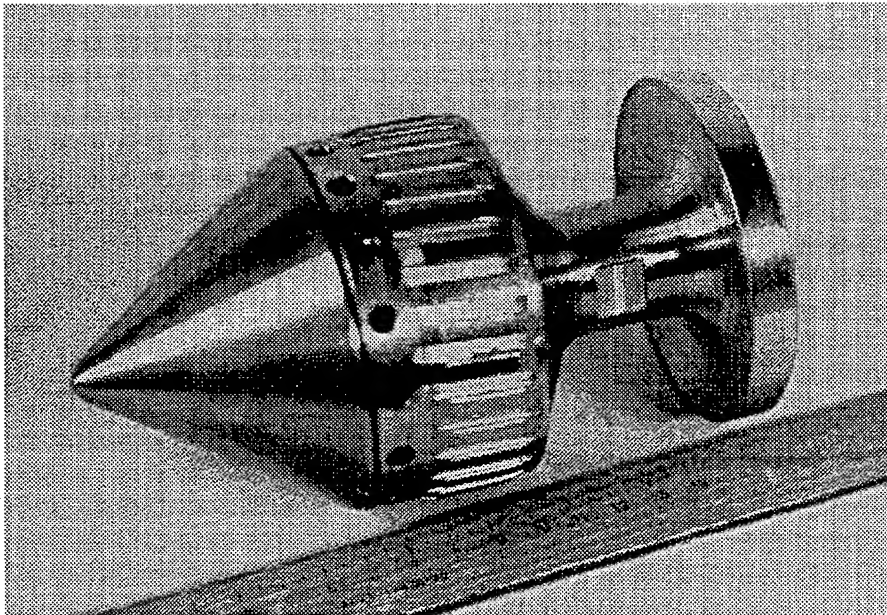


Figure 7

Projectile design

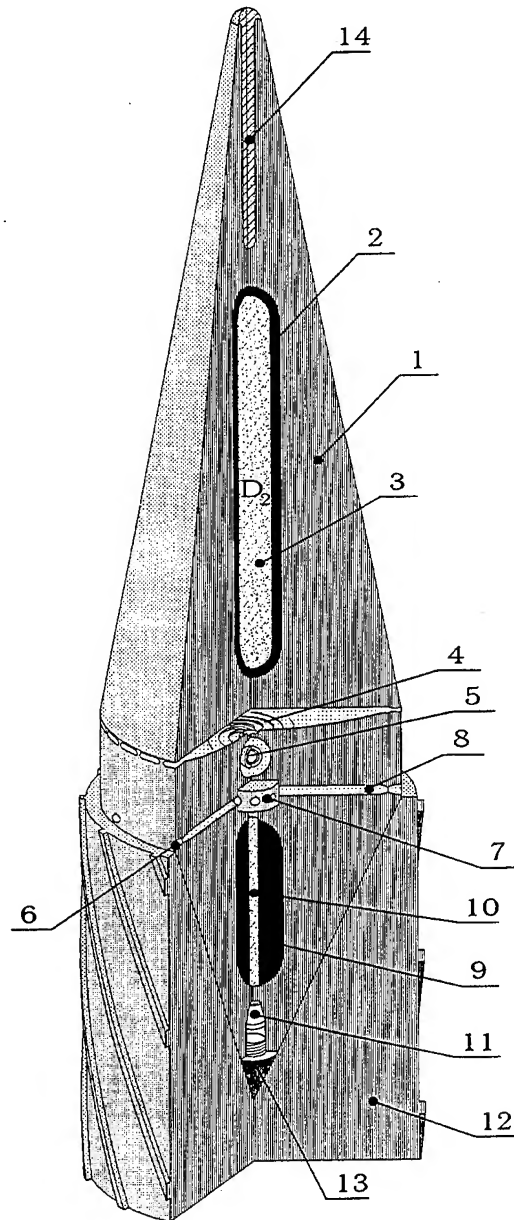
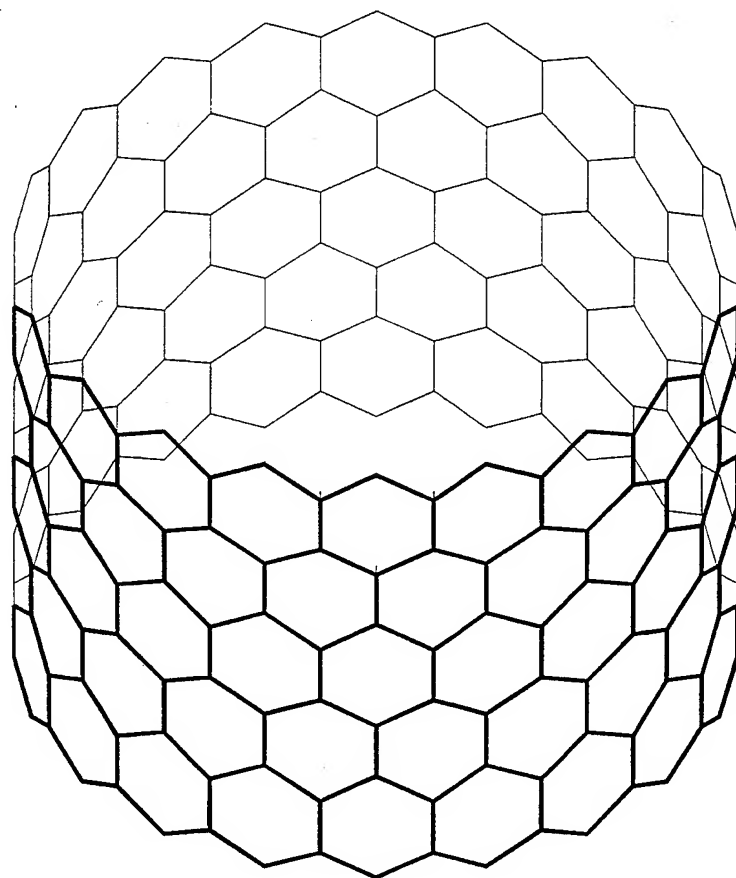


Figure 8

1 - projectile body, 2 - lead capsule, 3 - energy source, 4 - turbocumulative accelerator, 5 - spherical thermonuclear target, 6 - fluidblast nozzles, 7 - guidance valve assembly, 8 - accelerating conduit, 9 - consumable working liquid (mercury), 10 - working liquid vapor, 11 - laser beam reflector & sensor, 12 - sabot, 13 - protective screw, 14 - powder gasgenerator

Cylinder-Shaped Atomic Layer of Graphite Monocrystal



Utmost Rupture Stress
along the Atomic Layer . . . up to 20 GPa

Density. about 2260 kg/cu.m

Fig. 9

Estimated Parameters of Antiasteroid Defence Projectile

Projectile material. Cylindric lattice monocrystal graphite

Mass w/o sabot 300 kg

Muzzle velocity 13 km/s

Atmosphere escape velocity better than 11.5 km/s

Aerodynamic drag factor 0.01

Overload up to 10^4 g

Angular rate 2000 rps

Max normal velocity component
for maneuvers up to 1 km/s

Consumable mass for maneuvers 100 kg

Energy source density 4 ρ_{LD2}

$\rho \cdot d$ value at impact with asteroid ~ 30 g/cm²

Initiation temperature ~ 100 KeV

Energy of initiated event about 10 GJ

Type of projectile
guidance external, thru command channel

Fig. 10